



**Università  
degli Studi  
di Ferrara**

**DOCTORAL COURSE IN  
CHEMICAL SCIENCES**

CYCLE XXXIV

DIRECTOR Prof. Cavazzini Alberto

***CHARACTERIZATION OF NANOSTRUCTURED ADSORBENT MATERIALS FOR  
ENVIRONMENTAL APPLICATIONS***

Scientific/Disciplinary Sector (SDS) CHIM/01

**Candidate**

Dott. Stevanin Claudia

**Supervisor**

Prof. Pasti Luisa

**Co-Supervisor**

Prof. Cavazzini Alberto

2018/2021

# CONTENTS

<b>1 Introduction</b>	1
1.1 Aim of the work	2
<b>2 Contaminants of emerging concern</b>	4
2.1 Pharmaceuticals	5
2.1.1 Atenolol	6
2.1.2 Carbamazepine	7
2.1.3 Ketoprofen	8
2.1.4 Levofloxacin	8
2.1.5 Hydrochlorotiazide	9
2.1.6 Propranolol	10
2.1.7 Sulfamethoxazole	10
2.2 Perfluorinated alkyl compounds	11
2.2.1 PFOA & PFOS	12
2.3 Pesticides	13
2.3.1 Chlorobenzene	14
2.4 References	15
<b>3 Adsorbent materials</b>	18
3.1 Zeolites	18
3.1.1 Ag-zeolites	25
3.1.2 ZSM-5	27
3.1.3 BETA	28
3.1.4 Zeolite Y	30
3.2 Graphene	31
3.2.1 Carbon Nanostructured Advanced Material	32
3.3 Mixed matrix membranes	38
3.4 References	42

<b>4 Adsorption</b>	47
4.1 Adsorption isotherms	48
4.2 Adsorption kinetics	58
4.3 References	64
<b>5 Semiconductors and photocatalysis</b>	66
5.1 Band theory and electronic band structure of a solid	66
5.2 Electrochemistry of semiconductor electrolyte interface	70
5.3 Semiconductor-electrolyte interface under illumination	74
5.4 Photocatalysis	76
5.5 Photocatalysts based on heteropolytungstates	77
5.5.1 Decatungstate photocatalysis	78
5.5.2 Tungsten trioxide	80
5.6 Heterogeneous polyoxotungstates as photocatalysts	81
5.7 References	83
<b>6 Experimental</b>	85
6.1 Drugs adsorption on zeolites	85
6.2 Adsorption of chlorobenzene onto zeolites	107
6.3 Photodegradation of contaminants using semiconductor $W_{10}O_{32}^{2-}$	129
6.4 Water remediation using $\beta$ 25/ $WO_3$	150
6.5 Adsorption of PFAS onto Mixed matrix membranes	174
6.6 Comparison of the adsorption process between Y zeolites	182
6.7 Characterization and activity of Aqueous Extracts from <i>Asparagus officinalis</i> L. Byproducts	196
<b>7 Conclusions</b>	223
<b>8 Papers</b>	225

# 1 Introduction

The environmental pollution is growing on a massive and unprecedented scale, mainly due to the burning of fossil fuels and the release of materials and chemicals into the environment, especially contaminants of emerging concern (CECs), for which there is no established treatment strategy.

CECs is a term used to describe pollutants that have been detected in water bodies, that may cause harmful effects to the ecosystem or to human health, and typically are not regulated under current environmental laws.

The main groups of CECs reported are pharmaceuticals, personal care products, endocrine disruptors, surfactants, persistent organic contaminants (*i.e.* flame retardants and perfluorinated compounds), industrial additives and artificial sweeteners. These contaminants are difficult to be traced due to the need of specific detection methods, raising the question on how long these contaminants have been prevalent in the ecosystem and how the contamination process can be reversed or reduced.

The industrial development and other anthropogenic actions for better living conditions and lifestyle increased the release of contaminants to the environment, particularly to the soil and water bodies. For instance, the application of pesticides, the use of activated sludge contaminated with CECs and the reuse of domestic polluted wastewater for agriculture irrigation - to prevent water scarcity, are increasing the soil contamination. In the soil, contaminants can eventually be adsorbed, degraded by microorganisms and/or uptake by crops. On the other hand, drainage of contaminated soil or landfill leachates can contribute to the contamination of freshwater - both surface and groundwater. Consequently, sludge discharged from wastewater treatment plants, untreated sewage and ineffectively treated wastewater are some of the vectors affecting the quality and safety of water resources.

The potential impact on public health of selected CECs has been investigated typically in bacteria and fish. Effects such as reduced growth, increased antimicrobial resistance and altered behaviour were detected in bacteria present in the sediments of water bodies, where the levels of CECs are augmented. Additionally, some disruptive effects in the reproductive system were observed in fish and other aquatic organisms as well as the

potential to affect the immunological system and create imbalances in the host/pathogen interaction. Hence, effective strategies for CECs treatment are required. However, the conventional processes for wastewater treatment are not capable or efficient for what concerns CECs removal, due to their chemical structure and properties. For instance, chemical oxidation, adsorption with conventional adsorbent material, such as active carbon and ion-exchange resins, or biological methods are not effective for the removal of estrogens or androgens from wastewaters due to the stability of their chemical structure and low bioavailability.

### **1.1 Aim of the work**

The main objective of this work of thesis is to evaluate the efficiency of different adsorbent materials in the removal of some classes of contaminants from water matrix. The adsorption process was studied to determine both thermodynamics and kinetics properties of the adsorption process. The selected adsorbent materials employed in the present study differs from each other in structure and chemical composition. They can be categorised in two main classes: (i) silico aluminate synthetic microporous adsorbent (zeolites) and (ii) mixed matrix membranes carbon based (MMMs).

In particular, MMMs, that are composed by a continuous polymer phase and a dispersed inorganic filler have gained importance due to their fouling, permeate quality and longevity characteristics. In this work nanostructured carbon material has been included in several formulations of hydrogels which differ in hydrophilicity, cross-linking and swelling, and the contaminants adsorption efficiency of all the formulations had been determined and compared to the adsorption of powder nanostructured carbon.

Zeolites are classified according to the typology of the framework; every zeolite is characterised by regular channels and cavities systems with different dimensions. Moreover, the hydrophobic/hydrophilic behaviour of these materials is related to the silica/alumina ratio (SAR): the higher the content of  $Al_2O_3$  in the zeolite structure, the lower the SAR, a zeolite with a SAR lower than 5 is hydrophilic, whereas a zeolite with a SAR higher than 5 is hydrophobic.

In this work, zeolites with different framework typologies and SAR were selected to optimise the adsorption of the different contaminants considered.

This study includes a work on silver substituted zeolites; silver was introduced by wet impregnation (adsorption) on three Y zeolites and the obtained materials were characterised combining adsorption isotherms and X ray powder diffraction to determine the nature of the Ag<sup>+</sup> sites. In such a case adsorption has been used to generate a material with interesting characteristics that can be applicable in water remediation application because of its adsorption capacity and its antimicrobial and antifungal activity.

Furthermore, this thesis includes a study on advanced oxidation processes by photocatalysts for the degradation of pharmaceuticals in aqueous environment. The selected photocatalysts were: (i) sodium decatungstate (Na<sub>4</sub>W<sub>10</sub>O<sub>32</sub>) and (ii) tungsten trioxide (WO<sub>3</sub>). The common feature of all these materials is the ability to photoproduce .OH radicals, whose oxidation potential (E°=2.1 V vs NHE) allows for the oxidation of a variety of organic compounds leading, with sufficient time, to their mineralization. Photocatalytic degradation kinetics was evaluated, and by-products were investigated by HPLC/MS analysis.

The final part of this work of thesis includes a study on aqueous extracts derived from the non-edible portion of the asparagus plant (hard stem) which were prepared and characterized to investigate the chemical content. Furthermore, the biocompatibility and bioactivity of asparagus aqueous extracts were assessed in vitro on normal fibroblasts and on breast cancer cell lines.

This approach can be used as an investigation method applicable also to environmental pollutants and their derivatives, such as by-products and degradation intermediates, using different cell lines as bioindicators of water pollution.

## 2 Contaminants of emerging concern

Contaminants of emerging concern (CECs) may be defined as chemicals or materials found in the environment at trace concentrations with potential, perceived, or real risk to the animal and human health and to the environment. The industrial development and other anthropogenic actions for better living conditions and lifestyle increased the release of contaminants to the environment, particularly to the soil and water bodies. Aqueous environment pollution arising from a wide variety of the contaminants of emerging concerns (CECs) namely, endocrine-disrupting compounds, flame retardants, pharmaceuticals and personal care products, artificial sweeteners, pesticides, and their metabolites is an issue of major concern[1], [2]. It is well known that CECs have a negative impact especially on aqueous ecosystems and human health[3]. The frequent detection of various CECs in wastewater treatment plant (WWTP) effluents reveals that CECs are susceptible to poor removal during conventional waste-water treatment processes.

Therefore, WWTPs are source of inductive release of CECs into the environment [2], [4]. The discharge of poor effluent treatment by WWTPs contributes to river, groundwater, watershed contamination, and ultimately drinking water.

This wide range of contaminants is characterized by different chemical-physical properties, in Figure 2.1, these compounds are divided up on the basis of polarity and volatility.

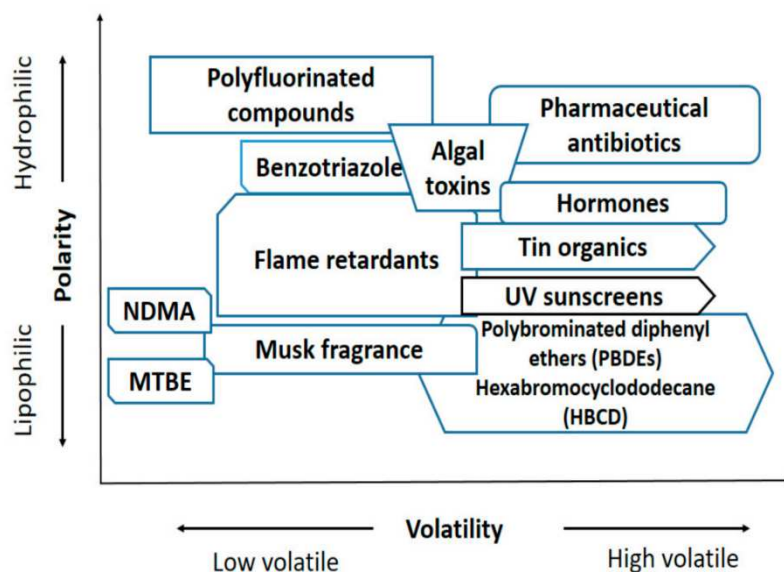


Fig 2.1 Emerging pollutants volatility and polarity[2]

Water treatment technologies, such as activated carbon and reverse osmosis membranes, have been commonly applied for the removal of CECs. Alternatively, advanced oxidation processes (AOP) have been introduced as suitable techniques for the elimination of organic contaminants because they are among the most practical technologies to improve biodegradation and detoxification of WWTP effluent waste[5].

## **2.1 Pharmaceuticals**

The increase in the human life expectancy coupled with the rise in population is expected to increase the use of pharmaceuticals[6], [7] and thus, intensify the presence of antibiotics, analgesics, anti-inflammatory, antihistaminic, antiepileptic and other type of drugs in aquatic environments. This contributes to the increase in the ecotoxicology of lakes and rivers that can be harmful to aquatic organisms [8]. Additionally, the presence of pharmaceuticals can lead to the development of antibiotic resistance genes potentially causing antibiotic-resistant bacteria or so-called superbugs.

For these motives pharmaceuticals can be classified as Contaminants of emerging concern (CEC), in fact are commonly found in urban and industrial wastewater are a potential threat to human health and have negative environmental impact.

Pharmaceuticals are present in the environment as a consequence of pharmaceutical production and formulation, patient use, use in food production and improper disposal. After passing through the human or animal body, active pharmaceutical ingredients are excreted either in an unchanged active form or as metabolites, which may be active or inactive, and have the potential for further breakdown into numerous transformation products in WWTPs or in the environment. Pharmaceuticals can disperse through the environment via multiple pathways as illustrated in Figure 2.2. The presence of pharmaceuticals in freshwater and terrestrial ecosystems can result in the uptake of pharmaceuticals into wildlife and have the potential to bioaccumulate[9]. Humans can subsequently be exposed through drinking water, and ingestion of pharmaceutical residues in plant crops, fish, dairy products, and meat.



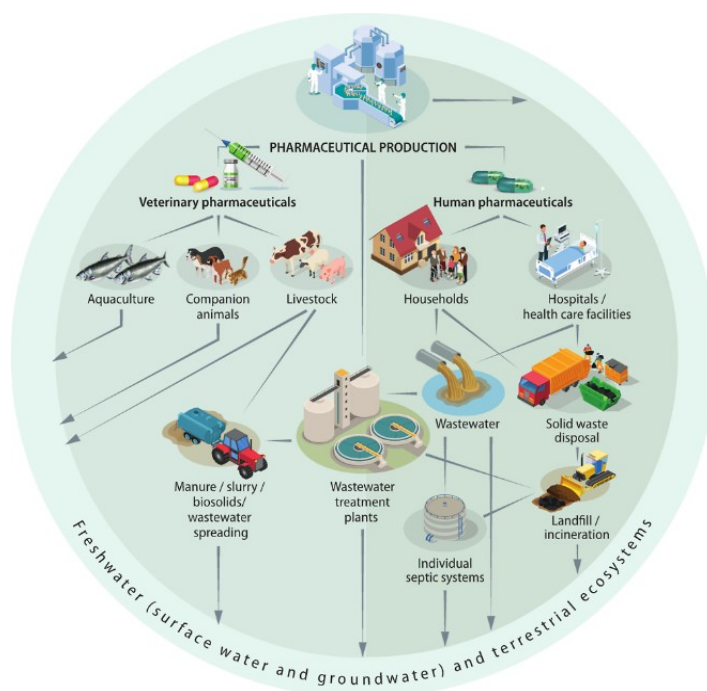


Fig 2.2 Origins, entry-pathways of pharmaceuticals in the environment

Most WWTPs cannot efficiently remove these compounds and therefore, many pharmaceuticals end up in aquatic ecosystems, inducing problems such as toxicity and antibiotic-resistance.

In this work, the interaction between different contaminants belonging to the above-mentioned classes and different mesoporous and microporous materials was systematically investigated by considering the effect of surrounding pH, ionic strength, and thus chemical state of compounds, to evaluate the role of hydrophobic and electrostatic forces in the interaction between the selected molecule and the adsorbent. In the following some characteristics of the studied compounds are reported.

### 2.1.1 Atenolol (ATN)

Atenolol is a selective  $\beta_1$  receptor antagonist, a drug belonging to the group of beta blockers ( $\beta$ -blockers), a class of drugs used primarily in cardiovascular diseases. Introduced in 1976, atenolol was developed as a replacement for propranolol in the treatment of hypertension. Unlike propranolol, atenolol does not pass through the blood–brain barrier thus avoiding various central nervous system side effects. Atenolol is used for several conditions including hypertension, angina, acute myocardial infarction, supraventricular tachycardia, ventricular tachycardia, and the symptoms of

alcohol withdrawal. Its structure shows three donor sites of hydrogen bonds and four hydrogen bond acceptor sites.

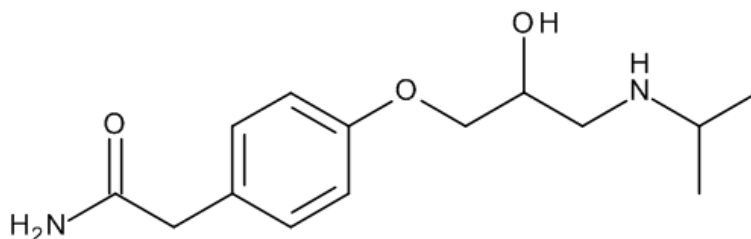


Fig 2.3 Atenolol

### 2.1.2 Carbamazepine (CBZ)

Carbamazepine is one of the oldest antiepileptic drugs, discovered by Walter Schindler in 1953, and is still commonly used in first-line therapy of partial, generalized tonic-clonic, and mixed seizure patterns [10]. It is also approved for use in the treatment of bipolar disorders, post-traumatic stress disorders, schizophrenia, neuropathic pain, and trigeminal neuralgia. The pharmacokinetic profile of carbamazepine is complex and variable. Carbamazepine is largely metabolized in the liver by CYP3A4 to its active and potentially toxic metabolite, carbamazepine-10,11-epoxide (CBZE). Following an acute dose, the initial elimination half-life is 25–65 hours, decreasing to 4–17 hours with repeated doses [11]. Common side effects of carbamazepine include nausea, vomiting, dry mouth, hyponatremia, fatigue, tremor, and dizziness. Rare serious adverse effects of carbamazepine and CBZE include toxic epidermal necrolysis, Stevens-Johnson syndrome, aplastic anemia, and agranulocytosis. Other reactions to carbamazepine may include hepatotoxicity, pancreatitis, vitamin D metabolism disturbances. Serum levels of the free fraction of carbamazepine show significant intra- and inter-individual variability. It is affected by many factors such as the presence of other diseases, drug interactions, age, pregnancy, race, and non-compliance.

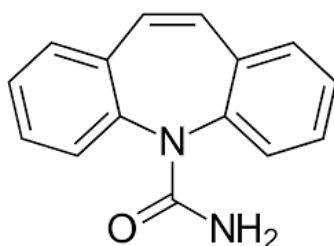


Fig 2.4 Carbamazepine

### 2.1.3 Ketoprofen (KTP)

Ketoprofen, (RS)2-(3-benzoylphenyl)-propionic acid, is one of the propionic acid classes of Non-Steroidal Anti-Inflammatory Drugs (NSAID) with analgesic and antipyretic effects. It acts by inhibiting the body's production of prostaglandin. The main mechanism of action of the drug is due to the inhibition of cyclo-oxygenase leading to block the synthesis of prostaglandins responsible for inflammation and tissue damage. The drug is light sensitive, so it is necessary to avoid exposure to direct sunlight: in some cases, in fact, there has been the emergence of photo-allergic and photo-toxicity. KTP is also employed as antipyretic and analgesic in veterinary field. Recent studies have found KTP, like diclofenac, causing lethal effects in red-headed vultures: vultures feeding on the carcasses of recently treated livestock suffer acute kidney failure within days of exposure. There is a chiral center in the carbon  $\alpha$  to the carbonyl. Furthermore, it presents a site donor and acceptor sites of three hydrogen bonds.

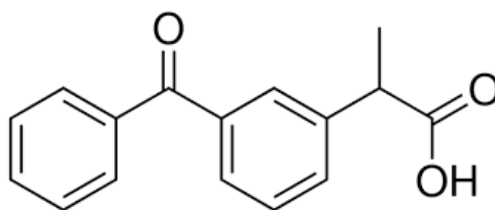


Fig 2.5 Ketoprofen

### 2.1.4 Levofloxacin (LEVO)

Levofloxacin is a third-generation fluoroquinolones antibiotic which is widely applied in human and animal patients for the treatment of bacterial infections, pneumonia and immunodeficiency virus. However, the overuse of levofloxacin not only causes antimicrobial resistance but leaves drug residues which adversely affect human health. LEVO, sold under the brand name Levaquin among others, is an antibiotic medication. It is used to treat several bacterial infections including acute bacterial sinusitis, pneumonia, urinary tract infections, chronic prostatitis, and some types of gastroenteritis. Along with other antibiotics it may be used to treat tuberculosis, meningitis, or pelvic inflammatory disease. Use is generally recommended only when other options are not available. It is available by mouth, intravenously, and in eye drop form.

Common side effects include nausea, diarrhea, and trouble sleeping. Serious side effects may include tendon rupture, tendon inflammation, seizures, psychosis, and potentially permanent peripheral nerve damage.

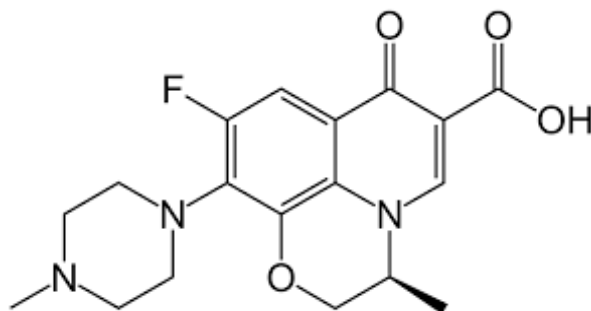


Fig 2.6 Levofloxacin

### 2.1.5 Hydrochlorothiazide (HTC)

Hydrochlorothiazide is a diuretic drug of the thiazide class that acts by inhibiting the kidneys' ability to retain water. This reduces the volume of the blood, decreasing blood return to the heart and thus cardiac output and, by other mechanisms, is believed to lower peripheral vascular resistance. HTC is frequently used for the treatment of hypertension, congestive heart failure, symptomatic edema, diabetes insipidus, renal tubular acidosis and the prevention of kidney stones. Thiazides are also used in the treatment of osteoporosis. Thiazides decrease mineral bone loss by promoting calcium retention in the kidney, and by directly stimulating osteoblast differentiation and bone mineral formation. Five centers' acceptors of hydrogen bonds and three centers donors of hydrogen bonds are present.

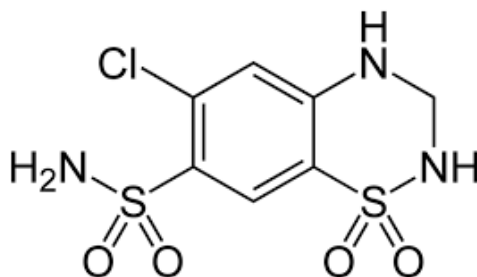


Fig 2.7 Hydrochlorothiazide

### 2.1.6 Propranolol (PRP)

Propranolol is a medication of the beta blocker class. It is used to treat high blood pressure, a number of types of irregular heart rate, thyrotoxicosis, capillary hemangiomas, performance anxiety, and essential tremors, as well to prevent migraine headaches, and to prevent further heart problems in those with angina or previous heart attacks.

The formulation that is taken by mouth comes in short-acting and long-acting versions. Propranolol appears in the blood after 30 minutes and has a maximum effect between 60 and 90 minutes when taken by mouth. Common side effects include nausea, abdominal pain, and constipation. It is a non-selective beta blocker which works by blocking  $\beta$ -adrenergic receptors.

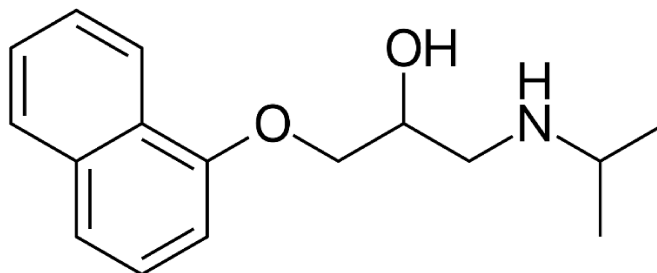


Figure 2.8 Propranolol

### 2.1.7 Sulfamethoxazole (SMX)

Sulfamethoxazole (SMZ or SMX) is an antibiotic. It is used for bacterial infections such as urinary tract infections, bronchitis, and prostatitis and is effective against both gram negative and positive bacteria such as *Listeria monocytogenes* and *E. coli*.

Common side effects include nausea, vomiting, loss of appetite, and skin rashes. It is a sulfonamide and bacteriostatic. It resembles a component of folic acid. It prevents folic acid synthesis in the bacteria that must synthesize their own folic acid. Mammalian cells, and some bacteria, do not synthesize but require preformed folic acid (vitamin B9); they are therefore insensitive to sulfamethoxazole.

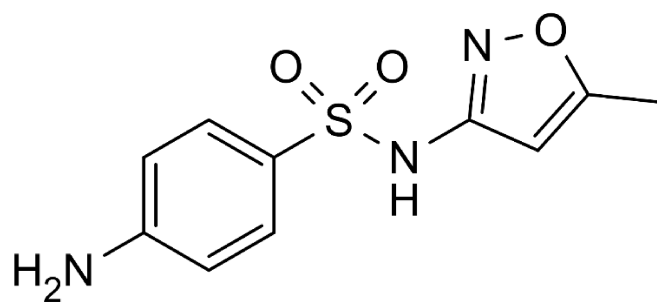


Figure 2.9 Sulfamethoxazole

## 2.2 Perfluorinated alkyl compounds

Concern about fluorinated organic compounds, especially perfluorinated (fully fluorinated) compounds, is increasing. Perfluoroalkyl substances (PFAS) are a group of synthetic, persistent chemicals with broad applications in many industrial and consumer products. Due to the strong electronegativity and small atomic size of fluorine, PFAS have high surface activity, stability, and water- and oil-repellency. Alkyl perfluorinated compounds (PFCs) belong to the category of emerging contaminants: these molecules have received increasing attention as environmental contaminants in recent years due to their consistent detection in various environmental matrices [12] and their negative effects in animal toxicity studies [13], [14]. The two groups most examined so far have been perfluoroalkylsulfonates (PFSA) and perfluorocarboxylic acids (PFCA) and the most representative compounds of these groups are perfluorooctane sulfonate (PFOS) and perfluorooctanoic acid (PFOA).

These compounds have been produced commercially since the 1950s and used in a variety of industrial and consumer applications, including oil and water repellent surface coatings for packaging and textiles, surfactants and aqueous firefighting foams [15]. In 2009, PFOS was added to the Stockholm Convention on Persistent Organic Pollutants [16].

Production of PFOS and similar perfluorooctyl products was phased out in the United States and Europe in 2000-2002, however production continues elsewhere. PFOA and its salts continue to be used as processing agents in fluoropolymer manufacturing, but efforts have been made to reduce emissions from fluoropolymer manufacturing plants.

PFOS and PFOA have been detected in surface, marine, groundwater and even tap waters around the world [17]: industrial and municipal wastewater treatment plants are the main sources of PFOS and PFOA entering natural waters [18] because these compounds are inefficiently removed from primary and secondary wastewater treatment [19]. Various concentrations of PFOS and PFOA at the ng / L and µg / L levels have been observed in the tributaries and effluents of wastewater treatment plants.

Long chain PFCs ( $\geq 7$  perfluorinated carbons) are persistent organic pollutants that cannot be hydrolyzed, directly photolysed or biodegraded under environmental conditions. PFCs have been found in fish, birds and mammals from mid-latitudes to the poles. PFCs have relatively high solubility in water (i.e. 9.5 g / L for PFOA and 0.26 g / L for perfluorododecanoic acid PFDA) and low volatility and absorption potentials.

The selected alkyl perfluorinated compounds are PFOS and PFOA because, unlike other PFCs, they are highly soluble in water and therefore easily transportable in an aquatic environment. At the same time, the hydrophobic chain and hydrophilic functional groups can provide opportunities for the absorption of PFOA and PFOS on the surfaces of a variety of environmental solid matrices.

### **2.2.1 PFOA & PFOS**

PFOA is a synthetic chemical that does not occur naturally in the environment. In 1951, the American chemical company DuPont started using PFOA in the manufacturing of fluoropolymers, substances which impart fire resistance and oil, stain, grease and water repellency. They provide non-stick surfaces on cookware and waterproof, breathable membranes for clothing, and are used in many industry segments, such as aerospace, automotive, building/construction, chemical processing, electronics, semiconductors and textile industries.

PFOS is a fluorinated surfactant that lowers the surface tension of water more than normal hydrocarbon surfactants. The C<sub>8</sub>F<sub>17</sub> chain is hydrophobic, while the sulfonic acid/sulfonate group confers polarity to the molecule.

By virtue of the nature and strength of the carbon-fluorine bond, PFOS is a compound of exceptional stability both for industrial applications and in the environment, in which

it persists and bioaccumulates. Attention is usually focused on the linear chain isomer (n-PFOS) illustrated in Figure 2.10, which is the dominant species in commercial products and environmental samples, but there are numerous linear or branched congeners that have different physical, chemical properties and toxicological.

In 1999 the United States Environmental Protection Agency (US-EPA) began investigating perfluorinated chemicals, founding that PFOA and PFOS are very persistent in the environment and causes adverse effects in laboratory animals [US-EPA PFOA]: for these reasons, in 2000 PFOA, PFOS and related products production was phased-out.

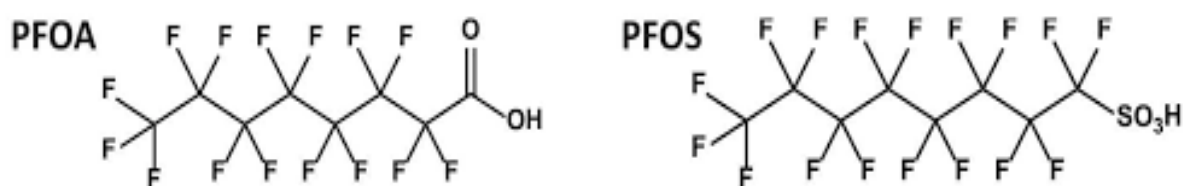


Fig 2.10 PFOA and PFOS structures

## 2.3 Pesticides

Pesticides are chemical substances intended for preventing, destroying, repelling and mitigating any pest, although they can also be used as a plant regulator, defoliant or desiccant. The widespread use of thousands of tons of these compounds in domestic, industrial and agricultural activities throughout the world, especially in developed countries, generates large volumes of contaminated waste waters, whose direct disposal into natural channels causes their accumulation in the environment [20]. Therefore, it is necessary to control the emission sources, to reduce the transfer of pesticides into the environment and to treat contaminated media using biological processes, filtration, coagulation, adsorption, membrane processes, chemical oxidation, etc.

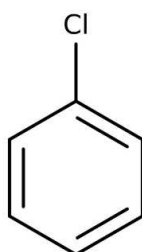
People are exposed to these chemicals from a variety of sources, with various exposure levels. Direct, generally high exposure occurs in occupational, agricultural, or residential settings when pesticides are applied, mixed by hand, loaded from one place to another, when seeds with pesticides are handled, and when pesticide containers are cleaned. Indirect, generally chronic low-level exposure occurs through residues in food, drinking



water, air, and soil. In contrast to these occupational exposures, nonoccupational exposure to pesticides occurs primarily via diet [21]. Pesticide exposure has profound effects on human health, including increased risk of cancer, diabetes, genetic disorders, and neurotoxicity [22], [23]. Although it is established that neurotoxicity can result from high-level exposure to most types of pesticides, the neurotoxic effects of chronic exposure to moderate levels has been a matter of controversy.<sup>6</sup> Robust animal data and large prospective epidemiological studies provide evidence for the neurotoxic properties of pesticides such as organophosphate and organochlorine pesticides, both through interfering with the functioning of the brain and damaging the developing brain [24].

### 2.3.1 Chlorobenzene (CB)

The major use of chlorobenzene is as an intermediate in the production of commodities such as herbicides, dyestuffs, and rubber. CB is produced by chlorination of benzene in the presence of a Lewis acid catalyst such as ferric chloride, sulfur dichloride and anhydrous aluminium chloride. It was used in the past to produce chemicals such as phenol and DDT, formerly on a large scale, but their production from chlorobenzene has been almost entirely discontinued due to the development of new processes and legislation forbidding the use of DDT [25]. Nowadays, CB is mainly used as a solvent for pesticide formulations, as a degreaser, and to produce other chemicals. Chlorobenzene is also used as a high-boiling solvent in many industrial applications as well as in the laboratory. Chlorobenzene can enter the environment from different sources including industrial and agricultural discharges, drinking water and wastewater chlorine disinfection by-products and incineration wastes.



*Fig 2.11 Chlorobenzene*

## 2.4 References

- [1] S. D. Richardson and S. Y. Kimura, "Water Analysis: Emerging Contaminants and Current Issues," *Analytical Chemistry*, vol. 88, no. 1. American Chemical Society, pp. 546–582, Jan. 05, 2016. doi: 10.1021/acs.analchem.5b04493.
- [2] I. C. Vasilachi, D. M. Asiminesei, D. I. Fertu, and M. Gavrilescu, "Occurrence and fate of emerging pollutants in water environment and options for their removal," *Water (Switzerland)*, vol. 13, no. 2. MDPI AG, Jan. 02, 2021. doi: 10.3390/w13020181.
- [3] D. M. dos Santos *et al.*, "Multiresidue determination and predicted risk assessment of contaminants of emerging concern in marine sediments from the vicinities of submarine sewage outfalls," *Marine Pollution Bulletin*, vol. 129, no. 1, pp. 299–307, Apr. 2018, doi: 10.1016/j.marpolbul.2018.02.048.
- [4] B. D. Blair, J. P. Crago, C. J. Hedman, and R. D. Klaper, "Pharmaceuticals and personal care products found in the Great Lakes above concentrations of environmental concern," *Chemosphere*, vol. 93, no. 9, pp. 2116–2123, 2013, doi: 10.1016/j.chemosphere.2013.07.057.
- [5] M. Salimi *et al.*, "Contaminants of emerging concern: a review of new approach in AOP technologies," *Environmental Monitoring and Assessment*, vol. 189, no. 8, Aug. 2017, doi: 10.1007/s10661-017-6097-x.
- [6] D. G. J. Larsson, "Pollution from drug manufacturing: Review and perspectives," *Philosophical Transactions of the Royal Society B: Biological Sciences*, vol. 369, no. 1656. Royal Society of London, Nov. 19, 2014. doi: 10.1098/rstb.2013.0571.
- [7] P. Verlicchi, M. al Aukidy, and E. Zambello, "Occurrence of pharmaceutical compounds in urban wastewater: Removal, mass load and environmental risk after a secondary treatment-A review," *Science of the Total Environment*, vol. 429, pp. 123–155, Jul. 01, 2012. doi: 10.1016/j.scitotenv.2012.04.028.
- [8] P. Verlicchi, A. Galletti, M. Petrovic, and D. Barceló, "Hospital effluents as a source of emerging pollutants: An overview of micropollutants and sustainable treatment options," *Journal of Hydrology*, vol. 389, no. 3–4. pp. 416–428, Aug. 2010. doi: 10.1016/j.jhydrol.2010.06.005.
- [9] K. E. Arnold, A. R. Brown, A. R. Brown, G. T. Ankley, and J. P. Sumpter, "Medicating the environment: Assessing risks of pharmaceuticals to wildlife and ecosystems," *Philosophical Transactions of the Royal Society B: Biological Sciences*, vol. 369, no. 1656, Nov. 2014, doi: 10.1098/rstb.2013.0569.
- [10] A. Wahab, "Difficulties in treatment and management of epilepsy and challenges in new drug development," *Pharmaceuticals*, vol. 3, no. 7. MDPI AG, pp. 2090–2110, 2010. doi: 10.3390/ph3072090.

- [11] J. L. Russell, H. A. Spiller, and D. D. Baker, "Markedly elevated carbamazepine-10,11-epoxide/carbamazepine ratio in a fatal carbamazepine ingestion," *Case Reports in Medicine*, vol. 2015, 2015, doi: 10.1155/2015/369707.
- [12] K. Kannan *et al.*, "Concentrations of perfluorinated acids in livers of birds from Japan and Korea." [Online]. Available: [www.elsevier.com/locate/chemosphere](http://www.elsevier.com/locate/chemosphere)
- [13] M. E. Andersen *et al.*, "Perfluoroalkyl acids and related chemistries - Toxicokinetics and modes of action," *Toxicological Sciences*, vol. 102, no. 1. pp. 3–14, Mar. 2008. doi: 10.1093/toxsci/kfm270.
- [14] R. Grønnestad *et al.*, "Effects of an environmentally relevant PFAS mixture on dopamine and steroid hormone levels in exposed mice," *Toxicology and Applied Pharmacology*, vol. 428, Oct. 2021, doi: 10.1016/j.taap.2021.115670.
- [15] R. C. Buck *et al.*, "Perfluoroalkyl and polyfluoroalkyl substances in the environment: Terminology, classification, and origins," *Integrated Environmental Assessment and Management*, vol. 7, no. 4, pp. 513–541, Oct. 2011, doi: 10.1002/ieam.258.
- [16] "Stockholm Convention on Persistent Organic Pollutants (POPs)."
- [17] C. Kunacheva *et al.*, "Worldwide surveys of perfluorooctane sulfonate (PFOS) and perfluorooctanoic acid (PFOA) in water environment in recent years," *Water Science and Technology*, vol. 66, no. 12, pp. 2764–2771, 2012, doi: 10.2166/wst.2012.518.
- [18] K. Prevedouros, I. T. Cousins, R. C. Buck, and S. H. Korzeniowski, "Sources, fate and transport of perfluorocarboxylates," *Environmental Science and Technology*, vol. 40, no. 1. pp. 32–44, Jan. 01, 2006. doi: 10.1021/es0512475.
- [19] B. G. Loganathan, K. S. Sajwan, E. Sinclair, K. Senthil Kumar, and K. Kannan, "Perfluoroalkyl sulfonates and perfluorocarboxylates in two wastewater treatment facilities in Kentucky and Georgia," *Water Research*, vol. 41, no. 20, pp. 4611–4620, 2007, doi: 10.1016/j.watres.2007.06.045.
- [20] A. Ouni *et al.*, "Removal of pesticide chlorobenzene by anodic degradation: Variable effects and mechanism," *Journal of Saudi Chemical Society*, vol. 25, no. 10, p. 101326, Oct. 2021, doi: 10.1016/j.jscs.2021.101326.
- [21] S. A. Korrick and S. K. Sagiv, "Polychlorinated biphenyls, organochlorine pesticides and neurodevelopment," *Current Opinion in Pediatrics*, vol. 20, no. 2. pp. 198–204, Apr. 2008. doi: 10.1097/MOP.0b013e3282f6a4e9.
- [22] P. Grandjean and P. J. Landrigan, "Developmental neurotoxicity of industrial chemicals," *www.thelancet.com*, doi: 10.1016/S0140.
- [23] S. Weichenthal, C. Moase, and P. Chan, "A review of pesticide exposure and cancer incidence in the agricultural health study cohort," *Environmental Health Perspectives*, vol. 118, no. 8. pp. 1117–1125, 2010. doi: 10.1289/ehp.0901731.

- [24] A. Miodovnik, "Environmental neurotoxicants and developing brain," *Mount Sinai Journal of Medicine*, vol. 78, no. 1, pp. 58–77, Jan. 2011, doi: 10.1002/msj.20237.
- [25] M. Rossberg *et al.*, "Chlorinated Hydrocarbons", doi: 10.1002/14356007.a06.

### 3 Adsorbent materials

Micro- and mesoporous materials are solids characterised by the presence of pores with diameters lower than 2 nm for microporous materials, and between 2 and 50 nm for mesoporous materials. Ordered micro- and mesoporous materials are used in many applications as catalysts, highly selective adsorbent, but also, they can be modified to create materials with additional functionality [1]. Zeolites are a class of microporous materials, widely found in nature, whose characteristics allow their use in many industrial applications. Another very common mesoporous material is activated carbon which is typically composed of a carbon framework with both mesoporosity and microporosity depending on the conditions under which it was synthesized. However, the flagship of mesoporous materials is mesoporous carbon, which has direct applications in energy storage devices. Mesoporous carbon has porosity within the mesopore range and this significantly increases the specific surface area.

#### 3.1 Zeolites

Among silicates, zeolites represent a wide class of porous materials counting more than forty natural species, plus a much larger number of synthetic types. Zeolites were discovered in 1756 by the Swedish mineralogist A. F. Cronstedt who observed that after heating rapidly the mineral, it produced large amounts of steam from water adsorbed on the material, so he coined the term zeolite from the Greek ζέω (zéō), meaning "to boil" and λίθος (líthos), meaning "stone".

Zeolites are crystalline aluminosilicate microporous materials with chemical formula  $\text{Na}_{12}[(\text{SiO}_2)_{12}(\text{AlO}_2)_{12}] \cdot 27\text{H}_2\text{O}$ ; the three-dimensional structure is formed by tetrahedral units  $\text{TO}_4$  called primary building units (PBU) composed of  $[\text{SiO}_4]^{4-}$  and  $[\text{AlO}_4]^{5-}$  units connected to each other through oxygen atoms (fig. 3.1).

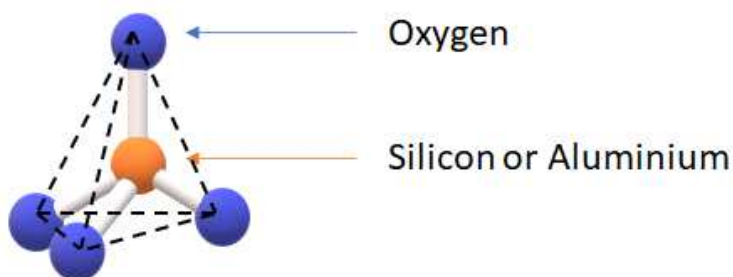
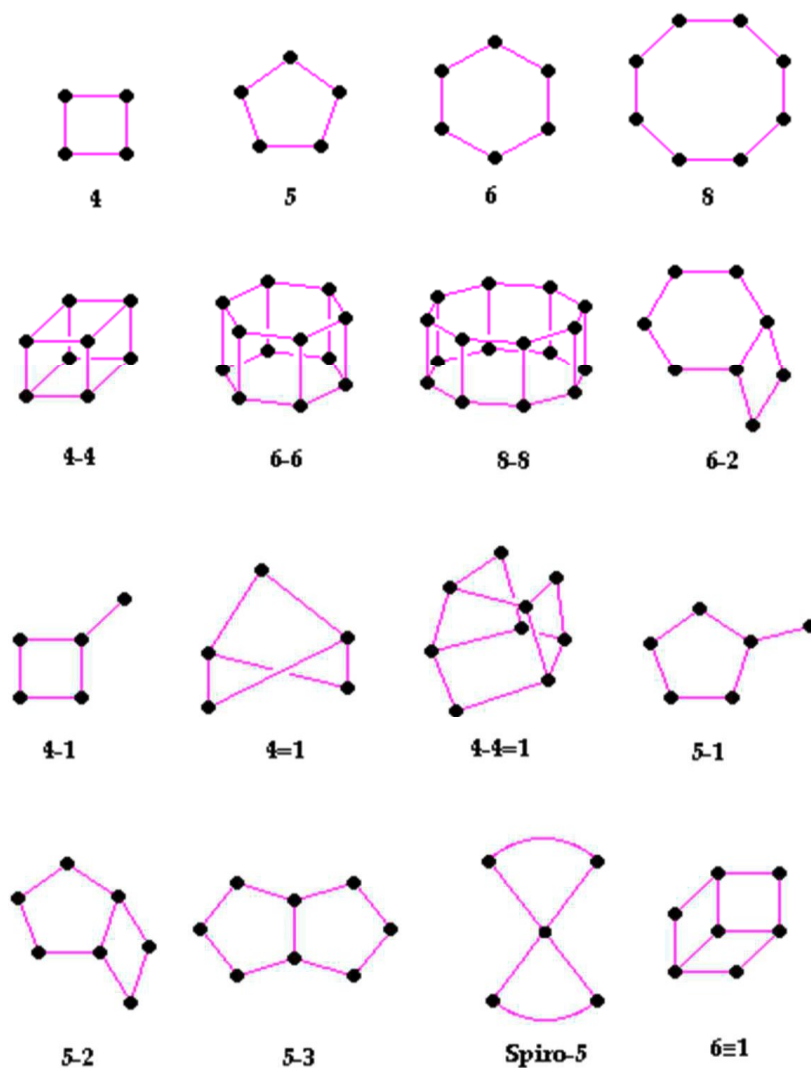


Figure 3.1 TO<sub>4</sub> unit

The combination of  $TO_4$  units leads to the formation of different more complex structural blocks known as secondary building units (SBU). SBUs are the simplest units in which a single zeolite structure can be decomposed, there are 23 different SBU's observed which can contain up to 16 T-atoms [2]. The main SBU's are represented in figure 3.2.



**Figure 3.2** Secondary Building Units (SBU).

When secondary building units are combined, they create complex frameworks with different structures containing regular cavities and channels with molecular dimensions. Due to the wide range of structure typologies found in zeolites, these materials are classified by the “structure commission” of the International Zeolite

Association according to their crystalline structure and divided into structure types indicated by a three letters code (e.g., MFI).

In zeolites, the ratio of silicon and aluminium can vary, due to the fact that Al-O-Al bonds are not possible and only Si-O-Si or Si-O-Al bonds are allowed; according to the Si/Al ratio (SAR) zeolites can be divided into two classes:

- Zeolites with a low Si/Al (SAR < 5)
- Zeolites with a high Si/Al (SAR > 5)

A higher amount of aluminium in the structure gives to the zeolite framework a more negative overall charge giving to the material hydrophilic properties, on the other hand, zeolites with higher silicon content show hydrophobic behaviour.

### Properties

Zeolites belongs to a particular category of microporous materials known as molecular sieves, this classification is due to the characteristic of zeolites of having uniform cavities and channels interconnected with each other and with dimensions from 3 to 10 Å that results in high superficial areas and internal volumes. These features allow zeolites to host molecular or ionic species acting as molecular sieves.

The maximum dimension of the host molecule depends strictly on the dimensions of the zeolite channels defined as the diameter of the ring opening of the pore. The substitution of Si<sup>4+</sup> atoms with Al<sup>3+</sup> in some TO<sub>4</sub> units results in a net negative charge in the framework, this charge arises from the different formal valency of [SiO<sub>4</sub>]<sup>4-</sup> and [AlO<sub>4</sub>]<sup>5-</sup> tetrahedral units and is located on one of the oxygen atoms connected to the aluminium. The resulting negative charges present on the zeolite framework are balanced by counterions such as Na<sup>+</sup>, Mg<sup>2+</sup> and Ca<sup>2+</sup>. These cations are bond to the aluminosilicate framework through weak electrostatic interactions[3] and they can be exchanged with solutes present in the solution in contact with the material. This allows the use of zeolites as cations exchangers, the cation exchange capacity defines the maximum number, expressed as milliequivalent, of ions that can be substituted per gram of zeolitic material.

This value depends on the Si/Al ratio and it is higher for zeolites with low SAR, since a higher amount of Al<sup>3+</sup> in the structure means more negative charges on the framework and, therefore, more extra-framework species are present in the pores of the zeolite [4].

### Applications

Zeolites are widely used in different industrial, agricultural and medical applications as catalysts, adsorbents or ionic exchangers.

The regular porous structure and the fact that the dimensions and shape of the cavities can be modulated in synthesised zeolites, allow to employ these materials as molecular sieves in adsorption and separation technologies. The properties that make zeolites suitable materials for adsorption applications are the following:

**High efficiency.** Zeolites have been used for the irreversible removal of high concentration of pharmaceuticals from water, such as atenolol (ANT), levofloxacin (LEVO), carbamazepine (CBZ), ketoprofen (KTP) and hydrochlorothiazide (HTC). The adsorption kinetics for the single drugs in zeolite Y showed a very fast uptake, with the complete removal of the contaminant from water achieved in less than one minute. Furthermore, it has been proved that the efficiency of zeolite is not modified when dissolved natural organic matter is present in the water stream that is being treated.

**Shape selectivity.** One of the most important features of zeolites is their highly selective adsorption towards host molecules, strongly affected by the internal pore structure, especially shape and dimension of channels and cages. Adsorption phenomena are found in many domains including catalysis, pollution control, gas separation and storage. Recent environmentally driven applications have arisen using the hydrophobic molecular sieves as adsorbent for the removal and recovery of VOCs which offers the promise of significant market growth. A new scientific direction has emerged over the last few years for exploring molecular sieves as advanced solid-state materials: this research includes zeolite electrodes, batteries and chemical sensors [5].

**Stability.** Zeolites should keep their activity for long periods, the operational life is expected to be 10 to 20 years. However, experience over such period is not yet



available. The replacement or regeneration of zeolites can be easily achieved: after adsorption, the exhausted zeolites are generally subjected to a regeneration process which involves operating at high temperatures, normally from 250° and 350°C for a time ranging from 30 minutes to 1.5 hours, and in presence of an air flow (from 1.5 to 2.5 m<sup>3</sup>/hr). Under these conditions zeolites maintain their structural integrity, in this way they can be regenerated many times without changing their adsorption properties.

**Environmental compatibility.** Zeolites do not represent a source of contamination itself by solubilisation or other mobilisation mechanisms; moreover, when reacting with contaminants they do not form any by products. Zeolites have been employed as catalysts in many industrial chemical reactions, for example petroleum cracking, isomerisation and alkylation reactions for the production of fine chemicals, dyestuffs, detergents and scents [3].

**Availability and cost.** Permeable reactive barrier (PRB) containing zeolites has been recognised as a cost-effective technology for water remediation. Both natural and synthetic zeolites are commercially available at low prices.

The use of zeolites as catalysts is mainly due to their 3D structure with cavities and channels that can accommodate reactive molecules with dimensions comparable with those of the zeolite channels. In this way, the reactive molecules are enclosed in a confined space and can react more efficiently.

The catalytic process is mainly due to the presence of Brønsted and Lewis acid sites on the zeolite framework, in particular catalytic reactions are influenced by:

The presence of hydroxyl groups on the zeolite framework that act as Brønsted acid sites via reversible transfer of a proton to the adsorbed molecule;

Oxygen vacancy in the framework that generate a Lewis acid site on the tetrahedral cation due to the residual positive charge on it;

The interaction with metal ions or clusters.

The existence of electrostatic field gradients that create Lewis acid sites that are able to polarise bonds of the adsorbed molecule;

The zeolitic acid sites are described with the classic models of Brønsted and Lewis: Brønsted acids are species that can donate a proton (Brønsted acid sites are present in zeolites with H<sup>+</sup> as the extra-framework ion); Lewis acids are those that can accept an electron pair from another species, this is the case mainly for zeolites with Al tri-coordinated that can accept an electron pair and act as a Lewis acid.

## **Characterization**

### Thermal analysis

Thermal analysis is a family of techniques in which the properties of materials are studied as they change with temperature. Thermal analysis includes several methods that differ from each other by the property which is measured. Thermogravimetric analysis (TGA) is a method in which sample weight changes are monitored as a function of increasing temperature (with constant heating rate), or as a function of time (with constant temperature and/or constant mass loss). This measurement provides information about physical phenomena, such as absorption, phase transitions, adsorption and desorption; as well as chemical phenomena including chemisorption, thermal decomposition, and solid-gas reactions (e.g., oxidation or reduction). TGA can be used to determine material stability, if the material is thermally stable, there will be no observed mass change.

TGA is commonly used to qualify selected characteristics of materials that report oxidation or loss of volatiles, such as moisture, either mass loss or gain due to decomposition. Materials characterization can be obtained through TG analysis evaluating degradation mechanisms, reaction kinetics and characteristic decomposition patterns.

Differential thermal analysis (DTA) is a thermoanalytic technique, where the material under study and an inert reference undergo identical thermal cycles, while recording the temperature difference between sample and reference. The differential temperature is plotted against time or temperature (DTA curve, or thermogram), in this way, changes in the sample, either exothermic or endothermic, can be detected relative to the inert reference. A DTA curve provides information on the

transformations that have occurred, such as glass transitions, crystallisation, melting and sublimation. The area under a DTA peak is the enthalpy change and it is not affected by the heat capacity of the sample. A DTA curve can be used only as a fingerprint for identification purposes but usually the applications of this method are the determination of phase diagrams, heat change measurements and decomposition in various atmospheres.

### X ray powder diffraction

The efficiency and use of many zeolites are closely linked to their long-range crystalline architecture, which is why it is very important to study and clearly understand the structure of zeolites. To define zeolite long-range crystalline structure, it is necessary to use radiation diffraction methods, whose wavelength is of the same order of magnitude as the distances between the atoms in the material structure. X rays are the most widely used radiation, but neutron and electrons can also be applied.

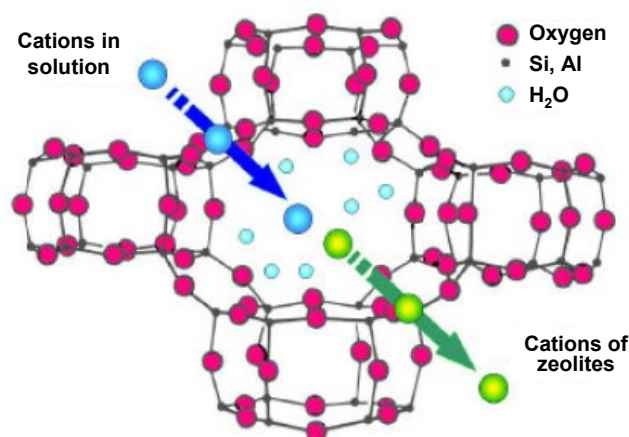
Powder X-ray diffraction (XRD) is a fast analytical technique used to obtain information on unit cell sizes and for phase identification of a crystalline material. The XRD represents one of the basic techniques for the characterization of the zeolite, the XRD pattern of a zeolite is a typical fingerprint that allows to determine the degree of crystallinity or the size of a unit cell of the zeolite and the impurity of the sample. An XRD pattern is a graph of the intensity of X-rays scattered at different angles by the sample. The characteristics of an XRD pattern are the peak positions, their relative intensity, their widths and background.

The peaks positions are measured as  $2\theta$  and determined by the geometry of the unit cell, which describes the 3-dimensional repetition unit of a crystal structure. Relative intensities are determined by the position and type of the various atoms within the unit cell, while the width of the peaks in the pattern gives an indication of the crystalline quality of the sample. Finally, the background is an indication of whether or not an amorphous phase is present in the sample. A change in the relative intensities of the peaks indicates that a structural change has occurred, if a change in the positions of the peaks is observed the unit cell has been deformed, narrower or wider peaks indicate that the crystallinity has improved or deteriorated. More details can be

extracted from the powder model if a complete refinement of the Rietveld structure is performed to obtain information on the full profile.

### 3.1.1 Ag-zeolites

Zeolites having an high Al content show high ionic exchange capacity of their extra-framework cations: as represented in Figure 3.3, extra-framework cations can be reversibly substituted with other cations.



**Figure 3.3** Representation of cationic exchange

Cationic exchange leads to extraction from solutions of ions which better fit to zeolitic structure, based on their charge, ionic radius and dimension: this feature represents the high selectivity of zeolites towards host ions or molecules.

Transition metal exchanged zeolites have attracted a great deal of attention for their superior catalytic and adsorptive properties. These materials have been used for many industrial applications based on the adsorptive systems considered such as olefin/paraffin separation, purification of low molecular weight olefins (ethylene and propylene), desulfurization of transportation fuels (gasoline, diesel, and jet fuels), hydrogen storage, and CO removal for fuel cell technology [6], [7]. These materials were also found to be active catalysts in some synthesis reactions of organic molecules[6].

In the field of biomedicine, the production of materials applied for anticancer treatment remains an important area of scientific research. The World Health

Organization (WHO) reports that cancer is the second leading cause of death globally, accounting for approximately 9.6 million deaths occurred in 2018.

The use of silver nanomaterials has become one of the most predominant biomedical applications in the emerging field of nanotechnology to eliminate cancer cells [8], [9]. The materials' biological activity depends on factors such as surface chemistry, size, shape, distribution, and morphology particles, among others.

Silver (Ag) has been known to possess a broad-spectrum against bacteria and limited toxicity towards mammalian cells[10]. Significantly, zeolites incorporated with functional ions Ag also show excellent antibacterial properties [11] . Wang et al. reported the Ag-incorporated zeolites coated on Ti-6Al-4V have potential application in orthopedic implants as antibacterial and antiadhesive materials, which is clinically important for the treatment of postoperative infections in the orthopedic trauma surgery [12]. Despite the substantial advantages of zeolites in biomedical fields, the negative influences of zeolites cannot be ignored. To date, zeolites incorporated with functional ions for tissue engineering are dominant by aluminosilicates, which inevitably release harmful aluminum during usage, and disturb the mineral metabolism of organism [13]. Therefore, it is of great significance to develop aluminum-free zeolites-based scaffolds with good biological properties and antimicrobial activities.

In addition, hybrid systems have been developed for photocatalytic and antibacterial purposes such as Ag-ion-exchanged zeolite/TiO<sub>2</sub> catalyst. The idea is to propose a method to fix nano-sized TiO<sub>2</sub> particles on a zeolite framework, which is also activated by entering Ag ions into its structure. The environmental contaminants, industrial wastes, hospital wastewater and organic pollutants are getting increasingly complicated. This necessitates using highly functional hybrid disinfection methods, based on nanocomposite materials. The novelty of this research is the modification of natural zeolite using Ag-ion-exchange, and TiO<sub>2</sub> deposition for the development of a low-cost catalyst powder for simultaneous degradation of antibiotics and bacteria in a simulated hospital wastewater [14].

### 3.1.2 ZSM-5 (MFI)

The most important member of the MFI family is the ZSM-5 zeolite because it possesses unusual catalytic properties and have high thermal stability [15]. The pure silica form of ZSM-5 zeolite is known as silicalite. The MFI framework is presented in Figure 3.4.

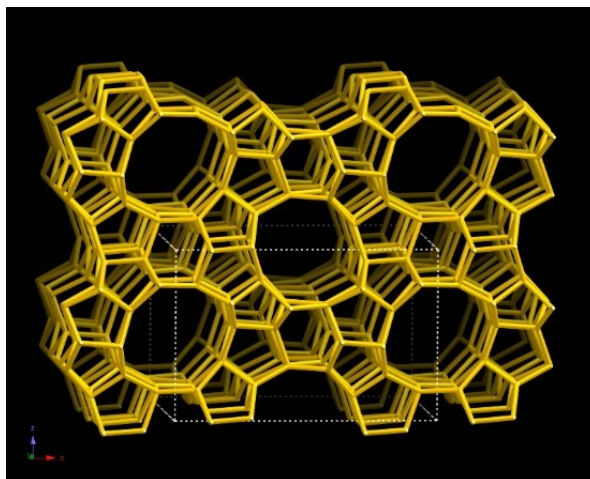


Figure 3.4 ZMS-5 framework viewed along (010) [IZA]

Zeolite ZSM-5 is constructed from pentasil units that are linked together in pentasil chains. Mirror images of these chains are connected by oxygen bridges to form corrugated sheets with ten-ring channel openings. Oxygen bridges link each sheet to the next to form a three-dimensional structure with straight ten-ring channels parallel to the corrugations along  $y$  intersected by sinusoidal ten-ring channels perpendicular to the sheets along  $z$ . The minor and major axis dimensions are  $5.1 \times 5.5 \text{ \AA}$  for the sinusoidal channels and  $5.3 \times 5.6 \text{ \AA}$  for the straight channels (Figure 3.5) [IZA].

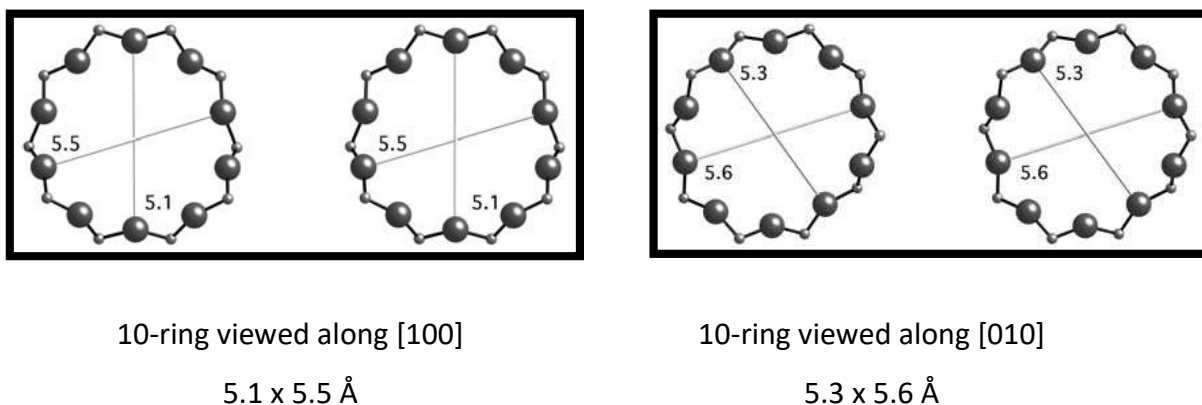


Figure 3.5 ZSM-5 channels.

### 3.1.3 BETA (BEA)

Beta zeolite (BEA) is a microporous material with large pores which was synthesized for the first time from Wandlinger for the Mobile Oil Corporation in 1967, by employing tetraethylammonium (TEA) as templating.

The crystalline structure of Beta was first resolved in 1988 by Newsam, who defined this zeolite as a hybrid grown of two distinct but strictly connected structures, that is two different polytypes [16]. The two principal polytypes, named polytype A and polytype B which are shown in Figure 3.6, are tetragonal and monoclinic, respectively; reported that the synthetic Beta zeolite is composed by monoclinic polytype B for its 56%. [2], [17].

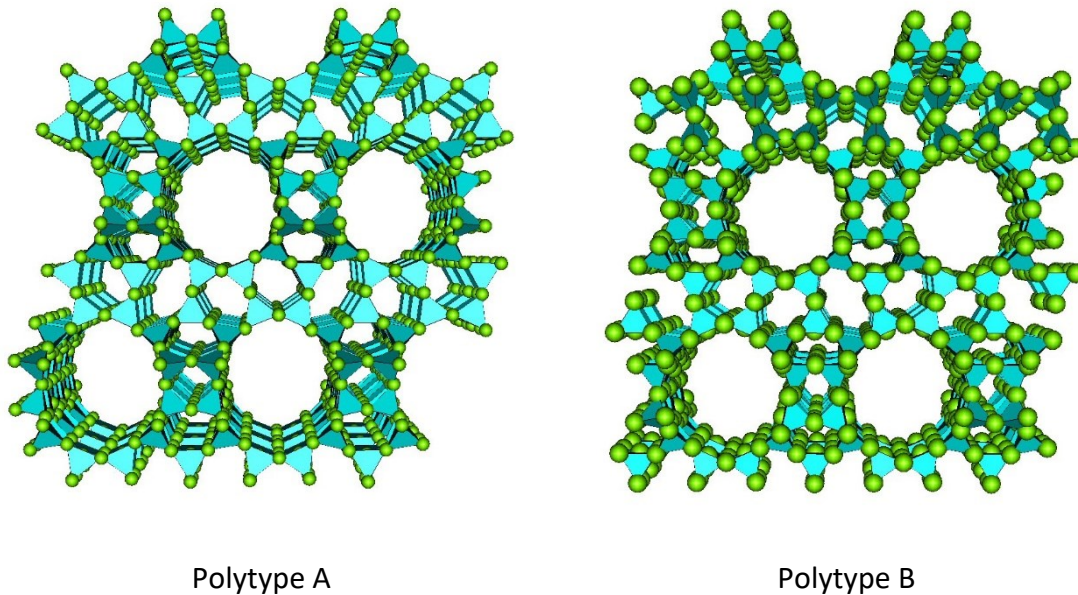
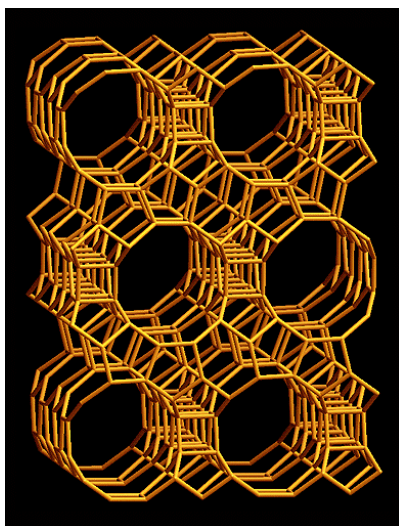


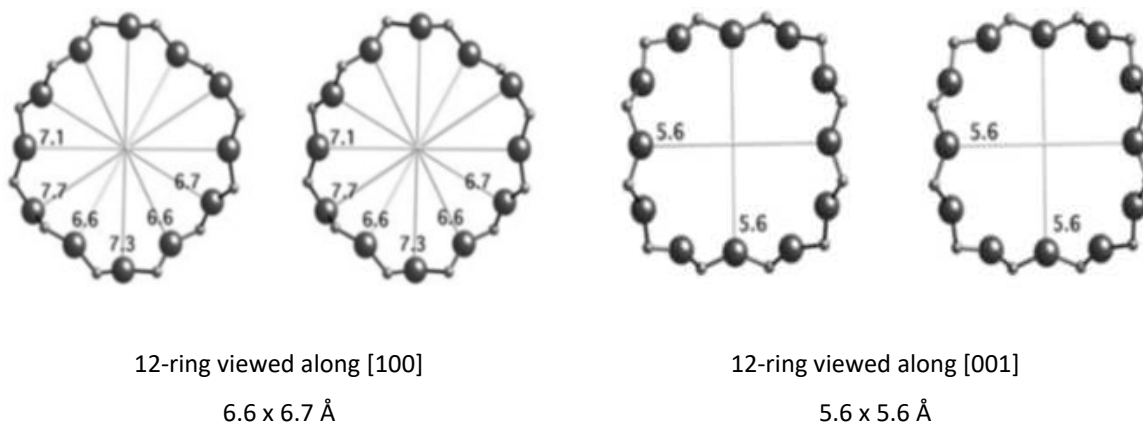
Figure 3.6 Two polytypes of Beta zeolite

Beta zeolites have well-defined layers comprised of four 5-ring subunits joined by 4-ring subunits that are stacked in a disordered way along the z direction: the whole structure is represented in Figure 3.7.



**Figure 3.7** Beta framework viewed along (100) [IZA]

Despite this disorder, a three-dimensional 12-ring channel system is formed [2]. The tetragonal polytype A presents two 12-ring channels highly elliptical, parallel to [100] and [010] directions, with pore dimensions of about  $7.3 \times 5.8\text{-}6.6 \text{ \AA}$ , and a more contorted 12-ring channel parallel to [001] direction, with pore dimensions of about  $5.6\text{-}5.8 \times 5.6\text{-}5.8 \text{ \AA}$  (Figure 3.8) [IZA].



**Figure 3.8** BETA channels in polytype A

The porous structure and the strong acidity, both as Brønsted and as Lewis sites, make Beta zeolites highly selective towards host molecules and catalytically active, so that it is employed in a huge number of industrial processes.



### 3.1.4 Zeolite Y

Faujasite is a mineral group in the zeolite family of silicate minerals and it was discovered in 1842 in Limberg quarries, Germany. Faujasite occurs in vesicles within basalt and phonolite lava and tuff as an alteration or authigenic mineral. It occurs with other zeolites, olivine, augite and nepheline.

Zeolite Y belongs to the faujasite group with chemical formula  $(Ca, Mg, Na_2)_{29} (H_2O)_{240} [Al_{58}Si_{134}O_{384}]$ -FAU and FAU framework type. The structure (Fig. 3.9) is composed of sodalite cages connected to each other through hexagonal prisms.

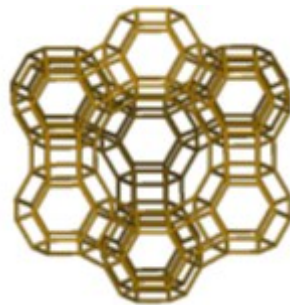
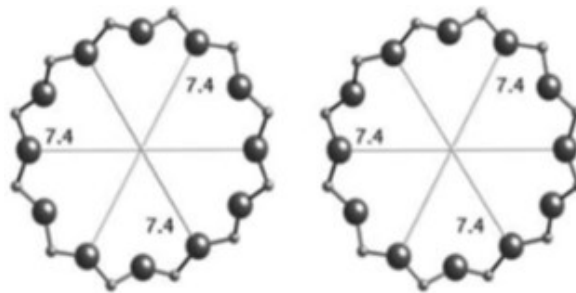


Figure 3.9 FAU framework viewed along (111) [IZA]

The pore system consists in 12-membered rings, shown in figure 3.10, with large openings (7.4 Å diameters) that lead to the inner cavity which has a diameter of 12 Å and is surrounded by 10 sodalite cages.



12-ring viewed along [111]

7.4 x 7.4 Å

Figure 3.10 Y channels

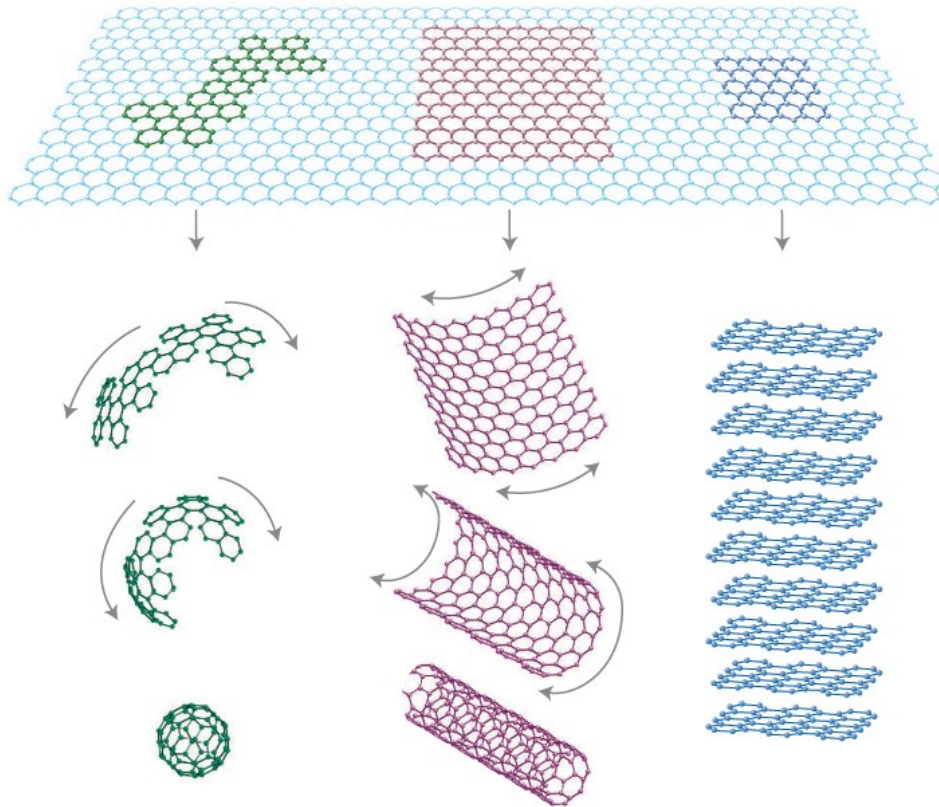
The main use of Faujasite zeolites is as a catalyst in fluid catalytic cracking for the conversion of high-boiling fractions of petroleum crude to more valuable petrol, diesel and other products. Zeolite Y has replaced zeolite X in this use because it is both more active and more stable at high temperatures due to the higher Si/Al ratio. It is also

used in the hydrocracking units as a platinum/palladium support to increase aromatic content of reformulated refinery products.

### **3.2 Graphene**

Graphene is the name given to a flat monolayer of carbon atoms tightly packed into a two-dimensional (2D) honeycomb lattice, and is a basic building block for graphitic materials of all other dimensionalities. It can be wrapped up into 0D fullerenes, rolled into 1D nanotubes or stacked into 3D graphite [18], [19] (Fig. 3.11).

The name is derived from "graphite" and the suffix-ene, reflecting the fact that the graphite allotrope of carbon contains numerous double bonds. Each atom in a graphene sheet is connected to its three nearest neighbors by a  $\sigma$ -bond and contributes one electron to a conduction band that extends over the whole sheet. This is the same type of bonding seen in carbon nanotubes and polycyclic aromatic hydrocarbons, and (partially) in fullerenes and glassy carbon [20]. These conduction bands make graphene a semimetal with unusual electronic properties that are best described by theories for massless relativistic particles.[18] Charge carriers in graphene show linear dependence of energy on momentum, and field-effect transistors with graphene can be made that show bipolar conduction. Charge transport is ballistic over long distances; the material exhibits large quantum oscillations and large and nonlinear diamagnetism. Graphene conducts heat and electricity very efficiently along its plane. The material strongly absorbs light of all visible wavelengths,[21], [22] which accounts for the black color of graphite; yet a single graphene sheet is nearly transparent because of its extreme thinness. The material is also about 100 times stronger than would be the strongest steel of the same thickness.



**Figure 3.11** Mother of all graphitic forms. Graphene is a 2D building material for carbon materials of all other dimensionalities. It can be wrapped up into 0D buckyballs, rolled into 1D nanotubes or stacked into 3D graphite. [18]

Scientists theorized the potential existence and production of graphene for decades. It has likely been unknowingly produced in small quantities for centuries, through the use of pencils and other similar applications of graphite. It was originally observed in electron microscopes in 1962, but only studied while supported on metal surfaces. The material was later rediscovered, isolated and investigated in 2004 by Andre Geim and Konstantin Novoselov at the University of Manchester[23], who were awarded the Nobel Prize in Physics in 2010 for their "groundbreaking experiments regarding the two-dimensional material graphene".

Graphene has become a valuable and useful nanomaterial due to its exceptionally high tensile strength, electrical conductivity, transparency, and being the thinnest two-dimensional material in the world. The global market for graphene was \$9 million in 2012, with most of the demand from research and development in semiconductor, electronics, electric batteries, and composites.

The IUPAC (International Union for Pure and Applied Chemistry) recommends use of the name "graphite" for the three-dimensional material, and "graphene" only when the reactions, structural relations or other properties of individual layers are discussed.[24] A narrower definition, of "isolated or free-standing graphene" requires that the layer be sufficiently isolated from its environment but would include layers suspended or transferred to silicon dioxide or silicon carbide.[25]

## Structure

### Bonding

Graphene has a remarkable band structure thanks to its crystal structure. Carbon atoms form a hexagonal lattice on a two-dimensional plane. Each carbon atom is about  $a = 1.42 \text{ \AA}$  from its three neighbors, with each of which it shares one  $\sigma$  bond. Carbon orbitals  $2s$ ,  $2p_x$ ,  $2p_y$  form the hybrid orbital  $sp^2$  with three major lobes at  $120^\circ$ . The remaining orbital,  $p_z$ , is sticking out of the graphene's plane. Sigma bonds result from an overlap of  $sp^2$  hybrid orbitals, whereas pi bonds emerge from tunneling between the protruding  $p_z$  orbitals. Three of the four outer-shell electrons of each atom in a graphene sheet occupy three  $sp^2$  hybrid orbitals, a combination of orbitals  $s$ ,  $p_x$  and  $p_y$ , that are shared with the three nearest atoms, forming  $\sigma$ -bonds. The remaining outer-shell electron occupies a  $p_z$  orbital that is oriented perpendicularly to the plane. These orbitals hybridize together to form two half-filled bands of free-moving electrons,  $\pi$  and  $\pi^*$  (fig. 3.12), which are responsible for most of graphene's notable electronic properties.[26]

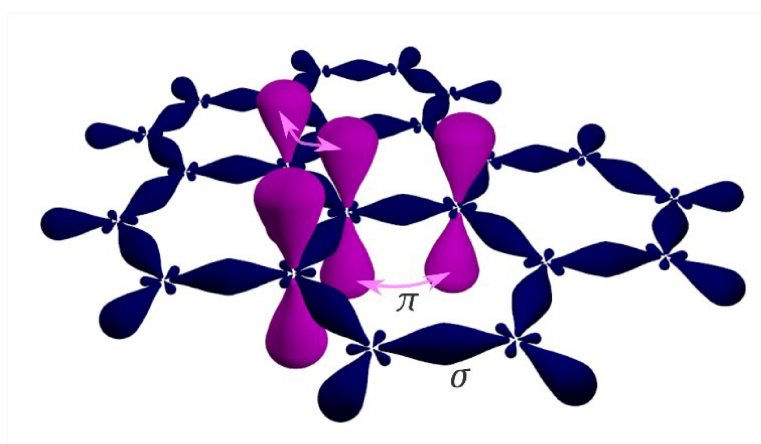


Figure 3.12  $\sigma$  and  $\pi$  bonds in graphene

## Geometry

The hexagonal lattice structure of isolated, single-layer graphene can be directly seen with transmission electron microscopy (TEM) of sheets of graphene suspended between bars of a metallic grid [27]. The hexagonal structure is also seen in scanning tunneling microscope (STM) images of graphene supported on silicon dioxide substrates. The rippling seen in these images is caused by conformation of graphene to the substrate's lattice and is not intrinsic.[28]

## **Properties**

### Electronic

Graphene behaves like a zero-gap semiconductor. Its particular electronic structure means that it can behave both as a P semiconductor and as an N semiconductor in the absence of doping, for mere electronic control (gating). Other uses are in solar cells, flow batteries and lithium-ion batteries. Recently, so-called "graphene" lithium-ion batteries have been placed on the market, which would use graphene as an anodic material. However, it should be noted that the absence of international standards defining what can or cannot be called graphene means that many "graphene" products simply use micronized graphites.

### Thermal conductivity

Thermal transport in graphene is an active area of research, which has attracted attention because of the potential for thermal management applications. Following predictions for graphene and related carbon nanotubes,[29] early measurements of the thermal conductivity of suspended graphene reported an exceptionally large thermal conductivity up to  $5300 \text{ W}\cdot\text{m}^{-1}\cdot\text{K}^{-1}$ , compared with the thermal conductivity of pyrolytic graphite of approximately  $2000 \text{ W}\cdot\text{m}^{-1}\cdot\text{K}^{-1}$  at room temperature.[30]

### Chemical

Graphene has a theoretical specific surface area (SSA) of  $2630 \text{ m}^2/\text{g}$ . This is much larger than that reported to date for carbon black (typically smaller than  $900 \text{ m}^2/\text{g}$ ) or for carbon nanotubes (CNTs), from  $\approx 100$  to  $1000 \text{ m}^2/\text{g}$  and is similar to activated carbon [31]. Graphene is the only form of carbon (or solid material) in which every atom is

available for chemical reaction from two sides (due to the 2D structure). Atoms at the edges of a graphene sheet have special chemical reactivity. Graphene has the highest ratio of edge atoms of any allotrope. Defects within a sheet increase its chemical reactivity. The onset temperature of reaction between the basal plane of single-layer graphene and oxygen gas is below 260 °C (530 K) [31], [32] .

Graphene burns at very low temperature (e.g., 350 °C (620 K)). Graphene is commonly modified with oxygen- and nitrogen-containing functional groups and analyzed by infrared spectroscopy and X-ray photoelectron spectroscopy. However, determination of structures of graphene with oxygen and nitrogen functional groups requires the structures to be well controlled [33], [34].

In 2013, Stanford University physicists reported that single-layer graphene is a hundred times more chemically reactive than thicker multilayer sheets [35].

Graphene can self-repair holes in its sheets, when exposed to molecules containing carbon, such as hydrocarbons. Bombarded with pure carbon atoms, the atoms perfectly align into hexagons, completely filling the holes.

### Biological

Despite the promising results in different cell studies and proof of concept studies, there is still incomplete understanding of the full biocompatibility of graphene-based materials [36]. Different cell lines react differently when exposed to graphene, and it has been shown that the lateral size of the graphene flakes, the form and surface chemistry can elicit different biological responses on the same cell line [37].

There are indications that Graphene has promise as a useful material for interacting with neural cells; studies on cultured neural cells show limited success. Graphene also has some utility in osteogenics. Researchers at the Graphene Research Centre at the National University of Singapore (NUS) discovered in 2011 the ability of graphene to accelerate the osteogenic differentiation of human Mesenchymal Stem Cells without the use of biochemical inducers [38]. Graphene can be used in biosensors; in 2015 researchers demonstrated that a graphene-based sensor can use to detect a cancer risk biomarker. In particular, by using epitaxial graphene on silicon carbide, they were

repeatably able to detect 8-hydroxydeoxyguanosine (8-OHdG), a DNA damage biomarker [39].

### 3.2.1 Carbon Nanostructured Advanced Material

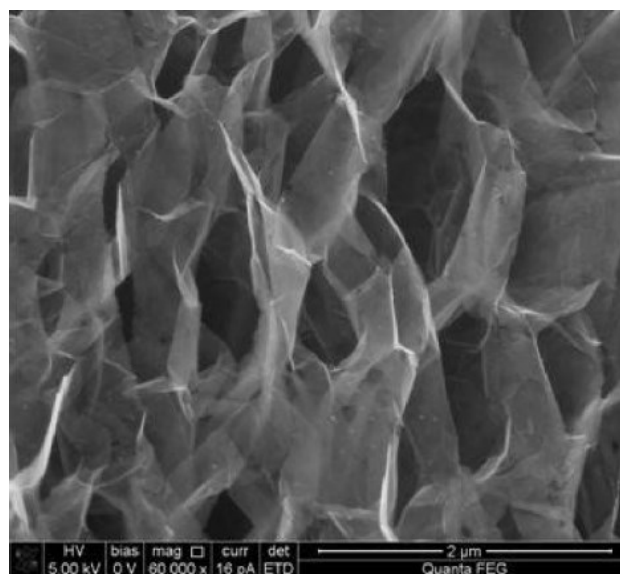
All these peculiar properties have allowed nanostructured materials to find applications in many fields and products, even for everyday use such as batteries, antibacterial clothing, coatings, paints, cosmetics, equipment and pharmaceutical products. Nanostructured materials also find application in the field of environmental remediation, where they are used as filters for water treatment, to inhibit the growth of algae or to remove heavy metals from wastewater. Many of the nanomaterials used in this field are carbon-based, in the form of fullerenes, nanotubes, nanospheres and graphene, such as the material studied in this work, CANAM (Carbon Nanostructured Advanced Material), produced by the Swiss company Vyridis.

**Table 3.1** Main physical properties of CANAM

Parameter	Values / Description
Product form	Powder / fluff
Crystalline structure	Crystallinity increases with pressure
Chemical composition	>99.76% of carbon with silicon, iron, magnesium and alkali residues but not trace of heavy metals
Density in current state	0.01-0.001 g/cm <sup>3</sup>
Wettability and contact angle	Hydrophobic material, with contact angle greater than 90°
Thermal characteristic	Stable material up to 600°C, after which it loses weight until consumption
Zeta potential or electrokinetic	Neutrality potential at pH 4.8
Microscopic structure	Micropores with constant diameter of 0.2-2.0 nm, remaining constant with the pressure. Diffuse porosity between 2 and 100 nm. The product has an apparent porosity of 54%.
Morphology and mesoscopic structure	Flakes with very high volume versus surface
Percentage of nano-tubes	20%
Specific surface area	Ca. 70 m <sup>2</sup> /g in the product as is. The specific surface area increase by increasing the material compaction pressure. It reaches

	2000 m <sup>2</sup> /g for a compaction pressure of 2 kg/cm <sup>2</sup>
Colour	Dark gray
General properties	Inert, conductor of electricity, stable towards chemically aggressive substances, does not exhibit any release phenomena of substances into environment.

CANAM is made up of graphene sheets, carefully modeled and oriented during the manufacturing process, in order to obtain nano-tubes and fullerenes that form a regular structure of cells and channels. Therefore, CANAM is a material that has a mesopore structure with a high surface area. The dark gray color of the powder of the granular powder, it is in this form that it is sold, is due to the fact that it is made up of 99.760% carbon, in the form of graphene sheets. In addition to carbon, a low percentage of chlorine, sulfur, iron, silica, magnesium and sodium are found. On the other hand, traces of heavy metals are absent. CANAM is an inert material, stable up to 600 ° C and to chemically aggressive substances, electrical and hydrophobic conductor. The structure has micropores with a diameter ranging from 0.2 to 2.0 nm, while the porosity varies between 2.0 and 100.0 nm (Fig. 3.13). One of the main applications for CANAM is certainly to be used as a material for nano filtration, as a technology for the fluid purification process.



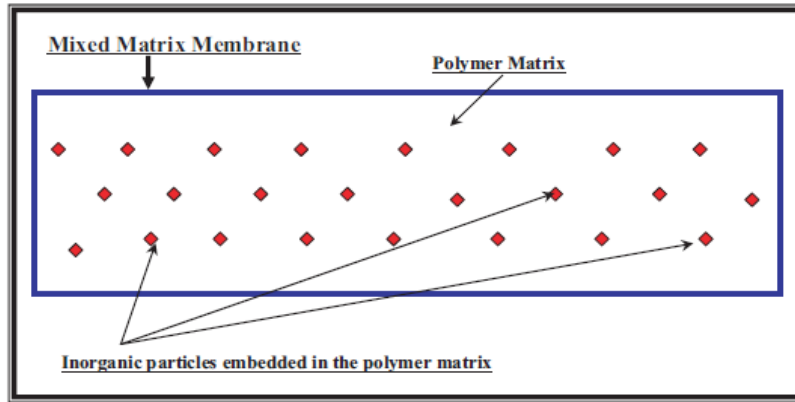
**Figure 3.13** Detail of a sheet structure, the hexagonal structure of the surface of the cells



### 3.3 Mixed matrix membranes

Over the past few decades, membrane separation process was found to be promising for various medical and industrial applications (air separation, hydrogen recovery and CO<sub>2</sub> removal)[40], [41]. Membrane technology is an attractive separation approach due to such advantages offered by the process, like: high stability and efficiency, ease of operation, low operating cost and energy requirement [42]. The major issue of current membrane research is developing of highly permeable and selective membrane materials, that also show sufficient resistance. Because of that the development of new polymers or the modification of existing polymers for gas separation is a very important factor. These polymers can be easily modified by various substitutions and insertion of the metal cations, like: Na<sup>+</sup>, Mg<sup>2+</sup>, Al<sup>3+</sup>, a production of copolymers or carbon membranes received by pyrolysis of polymer precursors[43], [44]. The next, very promising strategy for improving the mass transport through polymer films is the incorporation of inorganic materials (zeolites, carbon molecular sieve, silica nanoparticles, etc.) into a polymer matrix. This new class of membrane materials, that offers the significant potential in membrane separation technology is called mixed matrix membranes (MMMs). These membranes combine the selectivity of fillers and the simplicity of polymer membrane processing [45]. The successful application of MMMs depends mainly on the polymer matrix selection, the inorganic filler as well as the interaction between these two phases. Recently, much attention has been devoted to usage of aromatic polyimides (PIs) as the polymer matrices, especially because of their high selectivity in gas separation and their excellent thermal, chemical and mechanical stability[46], [47].

As mentioned above, mixed matrix is a blend of inorganic particles in a polymer matrix. Fig. 3.14 shows the mixed matrix membranes schematically.



**Figure 3.14** A schematic diagram of the inorganic dispersed phase embedded in the polymer matrix

Therefore, the procedure of the fabrication of mixed matrix membranes is very similar to ordinary polymer membrane fabrication. The first step of mixed matrix membrane fabrication is preparing a homogeneous solution of polymer and particles. For this purpose, the following methods can be used:

1. Particles are dispersed into the solvent and stirred for a predetermined period of time and then the polymer is added [48] (Fig. 3.15 a).
2. The polymer is dissolved in the solvent and stirred; a predetermined mass of inorganic particles is then added to the polymer solution [49] (Fig. 3.15 b).
3. Particles are dispersed into the solvent and stirred for a predetermined period of time and the polymer is dissolved in a solvent separately. The particle suspension is then added to the polymeric solution [50] (Fig. 3.15 c).

Among these methods, the first and third methods are used for better distribution of inorganic particles because in a dilute suspension, the particles are prevented from agglomerating by high shear rate during stirring. The second method is used commonly for nanoparticles distribution in the polymer matrix. Fig. 3.15 (a–c) illustrates the different methods of mixed matrix dope preparation.

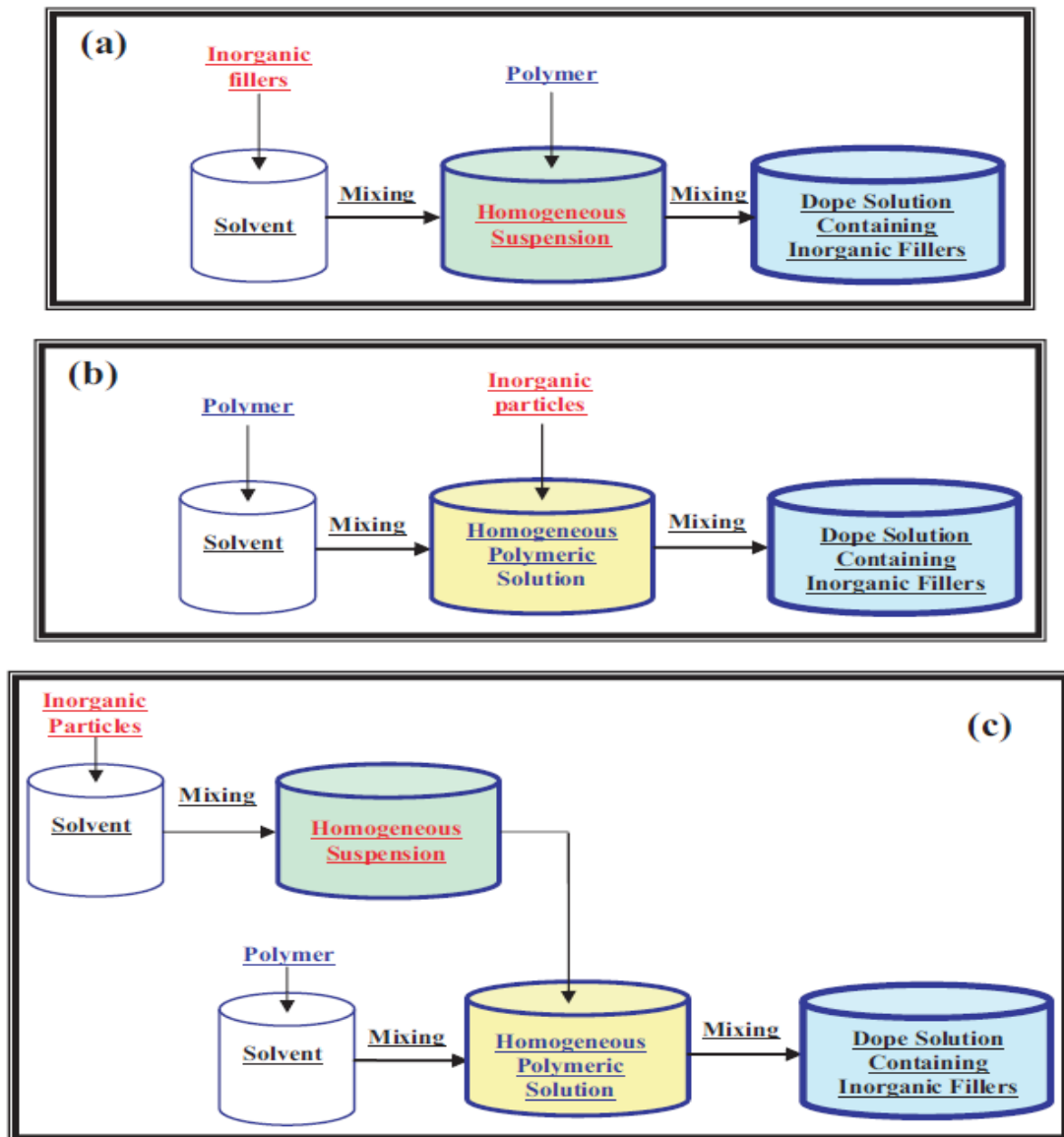
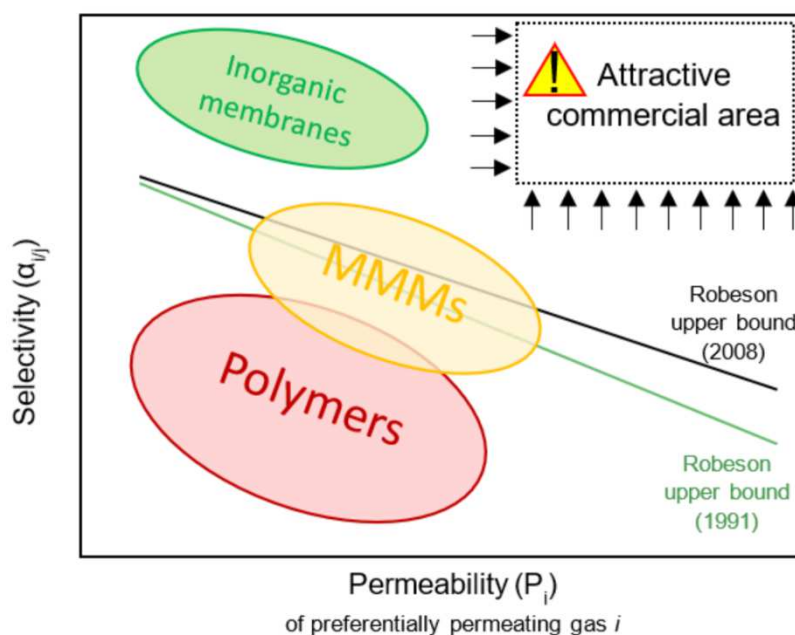


Figure 3.15 Different methods for mixed matrix dope preparation

The effect of the inorganic dispersed phase on the mixed matrix membrane properties is related to its chemical structure, surface chemistry and the type of particles. The inorganic materials used for MMMs can be classified into porous and nonporous types. The effect of porous fillers on the mixed matrix membrane is different from nonporous inorganic fillers and can be related to their structure and their pore size. Generally, porous fillers act as molecular sieving agents in the polymer matrix [51] and separate gas molecules by their shape or size. Due to their concise apertures, porous inorganic particles have usually high permeability and selectivity which is above the Robeson upper bound (fig.3.16).



**Figure 3.16** Relationship between permeability and selectivity. Current situation between different membrane composition regarding Robeson upper bound and the attractive commercial area. [52]

Therefore, when these highly selective porous fillers are added to the polymer matrix, they selectively allow the desired component to pass through the pores and thus a mixed matrix membrane, whose permselectivity is higher than that of the neat polymeric membrane, can be obtained. In other words, addition of porous inorganic fillers to a polymer matrix not only increases the permeability of the desired component but also increases the overall selectivity of the desired component relative to the undesired component. That is, addition of porous fillers to the polymer matrix is an ideal way to overcome the traditional permeability-selectivity trade-off of the polymeric membranes. It is very important to note that the above mentioned ideal effect is justified when the polymer chains wet the porous particles completely and there are no defects in the polymer–particle interface.

In this work some MMMs were studied for the removal of PFAS from aqueous solutions. The selected filler was CANAM that was incorporated into three different polymeric matrices (hydrogels) with different characteristics about crosslinking, swelling and hydrophilicity.

### 3.4 References

- [1] F. Schüth and W. Schmidt, "Microporous and Mesoporous Materials\*\*."
- [2] C. Baerlocher, L. B. Mccusker, and D. H. Olson, "AtlAs of Zeolite frAmework types."
- [3] M. Moshoeshoe, M. Silas Nadiye-Tabbiruka, and V. Obuseng, "A Review of the Chemistry, Structure, Properties and Applications of Zeolites," *American Journal of Materials Science*, vol. 2017, no. 5, pp. 196–221, 2017, doi: 10.5923/j.materials.20170705.12.
- [4] S. L. B. Sersale R., *Natural zeolites. Occurrences, properties and uses*. Elmsford, 1978.
- [5] van B. H. , C. A. , S. F. Čejka J., *Introduction to Zeolite Science and Practice*, 3RD revised edition., vol. 168. 2007.
- [6] M. Guisnet and J.-P. Gilson, "Zeolites for Cleaner Technologies edited by."
- [7] A. , C. T. , W. Z. Varin, *Nanomaterials for Solid State Hydrogen Storage*. 2009.
- [8] H. Qu, B. Ma, H. F. Yuan, Z. Y. Wang, S. J. Guo, and J. Zhang, "Effect of salinomycin on metastasis and invasion of bladder cancer cell line T24," *Asian Pacific Journal of Tropical Medicine*, vol. 8, no. 7, pp. 578–582, Jul. 2015, doi: 10.1016/j.apjtm.2015.06.004.
- [9] F. , B. Y. , M. P. Benaliouche, "Fluid Transport in Nanoporous Materials," *NATO Sciences Series*, vol. 219, 2006.
- [10] V. K. Sharma, R. A. Yngard, and Y. Lin, "Silver nanoparticles: Green synthesis and their antimicrobial activities," *Advances in Colloid and Interface Science*, vol. 145, no. 1–2. pp. 83–96, Jan. 30, 2009. doi: 10.1016/j.cis.2008.09.002.
- [11] P. Tavolaro, S. Catalano, and A. Tavolaro, "Anticancer activity modulation of an innovative solid formulation of extra virgin olive oil by cultured zeolite scaffolds," *Food and Chemical Toxicology*, vol. 124, pp. 139–150, Feb. 2019, doi: 10.1016/j.fct.2018.11.061.
- [12] J. Wang *et al.*, "Antibacterial and anti-adhesive zeolite coatings on titanium alloy surface," *Microporous and Mesoporous Materials*, vol. 146, no. 1–3, pp. 216–222, Dec. 2011, doi: 10.1016/j.micromeso.2011.04.005.
- [13] K. K. Turner, B. D. Nielsen, C. I. O'Connor-Robison, F. H. Nielsen, and M. W. Orth, "Tissue response to a supplement high in aluminum and silicon," *Biological Trace Element Research*, vol. 121, no. 2, pp. 134–148, Feb. 2008, doi: 10.1007/s12011-007-8039-x.
- [14] N. Torkian *et al.*, "Synthesis and characterization of Ag-ion-exchanged zeolite/TiO<sub>2</sub> nanocomposites for antibacterial applications and photocatalytic

- degradation of antibiotics," *Environmental Research*, p. 112157, Oct. 2021, doi: 10.1016/j.envres.2021.112157.
- [15] G. T. , L. S. L. , O. D. H. , M. W. M. Kokotailo, "Structure of synthetic zeolite ZSM-5," *Nature*, vol. 272, pp. 437–438, 1978.
- [16] H. U. Blaser and H.-Jurgen. Federsel, *Asymmetric catalysis on industrial scale : challenges, approaches and solutions*. Wiley-VCH, 2010.
- [17] J. Stelzer, M. Paulus, M. Hunger, and J. Weitkamp, "Hydrophobic properties of all-silica zeolite beta1," 1998.
- [18] A. K. Geim and K. S. Novoselov, "The rise of graphene." [Online]. Available: [www.nature.com/naturematerials](http://www.nature.com/naturematerials)
- [19] N. M. R. Peres and R. M. Ribeiro, "Focus on graphene," *New Journal of Physics*, vol. 11, Sep. 2009, doi: 10.1088/1367-2630/11/9/095002.
- [20] A. D. Zdetsis and E. N. Economou, "A Pedestrian Approach to the Aromaticity of Graphene and Nanographene: Significance of Huckel's  $(4n+2)\pi$  Electron Rule," *Journal of Physical Chemistry C*, vol. 119, no. 29, pp. 16991–17003, Jul. 2015, doi: 10.1021/acs.jpcc.5b04311.
- [21] R. R. Nair *et al.*, "Fine structure constant defines visual transparency of graphene," *Science*, vol. 320, no. 5881, p. 1308, Jun. 2008, doi: 10.1126/science.1156965.
- [22] S. E. Zhu, S. Yuan, and G. C. A. M. Janssen, "Optical transmittance of multilayer graphene," *EPL*, vol. 108, no. 1, Oct. 2014, doi: 10.1209/0295-5075/108/17007.
- [23] K. S. Novoselov *et al.*, "Electric Field Effect in Atomically Thin Carbon Films," Kluwer, 2000. [Online]. Available: [www.arXiv.org/quant-ph/pac199567030473](http://www.arXiv.org/quant-ph/pac199567030473).
- [24] "pac199567030473".
- [25] C. Riedl, C. Coletti, T. Iwasaki, A. A. Zakharov, and U. Starke, "Quasi-free-standing epitaxial graphene on SiC obtained by hydrogen intercalation," *Physical Review Letters*, vol. 103, no. 24, Dec. 2009, doi: 10.1103/PhysRevLett.103.246804.
- [26] D. R. Cooper *et al.*, "Experimental Review of Graphene," *ISRN Condensed Matter Physics*, vol. 2012, pp. 1–56, Apr. 2012, doi: 10.5402/2012/501686.
- [27] J. C. Meyer, A. K. Geim, M. I. Katsnelson, K. S. Novoselov, T. J. Booth, and S. Roth, "The structure of suspended graphene sheets," *Nature*, vol. 446, no. 7131, pp. 60–63, Mar. 2007, doi: 10.1038/nature05545.
- [28] M. Ishigami, J. H. Chen, W. G. Cullen, M. S. Fuhrer, and E. D. Williams, "Atomic structure of graphene on SiO<sub>2</sub>," *Nano Letters*, vol. 7, no. 6, pp. 1643–1648, Jun. 2007, doi: 10.1021/nl070613a.

- [29] S. Berber, Y.-K. Kwon, and D. Tománek, "Unusually High Thermal Conductivity of Carbon Nanotubes," 2000.
- [30] A. A. Balandin *et al.*, "Superior thermal conductivity of single-layer graphene," *Nano Letters*, vol. 8, no. 3, pp. 902–907, Mar. 2008, doi: 10.1021/nl0731872.
- [31] F. Bonaccorso *et al.*, "Graphene, related two-dimensional crystals, and hybrid systems for energy conversion and storage," *Science*, vol. 347, no. 6217. American Association for the Advancement of Science, Jan. 02, 2015. doi: 10.1126/science.1246501.
- [32] P. A. Denis and F. Iribarne, "Comparative study of defect reactivity in graphene," *Journal of Physical Chemistry C*, vol. 117, no. 37, pp. 19048–19055, Sep. 2013, doi: 10.1021/jp4061945.
- [33] Y. Yamada, H. Yasuda, K. Murota, M. Nakamura, T. Sodesawa, and S. Sato, "Analysis of heat-treated graphite oxide by X-ray photoelectron spectroscopy," *Journal of Materials Science*, vol. 48, no. 23, pp. 8171–8198, Dec. 2013, doi: 10.1007/s10853-013-7630-0.
- [34] Y. Yamada, J. Kim, S. Matsuo, and S. Sato, "Nitrogen-containing graphene analyzed by X-ray photoelectron spectroscopy," *Carbon*, vol. 70, pp. 59–74, Apr. 2014, doi: 10.1016/j.carbon.2013.12.061.
- [35] G. Diankov, M. Neumann, and D. Goldhaber-Gordon, "Extreme monolayer-selectivity of hydrogen-plasma reactions with graphene," *ACS Nano*, vol. 7, no. 2, pp. 1324–1332, Feb. 2013, doi: 10.1021/nn304903m.
- [36] C. J. Bullock and C. Bussy, "Biocompatibility Considerations in the Design of Graphene Biomedical Materials," *Advanced Materials Interfaces*, vol. 6, no. 11. Wiley-VCH Verlag, Jun. 07, 2019. doi: 10.1002/admi.201900229.
- [37] K. H. Liao, Y. S. Lin, C. W. MacOsko, and C. L. Haynes, "Cytotoxicity of graphene oxide and graphene in human erythrocytes and skin fibroblasts," *ACS Applied Materials and Interfaces*, vol. 3, no. 7, pp. 2607–2615, Jul. 2011, doi: 10.1021/am200428v.
- [38] T. R. Nayak *et al.*, "Graphene for controlled and accelerated osteogenic differentiation of human mesenchymal stem cells," *ACS Nano*, vol. 5, no. 6, pp. 4670–4678, Jun. 2011, doi: 10.1021/nn200500h.
- [39] Z. Tehrani *et al.*, "Generic epitaxial graphene biosensors for ultrasensitive detection of cancer risk biomarker," *2D Materials*, vol. 1, no. 2, Sep. 2014, doi: 10.1088/2053-1583/1/2/025004.
- [40] N. , F. A. G. , W. H. W. S. , M. T. Li, *Advanced Membrane Technology and Applications*, 1st Edition.

- [41] X. G. Li and M. R. Huang, "Water-casting ultrathin-film composite membranes for air separation," *Separation Science and Technology*, vol. 31, no. 5. Marcel Dekker Inc., pp. 579–603, 1996. doi: 10.1080/01496399608000706.
- [42] H. Strathmann, L. Giorno, and E. Drioli, "An Introduction to Membrane Science and Technology," 2006.
- [43] H. J. Lee, D. P. Kim, H. Suda, and K. Haraya, "Gas permeation properties for the post-oxidized polyphenylene oxide (PPO) derived carbon membranes: Effect of the oxidation temperature," *Journal of Membrane Science*, vol. 282, no. 1–2, pp. 82–88, Oct. 2006, doi: 10.1016/j.memsci.2006.05.006.
- [44] B. Kruczek and T. Matsuura, "Development and characterization of homogeneous membranes de from high molecular weight sulfonated polyphenylene oxide."
- [45] P. S. Goh, A. F. Ismail, S. M. Sanip, B. C. Ng, and M. Aziz, "Recent advances of inorganic fillers in mixed matrix membrane for gas separation," *Separation and Purification Technology*, vol. 81, no. 3. Elsevier B.V., pp. 243–264, Oct. 10, 2011. doi: 10.1016/j.seppur.2011.07.042.
- [46] J. P. G. Villaluenga, B. Seoane, J. Hradil, and P. Sysel, "Gas permeation characteristics of heterogeneous ODPa-BIS P polyimide membranes at different temperatures," *Journal of Membrane Science*, vol. 305, no. 1–2, pp. 160–168, Nov. 2007, doi: 10.1016/j.memsci.2007.08.002.
- [47] K. Friess *et al.*, "Comparison of transport properties of hyperbranched and linear polyimides," *Desalination and Water Treatment*, vol. 14, no. 1–3, pp. 165–169, 2010, doi: 10.5004/dwt.2010.1022.
- [48] T. W. Pechar *et al.*, "Fabrication and characterization of polyimide-zeolite L mixed matrix membranes for gas separations," *Journal of Membrane Science*, vol. 277, no. 1–2, pp. 195–202, Jun. 2006, doi: 10.1016/j.j.memsci.2005.10.029.
- [49] S. Kim, L. Chen, J. K. Johnson, and E. Marand, "Polysulfone and functionalized carbon nanotube mixed matrix membranes for gas separation: Theory and experiment," *Journal of Membrane Science*, vol. 294, no. 1–2, pp. 147–158, May 2007, doi: 10.1016/j.memsci.2007.02.028.
- [50] S. Husain and W. J. Koros, "Mixed matrix hollow fiber membranes made with modified HSSZ-13 zeolite in polyetherimide polymer matrix for gas separation," *Journal of Membrane Science*, vol. 288, no. 1–2, pp. 195–207, Feb. 2007, doi: 10.1016/j.memsci.2006.11.016.
- [51] C. v. Funk and D. R. Lloyd, "Zeolite-filled microporous mixed matrix (ZeoTIPS) membranes: Prediction of gas separation performance," *Journal of Membrane Science*, vol. 313, no. 1–2, pp. 224–231, Apr. 2008, doi: 10.1016/j.memsci.2008.01.002.



- [52] J. Dechnik, J. Gascon, C. J. Doonan, C. Janiak, and C. J. Sumby, "Mixed-Matrix-Membranen," *Angewandte Chemie*, vol. 129, no. 32, pp. 9420–9439, Aug. 2017, doi: 10.1002/ange.201701109.

## 4 Adsorption

Adsorption is present in many natural (physical, chemical and biological) systems and is a phenomenon of considerable industrial importance, been a major part of many processes including chemical and bio-chemical reactions, purification and filtration. Moreover, applications of technologies involving adsorption processes for air pollution control and water treatment are well known.

Adsorption is a physico-chemical process in which substances present in liquid and/or gas phase (adsorbate) interact with a solid phase (adsorbent). Adsorption is a surface phenomenon, in the bulk of a material all the bonding requirements (ionic, covalent or metallic) of the constituent atoms of the material are filled by other atoms in the material.

On the other hand, atoms localised on the surface of the adsorbent material are not completely surrounded by other atoms, so they can attract adsorbate molecules. The nature of the bonding depends on the species involved, but in general the process is classified as physical adsorption (physisorption) or chemical adsorption (chemisorption).

In physical adsorption, van der Waals interactions between the adsorbate molecules and the adsorbent surface are involved; these are weak interactions that allow the adsorbate molecules to move across the adsorbent surface (Fig. 4.1 a). In chemisorption chemical bonds between adsorbate and adsorbent are formed, ionic or covalent, strong and localised, forbidding in this case any transition on the surface (Fig. 4.1 b).

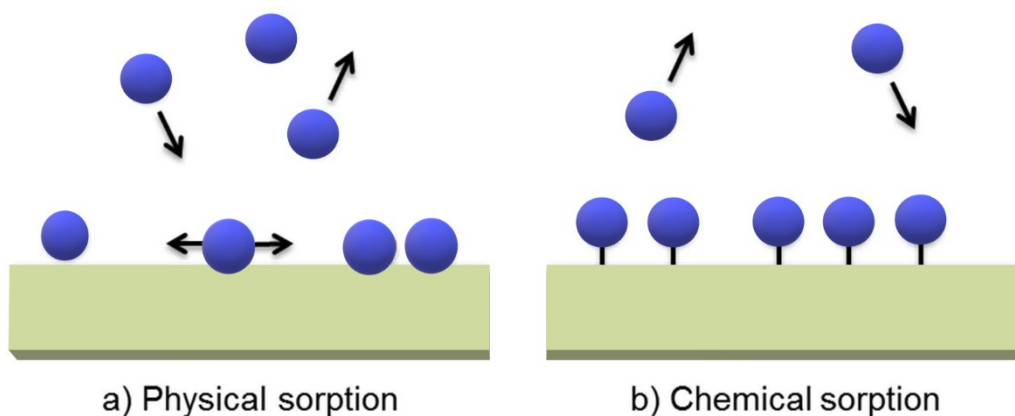


Fig. 4.1 Physical and Chemical sorption of a solute onto an adsorbent material.

**PHYSISORPTION****CHEMISORPTION**

Low degree of specificity	Dependent on the reactivity of the adsorbent and adsorptive
At high relative pressure, it general occurs as a multilayer	It is usually limited to a monolayer
A physisorbed molecule keeps its identity and on desorption returns to the fluid phase in its original form	If a chemisorbed molecule undergoes reaction or dissociation, it loses its identity and cannot be recovered by desorption
It is always exothermic and the energy involved is not much larger than the energy of condensation of the adsorptive	The energy is the same order of magnitude as the energy change in a comparable chemical reaction
Physisorption systems generally attain equilibrium fairly rapidly, but equilibration may be slow if the transport process is rate-determining	An activation energy is often involved and at low temperature the system may not have sufficient thermal energy to attain thermodynamic equilibrium

**4.1 Adsorption isotherms**

Theory regarding adsorption processes has been developed, however the mechanism of the interaction between contaminants and the solid materials used for their removal is still poorly understood in many cases, thus many experiments are carried out in order to compare experimental data.

Regarding contaminants attenuation, adsorption consists in the removal of the solute from a solution resulting in its concentration onto a surface, until the amount of solute remaining in the solution is in equilibrium with that adsorbed on the surface. This equilibrium condition is described by expressing the amount of solute adsorbed per unit weight of adsorbent ( $q_e$ ) as a function of the concentration of solute remaining in the

solution phase ( $C_e$ ). A representation of this type is called an adsorption isotherm (Fig. 4.2).

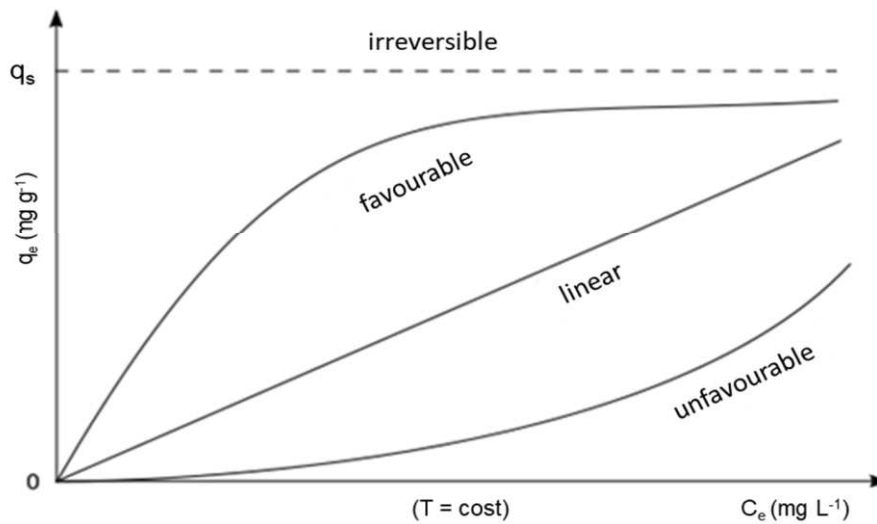


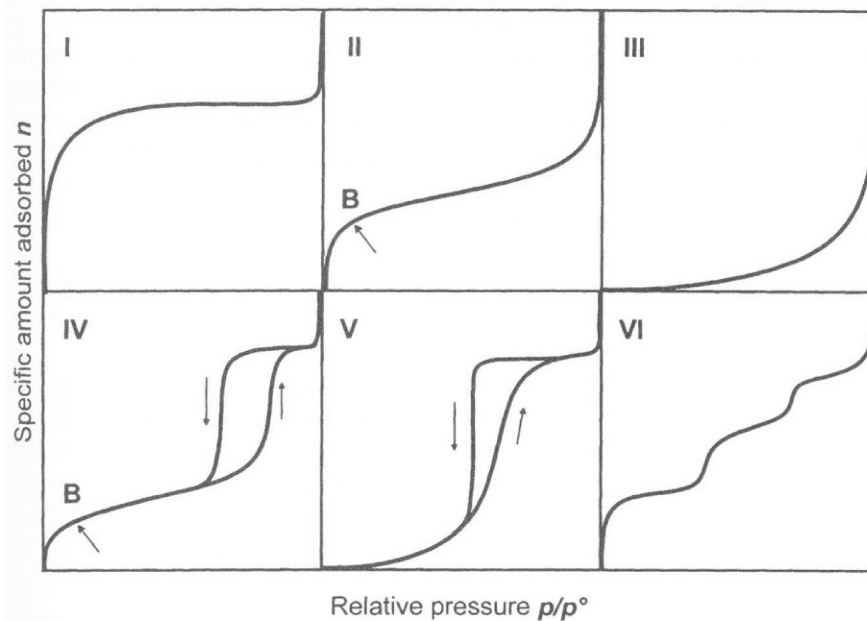
Fig. 4.2 Representation of adsorption isotherms.

The adsorption isotherms represent the variation of the adsorption capacity with respect to the solute concentration in the solution. Isotherms can be favourable when they show a concavity downwards, unfavourable when they are concave upwards, or linear when the solute mass varies linearly with the adsorbent mass. Finally, when the interaction between solute and adsorbent is so strong that it is not possible to reverse the reaction, the isotherm can be considered irreversible.

The earliest studies were focused on gas adsorption on solid phase, due to the greater simplicity than a liquid-solid system. In the case of gas-solid adsorption, the adsorbable specie is a pure compound and no interactions with other components must be considered. The first theoretical elaborations were applied on gas-solid adsorption and only at a later stage they were extended on the much complex liquid-solid systems.

The amount of gas adsorbed by the mass of solid is dependent on the equilibrium pressure, temperature and the nature of the gas-solid system. Functions describing the relationship between the amount adsorbed by unit mass of solid and the equilibrium pressure (or relative pressure) at a specific and constant temperature (isothermal conditions) are called adsorption isotherms. Several different adsorption isotherm models are available for describing single component as well as n-component systems

at constant temperature. Most of these isotherms which result from physical adsorption may be grouped into six classes in the IUPAC classification, as shown in Figure 4.3.



**Fig.4.3** Main types of gas physisorption isotherms according to IUPAC 1985 classification [1]

In Type I isotherm, the amount adsorbed by the unit mass of solid approaches a limiting value as the relative pressure approaches to 1. This isotherm is suitable when adsorbent-adsorbate interactions occur in micropores of molecular dimensions. A decrease in the micropores width results in both an increase in the adsorption energy and a decrease in the relative pressure at which the filling occurs.

The Type II isotherm indicates the formation of an adsorbed layer whose thickness increases progressively with increasing relative pressure. The uptake at point B is usually considered to represent the completion of the monolayer and the beginning of the formation of the multilayer. The ordinate of point B represents the amount of adsorbate required to cover the unit mass of solid surface (monolayer capacity). This isotherm is obtained with non-porous or macroporous adsorbents.

The Type III isotherm is not common and indicates weak adsorbent-adsorbate interactions.

The Type IV isotherm exhibits a hysteresis loop, which is usually associated with the filling and emptying of mesopores.

Type V isotherm, similar to Type III isotherm, is rare and is associated with weak adsorbent-adsorbate interactions. This isotherm shows a hysteresis loop.

Finally, the Type VI isotherm, which is relatively rare, is associated with layer-by-layer adsorption on a highly uniform surface.

This classification is only applicable to the adsorption of a single-component gas within its condensable range of temperature.

In the text below, an introduction about the thermodynamic quantities for the processing and interpretation of adsorption isotherm is reported.

It can be supposed that the local concentration  $c = dn/dV$  of the adsorbable component decreases progressively with the increased distance  $z$  from the adsorbent surface; at distance  $z = t$  ( $t$  is the thickness of the adsorbed layer), this concentration reaches the constant value of the gas phase  $c^g$ . The volume  $V^a$  of the adsorbed layer can be expressed as

$$V^a = At \quad (\text{Eq. 4.1})$$

where  $A$  is the interfacial area. The amount adsorbed  $n^a$  in the adsorbed layer is defined as

$$n^a = \int_0^{V_a} cdV = A \int_0^t cdz \quad (\text{Eq. 4.2})$$

The total amount  $n$  of the adsorbable substance in the whole system can be divided into two contributes, the amount adsorbed and the amount remaining in the gas phase:

$$n = A \int_0^t cdz + c^g V^g \quad (\text{Eq. 4.3})$$

where  $V^g$  is the volume occupied by the gas at the concentration  $c^g$ . Therefore

$$n^a = n - c^g V^g \quad (\text{Eq. 4.4})$$

The evaluation of  $n^a$  requires the knowledge of either the exact value of  $V^g$  or of the variation of the local concentration  $c$  with respect to  $z$ , but it isn't easy to attain either of these requirements.

To resolve this problem Gibbs introduced the concept of "surface excess" to quantify the amount adsorbed. A reference system is divided into two zones by an imaginary surface, named Gibbs dividing surface (GDS), which is placed parallel to the adsorbent surface. Surface excess is the difference between the amount of a component actually present in the system and that which would be present in a reference system if the bulk concentration in the adjoining phases were maintained up to a chosen GDS, i.e. as though the interface had no effect. Schematically

$$[n_i]_{\text{surface}} = [n_i]_{\text{real}} - [n_i]_{\text{reference}} \quad (\text{Eq. 4.5})$$

where  $[n_i]_{\text{surface}} = n_i^\sigma$  is the surface excess amount of component  $i$ ,  $[n_i]_{\text{real}} = n_i$  is the total amount of that component in the real system and  $[n_i]_{\text{reference}}$  is the amount which would be present in the volume  $V^{g,\circ}$  of the reference system if the final equilibrium concentration  $c^g$  was constant up to the GDS. Thus

$$n^\sigma = n - c^g V^{g,\circ} \quad (\text{Eq. 4.6})$$

It is convenient to locate GDS exactly on the surface which is accessible, so that  $V^{g,\circ} = V^a + V^g$ . Under these conditions:

$$n^\sigma = n - c^g V^g - c^g V^a \quad (\text{Eq. 4.7})$$

Combining equation 4.7 with 4.4, it can obtain:

$$n^a = n^\sigma + c^g V^a \quad (\text{Eq. 4.8})$$

Usually in the experimental conditions the final concentration  $c^g$  of the gas is small and the volume  $V^a$  of the adsorbed layer is negligible compared with the gas volume  $V^g$ , so

$$n^a \approx n^\sigma \quad (\text{Eq. 4.9})$$

In the case of solution adsorption, the competition between solvent and solute must be considered. The adsorption of the solute at the liquid-solid interface is usually evaluated as the decrease in its concentration when kept in contact with the adsorbent. The surface excess amount  $n_i^\sigma$  is defined as

$$n_i^\sigma = n_i - c_i^l V^{l,\circ} \quad (\text{Eq. 4.10})$$

where  $n_i$  is the total amount of the component  $i$  in the system,  $c_i^l$  is its concentration in the liquid after adsorption and  $V^{l,\circ}$  is the volume of the liquid. The surface excess amount depends on the position of GDS because any displacement of the GDS normal to the surface produces a change in the volume  $V^{l,\circ}$ . To replace  $n_i^\sigma$  by a quantity invariant with respect to the position of GDS, equation 3.10 can be written for each component (1 and 2):

$$n_2^\sigma - n_1^\sigma \frac{c_2^l}{c_1^l} = n_2 - n_1 \frac{c_2^l}{c_1^l} \quad (\text{Eq. 4.11})$$

The variables both on the right and on the left side are independent of the position of GDS; variables on the right are experimental quantities while the ones on the left represent the **relative surface excess** of component 2 respect to component 1 ( $n_2^{\sigma(1)}$ ), defined as

$$n_2^{\sigma(1)} = n_2^\sigma - n_1^\sigma \frac{c_2^l}{c_1^l} \quad (\text{Eq. 4.12})$$

$$n_2^{\sigma(1)} = n_2 - n_1 \frac{c_2^l}{c_1^l} \quad (\text{Eq. 4.13})$$

The corresponding equations for the relative surface excess of the component 1 with respect the component 2 are:

$$n_1^{\sigma(2)} = n_1^\sigma - n_2^\sigma \frac{c_1^l}{c_2^l} = n_1 - n_2 \frac{c_1^l}{c_2^l} \quad (\text{Eq. 4.14})$$

The ratio of concentrations expressed as amounts per unit volume can be replaced by the ratio of molar fractions  $x_2^l/x_1^l$ ; considering that  $x_1^l=1-x_2^l$ , equations 4.11 and 4.12 can be transformed as:

$$n_2^{\sigma(1)} = n_2 - n_1 \frac{x_2^l}{x_1^l} = n^\circ \frac{\Delta x_2^l}{x_1^l} \quad (\text{Eq. 4.15})$$

where  $n^\circ = n_1+n_2$ ,  $n_2 = n^\circ x_2^{l,\circ}$  and  $\Delta x_2^l = x_2^{l,\circ} - x_2^l$  is the change due to adsorption.

Another function independent with respect the position of GDS is the reduced surface excess amount and it is derived from equation 4.10 as

$$n_2^\sigma = n_2 - V^{l,\circ} c_2^l \quad (\text{Eq. 4.16})$$

$$n^\sigma = n_2^\sigma - V^{l,\circ} c^l \quad (\text{Eq. 4.17})$$

where  $n^\sigma = n_1^\sigma + n_2^\sigma$ ,  $n^\circ = n_1 + n_2$  and  $c^l = c_1^l + c_2^l$ . Replacing  $c_2^l/c^l$  with  $x_2^l$ , the following equation is obtained:

$$n_2^\sigma - n^\sigma x_2^l = n_2 - n^\circ x_2^l = n^\circ \Delta x_2^l \quad (\text{Eq. 4.18})$$

The right side depends only on experimentally measurable quantities and not on the position of GDS: this function is defined as the reduced surface excess amount of component 2:

$$n_2^{\sigma(n)} = n_2^\sigma - n^\sigma x_2^l \quad (\text{Eq. 4.19})$$

By combining equations 4.15, 4.18 and 4.19, the relationship between the relative and the reduced surface quantities is obtained

$$n_2^{\sigma(1)} = n_2^{\sigma(n)} / x_1^l \quad (\text{Eq. 4.20})$$

The reduced surface excess amounts offer the most convenient way of reporting experimental results [1]. The quantity plotted to represent adsorption of component 2 is often in the form  $n^\circ \Delta x_2^l$ , according to equation 4.18. The isotherm obtained is generally named "composite isotherm" or "isotherm of apparent adsorption": the term



“composite” refers to the fact that the single isotherm contains information about the adsorption of both components 1 and 2. Figure 4.4 gives the two most important shapes of reduced surface excess isotherms (S-shape and U-shape) for completely miscible liquids.

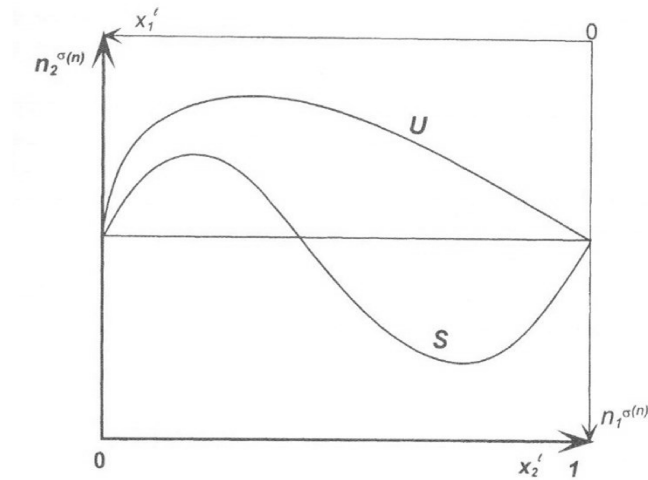


Figure 4.4 Two basic shapes of reduced surface excess isotherms: S-shaped (S) and inverted U-shaped (U) [1]

When the adsorption from dilute solutions is studied, the solvent is considered as component 1 and hence  $x_1^l = 1 - x_2^l \approx 1$ : from equations 4.15, 4.18 and 4.20

$$n_2^{\sigma(1)} \approx n_2^{\sigma(n)} \approx n_2^{\sigma} \quad (\text{Eq. 4.21})$$

Any of these quantities can be plotted to represent the adsorption data in the isotherm. Although many shapes have been distinguished, three main shapes are particularly interesting and they are represented in Figure 4.5: a L-shaped (analogous to Type I of IUPAC classification) as in the Langmuir or Tóth models, a S-shaped (analogous to Type V of IUPAC classification) as in the Moreau model, or a less common stepwise (analogous to Type VI of IUPAC classification).

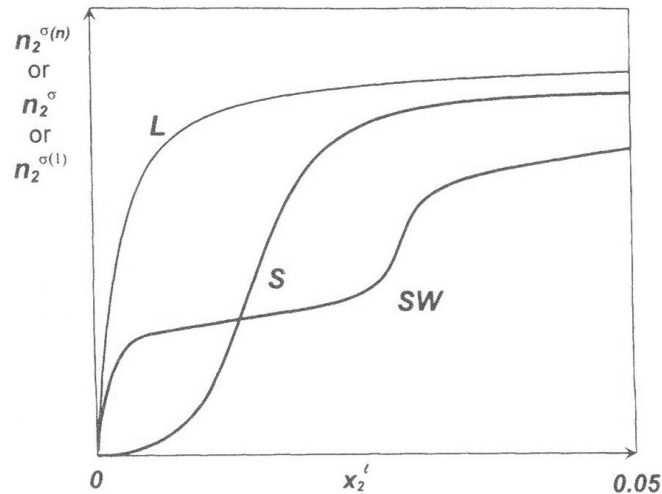


Figure 4.5 Shapes of surface excess isotherms from dilute solutions: L-shaped (L), S-shaped (S) and stepwise (SW) [1]

If higher concentrations can be attained, the reduced surface excess eventually reaches a maximum and then decreases as shown in Figure 4.4. However, if the solute solubility is low, the saturation at high concentrations cannot be determined.

#### Henry adsorption isotherm

This is the simplest adsorption isotherm model, generally used for gas – solid systems, it is expressed by the linear relationship (Eq. 4.22)

$$q = K_H * C \quad (Eq. 4.22)$$

Where  $q$  is the amount of solute adsorbed on the surface,  $C$  is the concentration (or pressure), and  $K_H$  is the Henry's adsorption constant. This model follows the Henry's law, it assumes that there is no interaction between the adsorbed molecules and that the degree of coverage of the adsorbate onto the adsorbent surface is low [2]

This linear model can be used to describe the initial part of many practical adsorption isotherms, including the Langmuir isotherm, when the low concentration range is considered.

### Langmuir isotherm model

It was originally formulated to describe gas-solid-phase adsorption onto activated carbon, it assumes monolayer adsorption that can only occur at a finite number of definite localised sites, identical and equivalent, with no lateral interaction between the adsorbed molecules.

It refers to homogeneous adsorption, and graphically is characterised by a plateau that indicates the equilibrium saturation capacity, where no further adsorption can take place.

$$q_e = \frac{q_s b C_e}{1 + b C_e} \quad (\text{Eq. 4.23})$$

Where  $q_e$  is the amount of solute adsorbed at the equilibrium ( $\text{mg g}^{-1}$ ),  $C_e$  is the equilibrium concentration ( $\text{mg L}^{-1}$ ),  $q_s$  is the saturation capacity of the adsorbent material ( $\text{mg g}^{-1}$ ) and  $b$  the adsorption constant ( $\text{L mg}^{-1}$ ).

### Freundlich isotherm model

The Freundlich isotherm equation is an empirical equation and may be derived by assuming a heterogeneous surface with adsorption on each class of sites that have obeyed the Langmuir equation [3]. The Freundlich equation is commonly used as

$$q = K C_e^{1/n} \quad (\text{Eq. 4.24})$$

where  $q$  is the adsorption capacity,  $C_e$  is the adsorption equilibrium concentration and  $K$  and  $n$  are empirical constants, which depend on the nature of adsorbent and adsorbate and on the temperature.

The Freundlich isotherm accounts for the adsorption of strongly polar compounds on polar or strongly polar adsorbents (inhomogeneous surface) in low- or medium polarity solvents, but it isn't restricted to the formation of monolayers [4]. If  $n = 1$  the adsorption is linear: this means that the adsorption sites are homogeneous in energy and no interaction take place between the adsorbed species. If  $1/n < 1$  then the sorption

capacity increases and new adsorption sites occur, reflecting favourable adsorption. When  $1/n \gg 1$ , the adsorption bond becomes weak: unfavourable adsorption takes place, due to the decrease in adsorption capacity [5]

Toth isotherm model

The Tóth isotherm [3] was originally derived for the study of gas-solid equilibria, however, like the Langmuir isotherm model, it can be extended to the description of liquid-solid system. The Tóth isotherm accounts for adsorption on a heterogeneous surface, with no adsorbate-adsorbate interactions. The equation of the Tóth isotherm is:

$$q_e = \frac{q_s K_T C_e}{[1+(K_T C_e)^u]^{1/u}} \quad (\text{Eq. 4.25})$$

Where,  $q_e$  is the amount of solute adsorbed at the equilibrium ( $\text{mg g}^{-1}$ ),  $q_s$  is the saturation capacity,  $K_T$  the affinity constant, and  $u$  represents the heterogeneity parameter.

Brunauer – Emmett – Teller (BET) isotherm model

This theoretical model, widely used in the gas – solid equilibrium systems, was developed for multilayer adsorption, that is, solute molecules can be adsorbed either on the bare surface of the adsorbent material or on a layer of solute already adsorbed. The BET model is expressed by the following equation:

$$q_e = \frac{q_s C_{BET} C_e}{(C_s - C_e)[1+(C_{BET}-1)(C_e/C_s)]} \quad (\text{Eq. 4.26})$$

Where  $q_e$  is the amount of solute adsorbed at the equilibrium ( $\text{mg g}^{-1}$ ),  $C_e$  is the equilibrium concentration ( $\text{mg L}^{-1}$ ),  $q_s$  is the theoretical saturation capacity ( $\text{mg g}^{-1}$ ),  $C_{BET}$  the BET adsorption constant ( $\text{L mg}^{-1}$ ), and  $C_s$  the adsorbate monolayer saturation concentration ( $\text{mg L}^{-1}$ ) [6].

## 4.2 Adsorption kinetics

The adsorption of a solute onto an adsorbent material is a time-dependent process. Since the adsorption is a phenomenon important in many systems, it is necessary to evaluate the rate of this process in order to compare the performances of different adsorbents and to optimise the adsorption process itself. For these reasons, it is useful to recognise the adsorption kinetics and to determine the phenomenological coefficients which characterise the transport of the adsorbate molecules within the adsorbents [7].

The adsorption mechanism can be well described in four steps as indicated below:

1. transport of solute in the bulk solution.
2. diffusion of solute through the liquid film surrounding the adsorbent particles;
3. diffusion of solute in the pores of the sorbent (intraparticle diffusion);
4. chemical reaction as adsorption and desorption on the solid surface.

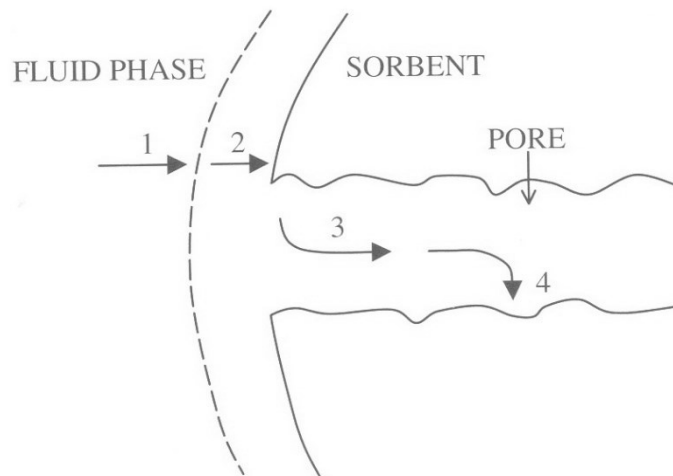


Figure 4.6 Representation of adsorption mechanism [8]

The overall rate of the sorption process may be controlled by any of these steps or in some cases by combination of two steps. Various kinetic models have been used for solid/solution adsorption batch systems. For example, Langmuir, statistical rate theory (SRT), pseudo first-order (PFO), pseudo second order (PSO), Elovich and intraparticle diffusion model (IDM) are the most well-known sorption kinetic models. Among the

mentioned equations, the intraparticle diffusion model is applicable when the rate determining step is the mass transfer of adsorbate to the solid surface sites (step 3), whereas the other ones are used for description of adsorption kinetics when the overall sorption rate is controlled by the rate of surface reaction (step 4) [9].

Rudzinski et al. [10] demonstrated that the common pseudo-first and the pseudo-second order kinetic equations are only simplified forms of a more general kinetic equation. One possible form of such general equation has been developed by applying the new approach to the rate of interfacial transport, called the Statistical Rate Theory.

The empirical kinetic equation proposed by Lagergren in 1898 [11] is still the most widely used rate equation for sorption of a solute from a liquid solution [10]:

$$\frac{dN_t}{dt} = k_1 (N^{(e)} - N_t) \quad (\text{Eq. 4.27})$$

where  $N_t$  is the amount of the solute adsorbed at a time  $t$ ,  $k_1$  and  $N^{(e)}$  are some constants. They can be easily found from the following linear regression of experimental data:

$$\ln(N^{(e)} - N_t) = \ln N^{(e)} - k_1 t \quad (\text{Eq. 4.28})$$

which represents the integral form of equation 4.27, corresponding to the boundary condition  $N_t(t=0) = 0$ . According to the commonly accepted interpretation,  $k_1$  is the pseudo-first order constant and  $N^{(e)}$  should be the amount adsorbed at equilibrium. This makes equation 4.27 a “pseudo-first order” equation, by comparison with the kinetic adsorption term of the “true” first-order equation in which  $N^{(e)}$  is the maximum amount that can be adsorbed.

By comparison with the adsorption term of the true first-order process, the form of equation 4.27 seemed to suggest a one-site-occupancy adsorption when the adsorbing molecule reacts with one adsorption site. Thus, it seemed natural to propose that in the case of two-site occupancy adsorption, i.e., when the solute molecule reacts with two adsorption sites, the rate of adsorption should be given by the following:

$$\frac{dN_t}{dt} = k_2 (N^{(e)} - N_t)^2 \quad (\text{Eq. 4.29})$$

Equation 4.29 has commonly been called the “pseudo-second-order rate equation” [[12]; [7]]. The integral form of this equation, obtained with the boundary condition  $N_t(t=0) = 0$ , can be written as:

$$\frac{t}{N_t} = \frac{1}{N^{(e)}} t + \frac{1}{k_2 (N^{(e)})^2} \quad (\text{Eq. 4.30})$$

The equation is usually applied for kinetic data by plotting of  $t/N_t$  versus  $t$ : a linear relationship should be obtained where  $1/N^{(e)}$  and  $1/k_2(N^{(e)})^2$  are the slope and the intercept, respectively.

However, it should be emphasized that both equations 4.27 and 4.29 are essentially empirical equations; Rudzinski et al., [10] assumed these equations are simplified forms of another rate equation, hence they searched for a more general rate equation having a well-established theoretical background, applying this to the Statistical Rate Theory of Interfacial Transport (SRT).

If the transport of molecules between two neighbouring phases through their phase boundary results primarily from single molecular events, the rate of molecular transport  $R_{12}$  between two phases 1 and 2 is expressed as

$$R_{12} = R_e \left[ \exp\left(\frac{\mu_1 - \mu_2}{kT}\right) - \exp\left(\frac{\mu_2 - \mu_1}{kT}\right) \right] \quad (\text{Eq. 4.31})$$

where  $\mu_1$  and  $\mu_2$  are the chemical potentials of the molecules in phases 1 and 2 at non-equilibrium conditions and  $R_e$  is the exchange rate at equilibrium to which the system would evolve after being closed and equilibrated. The new SRT approach may also explain the successful application of the empirical Lagergren equation for describing adsorption kinetics at the solid/solution interfaces. As the Lagergren kinetic equation has always been associated with the model of one-site-occupancy adsorption, Rudzinski et al. [10] accepted the Langmuir adsorption model in their theoretical investigation. Thus, they assumed that the chemical potential of the solute molecules adsorbed on a solid surface  $\mu_s$  can be expressed as:

$$\mu_s = kT \ln \frac{\Theta}{1 - \Theta} - kT \ln q_s \quad (\text{Eq. 4.32})$$

where  $\Theta = N_t/N_m$  and  $q_s$  is the molecular partition function of the adsorbed solute molecule. In equation 4.32,  $N_m$  is the maximum amount that can be adsorbed, usually called the adsorption capacity. In terms of the Langmuir model, this is the total number of the adsorption sites on the surface, available for adsorption of solute molecules. For the chemical potential of the solute molecules in the bulk solution  $\mu_b$ , the following expression was assumed:

$$\mu_b = \mu_b^\circ + kT \ln c \quad (\text{Eq. 4.33})$$

where  $c$  is the bulk solution concentration. equations 4.32 and 4.33 lead to the Langmuir adsorption isotherm at equilibrium (see equation 4.23):

$$\Theta^{(e)} = \frac{K_L c^{(e)}}{1 + K_L c^{(e)}} \quad (\text{Eq. 4.34})$$

where

$$K_L = q_s \exp\left(\frac{\mu_b^\circ}{kT}\right) \quad (\text{Eq. 4.35})$$

and the superscript <sup>(e)</sup> will always denote equilibrium conditions. The corresponding SRT expression for the adsorption kinetics is

$$\frac{d\Theta}{dt} = K_{is}' \left[ \exp\left(\frac{\mu_b - \mu_s}{kT}\right) - \exp\left(\frac{\mu_s - \mu_b}{kT}\right) \right] \quad (\text{Eq. 4.36})$$

in which  $K_{is}'$  is the rate of adsorption at equilibrium. In the Langmuir model of adsorption,  $K_{is}'$  is proportional to the frequency of the collisions of the solute molecules with the surface and to the number of the free molecules available for the adsorption sites ( $1 - \Theta^{(e)}$ ). Thus,  $K_{is}'$  can be written as:

$$K_{is}' = K_{is} c^{(e)} (1 - \Theta^{(e)}) \quad (\text{Eq. 4.37})$$

While assuming that the rate of desorption is proportional to  $\Theta^{(e)}$ , the Langmuir isotherm (equation 4.34) is again obtained. The classical kinetic equation of the fundamental TAAD approach (Theory of Activated Adsorption/Desorption), used throughout the last 20<sup>th</sup> century, is:

$$\frac{d\Theta}{dt} = K_a c (1 - \Theta)^s - K_d \Theta^s \quad (\text{Eq. 4.38})$$



where  $s$  is the number of sites occupied by one adsorbed molecule,  $K_a$  and  $K_d$  are temperature-dependent constants. From equation 4.38 one can arrive either at Lagergren ( $s = 1$ ), or at pseudo-second-order equation ( $s = 2$ ) by neglecting the desorption term in that fundamental TAAD equation, and yet defining  $\Theta$  as an “efficient” surface coverage equal to  $N_t/N^{(e)}$ .

The experiments show that the coefficients  $k_1$  and  $k_2$  in the empirical equations 4.28 and 4.30 depend, for instance, on the initial concentration but there is no theoretical explanation for that. The SRT equation explains it because  $c^{(e)}$  and the total adsorption coverage  $\Theta_t^{(e)}$  depend on the amount of solid adsorbent, the volume of the solute solution, and its initial concentration. There, we studied, for instance the case of “volume dominated” systems, when the amount of the bulk molecules dominates the amount of adsorbed molecules in experiment to such an extent that the bulk concentration is essentially unchanged during the kinetic experiment. In our case, it means that the concentration  $c$  can be identified with the equilibrium concentration  $c^{(e)}$ .

After several calculations reported in [10], the following equation is obtained:

$$\frac{d\Theta_t}{dt} = K_b c^{(e)} (1 - \Theta_t^{(e)} c^{(e)}) \left[ \exp\left(\frac{(\Theta_t^{(e)} - \Theta_t)(\varepsilon_m - \varepsilon_l)}{kT}\right) - \exp\left(-\frac{(\Theta_t^{(e)} - \Theta_t)(\varepsilon_m - \varepsilon_l)}{kT}\right) \right] \quad (Eq. 4.39)$$

where  $\varepsilon$  is the energy of adsorption.

The applicability of the Lagergren (equation 4.27) would suggest that  $d\Theta_t/dt$  is proportional to the difference  $(\Theta_t^{(e)} - \Theta_t)$ . So, it is possible to expand the exponents within the square bracket into Taylor series around  $\Theta_t = \Theta_t^{(e)}$ . With this assumption, the terms of order  $\geq 3$  are very small and, therefore, can be neglected. Now the pseudo-first order constant  $k_1$  is defined as:

$$k_1 = \frac{2K_b c^{(e)} (1 - \Theta_t^{(e)}) (\varepsilon_m - \varepsilon_l)}{kT} \quad (Eq. 4.40)$$

The SRT approach shows that the empirical Lagergren kinetic equations should apply best in the case of “volume dominated” kinetic experiments. When noticeable changes of the bulk concentration will be observed during a kinetic experiment, then deviations from the pseudo-first order Lagergren equation are to be expected.

In the cases where change of adsorbate concentration is noticeable, the terms of order  $\geq 3$  of Taylor expansions cannot be all neglected and other calculations leads to the pseudo-second order kinetic (equation 4.29): the pseudo-second order rate equation is just an intuitive generalization of the Lagergren equation.

Model investigations based on the general kinetic equations show that deviations of the observed kinetics from the behaviour predicted by the pseudo-first and the pseudo-second-order kinetic equations may be due to the approximate character of these equations.

### 4.3 References

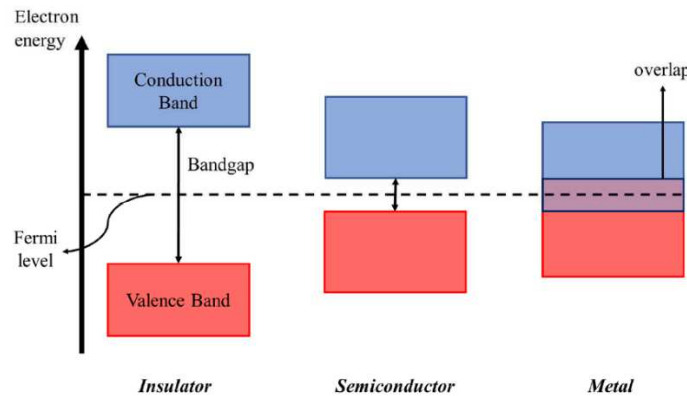
- [1] R. J. , S. K. Rouquerol F., "Adsorption by powders & porous solid. Principles, methodology and applications," *Academic Press* .
- [2] M. Silva Da Rocha, K. Iha, A. C. Faleiros, E. J. Corat, and M. Encarnación Vázquez Suárez-Iha, "Henry's Law as a Limit for an Isotherm Model Based on a Statistical Mechanics Approach," 1998.
- [3] J. Tòth, "State equations of the solid gas interface layer," *Acta Chimica Academiae Scientiarum Hungaricae*, vol. 69, pp. 311–317, 1971.
- [4] F. A. , S. D. G. , K. A. M. Guiochon G., *Fundamentals of Preparative and Nonlinear Chromatography*. 2006.
- [5] A. S. Özcan, B. Erdem, and A. Özcan, "Adsorption of Acid Blue 193 from aqueous solutions onto Na-bentonite and DTMA-bentonite," *Journal of Colloid and Interface Science*, vol. 280, no. 1, pp. 44–54, Dec. 2004, doi: 10.1016/j.jcis.2004.07.035.
- [6] K. Y. Foo and B. H. Hameed, "Insights into the modeling of adsorption isotherm systems," *Chemical Engineering Journal*, vol. 156, no. 1. pp. 2–10, Jan. 01, 2010. doi: 10.1016/j.cej.2009.09.013.
- [7] S. Azizian, "Kinetic models of sorption: A theoretical analysis," *Journal of Colloid and Interface Science*, vol. 276, no. 1, pp. 47–52, Aug. 2004, doi: 10.1016/j.jcis.2004.03.048.
- [8] T. P. A. Noble R.D., *Principles of chemical separations with environmental applications*.
- [9] M. Haerifar and S. Azizian, "Mixed surface reaction and diffusion-controlled kinetic model for adsorption at the solid/solution interface," *Journal of Physical Chemistry C*, vol. 117, no. 16, pp. 8310–8317, Apr. 2013, doi: 10.1021/jp401571m.
- [10] W. Rudzinski and W. Plazinski, "Kinetics of solute adsorption at solid/solution interfaces: A theoretical development of the empirical pseudo-first and pseudo-second order kinetic rate equations, based on applying the statistical rate theory of interfacial transport," *Journal of Physical Chemistry B*, vol. 110, no. 33, pp. 16514–16525, Aug. 2006, doi: 10.1021/jp061779n.
- [11] S. Lagergren, "Zur Theorie der Sogenannten Adsorption Gelöster Stoffe," *Kungliga Svenska Vetenskapsakademiens*, vol. 24, pp. 1–39, 1898.
- [12] G. Blanchard, M. Maunaye, and G. Martin, "REMOVAL OF HEAVY METALS FROM WATERS BY MEANS OF NATURAL ZEOLITES," 1984.

## 5 Semiconductors and photocatalysis

### 5.1 Band theory and electronic band structure of a solid

The electrons of a single, isolated atom occupy atomic orbitals, each of which has a discrete energy level (allowable state the electron may assume), according to the four-quantum number: the principal quantum number ( $n$ ), the orbital angular momentum quantum number ( $l$ ), the magnetic quantum number ( $m_l$ ) and the electron spin quantum number ( $m_s$ ). When atomic orbitals are combined together, their interaction will lead to a splitting in energy of each orbital. The resulting molecular orbitals (MOs) can be bonding MOs, full of electrons, if the bonding interaction between atomic orbitals brings to a constructive interaction that lowers the original orbitals energy, or antibonding MOs, empty, if the bonding interaction between atomic orbitals brings to a destructive interaction that raises the original orbitals energy. Due to the essentially infinite number of atoms and the consequential numbers of interacting orbitals that must be considered in a solid, the spacing of electronic energies becomes so small that they can be considered as a continuum of energy levels and the electronic structure of the solid could be discussed in terms of energy band. Therefore, the allowed bonding and antibonding electronic energies fall into different energy bands of closely spaced levels, where each band is separated by forbidden band-gaps.[1] The width of the band depends on the overlap of the orbitals involved, thus for deep levels the broadening is small, and they retain their atomic shell-like character, instead the broadening for the higher levels is so large that the  $s$ -,  $p$ - and where present,  $d$ -levels merge into a single band. The energy levels of interest are the “Highest Occupied” and the “Lowest Unoccupied”, respectively called the valence band (VB) and the conduction band (CB) according to the solid Band Theory (figure 5.1). The difference between the upper edge of the VB and the lower edge of the CB is the energy gap ( $E_g$ ), that determines the properties of the material. In an insulator the valence band is full, the conduction band is empty and a large amount of energy is required to shift electrons from the first to the second, so no net motion of charges results from the application of an electric field. In a conductor the uppermost energy band containing electrons is only partially filled, or a filled band overlaps an empty band. In this case many electrons are free to move and the current flows easily.

In a semiconductor the band gap is smaller than in an insulator and electrons can be thermally or optically promoted to the CB, while holes remain into the VB, resulting in electrical conductivity values in between those of metals and insulators, because semiconductors have comparatively less free charge carriers than the conductors.



**Figure 5.1** Representation of CB and VB in terms of band theory for a conductor (metal), a semiconductor and an insulator

The entity of the energy gap is determined essentially by the degree of overlap between the atomic orbitals involved. For metal oxides, the valence band derives from the filled 2p orbitals of  $O_2^-$ , while the conduction band results from the empty nd (n from 3 to 5) orbitals of the metal. In general, semiconductors have band gaps that range from 0.3 to 3.5 eV.

An important concept that is needed to describe the properties of a semiconductor is the electrochemical potential, or Fermi level ( $E_F$ ). The Fermi-Dirac distribution is (equation 5.1):

$$f(E) = \frac{1}{1 + e^{\frac{(E-E_F)}{kT}}} \quad Eq. 5.1$$

Where,  $f(E)$  is the probability to occupy a state with energy E,  $E_F$  is the Fermi Energy, k is the Boltzmann's constant and T is the absolute temperature. From this equation it can be noted that when E is equal to  $E_F$  and  $T > 0$ ,  $f(E)$  becomes  $\frac{1}{2}$ , so the Fermi level is a virtual energy level (there are no actual electronic states at this energy) that has the 50% of probability to be occupied by electrons.[2]

Furthermore, at absolute zero, the probability of finding an electron would go from 1 in the valence band to 0 in the conduction band.

From the electrochemical point of view the Fermi energy is the electrochemical potential of electrons in the solid, and could be defined with equation 5.2 valid for an intrinsic semiconductor (when under thermal equilibrium the number of electrons equals the number of holes):

$$E_F = \frac{E_c + E_v}{2} + \frac{kT}{2} \ln \frac{N_v}{N_c} \quad \text{Eq. 5.2}$$

Where  $N_v$  represents the effective density of VB levels with  $E_v$  energy and  $N_c$  is the effective density of CB levels with  $E_c$  energy.

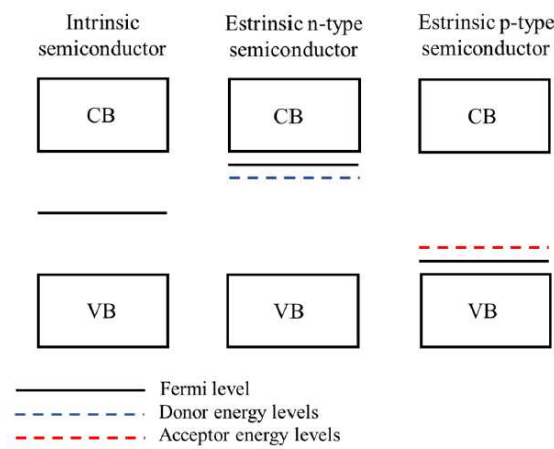
When a semiconductor gets in contact with a solution containing redox species, these two phases start to exchange electrons until the fermi level of the semiconductor will be equal to the electrochemical potential of the electrolyte phase (herein represented by the redox potential of the couple  $A/A^-$ ), described quantitatively by the Nernst equation:

$$\mu\left(\frac{A}{A^-}\right) = \mu^0\left(\frac{A}{A^-}\right) + RT \ln \frac{[A]}{[A^-]} \quad \text{Eq. 5.3}$$

In equation 5.3,  $\mu\left(\frac{A}{A^-}\right)$  is the actual electrochemical potential of the solution,  $\mu^0\left(\frac{A}{A^-}\right)$  is the formal electrochemical potential of the redox couple  $\left(\frac{A}{A^-}\right)$ ,  $R$  is the gas constant ( $8.315 \text{ J K}^{-1} \text{ mol}^{-1}$ ), and  $[A]$  and  $[A^-]$  are respectively the concentrations of the acceptor and donor species. The semiconductor lattice almost always presents impurity concentrations, in the order of 1 part per billion, due to oxygen vacancies in oxides, surface states where the physical contiguity of the atoms ceases, or the intentional introduction of foreign elements in the crystal lattice. The presence of electron-rich or electron-deficient atoms and defects in the lattice brings to the formation of ionizable levels, energetically near to the conduction band, in the first case, or to the valence band in the second.

Thus, the Fermi level position of the semiconductor will be shifted from mid-gap (figure 5.2): if donors (D) are present, the Fermi level will move closer to the CB (it will become more negative on the electrochemical potential scale), instead, if there are several acceptors, the Fermi level will shift nearby the VB (it will become more positive).

Thermal excitation of electrons from the donor band to the CB results in an excess of negative moving carriers ( $e^-$ ) that improve the conductivity of the material, while ionized donors ( $N_D^+$ ) are formed. The probability ( $N_D^+/N_D$ ) of the above mentioned process to take place depends on the Boltzmann distribution,  $N_D^+ = N_D \exp(-\Delta E/kT)$ , where  $\Delta E$  is the energetic difference between the CB and donor levels. Such semiconductors are known as n-type. A similar description could be used to explain the behavior of p-type semiconductors, in which the thermal excitation of electrons from the VB to the acceptor band leads to an excess of positive moving carriers (holes,  $h^+$ ) that increase the conductivity of the material, in the same way electrons do for n-type semiconductors.



**Figure 5.2** Band gap structure of intrinsic, n-type and p-type semiconductors.

In the dark, and in thermal equilibrium conditions, the electron's electrochemical potential ( $\mu_{e^-}$ ) is equal to the hole's one ( $\mu_{h^+}$ ), both corresponding to the Fermi level of the solid (equation 5.4 and 5.5).

$$Ef = \mu_{e^-} = E_c + kT \ln \frac{n}{N_c} \quad (Eq. 5.4)$$

$$Ef = \mu_{h^+} = E_v - kT \ln \frac{p}{N_v} \quad (Eq. 5.5)$$

The electron density  $n$  in the CB and the hole density  $p$  in the VB can be derived from the previous equations:

$$n = N_c \exp\left[-\frac{(E_c - Ef)}{kT}\right] \quad (Eq. 5.6)$$

$$p = N_v \exp\left[-\frac{(E_f - E_v)}{kT}\right] \quad (\text{Eq. 5.7})$$

## 5.2 Electrochemistry of semiconductor electrolyte interface

When a semiconducting is brought into contact with an electrolyte solution in dark conditions, a charge transfer at the semiconductor-electrolyte interface occurs until the electrochemical potential gets the same value throughout the system. The resulting flow of current through the junction continues as long as a potential difference is established at the interface. In the simplest case, ignoring the adsorption of ions or other molecules on the surface of the semiconductor, and any electrostatic interaction that can determine contact potentials between the two phases, the potential difference is:

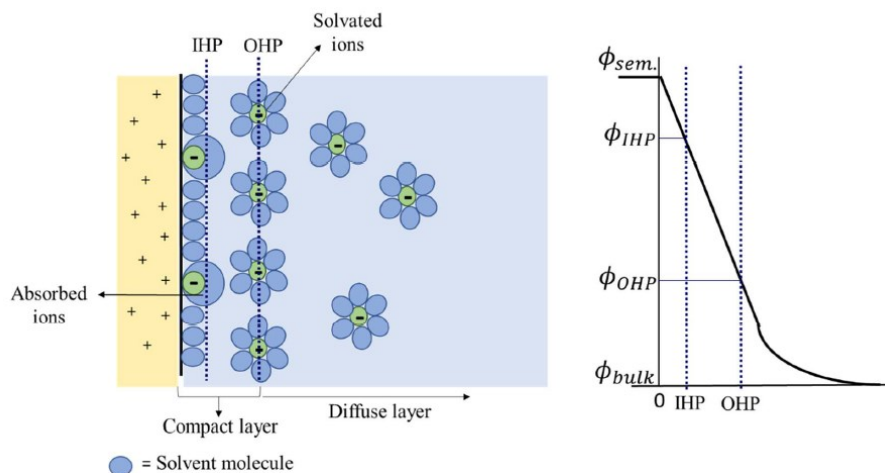
$$\mu_{e^- \text{-semiconductor}} - \mu_{e^- \text{-redox}} = eU \quad (\text{Eq. 5.8})$$

Where  $e$  is the electron charge and  $U$  is the potential difference between the two phases. The direction of the electronic flux depends on the relative potential position in the two phases. Electrons are transferred from the semiconductor to the solution if the semiconductor  $E_f$  is more negative than the electrolyte electrochemical potential; usually this situation occurs in an n-type semiconductor. In p-type semiconductors the inverse situation, where the  $E_f$  has a higher value than the electrolyte electrochemical potential, is more common, and electrolytes give electrons to the semiconductor. Despite the exchange of charges takes place in both phases, only the semiconductor Fermi level will shift in energy because the semiconductor density of charge carriers (about  $10^{15}$ - $10^{16}$  e<sup>-</sup>/cm<sup>3</sup>) is about  $10^7$  times lower than the concentration of redox species in solution (esteemed to be  $10^{22}$  particles/lit, considering a concentration of 0.1 M)[1]. The simplest way to describe what happens at the interface is in terms of “electric double layer”, consisting of a sheet of positive charges at the surface of the semiconductor and a sheet of negative charges (ions) next to the solution, or vice versa. An adsorbed layer of water molecules at the interface separates hydrated ions from the solid surface. The interfacial electric double layer can be explained in terms of a parallel plate condenser. At the interface charge neutrality occurs as  $q_s = q_{el}$  where  $q_s$  and  $q_{el}$  are respectively the charges near the semiconductor and electrolyte side of the interface.



This description can be extended considering that, during the equilibration between the semiconductor's and the electrolyte's Fermi levels, the semiconductor will be depleted of its majority charge carriers to a certain extent far from the surface and that ions will be distributed away from the plane of the closest approach of hydrated ions towards the bulk solution. On the solution side, when a semiconductor is brought in contact with an electrolyte solution, counterions are attracted towards charged surface in order to form a sheath, called the Helmholtz plane.

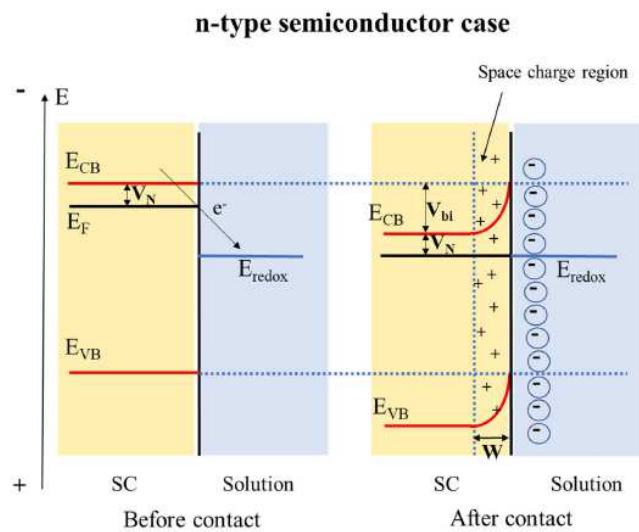
The inner part of the Helmholtz plane (IHP) is composed by solvent molecules and partially solvated ions absorbed on the material surface, while solvated ions form the outer Helmholtz plane (OHP) (see figure 5.3). Between the inner and outer Helmholtz layers a linear potential drop occurs. The values of this potential difference are not high, but the electrical potential gradient is still very intense because the interface thickness is extremely small. According to the Stern model, over the compact Helmholtz plane there is a diffused layer formed as a result of opposing tendencies of attractive coulombic forces and disordered thermal fluctuations, where the potential decays exponentially. If the electrolytes concentration is sufficiently high, the diffused layer reduces its thickness until it collapses on the OHP. Thus, in first approximation, in electrolytic solutions where the electrolyte concentration is higher than 0.1 M, the potential drop between the OHP and the solid surface occurs linearly.



**Figure 5.3** Scheme of the semiconductor-electrolyte interface and associated potential trend

On the semiconductor side, a diffuse layer of minority charge excess (ionized donors  $N_D^+$  or acceptor  $N_A^-$ ), called the space charge layer ( $W$ ), is formed (figure 5.4).

Examining the case of an n-type semiconductor, it is necessary to spend work to bring an electron from the bulk to the surface, due to the repulsive interaction with the attracted negative ions in solution. The potential barrier that must be overcome to get a charge transfer between the semiconductor and the electrolyte phase is called barrier height energy ( $\phi_b$ ) of the junction and is the sum of: I) the difference in the semiconductor electrostatic potential resulting from the formation of the junction, called built-in voltage ( $V_{bi}$ ); II) the difference between the semiconductor Fermi level and the conduction band edge ( $V_N$ ) (figure 5.4).



**Figure 5.4** Scheme representing the formation of the electric double layer in a n-type semiconductor.

If the charge density  $\rho$  in the semiconductor space charge layer is considered constant, then  $\rho = eN_D^+$  and it's possible to obtain the expression for both the electric field (equation 5.9) and the potential (equation 5.10) generated in the junction:

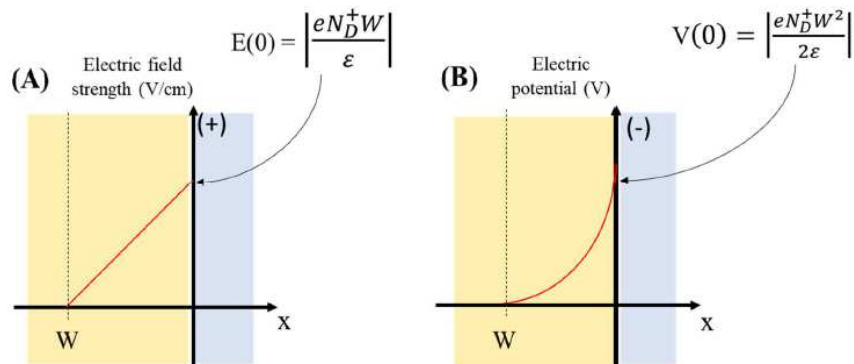
$$E(x) = \frac{eN_D^+}{\epsilon} (x - W) \quad (\text{Eq. 5.9})$$

$$V(x) = -\frac{eN_D^+}{2\epsilon} (x - W)^2 \quad (\text{Eq. 5.10})$$

Where  $\epsilon$  is the relative dielectric constant of the material,  $e$  is the electronic charge,  $N_D^+$  represents the donor density,  $x$  is the charge position compared to the surface ( $0 \leq x \leq W$ ).

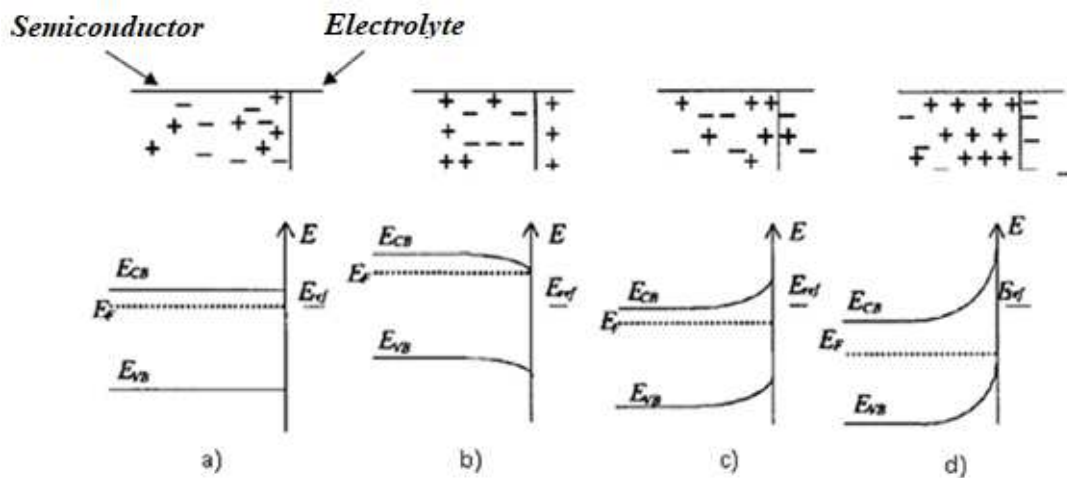
The electric field  $E(x)$  and the potential  $-V(x)$  increase moving from the bulk ( $x=W$ ) to the surface ( $x=0$ ), where both reach their maximum (figure 5.5), given by equation 5.11:

$$|V_{max}| = V_{ib} = \left| \frac{eN_D^+ W^2}{2\epsilon} \right| \quad (\text{Eq. 5.11})$$



**Figure 5.5** Electric field  $E(x)$  and potential  $-V(x)$  in an n-type semiconductor space charge layer

The semiconductor band edge pinning depends on the value of the ionic charge sign in the electrolytic solution and can be controlled by the application of an external bias or changing the energetics of the redox pair in solution [1], [3], [4]. Still considering a n-type semiconductor, four different situations can take place, as shown in figure 5.6:



**Figure 5.6** Development of the space charge region in the n-type semiconductor-electrolyte interface: a) flat band situation; b) enrichment layer; c) depletion layer; d) inversion layer

The potential at which there is no space charge region in the semiconductor is called the flat band potential ( $E_{fb}$ ). With good approximation, the flat band potential can be considered equal to the Fermi level, which in turn approximates the conduction band edge in a n-type semiconductor and the valence band edge in a p-type semiconductor (figure 5.6a). If the surface of semiconductor is enriched with majority carriers (electrons for a n-type and holes for a p-type semiconductor), an enrichment (also called accumulation) layer arises (figure 5.6b). This situation can be also obtained with the

application of an external high negative potential in n-type semiconductor, or a high positive potential in the p-type case. The depletion layer (figure 5.6c) is given by the ionized donors (or acceptors) formed after the charge transfer between the solution and the semiconductor. The electron transfer continues until the surface ionized donors (or acceptors) concentration is less than the intrinsic level. When the surface region is enriched with minority carriers so that their contribution to the space charge exceeds the contribution from majority carriers (in the bulk), the n-type semiconductor changes its surface behaviour acting like a p-type. In n-type semiconductor the inversion layer (figure 5.6d) is reached thanks to the application of extremely high positive potential that empties not only the conduction band, but also (partially) the valence band. For p-type semiconductors a very high negative potential must be applied.

The properties of the current-voltage (I-V) behavior of a semiconductor can be examined commenting the equation 5.12:

$$I = -I_0 \left[ \exp\left(-\frac{eV}{kT}\right) - 1 \right] \quad (\text{Eq. 5.12})$$

Where, V is the external applied potential and  $I_0$  is the value of current, called exchange current, present at equilibrium, that is dependent on the material characteristic and the redox couple. Equation 5.12 predicts that for  $V < 0$  (forward bias) the current is exponentially dependent on the voltage but essentially independent from it when  $V > 0$  (reverse bias). The current-voltage characteristic described by equation 2.12, where the current flow predominates in one direction under an applied bias, is called rectification and it is a typical characteristic of an electrical diode. Therefore, the equation is generally called diode equation.

### 5.3 Semiconductor-electrolyte interface under illumination

Under illumination, the semiconductor can absorb a photon with an energy greater than, or equal to its energy gap. This energy is used to promote an electron from the VB to the CB, leaving a hole in the VB. It is possible to define different electrochemical potentials, called quasi-Fermi levels, for the photogenerated electrons and holes (figure 5.7b), described by equations 5.13 and 5.14, where  $n^*$  and  $p^*$  are the carriers concentration under illumination.

$$\mu_{e-} = E_C + kT \ln \frac{n^*}{N_C} \quad (\text{Eq. 5.13})$$

$$\mu_{h+} = E_V + kT \ln \frac{p^*}{N_V} \quad (\text{Eq. 5.14})$$

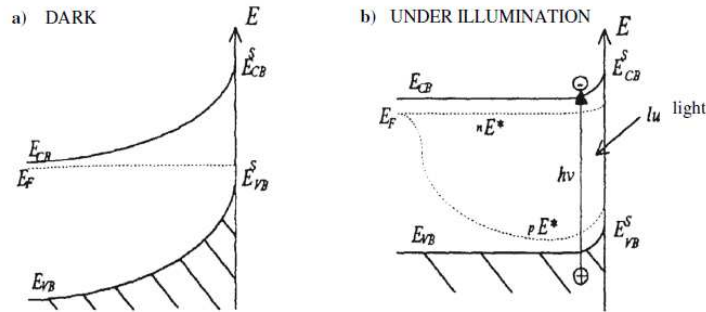


Figure 5.7 a) Fermi and b) quasi fermi levels of an n-type semiconductor

Light intensity and absorption properties of the material affect the quasi-Fermi levels. In an n-type semiconductor, for example, the electron quasi-Fermi level stays close to the original Fermi level because  $n^* = \Delta n + n_0 \sim n_0$ , since the concentration of photogenerated electrons ( $\Delta n$ ) is small compared to the thermally ionized one  $n_0$ . Instead, the hole quasi-Fermi level shift is considerable, due to the consistent growth of holes concentration under light compared to the one in the dark. The photogenerated electrons and holes can move towards the semiconductor in opposite directions under the electric field in the space charge layer[4]. If a depletion layer occurs, the minority carriers will travel toward the surface, where they participate in charge transfer reactions, while the majority carriers will move to the bulk. This flow of carriers provides a photocurrent. Such a migration induces also an inverse potential in the semiconductor, called photopotential ( $\Delta E_{ph}$ ) which reduces the potential drop across the space charge layer. When the  $\Delta E_{ph}$  equals the difference between the semiconductor dark potential and the  $E_{fb}$ , the band bending disappears, and an applied potential is needed to achieve photocurrent. To describe the current-voltage behaviour under light condition is convenient the partition of the current into two separate components: one that originates from majority carriers and one from minority carriers. The concentration of photogenerated majority carriers is usually small compared to that present from the thermal ionization of dopants atoms, so they should exhibit a I-V characteristic that is well described by the diode equation. On the other hand, illumination generally produces a substantial change in the concentration of minority carriers. If the electric

field is so strong that essentially all the photogenerated minority carriers are separated and then collected, the minority carrier current is approximately equal to  $I_{ph}$  (the photon flux absorbed by the semiconductor multiplied by the charge on an electron  $e$ ). The net current could be obtained by adding together, with the appropriate sign, the majority and minority carrier components:

$$I = I_{ph} - I_0 \left[ \exp\left(-\frac{eV}{kT}\right) - 1 \right] \quad (\text{Eq. 5.14})$$

The equation 5.14 is the diode curve of equation 5.12, offset by a constant amount,  $I_{ph}$ , over the voltage range of interest.

## 5.4 Photocatalysis

Photocatalysis is the acceleration of a photoreaction in the presence of a catalyst. In photocatalysis electrons are excited by the energy supplied by the incident photons; mobile electron / hole pairs are produced which make the semiconductor active to catalyze reactions on its surface. The water splitting, using solar energy, is a particularly interesting reaction to photo-produce Hydrogen, which in this way could thus be considered as an inexhaustible fuel source. The water splitting semi-reactions for water reduction (5.15) and oxidation (5.16) are:



Water reduction is a relatively fast reaction on several metals of the transition series, like Ni, Pt, Rh etc., usually requiring two reaction steps, whereas water oxidation is more complex because it needs the removal of four electrons and four protons to take place. The mechanism proposed for the water oxidation process may involve a concerted reaction to four electrons, or multiple steps from two to three electrons. For metal oxide semiconductors with wide band gap, the mechanism involves the formation of the hydroxyl radical intermediate which requires a potential of 2.85 V:



In order for hydrogen production to occur without an applied bias, the potential of the photogenerated electrons must be more negative than the  $\text{H}^+/\text{H}_2$  reduction potential and the potential of photogenerated holes must be more positive than  $\text{O}_2/\text{H}_2\text{O}$  oxidation

potential. This situation is not verified for many of the most common metal oxides able to absorb visible light. Indeed, many of them display a band gap greater than 2.3 eV, ideally suitable for the splitting of water with a single photon, but they do not possess a sufficiently negative conduction band to support the unassisted production of hydrogen (e.g.  $\text{WO}_3$  in figure 5.10)

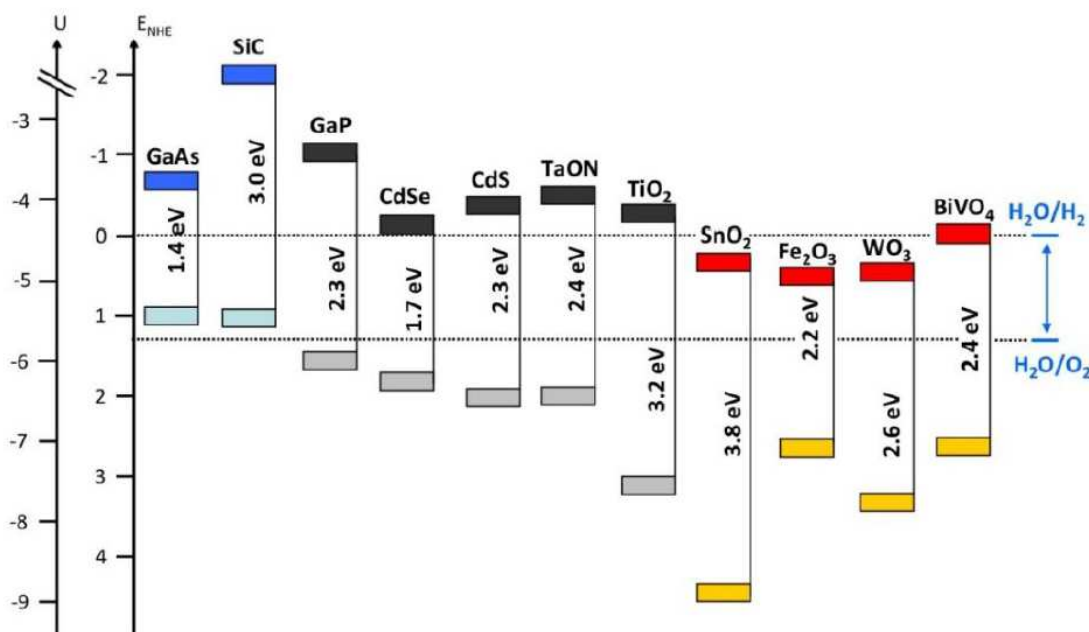


Figure 5.10 Band-gap and valence levels of some semiconductors at pH=0

## 5.5 Photocatalysts based on heteropolytungstates

Polyoxotungstates (POTs) are tungsten oxygen anion clusters of nanometric size characterized by a wide variety of structures [5]. Generally speaking, POTs can be divided into two main groups: isopolytungstates, constituted only by W and O atoms, and heteropolytungstates where a heteroatom ( $X = \text{Si}, \text{P}, \text{S}, \text{Ge}, \text{etc.}$ ) different from W and O is also present. The most important isopolytungstate is decatungstate anion that is viewed as the union of two  $\text{W}_5\text{O}_{18}$  units, bonded through shared oxygen in vertices with internal empty space. Each subunit is made up of  $\text{WO}_6$  octahedra that has sides and oxygen atoms in common. Among heteropolytungstates, Keggin ( $[\text{XM}_{12}\text{O}_{40}]^{n-}$ ) and Dawson ( $[\text{X}_2\text{M}_{18}\text{O}_{62}]^{n-}$ ) types represent the most common structures: a central tetrahedral  $\text{XO}_4$  unit is surrounded by a definite number of  $\text{WO}_6$  octahedra. POTs exhibit very peculiar structure-dependent chemical and physical properties (acid-base and redox properties) which are thermally and oxidatively stable and undergo photoinduced multielectron transfers without changing their structures. These features make them

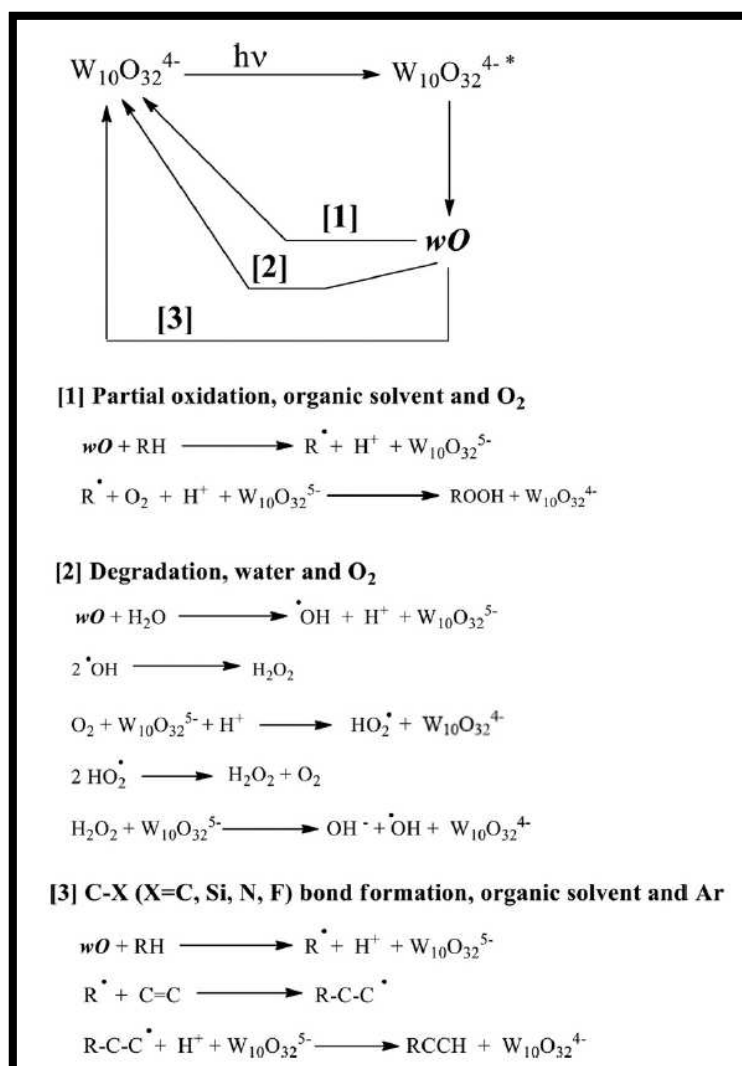
attractive materials for applications as redox catalysts. Moreover, irradiation with UV and/ or near UV light in the ligand to metal charge transfer band causes an intramolecular charge transfer from  $O^{2-}$ -based highest occupied molecular orbital (HOMO) to the  $W^{6+}$ -based lowest unoccupied molecular orbital (LUMO) leading to the formation of a photoexcited state. The resulting photoexcited POT is highly reactive both in oxidation and reduction reactions and can trigger chemical transformations on organic and inorganic molecules that are transparent in the wavelength range employed. The entire process is truly photocatalytic when the photoexcited POT is regenerated in its initial state at the end of the reaction cycle (as it happens for a thermal catalyst), while the light is a stoichiometric reagent. This is the base of the utilization of POTs as photocatalysts. Also, POTs have been applied to a wide range of new applications [6]–[8], and most of them have been recently reviewed [9].

### 5.5.1 Decatungstate photocatalysis

Considering photoredox applications in the liquid phase, POTs have common photochemical processes. However, decatungstate anion is the polyoxotungstate that has the absorption band at the highest wavelengths of all. In fact,  $[O^{2-} - W^{6+}]$  LMCT absorption band is in the UV region ( $\lambda_{max} = 324$  nm,  $\epsilon = 14,100 M^{-1} cm^{-1}$ ) with a tail that extends until 380 nm, partially overlapping to the UV solar emission spectrum. This renders the isopolyoxoanion, the king photocatalyst of the family, principally because UV light excites exclusively the decatungstate anion, and it is not absorbed by the organic substrates to be transformed that remain always in their ground state [10]. Moreover, the absorption spectrum of decatungstate anion in solution overlaps that of  $TiO_2$ , the benchmark material in photocatalysis, so that the polyoxoanion is considered the soluble model of the semiconductor (SC) [11]. Proper counter cation warrants solubility in various media: for example  $(n-Bu_4N)_4W_{10}O_{32}$  dissolves in  $CH_3CN$  and  $Na_4W_{10}O_{32}$  is soluble in water. The cascade of events that take place after light absorption by decatungstate anion has been deeply studied (Figure 5.11): the photoactivation of  $W_{10}O_{32}^{4-}$  leads to a LMCT excited state ( $W_{10}O_{32}^{4-*}$ ), in analogy to the photoinduced charge separation processes which occur in  $TiO_2$ . This state decays in few picoseconds to a very reactive transient, named **wO**, with an oxy radical character. The quantum yield for the generation of this species is around 0.5–0.6. The high reactivity of



**wO** has been recently quantified reporting that its redox potential is +2.44V vs SCE [12], [13].



**Figure 5.11** Photoactivation of decatungstate anion with UV light and subsequent possible reactive pathways

Thus, the transient **wO** can give rise to different processes depending on the experimental conditions. In organic solvent and in aerated conditions (Fig. 5.11 path [1]), **wO** can initiate the oxidation of several organic substrates (RH) through hydrogen atom abstraction or electron transfer mechanism, depending on the actual properties of the chosen substrate RH. Both mechanisms lead to the reduced form of decatungstate ( $W_{10}O_{32}^{5-}$  or  $HW_{10}O_{32}^{4-}$ ) and the substrate-derived radical ( $R^\bullet$ ). Oxidation of  $W_{10}O_{32}^{5-}$  by  $O_2$  restores starting  $W_{10}O_{32}^{4-}$ , closing the photocatalytic cycle.  $O_2$  is reductively activated to peroxy species. In aqueous solutions and aerated conditions (Fig. 5.11 path [2]), the direct reaction of water with **wO** leads to the formation of  $\cdot OH$  radicals. The occurrence

of this reaction has been the object of debate in literature for a long time until some researchers demonstrate with independent techniques the formation of  $\cdot\text{OH}$  radicals. Also, it has been demonstrated that hydroxyl radicals originate from both  $\text{H}_2\text{O}$  oxidation and  $\text{H}_2\text{O}_2$  reduction. The two pathways just described above opened to the possibility of photocatalyse oxidation reactions of organic molecules. In detail, reactions of path can be controlled and partial oxidation is achievable with the conversion of starting molecules into high-added value intermediates. Conversely, in aqueous environment (Fig. 5.11 path [2]), the formation of  $\cdot\text{OH}$  radicals, which are very reactive and unselective oxidant species, is suitable for photocatalytic degradative reactions where the main purpose is depollution [14]. Another possibility occurring in organic solvent and de-aerated conditions should be considered (Fig. 5.11 path [3]):  $\text{W}_{10}\text{O}_{32}^{5-}$  (recognizable because of its blue color) can be accumulated in the reaction vessel together with the substratederived radical ( $\text{R}\cdot$ ). These species could start a very large variety of reactions of interest in organic chemistry which results in the formation of C-C, C-N, C-Si, C-F bonds, opening to new and mild synthetic applications [15].

### 5.5.2 Tungsten trioxide

$\text{WO}_3$  is characterized by an octahedral coordination as  $\text{WO}_6$  [16], and presents different crystalline phases depending on temperature, pressure and preparation conditions. The tungsten trioxide crystal has at least five phases in a temperature range between 900 and  $-180^\circ\text{C}$ , changing with cooling in the following order: tetragonal, orthorhombic, monoclinic, triclinic, monoclinic. At room temperature,  $\text{WO}_3$  it is found in its monoclinic form, whose structure is shown in figure 5.12:

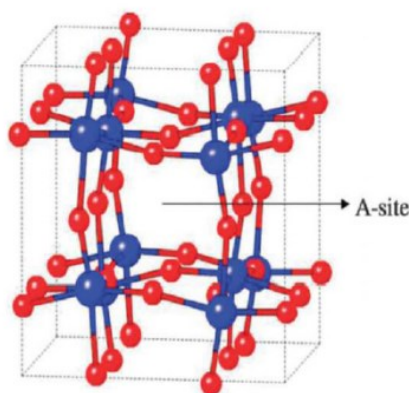


Figure 5.12  $\text{WO}_3$  monoclinic cell structure<sup>23</sup>. Color scheme: W=blue and O=red

$\text{WO}_3$  is a semiconductor possessing an indirect band gap, ranging between 2.6-2.7 eV depending on the preparation method. Such band gap allows for the absorption of the

<480 nm part of the visible spectrum. Today, it is a widely studied material for several applications, such as gas sensing, electrochromic display, photocatalytic degrader[17] and, of course, photoelectrochemical (PEC) cells.

Entering in the details of water-splitting application,  $\text{WO}_3$  is stable in acid aqueous conditions ( $\text{pH}<4$ ), the photogenerated carriers display high mobility[18] and it presents favourable energetics to promote oxygen evolution, while an external bias is request in order to support water reduction to hydrogen.  $\text{WO}_3$  PEC water-splitting performances are significantly sensitive to large number of defects in the crystal surface and to grain boundaries, which results in increased resistance and interfacial charge recombination.  $\text{WO}_3$  nanostructures with small size and controllable morphology can instead decrease the holes diffusion length and the number of grain boundaries, thus improving the charge separation. Furthermore, nanostructured semiconductors with high porosity have better photoelectrochemical activity than dense material, due to their larger active area, more active sites and better charge transport performance [17], [19], related to the reduced distance for the holes to reach semiconductor-electrolyte interface, thus inhibiting surface recombination. Furthermore, the electrolyte could penetrate better into the nanoporous films structure. Among the others, 2-D nanostructures (such as nanoplates, nanosheets and nanoflakes) are particularly promising due to their highly efficient and directional transport of electrons and holes [18].

## **5.6 Heterogeneous polyoxotungstates as photocatalysts**

The main shortcoming of homogeneous catalytic processes is the cumbersome separation of the catalyst (often expensive) from reaction products and its quantitative recovery in an active form. The growing need for the development of environmentally benign, recoverable catalysts which could replace the current homogeneous chemical procedures pushed the research towards the heterogenization of the catalysts on a solid carrier. In this framework, the use of heteropolyanions in their solid state led to the development of practical significance[20]. However, since their specific surface area was very low ( $1 \div 10\text{m}^2\text{g}^{-1}$ ), immobilization of polyoxotungstates onto a large surface area of a solid carrier was preferred[21]. In principle, dispersion of catalytic clusters on supports with high surface area should increase the accessibility of the catalytic sites for the molecule to be transformed so increasing the catalytic performance. Moreover, as most of the POTs are very soluble in water or organic solvents, their heterogenization

should provide more freedom in the choice of the dispersing medium. Easiness of recovery and the possibility of recycling the heterogenized catalyst are the other important advantages. Related to this aspect, when a heterogeneous catalyst is considered, one has to evaluate if there is a certain degree of release of the photocatalytic cluster in the solution or not. This factor is particularly important in the case of immobilized polyoxotungstates because they are also active as homogeneous photocatalysts. In fact, leaching of the photocatalyst during the reaction time inhibits the researcher to be sure that the process is truly heterogeneous. Also, when leaching occurs in some extent, the immobilized photocatalyst recovered at the end of the reaction contains a lower number of photoactive species with respect to the beginning and consequently the loss in efficiency during a consecutive run is obvious. Another fundamental parameter to be considered in a (photo)catalytic process aimed at the production of functionalized intermediates or complete mineralization of the substrate is selectivity. Heterogeneous system represents a suitable means to tailor selectivity through the control of the microscopic environment surrounding the photoactive center, that is immobilized on the surface or inside pores of the support. In detail, it is believed that the support should affect the physical and chemical properties of the (photo)catalytic system through specific and projected textural characteristics. Well-defined structures at the nanometer scale afford a good design of active sites for obtaining selective (photo)catalytic processes[22]. The ongoing interest in POTs heterogeneous photocatalysis has triggered the development of a variety of synthetic procedures.

## 5.7 References

- [1] N. B. Hannay, *Semiconductors*, 1st ed. Reinhold Publishing, 1959.
- [2] J. Leszczynski and U. Tien-Yau Luh, "Lecture Notes in Chemistry." [Online]. Available: <http://www.springer.com/series/632>
- [3] D. Li, *Electrokinetics in microfluidics*, vol. 2. London, 2004.
- [4] S. R. Morrison, *Electrochemistry at semiconductor and oxidized metal electrodes*, 1st ed. New York: Springer US, 1980.
- [5] M. T. Pope, *Heteropoly and isopoly oxometalates*, vol. 8. Springer-Verlag, 1983.
- [6] A. Sartorel *et al.*, "Polyoxometalate embedding of a tetraruthenium(IV)-oxo-core by template-directed metalation of  $[\gamma\text{-SiW}_{10}\text{O}_{36}]^{8-}$ : A totally inorganic oxygen-evolving catalyst," *Journal of the American Chemical Society*, vol. 130, no. 15, pp. 5006–5007, Apr. 2008, doi: 10.1021/ja077837f.
- [7] Y. v. Geletii, B. Botar, P. Kögerler, D. A. Hillesheim, D. G. Musaev, and C. L. Hill, "An all-inorganic, stable, and highly active tetraruthenium homogeneous catalyst for water oxidation," *Angewandte Chemie - International Edition*, vol. 47, no. 21, pp. 3896–3899, May 2008, doi: 10.1002/anie.200705652.
- [8] C. Ritchie *et al.*, "Polyoxometalate-mediated self-assembly of single-molecule magnets:  $\{[\text{XW}_9\text{O}_{34}]_2[\text{Mn}^{\text{III}}_4\text{Mn}^{\text{II}}_2\text{O}_4(\text{H}_2\text{O})_4]\}^{12-}$ ," *Angewandte Chemie - International Edition*, vol. 47, no. 30, pp. 5609–5612, Jul. 2008, doi: 10.1002/anie.200801281.
- [9] W. Deng, Q. Zhang, and Y. Wang, "Polyoxometalates as efficient catalysts for transformations of cellulose into platform chemicals," *Dalton Transactions*, vol. 41, no. 33. pp. 9817–9831, Sep. 07, 2012. doi: 10.1039/c2dt30637a.
- [10] M. Fagnoni, D. Dondi, D. Ravelli, and A. Albini, "Photocatalysis for the formation of the C-C bond," *Chemical Reviews*, vol. 107, no. 6. pp. 2725–2756, Jun. 2007. doi: 10.1021/cr068352x.
- [11] K. Suzuki, N. Mizuno, and K. Yamaguchi, "Polyoxometalate Photocatalysis for Liquid-Phase Selective Organic Functional Group Transformations," *ACS Catalysis*, vol. 8, no. 11. American Chemical Society, pp. 10809–10825, Nov. 02, 2018. doi: 10.1021/acscatal.8b03498.
- [12] D. C. Duncan, T. L. Netzel, and C. L. Hill, "Early-Time Dynamics and Reactivity of Polyoxometalate Excited States. Identification of a Short-Lived LMCT Excited State and a Reactive Long-Lived Charge-Transfer Intermediate following Picosecond Flash Excitation of  $[\text{W}_{10}\text{O}_{32}]^{*1234}$  in Acetonitrile," 1995. [Online]. Available: <https://pubs.acs.org/sharingguidelines>
- [13] V. de Waele, O. Poizat, M. Fagnoni, A. Bagno, and D. Ravelli, "Unraveling the Key Features of the Reactive State of Decatungstate Anion in Hydrogen Atom

- Transfer (HAT) Photocatalysis," *ACS Catalysis*, vol. 6, no. 10, pp. 7174–7182, Oct. 2016, doi: 10.1021/acscatal.6b01984.
- [14] P. Kormali, T. Triantis, D. Dimotikali, A. Hiskia, and E. Papaconstantinou, "On the photooxidative behavior of TiO<sub>2</sub> and PW12O<sub>40</sub><sup>3-</sup>: OH radicals versus holes," *Applied Catalysis B: Environmental*, vol. 68, no. 3–4, pp. 139–146, Nov. 2006, doi: 10.1016/j.apcatb.2006.07.024.
- [15] D. Ravelli, S. Protti, and M. Fagnoni, "Decatungstate Anion for Photocatalyzed 'window Ledge' Reactions," *Accounts of Chemical Research*, vol. 49, no. 10, pp. 2232–2242, Oct. 2016, doi: 10.1021/acs.accounts.6b00339.
- [16] S. D. Tilley, M. Cornuz, K. Sivula, and M. Grätzel, "Light-induced water splitting with hematite: Improved nanostructure and iridium oxide catalysis," *Angewandte Chemie - International Edition*, vol. 49, no. 36, pp. 6405–6408, Aug. 2010, doi: 10.1002/anie.201003110.
- [17] G. Zheng *et al.*, "Tungsten oxide nanostructures and nanocomposites for photoelectrochemical water splitting," *Nanoscale*, vol. 11, no. 41. Royal Society of Chemistry, pp. 18968–18994, Nov. 07, 2019. doi: 10.1039/c9nr03474a.
- [18] A. Stashans and S. Lunell, "Semiempirical Calculations on WO and 3 ( ) M WO Crystals M = H, Li, Na x 3," John Wiley & Sons, Inc, 1997.
- [19] N. A. Schwadron *et al.*, "Global anisotropies in TeV cosmic rays related to the sun's local galactic environment from IBEX," *Science*, vol. 343, no. 6174, pp. 988–990, 2014, doi: 10.1126/science.1245026.
- [20] G. Marcì, E. I. García-López, and L. Palmisano, "Heteropolyacid-Based Materials as Heterogeneous Photocatalysts," *European Journal of Inorganic Chemistry*, pp. 21–35, 2014.
- [21] M. D. Tzirakis, I. N. Lykakis, and M. Orfanopoulos, "Decatungstate as an efficient photocatalyst in organic chemistry," *Chem. Soc. Rec*, vol. 38, pp. 2609–2621, 2009.
- [22] F. Zaera, "The New Materials Science of Catalysis: Toward Controlling Selectivity by Designing the Structure of the Active Site," *The Journal of Physical Chemistry Letters*, vol. 1, pp. 621–627, 2010.

## 6 Experimental

### 6.1 Drugs adsorption on zeolites

The data herein reported are part of my work of thesis and have been published in: Elena Sarti, Tatiana Chenet, Claudia Stevanin, Valentina Costa, Alberto Cavazzini, Martina Catani, Annalisa Martucci, Nicola Precisvalle, Giada Beltrami and Luisa Pasti (2020). High-Silica Zeolites as Sorbent Media for Adsorption and Pre-Concentration of Pharmaceuticals in Aqueous Solutions. *Molecules* 25,3331.

The present work focused on the use of commercial zeolites with a high silica content as absorbent media for pharmaceutical products in an aqueous matrix. Some target molecules belonging to the category of emerging contaminants have been selected, being present at surface water level and in the effluents of wastewater treatment plants, which are unable to break down or eliminate these emerging contaminants effectively. As drug probes, ketoprofen, hydrochlorothiazide and atenolol were selected. The adsorption of pharmaceutical products was evaluated for two zeolites of the Faujasite topology with Silica / Alumina ratio 30 and 200. this silica/alumina ratio various gives different characteristics to the two zeolites. in fact, a higher amount of aluminium in the structure gives to the zeolite framework a more negative overall charge giving to the material hydrophilic properties, on the other hand, zeolites with higher silicon content show hydrophobic behaviour. The selected zeolites proved to be efficient absorbers towards all the pharmaceutical products studied, thanks to their high saturation capacities and constant binding. These results were confirmed by thermal and structural analyzes, which revealed that adsorption occurred within the porosities of the zeolite, causing changes in the lattice.

Finally, the zeolites were tested as pre-concentration medium in the solid phase dispersive extraction procedure. Recoveries greater than 95% were obtained for ketoprofen and hydrochlorothiazide and approximately 85% for atenolol, under conditions that promoted the dissolution of the neutral solute in a predominantly organic phase. The results were obtained using a short contact time (5 min) and a small extraction volume (500 L), without halogenated solvents. These attractive features

make the proposed procedure a time- and cost-saving method for sample enrichment and spent sorbent regeneration, rather than the more energy-expensive heat treatment.

### **6.1.1 Introduction**

The increasing use of pharmaceutical compounds in human and veterinary medicine has become an environmental problem, which received widespread attention from scientists over the past 20 years [1,2]. Hundreds of tonnes of pharmacologically active substances enter sewage treatment plants, where they are poorly removed. Consequently, they can enter into surface water collecting the plant effluents [3,4]. Indeed, the occurrence of pharmaceuticals in surface water and sediments has been extensively reviewed [5,6]. Likewise, “source-to-tap” studies concerning the fate of pharmaceuticals from wastewater to finished drinking water have been reported [7,8]. The concentrations measured in natural and drinking waters are very low, generally in the  $\text{ng L}^{-1}$  to  $\mu\text{g L}^{-1}$  [9,10], thus requiring accurate and sensitive methods for their detection. Likewise, to reduce the negative impact of pharmaceutical on biota and human health, new technologies should be investigated to improve the efficiency of water treatment plants in the removal of drugs. Therefore, it is important on one hand to develop analytical methods able to detect these molecules at a low concentration level to better evaluate their impact on the environment and, on the other hand, to enhance the efficiency of water remediation technologies in order to reduce water contamination. Sorption based technologies were demonstrated to be efficient and economical methods both for the enrichment of trace pollutants as well as for their removal from water [11–13]. Among the wide variety of adsorbents, zeolites are very promising for environmental application thanks to their properties such as high surface area, controlled pore size, thermal and chemical stability. Recent studies demonstrated the efficiency of zeolites in the adsorption of several organic pollutants from water, such as pharmaceuticals [14,15], polycyclic aromatic hydrocarbons [16,17], and petrol-derived compounds such as toluene [18], methyl tert-butyl ether [19], chlorobenzene [20]. In addition, zeolites were also investigated as materials for the enrichment of organic compounds in dilute aqueous solutions. Dispersive solid-phase extraction is a promising sample pre-treatment technique, first introduced by Anastassiades et al. [21], which is based on the SPE methodology, but the sorbent is dispersed in a sample



solution containing the target analytes instead of being immobilized inside a cartridge. This approach enables the sorbate to interact equally with all the sorbent particles and avoids channeling or blocking of cartridges or disks, as occurs in traditional SPE [22]. Other advantages with respect to the conventional SPE are the small sample volume required, reduced operational time, and high recoveries [23]. The dispersive-SPE has been successfully introduced for several analyses (i.e., pesticide residues in various matrices, antibiotics in animal tissues, pharmaceuticals in whole blood), with the purpose of sample clean-up and elimination of matrix interferences [24]. In the present work, the adsorptive properties of high-silica zeolites toward drugs in aqueous solutions were studied in order to investigate the efficiency of these siliceous materials in two applications, namely: (1) The removal of contaminants from the aqueous matrix, (2) the pre-concentration step for micropollutants analysis. An interesting future perspective of the present work could be the investigation of the possible reuse of zeolites after solvent extraction of sorbed analytes. Despite the fact that the thermal treatment usually requires high temperatures and long times, it still represents the most common regeneration technique of an exhausted adsorbent. It has been already demonstrated that exhausted zeolites maintain their adsorption efficiency after thermal regeneration [25,26]. Adsorbent regeneration by solvent extraction could be an attractive alternative to thermal treatment, because it is time-saving, requires less energy, and could permit the recovery of bioactive molecules from waste. Target pharmaceuticals were chosen based on their presence in effluents of wastewaters treatment plants and in surface waters [3,27,28].

In detail, the three investigated pharmaceuticals were ketoprofen (non-steroidal anti-inflammatory drug), hydrochlorothiazide (diuretic), and atenolol (beta-blocker), which are characterized by different physicochemical properties. As adsorbent media, commercial high-silica zeolites [29] (FAU and BEA framework type), differing in structure and surface properties, were considered. The release of sorbed pharmaceuticals from zeolites was evaluated by varying the pH and organic modifier of the extracting phase.

## **6.1.2 Results and Discussion**

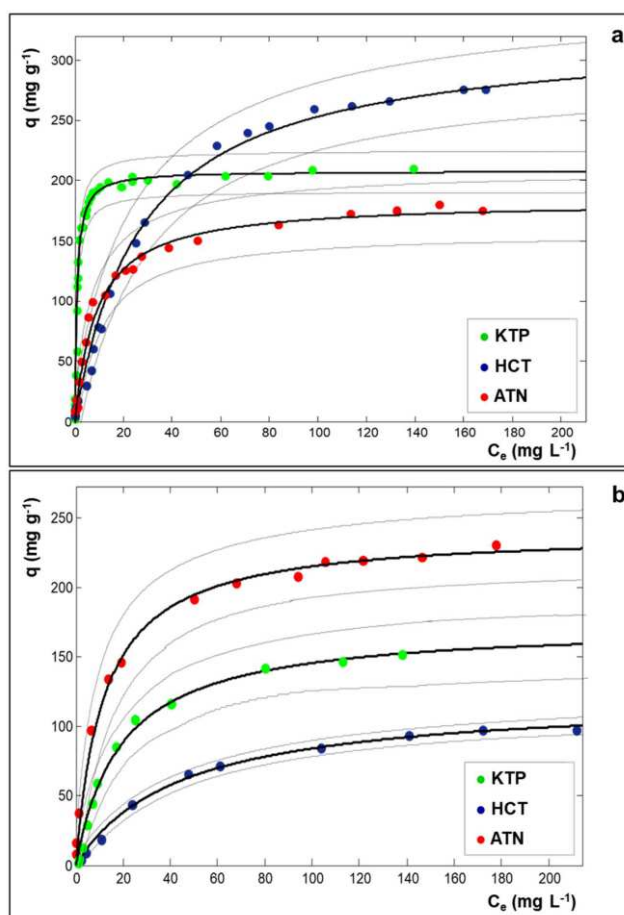
### **6.1.2.1 Adsorption**

The adsorption of pharmaceuticals from the aqueous solution onto zeolites was evaluated in a wide concentration range and by fitting the experimental data with the

proper mathematical model. In this case, good fits were obtained using Langmuir adsorption isotherm Equation (1) which has been already employed to investigate several organic molecule-zeolite systems [25,30,31]:

$$q = \frac{q_s b C_e}{1 + b C_e} \quad (\text{Eq. 1})$$

In Equation (1),  $q$  ( $\text{mg g}^{-1}$ ) is the adsorbed amount per unit weight of adsorbent,  $C_e$  ( $\text{mg L}^{-1}$ ) is the solute concentration at equilibrium,  $q_s$  ( $\text{mg g}^{-1}$ ) is the saturation capacity and  $b$  ( $\text{L mg}^{-1}$ ) is the Langmuir coefficient (binding constant). The adsorption isotherms of drugs adsorption on Y zeolites in Milli-Q water are shown in Figure 6.1.1 and the respective parameters estimated by non-linear fitting are reported in Table 6.1.1. Data concerning the drugs adsorption onto Beta25 are reported elsewhere [15].



**Figure 6.1.1.** Adsorption isotherms of ketoprofen (KTP: green symbols), hydrochlorothiazide (HCT: dark blue symbols), and atenolol (ATN: red symbols) on Y200 (a) and Y30 (b) in Milli-Q water. Dotted lines are the confidence limits at 95% of probability of the fitted curves.

**Table 6.1.1.** Parameters Estimated by Non-Linear Fitting, According to the Langmuir Model, of Three Drugs Adsorption on Y200 and Y30. The Confidence Limits at 95% of Probability of Parameters are Reported in Brackets.

Drug-Zeolite	b (L mg <sup>-1</sup> )	q <sub>s</sub> (mg g <sup>-1</sup> )	R <sup>2</sup>
KTP-Y200	0.91 (0.76; 1.1)	208 (202; 214)	0.9887
HCT-Y200	0.037 (0.029; 0.044)	322 (302; 342)	0.9856
ATN-Y200	0.11 (0.082; 0.14)	183 (171; 195)	0.9737
KTP-Y30	0.052 (0.035; 0.069)	173 (148; 197)	0.9756
HCT-Y30	0.022 (0.018; 0.026)	121 (114; 128)	0.9957
ATN-Y30	0.084 (0.058; 0.11)	240 (223; 257)	0.9727

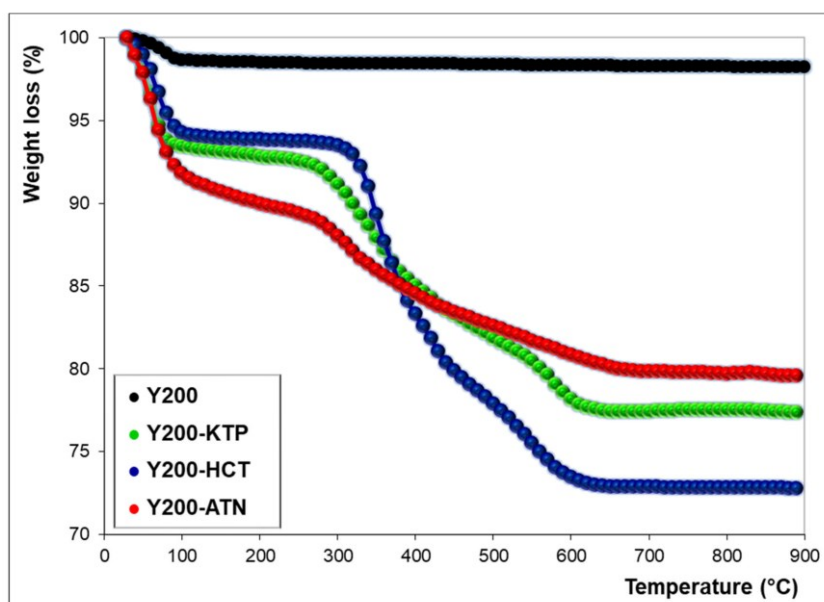
As can be seen in Table 6.1.1, both USY zeolites show high saturation capacities toward all the examined drugs. These data could be compared with saturation capacities approximately ranging from 20 to 100 mg g<sup>-1</sup> found by other studies for the adsorption of pharmaceuticals by different adsorbents, such as carbon black [32], granular or derivatized activated carbon [33,34], polymer clay composite [35]. In particular, by comparing the adsorptions on Y200, it can be noted that the highest saturation capacity (q<sub>s</sub>) was reached for HCT, but the isotherm slope (b), related to the adsorption constant, is the lowest one. At low concentrations, Y200 shows the greatest adsorption efficiency towards KTP. From the data of Table 6.1, it can also be observed that Y30 shows higher adsorption capacity and affinity for ATN than for the other pharmaceuticals. This last finding could be ascribed to electrostatic interactions between Y30, which is less hydrophobic than Y200, and ATN which is partially positively charged. By comparing the USY zeolites in terms of saturation capacities and binding constants (Table 6.1), the more hydrophobic Y200 generally demonstrated to offer higher efficiency than Y30, despite the lower surface area, thus confirming that the surface area is not exhaustive for predicting adsorption properties. In the light of above, further investigations were performed solely on Y200.

In order to obtain more information on the adsorption process, thermal and diffractometric analyses were carried on. Thermogravimetric curves of Y200 before and after saturation with drugs are shown in Figure 6.1.2.

The TG curves of as-synthesized Y200 show a total weight loss of 1.7% at 900°C. The thermal profile shows a sudden slope variation at a temperature below 100°C, thus

suggesting the presence of water molecules weakly bonded to the surface [14]. The TG curves of Y200 saturated with drugs display two main weight losses: The first one below 100°C can be attributed to the desorption of species (water and/or drug) weakly retained on the zeolite surface, while the second one at temperatures above 100°C can be ascribed to the decomposition of drug sorbed inside the zeolite porosities. According to the literature data [36–38], KTP and HCT present a stable profile until about 250 and 300°C, respectively, while the ATN thermal decomposition starts at lower temperatures (120–150 °C).

Thermogravimetric curves of Y200 after saturation with ATN, HCT, and KTP show weight losses at 900°C of 20.4%, 27.2%, and 22.6%, respectively. These results indicated that, at saturation conditions, the higher amount of sorbed drug was found for HCT, followed by KTP and ATN. The same trend can be observed by comparing the saturation capacities extrapolated from adsorption isotherms (see  $q_s$  in Table 6.1.1). Differences in the amounts obtained from TG and isotherm data can derive from different factors, such as the contribution of co-adsorbed water molecules to TG results. In addition, saturation capacity is a limit value estimated from non-linear fitting of experimental data (see Figure 6.1.1) and it does not refer to a single adsorption measurement.



**Figure 6.1.2.** Thermogravimetric curves of Y200 before (black) and after drugs adsorption (KTP: Green, HCT: Blue, ATN: Red).

The Y200 dealuminated zeolite is characterized by the presence of both microporosity and macroporosity mainly due to the dealumination process [39]. Although drug

adsorption can occur in both micro- and mesoporous structures, the deeply investigation of the adsorption site location lies beyond the aim of the present work. In order to have experimental evidence of the effective incorporation of the drug inside the zeolite porosity and not only on the zeolite surface, a structural investigation was carried out. Figure 6.1.3 shows the results attained for Y200-KTP and Y200-ATN systems. Structural analyses carried out on Y200 saturated with HCT led to results similar to those obtained for KTP: For this reason, the diffractometric data of HCT have not been reported here.

The XRD diffraction patterns of Y200 before and after KTP and ATN adsorption showed changes in the entire  $2\theta$  range investigated (Figure 6.1.3a) and especially in the low  $2\theta$  region (Figure 6.1.3b). After drugs adsorption, the intensity of the (111) reflection decreased and the full width at half maximum (FWHM), reported in Figure 3b, increased, thus indicating changes in crystallinity of the original sample. At the same time, shifts in the peaks positions revealed unit cell parameters modifications (Table 6.1.2) whereas variations in their intensity suggested modifications induced by KTP and ATN adsorption, indicating that the molecules are effectively penetrated inside the structural microporosities of Y200.

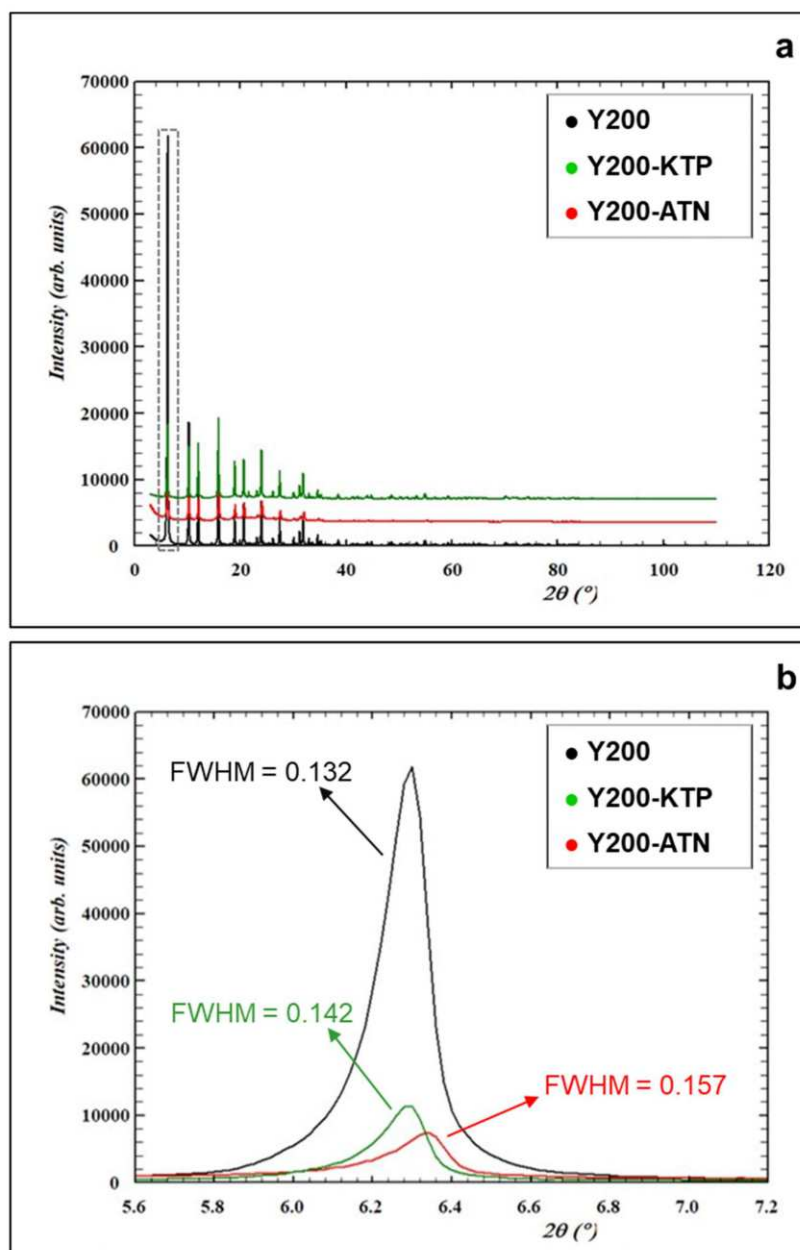


Figure 6.1.3. X-ray powders diffraction pattern in the entire  $2\theta$  range investigated (a) and in the low  $2\theta$  region (b) of as-synthesized Y200 (black), Y200 saturated with KTP (green), and ATN (red).

Table 6.2. Lattice Parameters for Y200 Before and After Pharmaceuticals Adsorption.

	Y200	Y200-KTP	Y200-ATN
Crystallite size ( $\text{\AA}$ )	668.5	621.5	563.4
$a = b = c$ ( $\text{\AA}$ )	24.259(1)	24.255(1)	24.159(1)
$V$ ( $\text{\AA}^3$ )	14,277.1(1)	14,269.1(1)	14,101.5(1)
O4-O4 ( $\text{\AA}$ )	9.81	10.30	9.90
O1-O1 ( $\text{\AA}$ )	9.70	9.63	9.58
C.F.A. ( $\text{\AA}^2$ )	39.07	41.43	38.90
Ellipticity ( $\epsilon$ )	1.01	1.07	1.03

Considering the structural difference between the channels, the framework oxygen distances between the pores give important indications in determining the stability of a sorption site. A guest molecule on a stable sorption site favors those distances that minimize the van der Waals interaction potentials. This means that due to the host-guest interactions, the pore sizes of the channels are roughly the same, but the precise structures of the channels are quite different. The bond lengths and angles in the framework geometry and the diagonal O—O internuclear distances in the 12-ring channel (12MR) are listed in Table 6.2. The 12MR diameters, calculated from the Rietveld structure refinement, are indicated by O1-O1 and O4-O4 distances, treating the framework oxygen atoms as cold hard spheres with van der Waals radius equal to 1.35 Å. The oblate spheroidal KTP and ATN profile “forced” the 12-ring channel to adapt to the host molecules geometry, with a consequent variation of Crystallographic Free Area (CFA). The 12MR had been compressed becoming more elliptical, as expressed by the channel ellipticity ( $\epsilon$ ), defined as the ratio between the smaller and the larger O—O “free diameters” of the 12-rings. The refined atomic occupancy factors gave rise to an adsorption of 19% and 18% in weight for KTP and ATN, respectively. This finding is in good agreement with those determined by adsorption isotherms (see  $q_S$  in Table 6.1.1) and by thermogravimetric analyses (see Figure 6.1.2).

The positions occupied by atenolol and ketoprofen atoms appeared strongly disordered due to real static disorder or to dynamic disorder. For these reasons, the complete geometry of selected molecules inside the supercage was not achieved. The benzene ring of the drugs molecule was recognized in the supercage and the adsorption site was partially occupied in both cases and each shows, on a statistical basis, four possible orientations. In particular, two and four orientations were identified for the tert-butyl and methoxyl groups, respectively. This result could indicate that structural and topological information contents may be significantly different, due to the geometry of extra-framework species, their ordering and respective symmetry lowering, framework distortions, etc. Consequently, we cannot exclude that the FAU framework could be in higher symmetry ( $Fd\bar{3}$ ) compared to the symmetry of the guest molecules. Moreover, the absence of cubic forbidden peaks indicating change in the space group does not get reported after adsorption, consequently, the  $Fd\bar{3}$  one was also adopted in the structure refinement.

Since it is known that the solution pH influences the adsorption of molecules with ionizable functional groups [40], adsorption experiments were carried out in water at different pH.

The pH-dependent adsorption behaviour was studied by measuring the amount of adsorbed drug ( $q$ ), normalized to the maximum value found in the investigated pH range ( $q_{\max}$ ) for each analyte vs. the pH of the solution (see Figure 6.1.4).

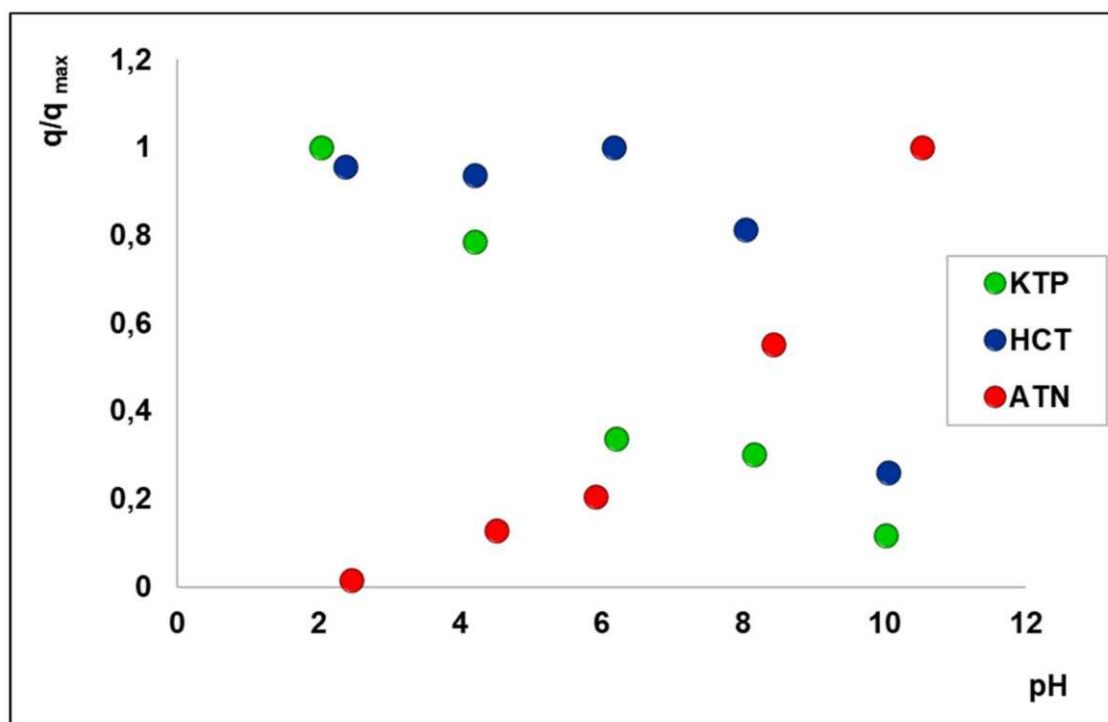


Figure 6.1.4. Normalized adsorbed amount ( $q/q_{\max}$ ) on Y200 of KTP (green), HCT (blue), and ATN (red) vs. pH.

At  $2 < \text{pH} < 12$ , the zeolite surface remains negatively charged due to the dissociation of the hydroxyl groups [41]. In the explored pH range, literature data [42] reported that the Y zeolite does not undergo degradation.

The  $\text{pK}_a$  of KTP is 4.0, hence at  $\text{pH} < 4$  KTP is mainly in its neutral form and at  $\text{pH} > 4$  it is negatively charged. As shown in Figure 6.1.4, the adsorption of KTP decreases as pH increases, due to repulsive electrostatic interactions between KTP and the zeolite surface, both negatively charged. Analogously to KTP, the molecule of HCT ( $\text{pK}_{a1} = 7.9$ ) is undissociated at  $\text{pH} < \text{pK}_{a1}$  and negatively charged in more alkaline solutions. The adsorption is almost constant until the HCT molecule remains neutral and decreases as the negatively charged molecule becomes dominant. These results demonstrated that KTP and HCT interact with the high-silica zeolite mainly in their neutral form thanks to hydrophobic interactions. The preferential adsorption of neutral organic



micropollutants by high-silica zeolites was observed also by Fukahori et al. [40] who reported that sulfa-drugs in neutral form could be more readily adsorbed onto FAU zeolites than those in cationic and anionic forms, based on the hydrophobic interactions. On the contrary, when the anionic forms are dominant under alkaline conditions, a reduction of adsorption capacity occurs [31]. Atenolol showed an opposite behaviour with respect to other two drugs, likewise to what was observed for BEA zeolites [15]. It should be minded that this molecule is cationic at  $\text{pH} < \text{pKa}$  and neutral at  $\text{pH} > \text{pKa}$  ( $\text{pKa} = 9.6$ ). As the pH increases, the conversion of cationic species in the neutral one may result in greater hydrophobic interactions with Y200 and, at the same time, a lower solubility of the neutral ATN [43] which displays higher affinity with the sorbent surface rather than the liquid phase. Both these aspects could be responsible of the increase of ATN adsorption with pH.

### **6.1.2.2 Release**

The performances of Y200 as a pre-concentration media for drugs enrichment was compared to a BEA zeolite having SAR 25, which was previously calcined (referred to as Beta25c), since it has been proved that this thermal treatment increases the adsorption efficiency of BEAs, thanks to the increase of acidity due to the thermal release of ammonia for  $\text{NH}_4$ -zeolites and to the increase of acidity as well as to surface and structural modifications induced by thermal treatments [15,18]. The extracting phases, at different pH and organic modifier contents, were selected in order to minimize the attractive interactions between the sorbed drug and the zeolite framework (see Figure 6.1.4) and, at the same time, to favour the analyte's dissolution in the liquid phase. In general, for each zeolite-drug system, the following extracting phases were tested: Water, an organic polar solvent (methanol and acetonitrile), aqueous solutions at pH values where the adsorption has demonstrated to be low, mixtures organic modifier/formic acid or organic modifier/ammonium hydroxide. Despite the fact that in some cases acidic or alkaline extracting phases were employed, the time of contact of 5 min with the loaded zeolite is too brief to induce structural degradation. Moreover, it should be considered that, in the studied pH range, it has been reported that zeolites [42,44] do not undergo degradation.

The release efficiency was calculated as a percentage recovery, according to Equation (2) [45]:

$$\%R = 100 \frac{C_f V_f}{C_i V_i} \quad (\text{Eq. 2})$$

where  $C_f$  corresponds to the concentration ( $\text{mg L}^{-1}$ ) of the released drug in the final volume  $V_f$  ( $0.2 \cdot 10^{-3}$  L),  $V_i$  is the initial volume ( $1 \cdot 10^{-3}$  L),  $C_i$  is the initial drug concentration (in the range  $0.05\text{--}1$   $\text{mg L}^{-1}$ ). In Table 6.3, the results obtained from dispersive-SPE applied to KTP, at an initial concentration of  $1$   $\text{mg L}^{-1}$ , are reported.

Table 6.3. Percentage Release of KTP at an Initial Concentration of  $1$   $\text{mg L}^{-1}$  from Y200 and Beta25c ( $\pm$ SD: Standard Deviation).

Extracting Phase	Y200	Beta25c
ACN	$53 \pm 4$	$53 \pm 5$
MeOH	$63 \pm 8$	$47 \pm 3$
MeOH:formic acid 90:10 pH 2.4	$94 \pm 14$	$115 \pm 17$
MeOH:formic acid 95:5 pH 2.5	$88 \pm 11$	$86 \pm 12$

For both zeolites, KTP is not at all released in water and the release is still negligible even by increasing the pH of water to 10. At this pH, KTP is negatively charged, hence electrostatic repulsions with a zeolite framework, negatively charged too, were expected. Percent recoveries higher than 80% were obtained with mixtures of methanol and formic acid, probably due to interactions between the neutral form of KTP at  $\text{pH} < \text{pK}_a$  and the extracting phase enriched in an organic modifier.

Some further experiments were carried out by varying the initial drug's concentration, in order to verify if such positive results could be achieved also in the low concentrations range. The results of the present work were compared with those obtained by other studies [8,46] focused on solid phase extraction of KTP by using a commercial adsorbent and the efficiency was found comparable. Figure 6.1.5 shows some of the results obtained by extraction of HCT with different phases from both zeolites.

The release of HCT in water from Y200 is low but not negligible. However, a higher release ( $61 \pm 6\%$  as shown in Figure 6.1.5a) was obtained by increasing the pH to 10, because of electrostatic repulsions between the negatively charged drug and the zeolitic framework. A high recovery of  $96 \pm 11\%$  was obtained with  $\text{MeOH:H}_2\text{O} = 70:30$  at pH

5.0: analogously to KTP, in these conditions ( $\text{pH} < \text{pKa}$ ) HCT is neutral and displays high affinity with the extracting phase which is mainly organic. Some experiments were carried out also at HCT concentrations lower than  $1 \text{ mg L}^{-1}$  (i.e.,  $0.1$  and  $0.05 \text{ mg L}^{-1}$ ): No significant differences were observed between the different concentrations, thus indicating that the dispersive SPE of the Y200-HCT system is effective also in the low concentrations range, similarly for what was observed for KTP. The recovery efficiency on Beta25c (Figure 6.1.5b) was evaluated by keeping constant the composition of the extracting phase and by varying the pH from 4 to 6. The highest recovery ( $71 \pm 7\%$ ) was obtained at pH 5 as already found for Y200, even if the extraction was less efficient. This could be due to higher affinities between HCT at low concentrations and Beta25c (a binding constant of  $0.60 \text{ L mg}^{-1}$  was found [15]) with respect to Y200 ( $b = 0.037 \text{ L mg}^{-1}$  as reported in Table 6.1). Finally, for that which concerns ATN, this drug was not at all released from Y200 in water at pH 3, despite the fact that it was found that the adsorption is negligible at strongly acidic pH (Figure 6.1.4). Other experiments were performed at acidic pH by adding an organic modifier, and the best result ( $71 \pm 5\%$ ) was obtained with a mixture (ACN:formic acid) (95:5) as an extracting phase.

Further tests were carried out at high pH values, by using extracting phases constituted by an organic modifier (MeOH, ACN, or a mixture of them) and ammonium hydroxide at different concentrations.

These alkaline conditions should promote the dissolution of neutral ATN into the liquid phase which is mainly organic. The highest efficiency ( $83 \pm 9\%$ ) was obtained with an extracting phase composed by (MeOH:ACN 40:60):(NH<sub>4</sub> OH 5%) = 70:30. The solute enrichment obtained with the proposed procedure could be improved by using higher volumes of the initial drug solution. Moreover, the extraction efficiency could be enhanced by using longer time contact or higher volume of extraction phases. However, the results herein presented could be considered a good compromise between the efficiency of the enrichment process ( $> 80\%$ ) and the cost and time saving of the concentration procedure. Unfortunately, for the Beta25c-ATN system, very low recoveries were obtained with several extracting phases, in fact the best result was reached with a mixture (MeOH:ACN 40:60):(NH<sub>4</sub>OH 5%) = 80:20 which led to a scarce  $13 \pm 2\%$ . The differences in terms of recovery efficiencies between the two selected zeolites could be ascribed to the binding constants. The  $b$  parameter of the Beta25c-ATN system was found to be  $5.8 \pm 2.8 \text{ L mg}^{-1}$  [15], while that of the Y200-ATN system was  $0.11 \pm 0.03$

L mg<sup>-1</sup> (Table 6.1). As already hypothesized for HCT and KTP, the lower recovery of ATN from Beta25c could be due to its higher affinity with respect to Y200.

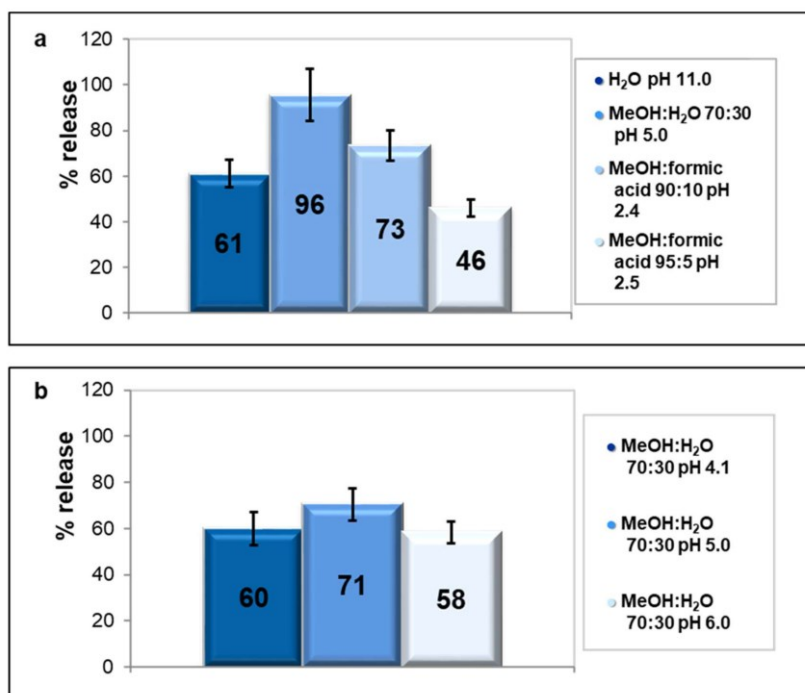


Figure 6.1.5. Release of HCT 1 mg L<sup>-1</sup> from Y200 with different extracting phases (a) and from Beta25c with mixture MeOH:H<sub>2</sub>O 70:30 at different pH (b).

### 6.1.3. Materials and Methods

#### 6.1.3.1. Materials

Technical grade (99% purity) ketoprofen (KTP), hydrochlorothiazide (HCT), and atenolol (ATN) were obtained from Sigma-Aldrich (Steinheim, Germany), as well as sodium phosphate monobasic for the HPLC eluent. HPLC grade acetonitrile (ACN) and methanol (MeOH) were purchased from VWR International PBI Srl (Radnor, PA, USA). The water was Milli-Q grade (Merck Millipore, Burlington, MA, USA). Formic acid and ammonium hydroxide solution were obtained from Merck (Darmstadt, Germany). Hydrochloric acid and sodium hydroxide (Alfa Aesar, Haverhill, MA, USA) were used for pH adjustment. The pH was measured with an Amel 2335 pH-meter (Milano, Italy). Zeolite powders were obtained from Zeolyst International (Conshohocken, PA, USA) and from Tosoh Corporation (Tokyo, Japan). In our study, two USY zeolites with a Silica/Alumina Ratio (SAR) of 30 and 200 (referred as Y30 and Y200) and a BEA with SAR of 25 (referred as Beta25) have been employed. According to C<sup>~</sup>ejka et al. [29], who discriminated between high-silica and low-silica zeolites when SAR was respectively above or below 5, the selected materials can be considered high-silica zeolites.

### 6.1.3.2. Sorption Studies

The adsorption experiments were carried out using the batch method, by putting in contact aqueous solutions of drugs at different concentrations in Milli-Q water with a known amount of zeolite.

It has been reported in previous studies [15] that the equilibrium is quite fast, nevertheless in this work a contact time of 24 h was employed. Batch experiments were carried out in duplicate in 25 mL crimp top reaction glass flasks sealed with PTFE septa (Supelco, Bellefonte, PA, USA). During the equilibration, the solutions were thermostated at a temperature of  $25.3 \pm 0.5$  °C and continuously stirred at 700 rpm. The solid was separated from the solution by centrifugation (Eppendorf 5418, Hamburg, Germany) at 14,000 rpm for 10 min. For each level of concentration, the amount of analyte in the solution, before and after the contact with the adsorbent, was determined by HPLC-DAD as described in Supporting Information. Thermogravimetric and diffractometric analyses were performed on zeolites before and after saturation with the selected drugs. Thermogravimetric (TG) measurements were performed in air up to 900 °C, at  $10$  °C  $\text{min}^{-1}$  heating rate, using an STA 409 PC LUXX® - Netzch Gerätebau GmbH (Verona, Italy). The X-ray diffraction analysis was carried out on a Bruker D8 Advance (Karlsruhe, Germany) diffractometer (Cu K<sub>1,2</sub> radiation) equipped with a Si (Li)SOL-X solid-state detector. The GSAS software and the EXPGUI graphical interface were employed for structural refinements through a full profile Rietveld analysis. Statistical elaborations were carried out through MATLAB® ver. 9.1 software (The MathWorks Inc., Natick, MA, USA).

### 6.1.3.3. Dispersive-SPE Studies

The dispersive-SPE procedure was carried out as follows: In a safe-lock microcentrifuge tube, 2 mg of zeolite were added to 1 mL of drug solution, in a concentration range of  $0.05\text{--}1$  mg  $\text{L}^{-1}$  in Milli-Q water, and mixed for 5 min by vortex (VWR International PBI Srl, Radnor, PA, USA) equipped with a specific adapter for microcentrifuge tubes. The resulting suspension was centrifuged at 14,000 rpm for 5 min and the supernatant was analyzed by HPLC-DAD, in order to quantify the adsorption.

In all cases, it was found that the drug concentration in the supernatant was below the instrumental limit of detection. Therefore, the drug was completely adsorbed in the

brief time of contact, thanks to the fast kinetic offered by the zeolites [14,15], especially in the low concentration range. After the supernatant's removal, the loaded zeolite was re-suspended for 5 min with 500  $\mu\text{L}$  of solutions having different compositions (i.e., pH and organic modifier concentration) and then centrifuged at 14,000 rpm for 5 min. Finally, the supernatant was dried by evaporation under a gentle stream of nitrogen gas, dissolved with 200  $\mu\text{L}$  of the HPLC mobile phase and analyzed by HPLC-DAD for the quantification of the released drug. With the proposed procedure, a five-fold enrichment was achieved. All measurements were performed in triplicate.

#### **6.1.4 Conclusions**

In this study, the adsorptive properties of two commercial high-silica Y zeolites, with a Silica/Alumina Ratio 30 and 200 (namely Y30 and Y200), toward drugs in a diluted aqueous solution were evaluated, with the aim to investigate their possible use in the enrichment step of the analysis.

In fact, the determination of pharmaceuticals at trace levels in natural waters requires advanced analytical methodologies enabling a more efficient detection with lower limits of quantitation. Owing to their high surface area, hydrophobicity and water stability, the selected materials were demonstrated to be efficient sorbents, both in terms of saturation capacity and binding constant. Among the two Y-zeolites, in general better performances were observed for Y200. The structural analyses of saturated zeolites revealed that drugs adsorption occurred inside the porosities of Y200 leading to modifications of lattice parameters and channel ellipticity. Pharmaceuticals pre-concentration from dilute aqueous solutions was carried out through the dispersive-solid phase extraction technique, thanks to its attractive features, such as the short experimental times and small reagents amount required. As a pre-concentration medium, in addition to Y200, a calcined Beta-zeolite with Silica/Alumina Ratio 25 was tested. The dispersive-solid phase extraction experiments led to high recoveries, especially for ketoprofen and hydrochlorothiazide. These results are promising, especially by considering the short operational times required for the entire procedure.

### 6.1.5 References

1. Charuaud, L.; Jarde, E.; Ja\_rezic, A.; Thomas, M.; le Bot, B. Veterinary pharmaceutical residues from natural water to tap water: Sales, occurrence and fate. *J. Hazard. Mater.* **2019**, *361*, 169–186.
2. Sharma, B.M.; Be\_ canová, J.; Scheringer, M.; Sharma, A.; Bharat, G.K.; Whitehead, P.G.; Klánová, J.; Nizzetto, L. Health and ecological risk assessment of emerging contaminants (pharmaceuticals, personal care products, and artificial sweeteners) in surface and groundwater (drinking water) in the Ganges River Basin, India. *Sci. Total Environ.* **2019**, *646*, 1459–1467.
3. Yang, Y.; Ok, Y.S.; Kim, K.H.; Kwon, E.E.; Tsang, Y.F. Occurrences and removal of pharmaceuticals and personal care products (PPCPs) in drinking water and water/sewage treatment plants: A review. *Sci. Total Environ.* **2017**, *596*, 303–320.
4. McCallum, E.S.; Krutzelmann, E.; Brodin, T.; Fick, J.; Sundelin, A.; Balshine, S. Exposure to wastewater e\_uent a\_ects fish behaviour and tissue-specific uptake of pharmaceuticals. *Sci. Total Environ.* **2017**, *605*, 578–588.
5. Wilkinson, J.; Hooda, P.S.; Barker, J.; Barton, S.; Swinden, J. Occurrence, fate and transformation of emerging contaminants in water: An overarching review of the field. *Environ. Pollut.* **2017**, *231*, 954–970.
6. Yang, H.; Lu, G.; Yan, Z.; Liu, J.; Dong, H.; Jiang, R.; Zhou, R.; Zhang, P.; Sun, Y.; Nkoom, M. Occurrence, spatial-temporal distribution and ecological risks of pharmaceuticals and personal care products response to water diversion across the rivers in Nanjing, China. *Environ. Pollut.* **2019**, *255*, 113–132.
7. Furlong, E.T.; Batt, A.L.; Glassmeyer, S.T.; Noriega, M.C.; Kolpin, D.W.; Mash, H.; Schenck, K.M. Nationwide reconnaissance of contaminants of emerging concern in source and treated drinking waters of the United States: Pharmaceuticals. *Sci. Total Environ.* **2017**, *579*, 1629–1642.
8. Caban, M.; Lis, E.; Kumirska, J.; Stepnowski, P. Determination of pharmaceutical residues in drinking water in Poland using a new SPE-GC-MS(SIM) method based on Speedisk extraction disks and DIMETRIS derivatization. *Sci. Total Environ.* **2015**, *538*, 402–411.
9. Comber, S.; Gardner, M.; Sörme, P.; Leverett, D.; Ellord, B. Active pharmaceutical ingredients entering the aquatic environment from wastewater treatment works: A

- cause for concern? *Sci. Total Environ.* **2018**, 613, 538–547.
10. Patrolecco, L.; Capri, S.; Ademollo, N. Occurrence of selected pharmaceuticals in the principal sewage treatment plants in Rome (Italy) and in the receiving surface waters. *Environ. Sci. Pollut. Res.* **2015**, 22, 5864–5876.
  11. Carmalin, S.A.; Eder, C.L. Removal of emerging contaminants from the environment by adsorption. *Ecotox. Environ. Safe* **2018**, 150, 1–17.
  12. Patiño, Y.; Díaz, E.; Ordóñez, S. Pre-concentration of nalidixic acid through adsorption–desorption cycles: Adsorbent selection and modelling. *Chem. Eng. J.* **2016**, 283, 486–494.
  13. Naing, N.N.; Li, S.F.Y.; Lee, H.K. Evaluation of graphene-based sorbent in the determination of polar environmental contaminants in water by micro-solid phase extraction-high performance liquid chromatography. *J. Chromatogr. A* **2016**, 1427, 29–36.
  14. Martucci, A.; Pasti, L.; Marchetti, N.; Cavazzini, A.; Dondi, F.; Alberti, A. Adsorption of pharmaceuticals from aqueous solutions on synthetic zeolites. *Micropor. Mesopor. Mat.* **2012**, 148, 174–183.
  15. Pasti, L.; Sarti, E.; Cavazzini, A.; Marchetti, N.; Dondi, F.; Martucci, A. Factors affecting drug adsorption on beta zeolites. *J. Sep. Sci.* **2013**, 36, 1604–1611.
  16. Costa, A.A.; Wilson, W.B.; Wang, H.; Campiglia, A.D.; Dias, J.A.; Dias, S.C.L. Comparison of BEA, USY and ZSM-5 for the quantitative extraction of polycyclic aromatic hydrocarbons from water samples. *Micropor. Mesopor. Mat.* **2012**, 149, 186–192.
  17. Wilson, W.B.; Costa, A.A.; Wang, H.; Campiglia, A.D.; Dias, J.A.; Dias, S.C.L. Pre-concentration of water samples with BEA zeolite for the direct determination of polycyclic aromatic hydrocarbons with laser-excited time-resolved Shpol'skii spectroscopy. *Microchem. J.* **2013**, 110, 246–255.
  18. Sarti, E.; Chenet, T.; Pasti, L.; Cavazzini, A.; Rodeghero, E.; Martucci, A. Effect of silica alumina ratio and thermal treatment of Beta zeolites on the adsorption of toluene from aqueous solutions. *Minerals* **2017**, 7, 22.
  19. Martucci, A.; Braschi, I.; Bisio, C.; Sarti, E.; Rodeghero, E.; Bagatin, R.; Pasti, L. Influence of water on the retention of methyl tertiary-butyl ether by high silica ZSM-5 and Y zeolites: A multidisciplinary study on the adsorption from liquid and gas phase. *RSC Adv.* **2015**, 5, 86997–87006.



20. Pasti, L.; Rodeghero, E.; Beltrami, G.; Ardit, M.; Sarti, E.; Chenet, T.; Stevanin, C.; Martucci, A. Insights into adsorption of chlorobenzene in high silica MFI and FAU zeolites gained from chromatographic and diffractometric techniques. *Minerals* **2018**, *8*, 80.
21. Anastassiades, M.; Lehotay, S.J.; Stajnbaher, D.; Schenck, F.J. Fast and easy multiresidue method employing acetonitrile extraction/partitioning and “dispersive solid-phase extraction” for the determination of pesticide residues in produce. *J. AOAC Int.* **2003**, *86*, 412.
22. Román, I.P.; Chisvert, A.; Canals, A. Dispersive solid-phase extraction based on oleic acid-coated magnetic nanoparticles followed by gas chromatography–mass spectrometry for UV-filter determination in water samples. *J. Chromatogr. A* **2011**, *1218*, 2467–2475.
23. Wang, P.; Yang, X.; Wang, J.; Cui, J.; Dong, A.J.; Zhao, H.T.; Zhang, L.W.; Wang, Z.Y.; Xu, R.B.; Li, W.J. Multi-residue method for determination of seven neonicotinoid insecticides in grains using dispersive solid-phase extraction and dispersive liquid–liquid micro-extraction by high performance liquid chromatography. *Food Chem.* **2012**, *134*, 3–1691.
24. Tsai, W.H.; Huang, T.C.; Huang, J.J.; Hsue, Y.H.; Chuang, H.Y. Dispersive solid-phase microextraction method for sample extraction in the analysis of four tetracyclines in water and milk samples by high-performance liquid chromatography with diode-array detection. *J. Chromatogr. A* **2009**, *1216*, 12–2263.
25. Rodeghero, E.; Martucci, A.; Cruciani, G.; Bagatin, R.; Sarti, E.; Bosi, V.; Pasti, L. Kinetics and dynamic behaviour of toluene desorption from ZSM-5 using in situ high-temperature synchrotron powder X-ray diffraction and chromatographic techniques. *Catal. Today* **2016**, *277*, 118–125.
26. Rodeghero, E.; Pasti, L.; Sarti, E.; Cruciani, G.; Bagatin, R.; Martucci, A. Temperature-induced desorption of methyl tert-butyl ether confined on ZSM-5: An in situ synchrotron XRD powder diffraction study. *Minerals* **2017**, *7*, 34.
27. Archer, E.; Petrie, B.; Kasprzyk-Hordern, B.; Wolfaard, G.M. The fate of pharmaceuticals and personal care products (PPCPs), endocrine disrupting contaminants (EDCs), metabolites and illicit drugs in a WWTW and environmental waters. *Chemosphere* **2017**, *174*, 437–446.
28. Fernández-Perales, M.; Sánchez-Polo, M.; Rozalen, M.; López-Ramón, M.V.; Mota,

- A.J.; Rivera-Utrilla, J. Degradation of the diuretic hydrochlorothiazide by UV/Solar radiation assisted oxidation processes. *J. Environ. Manag.* **2020**, *257*, 109973.
29. C̃ejka, J.; van Bekkum, H.; Corma, A.; Schüth, F. *Introduction to Zeolite Science and Practice*, 3rd ed.; Elsevier: Amsterdam, The Netherlands, 2007; Volume 168, pp. 50–51.
30. Hartig, D.; Schwindt, N.; Scholl, S. Using the local adsorption equilibrium distribution based on a Langmuir type adsorption model to investigate liquid phase adsorption of sugars on zeolite BEA. *Adsorption* **2017**, *23*, 433–441.
31. Jiang, N.; Shang, R.; Heijman, S.G.J.; Rietveld, L.C. High-silica zeolites for adsorption of organic micro-pollutants in water treatment: A review. *Water Res.* **2018**, *144*, 145–161.
32. Cuerda-Correa, E.M.; Domínguez-Vargas, J.R.; Olivares-Marín, F.J.; Beltrán de Heredia, J. On the use of carbon blacks as potential low-cost adsorbents for the removal of non-steroidal anti-inflammatory drugs from river water. *J. Hazard. Mater.* **2010**, *177*, 1046–1053.
33. Haro, N.K.; del Vecchio, P.; Marcilio, N.R.; Féris, L.A. Removal of atenolol by adsorption – Study of kinetics and equilibrium. *J. Clean. Prod.* **2017**, *154*, 214–219.
34. Fröhlich, A.C.; Foletto, E.L.; Dotto, G.L. Preparation and characterization of NiFe<sub>2</sub>O<sub>4</sub>/activated carbon composite as potential magnetic adsorbent for removal of ibuprofen and ketoprofen pharmaceuticals from aqueous solutions. *J. Clean. Prod.* **2019**, *229*, 828–837.
35. Arya, V.; Philip, L. Adsorption of pharmaceuticals in water using Fe<sub>3</sub>O<sub>4</sub> coated polymer clay composite. *Micropor. Mesopor. Mat.* **2016**, *232*, 273–280.
36. Wesolowski, M.; Rojek, B. Thermogravimetric detection of incompatibilities between atenolol and excipients using multivariate techniques. *J. Therm. Anal. Calorim.* **2013**, *113*, 169–177.
37. Silva Pires, M.A.; Souza dos Santos, R.A.; Sinisterra, R.D. Pharmaceutical composition of hydrochlorothiazide:  $\beta$ -cyclodextrin: Preparation by three different methods, physico-chemical characterization and in vivo diuretic activity evaluation. *Molecules* **2011**, *16*, 4482–4499.
38. Tiṭta, B.; Fulia,s, A.; Bandur, G.; Marian, E.; Tiṭta, D. Compatibility study between ketoprofen and pharmaceutical excipients used in solid dosage forms. *J. Pharm. Biomed.* **2011**, *56*, 221–227.

39. Braschi, I.; Gatti, G.; Bisio, C.; Berlier, G.; Sacchetto, V.; Cossi, M.; Marchese, L. The role of silanols in the interactions between methyl tert-butyl ether and high-silica Faujasite Y: An infrared spectroscopy and computational model study. *J. Phys. Chem. C* **2012**, *116*, 6943–6952.
40. Fukahori, S.; Fujiwara, T.; Ito, R.; Funamizu, N. pH-Dependent adsorption of sulfa drugs on high silica zeolite: Modeling and kinetic study. *Desalination* **2011**, *275*, 237–242.
41. Kuzniatsova, T.; Kim, Y.; Shqau, K.; Dutta, P.K.; Verweij, H. Zeta potential measurements of zeolite Y: Application in homogeneous deposition of particle coatings. *Micropor. Mesopor. Mat.* **2007**, *103*, 102–107.
42. Lee, E.F.T.; Rees, L.V.C. Dealumination of sodium Y zeolite with hydrochloric acid. *J. Chem. Soc. Faraday Trans.* **1987**, *83*, 1531–1537.
43. Schönherr, D.; Wollatz, U.; Haznar-Garbacz, D.; Hanke, U.; Box, K.J.; Taylor, R.; Ruiz, R.; Beato, S.; Becker, D.; Weitschies, W. Characterisation of selected active agents regarding pKa values, solubility concentrations and pH profiles by Sirius T3. *Eur. J. Pharm. Biopharm.* **2015**, *92*, 155–170.
44. Liu, X.; Mäki-Arvela, P.; Aho, A.; Vajglova, Z.; Gun'ko, V.M.; Heinmaa, I.; Kumar, N.; Murzin, D.Y. Zeta potential of beta zeolites: Influence of structure, acidity, pH, temperature and concentration. *Molecules* **2018**, *23*, 946.
45. Bosi, V.; Sarti, E.; Navacchia, M.L.; Perrone, D.; Pasti, L.; Cavazzini, A.; Capobianco, M.L. Gold-nanoparticle extraction reversed-electrode-polarity stacking mode combined to enhance capillary electrophoresis sensitivity for conjugated nucleosides and oligonucleotides containing thioether linkers. *Anal. Bioanal. Chem.* **2015**, *407*, 5405–5415.
46. Santos, J.L.; Aparicio, I.; Alonso, E.; Callejón, M. Simultaneous determination of pharmaceutically active compounds in wastewater samples by solid phase extraction and high-performance liquid chromatography with diode array and fluorescence detectors. *Anal. Chim. Acta* **2005**, *550*, 116–122.
47. Gantiva, M.; Martínez, F. Thermodynamic analysis of the solubility of ketoprofen in some propylene glycol + water cosolvent mixtures. *Fluid Phase Equilib.* **2010**, *293*, 242–250.
48. Radjenović, J.; Petrović, M.; Ventura, F.; Barceló, D. Rejection of pharmaceuticals in nanofiltration and reverse osmosis membrane drinking water treatment. *Water*

- Res. **2008**, 42, 3601–3610.
49. Kadam, Y.; Yerramilli, U.; Bahadur, A.; Bahadur, P. Micelles from PEO–PPO–PEO block copolymers as nanocontainers for solubilization of a poorly water soluble drug hydrochlorothiazide. *Colloid. Surface B* **2011**, 83, 49–57.
50. Küster, A.; Alder, A.C.; Escher, B.I.K.; Duis, K.; Fenner, K.; Garric, J.; Hutchinson, T.H.; Lapen, D.R.; Péry, A.; RöxF6;mbke, J. Environmental risk assessment of human pharmaceuticals in the European Union: A case study with the  $\beta$ -blocker atenolol. *Integr. Environ. Assess. Manag.* **2010**, 6, 514–523.

## 6.2 Adsorption of chlorobenzene onto zeolites

The data herein reported are part of my work of thesis and have been published in: Pasti L., Rodeghero E., Beltrami G., Ardit M., Sarti E., Chenet T., Stevanin C., Martucci A. (2018) Insights into Adsorption of Chlorobenzene in High Silica MFI and FAU Zeolites Gained from Chromatographic and Diffractometric Techniques. *Minerals*, 8, 80.

In this work, the capability of two commercial high silica zeolites (HSZs), namely ZSM-5 and Y, for the removal of chlorobenzene (CB) from water was investigated by combining chromatographic and diffractometric techniques. The two zeolites differ in the framework cages, Zeolite ZSM-5 is constructed from pentasil units that are linked together in pentasil chains, while zeolite Y is composed of sodalite cages connected to each other through hexagonal prisms. Furthermore, present different dimensions of the pores in fact, in the first one The minor and major axis dimensions are 5.1 x 5.5 Å for the sinusoidal channels and 5.3 x 5.6 Å for the straight channels, in the second one The pore system consists in 12-membered rings with large openings (7.4 Å diameters) that lead to the inner cavity which has a diameter of 12 Å and is surrounded by 10 sodalite cages. The adsorption isotherms and kinetics of CB on ZSM-5 and Y zeolites were determined from batch tests. The adsorption kinetics were very fast; the obtained values shown that the time to reach equilibrium was less than 10 min for the zeolites both. The equilibrium data of CB on the two HSZs showed dissimilarities that are particularly evident in the adsorption data concerning the low concentration range, where Y zeolite is characterized by low adsorption. On the contrary, at higher concentrations the adsorption capacity of Y is higher than that of ZSM-5.

The crystalline structures of Y and ZSM-5 saturated with CB were investigated by X-ray diffraction (XRD) techniques. Rietveld refinement analyses of XRD data allowed for quantitative probing of the structural modifications of both zeolites after CB adsorption and provided insight into the preferred zeolite adsorption sites in both microporous materials. The refined framework–extraframework bond distances confirm that interactions between the selected organic contaminant and hydrophobic zeolites are mediated via co-adsorbed H<sub>2</sub>O. The occurrence of H<sub>2</sub>O–CB–framework oxygen oligomers explains variations in both the unit cell parameters and the shape of the channels, clearly confirming that water plays a very relevant role in controlling the diffusion and adsorption processes in hydrophobic zeolites.

### 6.2.1 Introduction

Industrial and agricultural discharges, chlorine disinfection by-products (DBPs) of drinking water and wastewater, and incineration of wastes are the main sources of chlorine and organochlorine compounds (OCICs), such as chlorobenzene (CB). These compounds can cause toxic effects on both human health and environmental systems, even at low concentration [1]. In particular, the Environmental Protection Agency (EPA) fixed the maximum contaminant level (MCL) of CB at  $0.1 \text{ mg L}^{-1}$ ; above this threshold value CB can cause negative health effects, such as gastrointestinal irritations, hepatotoxicity and kidney damages [2]. Therefore, it is important to remove this pollutant from the environment and different methodologies have been proposed.

Actually, the physical method based on adsorption processes is a recuperative method exploited for in situ water treatments which combines high flexibility of the system, efficiency even at low concentration levels, low energy, cheap operating costs, and possible waste reductions [3]. Different adsorbent materials can be employed, and their efficiency depends on the host-guest interactions between sorbent and sorbate [4–13]. In general, carbonaceous adsorbents are low cost materials, widely employed in remediation technology. However, their applicability can be limited by fouling that cause a pore blocking (i.e., to the presence of dissolved organic matter), to low adsorption capacity, sharp rise of bed temperature and difficulty of regeneration [14–17]. In recent years, organic contaminants removal by single-walled carbon nanotubes (SWCNTs) has attracted great interest due to their chemical, electronic and mechanical properties [18]. However, the saturation capacity of these adsorbents for OCICs is moderate and functional groups on the surface of carbonaceous adsorbents can further reduce the adsorption features [19–21]. In the past few decades, surfactant modified clays have been proposed as a potential alternative to carbonaceous adsorbents for removing OCIC pollutants. Indeed, it has been proved that these materials are efficient and they can be easily regenerated. One of the main disadvantages is their limited stability due to a progressive release of surfactant which can have a negative impact on biota [22–25]. Synthetic and hydrophobic zeolites offer an attractive and efficient option for the removal of chlorine, and organochlorine compounds from water. The main advantages are related to their high surface area and porous structure, high specific capacity and organic pollutants selectivity. Additionally, fast kinetics, mechanical, biological and chemical stability make them promising and efficient adsorbents [4,6–

8,26–28]. Furthermore, their high thermal stability guarantees the possibility of regeneration through thermal treatments in order to reintroduce them in new adsorption processes [5,29–33].

This work is part of a wider study aimed at systematically evaluating the adsorptive capacity of high silica zeolites (HSZ) (e.g., mordenite, ZSM-5, faujasite, beta, ferrierite [4,7,10,29,30]) for fuel-based compounds differing in chemical properties (e.g., polarity, functional groups, size, host-guest interactions, etc.), which can provide useful information to accurately predict the behaviour of HSZs as well as improve their individual performance.

The objective of this study is to evaluate the capability of two commercial HSZs, ZSM-5 (MFI topology), and Y zeolite (FAU topology) [34], for removal of chlorobenzene (CB) from water. For that purpose, the adsorption process from water was investigated in order to gain information on the interactions between the selected organic contaminant and hydrophobic zeolites. The information gathered from this work provides a tool for the selection of adsorbent materials for environmental remediation. Additionally, the investigation of hostguest interactions can provide information on the fate and transport of OCICs in the environment, and in particular for the partition of those contaminants in the mineral fraction of soils, normally constituted by aluminosilicate.

## 6.2.2 Materials and Methods

High-silica Y (code HSZ-390HUA, 200 SiO<sub>2</sub>/Al<sub>2</sub>O<sub>3</sub> molar ratio, 750 m<sup>2</sup> g<sup>-1</sup> surface area, 0.05 wt % Na<sub>2</sub>O content) and ZSM-5 (code CBV 28014, 280 SiO<sub>2</sub>/Al<sub>2</sub>O<sub>3</sub> molar ratio, 400 m<sup>2</sup> g<sup>-1</sup> surface area, 0.01 wt % Na<sub>2</sub>O content) hydrophobic zeolites were purchased in their assynthesised form by Tosoh Corporation (Tokyo, Japan) and Zeolyst International (Conshohocken, PA, USA) respectively. Chlorobenzene (CB) in its anhydrous form (purity of 99.8%) was provided by Sigma-Aldrich (Steinheim, Germany) and used as received.

### Batch Adsorption

The adsorption isotherm was determined using the batch method. Batch experiments were carried out in duplicate in 20 mL crimp top reaction glass flasks sealed with PTFE septa (Supelco, Bellefonte, PA, USA). The flasks were filled in order to have the minimum headspace and a solid:solution ratio of 1:2 (mg mL<sup>-1</sup>) was employed. After equilibration,

for 24 h at a temperature of  $25.3 \pm 0.5^\circ\text{C}$  under stirring, the solids were separated from the aqueous solution using centrifugation (14,000 rpm for 30 min).

The concentration of contaminants in the aqueous solution, before and after the contact with the adsorbent was determined by Headspace Gas Chromatography coupled to Mass Spectrometry (HS-GC-MS). The analysis was carried out using an Agilent GC-MS system (Santa Clara, CA, USA) consisting of a GC 6850 Series II Network coupled to a Pal G6500-CTC injector and a Mass Selective Detector 5973 Network. HS autosampler injector conditions are: incubation oven temperature  $80^\circ\text{C}$ , incubation time 50 min, headspace syringe temperature  $85^\circ\text{C}$ , agitation speed 250 rpm, agitation on time 30 s, agitation off time 5 s, injection volume  $500\ \mu\text{L}$ , fill speed  $30\ \mu\text{L s}^{-1}$ , syringe pull-up delay 5 s, injection speed  $250\ \mu\text{L s}^{-1}$ , pre-injection delay 0 s, post injection delay 2 s, syringe flush 30 s with nitrogen.

A DB-624 UI GC column ( $L = 20\ \text{m}$ , I.D. =  $0.18\ \text{mm}$ ,  $df = 1.00\ \mu\text{m}$  film thickness, Agilent, Santa Clara, CA, USA) was used. High purity helium was the carrier gas with a constant flow rate of  $0.7\ \text{mL min}^{-1}$ . The oven temperature gradient started at  $40^\circ\text{C}$  for 4 min and then ramped to  $130^\circ\text{C}$  at  $15\ ^\circ\text{C min}^{-1}$ . The injector temperature was kept at  $150^\circ\text{C}$ . All samples were injected in split mode (10:1). The mass spectrometer operated in electron impact mode (positive ion,  $70\ \text{eV}$ ). The source temperature and the quadrupole temperature were set to  $230^\circ\text{C}$  and  $150^\circ\text{C}$ , respectively. The mass spectra were acquired in full scan mode.

The electronic scan speed was  $1562\ \text{amu s}^{-1}$  in a mass range from 30 to 300 amu. For identification and quantification of the target analyte the SIM (selected ion monitoring) chromatograms were extracted from the acquired signal by selecting the most abundant characteristic fragments at  $m/z = 112$ . Chromatographic peak of analytes was identified by comparison of the retention time and the mass spectrum with standard compound and library data; quantitative analysis was performed using calibration curves.

## **Thermal Analyses**

The Netzsch STA 409 PC LUXX® (Gerätebau, Germany) simultaneous TG/DTA thermogravimetric balance was employed in order to carry out both thermogravimetric (TG) and differential thermal analyses (DTA) on Y and ZSM-5 zeolites before and after



CB loading. The measurements were performed in constant air flux conditions using a heating rate of  $10^{\circ}\text{C min}^{-1}$ , from room temperature (RT) to  $900^{\circ}\text{C}$ .

### **X-ray Powder Diffraction Data Collection and Refinement Strategy**

X-ray diffraction patterns on powders of Y and ZSM-5 zeolites loaded with CB were carried out on a Bruker D8 Advance (Karlsruhe, Germany) diffractometer (Cu  $\text{K}\alpha_{1,2}$  radiation) equipped with a Sol-X detector. Diffraction data were collected at RT, in  $3^{\circ}$ – $110^{\circ}$   $2\theta$  (for ZSM-5) and  $3^{\circ}$ – $100^{\circ}$   $2\theta$  (for Y zeolite)  $2\theta$  ranges respectively, with a counting time of 12 s each  $0.02^{\circ}$   $2\theta$ . GSAS software [35] and the EXPGUI graphical interface [36] were employed for Y–CB and ZSM-5–CB structural refinements through a full profile Rietveld analysis. Unitcell and structural parameters were determined starting from the monoclinic P21/n (for ZSM-5) and the cubic Fd-3 (for Y) space groups of Martucci et al. [10], and Braschi et al. [11] structural models, respectively. The Bragg peak profiles were modelled by a Pseudo-Voigt function with 0.001% cut-off peak intensity. Refined coefficients were: two Gaussian terms (i.e., the  $\tan 2\theta$  dependent GU and the  $\theta$  independent GW), and two Lorentzian terms (i.e.,  $\cos\theta-1$  dependent LX,  $\tan\theta$  dependent LY), respectively. A Chebyshev polynomial function with 24 and 22 coefficients was used in order to empirically fit the instrumental background for Y and ZSM-5, respectively. In both structural refinements, scale factor,  $2\theta$ -zero shift and unit-cell parameters were also refined. Soft constraints were initially imposed on Si–O, O–O, C–C and C–Cl bond distances (tolerance ( $\sigma$ ) value of  $0.04 \text{ \AA}$ ) and completely removed in the final cycles. Finally, atomic coordinates, site occupancy and isotropic atomic displacement parameters were refined. Furthermore, the displacement parameters for a given atom type were constrained to be equivalent (i.e., Si and O sites), thus limiting the number of refined atomic displacement parameters to two. Additionally, in Y–CB  $x/a$  and  $y/b$  parameters of the chlorobenzene molecule were constrained to be equal in order to maintain the planarity. Table 6.2.1 reports the details of the data collection and Rietveld refinements.

Parameter	ZSM-5	ZSM-5-CB	Y	Y-CB
	[Si <sub>96</sub> O <sub>192</sub> ]	[Si <sub>96</sub> O <sub>192</sub> ]·6(C <sub>6</sub> H <sub>5</sub> Cl)·8(H <sub>2</sub> O)	[Si <sub>192</sub> O <sub>384</sub> ]	[Si <sub>192</sub> O <sub>384</sub> ]·32(C <sub>6</sub> H <sub>5</sub> Cl)·70(H <sub>2</sub> O)
Space group	<i>P2<sub>1</sub>/n</i>	<i>P2<sub>1</sub>/n</i>	<i>Fd-3m</i>	<i>Fd-3</i>
<i>a</i> (Å)	19.899(5)	19.919(1)	24.259(1)	24.263(1)
<i>b</i> (Å)	20.117(6)	20.107(1)	24.259(1)	24.263(1)
<i>c</i> (Å)	13.389(4)	13.3967(1)	24.259(1)	24.263(1)
$\alpha$ (°)	90	90	90	90
$\beta$ (°)	90.546(3)	90.528(3)	90	90
$\gamma$ (°)	90	90	90	90
<i>V</i> (Å <sup>3</sup> )	5359.9(3)	5365.7(5)	14,277.1(1)	14,284.4(6)
Wavelength (Å): Cu K $\alpha$ <sub>1</sub>	1.540593	1.540593	1.540593	1.540593
Cu K $\alpha$ <sub>2</sub>	1.544427	1.544427	1.544427	1.544427
Refined 2 $\theta$ (°) range	3°–110°	3°–110°	3°–100°	3°–100°
Contributing reflections	5861	6362	620	620
<i>N</i> <sub>obs</sub>	5350	5350	4850	4850
<i>N</i> <sub>var</sub>	289	301	40	40
<i>R</i> <sub>wp</sub> (%)	10.3	13.3	12.8	12.9
<i>R</i> <sub>p</sub> (%)	9.4	10.4	12.5	12.6
<i>R</i> <sub>F</sub> <sup>2</sup> (%)	7.00	7.25	9.95	10.0

$R_p = \sum |Y_{io} - Y_{ic}| / \sum Y_{io}$ ;  $R_{wp} = [\sum w_i(Y_{io} - Y_{ic})^2 / \sum w_i Y_{io}^2]^{0.5}$ ;  $R_F^2 = \sum |F_o^2 - F_c^2| / |F_o^2|$

**Table 6.2.1** Details of the data collection and Rietveld refinements.

## 6.2.3 Results and Discussion

### *Adsorption Isotherms from Aqueous Solutions*

The uptake  $q$  (mg g<sup>-1</sup>) was calculated as follows:

$$q = \frac{(C_0 - C)V}{m} \quad (\text{Eq. 3})$$

where  $C_0$  is the initial concentrations in solution (mg L<sup>-1</sup>),  $C$  is the concentration at time  $t$  in kinetics experiments (mg L<sup>-1</sup>),  $V$  is the solution volume (L) and  $m$  is the mass of sorbent (g). In Figure 6.2.1 the uptake data for CB on Y and ZSM-5 are reported.

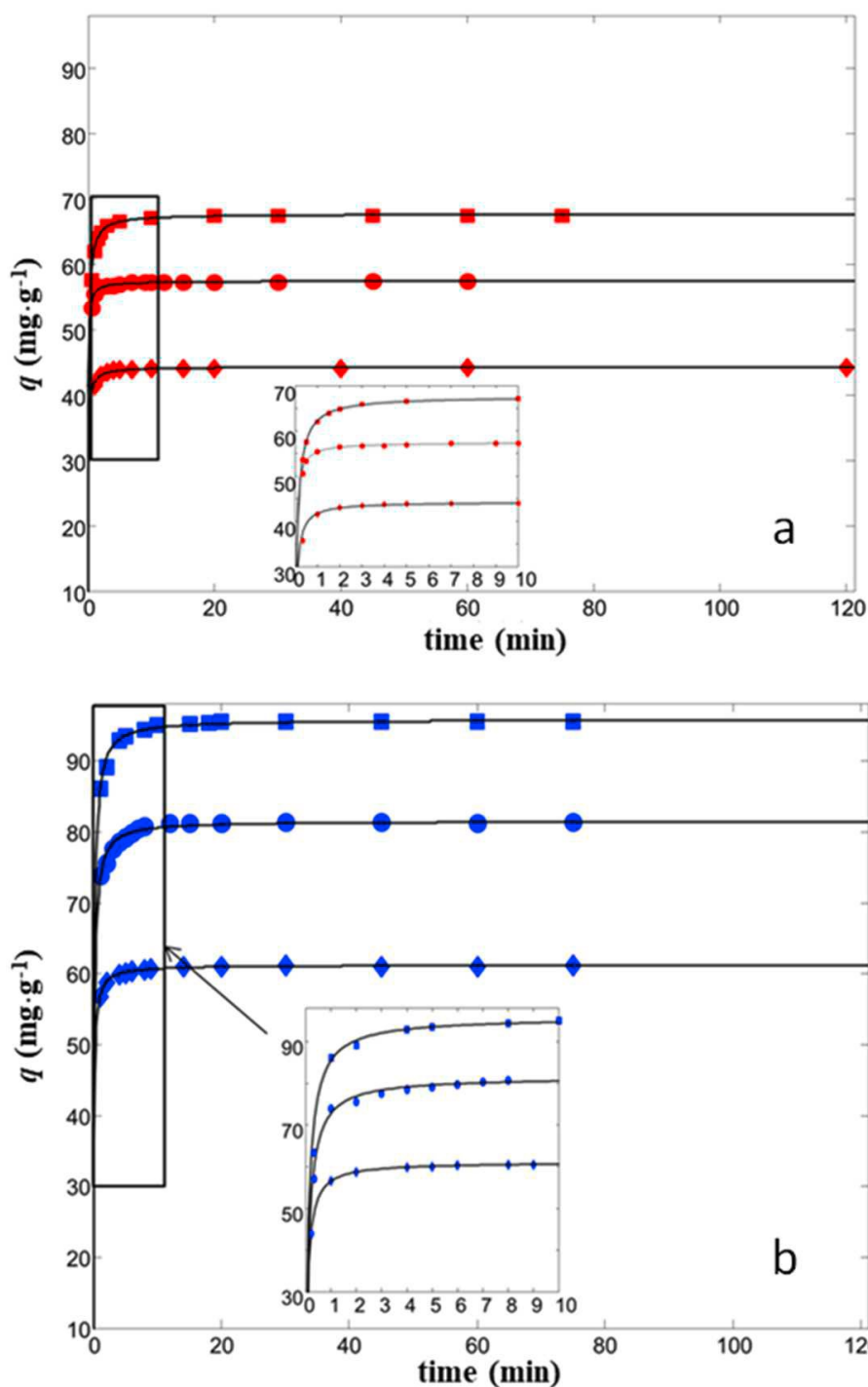


Figure 6.2.1 Chlorobenzene (CB) uptake vs. contact time for ZSM-5 (a) and Y (b) for initial concentration of 35, 25, 15 mg/L. The insets: enlarged image of the boxed regions.

It can be seen that the kinetics of the adsorption process was very fast; the equilibrium was reached in about 10 min. Similar behaviours were also observed for the adsorption of other aqueous contaminants, such as dichloroethane and toluene onto ZSM-5 and Y zeolites [5– 10,13]. We have previously verified [5–10,13] that uptake data of the investigated zeolites can be fitted by the pseudo-second order model as:

$$q_t = \frac{k_2 q_e^2 t}{1 + k_2 q_e t} \quad (\text{Eq.4})$$

where  $q_t$  and  $q_e$  are the amounts of solute adsorbed per mass of sorbent at time  $t$  and at equilibrium, respectively, and  $k_2$  is the second-order adsorption rate constant. The values of equilibrium uptake  $q_e$  and the adsorption rate constant  $k_2$  were obtained from non-linear fit of  $q_t$  vs.  $t$  (see Table 6.2.2). Analogous to what was observed for the adsorption of other aqueous contaminants, the uptake data of CB can be modelled by a pseudo-second order kinetic model, as indicated from the high coefficient of determination.

	$C_0$ (mg L <sup>-1</sup> )	$q_t$ (mg g <sup>-1</sup> )	$k_2$ (g L <sup>-1</sup> mg <sup>-1</sup> )	$R^2$
ZSM-5	15	23.4 (23.3, 23.5)	0.44 (0.41, 0.47)	0.9845
	25	44.3 (44.2, 44.3)	0.37 (0.33, 0.41)	0.9803
	35	67.6 (67.5, 67.6)	0.21 (0.19, 0.23)	0.9985
Y	25	39.3 (39.2, 39.4)	0.14 (0.11, 0.17)	0.9822
	35	70.3 (70.2, 70.3)	0.13 (0.11, 0.15)	0.9969
	45	82.3 (82.4, 82.5)	0.10 (0.085, 0.12)	0.9935

**Table 6.2.2** Estimated kinetics parameters (see Equation (4)). The confidence limits at 95% of probability of the estimated parameters are reported in brackets.

Furthermore, for the adsorption of CB it can be noted that the kinetic constant decreases by increasing the initial concentration [37], and that the adsorption onto Y zeolites is characterised by a lower kinetic constant than that found for ZSM-5. These findings allow us to generalise the difference observed in the adsorption kinetics of these two zeolites. In particular, the adsorption kinetics of neutral organic molecules (namely, toluene, dichloroethane, methyl tert-butylether and CB), which differ from

each other in physicochemical properties and molecular dimensions, is faster on ZSM-5 than on Y zeolite. It has been already shown that adsorption of organics in aqueous solutions onto ZSM-5 hydrophobic zeolites are well fitted by the Langmuir equation [5,6,8,13], that assumes monolayer adsorption onto energetically equivalent adsorption sites and negligible sorbate– sorbate interactions. The relationships describing the Langmuir isotherm is [38]:

$$q = \frac{q_s b C_e}{1 + b C_e} \quad (\text{Eq. 5})$$

where  $b$  is the binding constant ( $\text{L mg}^{-1}$ ) and  $q_s$  is the saturation capacity of the adsorbent material ( $\text{mg g}^{-1}$ ). The experimental data obtained for the adsorption of CB on both ZSM-5 and Y are shown in Figure 6.4.2. It can be observed that the isotherms are shaped differently from each other; they can be classified as concave (Type I) and sigmoidal (Type V) isotherms, respectively.

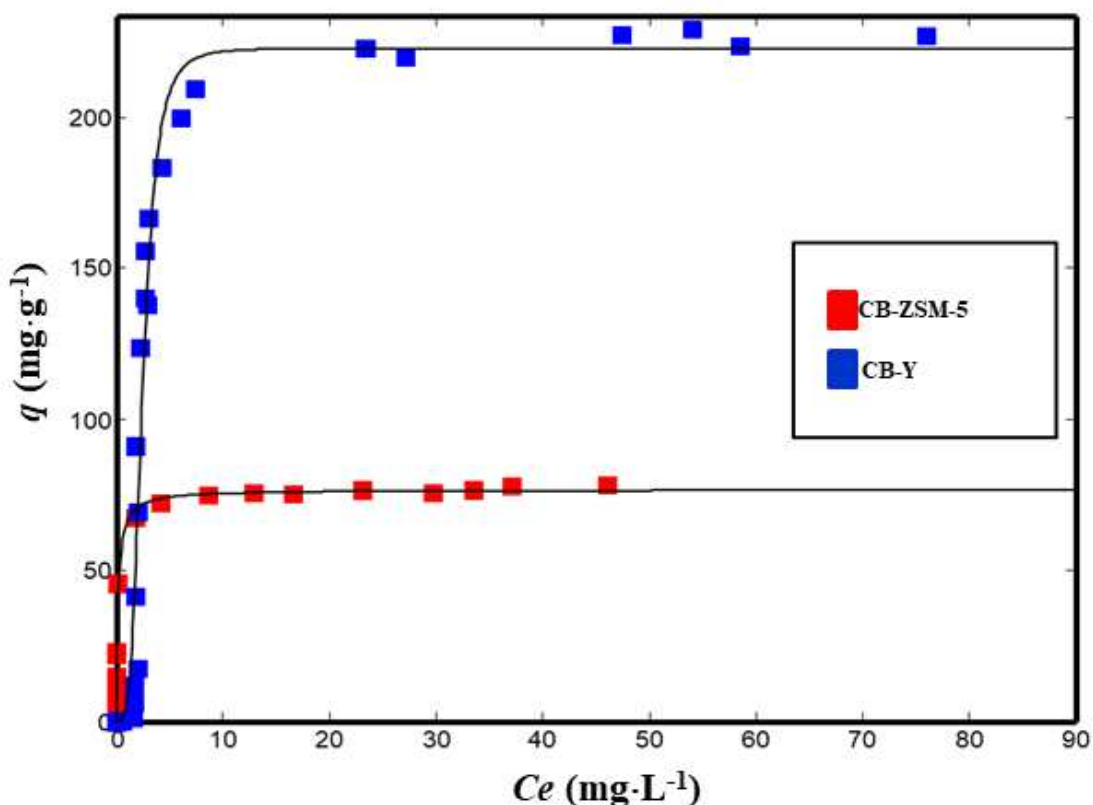


Figure 6.2.2 Adsorption isotherms of CB for ZSM-5 (red squares) and Y (blue squares).

Similar differences in the adsorption of polar organic compound from aqueous solution onto ZSM-5 and Y were also observed for methyl tert-butylether and toluene. In such cases, a Hill isotherm model was employed:

$$q_e = q_s \frac{c_e^n}{K_H + c_e^n} \quad (\text{Eq. 6})$$

where  $K_H$  is the Hill constant, and  $n$  is the Hill coefficient which is related to the degree of cooperativity. The Hill isotherm is often employed to describe cooperative adsorption in biological systems, and it has also been used to model adsorption data on zeolites due to evidence of the presence of water-organic compound clusters [39] inside the zeolite frameworks. Since the tendency to form clusters increases by increasing the porosity dimensions, the clusters are more probably formed in the large cage of Y than in the channel system of ZSM-5 [40]. To evaluate if clusters can be formed for CB, a structural investigation was carried out (vide infra). In Table 6.2.3, the isotherm parameters for ZSM-5 and Y estimated by non linear fitting of Equations 6.4.3 and 6.4.4 respectively, are reported. It can be seen that the saturation capacity of these zeolites are higher than those obtained with graphite materials (i.e., 28.3 mg g<sup>-1</sup> for dichlorobenzene) [41], and in particular Y zeolite has a saturation value higher than adsorbents single-walled carbon nanotubes, especially if they are partially oxidized [42]. In addition, HSZs can be regenerated without significant loss of their adsorption properties [5,6,29,30]. Therefore, hydrophobic zeolites are very promising adsorbents for the removal of chlorinated aromatic compounds from water.

			$R^2$	SSE*
Langmuir				
CB-ZSM-5	$q_s$	76.6 (74.8, 79.5)	0.9874	198
	$b$	5.0 (3.7, 6.6)		
Hill				
CB-Y	$q_s$	227 (218, 245)	0.9654	2135
	$K_H$	9.2 (6.6, 12.1)		
	$n$	5.5 (4.3, 6.7)		

**Table 6.2.3 Isotherm parameters for the adsorption of CB on ZSM-5 and Y. (\*SSE: sum of squared errors)**

#### *Structural Modifications upon Chlorobenzene Adsorption on High Silica Zeolites*

##### Y-CB

Y zeolite (FAU framework topology [34]) is built up of large cavities ( $\alpha$  cages or supercages) with a diameter of 12 Å linked to four other supercages through 12 membered-ring windows (diameter of 7.4 Å) and cuboctahedral  $\beta$  cages connected each

other through double hexagonal rings (D6R). Topological symmetry of the unloaded material is cubic  $Fd-3m$ , but it has been highlighted that the embedding of organic compounds can decrease the symmetry to  $Fd-3$  [10–13,43]. A careful examination of powder diffraction patterns after chlorobenzene adsorption highlights that Y–CB peak positions are quite similar to those of the as-synthesised material in all the  $2\theta$  range investigated. Contrariwise, peak intensities strongly decrease after pollutant incorporation, especially at low  $2\theta$  angles (Figure 6.2.3).

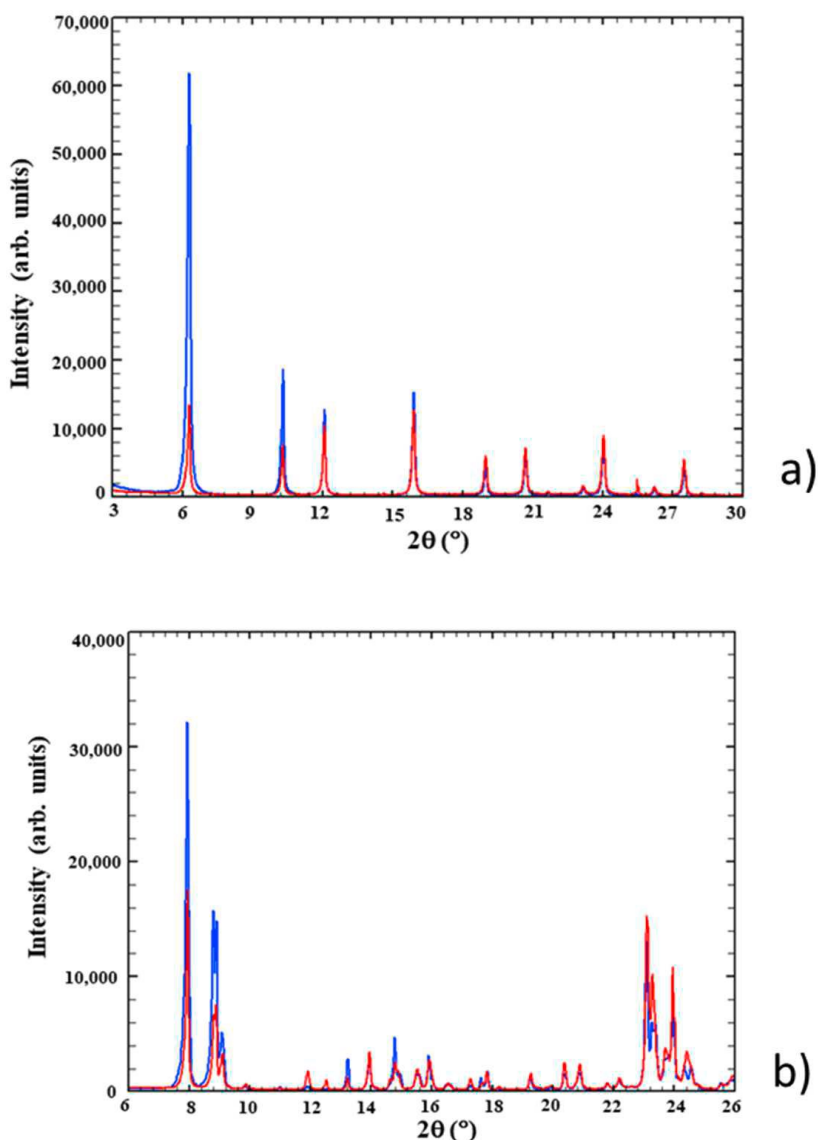


Figure 6.2.3 Observed powder diffraction patterns of Y–CB (a) and ZSM-5–CB (b), respectively, showing differences both in intensity and position of the diffraction peaks in the low and intermediate  $2\theta$  regions. Blue lines represent the unloaded samples, red lines the loaded ones.

These differences suggest variations in the extraframework species content as well as in the lattice parameters (Table 6.2.1), thus attesting to CB adsorption into the porous structure of the zeolite. After adsorption, the T1–O and T2–O mean distances are 1.621 and 1.620 Å, respectively, the O–T–O angles range from 103.3° to 112.3°. The T–O–T

bond angles adopt a wide range of values from 125° to 171° (mean value = 142°). The T–O, T–O–T and O–T–O grand mean values are in high agreement with those reported for other pure silica zeolites (PSZ) [44]. Furthermore, after adsorption the channel ellipticity  $\epsilon$  (defined as the ratio between the smaller and larger O–O “free diameters” of the 12-rings) changed ( $\epsilon = 1.02$  in Y,  $\epsilon = 1.21$  in Y–CB) and at the same time, the openings reached a wider Crystallographic Free Area (C.F.A., sensu Baerlocher [34]) when compared with the assynthesised material (Table 6.2.4), thus confirming the high flexibility of FAU-type materials [45,46].

Parameter	Y–CB	Y [11]
O4–O4 distance (Å)	11.16	9.81
O1–O1 distance (Å)	9.68	9.70
Free diameter O4–O4 (Å)	8.46	7.11
Free diameter O1–O1 (Å)	6.98	7.00
Mean diameter (Å)	7.72	7.06
Mean radius (Å)	3.86	3.53
C.F.A. (Å <sup>2</sup> )	46.81	39.07
$\epsilon$	1.21	1.01

Table 6.2.4 Crystallographic Free Area and ellipticity ( $\epsilon$ ) comparison between unloaded Y [11] and Y–CB systems. C.F.A. =  $\pi \times (\text{mean radius})^2$  (Å<sup>2</sup>);  $\epsilon$  = ratio between the longest and the shortest pore dimensions.

Rietveld structural refinement allows us to detect 32 CB molecules per unit cell (corresponding to ~ 22.0% dry weight, dw %) located within the Y supercage (Figure 6.2.4a). Chlorobenzene molecules occupy one crystallographic independent and partially occupied site, and statistically can assume six different orientations (Figure 6.2.4a).

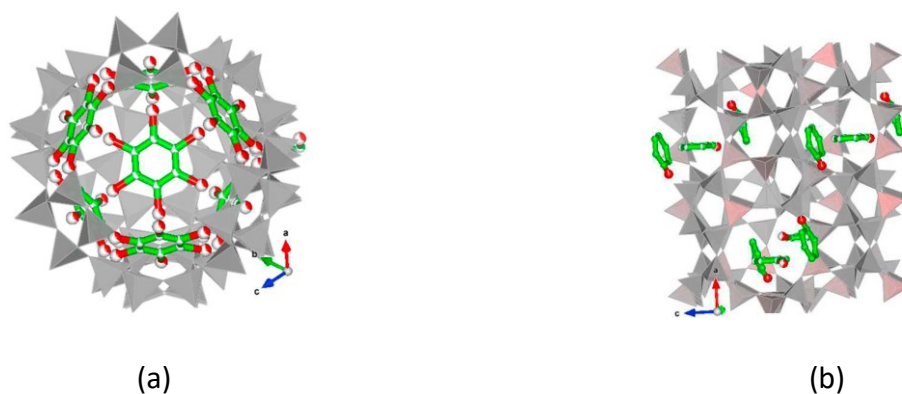
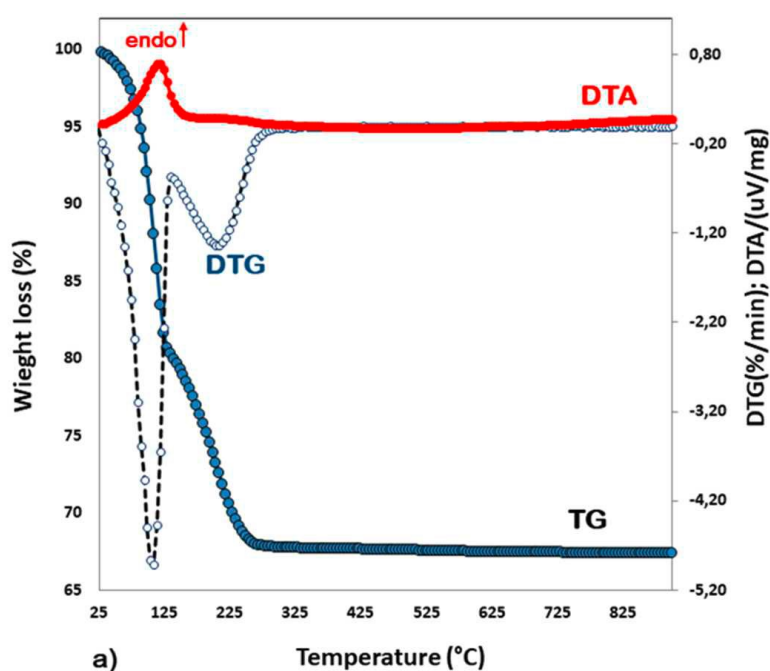
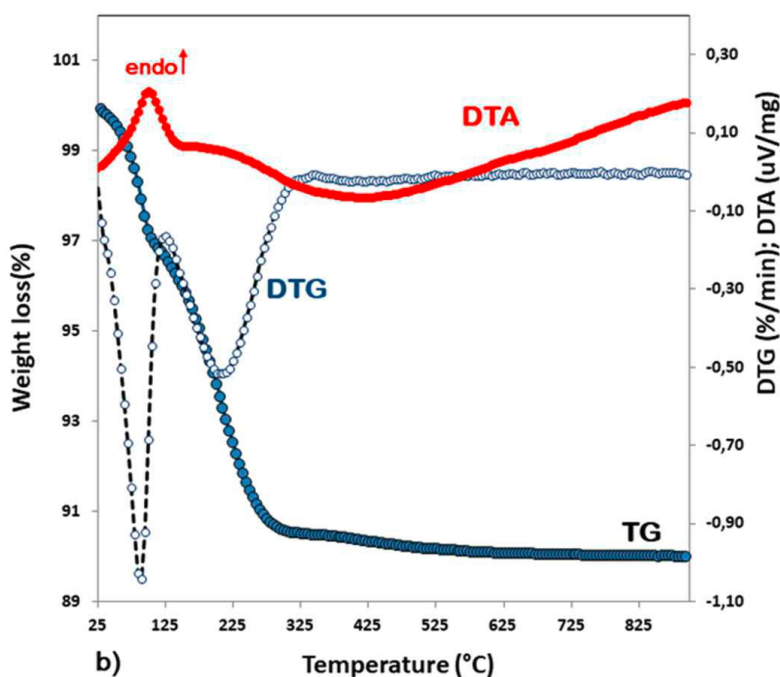


Figure 6.2.4 Distribution of CB molecules in Y (a) and ZSM-5 (b) zeolites, respectively. Chlorine (red circle) and carbon (green circle) are shown. Drawings produced by VESTA 3 [47].



Moreover, the evidence of relatively short Cl–O1 bond distances (i.e., Cl–O1 = 2.723(1) Å and 2.680 Å, respectively) proves that chlorobenzene directly interacts with framework oxygens. Furthermore, difference-Fourier maps of the electron density analysis revealed the presence of co-adsorbed H<sub>2</sub>O molecules hosted in three additional extraframework sites. Additionally, based on the W sites refined distance these sites interact with both each other and chlorine atoms forming oligomers (W2–W2 = 2.93 Å, W3–Cl = 3.21 Å and W1– W2 = 2.93 and 2.74 Å, respectively) that strongly interact with the framework oxygen atoms via chlorine (Figure 6.2.4a). According to the recent literature [5–8,10–13,29,44], the strong interactions among organic molecules–H<sub>2</sub>O short chain-frameworks play a relevant role in stabilising the guest structures within the zeolite porosity. On a whole, on the basis of Rietveld refinement 70 H<sub>2</sub>O molecules (~ 8% dw %) were detected in good agreement with the TG curve (Figure 6.2.5a), which shows two main weight losses: the first one (about 7.3 dw % zeolite, 25–110°C) is related to desorption of species retained on the surface, the second one (23.5 dw % zeolite, 110–900°C) to the removal from the structure of loaded CB and H<sub>2</sub>O molecules.





**Figure 6.2.5** Thermal analysis of Y (a) and ZSM-5 (b) loaded with chlorobenzene from room temperature to 900 °C. In blue and gray circles, the total weight loss curve (TG) and the derivative of it (DTG); in red the differential thermal analysis (DTA) curve.

## ZSM-5–CB

The ZSM-5 zeolite framework consists of two intersecting channel systems: a straight channel parallel to [010] direction and a sinusoidal one parallel to [100] direction [34]. Both channels are limited by 10MR of  $\text{TO}_4$  tetrahedra with free diameters of 5.4–5.6 Å and 5.1–5.5 Å for sinusoidal and straight channel, respectively. After CB adsorption, the evolution of the powder diffraction pattern indicates that ZSM-5 maintains its crystallinity as well as the monoclinic P21/n symmetry. In Table 6.2.1, the comparison between refined lattice parameters of starting material and of the ZSM-5–CB system highlights the occurrence of chlorobenzene adsorption in the ZSM-5 micropores. The structural characterisation was carried out starting with the model proposed by Rodeghero et al. [6] and an examination of the difference Fourier maps of the electron density suggested the presence of extraframework content. In detail, some of recognised maxima were reasonably attributed to chlorobenzene adsorption sites in both the sinusoidal channel (CB2 sites) and the intersection between sinusoidal and straight channels (CB1 sites) (Figure 6.2.4b). On the whole, a total amount of about 6 molecules per unit cell (p.u.c.) of organics were detected.

Besides, residual maxima of difference Fourier maps also indicate the presence of coadsorbed H<sub>2</sub>O molecules (~ 1.5 dw %) hosted at W1 and W2 sites. In particular, based on the refined distances between the extraframework content and framework oxygen atoms strong interactions among chlorobenzene molecules hosted in both adsorption sites (CB1 and CB2), H<sub>2</sub>O molecules (W1 and W2 sites), and framework oxygen atoms occur (i.e., O4–C10 = 3.01(1) Å, O18–C9 = 2.61(1) Å, O31–Cl1 = 2.69(1) Å, O47–Cl1 = 2.99(1) Å, W2–W2 = 3.15(1) Å, O26–Cl2 = 3.03(3) Å, W1–C1 = 3.16(3) Å) (Figure 6.2.4b). Additionally, thermogravimetric analysis (Figure 6.2.5b) indicated that relevant weight loss, occurring at temperatures higher than 100°C (7% in weight), is due to the expulsion from the structure of extraframework ions embedded in the ZSM-5 channels. The residual one at lower temperature can be ascribed to the expulsion of water and/or CB molecules bonded to the surface (3% in weight below ~100 °C). These results are quite well supported by the total amount of adsorbed molecules detected through both saturation capacity determined by the adsorption isotherm and the results obtained by Rietveld analysis. After adsorption, the T–O bond length ranges from 1.602 to 1.608 Å, the O–T–O angles varies from 96° to 125°, with a mean value of 109.4°. According to Wragg et al. [44] the T–O–T bond angles adopt a wide range of values from 124° to 178°. Regarding the channel geometry, after organics adsorption, any changes in both shape and channel dimension were also evaluated. Specifically, both straight and sinusoidal channels hosting the organic molecules change their shape and become more elliptical (Table 6.2.5).

Straight Channel										
O-O distance (Å)	O7-O1	O8-O2	O31-O37	O44-O46	O47-O48	$\epsilon$				
ZSM-5-CB	8.22	8.20	8.02	8.22	7.97	1.03				
ZSM-5	7.90	7.94	8.04	8.41	7.80	1.08				
Free diameter (Å)	O7-O1	O8-O2	O31-O37	O44-O46	O47-O48					
ZSM-5-CB	5.52	5.50	5.32	5.52	5.27	-				
ZSM-5	5.20	5.24	5.34	5.71	5.10	-				
Mean diameter (Å)						Mean radius (Å)	C.F.A. (Å <sup>2</sup> )			
ZSM-5-CB	5.43	2.71	23.12			-				
ZSM-5	5.32	2.66	22.20			-				
O-O distance (Å)	O11-O5	O20-O18	O21-O22	O27-O33	O28-O34	$\epsilon$				
ZSM-5-CB	8.08	7.89	8.11	8.22	8.08	1.04				
ZSM-5	8.19	8.35	7.98	8.13	7.76	1.08				
Free diameter (Å)	O11-O5	O20-O18	O21-O22	O27-O33	O28-O34					
ZSM-5-CB	5.38	5.19	5.41	5.52	5.38					
ZSM-5	5.49	5.65	5.28	5.43	5.06					
Mean diameter (Å)						Mean radius (Å)	C.F.A. (Å <sup>2</sup> )			
ZSM-5-CB	5.37	2.69	22.67							
ZSM-5	5.38	2.69	22.74							
Sinusoidal Channel										
O-O distance (Å)	O20-O15	O24-O26	O27-O2	O28-O1	O41-O46	$\epsilon$				
ZSM-5-CB	8.08	7.87	7.76	8.16	8.69	1.12				
ZSM-5	8.15	8.07	7.97	7.76	8.51	1.10				
Free diameter (Å)	O20-O15	O24-O26	O27-O2	O28-O1	O41-O46					
ZSM-5-CB	5.38	5.17	5.06	5.46	5.99					
ZSM-5	5.45	5.37	5.27	5.06	5.81					
Mean diameter (Å)						Mean radius (Å)	C.F.A. (Å <sup>2</sup> )			
ZSM-5-CB	5.41	2.71	23.01							
ZSM-5	5.39	2.70	22.82							
O-O distance (Å)	O17-O18	O23-O25	O30-O5	O31-O4	O44-O43	$\epsilon$				
ZSM-5-CB	7.50	8.58	8.20	7.89	7.75	1.14				
ZSM-5	7.30	8.31	8.32	8.05	7.95	1.14				
Free diameter (Å)	O17-O18	O23-O25	O30-O5	O31-O4	O44-O43					
ZSM-5-CB	4.80	5.88	5.50	5.19	5.05					
ZSM-5	4.60	5.61	5.62	5.35	5.25					
Mean diameter (Å)						Mean radius (Å)	C.F.A. (Å <sup>2</sup> )			
ZSM-5-CB	5.28	2.64	21.92							
ZSM-5	5.29	2.64	21.93							

**Table 6.2.5** C.F.A. and ellipticity ( $\epsilon$ ) comparison between unloaded ZSM-5 [13] and ZSM-5–CB systems. C.F.A. =  $(\text{mean radius})^2$  (Å<sup>2</sup>);  $\epsilon$  = ratio between the longest and the shortest pore dimensions.

## 6.2.4 Conclusions

This work aims to highlight the adsorptive capacity of commercial high silica zeolites ZSM-5 (MFI topology), and Y zeolite (FAU topology), for removal of chlorobenzene (CB)

from water. Both high silica ZSM-5 and Y zeolites are characterised by fast kinetics, that combined with good adsorption capacity, suggest they can be efficiently used as a sorbent media to control the concentration of chlorobenzene in water systems. In particular, ZSM-5 is more efficient in the removal of CB at low concentration level, while Y shows higher saturation capacity than ZSM-5. Difference Fourier maps of the electron density provide insight into the preferred zeolite adsorption sites in both microporous materials. The refined framework–extraframework bond distances highlight the existence of CB, and hydrophobic zeolites interactions mediated via co-adsorbed H<sub>2</sub>O molecules. Adsorption of CB on ZSM-5 and Y zeolites is accompanied by structural changes, i.e. variations in both unit-cell parameters and channel shape when compared to the as-synthesised microporous materials, clearly confirming the very relevant role of H<sub>2</sub>O molecules in both the diffusion and adsorption processes in hydrophobic zeolites. After adsorption, the channels become more distorted, thus indicating remarkable framework flexibility for both ZSM-5 and Y zeolites.

## 6.2.5 Refereces

- [1] Sennour R., Mimane G., Benghalem A., Taleb S. (2009) Removal of the persistent pollutant chlorobenzene by adsorption onto activated montmorillonite. *Appl. Clay Sci.*, 43, 503–506.
- [2] McClenny W. A., Oliver K. D., Jacumin H. H. Jr., Daughtrey E. H. Jr. (2002) Ambient level volatile organic compound (VOC) monitoring using solid adsorbents—Recent US EPA studies. *J. Environ. Monitor.*, 4, 695–705.
- [3] Khan F. I., Ghoshal A. K. (2000) Removal of Volatile Organic Compounds from Polluted air. *J. Prevent. Proc.*, 13, 527–545.
- [4] Sarti E., Chenet T., Pasti L., Cavazzini A., Rodeghero E., Martucci A. (2017) Effect of silica alumina ratio and thermal treatment of beta zeolites on the adsorption of toluene from aqueous solutions. *Minerals*, 7, 22.
- [5] Rodeghero E., Pasti L., Sarti E., Cruciani G., Bagatin R., Martucci A. (2017) Temperature-induced desorption of methyl tert-butyl ether confined on ZSM-5: An in situ synchrotron XRD powder diffraction study. *Minerals*, 7, 34.
- [6] Rodeghero E., Martucci A., Cruciani G., Bagatin R., Sarti E., Bosi V., Pasti L. (2016) Kinetics and dynamic behaviour of toluene desorption from ZSM-5 using in situ hightemperature synchrotron powder X-ray diffraction and chromatographic techniques. *Catal. Today*, 227, 118–125.
- [7] Arletti R., Martucci A., Alberti A., Pasti L., Nassi M., Bagatin R. (2012) Location of MTBE and toluene in the channel system of the zeolite mordenite: Adsorption and host–guest interactions. *J. Solid State Chem.*, 194, 135–142.
- [8] Pasti L., Rodeghero E., Sarti E., Bosi V., Cavazzini A., Bagatin R., Martucci A. (2016) Competitive adsorption of VOCs from binary aqueous mixtures on zeolite ZSM-5. *RSC Adv.*, 6, 54544–54552.
- [9] Pasti L., Sarti E., Cavazzini A., Marchetti N., Dondi F., Martucci A. (2013) Factors affecting drug adsorption on beta zeolites. *J. Sep. Sci.*, 36, 1604–1611.
- [10] Martucci A., Pasti L., Marchetti N., Cavazzini A., Dondi F., Alberti A. (2012) Adsorption of pharmaceuticals from aqueous solutions on synthetic zeolites. *Micropor. Mesopor. Mat.*, 148, 174–183.

- [11] Braschi I., Blasioli S., Gigli L., Gessa C.E., Alberti A., Martucci A. (2010) Removal of sulfonamide antibiotics from water: Evidence of adsorption into an organophilic zeolite Y by its structural modifications. *J. Hazard. Mater.*, 17, 218–225.
- [12] Blasioli S., Martucci A., Paul G., Gigli L., Cossi M., Johnston C.T., Marchese L., Braschi I. (2014) Removal of sulfamethoxazole sulfonamide antibiotic from water by high silica zeolites: A study of the involved host–guest interactions by a combined structural, spectroscopic, and computational approach. *J. Colloid. Interf. Sci.*, 419, 148–159.
- [13] Pasti L., Martucci A., Nassi M., Cavazzini A., Alberti A., Bagatin R. (2012) The role of water in DCE adsorption from aqueous solutions onto hydrophobic zeolites. *Micropor. Mesopor. Mat.*, 160, 182–193.
- [14] Guo Y., Li Y., Zhu T., Ye M., Wang X. (2013) Adsorption of SO<sub>2</sub> and chlorobenzene on activated carbon. *Adsorpt.*, 19, 1109–1116.
- [15] Crisafully R., Milhome M. A. L., Cavalcante R. M., Silveira E. R., De Keukeleire D., Nascimento R. F. (2008) Removal of some polycyclic aromatic hydrocarbons from petrochemical wastewater using low-cost adsorbents of natural origin. *Bioresource Technol.*, 99, 4515–4519.
- [16] Kim B. K., Ryu S. K., Kim B. J., Park S. J. (2006) Roles of Acid-Base Interactions in Hydrogen Chloride Removal by Activated Carbon Fibers. *J. Ind. Eng. Chem.*, 12, 121–126.
- [17] Park S. J., Kim B. J. (2004) Influence of oxygen plasma treatment on hydrogen Chloride removal of activated carbon fibers. *J. Colloid Interf. Sci.*, 275, 590–595.
- [18] Chin C. J. M., Shih M. W., Tsai H. J. (2010) Adsorption of nonpolar benzene derivatives on single-walled carbon nanotubes. *Appl. Surf. Sci.*, 256, 6035–6039.
- [19] Long C., Li Q., Li Y., Liu Y., Li A., Zhang Q. (2010) Adsorption characteristics of benzene–chlorobenzene vapor on hypercrosslinked polystyrene adsorbent and a pilotscale application study. *Chem. Eng. J.*, 160, 723–728.
- [20] Chen W., Duan L., Zhu D. (2007) Adsorption of polar and nonpolar organic chemicals to carbon nanotubes. *Environ. Sci. Technol.*, 41, 8295–8300.
- [21] Balamurugan K., Subramanian V. (2013) Adsorption of chlorobenzene onto (5,5) armchair single-walled Carbon nanotube and graphene sheet: Toxicity versus adsorption strength. *J. Phys. Chem. C*, 117, 21217–21227.

- [22] Lee J. J., Choi J., Park J. W. (2002) Simultaneous sorption of lead and chlorobenzene by organobentonite. *Chemosphere*, 49, 1309–1315.
- [23] Witthuhn B., Klauth P., Pernyeszi T., Vereecken H., Klumpp E. (2006) Organoclays for Aquifer Bioremediation: Adsorption of Chlorobenzene on Organoclays and its Degradation by RHODOCOCUS B528. *Water Air Soil Poll. Focus*, 6, 317–329.
- [24] Jarraya I., Fourmentin S., Benzina M., Bouaziz S. (2010) VOC adsorption on raw and modified clay materials. *Chem. Geol.*, 275, 1–8.
- [25] Altare C. R., Bowman R. S., Katz L. E., Kinney K. A., Sullivan E. J. (2007) Regeneration and long-term stability of surfactant-modified zeolite for removal of volatile organic compounds from produced water. *Micropor. Mesopor. Mat.*, 105, 305–316.
- [26] Anderson M. A. (2000) Removal of MTBE and Other Organic Contaminants from Water by Sorption to High Silica Zeolites. *Environ. Sci. Technol.*, 34, 725–727.
- [27] Damjanović L., Rakić V., Rac V., Stošić D., Auroux A. (2010) The investigation of phenol removal from aqueous solutions by zeolites as solid adsorbents. *J. Hazard. Mat.*, 184, 477–484.
- [28] Perego C., Bagatin R., Tagliabue M., Vignola R. (2013) Zeolites and related mesoporous materials for multi-talented environmental solutions. *Micropor. Mesopor. Mat.*, 166, 37–49.
- [29] Leardini L., Martucci A., Braschi I., Blasioli S., Quartieri S. (2014) Regeneration of highsilica zeolites after sulfamethoxazole antibiotic adsorption: A combined in situ hightemperature synchrotron X-ray powder diffraction and thermal degradation study. *Mineral. Mag.*, 78, 1141–1160.
- [30] Braschi I., Blasioli S., Buscaroli E., Montecchio D., Martucci A. (2016) Physicochemical regeneration of high silica zeolite Y used to clean-up water polluted with sulfonamide antibiotics. *J. Environ. Sci.*, 43, 302–312.
- [31] Vignola R., Cova U., Fabiani F., Sbardellati T., Sisto R., Vignola R. Process for the regeneration of nonpolar adsorbing zeolites used for the treatment of contaminated water. Patent WO/2009/000429, 31 December 2008.
- [32] Alberti A., Martucci A. (2005) Phase transformations and structural modifications induced by heating in microporous materials. *Stud. Surf. Sci. Catal.*, 155, 19–43.
- [33] Alberti A., Martucci A. (2011) Reconstructive phase transitions in microporous materials: Rules and factors affecting them. *Micropor. Mesopor. Mat.*, 141, 192, 198.



- [34] Baerlocher C., McCusker L. B., Olson D. H. (2007) Atlas of Zeolite Framework Types, 6th ed.; Elsevier: Amsterdam, The Netherland.
- [35] Larson A. C., Von Dreele R. B. (1994) GSAS General Structure Analysis System, LANSCE, MS-H805; Los Alamos National Laboratory: Los Alamos, NM, USA.
- [36] Toby B. H. (2001) EXPGUI, a graphical user interface for GSAS. *J. Appl. Crystallogr.*, 34, 210–213.
- [37] Azizian S., Haerifar M., Bashiri H. (2009) Adsorption of methyl violet onto granular activated carbon: Equilibrium, kinetics and modeling. *Chem. Eng. J.*, 146, 36–41.
- [38] De Moor B. A., Reyniers M. F., Gobin O. C., Lercher J. A., Marin G. B. (2011) Adsorption of C2-C8 n-Alkanes in Zeolites. *J. Phys. Chem. C*, 115, 1204–1219.
- [39] Martucci A., Braschi I., Bisio C., Sarti E., Rodeghero E., Bagatin R., Pasti L. (2015) Influence of water on the retention of methyl tertiary-butyl ether by high silica ZSM 5 and Y zeolites: A multidisciplinary study on the adsorption from liquid and gas phase. *RSC Advances*, 5, 86997–87006.
- [40] Martucci A., Braschi I., Marchese L., Quartieri S. (2014) Recent advances in clean up strategies of waters polluted with sulfonamide antibiotics: A review of sorbents and related properties. *Mineral. Mag.*, 78, 1115–1140.
- [41] Li X., Chen G. H. (2009) Surface modified graphite nanosheets used as adsorbent to remove 1,2-dichlorobenzene from water. *Mater. Lett.*, 63, 930–932.
- [42] Yu F., Ma J., Wu Y. (2011) Adsorption of toluene, ethylbenzene and m-xylene on multiwalled carbon nanotubes with different oxygen contents from aqueous solutions. *J. Hazard. Mater.*, 192, 1370–1379.
- [43] Krishna R., van Baten J. M. (2010) Highlighting a Variety of Unusual Characteristics of Adsorption and Diffusion in Microporous Materials Induced by Clustering of Guest Molecules. *Langmuir*, 26, 8450–8463.
- [44] Wragg D. S., Morris R. E., Burton A. W. (2008) Pure silica zeolite-type frameworks: A structural analysis. *Chem. Mater.*, 20, 1561–1570.
- [45] Leardini L., Martucci A., Alberti A., Cruciani G. (2013) Template burning effects on stability and boron coordination in boron lewyne studied by in situ time resolved synchrotron powder diffraction. *Micropor. Mesopor. Mater.*, 167, 117–126.
- [46] Baur W. H. (1992) Self-limiting distortion by antirotating hinges is the principle of flexible but noncollapsible frameworks. *J. Solid State Chem.*, 97, 243–247.

[47] Momma K., Izumi F. (2011) VESTA 3 for three-dimensional visualization of crystal, volumetric and morphology data. *J. Appl. Crystallogr.*, 44, 1272–1276.

### 6.3 Photodegradation of contaminants using semiconductor $W_{10}O_{32}^{2-}$

The data herein reported are part of my work of thesis and have been published in: Luisa Pasti, Elena Sarti, Annalisa Martucci, Nicola Marchetti, Claudia Stevanin, Alessandra Molinari (2018). An advanced oxidation process by photoexcited heterogeneous sodium decatungstate for the degradation of drugs present in aqueous environment. *Applied Catalysis B: Environmental* 239, 345–351

The aim of this work was to verify the photodegradation of organic contaminants in water media through the use of a photocatalyst. The main feature of the chosen photocatalyst, sodium decatungstate, is that in the presence of light it can produce OH radicals in aqueous solution. These radicals are not selective so they can react with a large number of molecules. After preliminary tests in which the catalyst in dispersed solution was used, it was immobilized in different supports.

The ability of the decatungstate anion ( $W_{10}O_{32}^{4-}$ ) to photoproduce OH· radicals from water is preserved when the polyoxanion is immobilized on solid supports and can be exploited as a heterogeneous photocatalytic process aimed at water reclamation.

It was possible to study the production of OH· radicals in solution for both working conditions, dispersed phase and heterogeneous phase, by means of EPR-spin trapping experiments.

However, we show that the interaction between OH· radicals and drug molecules depend on the physicochemical properties of the chosen medium. In fact, we demonstrate that the silica particles covered by decatungstate anions are not efficient in the degradation of carbamazepine and sulfamethoxazole (ubiquitous contaminants of natural waters) which are respectively neutral and negatively charged at an operating pH of 6. On the contrary, the entrapment of  $W_{10}O_{32}^{4-}$  within a mesoporous organosilic matrix it leads to a heterogeneous photocatalytic system with its own hydrophobic characteristics. Organic molecules enter the mesopores and easily leave the aqueous environment. Inside the pores the reaction between the photoproduced OH· radicals is favored. The mono and dihydroxylated products precede the fragmentation and degradation of the studied drug.

### 6.3.1 Introduction

Water scarcity is a well-recognized challenge to the sustainable development of many countries that claims for further efforts to develop and improve water treatment technologies. It is therefore necessary the development of processes capable to ensure the total elimination of trace of organic contaminants from waters [1,2].

The use of advanced oxidation processes (AOPs) has been demonstrated to be a possible approach for the remediation of contaminated waters [3,4]. AOPs are based on the insitu production of free radical species, such as ( $\text{OH}\cdot$ ), which being a strong oxidant characterized by a very high standard reduction potential ( $E^\circ = +2.80 \text{ V vs. SHE}$ ) rapidly oxidizes electron-rich organic compounds up to their mineralization [5]. Among the large variety of oxidation processes, photochemical methods offer the advantage of energy efficiency, rapidness and limited use of chemicals (oxidants), which together concur to the sustainability of the process [5]. In particular, photocatalysis with  $\text{TiO}_2$  has been demonstrated to be an efficient method for the destruction of low amounts of water-soluble organic pollutants [6–8], even if other semiconductor materials, such as  $\text{WO}_3$ , have been recently successfully utilized [9]. In water decontamination issue, the applicability of polyoxotungstates for the degradation and mineralization of chlorophenols, chloroacetic acids and herbicide has been also explored [10,11]. Among polyoxotungstates, decatungstate anionic cluster has light absorption properties very similar to those of  $\text{TiO}_2$  and for this similarity it can be considered a soluble analogue of the most employed semiconductor. In addition, it has been demonstrated that photoexcitation of  $\text{Na}_4\text{W}_{10}\text{O}_{32}$  dissolved in water produces  $\text{OH}\cdot$  radicals from water oxidation [12]. The interest for heterogeneous decatungstate photocatalyst in advanced oxidation processes framework has led to the development of several heterogenization procedures, such as impregnation on a solid support [13] and ion exchange [14,15]. Indeed, heterogeneous (photo)catalysis has the advantage of easy separation and recovery.

Recently, a heterogeneous photocatalytic system obtained by immobilization of the anionic decatungstate cluster on silica particles functionalized with  $-\text{NH}_2$  groups has been employed for the degradation of some contaminants of emerging concerns in aqueous matrix [16]. It was proved that the photocatalytic system was efficient and recyclable. The degradation process is achieved by photoexcitation of heterogeneous

decatungstate that results in the formation of OH• radicals as revealed by EPR spin trapping spectroscopy.

In addition, studies on the reaction mechanism of heterogeneous polyoxotungstates indicate that the selectivity and efficiency of these photocatalysts depend on the support characteristics. In general, pore structures, distributions of the active sites and hydrophilic–hydrophobic interactions with the substrate are key factors for the catalytic activity and selectivity of solid heterogeneous catalysts [17–19]. Therefore, the choice of support matrices is very important for highly efficient catalytic systems. In this paper, we show how support matrix properties can tune the degradation ability of immobilized decatungstate with respect to three target molecules in dilute aqueous solutions: propranolol, carbamazepine and sulfamethoxazole. These molecules are selected as probes since all of them are ubiquitous contaminants of natural waters. In particular, carbamazepine is a psychotic drug, resistant to conventional wastewater treatment and sulfamethoxazole is an antimicrobial largely employed, which has been detected in surface and drinking waters [20].

Two different heterogeneous photocatalysts, obtained either by immobilization of  $W_{10}O_{32}^{4-}$  by an ion exchange mechanism [16] or by encapsulation of the anionic cluster into a silicate structure [21], that were proved to be able to oxidize organic compounds, are here investigated. In particular, their photocatalytic degradation activity with respect to contaminants of emerging concern is evaluated and the observed differences are related to both the support and the drug molecule physical chemical properties. EPR spin trapping technique and HPLCMS analysis are employed to gain information about the operating degradative mechanism and the nature of reaction intermediates. In addition, composition and structural properties of the heterogeneous photocatalytic system are more deeply investigated. To the best of our knowledge, this is the first contribution where the photoactivity of decatungstate anion heterogenized on two different supports is compared, thus demonstrating that it is possible to tune the photocatalytic activity of the polyoxoanion by varying the chemical-physical properties of the support.

### 6.3.2. Experimental

#### Materials

Propranolol (PRP, purity 99.8%), carbamazepine (CBZ, purity 99.8%), sulfamethoxazole (SMX, purity 99.8%) and formic acid were purchased from Fluka (Fluka Chemie AG, Switzerland). Sodium hydroxide (Titolchimica, Rovigo, Italy), hydrochloric acid (Carlo Erba, Milano, Italy) of analytical grade were employed to adjust the pH of diluted drugs solutions. The pH was measured using an AMEL pHmeter (Milano, Italy). High-performance liquid chromatography (HPLC) grade acetonitrile (ACN) was purchased from Merck (Darmstadt, Germany). The water was Milli-Q® grade (Millipore, MA, USA).

#### Photocatalysts preparation

Sodium decatungstate ( $\text{Na}_4\text{W}_{10}\text{O}_{32}$ ) was synthesized following reported literature procedures [22,23]. The heterogeneous photocatalysts silica- $\text{NH}_3^+$ / $\text{Na}_3\text{W}_{10}\text{O}_{32}^-$  have been prepared carrying out the procedure recently published [16].  $\text{Na}_4\text{W}_{10}\text{O}_{32}/\text{SiO}_2/\text{BTESE}$  was prepared by simultaneous hydrolysis of tetraethylorthosilicate (TEOS, 23 mmol) and 1,2-bis(triethoxysilyl)ethane (BTESE, 2.3 mmol) in an acid aqueous solution of  $\text{Na}_4\text{W}_{10}\text{O}_{32}$  [21]. The obtained material has a content of decatungstate of 0.33 mmol/g. The composition was determined by Inductively Coupled Plasma-Optical Emission Spectrometer ICP-OES (Perkin-Elmer Optima 3100 XL) equipped with an axial torch, segmented array charge coupled device (SCD) detector and Babington-type nebulizer with cyclonic spray chamber for sample introduction. Plasma conditions were: RF power of 1.40 kW applied to the plasma; 15 L  $\text{min}^{-1}$  flow rate for plasma and 0.5 L  $\text{min}^{-1}$  for auxiliary gas. Nebulizer gas flow rate was 0.65 L  $\text{min}^{-1}$ . Sample uptake was 1.5 mL  $\text{min}^{-1}$  for each of three replicate scans. 0.5 g of samples were mineralized by microwave acid digestion ( $\text{HNO}_3$ , HF and  $\text{H}_3\text{BO}_3$ ) at 200 °C and high pressure (200 psi), with 20 min dwell time. At the end of preparation, UV-vis spectra of washing water aliquots showed that polyoxoanion was not released in the solution.

#### Photocatalytic experiments with homogeneous $\text{Na}_4\text{W}_{10}\text{O}_{32}$

An aerated aqueous solution (3 mL, final pH=6) containing dissolved  $\text{Na}_4\text{W}_{10}\text{O}_{32}$  ( $2 \cdot 10^{-4}$  M) and the drug of interest ( $C_0=10\text{mg L}^{-1}$ ) was put into a spectrophotometric cell (optical

path 1 cm) and placed in front of a Hg medium pressure lamp (Helios Italquartz, 15W cm<sup>-2</sup>). The solution is magnetically stirred and irradiation was carried out using a cut-off filter, placed between the lamp slit (1 cm x 3 cm) and the cuvette in order to select the suitable wavelength range (PRP,  $\lambda > 330$  nm, SMX  $\lambda > 335$  nm; CBZ,  $\lambda > 300$  nm). Selection of suitable cut off filter was performed in order to avoid direct photolysis of the drug compound. At the end of illumination, the sample was filtrated with 0.22  $\mu$ m PVDF membrane filters Captiva Econofilter Agilent Technologies (Santa Clara, CA, USA) and HPLC analysis was performed.

Samples containing dissolved decatungstate anion have been kept in the dark and then analyzed.

### **Photocatalytic experiments with heterogeneous Na<sub>4</sub>W<sub>10</sub>O<sub>32</sub>**

In a typical photocatalytic experiment, the optimal amount determined elsewhere [16,21] of silica-NH<sub>3</sub><sup>+</sup>/Na<sub>3</sub>W<sub>10</sub>O<sub>32</sub><sup>-</sup> (5 g/L) or of Na<sub>4</sub>W<sub>10</sub>O<sub>32</sub>/SiO<sub>2</sub>/BTESE (8 g/L) was kept in suspension in aqueous solution (3 mL, pH=6) containing the drug of interest (C<sub>0</sub>=10mg L<sup>-1</sup>) inside a spectrophotometric cell. Then, irradiation was carried out for the required period of time with the selected cut off filter (PRP,  $\lambda > 330$  nm, SMX  $\lambda > 335$  nm; CBZ,  $\lambda > 300$  nm) and at the end of irradiation the solution was analyzed as described above. After irradiation, the solutions were centrifuged to separate the heterogeneous photocatalysts and UV-vis spectra have been recorded to evaluate leaching of decatungstate anion. Moreover, these solutions have been subsequently irradiated to establish eventual photoactivity of traces of decatungstate cluster, leached into the solution and not detected by spectrophotometric analysis.

Some photocatalytic experiments have been carried out to evaluate the stability of decatungstate on the support, by recovering Na<sub>4</sub>W<sub>10</sub>O<sub>32</sub>/ SiO<sub>2</sub>/BTESE (8 g/L) after the first photocatalytic experiment, washing with aliquots of acetonitrile and drying in the oven at 373 K for 60 min. The photocatalytic system has been reused in a second experiment, suspending it in an aqueous solution (3 mL, pH=6) containing CBZ (C<sub>0</sub>=10mg L<sup>-1</sup>) and irradiated as described above. The irradiated solution was then analysed.

2.5. HPLC analysis A HPLC/DAD (Waters, MA, USA pump: Waters 515, DAD: Waters PDA 996) was employed under isocratic elution conditions, reported in Table 2. The flow rate was 1 mL min<sup>-1</sup>, while the column was thermostated at 25 °C. The column was 150x4.6mm (Phenomenex, CA, USA) and packed with a C18 silica-based stationary

phase with a particle diameter of 5  $\mu\text{m}$ . The injection volume was 20  $\mu\text{L}$  for all standards and samples.

### **HPLC/MS analysis**

HPLC/MS analyses were carried out by means of Surveyor Plus micro-HPLC hyphenated to a linear ion trap mass spectrometer (LTQ XL Thermo Scientific, Waltham, MA, USA). The HPLC apparatus was composed of a solvent delivery system, a quaternary pump (including a membrane degasser) and an autosampler (including a thermostated column compartment). The LTQ system was equipped with an electrospray ionization (ESI) ion source. The mobile phase was obtained as a mixture of ACN and formic acid 0.1% v/v: water formic acid 0.1% v/v. Chromatographic separation was performed under gradient elution conditions: 0–6 min 5% ACN, 6–14 min 5–70% ACN, 14–15 min 70% ACN, then held isocratically at 95% of ACN for 3 min before reconditioning the column. The flow rate was 100  $\mu\text{L min}^{-1}$ , while the column was thermostated at 25  $^{\circ}\text{C}$ . The column was 50 $\times$ 2.1mm (Restek, Bellefonte, PA, USA) packed with a C18 silica-based stationary phase with a particle diameter of 3  $\mu\text{m}$ . The injection volume was 5  $\mu\text{L}$  for all standards and samples. MS experimental conditions were as follows: spray voltage 4 kV, capillary temperature 275  $^{\circ}\text{C}$ , capillary voltage 11 V and tube lens 25 V for positive ESI conditions.

### **EPR-spin trapping experiments**

EPR-spin trapping experiments were carried out with a Bruker ER200 MRD spectrometer equipped with a TE201 resonator (microwave frequency of 9.4 GHz). The homogeneous samples were aqueous solutions containing 5,5'-dimethylpyrroline N-oxide (DMPO, 5  $10^{-2}$  M) as spin trap and  $\text{Na}_4\text{W}_{10}\text{O}_{32}$  ( $2 \cdot 10^{-4}$  M). In heterogeneous experiments, silica- $\text{NH}_3^+/\text{Na}_3\text{W}_{10}\text{O}_{32}^-$  was suspended in an analogous solution.

When requested, CBZ ( $C_0=10\text{mg L}^{-1}$ ) was introduced together with the spin trap. The samples were put into a flat quartz cell and directly irradiated in the EPR cavity with a medium pressure Hg lamp equipped with cut off filter ( $\lambda>300$  nm). No signals were obtained in the dark or during irradiation of the solution in the absence of decatungstate.



## XRD analysis

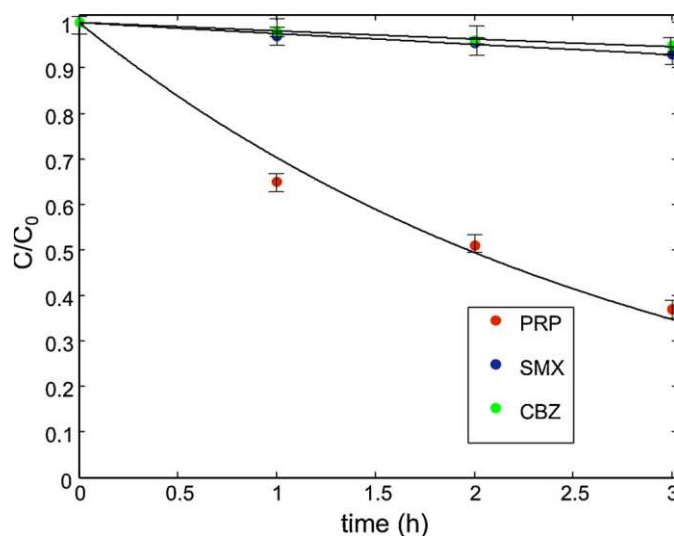
X-ray diffraction was used to verify the incorporation of BTESE on silica-based support. Powder patterns were measured on a Bruker D8 Advance Diffractometer equipped with a Sol-X detector, using Cu K $\alpha$ 1, $\alpha$ 2 radiation in the 3–110 2 $\theta$  range and a counting time of 12 s/ step. Table 2S reports reflection information for Na<sub>4</sub>W<sub>10</sub>O<sub>32</sub>/SiO<sub>2</sub>/ BTESE phase, where HKL are hkl, STOL is the value of  $\sin\theta/\lambda$ , TTH is the 2 $\theta$  position of the reflection, FWHM is the full width at half maximum of the reflection, FOSQ is Fo 2, SIG is an estimate  $\sigma$  Fo 2, FOBS is Fo. The GSAS LeBail computer program with the EXPGUI interface (Larson, A. C., & Von Dreele, R. B. General Structure Analysis System (GSAS); Los Alamos National Laboratory: Los Alamos, NM, 2000, 86–748).

## 6.3.3. Results and discussion

### 6.3.3.1 Sodium decatungstate heterogenized on modified silica particles (silica-NH<sub>3</sub><sup>+</sup>/Na<sub>3</sub>W<sub>10</sub>O<sub>32</sub><sup>-</sup>).

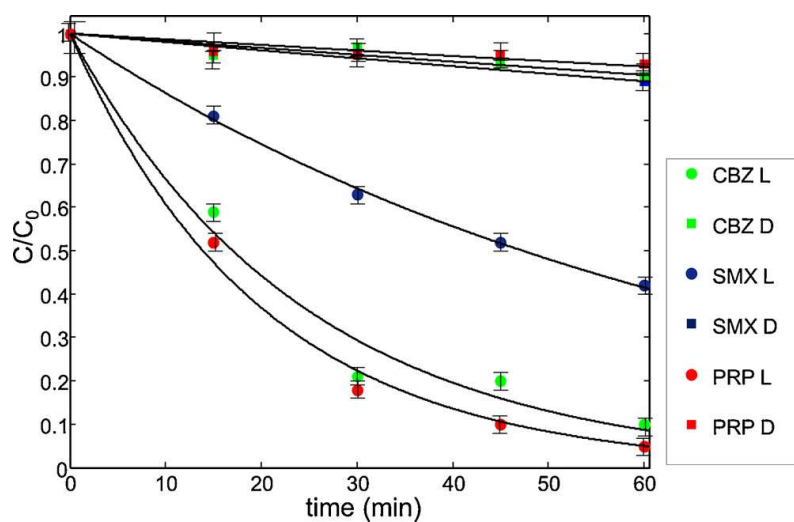
We recently demonstrated that a robust and recyclable photocatalytic system can be obtained by immobilization of the anionic cluster on silica particles functionalized with –NH<sub>2</sub> groups [16]. Moreover, photoexcitation of heterogeneous decatungstate (5 g/L) suspended in aqueous solutions (pH=6) containing one among levofloxacin or trimethoprim or atenolol (C<sub>0</sub> =10 mg/L) caused drug degradation mediated by OH $\cdot$  radicals, whose formation has been pointed out by EPR spin trapping spectroscopy [16]. With the aim of evaluating the wide scope of the found method, we decided both to confirm the observed performance by using propranolol (PRP), another  $\beta$ -blocker similar in structure to the previous studied atenolol, and to prove the photocatalytic method extending to other two drugs having different structure and physical chemical properties. In particular, we choose the antibiotic sulfamethoxazole (SMX, often used in combination with the studied trimethoprim) and the antidepressant carbamazepine (CBZ), which is known as a very recalcitrant drug. The degradation of each substrate is followed during irradiation time and it is expressed as ratio C/C<sub>0</sub> (where C is the drug concentration at a certain time and C<sub>0</sub> is the initial one). Interestingly, we observe (Fig. 6.3.1) that PRP behaves similarly to atenolol and after 3 h irradiation about 60–65% of degradation was obtained. On the contrary, irradiation of the silica-NH<sub>3</sub><sup>+</sup>/ Na<sub>3</sub>W<sub>10</sub>O<sub>32</sub><sup>-</sup>

system does not cause any appreciable photocatalytic degradation of both SMX and CBZ.

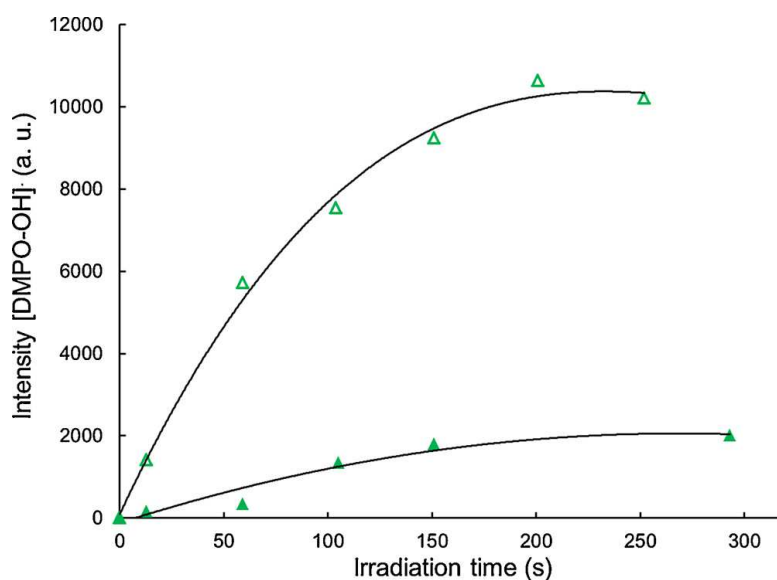


**Fig. 6.3.1.** Degradation kinetics of drugs by photoexcitation of silica-NH<sub>3</sub><sup>+</sup>/Na<sub>3</sub>W<sub>10</sub>O<sub>32</sub><sup>-</sup> (5 g/L) suspended in an aqueous solution (pH 6) containing propranolol (PRP), or sulfamethoxazole (SMX) or carbamazepine (CBZ). C<sub>0</sub>=10 mg/L. PRP, λ>330 nm, SMX λ>335 nm; CBZ, λ>300 nm.

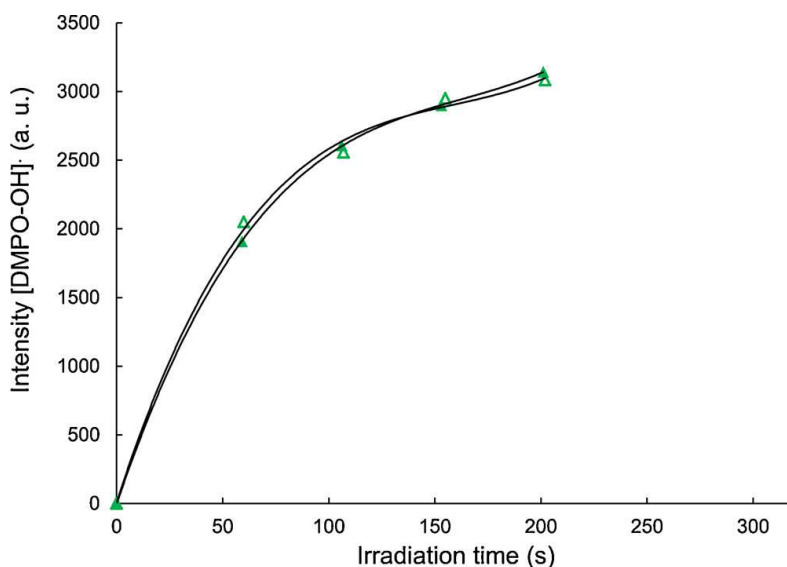
On the basis of these results, we propose that the inefficient degradation of both SMX and CBZ could be due to one of the following factors: i) low photoactivity of the polyoxoanion with respect to these molecules; ii) scarce affinity of the catalyst support for the two drugs; iii) combination of factors ascribable to decatungstate and its support. In order to evaluate the photocatalytic activity of decatungstate anion itself, experiments are carried out in homogeneous phase irradiating aqueous solutions containing dissolved Na<sub>4</sub>W<sub>10</sub>O<sub>32</sub> (2×10<sup>-4</sup> M) and CBZ, SMX or PRP (C<sub>0</sub>=10 mg/L). obtained results are reported in Fig.6.3.2 (circles), together with control experiments in which analogous samples are kept in the dark (squares). It is shown that around 90% of starting CBZ and PRP are degraded after 60 min of illumination in the presence of homogeneous sodium decatungstate, and a lower degradation efficiency is obtained with SMX that is, however, photodegraded of about 60% in the first hour of irradiation. This decrease is attributable to the photocatalytic activity of W<sub>10</sub>O<sub>32</sub><sup>4-</sup> since the decrease in the dark of CBZ, SMX or PRP never exceeds 10% (Fig.6.3.2, squares). Furthermore, EPR-spin trapping experiments support this statement.



**Fig.6.3.2.** Degradation kinetics of carbamazepine (CBZ), sulfamethoxazole (SMX) and propranolol (PRP) by photoexcitation of Na<sub>4</sub>W<sub>10</sub>O<sub>32</sub> ( $2 \times 10^{-4}$  M) dissolved in water at pH 6 (circles). Control experiments are carried out in the dark (squares). C<sub>0</sub>=10mg L<sup>-1</sup>. CBZ,  $\lambda > 300$  nm; SMX,  $\lambda > 335$  nm; PRP,  $\lambda > 330$  nm.

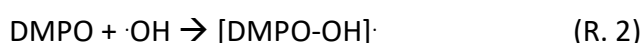
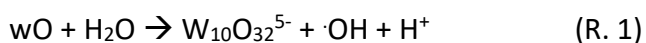


**Fig. 6.3.3.** Fixed-field signal intensity of the [DMPO-OH]· adduct in time upon irradiation ( $\lambda > 300$  nm) of Na<sub>4</sub>W<sub>10</sub>O<sub>32</sub> ( $2 \times 10^{-4}$  M) dissolved in water containing DMPO ( $5 \times 10^{-2}$  M): in the absence (full triangles) and in the presence (empty triangles) of CBZ (10 mg/L). Reported values are the mean of three repeated experiments. Errors do not exceed +10%.



**Fig.6.3.4.** Fixed-field signal intensity of the [DMPO-OH]· adduct in time upon irradiation ( $\lambda > 300$  nm) of silica-NH<sub>3</sub><sup>+</sup>/Na<sub>3</sub>W<sub>10</sub>O<sub>32</sub><sup>-</sup> suspended in an aqueous solution containing DMPO ( $5 \times 10^{-2}$  M): in the absence (full symbols) and in the presence of CBZ (10 mg/L) (empty symbols). Reported values are the mean of three repeated experiments. Errors do not exceed  $\pm 5\%$ .

In fact, photoexcitation of Na<sub>4</sub>W<sub>10</sub>O<sub>32</sub> dissolved in water in the presence of the spin trap DMPO causes the formation of a quartet 1:2:2:1 ( $a_N = a_H = 14.8$  G) ascribable to the paramagnetic adduct [DMPOOH]· in accordance to previous investigation [12]. As shown in Fig. 6.3.3, the intensity of this signal increases by increasing the irradiation time, showing that reactions:



solution causes an important decrease of [DMPO-OH]· signal. This could be an indication that CBZ competes with DMPO in the reaction with OH· radicals, and probably this reaction is the first step of the photocatalytic drug degradation pathway.

Analogous EPR spin trapping experiments carried out irradiating silica-NH<sub>3</sub><sup>+</sup>/Na<sub>3</sub>W<sub>10</sub>O<sub>32</sub><sup>-</sup> suspended in water containing DMPO show that the paramagnetic adduct [DMPO-OH]· is still formed, indicating that the primary photochemical process (Reaction 1) that produces OH· radicals is operating also with the heterogeneous system. Contrarily to what observed for homogeneous decatungstate, the addition of CBZ does not cause any decrease in the intensity of the paramagnetic adduct (Fig.6.3.4). This indicates that OH· radicals generated by photoexcited silica-NH<sub>3</sub><sup>+</sup>/Na<sub>3</sub>W<sub>10</sub>O<sub>32</sub><sup>-</sup> do not quickly react with

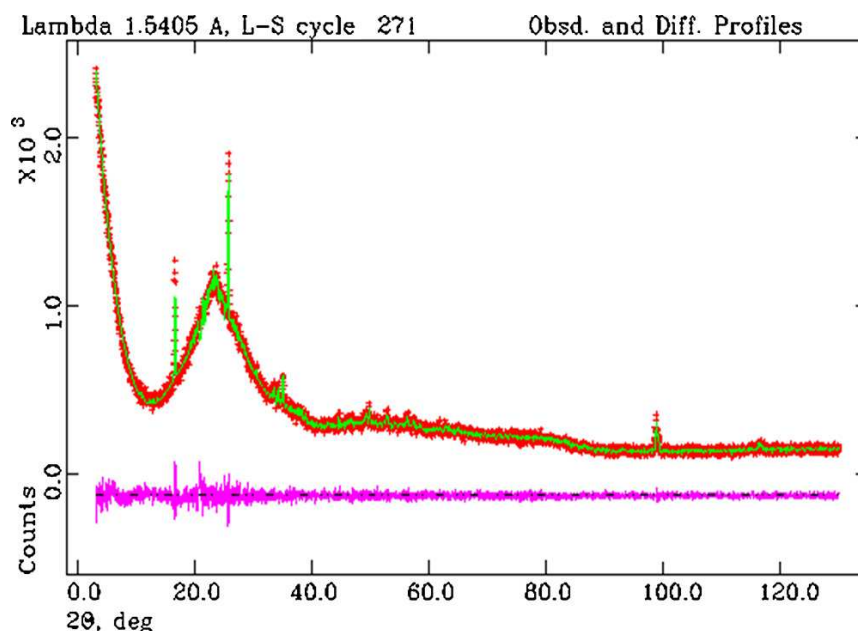
CBZ, in agreement with the absence of degradation of this drug shown in Fig. 6.3.1. Possibly, CBZ does not adequately approach the surface of the heterogeneous photocatalyst where OH<sup>·</sup> radicals are produced or CBZ concentration in the solution in contact with the particle is insufficient to favor the reaction between them two. The different behavior of silica-NH<sub>3</sub><sup>+</sup>/ Na<sub>3</sub>W<sub>10</sub>O<sub>32</sub><sup>-</sup> with respect to the studied drugs can be tentatively rationalized considering their distribution diagrams: at the operative pH of 6, while the β- blockers (PRP and atenolol, ATN) are mainly present in solution as cations, the same is not for CBZ and SMX. In fact, CBZ is in its neutral form and SMX presents an equilibrium between neutral and even negative form. Since the silica particles are covered by decatungstate anions, it can be supposed that immobilized decatungstate anions and CBZ or SMX are not sufficiently close each other, a needed requirement for the reaction between drug molecule and photogenerated OH<sup>·</sup> radicals.

### **6.3.3.2. Sodium decatungstate heterogenized on hydrophobic mesoporous silica support (SiO<sub>2</sub>/BTESE/ Na<sub>4</sub>W<sub>10</sub>O<sub>32</sub>)**

One of the main advantages of heterogeneous photocatalysis is the flexibility in choosing the support with the proper characteristics. Starting from the fact that silica-NH<sub>3</sub><sup>+</sup>/ Na<sub>3</sub>W<sub>10</sub>O<sub>32</sub><sup>-</sup> is not able to perform efficient photocatalytic degradation of CBZ and SMX (Fig. 6.3.1), we thought that a heterogeneous photocatalyst obtained by direct hydrolysis of TEOS and of an organotrialkoxy silane (BTESE) should be hydrophobic enough to favor the approach of organic drugs dissolved in an aqueous matrix. Morphological features of SiO<sub>2</sub>/BTESE/Na<sub>4</sub>W<sub>10</sub>O<sub>32</sub> have been determined: we have checked that SiO<sub>2</sub>/BTESE/Na<sub>4</sub>W<sub>10</sub>O<sub>32</sub> employed in this research presents similar morphological characteristics to those of an analogous heterogeneous system previously used [21]. In particular, the specific surface area is roughly 700m<sup>2</sup> g<sup>-1</sup> and about 80% of total pore volume are classified as mesopores. Additionally, FTIR spectra clearly showed that organic fragments (coming from BTESE) and silica moieties are distributed within the framework and microgravimetric adsorption isotherms pointed out that SiO<sub>2</sub>/BTESE/Na<sub>4</sub>W<sub>10</sub>O<sub>32</sub> enhances adsorption of toluene vapors with respect to that of water [21]. To complete the characterization, XRD was used to determine

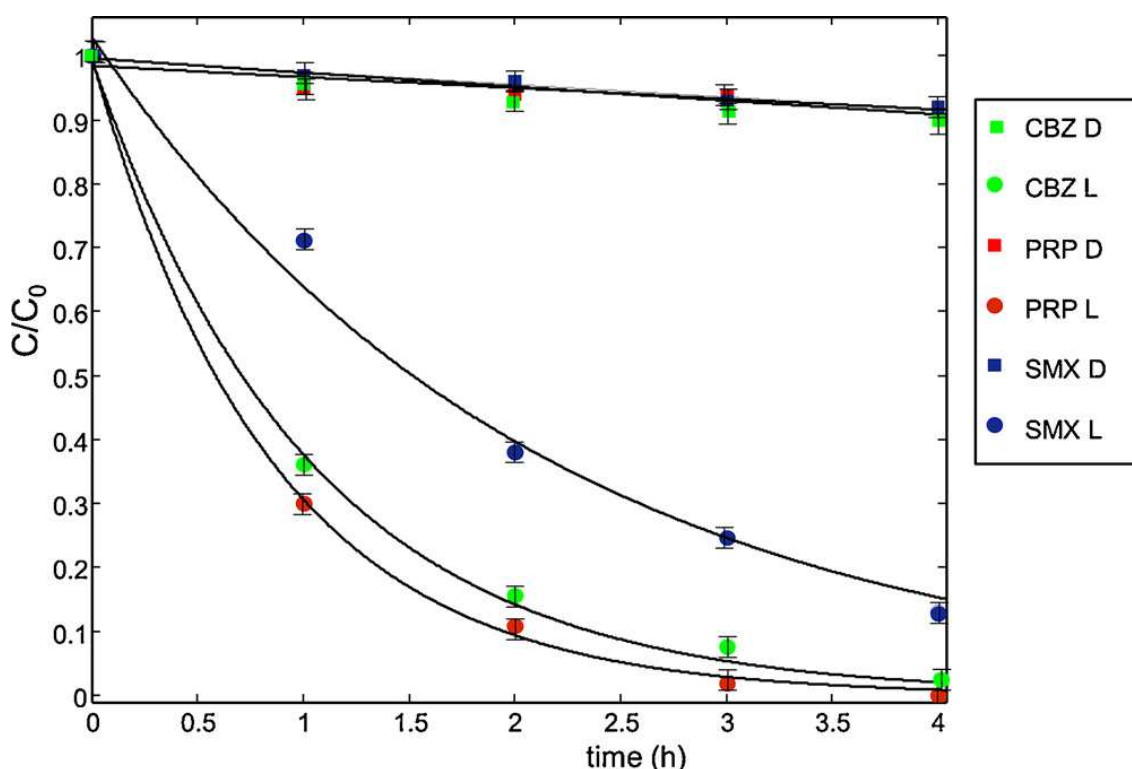
Na<sub>4</sub>W<sub>10</sub>O<sub>32</sub> unit cell parameters starting from the CIF file deposited with the Cambridge Crystallographic Data Center under number CCDC 1548831.

The Na<sub>4</sub>W<sub>10</sub>O<sub>32</sub>/SiO<sub>2</sub>/BTESE refined XRD pattern is shown in Fig. 6.3.5. From Fig. 6.3.5 the peaks at scattering angle (2θ) values of 16.52°, 25.57°, 34.22° and 35.04° were assigned to Na<sub>4</sub>W<sub>10</sub>O<sub>32</sub> respectively. The main crystallographic data and refinement results are as follows: triclinic crystal symmetry, space group P-1, a=11.9532(6) Å, b=12.2201(7) Å, c=12.1898(8) Å, α=75.343°(4) β=71.525°(4) γ=88.083°(5), cell volume=1631.70(17) Å<sup>3</sup>. Values in parenthesis represent the standard deviations of the parameters computed on the basis of 8467 independent observations. Final reliability factors over the observed reflections Rp=0.0403, Rwp=0.0535, χ<sup>2</sup>=1.029 (where Rp = Σ[Y<sub>io</sub> - Y<sub>ic</sub>]/ΣY<sub>io</sub>; Rwp = [Σw<sub>i</sub>(Y<sub>io</sub> - Y<sub>ic</sub>)<sup>2</sup>/Σw<sub>i</sub>Y<sub>io</sub><sup>2</sup>]<sup>0.5</sup>). These data allows us to infer that decatungstate anion is not significantly modified during the synthesis of the heterogeneous system via hydrolysis of TEOS and of BTESE. In addition, XRD analysis shows that it is encapsulated inside the mesoporous network. Finally, the decatungstate content was determined by ICP-OES measurement. As described in the Experimental Section, the synthesis process of SiO<sub>2</sub>/BTESE/Na<sub>4</sub>W<sub>10</sub>O<sub>32</sub> includes the hydrolysis of TEOS and of BTESE in the presence of an acid solution of sodium decatungstate. Silanol groups (^SiOH) can be protonated in the acidic medium to form ^SiOH<sub>2</sub><sup>+</sup>.



**Fig. 6.3.5.** Observed (red dotted line), calculated (green solid line) and difference (purple bottom line) X-ray powder diffraction patterns for Na<sub>4</sub>W<sub>10</sub>O<sub>32</sub>/SiO<sub>2</sub>/ BTESE. (For interpretation of the references to colour in this figure legend, the reader is referred to the web version of this article).

These groups, in turn, should act as counterions for decatungstate anion, that on the basis of XRD results is entirely encapsulated in the mesopores, leading to ( $^-\text{SiOH}_2^+$ ) ( $\text{Na}_3\text{W}_{10}\text{O}_{32}^-$ ) [24]. This strong interaction is confirmed by UV–vis spectra of washing water aliquots showing that polyoxoanion was not released in the solution. Therefore, this heterogeneous photocatalytic system was used for attempting the degradation of CBZ and SMX and, in a typical experiment,  $\text{SiO}_2/\text{BTESE}/\text{Na}_4\text{W}_{10}\text{O}_{32}$ , suspended in an aqueous solution containing the drug of interest, is irradiated for a desired time (see Experimental section). In parallel, samples prepared in an analogous way are kept in the dark for the same period. The degradation of each substrate is expressed, as before, in terms of  $C/C_0$  ratio vs time (Fig. 6.3.6).



**Fig. 6.3.6.** Degradation kinetics of carbamazepine (CBZ), sulfamethoxazole (SMX) and propranolol (PRP) by photoexcitation of  $\text{SiO}_2/\text{BTESE}/\text{Na}_4\text{W}_{10}\text{O}_{32}$  ( $500 \text{ g L}^{-1}$ ) suspended in water at pH 6 (circles). Control experiments are carried out in the dark (squares).  $C_0=10 \text{ mg L}^{-1}$ . CBZ,  $\lambda > 300 \text{ nm}$ ; SMX,  $\lambda > 335 \text{ nm}$ ; PRP,  $\lambda > 330 \text{ nm}$ .

One can observe that CBZ and SMX are now degraded upon photoexcitation of decatungstate. After 4 h illumination, more than 80% of CBZ and of SMX disappear from the aqueous solution. To verify the photoactivity of eventual leached polyoxoanion, the solution after one hour irradiation was separated from the heterogeneous photocatalyst, analyzed and then directly irradiated for an hour. The final analysis of these samples do not show a significant change ( $< 2\%$ ) in remained drug concentration

indicating that release of decatungstate into the solution is negligible. These results allow us to infer that the removal of CBZ and SMX occurs via the heterogeneous photocatalytic system employed.

Moreover, the charge taken by the drug molecule at pH 6 that was an obstacle in the case of silica-NH<sub>3</sub><sup>+</sup>/ Na<sub>3</sub>W<sub>10</sub>O<sub>32</sub><sup>-</sup> is overcome by this kind of support.

Concerning the stability of the material, SiO<sub>2</sub>/BTESE/Na<sub>4</sub>W<sub>10</sub>O<sub>32</sub> was recovered, washed with acetonitrile, dried at 373 K for 60 min and then used in a second experiment. The loss of activity in terms of both adsorption and photocatalytic degradation was within 10% after the two cycles, in agreement with the lack of release of anion during the experiment.

In Table 6.3.1 the kinetic constants obtained by fitting the data with a pseudo first order kinetic model are reported. A comparison can be made between homogeneous samples and heterogeneous experiments. One can additionally observe that SMX degradation kinetic is the slowest also with homogeneous sodium decatungstate, reinforcing the idea that the ionic charge of the drug molecule at pH 6 has a relevant role for the beginning of the oxidation process. From these results, we suggest that the ability of SiO<sub>2</sub>/BTESE/Na<sub>4</sub>W<sub>10</sub>O<sub>32</sub> to photodegrade CBZ and SMX can be attributed to the hydrophobicity induced by BTESE to the heterogeneous photocatalytic system. Moreover, the molecular dimensions are suitable with the pore sizes of the support where decatungstate anion is encapsulated. This can facilitate their approach to OH<sup>•</sup> radicals photoproduced nearby. In addition, SiO<sub>2</sub>/BTESE/Na<sub>4</sub>W<sub>10</sub>O<sub>32</sub> maintains a very good performance also in the degradation of PRP, showing that hydrophobicity introduced in the support does not preclude positively charged molecules from approaching the polyoxoanion. This result is particularly relevant since drugs photodegradation can be performed despite the form (charged or not) mainly present at the working conditions and answers to the requirement of general applicability.

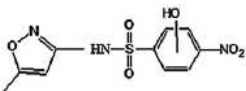
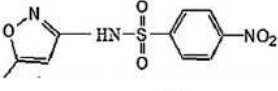
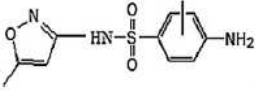
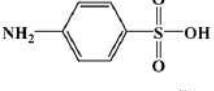
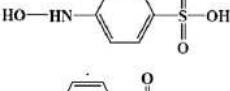
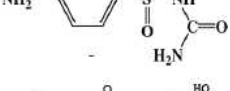
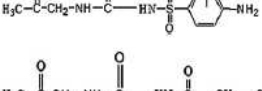
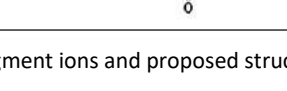


Photocatalyst	drug	k (h <sup>-1</sup> )	R <sup>2</sup>
Na <sub>4</sub> W <sub>10</sub> O <sub>32</sub> solution	CBZ	2.46 (2.10, 2.82)	0.9808
	PRP	2.94 (2.73, 3.05)	0.9934
	SMX	0.90 (0.89, 0.91)	0.9987
Silica-NH <sub>3</sub> <sup>+</sup> / Na <sub>3</sub> W <sub>10</sub> O <sub>32</sub> <sup>-</sup>	CBZ	0.024 (0.021, 0.027)	0.9837
	PRP	0.35 (0.28, 0.42)	0.9867
	SMX	0.021 (0.018, 0.024)	0.9881
SiO <sub>2</sub> /BTESE/Na <sub>4</sub> W <sub>10</sub> O <sub>32</sub>	CBZ	0.97 (0.83, 1.11)	0.9977
	PRP	1.18 (1.08, 1.28)	0.9982
	SMX	0.48 (0.36, 0.60)	0.9825

**Table 6.3.1** Kinetic constants obtained by fitting the experimental data with a first order kinetic equation ( $C/C_0 = \exp(-kt)$ ). Data in parenthesis are the confidence limits at 95% of probability.

### 6.3.3.3. HPLC/MS analysis

Degradation mechanism of drug molecules by SiO<sub>2</sub>/BTESE/Na<sub>4</sub>W<sub>10</sub>O<sub>32</sub> was investigated analyzing irradiated solution by HPLC-MS. Identification of the degradation byproducts was based on the analysis of the total ion current (TIC) and on the corresponding mass spectra. The identified intermediates for the case of SMX and of CBZ are reported in Tables 6.3.2 and 6.3.3 respectively. The intermediate with 301 m/z corresponds to a monohydroxylation of the aromatic ring and a nitration of the amino group of SMX. The product with 283 m/z derives from the oxidation of the amino group to nitro derivative, whereas the intermediate with 270 m/z correspond to the hydroxylation of SMX aromatic ring. Oxidation of the isoxazole ring of 270 m/z results in the formation of 288 m/z and 228 m/z intermediate and the intermediate with 216 m/z can derive from the opening of the isoxazole ring of SMX. The cleavage of bond between isoxazole ring and the amine group of SMX, can generate the 174 m/z by-product. The compound with 190 m/z was identified as an hydroxylated form of the amino group of 174 m/z derivative. Structures similar to those described were observed also in the photo-Fenton degradation of SMX [27].

Precursor Ion (m/z)	t <sub>r</sub> (min)	MS <sup>2</sup> (m/z)	Structure
301	9.18	177 133	
283	9.18	239 177 133	
270	10.25	206 228	
174	10.20	156	
190	3.76	158	
216	13.54	198	
288	14.46	270	
228	14.70		

**Table 6.3.2** SMX: degradation intermediates, retention times, fragment ions and proposed structures.

Precursor Ion (m/z)	t <sub>r</sub> (min)	MS <sup>2</sup> (m/z)	Structure
237.1	14.35	194.01 220.06	
251.1 253.1	12.3	208.0 210.0 236.0	
267.1	16.2	168 196.1 211.1	
271.1	9.6	210 253	

**Table 6.3.3** CBZ: degradation intermediates, retention times, fragment ions and proposed structures.

From Table 6.3.2 it is seen that hydroxylation of SMX by hydroxyl radical (OH·) attack could be an important reaction for the subsequent degradation of SMX. Indeed, three mono-hydroxylated byproducts (i.e. 301 m/z, 270 m/z and 288 m/z) are revealed.

Mono and dihydroxylated intermediates were also identified in the CBZ degradation by photoexcited /SiO<sub>2</sub>/BTESE/Na<sub>4</sub>W<sub>10</sub>O<sub>32</sub> catalyst in aqueous solution and they correspond to the intermediates 253 and 271 m/z respectively in Table 6.3.3. Further oxidation of both these compounds leads to the formation of 251 and 267 m/z intermediates. The detection of these intermediates indicates that hydroxylation and oxidation are the main reactions responsible for CBZ degradation. Based on reported and previous results we propose a reaction mechanism for photoexcited /SiO<sub>2</sub>/BTESE/Na<sub>4</sub>W<sub>10</sub>O<sub>32</sub> that can be considered general for pharmaceutical photocatalytic degradation. Photoexcitation of decatungstate anion dissolved or suspended in an aqueous environment causes the oxidation of water to OH· radicals [12], as shown in reaction 1. EPR spin trapping

experiments and HPLCMS point out that hydroxyl radicals attack drug molecules giving monoor dihydroxylated intermediates. Their formation is the prelude to fragmentation.

#### **6.3.4. Conclusions**

The ability of photoexcited sodium decatungstate to oxidize water producing OH· radicals, already observed in homogeneous conditions, is kept also when the polyoxoanion is heterogenized on siliceous supports. In this paper, we demonstrate that support characteristics are of paramount importance when reaction between OH· radicals and the organic molecule is the first step of its degradative pathway. In particular, silica-NH<sub>3</sub><sup>+</sup>/ Na<sub>3</sub>W<sub>10</sub>O<sub>32</sub><sup>-</sup> system, constituted by particles covered by decatungstate anions, is not efficient in the degradation of carbamazepine and sulfamethoxazole, which are neutral or negatively charged at the operating pH. On the contrary, entrapment of Na<sub>4</sub>W<sub>10</sub>O<sub>32</sub> inside a mesoporous organosilica matrix leads to a heterogeneous photocatalytic system with proper characteristic of hydrophobicity that is able to degrade not only carbamazepine and sulfamethoxazole but also all the other categories previously studied. In fact, the higher hydrophobicity of the organosilica support with respect to the aqueous environment favors adsorption of organic molecules, which enter the mesopores. Here, their proximity to photoproducted OH· radicals favors the hydroxylation of drug molecule. HPLC-MS investigation points out that mono- and di-hydroxylated products are formed and precede fragmentation pathways and degradation. Results obtained from the used independent techniques and methods allow us to formulate a general advanced oxidation process mechanism for the photocatalytic degradation of drug molecules by heterogeneous sodium decatungstate.

### 6.3.5 References

- [1] B. Subedi, K. Kannan, Mass loading and removal of select illicit drugs in two wastewater treatment plants in New York state and estimation of illicit drug usage in communities through wastewater analysis, *Environ. Sci. Technol.* 48 (2014) 6661-6670.
- [2] M.J. Benotti, R.A. Trenholm, B.J. Vanderford, J.C. Holady, B.D. Stanford, S.A. Snyder, pharmaceuticals and endocrine disrupting compounds in U.S. drinking water, *Environ. Sci. Technol.* 43 (2009) 597–603.
- [3] M.N. Chong, A.K. Sharma, S. Burn, C.P. Saint, Feasibility study on the application of advanced oxidation technologies for decentralised wastewater treatment, *J. Clean. Prod.* 35 (2012) 230–238.
- [4] J.L. Wang, L. Xu, Advanced oxidation processes for wastewater treatment: formation of hydroxyl radical and application, *Critic. Rev. Environ. Sci. Technol.* 42 (2012) 251-325.
- [5] U.I. Gaya, A.H. Abdullah, Heterogeneous photocatalytic degradation of organic contaminants over titanium dioxide: a review of fundamentals, progress and problems, *J. Photochem. Photobiol. C: Photochem. Rev.* 9 (2008) 1–12 and references therein.
- [6] M. Addamo, V. Augugliaro, A. Di Paola, E. Garcia-Lopez, V. Loddo, G. Marcì, Removal of drugs in aqueous systems by photoassisted degradation, *J. Appl. Electrochem.* 35 (2005) 765–774. [7] L.A. Ioannou, E. Hapeshi, M.I. Vasquez, D. Mantzavinos, D. Fatta-Kassinos, Solar/TiO<sub>2</sub> photocatalytic decomposition of  $\beta$  blockers atenolol and propranolol in water and wastewater, *Sol. Energy* 85 (2011), 1915–1926.
- [8] L. Haroune, M. Salaun, A. Menard, C.Y. Legault, J.P. Bellenger, Photocatalytic degradation of carbamazepine and three derivatives using TiO<sub>2</sub> and ZnO: effect of pH, ionic strength, and natural organic matter, *Sci. Total Environ.* 475 (2014) 16–22.
- [9] G. Longobucco, L. Pasti, A. Molinari, N. Marchetti, S. Caramori, V. Cristino, R. Boaretto, C.A. Bignozzi, Photoelectrochemical mineralization of emerging contaminants at porous WO<sub>3</sub> interfaces, *Appl. Catal. B: Environ.* 204 (2017) 273–282.
- [10] P. Kormali, D. Dimotikali, D. Tsipi, A. Hiskia, E. Papaconstantinou, Photolytic and photocatalytic decomposition of fenitrothion by PW12O<sub>40</sub> and TiO<sub>2</sub>: a comparative study, *Appl. Catal. B: Environ.* 48 (2004) 175–183.

- [11] P. Kormali, A. Troupis, T. Triantis, A. Hiskia, E. Papaconstantinou, Photocatalysis by polyoxometallates and TiO<sub>2</sub>: a comparative study, *Catal. Today* 124 (2007) 149-155.
- [12] A. Molinari, R. Argazzi, A. Maldotti, Photocatalysis with Na<sub>4</sub>W<sub>10</sub>O<sub>32</sub> in water system: formation and reactivity of OH• radicals, *J. Mol. Catal. A Chem.* 372 (2013) 23–28.
- [13] A. Maldotti, A. Molinari, G. Varani, M. Lenarda, L. Storaro, F. Bigi, R. Maggi, A. Mazzacani, G. Sartori, Immobilization of (n-Bu<sub>4</sub>N)<sub>4</sub>W<sub>10</sub>O<sub>32</sub> on mesoporous MCM 41 and amorphous silicas for photocatalytic oxidation of cycloalkanes with molecular oxygen, *J. Catal.* 209 (2002) 210–216.
- [14] E.S. Da Silva, V. Prevot, C. Forano, P. Wong-Wah Chung, H.D. Burrows, M. Sarakha, Heterogeneous photocatalytic degradation of pesticides using decatungstate intercalated macroporous layered double hydroxides, *Environ. Sci. Pollut. Res.* 21 (2014) 11218–11227.
- [15] A. Molinari, G. Varani, E. Polo, S. Vaccari, A. Maldotti, Photocatalytic and catalytic activity of heterogenized W<sub>10</sub>O<sub>32</sub>– in the bromide-assisted bromination of arenes and alkenes in the presence of oxygen, *J. Mol. Catal. A Chem.* 262 (2007) 156–163.
- [16] A. Molinari, E. Sarti, N. Marchetti, L. Pasti, Degradation of emerging concern contaminants in water by heterogeneous photocatalysis with Na<sub>4</sub>W<sub>10</sub>O<sub>32</sub>, *Appl. Catal. B: Environ.* 203 (2017) 9–17.
- [17] S.-S. Wang, G.-Y. Yang, Recent advances in polyoxometalate-catalyzed reactions, *Chem. Rev.* 115 (2015) 4893–4962.
- [18] F. Zaera, The new materials science of catalysis: toward controlling selectivity by designing the structure of the active site, *J. Phys. Chem. Lett.* 1 (2010) 621–627.
- [19] A. Maldotti, R. Amadelli, A. Molinari, M.G. Clerici, O. Kholdeeva (Eds.), *Liquid Phase Oxidation via Heterogeneous Catalysis*, Wiley, 2013, pp. 411–450 ch. 9.
- [20] A.J. Ebele, M. Abou-Elwafa Abdallah, S. Harrad, Pharmaceuticals and personal care products (PPCPs) in the freshwater aquatic environment, *Emerg. Contam.* 3 (2017)1–16.
- [21] A. Molinari, G. Magnacca, G. Papazzoni, A. Maldotti, HydrophobicW<sub>10</sub>O<sub>32</sub>–/silica photocatalyst for toluene oxidation in water system, *Appl. Catal. B: Environ.* 131-139 (2013) 446–452.
- [22] D.C. Duncan, T.C. Netzel, C.L. Hill, Early-time dynamics and reactivity of polyoxometalate excited states. identification of a short-lived LMCT excited state and

- a reactive long-lived charge-transfer intermediate following picosecond flash excitation of [W10O32]4- in acetonitrile, *Inorg. Chem.* 34 (1995) 4640–4646.
- [23] F. Bigi, A. Corradini, C. Quarantelli, G. Sartori, Silica-bound decatungstates as heterogeneous catalysts for H<sub>2</sub>O<sub>2</sub> activation in selective sulfide oxidation, *J. Catal.* 250 (2007) 222–230.
- [24] Y. Guo, C. Hu, X. Wang, Y. Wang, E. Wang, Microporous decatungstates: synthesis and photochemical behavior, *Chem. Mater.* 13 (2001) 4058–4064.
- [25] A. Martucci, L. Pasti, N. Marchetti, A. Cavazzini, F. Dondi, A. Alberti, Adsorption of pharmaceuticals from aqueous solutions on synthetic zeolites, *Microporous Mesoporous Mater.* 148 (2012) 174–183.
- [26] S. Blasioli, A. Martucci, G. Paul, L. Gigli, M. Cossi, C.T. Johnston, L. Marchese, I. Braschi, Removal of sulfamethoxazole sulfonamide antibiotic from water by high silica zeolites: a study of the involved host–guest interactions by a combined structural, spectroscopic, and computational approach, *J. Colloid Interface Sci.* 419 (2014) 148–159.
- [27] O. González, S. Carne, S. Esplugas, Sulfamethoxazole abatement by photo-Fenton: toxicity, inhibition and biodegradability assessment of intermediates, *J. Hazard. Mater.* 146 (2007) 459–464.

## 6.4 Water remediation using $\beta$ 25/ $\text{WO}_3$ system

The data herein reported are part of my work of thesis and have been published in: Vito Cristino, Gelsomina Longobucco, Nicola Marchetti, Stefano Caramori, Carlo Alberto Bignozzi, Annalisa Martucci, Alessandra Molinari, Rita Boaretto, Claudia Stevanin, Roberto Argazzi, Maurizio Dal Colle, Renzo Bertoncello, Luisa Pasti (2020). Photoelectrochemical degradation of pharmaceuticals at  $\beta$ 25 modified  $\text{WO}_3$  interfaces. *Catalysis Today* 340 302–310.

In this work we explored the applications of  $\text{WO}_3$ -based nanomaterials to the degradation of organic molecules belonging to the category of emerging pollutants such as Ketoprofen and Levofloxacin, selected among the anti-inflammatory and analgesic species and the most widely used antibiotics and which therefore represent omnipresent water contaminants.

$\text{WO}_3$  is a semiconductor which has an indirect band gap, between 2.6-2.7 eV. This band gap allows the absorption of the part  $<480$  nm of the visible spectrum. Compared to conventional photocatalytic conditions, which were not effective in oxidative degradation of ketoprofen, the application of electrical bias was successful in promoting 50% degradation of ketoprofen after 5 hours of illumination, with a constant degradation rate of 0.22 h<sup>-1</sup>. Similar improvement was seen with Levofloxacin. The degradation rate was further accelerated by exploiting  $\text{WO}_3$  films modified with 25 zeolites which obtained, on the same time scale, a degradation  $> 65\%$  with Ketoprofen and ca. 90% with Levofloxacin. The complete disappearance of the oxidation intermediates of these two drugs was observed on a time scale of ca. 20 h, indicative of the achievement of complete drug mineralization at the  $\beta$ 25 /  $\text{WO}_3$  illuminated interface under 1 solar illumination. the decrease in concentration was verified by HPLC analysis and subsequently the evaluation of the photoproducts was investigated by HPLC / MS analysis for both drugs.

### 6.4.1 Introduction

Among the wide variety of Contaminants of Emerging Concerns (CECs) pharmaceuticals, personal care products and their metabolites have especially alarmed the public and regulators. Although adverse human health consequences from the existing trace levels



of these substances in natural or drinking water are in general unlikely, their impact to aquatic ecosystems is more evident [1]. Some of these emerging pollutants are indeed very stable molecules, capable to survive the current potabilization and water remediation processes [2] and are thus able to reach and impact the aqueous environment with unaltered efficacy. In view of the growing world population, increasing industrialization of emerging countries and climate change, the re-use and re-cycle of water and the protection of aqueous ecosystems represent major societal challenges. Photocatalytic routes to the degradation of harmful organics, exploiting sunlight to trigger the formation of high energy electron/hole pairs (e/h) within dispersed semiconductor (nano)particles, to promote direct or indirect (mediated for example by oxidants like  $\%O_2^-$ ,  $H_2O_2$ ,  $\cdot OH$ ) oxidation reactions is an established approach, particularly with  $TiO_2$  [3–6] and  $ZnO$  [7–9] based materials. Some of the present authors also employed a decatungstate polyoxoanion heterogenized on silica particles in the photomineralization of pharmaceuticals [10]. The common feature of all these materials is the ability to photoproduce  $\cdot OH$  radicals, whose oxidation potential ( $E^\circ=2.1$  V vs NHE) allows for the oxidation of a variety of organic compounds leading, with sufficient time, to their mineralization [11]. In the absence of visible absorbing dye sensitizers [12,13], an important drawback of the materials and molecular clusters mentioned above is their limited capacity of harvesting the solar spectrum, with no practical photochemical activity beyond 420 nm.

Other semiconductors, and among them  $WO_3$ , offer a lower band gap (ca.  $2.7 \pm 0.1$  eV) [14] for harvesting a sizable portion of the visible region, up to 460 nm, with a valence band edge suitable for the production of  $\cdot OH$  radicals following mono-electronic oxidation of water [15]. The application of electric potential (bias) to a nanocrystalline thin film semiconductor, allows to optimize the charge separation at the Semiconductor/Electrolyte Interface (SEI), improving the rate of degradation of organic targets [16,17]. Recently, the photoelectrochemical approach employing  $WO_3$  photoanodes to the degradation of CECs, represented by either neutral (Carbamazepin, CBZ) or positively charged (Atenolol, ATN) molecular species, outperformed open circuit photocatalysis by a of three-to-five factor [18].

In this contribution we have focused on the degradation of Ketoprofen (KTP) and Levofloxacin (LFX) (Chart 6.4.1) in diluted aqueous electrolytes ( $[Na_2SO_4] = 7 \times 10^{-4}$  M) at pH 6. These targets were selected among the most widely used anti-inflammatory and

analgesic species (KTP) and antibiotics (LFX). LFX is an antibacterial fluoroquinolone widely used in the treatment of respiratory diseases and bacterial infections. The urinary excretion of fluoroquinolones delivers about 85% of the unmodified parent compounds, consequently a considerable amount of active drugs is present in waste waters [19]. Concerning the widely used KTP, roughly 80% of the administered dose is excreted in the urine, primarily as the glucuronide metabolite explaining its abundance in waste waters [20]. Additionally, these substances have been chosen as target molecules for their different acid/base characteristics, that allow us to investigate how the photocatalyst activity is influenced by the structure and physico-chemical properties of the target substrate. Indeed, KTP carries a carboxylic acid (see 1 in Chart 6.4.1), which dissociates at  $\text{pH} \geq 6$  having a typical  $\text{pK}_a \approx 4.5$  [21] resulting in an anionic species within the pH selected for the photodegradation experiments. LFX has a carboxylic group as well (5), but it also possesses two tertiary  $\text{sp}^3$  nitrogens (2–4) one of which can be protonated at neutral and acidic pH. The protonation constants indicate that this compound is present mainly as a zwitterionic form at pH 6, whereas at pH higher than 7 it prevails in the negative form [22]. Available nitrogen lone pairs in LFX might also interact with  $\text{W}6+$  acid groups at  $\text{WO}_3$  surface, favoring the contact between LFX and the oxidant species generated by the photocatalyst. Interestingly, while it has been found that LFX is effectively degraded under both photocatalytic (no bias) and photoelectrochemical (applied bias) conditions, in the case of KTP there is an extreme difference in the photochemical vs photoelectrochemical degradation kinetic: under conventional photocatalytic conditions, KTP does not show any appreciable photocatalytic degradation, whereas under applied bias its degradation is roughly 70% complete within a 5 h illumination cycle. This behavior was explained by the induction of a local excess of KTP at the  $\text{WO}_3$  SEI under positive potential, allowing a faster reaction with surface generated  $\cdot\text{OH}$  radicals. In the absence of positive bias, at pH 6, such interaction does not occur, due to electrostatic repulsion between the anionic KTP and the negatively charged  $\text{WO}_3$  surface, having zero zeta potential below pH 2. This indicates that besides modulating the charge separation rate at the SEI, the electric bias is useful to tune the solar degradation of otherwise impervious molecular species, ostensibly acting through double layer effects which result in an increased concentration of the molecular targets in proximity of the mesoporous photoactive material.

Finally, the degradation activity of  $\text{WO}_3$  was enhanced by incorporating an adsorbent material, in particular a Beta zeolite (BEA) having  $\text{SiO}_2/\text{Al}_2\text{O}_3$  ratio equal to 25 ( $\beta 25$ ) [23]. The use of composite materials based on  $\text{WO}_3$  modified with zeolites has been reported in catalysis, [24] sensor application [25] and, more recently, in gas phase photocatalysis [26], but, to the best of our knowledge, it was never reported for the degradation of these emerging contaminants in aqueous solution in a photoelectrochemical cell. The combination of the photocatalyst with the adsorbent allows to collect and trap contaminant molecules in proximity of the surface, where  $\cdot\text{OH}$  photogeneration occurs, allowing to increase the chance of bimolecular encounter between the target and this highly reactive oxidant. This strategy thus results in efficient degradation of species, such as KTP, even under purely photocatalytic (no bias) conditions.

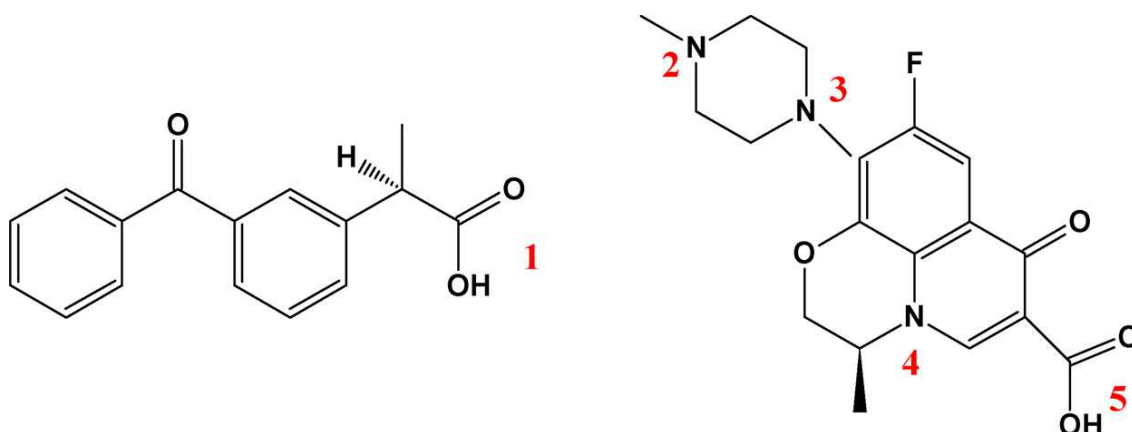


Chart 6.4.1. Molecular structures of KTP (left) and LFX (right). Both molecules are represented in their neutral form. Red numbers refer to the ionizable groups in their molecular structures.

## 6.4.2. Experimental

### 6.4.2.1 Chemicals for analytical and photo-electrochemical measurements

Levofloxacin (Fluka, purity>98%), ketoprofen (Sigma-Aldrich, purity>98%), sodium sulfate (Sigma-Aldrich, purity, 99%), sulfuric acid (Sigma-Aldrich, 95%), were used as received. Zeolite Beta (Zeolyst International) in its ammonium cation form, having a  $\text{Na}_2\text{O}$  content lower than 0.05% wt was employed after a calcination process. Calcination was carried out by raising the temperature from room temperature to 600 °C in 1 h, then holding at 600 °C for 4 h. Finally, the adsorbents were kept at room temperature for 3 h. High-performance liquid chromatography (HPLC) grade acetonitrile (ACN) was purchased from Merck (Darmstadt, Germany). The water was Milli-Q® grade (Millipore,

MA, USA). A dilute aqueous solution of sulfuric acid was employed to adjust at 6 the pH of the drug solution (in the range 30–2 ppm Levofloxacin or Ketoprofen) containing 0.7mM of sodium sulfate as supporting electrolyte. The saline concentration was chosen to reproduce the average salinity of freshwater [27]. The pH of the drug solutions was measured with a combined glass electrode connected to an AMEL pH-meter (Milano, Italy).

#### **6.4.2.2 Preparation of materials and thin films for photocatalysis and photoelectrocatalysis**

Nanocrystalline  $WO_3$  was prepared by following a published procedure [15]. Briefly,  $H_2WO_4$  was generated from 2.5 g of  $Na_2WO_4$  (Alfa Aesar) dissolved in 100 mL of Millipore water by addition of 20 ml of concentrated HCl (Sigma-Aldrich), followed by several washings in order to eliminate NaCl. The colloidal suspension of  $H_2WO_4$  nanoparticles was obtained by dissolving the  $H_2WO_4$  gel in 3M oxalic acid (2.5 ml) at 60 °C (Sigma-Aldrich) and stabilized by addition of 20% w/w Carbowax (Sigma-Aldrich, 15,000–20,000 u) and Triton X-100 (Fluka) (1 drop/2 g of colloidal precursor) which acted as densifier/sintering agent and tensioactive respectively.  $WO_3$  electrodes (active area 1 cm<sup>2</sup>) were fabricated by spin casting (600 rpm for 6 s followed by 2000 rpm for 20 s) colloidal  $H_2WO_4$  onto well cleaned FTO substrates (Fluorine Tin Oxide, Pilkington TEC 8) glass, followed by firing at 550 C°. This procedure was repeated six times in order to obtain films having a thickness of ca. 2 μm and a photoresponse up to 470 nm, as shown by a typical photoaction spectrum in sulfuric acid. Deposition of zeolites on  $WO_3$  electrodes was achieved by repeated spin coating (4×, 600 rpm for 6 s followed by 2000 rpm for 20 s) of a 4% w/v β25 suspension in water. After each deposition of β25, the electrode was heated at 550 °C to consolidate deposition.

β25/ $WO_3$  nanocrystalline powder was prepared by adding 0.1 g of β25 zeolite to the  $H_2WO_4$  gel obtained as previously described, followed by stirring for 24 h. The resulting solid was separated by centrifugation and heated at 550 C° for 8 h to obtain a powder.

#### **6.4.2.3. AFM**

Atomic force microscopy (AFM) images were collected using a Digital Instruments Nanoscope III scanning probe Microscope (Digital Instruments, CA). The instrument was

equipped with a silicon tip (RTESP-300 Bruker) and operated in tapping mode. Surface topographical analysis of raw AFM images was carried out with NanoScope analysis 1.5 and Gwyddion, a free modular program for SPM (scanning probe microscopy) data visualization.

#### **6.4.2.4. XRD and XPS**

X-ray diffraction (XRD) measurements were performed using a BRUKER D8 Advance X-ray diffractometer equipped with a Sol-X detector, working at 40 kV and 40 mA. The X-ray diffraction patterns were collected in a step-scanning mode with steps of  $\Delta 2\theta=0.01^\circ$  and a counting time of 12 s/step using Cu  $K\alpha_1$  radiation ( $\lambda=1.54056 \text{ \AA}$ ) in the  $2\theta$  range  $3-100^\circ$ . XPS experiments were conducted using a  $\Phi 5600\text{ci}$  X-Ray Photoelectron spectrometer (Perkin Elmer, Waltham, MA, USA) with an Mg K anode X-ray source (1253.6 eV) with a primary beam energy of 14 kV and an electron current of 20 mA. A CHA (Concentric Hemispherical Analyser) was used to collect the output signals.

Analysed areas were circles of 0.8mm in diameter. Multiplex scan mode was performed with a 0.125 eV steps (pass energy 23.50 eV). Bes were calibrated against the C1s peak (285 eV).

#### **6.4.2.5. Photocatalytic experiments**

In photocatalytic measurements the electrode (either  $\text{WO}_3$  or  $\beta 25/\text{WO}_3$ , having  $1 \text{ cm}^2$  geometric active area) was immersed in 10 mL of electrolyte solution comprising 0.7mM  $\text{Na}_2\text{SO}_4$  and KTP or LFX in 30–10 ppm concentration at pH 6. The photoanode was irradiated under open circuit conditions (disconnected wires) with a Hg medium pressure lamp at  $0.128 \text{ W/cm}^2$ . In order to avoid decomposition pathways arising from direct photochemical excitation of the pharmaceutical targets, appropriate cut-off filters were interposed between the source and the cell (360 nm for LFX, 380 nm for KTP, in accordance to the absorption threshold of the respective molecules). Typical photocatalytic experiments were carried out for five hours, monitoring the target concentration at 1, 3 and 5 h intervals.

#### **6.4.2.6. Photo-electrochemical experiments**

Photodegradation experiments under photo-electrochemical conditions were carried out in a two electrode cell (volume=10 mL) under potentiostatic conditions controlled

by an Eco Chemie PGSTAT 101 potentiostat/galvanostat running under Nova environment. The working electrode (photoanode) was either a  $\text{WO}_3$  or a  $\beta\text{25/WO}_3$  thin film supported on FTO, while the counter electrode was a platinum grid. An ABET sun simulator (AM 1.5 G with the appropriate cut offs) was used as an illumination source for photoelectrochemical experiments. Constant potential photoelectrolysis was conducted in aerated 0.7mM  $\text{Na}_2\text{SO}_4$  aqueous solutions at pH 6 by applying a constant bias of 1.2 V for KTP and 0.4 V for LFX respectively. These potential values were selected on the basis of the respective current density vs potential (J/V) curves (see Results and Discussion section). Typical experiments had a duration of 5 h, during which depolarization cycles at 0 V for 10 min were introduced between polarization cycles of the duration of 30 min in order to ensure a reproducible and stable operation of the photoelectrode. Longer experiments, aimed at the determination of decomposition intermediates were carried out for 20 h, by adopting the same electrochemical program specified above.

#### **6.4.2.7. HPLC/DAD analysis**

A HPLC/DAD (Waters, MA, USA pump:Waters 515, DAD:Waters PDA 996) was employed under isocratic elution condition, the eluent was 18:82 ACN: phosphate buffer 25mM at pH 4 and 60:40 MeOH: phosphate buffer 2mM at pH 3.3 for LFX and KTP respectively. The flow rate was 1 mL/min. The column was 4.6×150mm Kromasil Eternity-5-C18. The injection volume was 20  $\mu\text{L}$  for all standards and samples.

#### **6.4.2.8. HPLC/MS analysis**

HPLC/MS analyses were made by means of Surveyor micro-HPLC hyphenated to a linear trap quadrupole mass spectrometer (LTQ XL Thermo Scientific, Waltham, MA, USA). The HPLC apparatus was composed of a solvent delivery system, a quaternary pump (including a membrane degasser) and an autosampler (including a thermostated column compartment). The LTQ system was equipped with an electrospray ionization (ESI) ion source. The mobile phase was obtained as a mixture of acetonitrile (ACN) formic acid 0.1% v/v: water formic acid 0.1% v/v. Chromatographic separation was performed under gradient elution conditions: 0–6 min 5% ACN, 6–14 min 5–70% ACN, 14–15 min 70%

ACN, then held isocratically at 95% of ACN for 3 min before reconditioning the column. The flow rate was 100  $\mu\text{L}/\text{min}$ , while the column was thermostated at 25  $^{\circ}\text{C}$ . The column was 50 $\times$ 2.1mm (Restek, Bellefonte, PA, USA) and packed with a C18 silica-based stationary phase with a particle diameter of 3  $\mu\text{m}$ . The injection volume was 5  $\mu\text{L}$  for all standards and samples. MS experimental conditions were as follows: spray voltage 4 kV, capillary temperature 275  $^{\circ}\text{C}$ , capillary voltage 11 V and tube lens 25 V for positive ESI conditions.

### **6.4.3. Results and discussion**

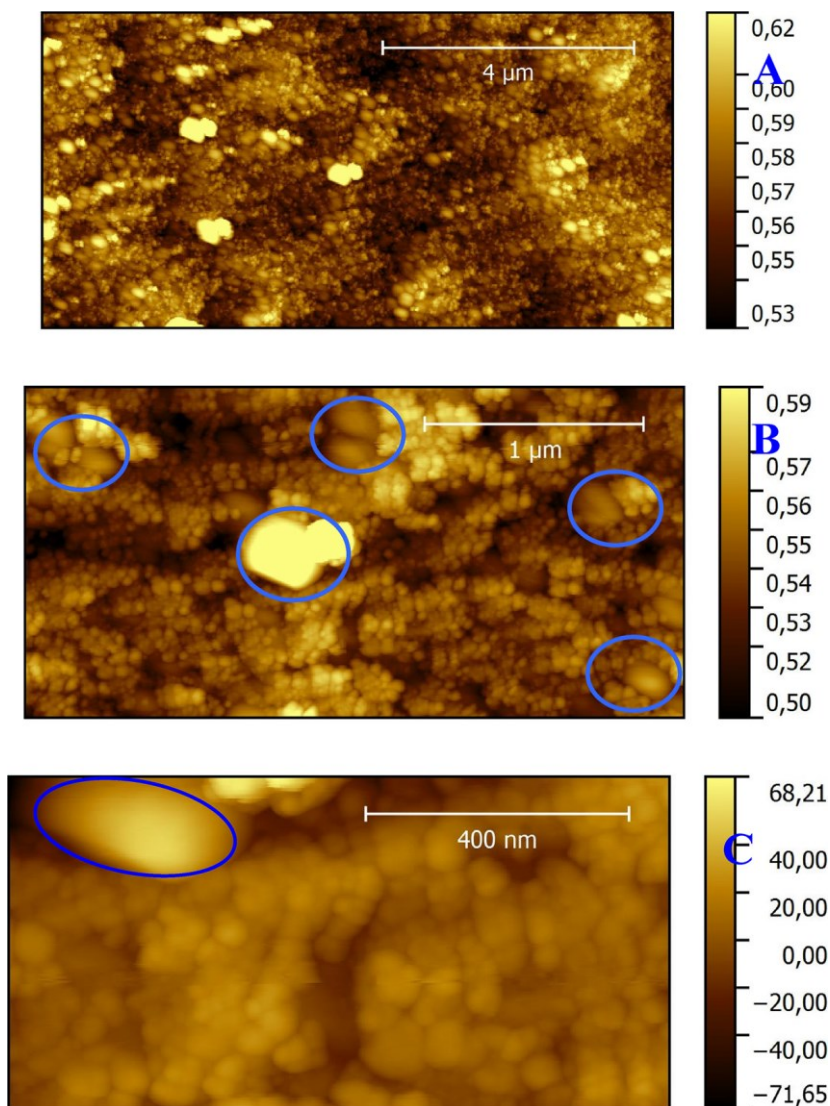
#### **6.4.3.1. Morphological, structural, optical and electrochemical properties**

Structural and morphological properties of colloidal  $\text{WO}_3$  films prepared by sequential spin coating-annealing cycles by our group, were reported previously [15,28]. AFM images taken on the  $\beta\text{T5}/\text{WO}_3$  composite are consistent with previous results taken on unmodified films, showing a network of rather polydisperse, partly fused, roughly spherical particles, whose diameter varies between 60 and 30 nm. The film shows mesopores of the order of 50–100 nm, which allow for electrolyte percolation through the film, more evident at intermediate magnification (scale bar 1  $\mu\text{m}$  in Fig. 6.4.1A, B). Smaller interstices are evident between nanoparticle interconnections at higher magnification in Fig. 6.4.1C.  $\beta\text{T5}$  modified  $\text{WO}_3$  displays the presence of comparatively larger elongated prismatic structures, having a ca. 1:2 aspect ratio and a length of ca. 200–250 nm assigned by comparison with pure  $\beta\text{T5}$  zeolites.

These are prevalingly distributed at the surface of the film, and are often embedded and surrounded by the outermost layers of  $\text{WO}_3$  nanoparticles. This is consistent with the two step preparation route of  $\beta\text{T5}$  modified  $\text{WO}_3$  surfaces which is based on the spin casting of zeolite suspensions on the pre-formed  $\text{WO}_3$  film. Attempts to disperse zeolites within the bulk of the film, by modifying with zeolites the colloidal precursor for one-step film deposition, were successful from the synthetic point of view, but led to photoanodes having poor photoelectrochemical reproducibility due to scarce film adhesion to the ohmic contact and were early abandoned for this work.

X-ray powder diffraction patterns of  $\beta\text{T5}$  before and after  $\text{WO}_3$  embedding are shown in Fig. 6.4.2. The strong changes in the XRD patterns can be interpreted by assuming the

presence of two phases:  $\beta$ 25 and tungsten trioxide  $\text{WO}_3$  with monoclinic symmetry. The evidence for the monoclinic-type phase of  $\text{WO}_3$  is strongly supported by the occurrence of new diffraction peaks (PDF file # 83-0951).  $\text{WO}_3$  phase showed a high intensity peak at (020) reflection as well as lower intensity ones corresponding to (212), (410), (240) reflections.

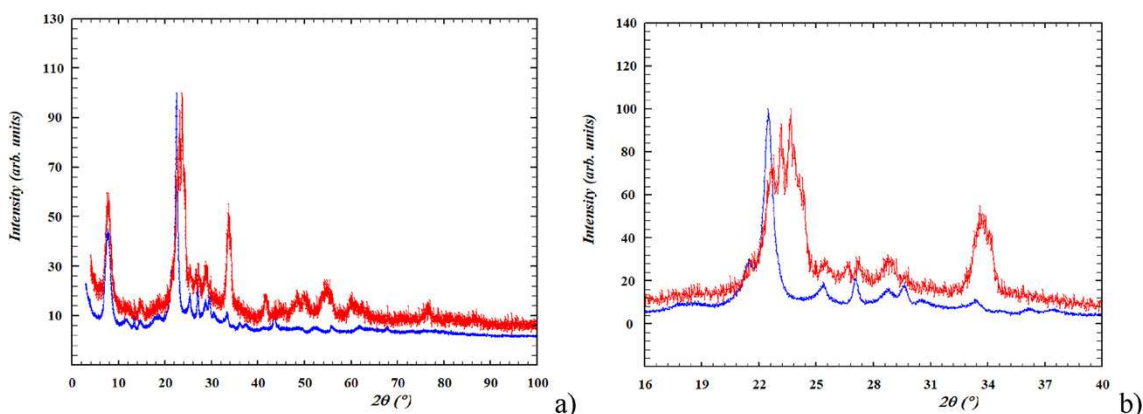


**Fig.6.4.1.** AFM micrographs showing the surface of  $\beta$ 25/ $\text{WO}_3$ . Blue circles indicate some zeolite structures at the surface and embedded within the outermost layers of much smaller  $\text{WO}_3$  particles. (For interpretation of the references to colour in this figure legend, the reader is referred to the web version of this article.)

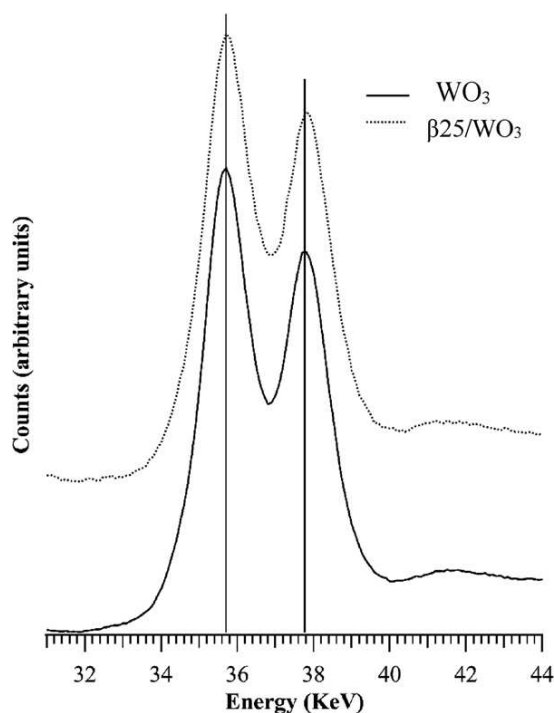
Comparative XPS measurements (Fig. 6.4.3) carried out on the thin film electrodes supported on FTO show that both the tungsten  $\text{W}4f_{7/2}$  and the  $\text{O}1s$  peaks associated to  $\text{WO}_3$  in the  $\beta$ 25 modified film are essentially unchanged with regard to binding energy, peak intensity ratio and FWHM (1.4 (W) and 1.6 (O) eV) with respect to the unmodified  $\text{WO}_3$  where BEs of 35.7 eV (W) and 530.5 (O) perfectly match with known literature data for such material ( $35.7 \pm 0.1$  and  $530.5 \pm 0.1$  eV for W and O in  $\text{WO}_3$  respectively) [29],



suggesting a negligible electronic perturbation to the W core levels upon physical deposition of  $\beta 25$  on the nanocrystalline  $\text{WO}_3$ .



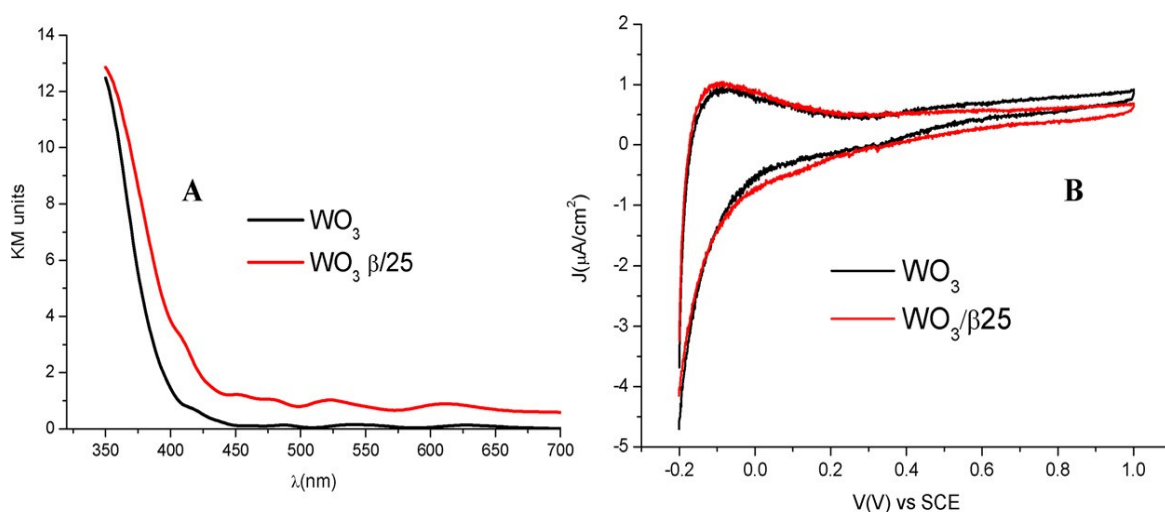
**Fig. 6.4.2.** (a) Intensity-normalized X-ray diffraction patterns of  $\beta 25$  (blue line) and  $\beta 25/\text{WO}_3$  in the  $3\text{-}100^\circ$   $2\theta$  range. (b) The occurrence of new peaks related to the embedding of  $\text{WO}_3$ . (For interpretation of the references to colour in this figure legend, the reader is referred to the web version of this article.)



**Fig. 6.4.3.**  $\text{W}4f_{7/2}$  XPS peaks observed in unmodified  $\text{WO}_3$  and  $\beta 25$  modified thin films supported on FTO.

Consistent with the XPS evidence, the electronic spectra and the cyclic voltammetry of pure  $\text{WO}_3$  and of  $\beta 25$  modified  $\text{WO}_3$  electrodes are substantially super-imposable, (Fig. 6.4.4 A,B) corroborating the fact that no new electronic levels in the semiconductor are introduced upon casting of the zeolite on the pre-formed  $\text{WO}_3$  thin films. In both unmodified and  $\beta 25$  modified materials, the absorption spectra are characterized by the same onset of the visible absorption at 450 nm, as one should expect from the forbidden gap value of  $\text{WO}_3$ . The presence of zeolites, larger than the average  $\text{WO}_3$  nanoparticles,

as shown by AFM, contributes to the increased light scattering from the  $\beta$ 25/ $\text{WO}_3$  film, evident from the increased background at  $\lambda > 450$  nm, where the electronic transitions of the semiconductor are absent. Cyclic voltammetry, reported in Fig. 6.4.4B, shows similar capacitive charging currents at positive potentials (i.e.  $> 0$  V vs SCE) where faradaic processes are absent. Also,  $\text{WO}_3$  and  $\beta$ 25/ $\text{WO}_3$  show the same onset of the  $\text{W}^{6+}/\text{W}^{5+}$  reduction (ca. 0 V vs SCE), corresponding to trapping of electrons in defects and surface states close to the conduction band edge, confirming the marginal impact coming from zeolite modification to the semiconductor energetics. In both  $\text{WO}_3$  and  $\beta$ 25/ $\text{WO}_3$ , the similar intensity of the faradaic reductive wave, where charge compensation of the  $\text{W}^{6+}/\text{W}^{5+}$  process occurs by movement of cations from the electrolyte (in our specific case  $\text{Na}^+$ ) to the porous semiconductor, indicates that after coating with zeolites the  $\text{WO}_3$  porous film maintains its permeability to the electrolyte, with an electrochemically active area comparable to that of pristine  $\text{WO}_3$ . This is again consistent with AFM, where the presence of rather sparse zeolitic structures decorating the surface of the semiconductor, cannot preclude the access of the electrolyte to most of the porous photoelectrode.



**Fig. 6.4.4.** Electronic absorption spectra (A) and cyclic voltammetry (20 mV/s) in 0.5M  $\text{Na}_2\text{SO}_4$  recorded on  $\text{WO}_3$  and  $\beta$ 25/ $\text{WO}_3$  electrodes.

#### 6.4.3.2. Photochemical and photoelectrochemical degradation of KTP and LFX at $\text{WO}_3$ electrodes

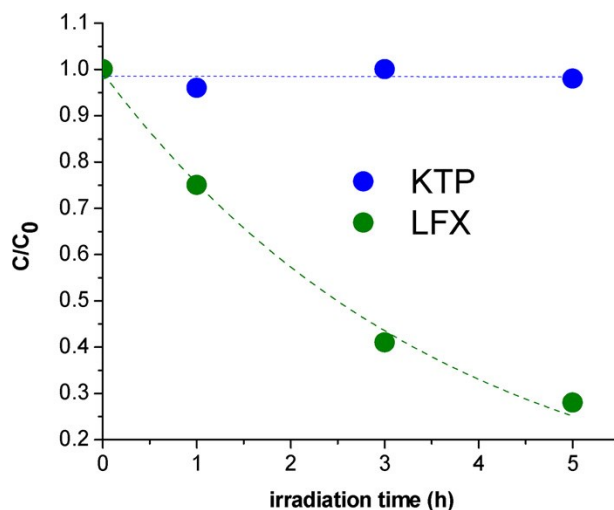
Photochemical degradation experiments were initially carried out on 0.7mM  $\text{Na}_2\text{SO}_4$  aqueous solutions containing 10 mg/L of drug (KTP or LFX) where the electrolyte was added to reproduce the overall ionic content of natural freshwaters and to provide, for comparative purposes, the same ionic environment established at the SEI under

photoelectrochemical conditions. In photochemical experiments, colloidal  $\text{WO}_3$  films were employed in the absence of applied potential bias. Under such conditions  $\text{WO}_3$  electrons are promoted by valence band excitation under  $\lambda > 360$  nm, into both delocalized (conduction band) and localized (trap) states, while holes, surviving recombination, are scavenged by water (leading to  $\cdot\text{OH}$  formation) or by direct reaction with the organics interacting with the  $\text{WO}_3$  surface. In the absence of surface co-catalysts [30], production of oxidizing intermediates via reduction of molecular oxygen by surface trapped electrons is considered to be slow and inefficient at  $\text{WO}_3$  nanoparticles having  $>30$  nm size, exhibiting no quantum confinement [31], thus the oxidation reactions are, in our case, mainly carried out by photogenerated holes.

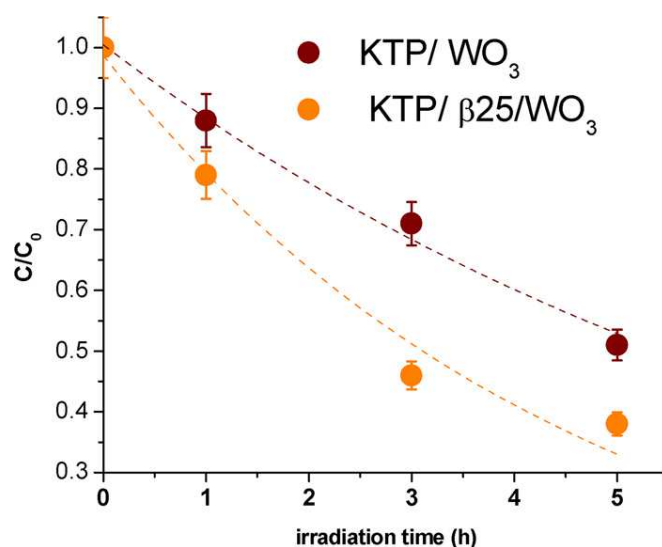
Clearly both the direct (via reaction with holes having an approximate quasi-Fermi potential of 2.7 V vs SCE) and the indirect pathway, via  $\cdot\text{OH}$  mediated oxidation, would lead to the oxidative degradation of these organic species.

Flat band conditions are quickly established in the solid under illumination due to electron accumulation, neutralizing the positive charges within the depletion layer formed upon initial Fermi level equilibration following contact between the solid and the liquid phases. In these stationary conditions no electric field should exist in the semiconductor film and transport of holes to the  $\text{WO}_3$  surface, where scavenging occurs, takes place solely by diffusion. Fig. 6.4.5 shows that photochemical degradation of 10 ppm LFX is ca. 75% complete after 5 h of illumination at ca.  $0.13 \text{ W/cm}^2$ , according to a monoexponential kinetic with a rate constant of  $0.27 \text{ h}^{-1}$ . On the contrary, in the same experimental conditions, KTP is not degraded, showing no deviations in the solution concentration from the initial 10 ppm value, which remains substantially constant, within the experimental error, during an irradiation cycle of 5 h. This finding can be possibly explained by considering the electrostatic repulsion between the negative charge of KTP at pH 6 and the negatively charged  $\text{WO}_3$  surface [32,33]. This would cause a depletion of KTP from the immediate proximity of the semiconductor surface reducing the probability of direct scavenging by reaction with holes and also the likelihood of bi-molecular reaction with  $\cdot\text{OH}$  which, being highly reactive species, are not expected to diffuse very far from the surface whereupon are generated under illumination. Competitive reaction of  $\cdot\text{OH}$  with  $\text{SO}_4^{2-}$  to form  $\text{S}_2\text{O}_8^{2-}$ , bi-molecular events yielding  $\text{H}_2\text{O}_2$  or electron recapture on the semiconductor surface leading to reformation of water will indeed limit the lifetime of  $\cdot\text{OH}$  and hence their diffusional path. In the

photoelectrochemical experiment, the application of a 1.2 V vs Pt potential bias to a  $\text{WO}_3$  film, significantly improves the degradation of KTP under simulated solar illumination (AM 1.5 G+380 nm cut off filter) resulting in a ca. 50% abatement of the initial concentration of KTP after 5 h of illumination, with a rate constant of  $0.13 \text{ h}^{-1}$  (Fig. 6.4.6, brown circles).



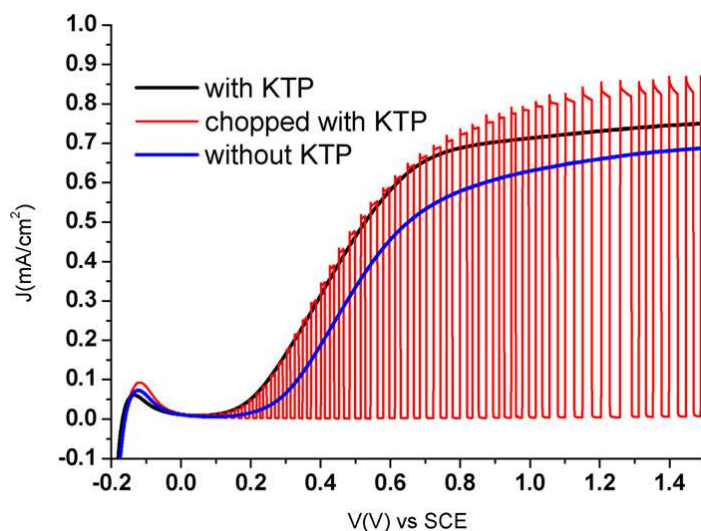
**Fig. 6.4.5.** Photocatalytic degradation kinetics (no applied potential) of 10 ppm KTP ( $\lambda > 380 \text{ nm}$ ) and of LFX ( $\lambda > 360 \text{ nm}$ ) on colloidal  $\text{WO}_3$  thin films (area=1  $\text{cm}^2$ ) at pH 6 in 0.7mM  $\text{Na}_2\text{SO}_4$ . Hg medium pressure mercury lamp 0.128  $\text{W}/\text{cm}^2$ .



**Fig. 6.4.6.** Photoelectrochemical degradation kinetics of 10 ppm KTP (AM 1.5 G and  $\lambda > 380 \text{ nm}$ ) at  $\text{WO}_3$  (area=1  $\text{cm}^2$ ) (brown) and at  $\beta 25/\text{WO}_3$  (orange) at pH 6 in 0.7mM  $\text{Na}_2\text{SO}_4$  under 1.2 V vs Pt bias.

degradation of KTP under simulated solar illumination (AM 1.5 G+380 nm cut off filter) resulting in a ca. 50% abatement of the initial concentration of KTP after 5 h of illumination, with a rate constant of  $0.13 \text{ h}^{-1}$  (Fig. 6.4.6, brown circles). The applied potential bias was set at 1.2 V since at this value no substantial dark anodic current is observed, while the photoanodic plateau (i.e. the maximum rate of hole extraction from the semiconductor) is reached. Additionally, from chronoamperometry data it can be

observed that the photocurrent is essentially constant and reproducible, with a steady state photoanodic current density of ca.  $100 \mu\text{A}/\text{cm}^2$ , during 10 polarization cycles at 1.2 V vs Pt, each of the duration of 30 min, confirming the stability of the photoanodic response of  $\text{WO}_3$  employed for the decontamination process. Since a 10 ppm concentration of KTP in the poorly conductive  $0.7\text{mM Na}_2\text{SO}_4$  solution was not ideal to observe the direct impact of the photo-oxidation of this drug on the resulting J-V characteristic of the  $\text{WO}_3$  photoelectrode, three electrode potentiodynamic experiments were carried out in  $0.5\text{M Na}_2\text{SO}_4$  at pH 6 in the presence of  $10^{-3}$  M KTP, representing the drug solubility limit in water at pH 6. Compared to the blank electrolyte made of  $0.5\text{M Na}_2\text{SO}_4$  at pH 6 (Fig. 6.4.7 blue line), the presence of  $10^{-3}$  M KTP (Fig. 6.4.7, black line) induces a ca. 100 mV anticipated photoanodic response, while the photocurrent in the activation region of the curve, i.e. between 0.2 and 0.4 V vs SCE, where minority carrier recombination is more significant, is ca. twice higher, with a good matching of the steady state JV with square shaped photoanodic transients (red line, Fig. 6.4.7). All these photoelectrochemical features provide unambiguous evidence of reduced photogenerated carrier recombination thanks to the participation of KTP to hole scavenging (or  $\cdot\text{OH}$  scavenging) processes at the SEI under positive polarization.

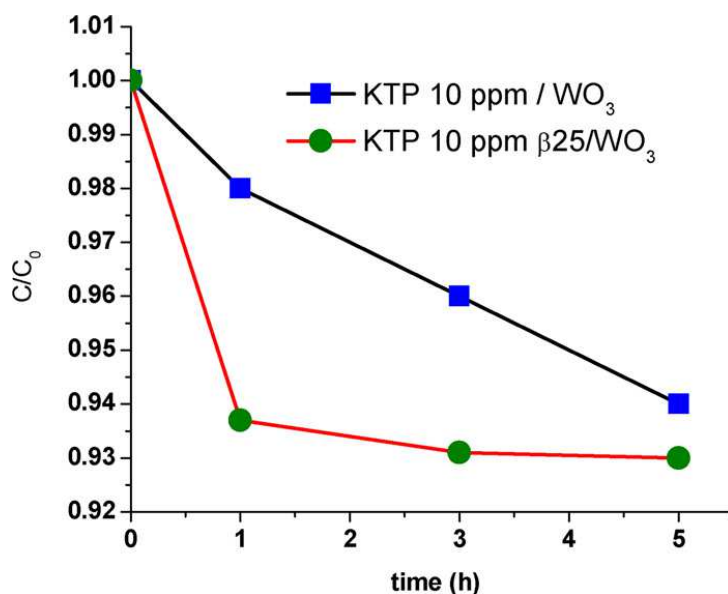


**Fig. 6.4.7.** J-V characteristic of colloidal  $\text{WO}_3$  thin films (area= $1 \text{ cm}^2$ ) under AM 1.5 illumination with 380 nm cut-off filter at pH 6 in  $0.5\text{M Na}_2\text{SO}_4$  in the presence (black and red curves) and in the absence of  $10^{-3}$  M KTP (blue). (For interpretation of the references to colour in this figure legend, the reader is referred to the web version of this article.)

The improved degradation of KTP under applied bias can be explained by the combination of two factors. First, the positive polarization reduces recombination, by continuously removing photogenerated electrons from conduction band and sub-band

gap states, increasing the flux of holes through the SEI where scavenging by the electrolyte occurs. Second, the positive charges induced on the electrode, comprising both the underlying FTO contact and mesoporous  $\text{WO}_3$  are counterbalanced by anionic species in the electrolyte. The ionic cloud surrounding the electrode is generally described in the framework of the Stern-Graham model, where the first linear potential drop in the electrolyte takes place within the Helmholtz plane, i.e. a compact sheet of ionic charge at a fixed distance from the electrodic surface, followed by a diffuse layer, where the potential drop, according to a linear approximation of the Poisson-Boltzmann equation occurs exponentially [34]. The induction of an ionic cloud, constituted by  $\text{SO}_4^{2-}$  and KTP, having charge opposite to that of the electrode surface, thus results in a local surface excess of KTP, favoring the effective bimolecular encounter with an increased flux of photogenerated  $\cdot\text{OH}$ , leading to enhanced oxidative degradation. Possible chemical interactions of KTP with the electrode surface, consisting for instance in the coordination of the carboxylate group to either  $\text{Sn}^{4+}$  of FTO or  $\text{W}^{6+}$  of  $\text{WO}_3$  could also result from the electrostatically increased surface excess of KTP. The local uptake of KTP by the mesoporous electrode under 1.2 V vs Pt polarization was confirmed by HPLC analysis carried out on 10 ppm KTP/0.7mM  $\text{Na}_2\text{SO}_4$ , within a time interval spanning 5 h, during which the solution was left to equilibrate with the electrode under positive polarization in the dark. We can indeed observe in Fig. 6.4.8 (blue squares) a slow depletion of KTP from the solution, slowly decreasing to a ca. 10% uptake after 5 h. Photoelectrochemical KTP degradation is further accelerated by exploiting the  $\beta$ 25 modified  $\text{WO}_3$  film, giving a >65% abatement (orange circles, Fig. 6.4.4) and a degradation rate constant of  $0.22 \text{ h}^{-1}$  within the same time interval and in otherwise identical conditions. The photoanodic current density, recorded during such experiment was also comparable with that delivered by the unmodified  $\text{WO}_3$  SEI, with a steady state value ranging between 100 and  $150 \mu\text{A}/\text{cm}^2$ .

Consistent with the degradation results, the  $\beta$ 25/ $\text{WO}_3$  electrode shows a much faster KTP uptake, (Fig. 6.4.8 green dots), with 90% of the relative variation occurring within the first hour, indicating a favorable trapping and confinement of KTP within the zeolites [35] embedded in the  $\text{WO}_3$  film.

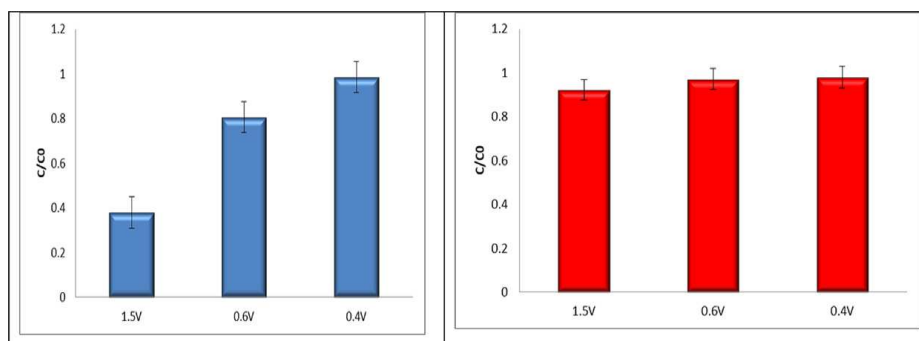


**Fig. 6.4.8.** KTP (10 ppm in 0.7mM Na<sub>2</sub>SO<sub>4</sub>) uptake by WO<sub>3</sub> (blue) and β25/WO<sub>3</sub> (green) in the dark under 1.2 V vs Pt polarization. (For interpretation of the references to colour in this figure legend, the reader is referred to the web version of this article.)

This well explains the faster degradation kinetics observed under photoelectrochemical conditions with the β25/WO<sub>3</sub> modified electrode. Imprisoning of KTP inside zeolites is also consistent with the high photoactivity of β25/WO<sub>3</sub> in the absence of applied bias where degradation of KTP was achieved with a time constant of 0.27 h<sup>-1</sup> under medium pressure Hg lamp ( $\lambda > 380$  nm) illumination. It should be recalled that in otherwise identical conditions, no significant KTP degradation was observed with the unmodified WO<sub>3</sub> film. This piece of evidence suggests that direct reaction of KTP with photogenerated holes at the SEI is not the likely mechanism for drug degradation, since in the case of KTP trapping inside β25, the direct contact between such organic species and the semiconductor surface is precluded. Rather, the degradation most probably involves reaction with ·OH diffusing away from the semiconductor surface upon primary hole scavenging by water.

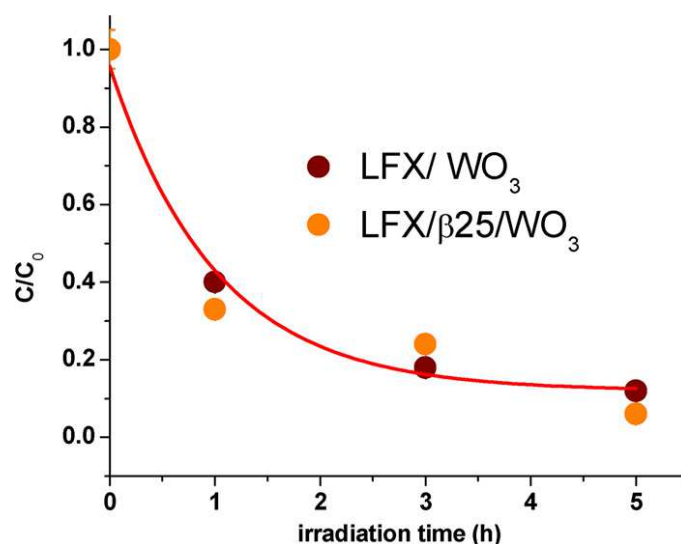
In the case of LFX, for which a satisfactory performance was already observed (see Fig. 6.4.1) under purely photocatalytic (no bias) conditions, the application of the potential to either WO<sub>3</sub> or β25/WO<sub>3</sub> also translates in a significant acceleration of the oxidative degradation of this drug at the SEI under illumination. Differently from KTP, which was essentially stable showing only a slight decrease at 1.5 V bias, probably due to surface uptake upon polarization, LFX is appreciably degraded by electrolysis at potential > 0.4 V vs. Pt, (Fig. 6.4.9), consistent with the observation of a dark electrochemical process, occurring at the exposed back contact (FTO) of the photoanode, having a threshold at

0.6 V vs Pt. In order to avoid spurious electrochemical contributions to drug degradation, the rate of LFX degradation was monitored at a bias of 0.4 V vs Pt, a potential at which only photoinduced charge separation within WO<sub>3</sub> should be active in triggering oxidative processes. Unsurprisingly, due to reduced bias, the photoanodic current generated by WO<sub>3</sub> in 10 ppm LFX dissolved in 0.7mM Na<sub>2</sub>SO<sub>4</sub> at pH 6, was smaller than in the KTP case, being in the order of ca. 50  $\mu$ A/cm<sup>2</sup>. Nevertheless, the photocurrent was satisfactorily stable and reproducible during prolonged experiments. Essentially, in this case the enhanced activity stems from an increased hole flux reaching the SEI: under 0.4 V vs Pt and AM 1.5 G (> 380 nm) illumination, causing the initial concentration of LFX to drop to less than 90% within 5 h, according to a rate constant of 0.69 h<sup>-1</sup> (Fig. 6.4.10). No obvious advantages were found from the use of a  $\beta$ 25 modified WO<sub>3</sub> thin film, given the fact that LFX is already likely to display a good interaction with the semiconductor surface, either through electrostatic interactions or by surface adsorption via nitrogen lone pairs. Compared to KTP, LFX is also an easier to oxidize species, which may react with a wider family of oxidant intermediates, like H<sub>2</sub>O<sub>2</sub>, generated upon primary water photooxidation by the coupling of two  $\cdot$ OH radicals.



**Fig. 6.4.9.** Electrodegradation of LFX (blue bars) and KTP (red bars) in the dark at the WO<sub>3</sub> SEI biased at various anodic potentials. The ratio of the concentration of either LFX or KTP with respect of their respective initial concentration (10 ppm) is reported after 3 h of anodic polarization at 0.4, 0.6 and 1.5 V vs Pt in the dark at pH 6 in 0.7mM Na<sub>2</sub>SO<sub>4</sub>. (For interpretation of the references to colour in this figure legend, the reader is referred to the web version of this article.)





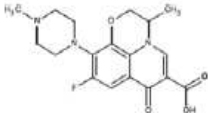
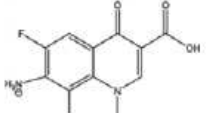
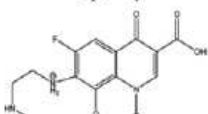
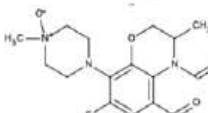
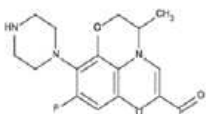
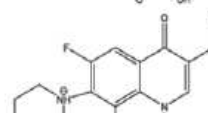
**Fig. 6.4.10.** Photoelectrochemical degradation kinetics of 10 ppm LFX, under AM 1.5 G and  $\lambda > 380$  nm illumination at WO<sub>3</sub> (area=1 cm<sup>2</sup>) (brown) and  $\beta$ 25/ WO<sub>3</sub> (orange) at pH 6 in 0.7mM Na<sub>2</sub>SO<sub>4</sub> under 0.4 V vs Pt bias.

#### 6.4.3.3. Drug mineralization and characterization of the degradation intermediates

The main degradation products of both KTP and LFX generated during the photoelectrocatalytic process were identified. The structural assignments of the intermediates were done on the basis of the comparison of the fragment ions detected in the MS-MS spectra with those reported in previous studies [36,37]. Concerning LFX, in addition to the parent molecule, five intermediate products were identified (Table 6.4.1) in the withdrawal solutions obtained during photoelectrochemical degradation. These compounds have molecular ions at m/z 335, 278, 337, 347 and 364. All of them correspond to the protonated molecule [M+H]<sup>+</sup>.

The byproduct having m/z 335 corresponds to the partial degradation of the piperazynilic ring, it is 27 Da lighter than LFX, and it could correspond to a secondary amine generated by the net loss of C<sub>2</sub>H<sub>2</sub> from the piperazynic moiety consistent with a previous observation by El Najjar et al. [38] The product with m/z 278 can be attributed to the oxidation of the piperazine side-chain in analogy to previously reported floxacine degradation products [39]. The intermediate with m/z of 364 possibly derives from the ring-opening at the N1 position (see Chart 6.4.1) followed by further oxidation via OH radical [40]. The fragment at m/z 347 may be generated through the transformation of the molecule chromophoric group. Additionally, literature data suggest that even the oxidation of quinolone moiety is mediated by %OH [41]. The product having m/z 347 possibly derives from demethylation (-14 Da) of the parent compound m/z 362. [40].

The exact concentrations of the intermediates have not been quantified since the corresponding standards for calibration are not commercially available.

Precursor ion	tr	MS <sup>2</sup>	Structure
362	7.18	362 318	
279	9.79	261	
336	6.96	261 235	
338	4.48	320 310 294 292	
348	7.10	304 284 261	
364	6.51	346 333 289 261 235	

**Table 6.4.1** Structure of the photoelectrochemical degradation products of LFX identified by mass spectrometry.

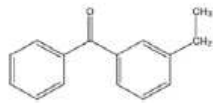
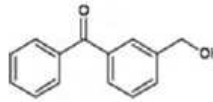
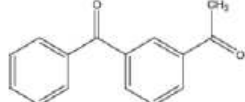
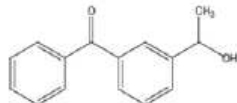
Precursor Ion	Tr	MS <sup>2</sup>	Structure
211	17.17	196 182 183 154	
212	14.35	105	
225	15.48	183 147 105	
227	13.59	76 105 209	

Table 6.4.2 Structures of the detected photoelectrochemical degradation products of KTP.

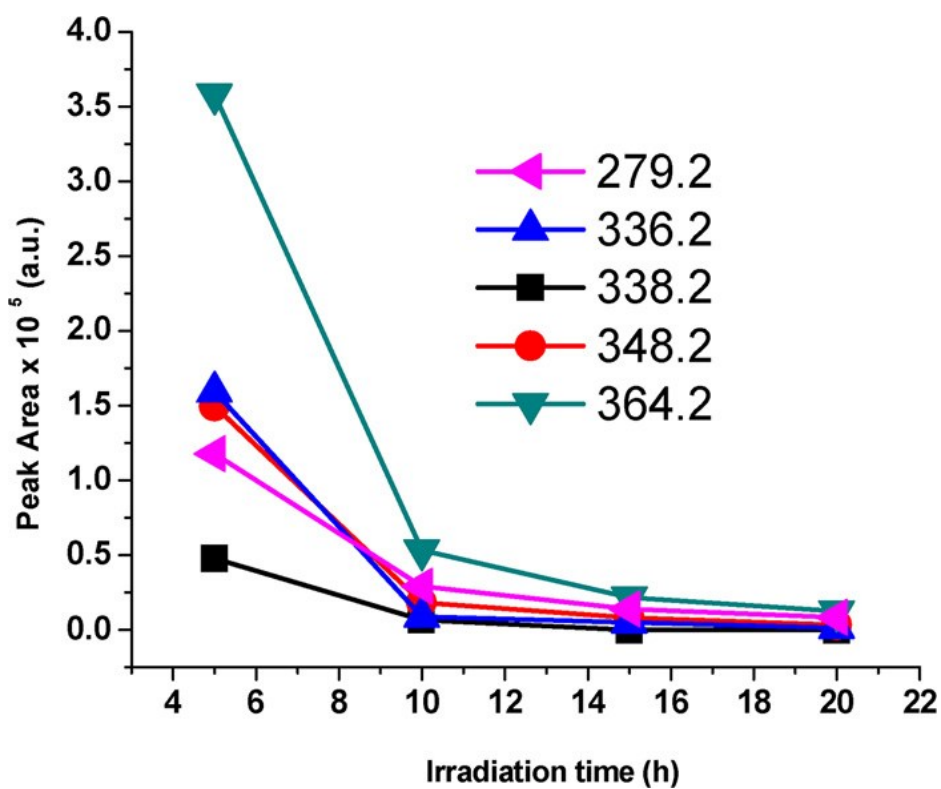


Fig. 6.4.11. Photoelectrochemical degradation of the LFX intermediates at the  $\beta$ 25/ $\text{WO}_3$  SEI under AM 1.5 G illumination with 380 nm cut off.

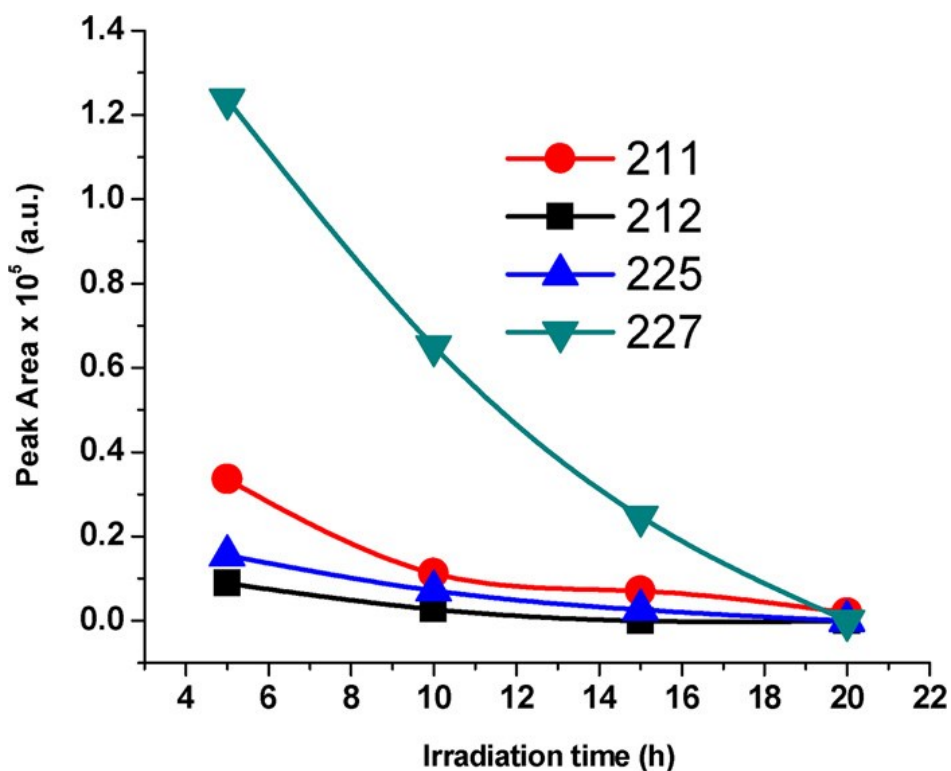


Fig. 6.4.12. Photoelectrochemical degradation of the KTP intermediates at the  $\beta$ 25/ $\text{WO}_3$  SEI under AM 1.5 G illumination and 380 nm cutoff.

However, the relative abundance of the oxidation products can be evaluated from their associated peak integral. Fig. 6.4.11 shows that the intermediates described above underwent a complete degradation, generally resulting below the detection limit of this analytical technique after 20 h of photoelectrolysis employing  $\beta$ 25- $\text{WO}_3$  photoelectrodes, consistent with the mineralization of LFX. In the degradation of KTP, the four most abundant intermediates observed have m/z 227, 225, 212 and 211 (see Table 6.4.2). The molecular weight of KTP is 254, whereas the intermediate having m/z 211, reported in Table 6.4.2, show a 44 Da decrease in the molar mass suggesting a decarboxylation of the parent compound. The most significant ( $\text{MS}^2$ ) fragments obtained from the m/z 211 compound, are reported in Table 6.4.2 alongside with the structural assignment performed on the basis of the comparison of the m/z fragments with the work by Szabò et al. [42]. It is thus possible to identify this compound as 3-ethylbenzophenone (EB). The m/z 212 intermediate seems to correspond to 3-hydroxymethyl-benzophenone, possibly deriving from oxidation of EB. On a similar basis, the fragment analysis of the intermediates with m/z 277 and 225 leads to 3-acetylbenzophenone and 3-hydroxyethyl benzophenone. The peak area of the fragments vs. irradiation time is reported in Fig. 6.4.12, where it can be observed that

also for KTP the intermediates become undetectable after 20 h of photoelectrolytic process, consistent with the achievement of drug mineralization.

#### **6.4.4. Conclusions**

In this contribution we have explored the applications of  $\text{WO}_3$  based nanomaterials to the degradation of Ketoprofen (KTP) and Levofloxacin (LFX), representing ubiquitous water contaminants of emerging concern. Interestingly, it was found that, while LFX is effectively degraded under both photocatalytic (no bias) and photoelectrochemical (applied bias) conditions, in the case of KTP there is an extreme difference in the photochemical vs. photoelectrochemical degradation kinetic: under conventional photocatalytic conditions, KTP does not show any appreciable degradation, whereas under applied bias its degradation is roughly 70% complete during a 5 h illumination cycle with  $\lambda > 380$  nm. This behavior was explained by the induction of a local excess of KTP at the  $\text{WO}_3$  SEI under positive potential, allowing a faster reaction with surface generated  $\cdot\text{OH}$  radicals. In the absence of positive bias, at pH 6, such interaction does not occur, due to electrostatic repulsion between the anionic KTP and the negatively charged  $\text{WO}_3$  surface, having point of zero charge at pH lower than 2. This indicates that besides modulating the charge separation rate at the SEI, the electric bias could be useful to tune the solar degradation of otherwise impervious molecular species via double-layer effects.

Further, in the case of KTP, the degradation activity of  $\text{WO}_3$  could be further enhanced by incorporating  $\beta 25$  zeolites into the photoactive semiconductor, allowing to trap and confine KTP in the immediate proximity of the  $\text{WO}_3$  surface, where the exposure to the flux of  $\cdot\text{OH}$  generated by monoelectronic oxidation of water should be optimal. Indeed, under appropriate photoelectrochemical conditions,  $\beta 25\text{-WO}_3$  led to the complete degradation of both KTP and LFX, as well as of their respective oxidation intermediates following 20 h of illumination. Our research is now directed towards the fabrication of thick  $\text{WO}_3$  films optimized for application under solar concentration and to the exploitation of  $\text{WO}_3/\text{BiVO}_4$  junctions, where the better light harvesting should allow for a considerable acceleration of the photoelectrochemical degradation of CECs.

## 6.4.5 References

- [1] M. La Farre, S. Perez, L. Kantiani, D. Barcelò, *Trends Analyt. Chem.* 27(2008)991-1007.
- [2] M. Schriks, M.B. Heringa, M.M. van de Krooi, P. de Voogt, A.P. van Wezel, *Water Res.* 44 (2010) 461–476.
- [3] K. Hashimoto, H. Irie, A. Fujishima, *Jpn. J. Appl. Phys.* 44 (2005) 8269–8285.
- [4] X. Chen, S.S. Mao, *Chem. Rev.* 107 (2007) 2891–2959.
- [5] M.A. Henderson, *Surf. Sci. Rep.* 66 (2011) 185–297.
- [6] J. Schneider, M. Matsuoka, M. Takeuchi, J. Zhang, Y. Horiuchi, M. Anpo, D.W. Bahnemann, *Chem. Rev.* 114 (2014) 9919–9986.
- [7] N. Daneshvar, D. Salari, A.R. Khataee, *J. Photochem. Photobiol. A: Chem.* 162(2004) 317–322.
- [8] E.S. Elmolla, M. Chaudhri, *J. Hazard. Mater.* 173 (2010) 445–449.
- [9] E.S. Elmolla, M. Chaudhuri, *Desalination* 256 (2010) 43–47.
- [10] A. Molinari, E. Sarti, N. Marchetti, L. Pasti, *Appl. Catal. B: Environ.* 203 (2017) 9–17.
- [11] A. Molinari, R. Argazzi, A. Maldotti, *J. Mol. Catal. A: Chem.* 372 (2013) 23–28.
- [12] G. Liu, T. Wu, H. Hidaka, N. Serpone, *Environ. Sci. Technol.* 33 (1999) 2081–2087.
- [13] C. Chen, W. Zhao, P. Lei, J. Zhao, N. Serpone, *Chem. Eur. J.* 10 (2004) 1956–1965.
- [14] A. Tanaka, K. Hashimoto, H. Kominami, *J. Am. Chem. Soc.* 136 (2013) 586–589.
- [15] V. Cristino, M. Sabrina, A. Molinari, S. Caramori, S. Carli, R. Boaretto, R. Argazzi, L. Meda, C.A. Bignozzi, *J. Mater. Chem. A* 4 (2016) 2995–3006.
- [16] I. Tantis, L. Bousiakou, Z. Frontistis, D. Mantzavinos, I. Konstantinou, M. Antonopoulou, G.-A. Karikas, P. Lianos, *J. Hazard. Mater.* 294 (2015) 57–63.
- [17] I. Tantis, E. Stathatos, D. Mantzavinos, P. Lianos, *J. Chem. Technol. Biotechnol.* 90 (2015) 1338–1344.
- [18] G. Longobucco, L. Pasti, A. Molinari, N. Marchetti, S. Caramori, V. Cristino, R. Boaretto, C.A. Bignozzi, *Appl. Catal. B: Environ.* 204 (2017) 273-228/272.
- [19] M. Ferech, S. Coenen, S. Malhotra-Kumar, K. Dvorakova, E. Hendrickx, C. Suetens, H. Goossens, *J. Antimicrob. Chemother.* 58 (2006) 423–427.
- [20] C. Tixier, H.P. Singer, S. Oellers, S.R. Muller, *Environ. Sci. Technol.* 37 (2003) 1061–1068.
- [21] H.R. Lozano, F. Martinez, *Braz. J. Pharm. Sci.* 42 (2006) 601–613.
- [22] J.A.O. Gonzalez, M.C. Mochon, F.J.B. de la Rosa, *Talanta* 52 (2000) 1149–1156.

- [23] J.M. Newsam, M.M.J. Treacy, W.T. Koetsier, C.B. De Grutyer, *Proc. R. Soc. Lond. Ser. A* 420 (1988) 375–405.
- [24] H. Liu, S. Huang, L. Zhang, S. Liu, W. Xin, *Catal. Commun.* 10 (2009) 544–558.
- [25] P. Varsani, A. Afonja, D.E. Williams, I.P. Parkin, R. Binions, *Sens. Actuators B* 160 (2011) 475–482.
- [26] I. Jansson, K. Yosshiiri, H. Hori, F.J. Garcia-Garcia, S. Rojas, B. Sanchez, B. Ohtani, S. Suarez, *Appl. Catal. A: Gen.* 521 (2016) 208–219.
- [27] [https://www3.epa.gov/caddis/ssr\\_ion\\_int.html](https://www3.epa.gov/caddis/ssr_ion_int.html).
- [28] L. Meda, G. Tozzola, A. Tacca, G.L. Marra, S. Caramori, V. Cristino, C.A. Bignozzi, *Sol. Energy. Mat. Sol. Cells* 94 (2010) 788–796.
- [29] [https://srdata.nist.gov/xps/main\\_search\\_menu.aspx](https://srdata.nist.gov/xps/main_search_menu.aspx).
- [30] H. Irie, S. Miura, K. Kamiya, K. Hashimoto, *Chem. Phys. Lett.* 457 (2008) 202–205.
- [31] T. Suzuki, H. Watanabe, Y. Oaki, H. Imai, *Chem. Commun.* 52 (2016) 6185–6188.
- [32] M. Anik, T. Cansizoglu, *J. Appl. Electrochem.* 36 (2006) 603–608.
- [33] S. Yamazaki, T. Yamate, K. Adachi, *Appl. Catal. A: Gen.* 454 (2013) 30–36.
- [34] J.O.M. Bockris, A.K.N. Reddy, M. Gamboa-Aldeco, *Modern Electrochemistry 2A: Fundamentals of Electrode Processes*, Kluwer Academic Publishers, New York, Boston, Dordrecht, London, Moscow, 2002.
- [35] L. Pasti, E. Sarti, A. Cavazzini, N. Marchetti, F. Dondi, A. Martucci, *J. Sep. Sci.* 36 (2013) 1604–1611.
- [36] Y. Gong, J. Li, Y. Zahng, M. Zhang, X. Tian, A. Wang, *J. Hazard. Mater.* 304 (2016) 320–328.
- [37] T. Kosjek, S. Perko, E. Heath, B. Kralj, D. Zigon, *J. Mass Spectrom.* 46 (2011) 391–401.
- [38] N.H. El Najjar, A. Touffet, M. Deborde, R. Journel, N.K.V. Leitner, *Chemosphere* 93 (2013) 604–611.
- [39] A.S. Maia, A.R. Ribeiro, C.L. Amorim, J.C. Barreiro, Q.B. Cass, P.M. Castro, M.E. Tiritan, *J. Chromatogr. A* 1333 (2014) 87–98.
- [40] I. Michael, E. Hapeshi, J. Acena, S. Perez, M. Petrovic, A. Zapata, D. Fatta-Kassinou, *Sci. Total Environ.* 461 (2013) 39–48.
- [41] P. Calza, C. Medana, F. Cabone, V. Giancotti, C. Baiocchi, *Rapid Commun. Mass Spectrom.* 22 (2008) 1533–1552.
- [42] R.K. Szabo, C. Megyeri, E. Illes, K. Gajda-Schranz, P. Mazellier, A. Dombi, *Chemosphere* 84 (2011) 1658–1663.

## **6.5 Adsorption of PFAS onto Mixed matrix membranes (MMMs)**

The data herein reported are preliminary results of a new project and further investigations will be carried out.

This work is focused on the study of the adsorption process on CANAM (carbon nanostructured advanced material) for PFAS removal from water matrix. CANAM is a mixture of graphene, carbon nanotubes, graphite, and fullerene to form mesoporous structures with a very high specific surface. The carbon material was incorporated into several polymeric matrices, which were obtained by polymerization reaction between two different PEGDEs and two different amino-functionalized monomers. The membranes obtained showed differences in crosslinking, swelling and hydrophilicity due to the intrinsic characteristics of monomers used in the formulations. Furthermore, a different percentage of carbon was added to each resulting mixed membrane matrix (MMMs). Porous fillers added to a polymer matrix not only increases the permeability of the desired component, but also increases the overall selectivity, overcoming the traditional permeability-selectivity trade-off of the polymeric membranes.

Among all the polyfluoroalkyl substances, PFOA was selected for its relevant use in industrial processes and products (due to its hydro-repellent and oleo-repellent characteristics) and for its presence in the environment, particularly in surface waters.

The adsorption and kinetic studies were carried out by batch method, in which a known amount of the adsorbent material was put in contact with a known concentration of PFOA in aqueous solution.

Kinetics studies showed that the kinetic equilibrium was reached in 3 hours for the MMMs, while it was faster for carbon powder (less of 30 minutes). Adsorption capacities were evaluated through the determination of adsorption isotherms for both the MMMs and the powdered carbon material; the results showed that higher adsorption capacities were obtained for MMMs than CANAM.

Furthermore, swelling tests were carried out to evaluate the swelling capacities for each formulation of the mixed matrix membrane.





- PEGDE propyl PEO-NH<sub>2</sub>. PEGDE Propyl was added to PEO-NH<sub>2</sub> in 8/1 ratio for the blank. To obtain the corresponding membrane, a quantity of CANAM at 5% w/w was added.

### 6.5.1.3 Batch Adsorption

Adsorption experiments were carried out into 20 mL polypropylene flasks and the solutions were stirred at room temperature for 24 hours. After the contact, an aliquot of the sample was centrifuged at 14000 rpm for 2 minutes and the supernatant was analyzed by HPLC-MS.

For each batch with increasing contaminant concentration (from 1 to 200 ppm of PFOA) the adsorbent to solution ratio w/v was 1: 1 mg / mL. Batch tests were performed for all adsorbent materials (MMMs) and compared with the respective blanks (hydrogels) and the carbon powder.

HPLC/MS analyses were made by means of Surveyor micro-HPLC hyphenated to a linear trap quadrupole mass spectrometer (LTQ XL Thermo Scientific, Waltham, MA, USA). The HPLC apparatus was composed of a solvent delivery system, a quaternary pump and an autosampler. The LTQ system was equipped with an electrospray ionization (ESI) ion source. The mobile phase was obtained as a mixture of acetonitrile (ACN) with formic acid 0.1% v/v and water with formic acid 0.1% v/v in a 60/40 ratio. Chromatographic separation was performed under isocratic elution conditions. The flow rate was 150  $\mu$ L/min, while the column was thermostated at 25 °C. The column used was Symmetry C18 100 $\times$ 2.1mm (Restek, Bellefonte, PA, USA) packed with a C18 silica-based stationary phase with a particle diameter of 2.1  $\mu$ m. The injection volume was 2  $\mu$ L for all standards and samples. MS experimental conditions were: spray voltage 3 kV, capillary temperature 275 °C, capillary voltage -4 V and tube lens -80 V for negative ESI conditions.

## 6.5.2 Result and Discussion

### 6.5.2.1 Adsorption Isotherm

Adsorption studies were carried out to evaluate saturation capacity ( $q_s$ ) for PFOA on each mixed membranes matrix and on CANAM powder (Figure 6.5.1).  $q_s$  (mg/g) corresponds to the maximum quantity of contaminant adsorbed per gram of adsorbent and is calculated using adsorption isotherm models.

The data obtained from batch experiments were fitted to the Langmuir isotherm model with the following equation:

$$q = \frac{q_s b C_e}{1 + b C_e}$$

where  $b$  is the binding constant ( $L\ mg^{-1}$ )  $q_s$  is the saturation capacity of the adsorbent material ( $mg\ g^{-1}$ ) and  $C_e$  is the equilibrium concentration. The Langmuir model describes an adsorption process on a homogenous surface, and it does not take into account adsorbate-adsorbate interactions and adsorbate-solvent interactions. Furthermore, the model represents an adsorbent characterized by energetically equivalent sites.

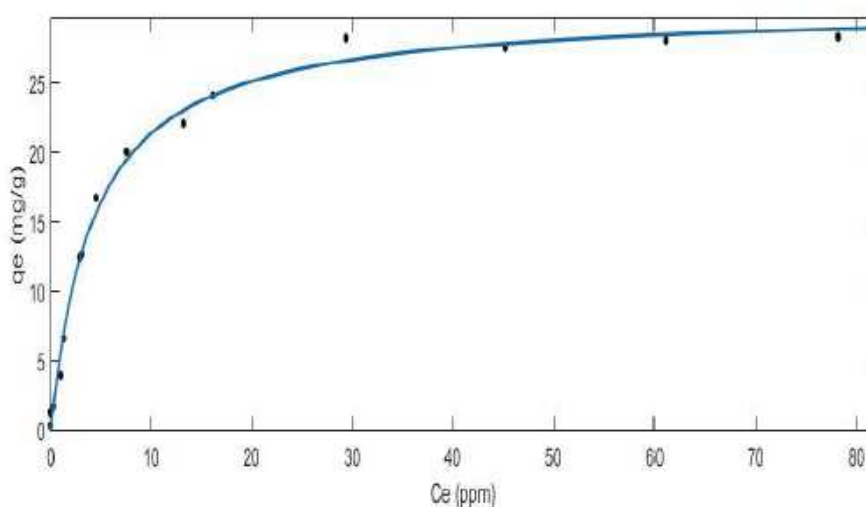


Fig.6.5.2 Adsorption isotherm of carbon powder

As can be seen in figure 6.5.2 the adsorption isotherm is concave and consists of a steep initial part and a saturation zone. The concave shape of the adsorption isotherm indicates a favorable adsorption of PFOA on CANAM, and therefore this material can be defined as a good adsorbent. The saturation capacity obtained is reported in Table 6.5.1

Table 6.5.1 Estimated parameters obtained using the Langmuir isotherm model, the confidence bonds at 95% of probability are reported in brackets.

$q_s$ ( $mg\ g^{-1}$ )	$b$ ( $L\ mg^{-1}$ )	$R^2$
30.5 (29.3; 31.8)	0.235 (0.198; 0.273)	0.9933

In Figure 6.5.2 the adsorption isotherms of the contaminant on MMMs are reported. Experimental data were fitted with the Hill isotherm model which describes the adsorption process as a cooperative phenomenon; the binding capacity of the ligand to

one site on the macromolecule can influence different binding sites on the same macromolecule.

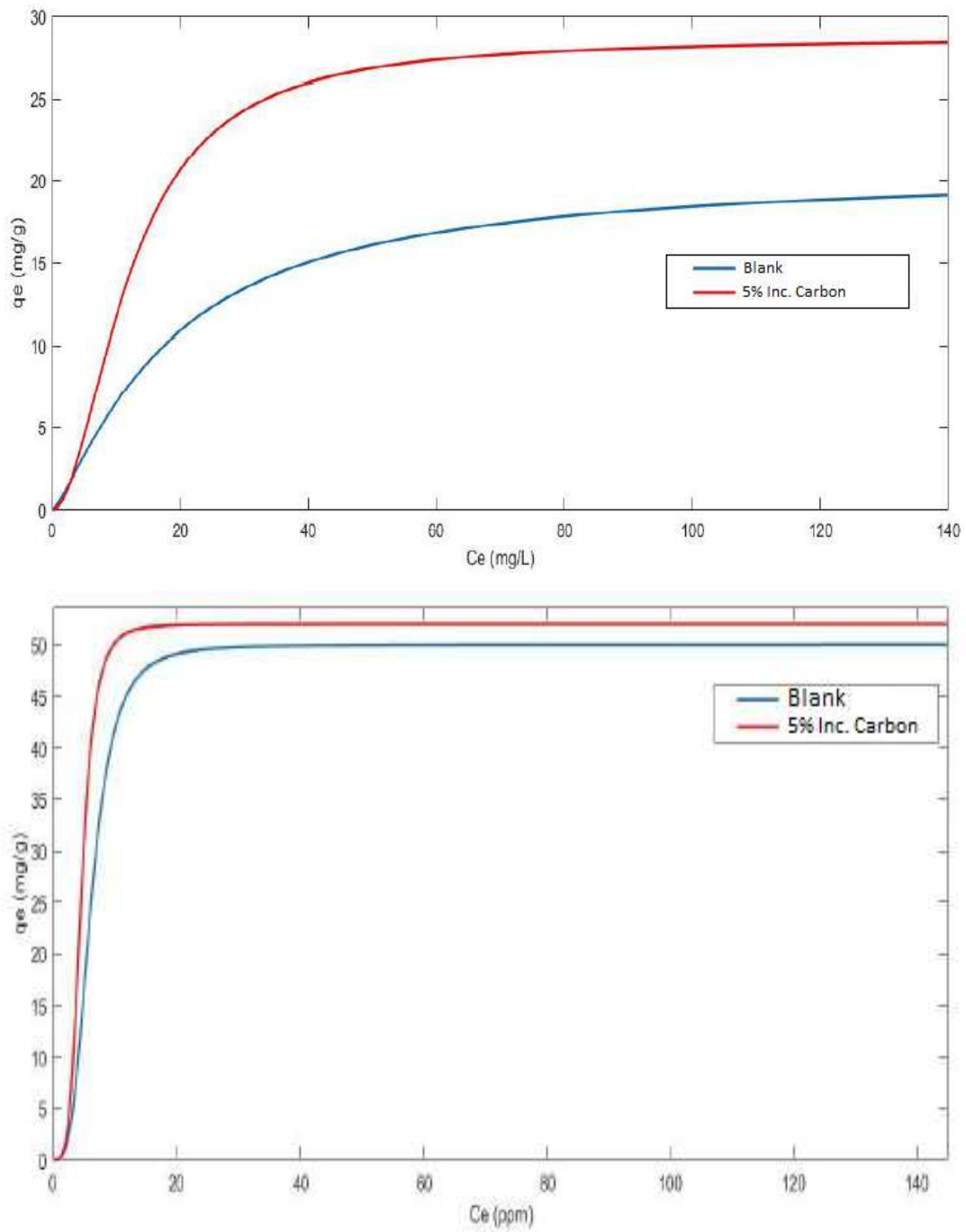


Figure 6.5.2 Adsorption isotherm comparison between: (a) PEGDE\_Ethyl\_PEONH2+5% carbon and Blank and (b) PEGDE\_Ethyl\_JEFF + 5% Carbonaceous material vs Blank

The mathematical expression of the Hill isotherm model is the follow:

$$q_e = \frac{q_{sH} C_e^{nH}}{K_D + C_e^{nH}}$$

Where  $q_e$  is the mass of adsorbate per adsorbent unit ( $\text{mg g}^{-1}$ ),  $q_{sH}$  is the maximum absorption saturation of the Hill isotherm ( $\text{mg L}^{-1}$ ),  $K_D$  is the Hill constant,  $nH$  is the Hill cooperativity coefficient of the bond interaction and  $C_e$  is the concentration of the species of interest at equilibrium ( $\text{mg L}^{-1}$ ).

The comparison of adsorption isotherms between blanks and the corresponding mixed matrix membranes (Fig.6.5.2), showed that in each case an increase of saturation capacity occurred when the filler was added to the polymeric matrices. This indicates that with the addition of CANAM, materials with a better adsorption capacity than the starting ones are obtained.

Furthermore, kinetic studies were carried out. To determine the kinetic parameters, experimental data were interpolated by the pseudo second order kinetic equation:

$$q_t = \frac{k_2 q_e^2 t}{1 + k_2 q_e t}$$

in which  $q_t$  represents the amount of adsorbed PFOA at the time  $t$ ,  $k_2$  the pseudo second order constant,  $q_e$  and the amount of adsorbed material at equilibrium.

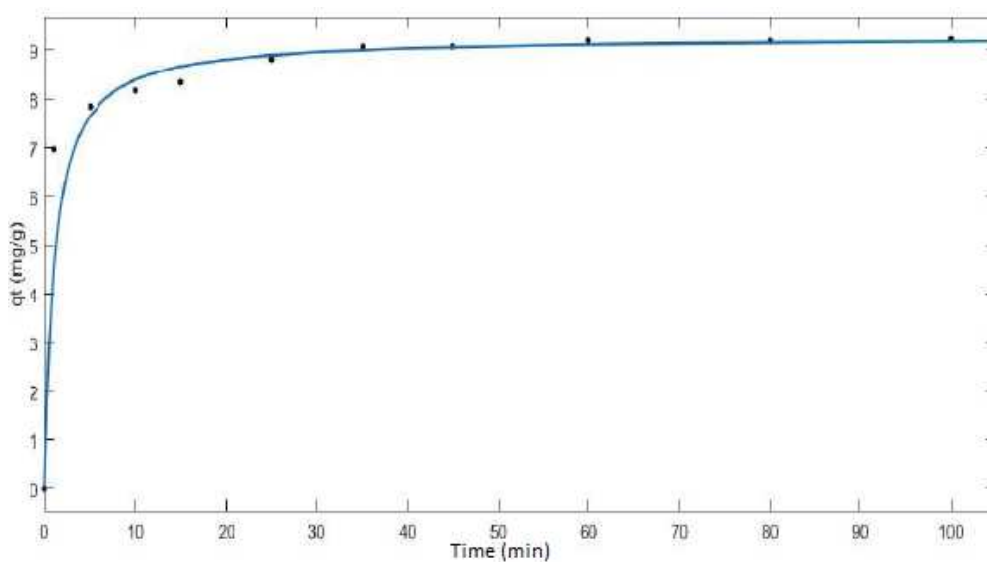


Figure 6.5.3 Adsorption kinetic of CANAM

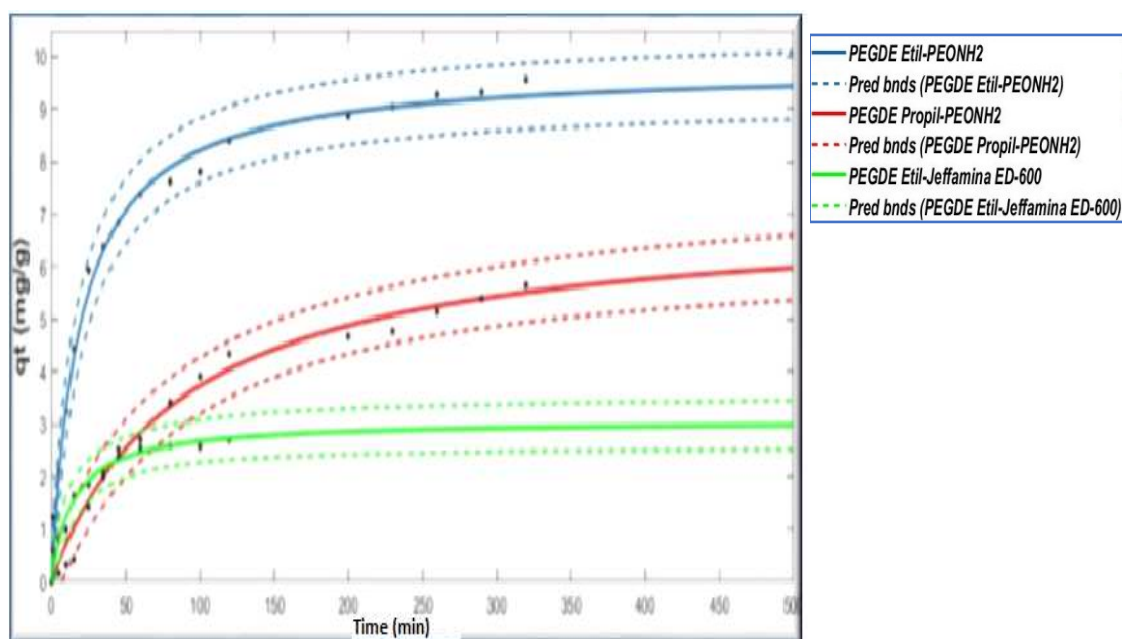


Figure 6.5.4 Comparison of adsorption kinetic trends of the polymeric matrices

Comparing the adsorption kinetics of the different adsorbent materials (Figure 6.5.3, 6.5.4) it can be seen that CANAM reaches the equilibrium faster than the various polymeric matrices. In fact, the carboneous powder reached equilibrium in less than 30 minutes, while in the case of the polymeric matrices the equilibrium was reached after 4 hours.

### 6.5.3 Swelling

Swelling percentage was evaluated weighting the sample at different contact time to evaluate the increases of mass and weight of the hydrogel sample. Experiments were carried out in water solution under stirred (25°C) for 24 hours. To obtain swelling percentage was used the following equation:

$$SW\% = \frac{SW_f - SW_i}{SW_i} * 100$$

Were  $SW_f$  corresponding to the weight of sample after a period of contact time, and  $SW_i$  is the weight of starting hydrogel. In figure 6.5.4 swelling percentages vs. contact time, are reported.

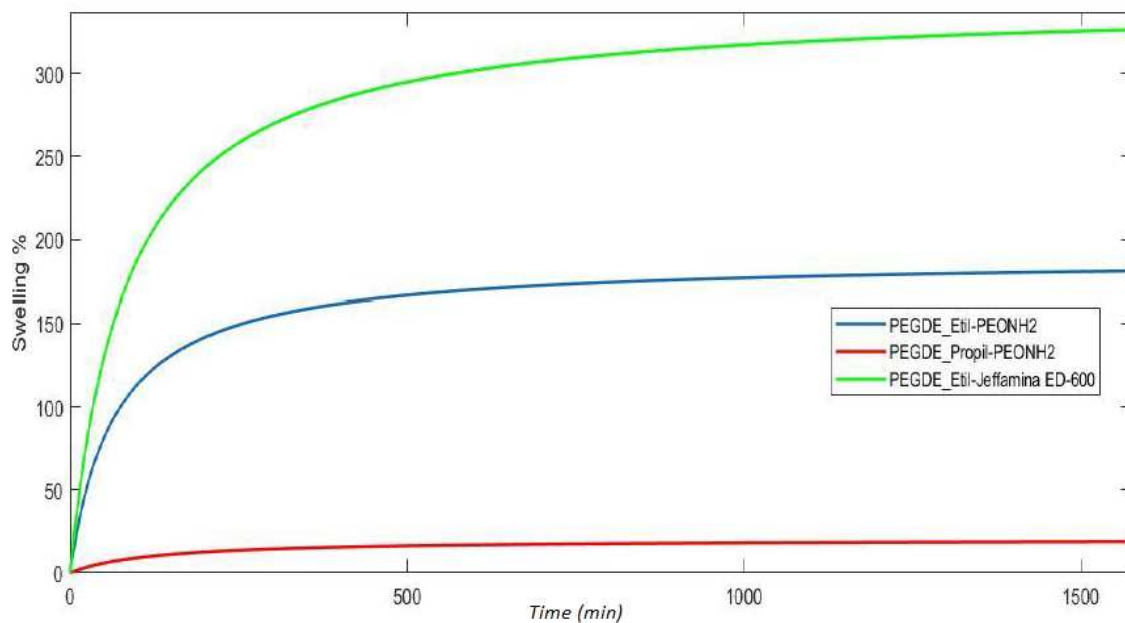


Figure 6.5.4 Swelling percentage of PEGDE\_Ethyl-Jeffamine ED-600 (green line), PEGDE\_Ethyl-PEONH<sub>2</sub> (blue line) and PEGDE\_Propyl-PEONH<sub>2</sub>

Experimental data shows that higher swelling percentage occurs for PEGDE\_Ethyl-JEFF and the followed, in order of swelling increase, are PEGDE\_Ethyl-PEONH<sub>2</sub> and PEGDE\_Propyl-PEONH<sub>2</sub>. As it can be seen in figure 6.5.1, the higher hydrophilic polymeric matrix is PEGDE\_Ethyl-JEFF; in view of this, it emerges that the swelling is linked to the hydrophilic characteristics of the material.

## 6.6 Comparison of the adsorption process between Y zeolites

Part of the results illustrated herein are included in an article in preparation.

Among the various removal approaches of PFAS contaminants, adsorption in low concentration from complex waste and surface waters through microporous materials has proven to be highly effective, albeit the PFOA and PFOS adsorption mechanism is not yet completely defined [1]. Due to their large surface area, controllable pore size, along with cost effective production on a large scale, eco-compatibility, long-life capability, high acid resistance and catalytic activity [2], zeolites have been widely used in water purification [3-5] organic solvent filtration, gas separation. Introduction of noble metals (e.g., Ag) nanoparticles NPs onto zeolites confers unique physical, chemical properties along with strong absorption property, good stability and good conductivity. Silver immobilized in the zeolite solid matrix has the most powerful antimicrobial activity against a range of both Gram-negative (e.g. *Acinetobacter*, *Escherichia*, *Pseudomonas*, *Salmonella* and, *Vibrio*) and Gram-positive bacteria (e.g. *Bacillus*, *Clostridium*, *Enterococcus*, *Listeria*, *Staphylococcus* and, *Streptococcus*), fungi (e.g. *Aspergillus niger*, *Candida albicans*, *Saccharomyces cerevisiae* and, *Penicillium citrinum*), virii (e.g Hepatitis B, and HIV-1), and antibiotic-resistant pathogens.

This work is focused on the adsorptive properties of Y zeolite with different silica/alumina ratio (SAR) towards PFOA and PFAS. This zeolite (FAU-type topology) is an inorganic microporous crystalline material whose three-dimensional framework is built up from  $TO_4$  tetrahedra giving rise to three-dimensional channels arranged in a cubic structure. The present work aims to investigate, for the first time by Rietveld structure refinements on, the structural evidences of PFOA and PFOS adsorption on Y zeolites with different silica/alumina ratio (SAR) before and after Ag-functionalization.

The objective was to investigate the host-guest interactions as well as demonstrate the potential application of these high selective microporous materials for PFOA removal from aqueous solutions.



## 6.6.1. Material and methods

### 6.6.1.1 Materials

High silica “Y” type faujausite zeolites powders CBV720 (30 SiO<sub>2</sub>/Al<sub>2</sub>O<sub>3</sub> molar ratio, 0.03 wt% Na<sub>2</sub>O), CBV760 (60 SiO<sub>2</sub>/Al<sub>2</sub>O<sub>3</sub> molar ratio, 0.03 wt% Na<sub>2</sub>O) and Y HSZ390HUA (500 SiO<sub>2</sub>/Al<sub>2</sub>O<sub>3</sub> molar ratio, 0.05 wt% Na<sub>2</sub>O), were purchased from Zeolyst International (Conshohocken, PA, USA) and Tosoh Corporation (Tokyo, Japan) respectively. More details are reported in Table 6.6.1. Silver Nitrate (AgNO<sub>3</sub> - ACS Reagent – purity ≥99.0% - 209139-25G) was purchased from Merck (Darmstadt, Germany). The water was Milli-Q grade (Millipore, Ma, USA). PFOA standard was purchased from Sigma-Aldrich (99% purity) while PFOS standard from LGC Standard (96% purity). Structures of perfluoroalkyl chemicals under investigation are reported in Figure 6.6.1.

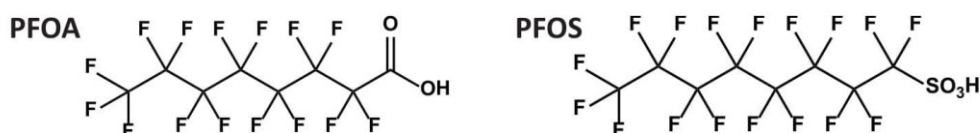


Figure 6.6.1 Molecular structures of PFOA and PFOS

Table 6.6.1 Characteristics of Y zeolites

Sample	Supplier and Product Code	SiO <sub>2</sub> /Al <sub>2</sub> O <sub>3</sub> Ratio	Surface Area (BET, m <sup>2</sup> /g)	Na <sub>2</sub> O (wt%)	Nominal Cation Form
Y720	Zeolyst International CBV720	30	780	0.03	Hydrogen
Y760	Zeolyst International CBV760	60	720	0.03	Hydrogen
Y390	Tosoh Corporation HSZ390HUA	500	630	0.05	Hydrogen

### 6.6.1.2 Preparation of silver-exchanged zeolites

The AgY zeolites were prepared using standard ion-exchange method. Caution was taken due to the silver photosensitivity. 1 g of each Y-zeolite was used as received and introduced in 250 mL of 0.05 M AgNO<sub>3</sub> aqueous solution and continuously stirred at 150 rpm for 24 h at 60 °C (ORBITAL INCUBATOR SI50 – Stuart Scientific) in darkness conditions. The solid was recovered by vacuum filtration on a membrane filter (mixed cellulose esters (MCE), 8 μm pore size, 47 mm diameter, MF-Millipore) and washed thoroughly with deionized water. The silver-exchanged zeolites were dried at room

temperature and atmospheric conditions in a dark area and were stored in a dryer before the analysis.

### **6.6.1.3 Batch experiments**

Adsorption experiments were performed with the batch method, where solutions of increasing concentration of PFAS were put in contact with known amounts of zeolite in 1:1 ratio (mg:mL). The PFAS, particularly PFOS, are adsorbed on glassy material, therefore, to evaluate the saturation capacity of the zeolites, it was necessary to use inert polypropylene volumetric flasks. During the contact time (24 hours) the solutions were continuously stirred at 25 ° C. After this period, an aliquot of sample solution was centrifuged at 14000 rpm for 5 minutes, and analyzed by HPLC / MS.

HPLC/MS analyses were carried out by means of Surveyor micro-HPLC hyphenated to a linear trap quadrupole (LTQ) mass spectrometer (LTQ XL Thermo Scientific, Waltham, MA, USA). The LTQ system was equipped with an electrospray ionization (ESI) ion source. The mobile phase was obtained as a mixture of acetonitrile (ACN) with formic acid 0.1% v/v and water with formic acid 0.1% v/v in 60/40 ratio. Chromatographic separation was performed under isocratic elution conditions and the flow rate was 150  $\mu$ L/min. The column used was Ascentis express C18 100 $\times$ 2.1mm (Supelco, USA) packed with a C18 silica-based stationary phase with a particle diameter of 2  $\mu$ m. The injection volume was 2  $\mu$ L for all standards and samples. MS experimental conditions were: spray voltage 3 kV, capillary temperature 275 °C, capillary voltage -4 V and tube lens -80 V for negative ESI conditions.

### **6.6.1.4 X-ray powder diffraction measurements and structure determination**

X-ray powder diffraction patterns (XRD) were measured on a D8 Advance X-Ray Diffractometer, with DAVINCI Design, (copper anode; operating conditions, 40 kV and 40 mA), and a linear array detector (LynxEye), coupled with a Ni filter to completely remove the Cu K $\beta$  component. Data scans were collected at RT in the 2 $\theta$  range 4-80°, 0.02° 2 $\theta$  step size, with point-detector equivalent counting times of 3 s/step. LeBail method get precise integrated intensities and refine accurately the lattice parameter a in Fd-3m space. Rietveld structure refinements were then performed using the GSAS package [6] with EXPGUI graphical interface [7]. Group starting from the structural

model reported by Braschi et al. (2010). The Bragg peak profiles were modelled by the third profile function described by Finger, Cox and Jephcoat (LX, LY, S/L, H/L) [n], with the peak cut-off set to 0.0005%. The instrumental background curve was fitted using a Chebyshev polynomial with 20 variable coefficients. The 2 $\theta$ -zero shift, scale factor, and unit-cell parameters were refined. Geometric soft constraints were initially imposed on tetrahedral Si-O, O-O, C-C, C-F bond distances (Si-O 1.62 $\pm$  0.04 Å, O-O 2.60 $\pm$  0.04 Å, C-C 1.40 $\pm$  0.02 Å, C-F 1.35 $\pm$  0.02 Å, respectively). Their weighting factor was then reduced in the last cycles of the refinement until reasonable bond lengths were obtained. The positions of extraframework sites were defined applying Fourier and Difference Fourier maps. Atomic coordinates, displacement factors and occupancies (Tables 1S-6S) of the organic molecules were refined during the early stage of the refinement and then fixed in the final stage of the refinement. The approximation of crystallite sizes of zeolites was achieved by the Scherrer equation and Williamson-Hall analysis.

## 6.6.2. Results and Discussion

### 6.6.2.1 Adsorption

The adsorption of PFAS from the aqueous solution onto zeolites was evaluated by fitting the experimental data with the Langmuir adsorption isotherm model. The uptake  $q$  (mg g<sup>-1</sup>) was calculated as follow:

$$q = \frac{q_s b C_e}{1 + b C_e}$$

where  $b$  is the binding constant (L·mg<sup>-1</sup>),  $q_s$  is the saturation capacity of the adsorbent material (mg·g<sup>-1</sup>) and  $C_e$  (mg L<sup>-1</sup>) is the solute concentration at equilibrium. The adsorption isotherms of PFOA and PFOS on Y and AgY zeolites are shown in Figure 6.6.2 and 6.6.3.

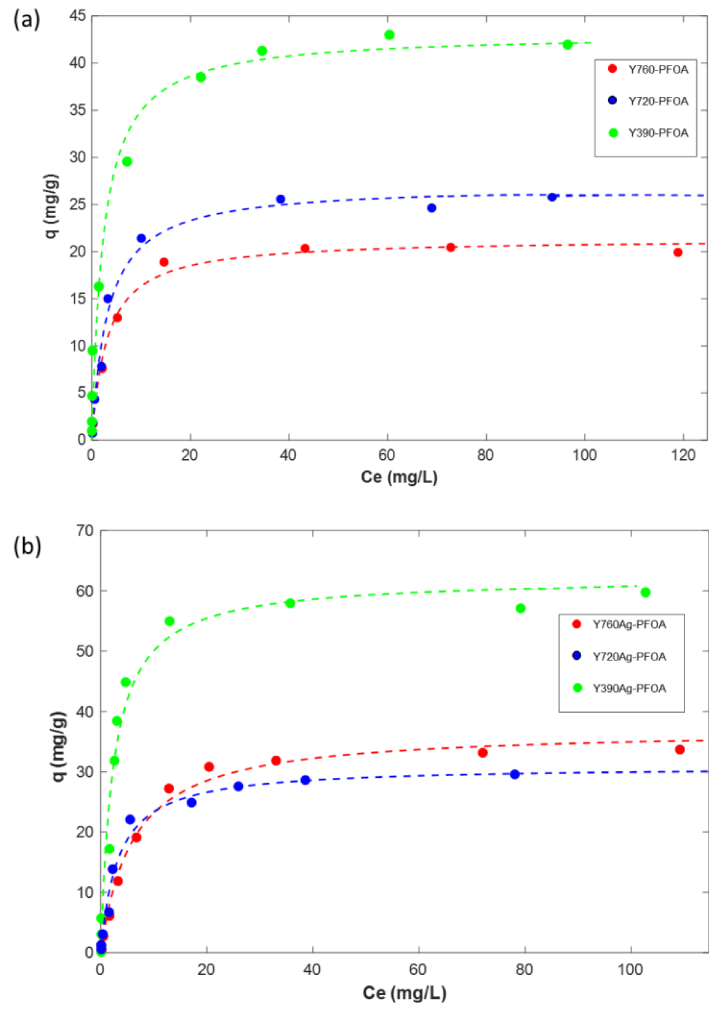


Figure 6.6.2 PFOA adsorption comparison between Y zeolites (a), PFOA adsorption comparison between AgY zeolites (b)

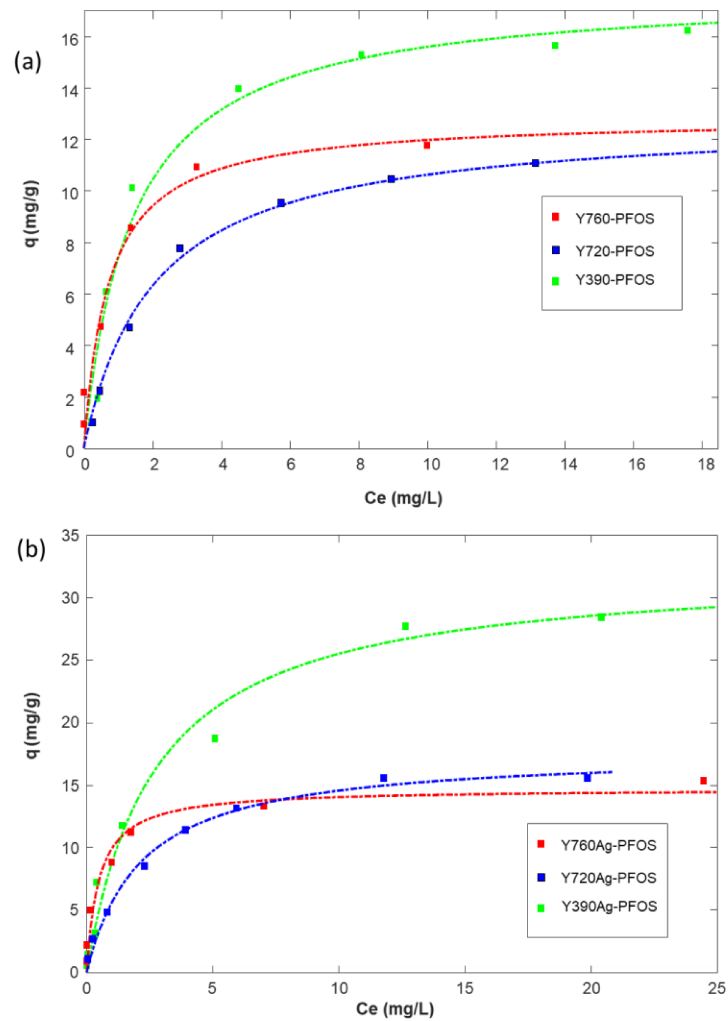


Figure 6.6.3 comparison of PFOS adsorption between Y zeolites (a), comparison PFOS adsorption between AgY zeolites (b)

As it can be seen in figure 6.6.2 and in figure 6.6.3 the saturation capacity is higher for the Y390 zeolite, whereas Y720 and Y760 have a similar uptake of PFOA and PFOS. By comparing the Y zeolites in terms of saturation capacities and binding constants (Table 6.6.2), the more hydrophobic Y390 generally demonstrated to offer higher efficiency than Y720 and Y760, despite the same surface area, thus confirming that the SAR of the zeolite is an important factor in the adsorption process.

Furthermore, the saturation capacity of each zeolite towards PFAS increases after adsorption of silver ions onto the material. Even in this case, the higher saturation capacity was reached for Y390 zeolite. Therefore, hydrophobic zeolites are very promising adsorbents for the removal of PFAS from water. Comparing the saturation capacities, it can be seen that the uptake of PFOA on all zeolites is higher than PFOS.

Furthermore, kinetic studies were carried out to evaluate the kinetic constants and the reaching of the kinetic equilibrium. Experimental data reported in Figure 6.6.4 can be fitted by the pseudo-second order model:

$$q_t = \frac{k_2 q_e^2 t}{1 + k_2 q_e t}$$

where  $q_t$  and  $q_e$  are the amounts of solute adsorbed per mass of sorbent at a time  $t$  and at the equilibrium, respectively, and  $k_2$  is the pseudo second-order adsorption rate constant.

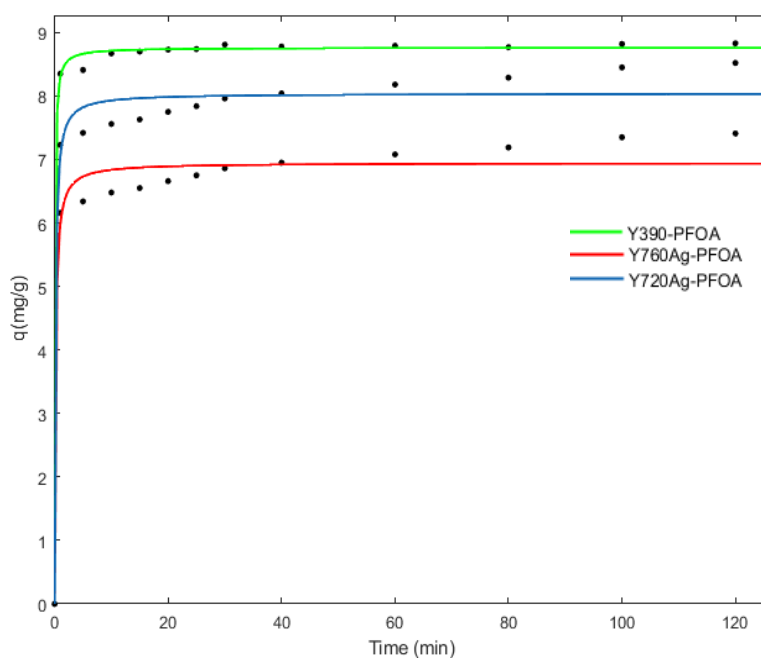


Figure 6.6.4. PFOA uptake vs. contact time for Y390 (green line), Y760 (red line) and Y720 (blue line) for initial concentration of 10 mg/L

Results showed that the adsorption kinetic process was very fast for all Y zeolites; the equilibrium was reached in about 20 min. The values of the uptake at the equilibrium,  $q_e$ , and the adsorption rate constant,  $k_2$ , obtained from the pseudo second order kinetic model, are reported in table 6.6.2.

Table 6.6.2 Kinetic parameters obtained from pseudo second order kinetic equation. The confidence limits at 95% of probability of the estimated parameters are reported in brackets.

Sample	$q$ ( $\text{mg g}^{-1}$ )	$K_2$ ( $\text{g L}^{-1}\text{mg}^{-1}$ )	$R^2$
Y390	8.87 (8.86 ; 8.8)	0.42 (0.39 ; 0.45)	0.9985
Y760	6.78 (6.77 ; 6.79)	0.33 (0.30 ; 0.36)	0.9898
Y720	7.98 (7.97 ; 7.99)	0.31 (0.28 ; 0.34)	0.9948

### 6.6.3 Characterization by X-ray diffraction

A careful characterization of all starting selected zeolites was carried out by the Rietveld method to define their unit cell parameters (Table 6.6.3), tetrahedral bond distances and angles. Mean Si-O bond lengths and Si-O-Si and O-Si-O angles do not differ significantly.

Table 6.6.3. Unit cell parameters of Y and AgY zeolites

Sample	Space group	a = b = c (Å)	V (Å <sup>3</sup> )
<b>Y720</b>	<i>Fd-3m</i>	24.3160(4)	14377.3(4)
<b>Y720-PFOA</b>	<i>Fd-3m</i>	24.2978(4)	14345.1(5)
<b>Y720-PFOS</b>	<i>Fd-3m</i>	24.3028(4)	14353.9(4)
<b>AgY720</b>	<i>Fd-3m</i>	24.3077(3)	14362.6(3)
<b>AgY720-PFOA</b>	<i>Fd-3m</i>	24.3054(3)	14358.5(3)
<b>AgY720-PFOS</b>	<i>Fd-3m</i>	24.2869(4)	14325.7(4)
<b>Y760</b>	<i>Fd-3m</i>	24.2789(6)	14311.6(6)
<b>Y760-PFOA</b>	<i>Fd-3m</i>	24.2865(4)	14324.9(4)
<b>Y760-PFOS</b>	<i>Fd-3m</i>	24.2809(4)	14315.1(4)
<b>AgY760</b>	<i>Fd-3m</i>	24.2844(4)	14321.3(4)
<b>AgY760-PFOA</b>	<i>Fd-3m</i>	24.2824(4)	14317.7(4)
<b>AgY760-PFOS</b>	<i>Fd-3m</i>	24.2869(4)	14325.7(4)
<b>Y390</b>	<i>Fd-3m</i>	24.2882(4)	14328.1(4)
<b>Y390-PFOA</b>	<i>Fd-3m</i>	24.2854(3)	14323.1(3)
<b>Y390-PFOS</b>	<i>Fd-3m</i>	24.2845(2)	14321.6(2)
<b>AgY390</b>	<i>Fd-3m</i>	24.2839(4)	14320.5(4)
<b>AgY390-PFOA</b>	<i>Fd-3m</i>	24.2824(4)	14317.7(4)
<b>AgY390-PFOS</b>	<i>Fd-3m</i>	24.2831(3)	14319.0(3)

Analysis of the Fourier maps highlighted the occurrence of co-adsorbed water molecules in the supercage (w1, w2, w3 and w4 sites, respectively), linked to each other to form 4 different water molecular oligomers (O4-w3-w1-w2-w4-w4-w3-O4; O4-w3-w2-w1-w1-

w3-O4;O4-w3-w1-w1-w2-w3-O4 and O4-w3-w1-w1-w2-w1-w1-w3-O4) hydrogen bonded to the O4 framework oxygen atom (Figure 6.6.4 a).

The unequal water molecules amount confined in structural pores (130, 94 and 86 water molecules per unit cell in Y720, Y760 and Y390, respectively) explains the different intensities of (111) and (220) reflections in the powder diffraction patterns.

After Ag-exchange, the comparison of the main peaks' intensity with those of the as-synthesized materials indicates a progressive variation of both intensity and position suggesting the entering of Ag ions inside the microstructural porosities. Moreover, no loss of crystallinity or new diffraction lines are observed thus excluding the formation of amorphous/secondary phases (Figure 6.6.4 b). A careful examination of the intra-framework bond lengths and angles highlighted that no significant deviations of the coordinates are detected for the framework atoms. The unit-cell parameters as well as the dimensions of the apertures were comparable with those of the pristine materials (Table 6.6.1). In all exchanged zeolites, the occurrence of co-adsorbed water hydrogen bonded to each other's and interacting with the O4 framework oxygen was also maintained (Figure 6.6.4b).



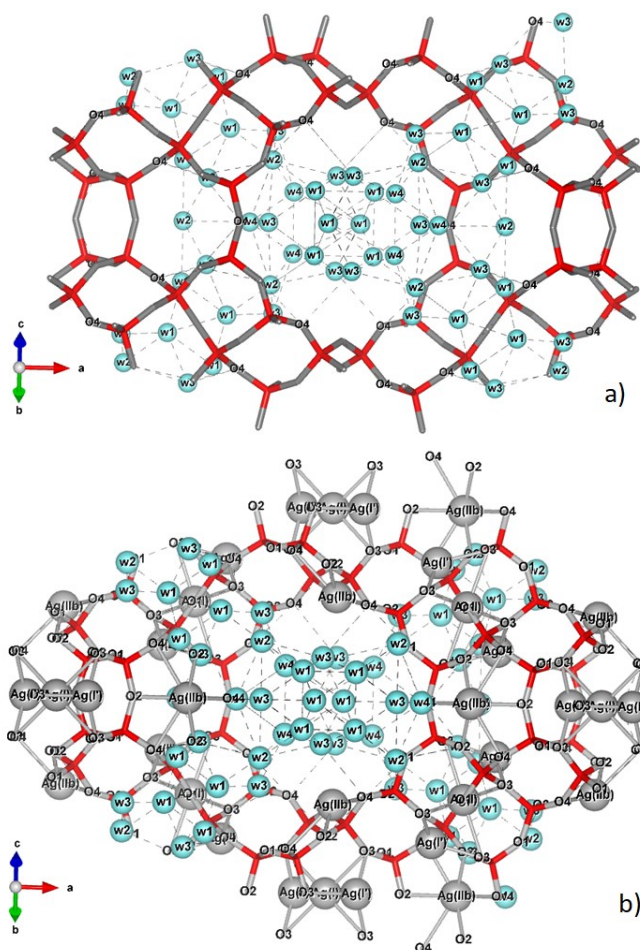


Figure 6.6.4 Fourier maps of a Y zeolite (a), fourier maps of a AgY zeolite (b)

Rietveld structure refinements highlighted that Ag ions were hosted in three disordered sites with partial occupancies interacting with the negatively charged framework oxygen atoms: site Ag(I) in the center of the hexagonal prism, closely surrounded by six oxygens (O3) of the two bases of the hexagonal prism; site Ag(I') on the external basis of the hexagonal prisms, just inside the sodalite cage and six-fold coordinated to O2 and O3 framework oxygens; site Ag(IIb) in the middle of the six-membered ring forming the frontier between the supercage and the sodalite cage, coordinated to water molecule at w3 site and to O2 and O3 oxygens of the framework (Figure 6.6.4 b). Silver ions at Ag(IIb) site acted as a bridge with the water oligomers thus forming continuous “tube” of water molecules H-bonded (Figure 6.6.4 b) to framework oxygens (Ag(IIb)-O4-w3-w1-w2-w4-w4-w3-O4-Ag(IIb)-O4-w3-w2-w1-w1-w3-O4- Ag(IIb) O4-w3-w1-w1-w2-w3-O4-Ag(IIb)-O4-w3-w1-w1-w2-w1-w1-w3-O4-Ag(IIb)).

According to Hutson et al. (2000) [8] the short Ag(I)-Ag(I') bond distances (1.98 and 1.49 Å in Ag(Y)760 and Ag(Y)390, respectively) prevented the formation of Ag<sup>+</sup>-Ag<sup>0</sup> (the sum of the ionic radius of Ag<sup>+</sup> and the atomic radius of Ag metal, 1.26 + 1.445 = 2.705 Å) or Ag<sup>0</sup>-Ag<sup>0</sup> (Ag<sup>0</sup>-Ag<sup>0</sup> distance in silver metal, 2.89 Å) bonds at these sites but the Ag<sup>+</sup>-Ag<sup>+</sup> (the sum of the ionic radius of Ag<sup>+</sup> ions 1.26 + 1.26 = 2.52 Å) occurrence was physically possible in Ag(Y)720 (Ag(I)-Ag(I') ≈ 2.39 Å). The total number of Ag ions per formula unit obtained by the structural refinement (~2.5 a.u.c in both AgY720 and AgY760, ~ 1 a.u.c. in AgY390).

After loading all selected Y samples with PFOA and PFAS, the PXRD patterns showed strong differences in the Bragg's peak intensities, especially at low 2θ angles suggesting modifications of the extraframework content. The check of the unit cell did not reveal phase change to the Fd-3m symmetry. The Rietveld procedure was started with the introduction of the framework coordinates (taken from our refinements of Y samples with different Si/Al ratio) without an inclusion of the adsorbed guest molecules. At this stage of the refinement, a careful analysis of difference Fourier maps highlighted the occurrence of groups of electron density peaks around the center of the large 'supercage' ([4<sup>18</sup>6<sup>4</sup>12<sup>4</sup>]). Except for slight variations in the thermal motions of the organic molecules, a general convergence between the electron density maps has been observed, thus providing a good picture of the real location of hosted ions and molecules. The most intense peaks are due to the PFAS/PFOA molecules, which had not yet been inserted in the structural model (Figure 6.6.5).

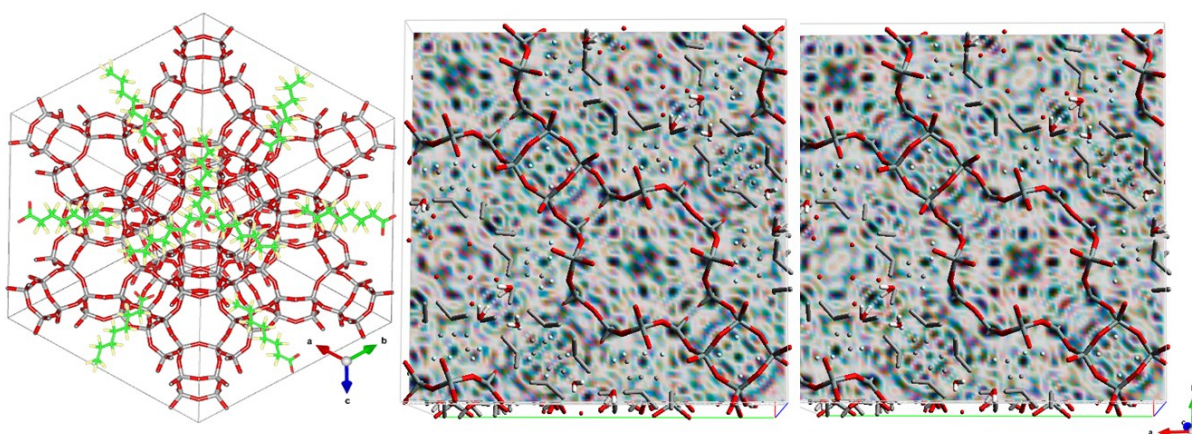


Figure 6.6.5 Interaction between PFOA and a Y zeolite

At the same time, the residual ones were assigned to co-adsorbed water molecules. The extra-framework sites detected by difference Fourier maps were optimized using the EXPO2014 program (by plane wave DFT with dispersion correction, DFT-D [9] and then the optimized structure coordinates were fixed in the final cycles of Rietveld refinement to secure a stable refinement.

In all structural refinements, PFOS and PFOA molecules are arranged at the center of the supercell, thus assuming six different molecular orientations, all partially statistically occupied (Figure 6.6.5).

In silver functionalized systems, the concentration Ag ions as well as those of PFAS were unchanged thus attesting that Ag did not compete with their adsorption (Figure 6.6.6).

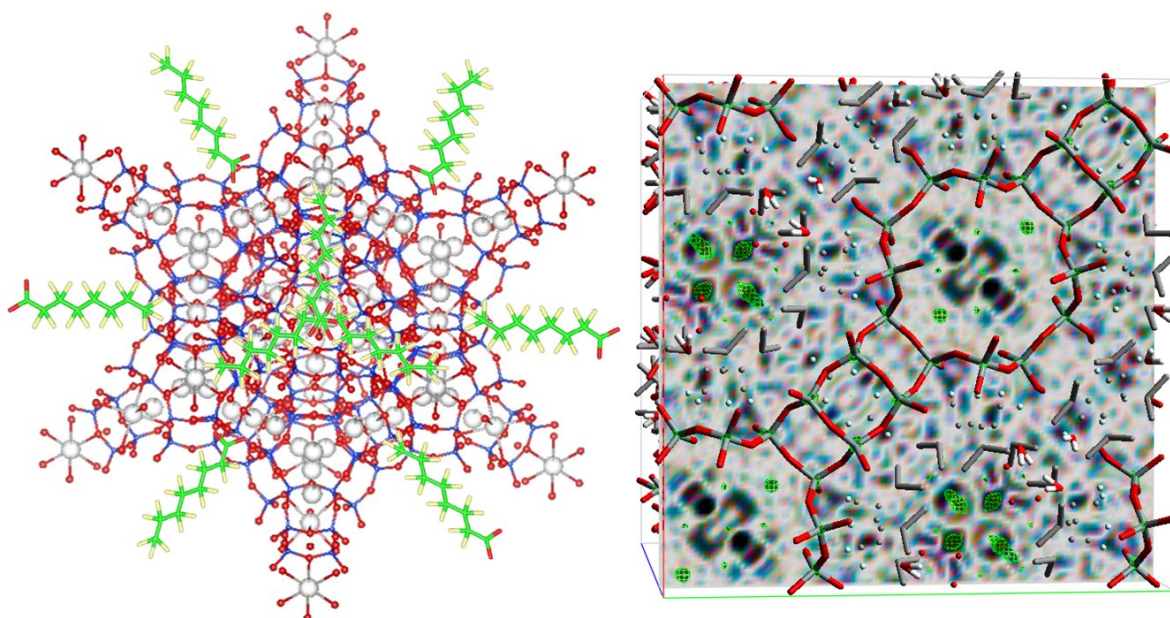


Figure 6.6.6 Interaction between PFOA and an AgY zeolite

The Ag(I') cations migrate towards Ag(I) site, located in the center of the hexagonal prism, closely surrounded by six oxygens (O3) of the two bases of the hexagonal prism. At the same time, Ag(IIb) is coordinated with three water molecules at w3 site, and these last are hydrogen bonded to water in w1 thus forming Ag-PFAS/PFOS oligomers interact strongly with the framework oxygens thus immobilizing the pollutants in the zeolite microporosities. The presence of these oligomers with weak changes of their intermolecular distances can explain why the channel systems of all investigated

systems are affected by structural distortion in the O4–O4 direction of the 12-ring channel.

#### **6.6.4 Conclusions**

This work aims to highlight the adsorption capacity of commercial high silica zeolites for the removal of PFAS from water. All high silica Y zeolites investigated are characterized by a good adsorption capacity and fast kinetics, suggesting that they can be efficiently used as a sorbent media towards PFOA and PFOS in water matrices. In particular, Y390 is the most efficient in the removal of PFAS, and shows higher saturation capacity than Y720 and Y760 zeolites. An increase of saturation capacity occurred when Y zeolites were exchanged with Ag<sup>+</sup> ions. Characterization of framework–extraframework bond distances after Ag-exchange, indicates a progressive variation in intensity and position, suggesting the entering of Ag<sup>+</sup> ions inside the microstructural porosities.

In all structural refinements, PFOS and PFOA molecules are arranged at the center of the supercage of the zeolite. In each case the uptake of PFOA onto all zeolites is higher than PFOS, probably due to the steric hindrance of the sulfonic group. The higher dimension of sulfonic substituent could be responsible for the lower adsorption of PFOS onto zeolites.

## 6.6.5 References

- [1] Matthias Van den Bergh, Andraž Krajnc, Stefan Voorspoels, Sergio Rodrigues Tavares, Steven Mullens, Prof. Isabelle Beurroies, Prof. Guillaume Maurin, Gregor Mali, Prof. Dirk E. De Vos Highly Selective Removal of Perfluorinated Contaminants by Adsorption on All-Silica Zeolite Beta *Angew. Chem. Int. Ed.* 2020, 59, 14086–14090
- [2] I. Braschi S. Blasioli E. Buscaroli D. Montecchio A. Martucci Physicochemical regeneration of high silica zeolite Y used to clean-up water polluted with sulfonamide antibiotics *J. of Environ. Sci.* 43 (2016) 302–12.
- [3] Elena Sarti, Tatiana Chenet, Claudia Stevanin, Valentina Costa, Alberto Cavazzini, Martina Catani, Annalisa Martucci, Nicola Precisvalle, Giada Beltrami and Luisa Pasti. High-Silica Zeolites as Sorbent Media for Adsorption and Pre-Concentration of Pharmaceuticals in Aqueous Solutions. *Molecules*, 2020, 25, 3331.
- [4] Sonia Blasioli, Annalisa Martucci, Geo Paul, Lara Gigli, Maurizio Cossi, Cliff T. Johnston, Leonardo Marchese, Ilaria Braschi. Removal of sulfamethoxazole sulfonamide antibiotic from water by high silica zeolites: A study of the involved host–guest interactions by a combined structural, spectroscopic, and computational approach. *Journal of Colloid and Interface Science*, 2014, 419.
- [5] Valeria Ochoa-Herrera Reyes Sierra-Alvarez. Removal of perfluorinated surfactants by sorption onto granular activated carbon, zeolite and sludge *Chemosphere*, 2008, 72, 1588–1593.
- [6] A.C. Larson and R.B. Von Dreele. General Structure Analysis System (GSAS), Los Alamos National Laboratory Report LAUR, 2004, 86-748
- [7] B.H. Toby EXPGUI, a graphical user interface for GSAS *J. Appl. Cryst.*, 2001, 34, 210-213
- [8] Nick D. Hutson, Ralph T. Yang. Structural effects on adsorption of atmospheric gases in mixed Li, Ag–X-zeolite *AIChE Journal*, 2021, Volume 46, Issue 11, 2305-2317
- [9] A. Altomare, C. Cuocci, C. Giacovazzo, A. Moliterni, R. Rizzi, N. Corriero, A. Falcicchio EXPO2013: a kit of tools for phasing crystal structures from powder data *J. Appl. Crystallogr.*, 46 (2013), pp. 1231-1235

## **6.7 Characterization and activity of Aqueous Extracts from *Asparagus officinalis* L. Byproducts**

The data herein reported are part of my work of thesis and have been published in: Arianna Romani, Fabio Casciano, Claudia Stevanin, Annalisa Maietti, Paola Tedeschi, Paola Secchiero, Nicola Marchetti and Rebecca Voltan (2021) Anticancer Activity of Aqueous Extracts from *Asparagus officinalis* L. Byproduct on Breast Cancer Cells. *Molecules* 26, 6369.

Cultivation of asparagus (*Asparagus officinalis* L.; Asp) for food and medicinal use has taken place since the early Roman Empire. Today, Asp represents a worldwide diffuse perennial crop. Lower portions of the spears represent a food industry waste product that can be used to extract bioactive molecules. In this study, aqueous extracts derived from the non-edible portion of the plant (hard stem) were prepared and characterized for chemical content. Furthermore, the biocompatibility and bioactivity of Asp aqueous extracts were assessed in vitro on normal fibroblasts and on breast cancer cell lines. Results showed no interference with fibroblast viability, while a remarkable cytostatic concentration-dependent activity, with significant G1/S cell cycle arrest, was specifically observed in breast cancer cells without apoptosis induction. Asp extracts were also shown to significantly inhibit cell migration. Further analyses showed that Asp extracts were characterized by specific pro-oxidant activity against tumoral cells, and, importantly, that their combination with menadione resulted in a significant enhancement of oxidants production with respect to menadione alone in breast cancer cells but not in normal cells. This selectivity of action on tumoral cells, together with the easiness of their preparation, makes the aqueous Asp extracts very attractive for further investigation in breast cancer research, particularly to investigate their role as possible co-adjuvant agents of clinical drug therapies.

### **6.7.1 Introduction**

Breast cancer (BC) is the most common cancer among women [1]. It is classified mainly based on the expression of three receptors that determine its pharmacological response and, therefore, severity: estrogen receptor (ER), progesterone receptor (PgR), and

epidermal growth factor receptor 2 (HER2). The majority of cases are hormone-dependent, showing overexpression of ER and PgR [2]. In those patients, endocrine-based treatment is used as a first-line treatment; however, after its initial efficacy, about 50% of patients develop endocrine resistance and treatment failure, requiring different choices or use of combined therapy [3]. Triple-negative breast cancers (TNBC; ER-, PgR-, HER2-), on the other hand, account for 10–15% of cases and still do not have efficient treatment. Since TNBC show an unfavorable prognosis and hormone-dependent BC has a 5-year survival rate of 25%, it is important to find an efficient and relatively safe cure to improve patients' survival [4]. Increasing attention in novel drug research has been focused on natural products as a source of compounds that exhibit few adverse effects [5,6]. One of the most common vegetables reported with therapeutic proprieties is asparagus, a plant nutritionally and commercially important belonging to the Asparagaceae family. Worldwide, more than 200 species have been identified [7], and among them, *Asparagus officinalis* L. (Asp) is the main species cultivated and commercialized [8]. The 2019 survey by FAO (<http://www.fao.org/faostat/en/#data>, on 5 October 2021 ) evidenced that asparagus cultivation is distributed worldwide, even if only six countries demonstrate major production: China (over 8 million tons); Peru (367,000 tons); Mexico (272,000 tons); Germany (131,000 tons); Spain (59,000 tons); Italy (50,000 tons). Italy has the largest yield in Europe and holds third place globally (7 tons per hectare), while the top yield globally belongs to Peru (11.5 tons per hectare). In Italy, asparagus production is focused only on five regions, with nearly 10,000 hectares cultivated (CSO Italy, Centro Servizi Ortofrutticoli, <https://www.csoservizi.com/focus-prodotti/asparagi/>, on 5 October 2021) by large agri-food farms. Hence, it is promptly understandable that potential solutions facing the recovery of bioactive molecules with asparagus waste material (i.e., hard stems, roots, plant aerial parts) might have a great impact on this agri-food chain. Different factors, including species, type of cultivation, seasons, or plant section used greatly change the content of the active biological molecules extracted [9]. Previous studies, focused mainly on the stem portion, have identified phenolic compounds, saponins, sterols, sulfur-containing acid, carotenoid, and amino acids as the main bioactive components [10]. Components such as flavonoids and carotenoids are well known for their antioxidant activity; others, such as saponins, have been reported to possess cell cycle modulatory

activity in cancer cells [11]. Lately, asparagus methanol extracts from *Asparagus laricus* have been reported to induce cytotoxicity in breast and prostate cancer cell lines [12]. More recently, Asp has become of interest for the possibility to extract bioactive molecules from non-edible portions [13]. Indeed, besides edible stems used in industrial processing, hard stems and roots, which are normally discarded, have been suggested to be used to extract phytochemicals with biological activities [7,14]. Recycling food industry byproducts will be beneficial from both economic and ecological points of view. Therefore, the present study first had the purpose of characterizing the chemical composition of hard stem Asp extracts prepared by a simple aqueous method that does not alter the structure nor the biological activity of important functional molecules. Then, the next aim of the study was to investigate in vitro the biological effects of the water extracts on survival and proliferation, oxidative balance and migration of BC cell lines belonging to different phenotypes, as well as in a normal cell line. The simple procedure to obtain water extracts of Asp hard stem, its chemical composition and its bioactivity on breast cancer cell lines represent the most innovative key-points of this study.

## **6.7.2 Results**

### **6.7.2.1 Asparagus Extraction**

Asparagus matrix has a moisture content of about  $89.9\% \pm 0.1\%$  w/w, as estimated by freeze-drying. The yield of water extraction was  $7.25\% \pm 0.23\%$  w/w. The estimation of total phenolic content (TPC), total flavonoid content (TFC) and antioxidant activity (DPPH and ABTS) for aqueous extract are reported in Table 6.7.1. TPC value evidenced a moderate amount of phenols extracted in Asp hard stem, confirmed also by low levels of antioxidant activity. As a matter of fact, the water extract contains 3.6% of phenolic compounds and 4% of flavonoids that constitute the hard stem matrix. It seems, therefore, that the aqueous extract is made of similar relative amounts of TPC and TFC than those available in ASP hard stem for extraction. Interestingly, flavonoids represent about 92.3% of water-extracted phenolic compounds, while in the hard stem, their relative amount is 83.8% of total phenolics on a dry matter basis. Thus, since phenolic compounds and flavonoids are water-extracted to the same extent (3.6% and 4%, respectively), and the relative amount of flavonoids is about 8.5% higher in dry water



extracts than in dry hard stems, this can be interpreted in two ways: the dry water extract contains a slightly larger representative fraction of flavonoids than ASP hard stem matrix; or part of the waterextracted phenolics are lost during the lyophilization process and the relative amount of flavonoids results a bit higher.

**Table 6.7.1.** Values of total phenolic content (TPC), total flavonoid content (TFC) and antioxidant activities (DPPH and ABTS) in water extracts from asparagus hard stem byproducts. Values are expressed in terms of gallic acid equivalents (GAE) and Trolox equivalents (TE) per mg of dry extract (mg<sub>de</sub>).

TPC ( $\mu\text{g}_{\text{GAE}}/\text{mg}_{\text{de}}$ )	10.09 $\pm$ 1.23
TFC ( $\mu\text{g}_{\text{GAE}}/\text{mg}_{\text{de}}$ )	9.31 $\pm$ 0.74
DPPH ( $\mu\text{mol}_{\text{TE}}/\text{mg}_{\text{de}}$ )	0.010 $\pm$ 0.006
ABTS ( $\mu\text{mol}_{\text{TE}}/\text{mg}_{\text{de}}$ )	0.017 $\pm$ 0.006

## 6.7.2.2 LC-MS/MS Analysis of Asparagus Extracts

### 6.7.2.2.1 Free Amino Acid Profile

Proteins and peptides in the hard stem represent about 1.85% w/w on a fresh matter basis and exhibit antioxidant and ACE inhibitory properties, as already evidenced recently [15]. Here, we mainly focused on the free aminoacidic profile. Single amino acid concentrations are reported in Table 6.7.2. Ion transitions (i.e., MRM (m/z) column) allowed us to correctly identify all amino acids, except for leucine (LEU) and Isoleucine (ILE). These two were quantified together. The total amount of free amino acids in the hard stem is noticeably higher (i.e., 45  $\mu\text{g}/\text{mg}_{\text{de}}$ ) than in the edible stem (i.e., 32.7  $\mu\text{g}/\text{mg}_{\text{de}}$ ) (data not published). The most abundant free amino acids in the hard stem are lysine (56.3%) and asparagine (30.3%). Proline, alanine, valine and glutamic acid are in the range 1–3%. Arginine, aspartic acid, histidine, leucine and isoleucine, methionine, phenylalanine, serine, threonine and tryptophan are in the range 0.1–0.9%, while only tyrosine is below 0.1%. Tryptophane is about 35 times more concentrated in the hard stem than in the edible part of the stem, while histidine and arginine are only 1.9 and 1.5 times higher in the hard stem. Additionally, levels of lysine and asparagine are higher in the hard stem than in the whole edible stem and spear: even though they are still the most abundant amino acids in the edible part, lysine is about 1.4 times and asparagine is 1.7 times more abundant in the hard stem.

**Table 6.7.2.** Quantitative determination of free amino acids in asparagus hard stem byproducts.

Amino Acid	Concentration ( $\mu\text{g}/\text{mg}_{\text{de}}$ )	MRM ( $m/z$ )
ALA	$0.101 \pm 0.023$	90.2 $\rightarrow$ 44.2
ARG	$0.369 \pm 0.019$	175.1 $\rightarrow$ 70.1
ASN	$13.65 \pm 1.12$	133.1 $\rightarrow$ 74.1
ASP	$0.322 \pm 0.022$	134.1 $\rightarrow$ 74.1
GLU	$0.451 \pm 0.027$	148.2 $\rightarrow$ 84.2
HIS	$0.254 \pm 0.015$	156.1 $\rightarrow$ 110.2
LEU+ILE	$0.368 \pm 0.018$	132.1 $\rightarrow$ 86.1
LYS	$25.33 \pm 1.75$	147.1 $\rightarrow$ 84.1
MET	$0.069 \pm 0.004$	150.2 $\rightarrow$ 104.1
PHE	$0.117 \pm 0.012$	166.2 $\rightarrow$ 120.2
PRO	$1.434 \pm 0.068$	116.1 $\rightarrow$ 70.1
SER	$0.364 \pm 0.016$	106.1 $\rightarrow$ 60.1
THR	$0.253 \pm 0.011$	120.1 $\rightarrow$ 74.1
TRP	$0.144 \pm 0.009$	205.2 $\rightarrow$ 146.2
TYR	$0.039 \pm 0.007$	182.2 $\rightarrow$ 136.2
VAL	$0.814 \pm 0.034$	118.1 $\rightarrow$ 72.1

#### 6.7.2.2.2 Organic Acids, Phenolic Acids, Polyphenols and Derivatives

Few secondary metabolites were identified in water extracts. Their tentative LCMS/MS identification is reported in Table 6.7.3. Compounds are grouped based on their most intense ionization mode. The second column presents the precursor ion, while the third column contains all informative fragment ions useful for compound identification. Numbers in parenthesis are the ion relative intensity. The last column reports the relative abundance for each identified compound, calculated on the basis of peak area.

**Table 6.7.3.** Tentative LC-MS/MS identification of most abundant compounds in asparagus hard stem.

Compound	[M – H] <sup>-</sup> ( <i>m/z</i> )	MS/MS Fragments ( <i>m/z</i> )	Relative Abundance
Dicaffeoyltartaric acid	473	311 (100), 293 (80) 179 (5), 149 (3)	0.5%
Caftaric acid	311	149 (100), 179 (55), 135 (5)	6.7%
Caffeoylquinic acid	353	191 (100), 179 (5)	0.27%
Malic acid	133	115 (100)	48.8%
Myricetin-O-rhamnoside	463	316 (100), 317 (50), 271 (15)	0.40%
Quinic acid	191	111 (100), 173 (20)	38.0%
Feruloylquinic acid	367	191 (100), 173 (5)	0.04%
Quercetin	301	179 (100), 151 (75), 273 (15), 257 (10)	0.03%
Tricin-O-glucoside	491	476 (100), 329 (70), 328 (15), 314 (5)	0.2%
Isorhamnetin-O-glucuronide	491	315 (100), 255 (10), 151 (5)	0.02%
<b>[M + H]<sup>+</sup> (<i>m/z</i>)</b>			
Laricitrin-O-glucoside	495	333 (100)	0.04%
Syringetin	347	291 (100), 153 (50), 287 (20)	0.08%
Kaempferol	287	153 (100), 121 (50), 213 (20), 229 (5)	0.1%
Apigenin	271	153 (100), 229 (30), 225 (30), 119 (10)	0.3%
Rutin	611	303 (100), 465 (30)	2.4%
Genistein	271	153 (100), 215 (85), 243 (60), 149 (25)	0.2%
Prunetin	285	229 (100), 257 (60), 267 (30), 163 (25)	1.2%
<b>[M]<sup>+</sup> (<i>m/z</i>)</b>			
Petunidin-O-pentoside	449	317 (100)	0.4%
Malvidin-O-pentoside	463	331 (100)	0.3%

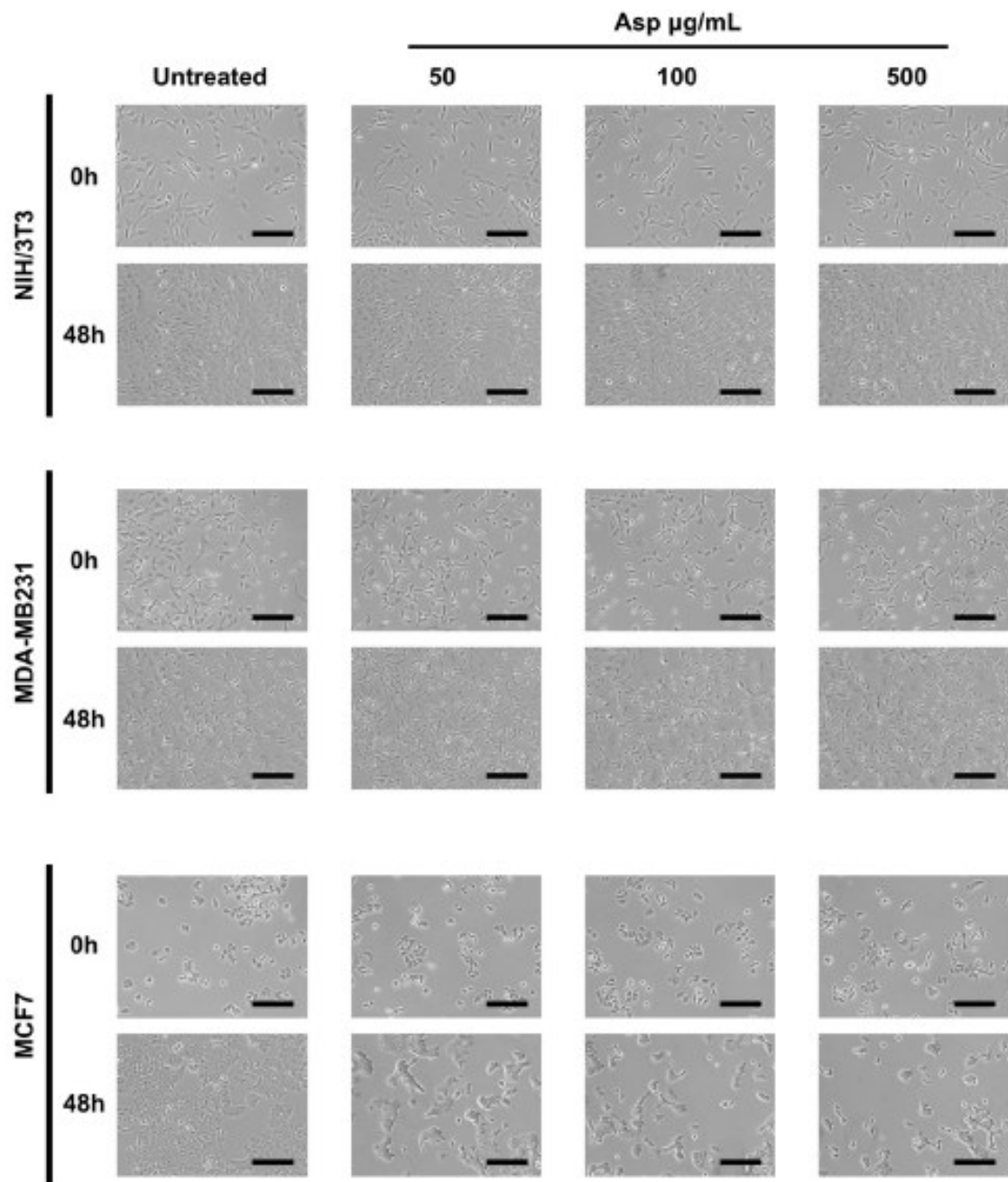
Among common organic acids (i.e., malic and quinic) and phenolic acid esters (i.e., dicaffeoyltartaric acid, caftaric acid, caffeoylquinic acid, feruloylquinic acid), important free aglycones were found: three flavonols (i.e., quercetin, kaempferol and syringetin), two isoflavones (i.e., genistein and prunetin) and one flavone (i.e., apigenin). Additionally, some common and less common glycosylated flavonoids were identified, such as myricetin-O-rhamnoside, triclin-O-glucoside, isorhamnetin-O-glucuronide, laricitrin-O-glucoside and rutin. Interestingly, two anthocyanins were identified (i.e., petunidin- and malvidin-O-pentoside derivatives) and listed separately as [M]<sup>+</sup>.

Both isoflavones and flavonols are known to play important bioactive roles as estrogens and antioxidants. Hence, alone or in synergy with all compounds identified in water extracts, they may have captivating effects on cancer cells. Compounds tentatively identified in Asp hard stem aqueous extracts are in accordance with literature works,

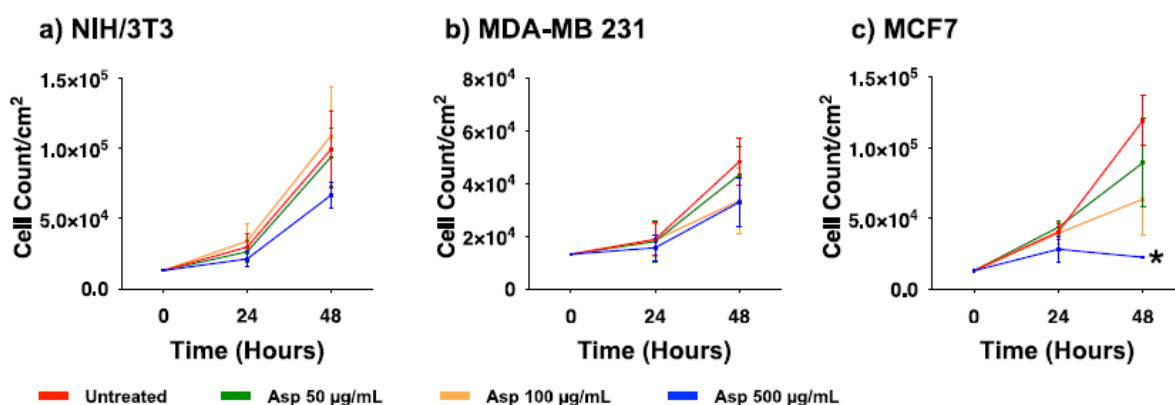
although most of them concerned more exhaustive hydroalcoholic extracts and most of the extensive chemical characterization regards the edible part [11,16–20].

### **6.7.2.2.3 Asparagus Extracts Affect Viability of MCF-7 Breast Cancer Cells through Cell Cycle Block**

To evaluate the biological effects of Asp extracts on cellular activities, cellular morphology, replication and apoptosis were assessed on NIH/3 T3 fibroblasts and breast cancer cell lines MDA-MB231 and MCF7, before and after treatments with several doses of Asp extracts. As shown in Figure 6.7.1, no changes in morphology and distribution were observed in NIH/3T3 as well as in MDA-MB231 cells until 48 h after treatments. However, a remarkable reduction in cell density coupled with cell size increase (typical of cellular senescence) was observed in MCF7 cells treated for 48 h with Asp with respect to the untreated. In agreement, as reported in the panels in Figure 6.7.2a,b, no significant changes in the number of viable cells were identified in NIH/3T3 and MDA-MB231 cells. On the contrary, a significant reduction in the number of viable cells was identified in the MCF7 cell line treated with 500 µg/mL Asp extracts for 48 h, compared with untreated cells maintained in culture in the same condition (Figure 6.7.2c; p-value 0.0434).



**Figure 6.7.1.** Representative images were taken by light microscopy of NIH/3T3, MDA-MB231 and MCF7 cells untreated or treated with 50, 100, and 500  $\mu\text{g/mL}$  of Asparagus extracts (Asp) for 48 h. Magnification 10x, scale bar 200  $\mu\text{m}$ .



**Figure 6.7.2.** Cell viability of (a) NIH/3T3, (b) MDA-MB231, (c) MCF7 exposed to 50, 100, and 500 µg/mL of Asp for 24 and 48 h. Data are reported as mean  $\pm$  standard error of the mean from three independent experiments. Statistical analysis was performed by ANOVA followed by Bonferroni's post hoc test. \*  $p \leq 0.05$  vs. untreated at the same incubation time.

Next, we investigated whether induction of apoptosis was responsible for the observed effects on cell viability. As reported in Figure 6.7.3, there were no significant differences between treated and untreated samples for all three cell lines, analyzing early and late apoptotic events, as well as necrotic events. Only for the MCF7 cell line, an increasing trend was observed for late apoptotic population in response to increasing concentrations of extracts, even if it was not significant with respect to the untreated control.

To further investigate the possible implication of Asp extracts on cell proliferation, the cell cycle was analyzed by flow cytometry upon BrdU incorporation. In agreement with cell viability results, Asp treatment on NIH/3T3 and MDA-MB-231 cells did not modify the cell cycle phase distribution either after 24 h or 48 h of treatment (Figure 6.7.4). By contrast, in MCF7 cells, Asp (500 µg/mL) induced a relevant contraction of the number of cells in S phase already after 24 h, when compared with untreated ( $p$ -value = 0.0169). Extending the treatment to 48 h, the alteration of cell cycle phases was more marked, showing a concentration-dependent effect with a significant reduction in cells in the S phase (100 µg/mL vs. untreated,  $p$ -value = 0.0469; 500 µg/mL vs. untreated,  $p$ -value = 0.0016; Asp 50 µg/mL vs. Asp 500 µg/mL,  $p$ -value = 0.0205), accumulation in G1 (500 µg/mL vs. untreated,  $p$ -value = 0.0169) and consequent induction of cell cycle blockade.

#### 6.7.2.2.4. Asparagus Extracts Cause ROS Production in Breast Cancer Cells but Not in Normal Cells

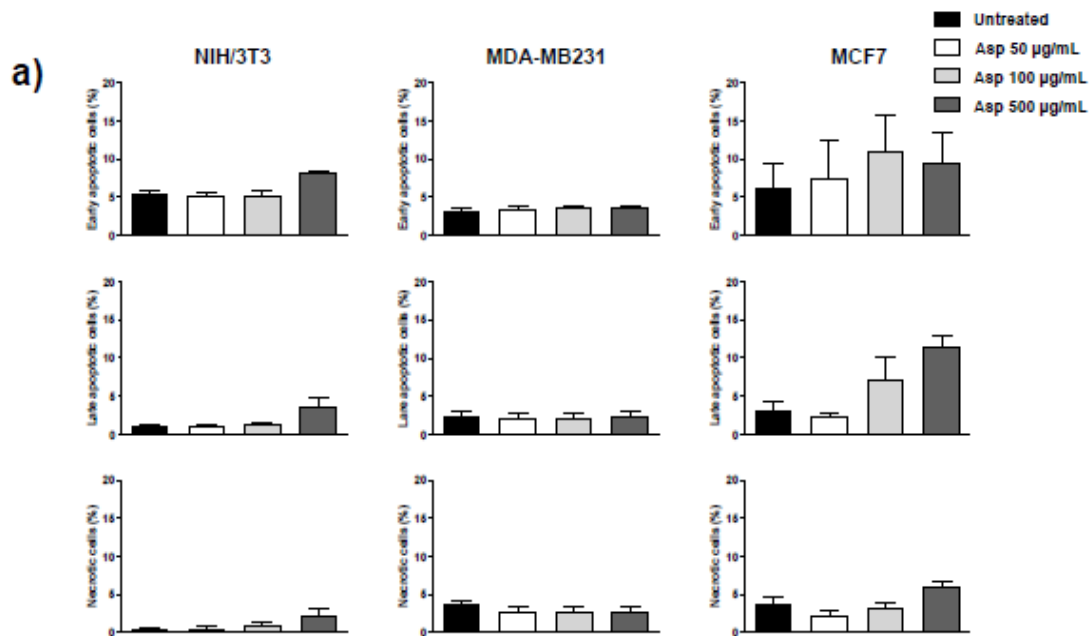
To further study the biological effects of Asp extracts in normal (NIH/3T3) and tumoral (MCF7) cell lines, a possible role of Asp in modulating the production of oxidants upon

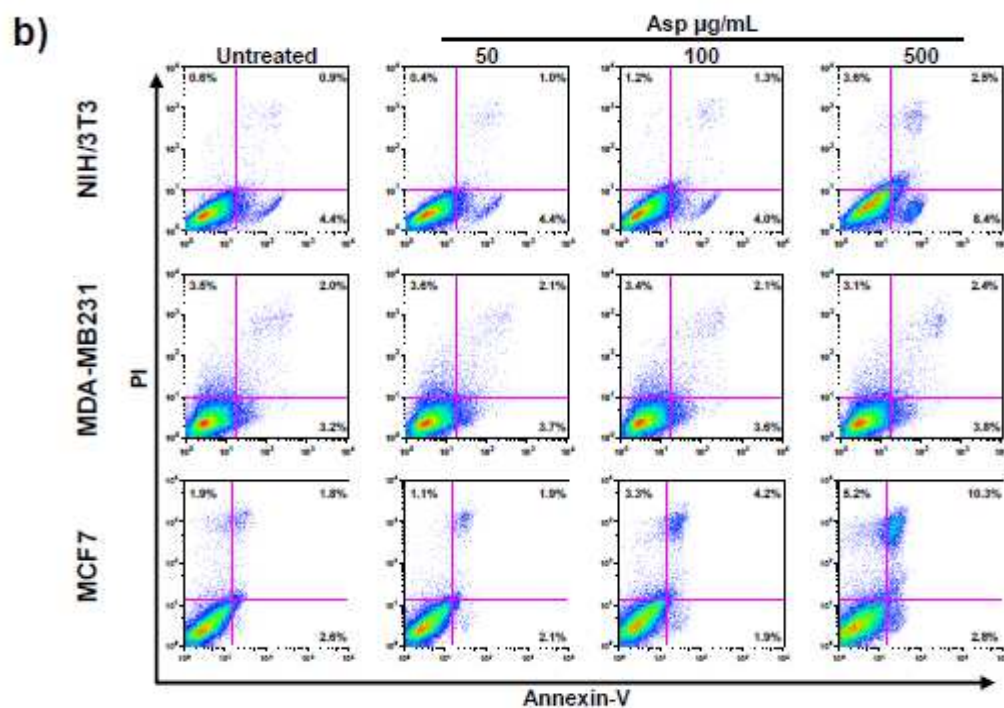
treatment was assessed by a method that enables the flow cytometric detection of reactive oxygen species (ROS) in live cells (CellROX Green Flow Cytometry Assay).

As depicted in Figure 6.7.5, following exposure to several Asp concentrations, normal cells did not significantly change their ROS level, while a significant increase in the production of oxidant species was observed in breast cancer MCF7 cells treated with 500 µg/mL of Asp for 48 h, with respect to the untreated sample (Asp 0 µg/mL) (p-value = 0.0126).

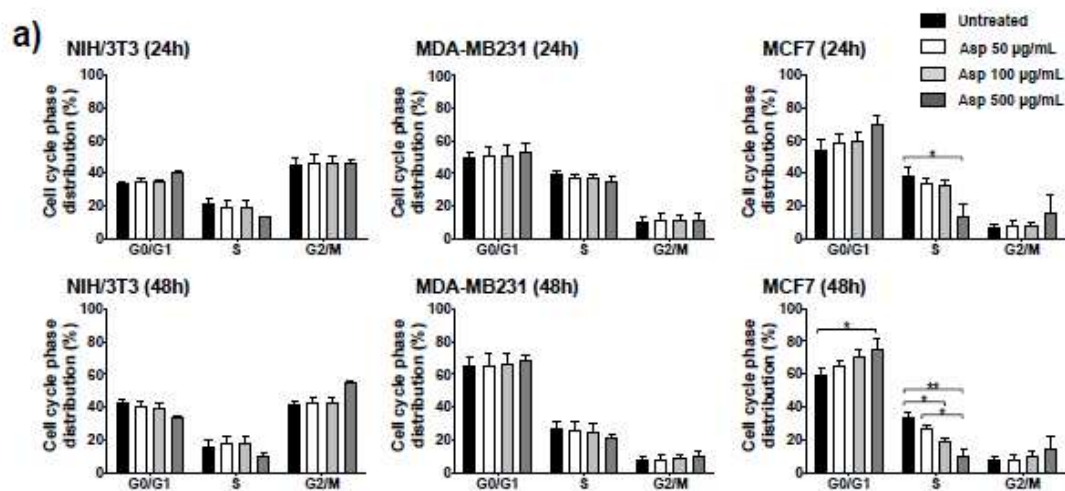
#### 6.7.2.2..5. Asparagus Extracts Increase Oxidant Activity of Menadione in Breast Cancer Cells

In order to investigate the role of Asp extracts on oxidative balance, both normal (NIH/3T3) as well as tumoral cells (MCF7) were exposed to Asp and then triggered with a pro-oxidant concentration of menadione (Figure 6.7.6). Asp 50 µg/mL was chosen as the pre-treatment dose to exclude concomitant effects derived from an alteration in viability or cell cycle modulation.

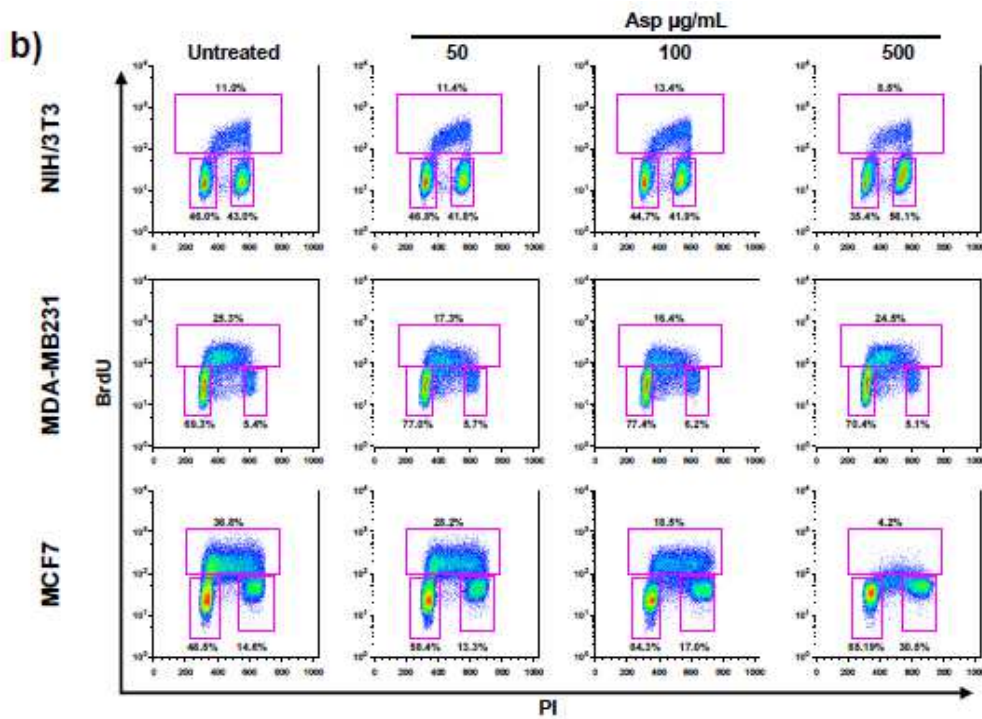




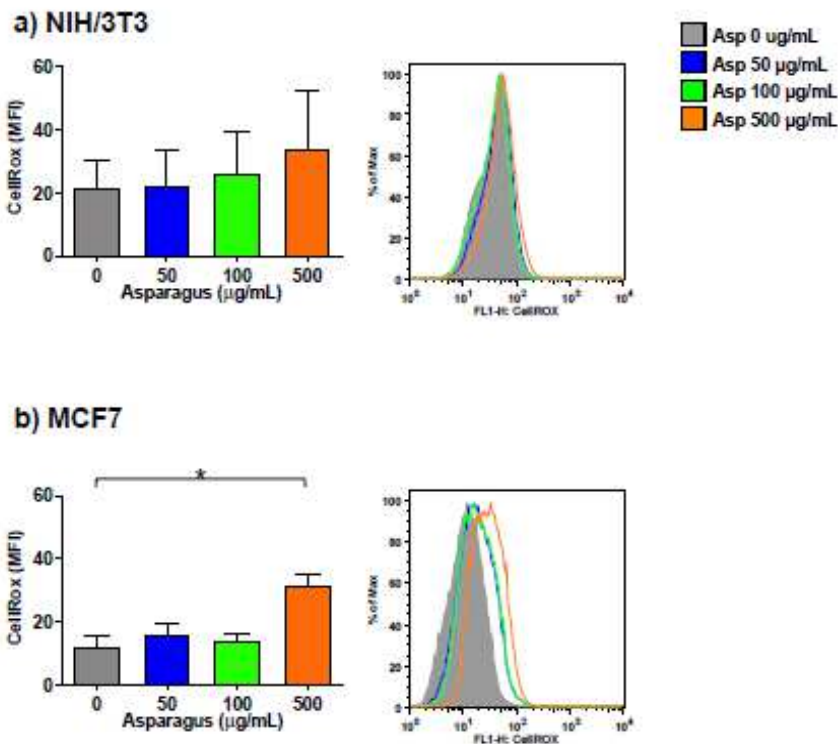
**Figure 6.7.3.** NIH/3T3; MDA-MB231; MCF7 percentage of apoptotic cells after 48 h, calculated from the flow cytometry dot plots after Annexin V/PI staining. (a) Results from untreated or treated with 50, 100, and 500  $\mu\text{g/mL}$  Asp extracts were expressed as a percentage of the total population. Data are reported as mean  $\pm$  standard error from three independent experiments. (b) Representative flow cytometry dot plots. The axis scales for fluorescence are reported as logarithmic.







**Figure 6.7.4.** NIH/3T3; MDA-MB231; MCF7 cell distribution in the different phases of the cell cycle calculated from the flow cytometry dot plots after BrdU/PI staining of cultures after 24 or 48 h. (a) Results from cells untreated or treated with 50,100, and 500 µg/mL of Asp extracts were expressed as a percentage of the total population. Data are reported as mean ± standard error from three independent experiments. Statistical analysis was performed by ANOVA followed by Bonferroni's post hoc test.  $p$ -values ≤ 0.05 were considered significant: \*  $p$  ≤ 0.05, \*\*  $p$  ≤ 0.01; (b) Representative flow cytometry dot plots of cell cycle profiles after 48 h of treatments. The PI axes scale is reported as linear and the BrdU axes scale is reported as logarithmic.

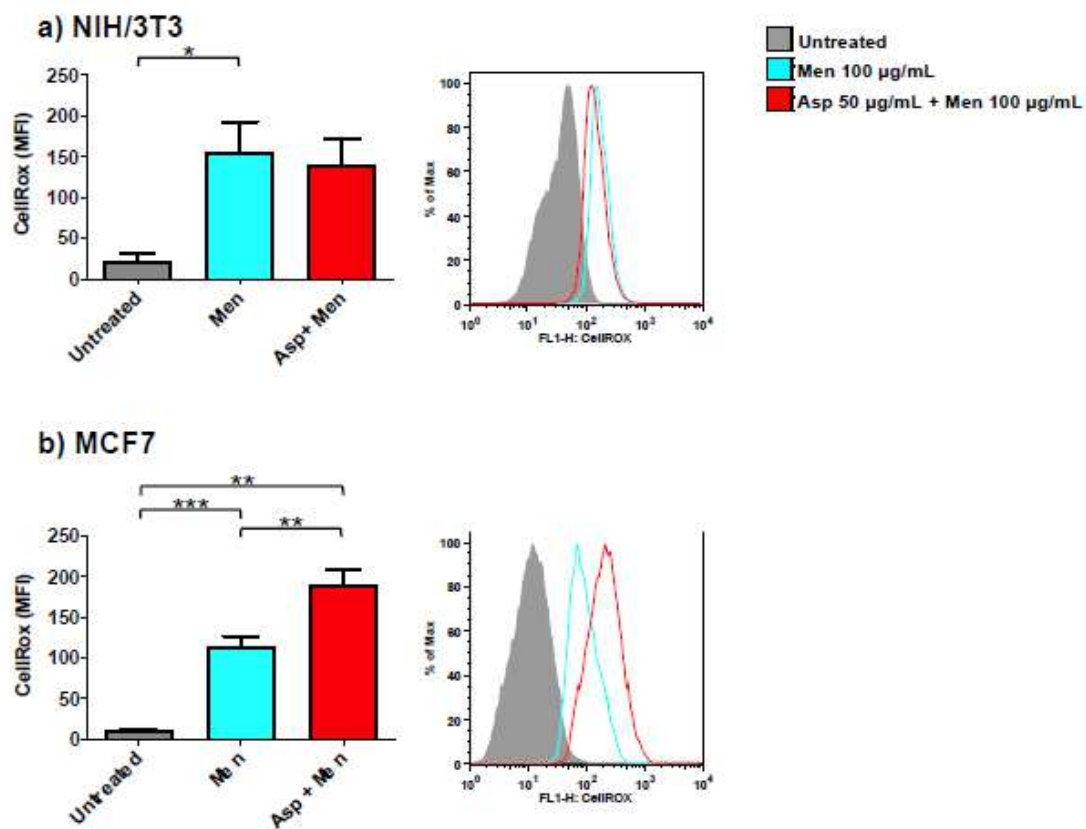


**Figure 6.7.5.** NIH-3T3 (a) or MCF7 (b) cells were treated with 0, 50, 100 or 500 µg/mL of Asp extracts for 48 h and incubated with CellROX Green Reagent to investigate the oxidation level (stress) of the cells. Left panels: MFI data are reported as mean ± standard error of results from three independent experiments; right panels: super imposed graphs from flow cytometry dot plots data of a representative experiment. The axes scale for fluorescence is reported as logarithmic. Statistical analyses were performed by ANOVA followed by Bonferroni's post hoc test. \*  $p < 0.05$ .

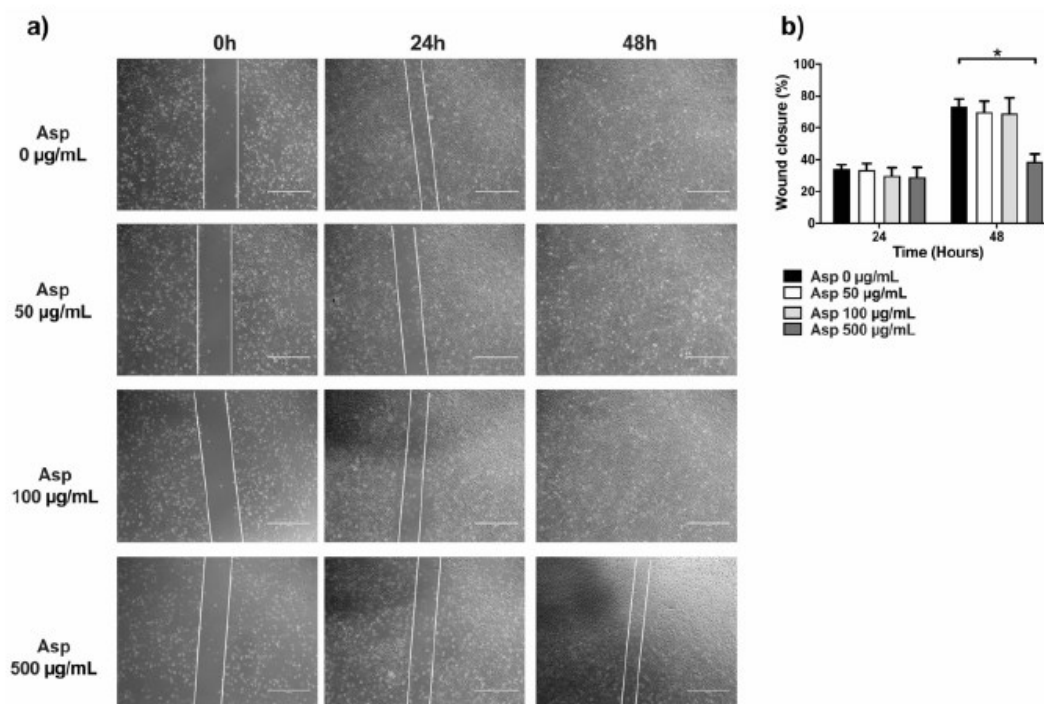
As expected, cells treated only with Menadione (positive control) showed a significant increase in oxidation production compared to untreated cells (p-value 0.0425 and p-value < 0.0001 for NIH/3T3 and MCF7, respectively). Interestingly, cells pre-treated with Asp extracts showed an opposite response in normal and cancerous cells when triggered with Menadione. Indeed, in fibroblasts (Fig. 6.7.6a) Asp did not induce a significant variation with respect to Menadione; however, in MCF7 cells (Fig. 6.7.6b), a combination of Asp and menadione significantly enhanced oxidation production compared to cells treated with Menadione alone (p-value =0.0038).

#### **6.7.2.2.6. Asparagus Extracts Impair Cell Migration**

To complete the characterization of biological activities of Asp on cells, we first assessed effects on migration by using traditional wound repair. A single scratch was manually performed on NIH/3T3 cells grown with a reduced concentration of serum (5% FBS) to lower interference from normal cell replication. Cells were treated with Asp at different doses and pictures were taken at different time points until 48 h of incubation (Figure 6.7.7). At 24 h, no significant variation in wound area was found, although a significant reduction in wound closure was observed in fibroblasts treated with 500 µg/mL of Asp compared with untreated cells (Asp 0 µg/mL) after 48 h of treatment (p-value = 0.0103).

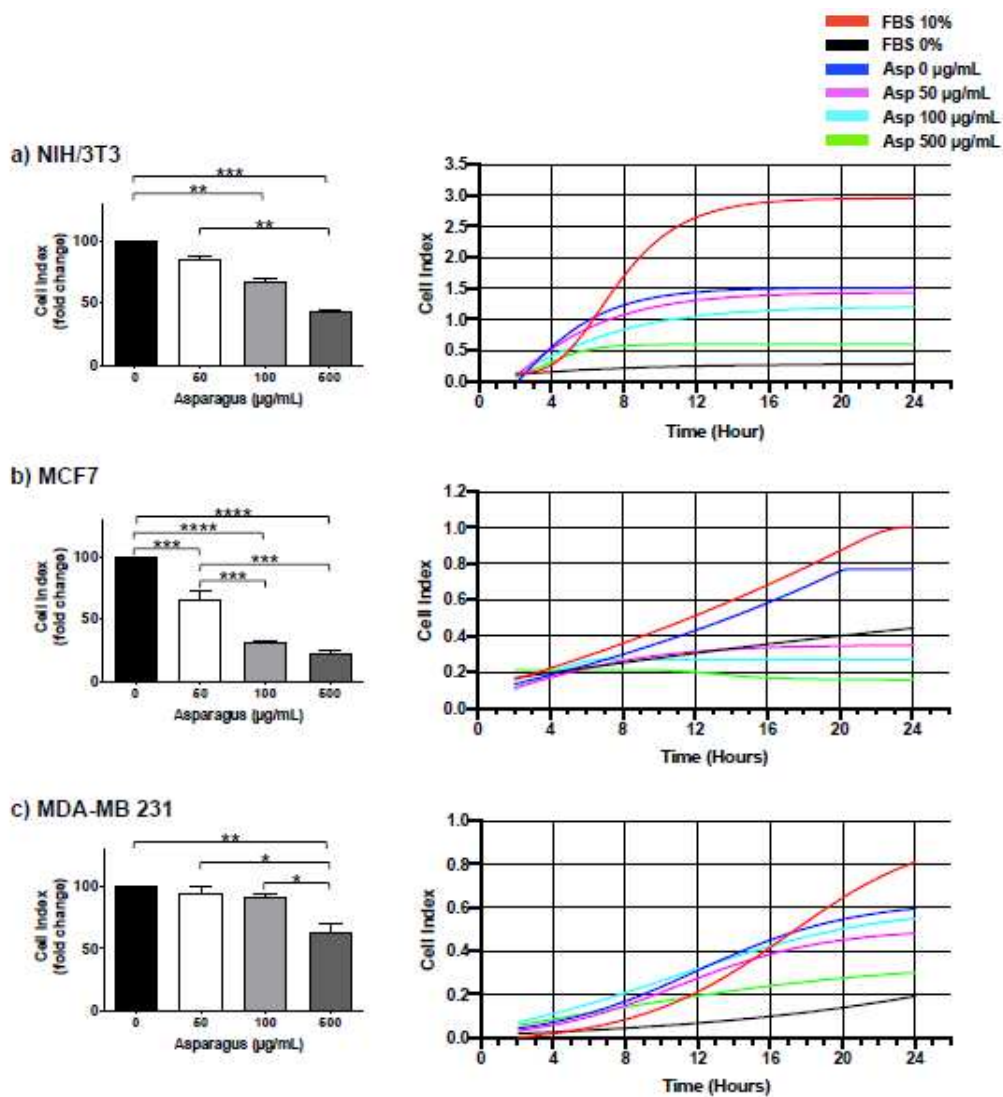


**Figure 6.7.6.** NIH/3T3 (a) or MCF7 (b) were treated with 50  $\mu\text{g}/\text{mL}$  Asp for 48 h and then triggered with oxidative stimulation performed by Menadione (Men) 100  $\mu\text{M}$  for 30 min. The left panels reported data as mean  $\pm$  standard error of results from at least three independent experiments. Right panels: representative flow cytometry dot plots. The axes scale for fluorescence is reported as logarithmic. Statistical analysis was performed by ANOVA followed by Bonferroni post hoc test; \*  $p < 0.05$ , \*\*  $p < 0.01$  and \*\*\*  $p < 0.001$ .



**Figure 6.7.7.** Scratch assay performed on fibroblasts (NIH/3T3). (a) Representative images were taken under light microscopy of fibroblast monolayers untreated or treated with 50, 100, and 500  $\mu\text{g}/\text{mL}$  of asparagus (Asp) at 0 h (immediately after scratch were performed), 24 or 48 h. Scale bar 1000  $\mu\text{m}$ . (b) Data from four independent experiments are reported as mean  $\pm$  standard error. Statistical analyses were performed by ANOVA followed by Bonferroni's post hoc test. \*  $p < 0.05$ .

To deeply investigate the role of Asp extracts in cell motility, dynamic high-resolution assessments of migration using the xCELLigence assay were performed on both normal and breast cancer cells. Results showed a significant inhibitory effect on cell migration mediated by Asp extracts, with respect to untreated, in all cell line tested (Figure 8). In detail, a significant reduction in NIH/3T3 cell migration was observed in response to 100 and 500  $\mu\text{g}/\text{mL}$  ( $p$ -value 0.0068 and  $\leq 0.0001$ , respectively), confirming data from wound repair. Importantly, MCF7 cell lines showed a significant reduction in migration in a concentration-dependent manner ( $p$ -value  $\leq 0.0001$  for all dosed vs. untreated;  $p$ -value  $\leq 0.001$  for 100  $\mu\text{g}/\text{mL}$  and 500  $\mu\text{g}/\text{mL}$  vs. 50  $\mu\text{g}/\text{mL}$ ), reducing the migration of this cell line below the basal threshold (0% FBS). Of note, migration was also significantly impaired in triple-negative MDA-MB231 cells after treatment with Asp 500  $\mu\text{g}/\text{mL}$  ( $p$ -value 0.0038 vs. untreated;  $p$ -value 0.0115 vs. Asp 50  $\mu\text{g}/\text{mL}$ ;  $p$ -value 0.0162 vs. Asp 100  $\mu\text{g}/\text{mL}$ ).



**Figure 6.7.8.** NIH-3T3 (a), MCF7 (b) and MDA-MB231 (c) cells were seeded in the upper chamber of CIM plate and monitored for migration through the lower chamber in response to different concentrations of Asp (0–500 µg/mL) with the xCelligence system (DP-RTCA) for 24 h. Positive controls were performed by using medium with 10% FBS in the lower chamber as the chemoattractant, while negative controls were performed by using medium without FBS (0% FBS). In the left panels, data are expressed as fold change compared to untreated cells of results from three independent experiments and are reported as mean ± standard error. Statistical analysis was performed by ANOVA followed by Bonferroni's post hoc test. p-values ≤ 0.05 were considered significant: \* p ≤ 0.05, \*\* p ≤ 0.005, \*\*\* p ≤ 0.001 \*\*\*\* p ≤ 0.0001. Right panels show representative graphs from RTCA software reporting overtime cell index.

### 6.7.3 Discussion

In recent years, increasing attention has been paid to sustainable recycling of food waste, mainly focusing on recovering bioactive molecules. This might represent a new source for drug production [21], especially for fields such as cancer where drug resistance or side effects still cause treatment interruption or failure. In the present study, we characterized the chemical composition and biological activities of hard stem asparagus aqueous extracts obtained from food industry waste recycling.

The chemical composition analyses revealed the absence of many antioxidants that were frequently found on edible stems of asparagus. However, the presence of

isoflavones, flavonols and flavones together with other glycosylated flavonoids might result in an effective pool of molecules with bioactivity on breast cancer cells. In particular, a relevant feature is represented by the presence of two isoflavones (i.e., prunetin and genistein) and one flavone (i.e., apigenin), counting all three together for the 1.7% relative amount in the extracts. It is known that these compounds might exert some antiestrogenic activity on estrogen-receptor- $\alpha$  positive tumor cells, such as MCF7. Indeed, we demonstrated in vitro, on cellular models of breast cancer with different phenotypes, specific anticancer effects, mainly attributable to cell cycle arrest, migration inhibition and oxidant production.

Firstly, we observed a significant reduction in the proliferation rate of the MCF7 breast cancer cell line (expressing HR+/HER2- phenotype), associated with a significant blockade of the cell cycle and low levels of apoptosis. This evidence is in accordance with other reports demonstrating cell cycle arrest in different cancer cell types following treatment with asparagus extracts [11,12]. However, studies are difficult to compare, since they use different raw materials and different methods for the extraction. We believe that the antiproliferative effect of Asp extracts on these cells might be the final result due to the combined effects of antiestrogenic phytochemicals and other antioxidants, mainly rutin, which is the most abundant flavonoid (i.e., 2.4%). Undoubtedly, the copresence of different components with activities connected to antitumor effects (i.e., anti-inflammatory), together with the antioxidant one (see rutin), might end up with particularly efficacious bioactivity against hormone-sensitive tumor cells. On the contrary, no direct involvement in these types of effects concerns the two organic acids (i.e., malic and quinic acids), which are the most abundant compounds in the extracts (i.e., 49% and 38%, respectively) and they are known to have antibacterial and anticholinesterase properties. Nonetheless, it is possible that malic and quinic acids can contribute somehow to the overall antioxidant property of the extract, as well as kaempferol and the other glycosylated flavonoids. Instead, three phenolic acids, such as caftaric (6.7%), dicaffeoyltartaric (0.5%) and caffeoylquinic (0.3%), can play a supportive role in affecting the tumor cell cycle and its response to other compounds.

Our results also indicated that any significant changes in proliferation, cell cycle and apoptosis were observed in MDA-MB-231 triple-negative cells (representative of a more aggressive phenotype of breast cancer), but not in NIH/3T3 noncancer cells.

Phytochemicals are commonly associated with beneficial effects, mainly for the presence of antioxidant molecules; however, the asparagus extracts used in our study, derived from the portion discarded from the food industry, were characterized by poor antioxidant content. This apparent defect translated into an advantage when we assessed the extracts on MCF7 tumoral cells. Indeed, in this model, we demonstrated a specific significant prooxidant activity of the extracts used alone at high dosage and, importantly, their capability at low dosage to enhance the level of ROS production induced by menadione. To explain this last feature, we can assume that the antioxidant molecules, even if present at low levels in the extracts, might be sufficient to induce redox amplification, cooperating in the ROS production prompted by menadione. This concept is supported by other authors that previously demonstrated an interaction between menadione and antioxidant molecules, resulting in increased oxidative stress in the same model—the MCF7 cells [22]. They reported apoptosis induction by ascorbate/menadione combination treatment, suggesting inhibition of ERK2 induced by H<sub>2</sub>O<sub>2</sub> generated from menadione redox cycling, with specific action on cancer cells. Our results similarly showed a specific cooperative effect on HR+/HER2- cells (MCF7), while preserving normal control fibroblasts. To further support our theory, it is of interest to cite Bakalova et al., who demonstrated that using menadione/ascorbate in combination with 13 conventional clinically used drugs for leukemia treatment did not induce cytotoxicity in cancer cells, but instead, caused irreversible metabolic changes, increasing sensitivity toward conventional therapy [23]. These observations are particularly important because they lay the foundations for future use of extracts to enhance the effects of clinically used drugs that act on breast cancer cells through the induction of oxidative stress, such as tamoxifen (used for hormonal therapy) or paclitaxel (used for chemotherapy). This aspect deserves further preclinical studies to evaluate its feasibility and effectiveness.

Next, we observed a significant inhibition of concentration-dependent migration of MCF7 cells and, surprisingly, even of the triple negative MDA-MB-231 cells. In particular, for MCF7, which showed a low degree of apoptosis after treatment with ASP, we exclude the role of cell death due to the intrinsic characteristics of the assay that allows seeding of the cells in the upper chamber, while the medium with treatment is placed only in the lower chamber. Inhibition of cell migration on MDA-MB-231 cell models has been described following treatments with traditional anticancer drugs (e.g., cisplatin) [24] and

purified molecules (e.g., curcumin) [25]. Interference with cellular migration represents a pivotal effect of the anticancer activity of the extracts, suggesting a possible role in inhibition of the metastatic process. A separate explanation is needed to interpret the data obtained on the migration of NIH/3T3 noncancer cells. In fact, these cells are fibroblasts and, as cells normally present in the connective tissue, in the case of tumors, they become part of the tumor microenvironment. Here, they are known to release substances that promote tumor proliferation [26]. In addition, they are also able to migrate to tumor implantation sites (or metastases) to support their growth through the induction of angiogenesis [27]. Therefore, inhibiting the migration of these cells, even if of the nontumor phenotype, has important implications in preventing the development of a tumor-friendly microenvironment. This is a preliminary study that will need more investigations to comprehend the molecular mechanisms involved in the observed biological effects, as well as to understand the efficacy of the combined use of Asp extracts with traditional drugs by using preclinical in vitro and in vivo models. Nonetheless, we believe that our results will open up new opportunities to use natural products, alone or combined with traditional treatment, to improve therapy for BC. In particular, observations reporting the inhibition of proliferation and menadione combined oxidant production in HR+ cells, as well as migration reduction in both HR+ and TNBC cells, seem to be particularly relevant for patients who develop drug resistance.

#### **6.7.4. Materials and Methods**

##### **6.7.4.1. Preparation of Asparagus Extracts, Phenolic Content, Total Flavonoids and Antioxidant Activity**

Asp hard stem samples employed in this study were from a farm located in the Province of Rovigo (Veneto Region, Italy). They were waste materials from greenhouse cultivation of Asp obtained when harvested spears are sorted and packed for the market. Aqueous extracts from lyophilized Asp hard stems were obtained by the following procedure, which has already been applied with modifications to other vegetable matrices [15,28–30]: ultraturrax (T18 model by IKA-Werke, Staufen, Germany) mechanical homogenization of 1 gram (dry matrix) in 25 mL of water (1:25 w/v) for 1 min; ultrasound bath (Elmasonic S 30 H, Elma Schmidbauer, Singen, Germany) for 10 min at 37 kHz (80 W effective ultrasonic power); suspension centrifuged at 10,000 g for 10 min (model



PK121R, Thermo Fisher Scientific, Waltham, MA, USA). Then, water supernatants were recovered, and the extract was lyophilized.

Phenolic content and antioxidant activity were determined by means of four different parameters: total phenolic compounds (TPC); total flavonoids (TFC); two Trolox equivalent antioxidant capacity (TEAC) assays based on DPPH and ABTS radicals. TPC and TFC are reported as  $\mu\text{g}$  of gallic acid equivalents per mg of dry extract ( $\mu\text{gGAE/mgde}$ ) and they were determined in accordance with Singleton [31] and the aluminum chloride colorimetric method [32,33], respectively. Results for DPPH and ABTS assays were calculated as  $\mu\text{mol}$  of Trolox equivalents per mg of dry extract ( $\mu\text{molTE/mgde}$ ).

These parameters were also estimated for hard stems (on dry basis) by using an overnight hydroalcoholic extraction (80:20 methanol:water + 0.1% v/v of formic acid) [25].

They were similarly expressed as  $\mu\text{gGAE/mgdm}$  and  $\mu\text{molTE/mgdm}$ , where mgdm means mg of dry matter (i.e., lyophilized ASP byproducts).

#### **6.7.4.2. LC-MS/MS Analysis of Asparagus Extracts**

##### **6.7.4.2.1. Free Amino Acid Profile**

Protein content and bioactive peptides in this byproduct matrix have already been investigated by the same authors [14]. Thus, here, we focused more on the determination of free amino acids. They were determined by external calibration method. Liquid chromatographic separation was obtained on a Restek Raptor Polar X column (100 \* 2.1 mm) packed with superficially porous particles (diameter 2.7  $\mu\text{m}$ ). The mobile phase was a mixture of water + formic acid 0.1% (v/v) (A) and acetonitrile + formic acid 0.1% (v/v) (B). Chromatographic runs were conducted under gradient elution conditions (from 25% to 70% of A in 10 min) at a mobile phase flow rate of 150  $\mu\text{L}/\text{min}$ . MS/MS detection was carried out under MRM mode (multiple reaction monitoring) with the positive ESI mode (see Section 2.2.1 for ion transitions and results).

##### **6.7.4.2.2. Organic Acids, Phenolic Acids, Polyphenols and Derivatives**

Untargeted LC-MS/MS analysis of phenolics was carried out by means of a 2.1 \* 150mm Symmetry C18 column (Waters, Milford, MA, USA), packed with 3.0 mm fully porous particles, thermostated at 30 °C, under gradient elution conditions. Mobile phases were

mixtures of water and formic acid 0.1% (v/v), channel A, and acetonitrile and formic acid 0.1% (v/v), channel B. The gradient elution was obtained with 5% to 70% channel B in 25 min. MS detection was achieved with a Thermo LTQ XL linear ion trap, equipped with an ESI interface (both positive and negative ionization modes were used).

#### **6.7.4.3. Cell Culture and Treatment**

Mouse embryo fibroblasts (NIH/3T3) and human breast cancer cell lines MDA-MB- 231 (TNBC) and MCF7 (ER+, HER2-) were purchased from Lonza (Basel, Switzerland) and grown in DMEM (4.5 g/L glucose) containing 10% FBS, 1% pen/step and L-glut (all from Life Technologies, Monza, Italy). Cells were maintained at 37 °C in a humidified atmosphere with 5% CO<sub>2</sub>. Doubling times of the three cell lines were determined by the calculator available at <http://www.doubling-time.com/compute.php> on 28 September 2021 (Roth V. 2006 Doubling Time Computing; NIH/3T3: 15 ± 1 h; MCF7: 15 ± 2 h; MDA-MB231: 22 ± 2 h). Lyophilized Asp extracts were dissolved in DMEM containing 1% FBS, 1% pen/strep, and L-glut, sterilized by filtration and used for in vitro treatment at predetermined concentrations of 50, 100, and 500 µg/mL for 24 and 48 h on NIH/3T3, MDA-MB231 and MCF7 cells seeded at the density of 25,000 cells/cm<sup>2</sup>. Cells were analyzed for cell shape and growth changes. Phase-contrast images were recorded with an EVOS digital microscope (Advanced Microscopy Group, Bothell, WA, USA). Recorded images were normalized for brightness with Fiji software [34].

#### **6.7.4.4. Assessment of Cell Viability, Cell Cycle Profile and Apoptosis**

Twenty-four and 48 hours after treatment with Asp extracts, cell viability was examined by Trypan blue exclusion dye. Cell cycle profiles were analyzed by 5-bromodeoxyuridine (BrdU; Sigma, St Louis, MO, USA) incorporation, as previously described [35]. Briefly, cells after incubation with 50 µM BrdU for 1 h at 37 °C were stained with primary mouse anti-BrdU antibody (clone 3D4, BD Bioscience, San José, CA, USA), goat F(ab')<sub>2</sub> antimouse IgG (H+L) fluorescein isothiocyanate-conjugated secondary antibody (Beckman Coulter, Brea, CA) and propidium iodide (PI; Sigma, St Louis, MO, USA), and were acquired using an FACS Calibur flow cytometer (BD Bioscience, San José, CA, USA) [36].

Apoptosis was analyzed in flow cytometry by Annexin V-FITC/propidium iodide (PI) staining (Immunotech, Marseille, France), as previously reported [36]. Flow cytometric acquisition was analyzed with the FlowJo software (Tree Star, Ashland, OR, USA).

#### **6.7.4.5. Analysis of ROS**

Changes in intracellular reactive oxygen species (ROS) levels were determined by cell-permeable CellRox® Green Oxidative Stress Reagent (Molecular Probes, Life Technologies) and analyzed using FACS Calibur flow cytometer. CellRox® is a nonfluorescent (or very weak fluorescent) dye in a reduced state, which is used for ROS measurement in live cells based on the strong fluorogenic signal developed after oxidation. Briefly, 50,000 NIH/3T3 or MCF7 cells were seeded on 24-well plates and grown for 24 h. The next day, the medium was removed, and cells were treated with 50 µg/mL of Asp extracts (diluted in fresh medium) for 48 h or left untreated as a negative control. As a positive ROS control, cells were treated with 100 µM Menadione (Sigma-Aldrich, St Louis, MO, USA) for 30 min. Cells were then stained with 2.5 µM CellRox® reagent for 30 min at 37 °C protected from light.

Cells were harvested by trypsinization, washed with PBS and centrifuged at 125xg for 5 min. In the end, cells were re-suspended in PBS with 0.5 µg/mL 7-AAD (BD Bioscience, San José, CA, USA) and analyzed by flow cytometry. Dead cells, positive for 7-AAD staining, were excluded from the analysis. Flow cytometric acquisition was analyzed with the FlowJo software (Tree Star, Ashland, OR, USA).

In some experiments, 100 µM menadione was added for 30 min to NIH/3T3 or MCF7 pretreated with 50 µM Asp for 48 h and then stained with 2.5 µM CellRox® reagent for 30 min at 37 °C protected from light. Flow cytometric acquisition was performed as reported above.

#### **4.6. Wound Healing Assay**

NIH-3T3 cells were seeded on a 6-well plate (13,000 cell/cm<sup>2</sup>) in DMEM, 5% FBS, 1% sodium pyruvate, 1% pen/strep and L-glut and left to grow for 24 h. A linear scratch was performed in the middle of each well using a p200 tip; then, the medium was removed and cells were washed twice with PBS before adding fresh media containing a predetermined concentration of 5% FBS and Asp extracts (0, 50, 100 or 500 µg/mL). Phase-contrast images were recorded with an EVOS digital microscope. Four frames for

each well were taken following the scratch length at different time points (immediately after the scratch was performed, after 24 and 48 h). For each well, analysis of the scratched area was performed by the Fiji software edge recognition tool and calculated by the following formula:

$$\text{Wound closure (\%)} = \left[ \frac{A_{t_0} - A_{\Delta t}}{A_{t_0}} \right] * 100$$

where  $A_{t_0}$  is the average of four frames measured immediately after scratching and  $A_{\Delta t}$  is the average of four frames measured after 24 or 48 h after scratching. Wound closure in cells treated with Asp extracts was compared with untreated cells at the same time point.

#### **6.7.4.7. Assessment of Cell Migration**

Cell migrations were performed using a DP-RTCA xCELLigence real-time cell analyzer (F. Hoffmann-La Roche SA, Basel, Switzerland) which records changes in impedance (reported as Cell Index) over time in a non-invasive system. Migration assay was performed using RTCA DP CIM-Plates 16. Cells were starved for 2 h with DMEM containing 0.2% FBS, 1% pen/strep, and L-glut and then seeded (40,000 cells/well) in the upper chamber in DMEM containing 1% FBS, 1% pen/strep, and L-glut. A 1% FBS concentration was experimentally established to support the length (24 h) of the experiments. Each condition was run in triplicate. Cells were left to equilibrate at RT for 30 min. Migration kinetics were analyzed in the presence of Asp (0, 50, 100, 500  $\mu\text{g}/\text{mL}$  in DMEM containing 1% FBS, 1% pen/strep, and L-glut) in the lower chamber and recorded every 15 min for 48 h. The positive control was performed using DMEM containing 10% FBS in the lower chamber as the chemoattractant. Data were analyzed using the RTCA software (F. Hoffmann-La Roche, version 1.2.1, Basel, Switzerland) and expressed as fold change  $\pm$  SEM of CI of migration with respect to untreated cultured set.

#### **6.7.4.8. Statistical Analysis**

All data, obtained from independent experiments, were tested for normal distribution by the Shapiro–Wilk normality test and for homogeneity of variance by the Brown–

Forsythe test. Results were evaluated by one-way ANOVA followed by Bonferroni post hoc test (from multiple corrections) using GraphPad Prism (GraphPad Software, San Diego, CA, USA). Results were expressed as mean  $\pm$  standard error of the mean (SEM) of replicate experiments. Statistical significance was defined as  $p < 0.05$ .

#### 6.7.5 References

- [1] Siegel, R.L.; Miller, K.D.; Jemal, A. Cancer Statistics. *CA Cancer J. Clin.* **2019**, *69*, 7–34.
- [2] Tagliaferri, B.; Quaquarini, E.; Palumbo, R.; Balletti, E.; Presti, D.; Malovini, A.; Agozzino, M.; Teragni, C.M.; Terzoni, A.; Bernardo, A.; et al. Role of Androgen Receptor Expression in Early Stage ER+/PgR $\square$ /HER2– Breast Cancer. *Ther. Adv. Med. Oncol.* **2020**, *12*, 1758835920958355.
- [3] Kwapisz, D. Cyclin-Dependent Kinase 4/6 Inhibitors in Breast Cancer: Palbociclib, Ribociclib, and Abemaciclib. *Breast Cancer Res. Treat.* **2017**, *166*, 41–54.
- [4] Presti, D.; Quaquarini, E. The PI3K/AKT/MTOR and CDK4/6 Pathways in Endocrine Resistant HR+/HER2 $\square$  Metastatic Breast Cancer: Biological Mechanisms and New Treatments. *Cancers* **2019**, *11*, 1242.
- [5] Almehdar, H.; Abdallah, H.M.; Osman, A.-M.M.; Abdel-Sattar, E.A. In Vitro Cytotoxic Screening of Selected Saudi Medicinal Plants. *J. Nat. Med.* **2012**, *66*, 406–412.
- [6] Sethi, G.; Shanmugam, M.; Warriar, S.; Merarchi, M.; Arfuso, F.; Kumar, A.; Bishayee, A. Pro-Apoptotic and Anti-Cancer Properties of Diosgenin: A Comprehensive and Critical Review. *Nutrients* **2018**, *10*, 645.
- [7] Chitrakar, B.; Zhang, M.; Adhikari, B. Asparagus (*Asparagus officinalis*): Processing Effect on Nutritional and Phytochemical Composition of Spear and Hard-Stem Byproducts. *Trends Food Sci. Technol.* **2019**, *93*, 1–11.
- [8] Adouni, K.; Chahdoura, H.; Mosbah, H.; Santos-Buelga, C.; González-Paramás, A.M.; Ciudad-Mulero, M.; Fernandes, Â.; Calhelha, R.C.; Morales, P.; Flamini, G.; et al. Revalorization of Wild *Asparagus stipularis* Forssk. as a Traditional Vegetable with Nutritional and Functional Properties. *Food Funct.* **2018**, *9*, 1578–1586.
- [9] Singh, R. *Asparagus racemosus*: A Review on Its Phytochemical and Therapeutic Potential. *Nat. Prod. Res.* **2016**, *30*, 1896–1908.
- [10] Rodríguez, R.; Jaramillo, S.; Rodríguez, G.; Espejo, J.A.; Guillén, R.; Fernández-Bolaños, J.; Heredia, A.; Jiménez, A. Antioxidant Activity of Ethanolic Extracts from Several *Asparagus* Cultivars. *J. Agric. Food Chem.* **2005**, *53*, 5212–5217.

- [11] Zhang, F.; Zhang, Y.-Y.; Sun, Y.-S.; Ma, R.-H.; Thakur, K.; Zhang, J.-G.; Wei, Z.-J. Asparanin A from *Asparagus officinalis* L. Induces G0/G1 Cell Cycle Arrest and Apoptosis in Human Endometrial Carcinoma Ishikawa Cells via Mitochondrial and PI3K/AKT Signaling Pathways. *J. Agric. Food Chem.* 2020, 68, 213–224.
- [12] Mfengwana, P.H.; Mashele, S.S.; Manduna, I.T. Cytotoxicity and Cell Cycle Analysis of *Asparagus Laricinus* Burch. and *Senecio Asperulus* DC. on Breast and Prostate Cancer Cell Lines. *Heliyon* 2019, 5, e01666.
- [13] Fuentes-Alventosa, J.M.; Jaramillo-Carmona, S.; Rodríguez-Gutiérrez, G.; Guillén-Bejarano, R.; Jiménez-Araujo, A.; Fernández-Bolaños, J.; Rodríguez-Arcos, R. Preparation of Bioactive Extracts from *Asparagus* By-Product. *Food Bioprod. Process.* 2013, 91, 74–82.
- [14] Montone, C.M.; Zenezini Chiozzi, R.; Marchetti, N.; Cerrato, A.; Antonelli, M.; Capriotti, A.L.; Cavaliere, C.; Piovesana, S.; Laganà, A. Peptidomic Approach for the Identification of Peptides with Potential Antioxidant and Anti-Hypertensive Effects Derived From *Asparagus* By-Products. *Molecules* 2019, 24, 3627.
- [15] Bergantin, C.; Maietti, A.; Tedeschi, P.; Font, G.; Manyes, L.; Marchetti, N. HPLC-UV/Vis-APCI-MS/MS Determination of Major Carotenoids and Their Bioaccessibility from “Delica” (*Cucurbita Maxima*) and “Violina” (*Cucurbita Moschata*) Pumpkins as Food Traceability Markers. *Molecules* 2018, 23, 2791.
- [16] Zhao, J.; Zhang, W.; Zhu, X.; Zhao, D.; Wang, K.; Wang, R.; Qu, W. The Aqueous Extract of *Asparagus officinalis* L. by-Product Exerts Hypoglycaemic Activity in Streptozotocin-Induced Diabetic Rats. *J. Sci. Food Agric.* 2011, 91, 2095–2099.
- [17] Fan, R.; Yuan, F.; Wang, N.; Gao, Y.; Huang, Y. Extraction and Analysis of Antioxidant Compounds from the Residues of *Asparagus officinalis* L. *J. Food Sci. Technol.* 2015, 52, 2690–2700.
- [18] Rodríguez, R.; Jaramillo, S.; Guillén, R.; Jiménez, A.; Fernández-Bolaños, J.; Heredia, A. Cell Wall Phenolics of White and Green *Asparagus*. *J. Sci. Food Agric.* 2005, 85, 971–978.
- [19] Fuentes-Alventosa, J.M.; Jaramillo-Carmona, S.; Rodríguez-Gutiérrez, G.; Rodríguez-Arcos, R.; Fernández-Bolaños, J.; Guillén-Bejarano, R.; Espejo-Calvo, J.A.; Jiménez-Araujo, A. Effect of the Extraction Method on Phytochemical Composition and Antioxidant Activity of High Dietary Fibre Powders Obtained from *Asparagus* By-Product. *Food Chem.* 2009, 116, 484–490.

- [20] Fuentes-Alventosa, J.M.; Rodríguez-Gutiérrez, G.; Jaramillo-Carmona, S.; Espejo-Calvo, J.A.; Rodríguez-Arcos, R.; Fernández-Bolaños, J.; Guillén-Bejarano, R.; Jiménez-Araujo, A. Effect of Extraction Method on Chemical Composition and Functional Characteristics of High Dietary Fibre Powders Obtained from Asparagus By-Products. *Food Chem.* 2009, 2, 665–671.
- [21] Kumar, K.; Yadav, A.N.; Kumar, V.; Vyas, P.; Dhaliwal, H.S. Food Waste: A Potential Bioresource for Extraction of Nutraceuticals and Bioactive Compounds. *Bioresour. Bioprocess.* 2017, 4, 18.
- [22] Beck, R.; Verrax, J.; Dejeans, N.; Taper, H.; Calderon, P.B. Menadione Reduction by Pharmacological Doses of Ascorbate Induces an Oxidative Stress That Kills Breast Cancer Cells. *Int. J. Toxicol.* 2009, 28, 33–42.
- [23] Bakalova, R.; Semkova, S.; Ivanova, D.; Zhelev, Z.; Miller, T.; Takeshima, T.; Shibata, S.; Lazarova, D.; Aoki, I.; Higashi, T. Selective Targeting of Cancerous Mitochondria and Suppression of Tumor Growth Using Redox-Active Treatment Adjuvant. *Oxid. Med. Cell. Longev.* 2020, 2020, e6212935.
- [24] Yang, M.-D.; Sun, Y.; Zhou, W.-J.; Xie, X.-Z.; Zhou, Q.-M.; Lu, Y.-Y.; Su, S.-B. Resveratrol Enhances Inhibition Effects of Cisplatin on Cell Migration and Invasion and Tumor Growth in Breast Cancer MDA-MB-231 Cell Models In Vivo and In Vitro. *Molecules* 2021, 26, 2204.
- [25]. Mukherjee, S.; Mazumdar, M.; Chakraborty, S.; Manna, A.; Saha, S.; Khan, P.; Bhattacharjee, P.; Guha, D.; Adhikary, A.; Mukherjee, S.; et al. Curcumin Inhibits Breast Cancer Stem Cell Migration by Amplifying the E-Cadherin/ $\beta$ -Catenin Negative Feedback Loop. *Stem Cell Res. Ther.* 2014, 5, 116.
- [26] Shiga, K.; Hara, M.; Nagasaki, T.; Sato, T.; Takahashi, H.; Takeyama, H. Cancer-Associated Fibroblasts: Their Characteristics and Their Roles in Tumor Growth. *Cancers* 2015, 7, 2443–2458.
- [27] Wan, X.; Guan, S.; Hou, Y.; Qin, Y.; Zeng, H.; Yang, L.; Qiao, Y.; Liu, S.; Li, Q.; Jin, T.; et al. FOSL2 Promotes VEGF-Independent Angiogenesis by Transcriptionally Activating Wnt5a in Breast Cancer-Associated Fibroblasts. *Theranostics* 2021, 11, 4975–4991.
- [28] Marchetti, N.; Bonetti, G.; Brandolini, V.; Cavazzini, A.; Maietti, A.; Meca, G.; Mañes, J. Stinging Nettle (*Urtica dioica* L.) as a Functional Food Additive in Egg Pasta:

- Enrichment and Bioaccessibility of Lutein and  $\beta$ -Carotene. *J. Funct. Foods* 2018, 47, 547–553.
- [29] Alonso-Garrido, M.; Tedeschi, P.; Maietti, A.; Font, G.; Marchetti, N.; Manyes, L. Mitochondrial Transcriptional Study of the Effect of Aflatoxins, Enniatins and Carotenoids in Vitro in a Blood Brain Barrier Model. *Food Chem. Toxicol.* 2020, 137, 111077.
- [30] Bergantin, C.; Maietti, A.; Cavazzini, A.; Pasti, L.; Tedeschi, P.; Brandolini, V.; Marchetti, N. Bioaccessibility and HPLC-MS/MS Chemical Characterization of Phenolic Antioxidants in Red Chicory (*Cichorium Intybus*). *J. Funct. Foods* 2017, 33, 94–102.
- [31] Singleton, V.L.; Orthofer, R.; Lamuela-Raventós, R.M. Analysis of Total Phenols and Other Oxidation Substrates and Antioxidants by Means of Folin-Ciocalteu Reagent. *Methods Enzymol.* 1999, 299, 152–178.
- [32] Miliuskas, G.; Venskutonis, R.P.; Beek, T.A. van Screening of Radical Scavenging Activity of Some Medicinal and Aromatic Plant Extracts. *Food Chem.* 2004, 85, 231–237.
- [33] Chang, C.; Yang, M.; Wen, H.; Chern, J. Estimation of Total Flavonoid Content in Propolis by Two Complementary Colometric Methods. *J. Food Drug Anal.* 2002, 10, 178–182.
- [34] Schindelin, J.; Arganda-Carreras, I.; Frise, E.; Kaynig, V.; Longair, M.; Pietzsch, T.; Preibisch, S.; Rueden, C.; Saalfeld, S.; Schmid, B.; et al. Fiji: An Open-Source Platform for Biological-Image Analysis. *Nat. Methods* 2012, 9, 676–682.
- [35] Trapella, C.; Rizzo, R.; Gallo, S.; Alogna, A.; Bortolotti, D.; Casciano, F.; Zauli, G.; Secchiero, P.; Voltan, R. HelixComplex Snail Mucus Exhibits Pro-Survival, Proliferative and pro-Migration Effects on Mammalian Fibroblasts. *Sci. Rep.* 2018, 8, 17665.
- [36] Voltan, R.; Rimondi, E.; Melloni, E.; Rigolin, G.M.; Casciano, F.; Arcidiacono, M.V.; Celeghini, C.; Cuneo, A.; Zauli, G.; Secchiero, P. Ibrutinib Synergizes with MDM-2 Inhibitors in Promoting Cytotoxicity in B Chronic Lymphocytic Leukemia. *Oncotarget* 2016, 7, 70623–70638.



## 7 Conclusions

In this work of thesis, different nanostructured adsorbent materials were employed for the removal of some classes of contaminants from aqueous solutions.

The study of the thermodynamics and the kinetics of the adsorption process of organic contaminants in aqueous solution onto zeolites provided the following results:

- ✓ The adsorption process is very fast for all the studied zeolites towards several classes of pollutants. Also, the adsorption kinetic of PFAS on microporous materials is satisfying if compared with literature data dealing with other types of adsorbents, with the equilibrium reached within 10 minutes.
- ✓ The adsorption capacities of zeolites depend on their structure, surface area and SAR. High adsorption capacities have been observed for zeolite Y and BEA, with respect of different organic compounds. ZSM-5 has generally lower adsorption capacity. However, ZSM-5 can be applied in water remediation since it is more efficient than Y in the removal of contaminants from very dilute solutions. Therefore, it can be used as adsorbent in finishing adsorption units, where the regulation limits of concentration of contaminants in the effluent are low.
- ✓ The zeolites with high silica/alumina ratio were tested as pre-concentration media in the dispersive-solid phase extraction procedure, extraction experiments led to high recoveries, especially for ketoprofen and hydrochlorothiazide with recoveries above 95% for KTP and HCT and approximately 85% for ATN. Among all zeolites, in general better adsorption performances were observed for zeolites with higher silica/alumina ratio.
- ✓ The zeolites exchanged with silver ions were also studied to obtain new adsorbent materials and determine the influence of this metal on the adsorption process. In all cases, zeolites showed fast kinetics and high saturation capacities towards the PFAS, higher than those of the starting materials. In each case, zeolites proved to be excellent adsorbent materials for the adsorption of organic contaminants of great concern from water matrices.
- ✓ Mixed matrix membranes, that are composed by a continuous polymer phase and a dispersed inorganic filler, were employed for the adsorption of PFAS from water matrix. Nanostructured carbon material (CM) has been included in several

formulations of hydrogels which differ in hydrophilicity, cross-linking and swelling. Kinetic studies showed that within 4 hours the kinetic equilibrium is reached for all the MMMs considered. In all cases, the addition of inorganic filler (CANAM) into polymeric matrix leads to higher saturation capacities, among the MMMs better adsorption performances were observed for the material with intermediate hydrophilicity and swelling (PEGDE\_Ethyl-PEONH<sub>2</sub> + 5% CANAM).

In this work of thesis, advanced oxidation processes were studied for the degradation of some pharmaceuticals, representing ubiquitous water contaminants of emerging concern.

- ✓ The ability of photocatalysts to oxidize water producing ·OH radicals, already observed in homogeneous conditions, is kept also when the materials are heterogenized on different supports.
- ✓ The entrapment of Na<sub>4</sub>W<sub>10</sub>O<sub>32</sub> and WO<sub>3</sub> inside porous matrices leads to a heterogeneous photocatalytic system with proper characteristics of hydrophobicity that is able to degrade pharmaceuticals (i.e. carbamazepine and sulfamethoxazole). The different hydrophobicity of the support employed favors adsorption of organic molecules, which enter into the pores. Here, their proximity to photoproducted ·OH radicals favors the degradation of contaminant.



The final part of this work of thesis includes a study about the bioactivity and biocompatibility of Asp aqueous extracts on normal fibroblasts and on breast cancer cell lines. The chemical composition analyses revealed the absence of many antioxidants that were frequently found on edible stems of asparagus. By in vitro tests it was observed a significant reduction in the proliferation rate of the MCF7 breast cancer cell line (expressing HR+/HER2- phenotype), associated with a significant blockade of the cell cycle and low levels of apoptosis. Results also indicated that any significant changes in proliferation, cell cycle and apoptosis were observed in MDA-MB-231 triple-negative cells (representative of a more aggressive phenotype of breast cancer), but not in NIH/3T3 noncancer cells.

## 8 Papers

- Elena Sarti, Tatiana Chenet, Claudia Stevanin, Valentina Costa, Alberto Cavazzini, Martina Catani, Annalisa Martucci, Nicola Precisvalle, Giada Beltrami and Luisa Pasti, “High-Silica Zeolites as Sorbent Media for Adsorption and Pre-Concentration of Pharmaceuticals in Aqueous Solutions”, *Molecules* 2020,25, 3331; doi:10.3390/molecules25153331
- Luisa Pasti, Elisa Rodeghero, Giada Beltrami, Matteo Ardit, Elena Sarti, Tatiana Chenet, Claudia Stevanin and Annalisa Martucci, “Insights into Adsorption of Chlorobenzene in High Silica MFI and FAU Zeolites Gained from Chromatographic and Diffractometric Techniques”, *Minerals* 2018,8,80 doi:10.3390/min8030080
- Luisa Pasti, Elena Sarti, Annalisa Martucci, Nicola Marchetti, Claudia Stevanin, and A. Molinari, “An advanced oxidation process by photoexcited heterogeneous sodium decatungstate for the degradation of drugs present in aqueous environment”, *Applied Catalysis B: Environmental*, vol.2390, pp.345-351, Dec.2018, doi:10.1016/j.apcatb.2018308.015
- Vito Cristino, Gelsomina Longobucco, Nicola Marchetti, Stefano Caramori, Carlo Albergo Bignozzi, Annalisa Martucci, Alessandra Molinari, Rita Boaretto, Claudia Stevanin, Roberto Argazzi, Maurizio Dal Colle, Renzo Bertoncetto, Luisa Pasti. “Photoelectrochemical degradation of pharmaceuticals at  $\beta$ 25 modified  $WO_3$  interfaces” *Catalysis Today*, Vol. 340 pp. 302-310, doi:10.1016/j.cattod.2018.09.020
- Arianna Romani, Fabio Casciano, Claudia Stevanin, Annalisa Maietti, Paola Tedeschi, Paola Secchiero, Nicola Marchetti, and Rebecca Voltan, “Anticancer Activity of Aqueous Extracts from *Asparagus officinalis* L. Byproduct on Breast Cancer Cells”, *Molecules* 2021, 26, 6369, <https://doi.org/10.3390/molecules26216369>

Article

# High-Silica Zeolites as Sorbent Media for Adsorption and Pre-Concentration of Pharmaceuticals in Aqueous Solutions

Elena Sarti <sup>1,\*</sup>, Tatiana Chenet <sup>1</sup>, Claudia Stevanin <sup>1</sup>, Valentina Costa <sup>1</sup> , Alberto Cavazzini <sup>1</sup>, Martina Catani <sup>1</sup>, Annalisa Martucci <sup>2</sup>, Nicola Precisvalle <sup>2</sup> , Giada Beltrami <sup>2</sup> and Luisa Pasti <sup>1</sup> 

<sup>1</sup> Department of Chemical and Pharmaceutical Sciences, University of Ferrara, Via Luigi Borsari 46, 44121 Ferrara, Italy; tatiana.chenet@unife.it (T.C.); claudia.stevanin@unife.it (C.S.); valentina.costa@unife.it (V.C.); alberto.cavazzini@unife.it (A.C.); martina.catani@unife.it (M.C.); luisa.pasti@unife.it (L.P.)

<sup>2</sup> Department of Physics and Earth Sciences, University of Ferrara, Via Giuseppe Saragat 1, 44122 Ferrara, Italy; annalisa.martucci@unife.it (A.M.); nicola.precisvalle@unife.it (N.P.); giada.beltrami@unife.it (G.B.)

\* Correspondence: elena.sarti@unife.it; Tel.: +39-0532-455189; Fax: +39-0532-455507

Academic Editor: Susana Valencia

Received: 23 June 2020; Accepted: 17 July 2020; Published: 22 July 2020



**Abstract:** The present work focused on the use of high-silica commercial zeolites as sorbent media for pharmaceuticals in an aqueous matrix. As drug probes, ketoprofen, hydrochlorothiazide, and atenolol were selected, because of their occurrence in surface waters and effluents from wastewater treatment plants. Pharmaceuticals adsorption was evaluated for two Faujasite topology zeolites with Silica/Alumina Ratio 30 and 200. The selected zeolites were demonstrated to be efficient sorbents towards all investigated pharmaceuticals, thanks to their high saturation capacities (from 12 to 32% w/w) and binding constants. These results were corroborated by thermal and structural analyses, which revealed that adsorption occurred inside zeolite's porosities, causing lattice modifications. Finally, zeolites have been tested as a pre-concentration media in the dispersive-solid phase extraction procedure. Recoveries higher than 95% were gained for ketoprofen and hydrochlorothiazide and approximately 85% for atenolol, at conditions that promoted the dissolution of the neutral solute into a phase mainly organic. The results were obtained by using a short contact time (5 min) and reduced volume of extraction (500  $\mu$ L), without halogenated solvents. These appealing features make the proposed procedure a cost and time saving method for sample enrichment as well as for the regeneration of exhausted sorbent, rather than the more energetically expensive thermal treatment.

**Keywords:** adsorption; emerging contaminants; pre-concentration; sorbent regeneration; zeolites

## 1. Introduction

The increasing use of pharmaceutical compounds in human and veterinary medicine has become an environmental problem, which received widespread attention from scientists over the past 20 years [1,2]. Hundreds of tonnes of pharmacologically active substances enter sewage treatment plants, where they are poorly removed. Consequently, they can enter into surface water collecting the plant effluents [3,4]. Indeed, the occurrence of pharmaceuticals in surface water and sediments has been extensively reviewed [5,6]. Likewise, "source-to-tap" studies concerning the fate of pharmaceuticals from wastewater to finished drinking water have been reported [7,8]. The concentrations measured in natural and drinking waters are very low, generally in the  $\text{ng L}^{-1}$  to  $\mu\text{g L}^{-1}$  [9,10], thus requiring accurate and sensitive methods for their detection. Likewise, to reduce the negative impact of pharmaceutical on biota and human health, new technologies should be investigated to improve the

efficiency of water treatment plants in the removal of drugs. Therefore, it is important on one hand to develop analytical methods able to detect these molecules at a low concentration level to better evaluate their impact on the environment and, on the other hand, to enhance the efficiency of water remediation technologies in order to reduce water contamination. Sorption based technologies were demonstrated to be efficient and economical methods both for the enrichment of trace pollutants as well as for their removal from water [11–13]. Among the wide variety of adsorbents, zeolites are very promising for environmental application thanks to their properties such as high surface area, controlled pore size, thermal and chemical stability. Recent studies demonstrated the efficiency of zeolites in the adsorption of several organic pollutants from water, such as pharmaceuticals [14,15], polycyclic aromatic hydrocarbons [16,17], and petrol-derived compounds such as toluene [18], methyl tert-butyl ether [19], chlorobenzene [20]. In addition, zeolites were also investigated as materials for the enrichment of organic compounds in dilute aqueous solutions. Dispersive solid-phase extraction is a promising sample pre-treatment technique, first introduced by Anastassiades et al. [21], which is based on the SPE methodology, but the sorbent is dispersed in a sample solution containing the target analytes instead of being immobilized inside a cartridge. This approach enables the sorbate to interact equally with all the sorbent particles and avoids channeling or blocking of cartridges or disks, as occurs in traditional SPE [22]. Other advantages with respect to the conventional SPE are the small sample volume required, reduced operational time, and high recoveries [23]. The dispersive-SPE has been successfully introduced for several analyses (i.e., pesticide residues in various matrices, antibiotics in animal tissues, pharmaceuticals in whole blood), with the purpose of sample clean-up and elimination of matrix interferences [24]. In the present work, the adsorptive properties of high-silica zeolites toward drugs in aqueous solutions were studied in order to investigate the efficiency of these siliceous materials in two applications, namely: (1) The removal of contaminants from the aqueous matrix, (2) the pre-concentration step for micropollutants analysis. An interesting future perspective of the present work could be the investigation of the possible reuse of zeolites after solvent extraction of sorbed analytes. Despite the fact that the thermal treatment usually requires high temperatures and long times, it still represents the most common regeneration technique of an exhausted adsorbent. It has been already demonstrated that exhausted zeolites maintain their adsorption efficiency after thermal regeneration [25,26]. Adsorbent regeneration by solvent extraction could be an attractive alternative to thermal treatment, because it is time-saving, requires less energy, and could permit the recovery of bioactive molecules from waste. Target pharmaceuticals were chosen based on their presence in effluents of wastewaters treatment plants and in surface waters [3,27,28]. In detail, the three investigated pharmaceuticals were ketoprofen (non-steroidal anti-inflammatory drug), hydrochlorothiazide (diuretic), and atenolol (beta-blocker), which are characterized by different physicochemical properties. As adsorbent media, commercial high-silica zeolites [29] (FAU and BEA framework type), differing in structure and surface properties, were considered. The release of sorbed pharmaceuticals from zeolites was evaluated by varying the pH and organic modifier of the extracting phase.

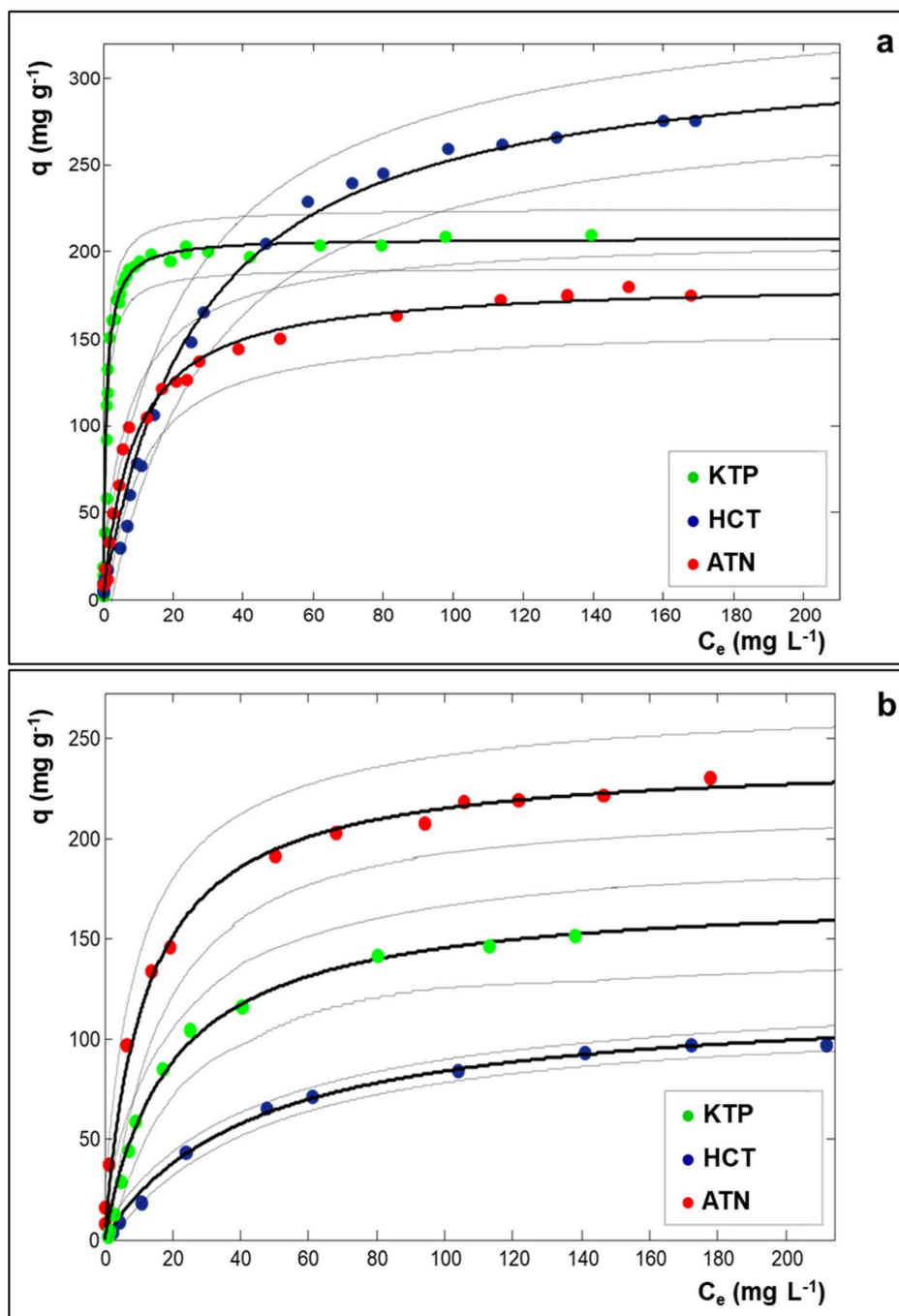
## 2. Results and Discussion

### 2.1. Adsorption

The adsorption of pharmaceuticals from the aqueous solution onto zeolites was evaluated in a wide concentration range and by fitting the experimental data with the proper mathematical model. In this case, good fits were obtained using Langmuir adsorption isotherm Equation (1) which has been already employed to investigate several organic molecule-zeolite systems [25,30,31]:

$$q = \frac{q_s b C_e}{1 + b C_e} \quad (1)$$

In Equation (1),  $q$  ( $\text{mg g}^{-1}$ ) is the adsorbed amount per unit weight of adsorbent,  $C_e$  ( $\text{mg L}^{-1}$ ) is the solute concentration at equilibrium,  $q_s$  is the saturation capacity ( $\text{mg g}^{-1}$ ) and  $b$  ( $\text{L mg}^{-1}$ ) is the Langmuir coefficient (binding constant). The adsorption isotherms of drugs adsorption on Y zeolites in Milli-Q water are shown in Figure 1 and the respective parameters estimated by non-linear fitting are reported in Table 1. Data concerning the drugs adsorption onto Beta25 are reported elsewhere [15].



**Figure 1.** Adsorption isotherms of ketoprofen (KTP: green symbols), hydrochlorothiazide (HCT: dark blue symbols), and atenolol (ATN: red symbols) on Y200 (a) and Y30 (b) in Milli-Q water. Dotted lines are the confidence limits at 95% of probability of the fitted curves.

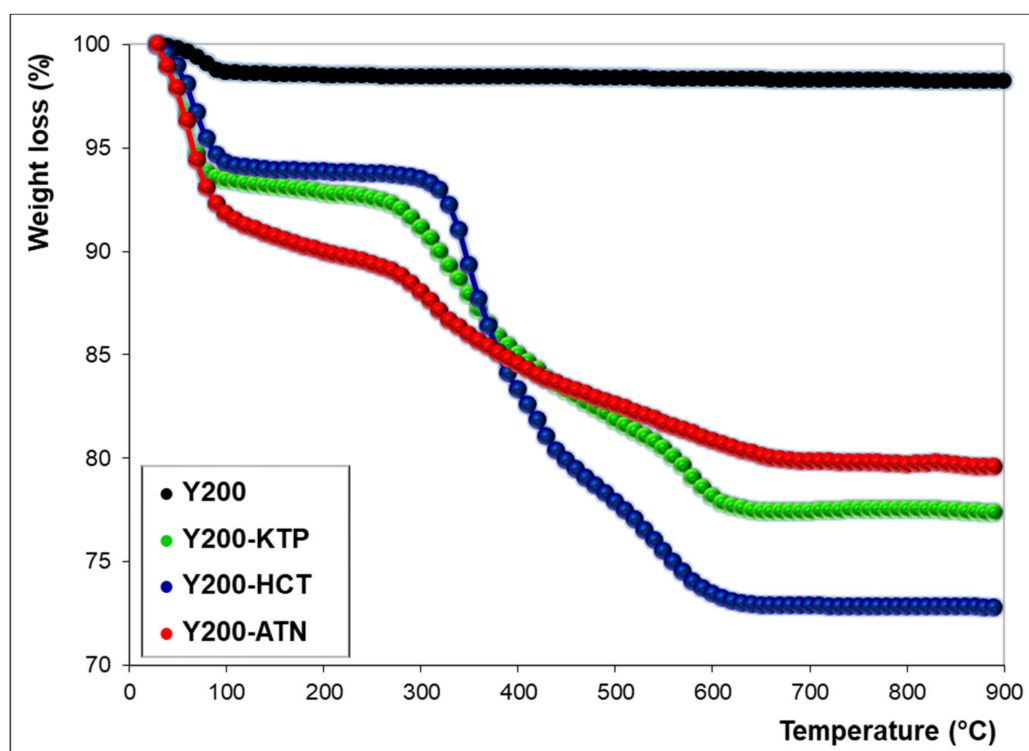
**Table 1.** Parameters Estimated by Non-Linear Fitting, According to the Langmuir Model, of Three Drugs Adsorption on Y200 and Y30. The Confidence Limits at 95% of Probability of Parameters are Reported in Brackets.

Drug-Zeolite	b (L mg <sup>-1</sup> )	q <sub>s</sub> (mg g <sup>-1</sup> )	R <sup>2</sup>
KTP-Y200	0.91 (0.76; 1.1)	208 (202; 214)	0.9887
HCT-Y200	0.037 (0.029; 0.044)	322 (302; 342)	0.9856
ATN-Y200	0.11 (0.082; 0.14)	183 (171; 195)	0.9737
KTP-Y30	0.052 (0.035; 0.069)	173 (148; 197)	0.9756
HCT-Y30	0.022 (0.018; 0.026)	121 (114; 128)	0.9957
ATN-Y30	0.084 (0.058; 0.11)	240 (223; 257)	0.9727

As can be seen in Table 1, both USY zeolites show high saturation capacities toward all the examined drugs. These data could be compared with saturation capacities approximately ranging from 20 to 100 mg g<sup>-1</sup> found by other studies for the adsorption of pharmaceuticals by different adsorbents, such as carbon black [32], granular or derivatized activated carbon [33,34], polymer clay composite [35]. In particular, by comparing the adsorptions on Y200, it can be noted that the highest saturation capacity (q<sub>s</sub>) was reached for HCT, but the isotherm slope (b), related to the adsorption constant, is the lowest one. At low concentrations, Y200 shows the greatest adsorption efficiency towards KTP. From the data of Table 1, it can also be observed that Y30 shows higher adsorption capacity and affinity for ATN than for the other pharmaceuticals. This last finding could be ascribed to electrostatic interactions between Y30, which is less hydrophobic than Y200, and ATN which is partially positively charged. By comparing the USY zeolites in terms of saturation capacities and binding constants (Table 1), the more hydrophobic Y200 generally demonstrated to offer higher efficiency than Y30, despite the lower surface area (see Table S1), thus confirming that the surface area is not exhaustive for predicting adsorption properties. In the light of above, further investigations were performed solely on Y200. In order to obtain more information on the adsorption process, thermal and diffractometric analyses were carried on. Thermogravimetric curves of Y200 before and after saturation with drugs are shown in Figure 2.

The TG curves of as-synthesized Y200 show a total weight loss of 1.7% at 900 °C. The thermal profile shows a sudden slope variation at a temperature below 100 °C, thus suggesting the presence of water molecules weakly bonded to the surface [14]. The TG curves of Y200 saturated with drugs display two main weight losses: The first one below 100 °C can be attributed to the desorption of species (water and/or drug) weakly retained on the zeolite surface, while the second one at temperatures above 100 °C can be ascribed to the decomposition of drug sorbed inside the zeolite porosities. According to the literature data [36–38], KTP and HCT present a stable profile until about 250 and 300 °C, respectively, while the ATN thermal decomposition starts at lower temperatures (120–150 °C).

Thermogravimetric curves of Y200 after saturation with ATN, HCT, and KTP show weight losses at 900 °C of 20.4%, 27.2%, and 22.6%, respectively. These results indicated that, at saturation conditions, the higher amount of sorbed drug was found for HCT, followed by KTP and ATN. The same trend can be observed by comparing the saturation capacities extrapolated from adsorption isotherms (see q<sub>s</sub> in Table 1). Differences in the amounts obtained from TG and isotherm data can derive from different factors, such as the contribution of co-adsorbed water molecules to TG results. In addition, saturation capacity is a limit value estimated from non-linear fitting of experimental data (see Figure 1) and it does not refer to a single adsorption measurement.

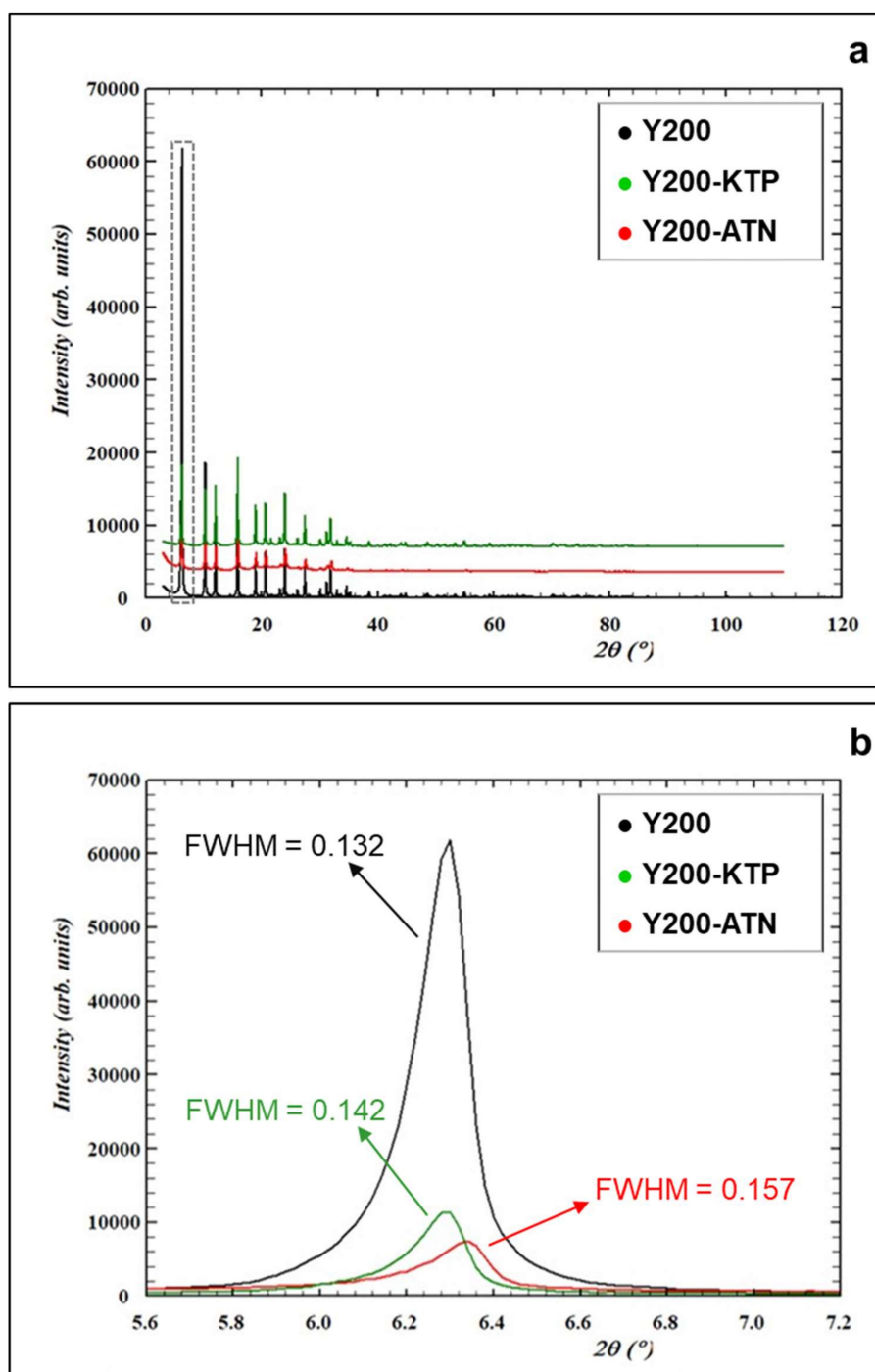


**Figure 2.** Thermogravimetric curves of Y200 before (black) and after drugs adsorption (KTP: Green, HCT: Blue, ATN: Red).

The Y200 dealuminated zeolite is characterized by the presence of both microporosity and macroporosity mainly due to the dealumination process [39]. Although drug adsorption can occur in both micro- and mesoporous structures, the deeply investigation of the adsorption site location lies beyond the aim of the present work. In order to have an experimental evidence of the effective incorporation of the drug inside the zeolite porosity and not only on the zeolite surface, a structural investigation was carried out. Figure 3 shows the results attained for Y200-KTP and Y200-ATN systems. Structural analyses carried out on Y200 saturated with HCT led to results similar to those obtained for KTP: For this reason, the diffractometric data of HCT have not been reported here.

The XRD diffraction patterns of Y200 before and after KTP and ATN adsorption showed changes in the entire  $2\theta$  range investigated (Figure 3a) and especially in the low  $2\theta$  region (Figure 3b). After drugs adsorption, the intensity of the (111) reflection decreased and the full width at half maximum (FWHM), reported in Figure 3b, increased, thus indicating changes in crystallinity of the original sample. At the same time, shifts in the peaks positions revealed unit cell parameters modifications (Table 2) whereas variations in their intensity suggested modifications induced by KTP and ATN adsorption, indicating that the molecules are effectively penetrated inside the structural microporosities of Y200.





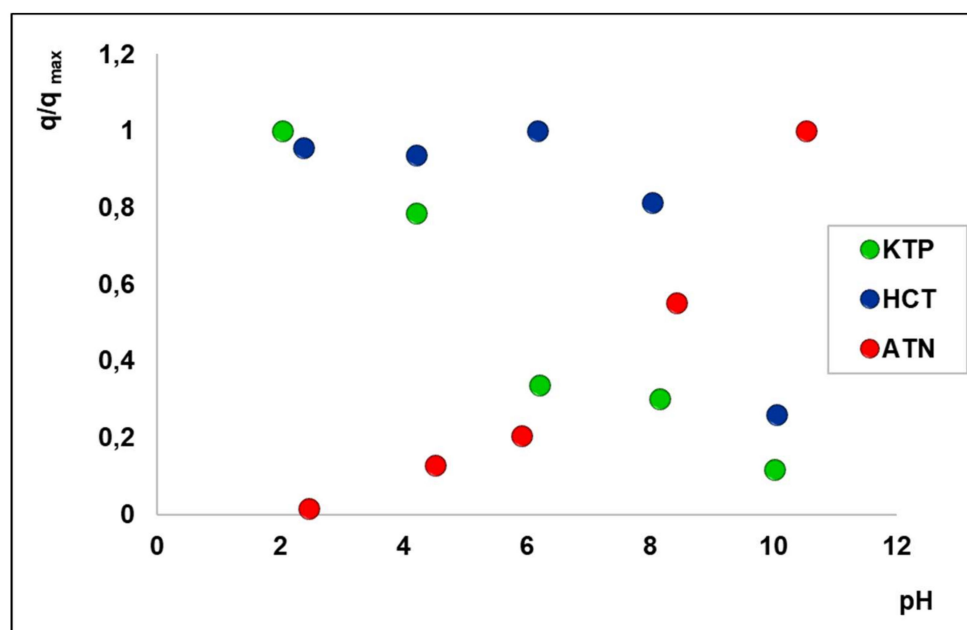
**Figure 3.** X-ray powders diffraction pattern in the entire  $2\theta$  range investigated (a) and in the low  $2\theta$  region (b) of as-synthesized Y200 (black), Y200 saturated with KTP (green), and ATN (red).

**Table 2.** Lattice Parameters for Y200 Before and After Pharmaceuticals Adsorption.

	Y200	Y200-KTP	Y200-ATN
Crystallite size (Å)	668.5	621.5	563.4
a = b = c (Å)	24.259(1)	24.255(1)	24.159(1)
V (Å <sup>3</sup> )	14,277.1(1)	14,269.1(1)	14,101.5(1)
O4-O4 (Å)	9.81	10.30	9.90
O1-O1 (Å)	9.70	9.63	9.58
C.F.A. (Å <sup>2</sup> )	39.07	41.43	38.90
Ellipticity (ε)	1.01	1.07	1.03

Considering the structural difference between the channels, the framework oxygens distances between the pores give important indications in determining the stability of a sorption site. A guest molecule on a stable sorption site favors those distances that minimize the van der Waals interaction potentials. This means that due to the host-guest interactions, the pore sizes of the channels are roughly the same, but the precise structures of the channels are quite different. The bond lengths and angles in the framework geometry and the diagonal O—O internuclear distances in the 12-ring channel (12MR) are listed in Table 2. The 12MR diameters, calculated from the Rietveld structure refinement, are indicated by O1-O1 and O4-O4 distances, treating the framework oxygen atoms as cold hard spheres with van der Waals radius equal to 1.35 Å. The oblate spheroidal KTP and ATN profile “forced” the 12-ring channel to adapt to the host molecules geometry, with a consequent variation of Crystallographic Free Area (CFA). The 12MR had been compressed becoming more elliptical, as expressed by the channel ellipticity (ε), defined as the ratio between the smaller and the larger O—O “free diameters” of the 12-rings. The refined atomic occupancy factors gave rise to an adsorption of 19% and 18% in weight for KTP and ATN, respectively. This finding is in good agreement with those determined by adsorption isotherms (see  $q_s$  in Table 1) and by thermogravimetric analyses (see Figure 2). The positions occupied by atenolol and ketoprofen atoms appeared strongly disordered due to real static disorder or to dynamic disorder. For these reasons, the complete geometry of selected molecules inside the supercage was not achieved. The benzene ring of the drugs molecule was recognized in the supercage (Figure S1 in Supporting Information) and the adsorption site was partially occupied in both cases and each shows, on a statistical basis, four possible orientations. In particular, two and four orientations were identified for the tert-butyl and methoxyl groups, respectively. This result could indicate that structural and topological information contents may be significantly different, due to the geometry of extra-framework species, their ordering and respective symmetry lowering, framework distortions, etc. Consequently, we cannot exclude that the FAU framework could be in higher symmetry (F d -3) compared to the symmetry of the guest molecules. Moreover, the absence of cubic forbidden peaks indicating change in the space group does not get reported after adsorption, consequently, the F d -3 one was also adopted in the structure refinement.

Since it is known that the solution pH influences the adsorption of molecules with ionizable functional groups [40], adsorption experiments were carried out in water at different pH. The pH-dependent adsorption behaviour was studied by measuring the amount of adsorbed drug (q), normalized to the maximum value found in the investigated pH range ( $q_{max}$ ) for each analyte vs. the pH of the solution (see Figure 4). The  $pK_a$  values of analytes are reported in Supplementary Materials (Table S2).



**Figure 4.** Normalized adsorbed amount ( $q/q_{\max}$ ) on Y200 of KTP (green), HCT (blue), and ATN (red) vs. pH.

At  $2 < \text{pH} < 12$ , the zeolite surface remains negatively charged due to the dissociation of the hydroxyl groups [41]. In the explored pH range, literature data [42] reported that the Y zeolite does not undergo degradation.

The  $\text{pK}_a$  of KTP is 4.0, hence at  $\text{pH} < 4$  KTP is mainly in its neutral form and at  $\text{pH} > 4$  it is negatively charged. As shown in Figure 4, the adsorption of KTP decreases as pH increases, due to repulsive electrostatic interactions between KTP and the zeolite surface, both negatively charged. Analogously to KTP, the molecule of HCT ( $\text{pK}_{a1} = 7.9$ ) is undissociated at  $\text{pH} < \text{pK}_{a1}$  and negatively charged in more alkaline solutions. The adsorption is almost constant until the HCT molecule remains neutral and decreases as the negatively charged molecule becomes dominant. These results demonstrated that KTP and HCT interact with the high-silica zeolite mainly in their neutral form thanks to hydrophobic interactions. The preferential adsorption of neutral organic micropollutants by high-silica zeolites was observed also by Fukahori et al. [40] who reported that sulfa-drugs in neutral form could be more readily adsorbed onto FAU zeolites than those in cationic and anionic forms, based on the hydrophobic interactions. On the contrary, when the anionic forms are dominant under alkaline conditions, a reduction of adsorption capacity occurs [31]. Atenolol showed an opposite behaviour with respect to other two drugs, likewise to what was observed for BEA zeolites [15]. It should be minded that this molecule is cationic at  $\text{pH} < \text{pK}_a$  and neutral at  $\text{pH} > \text{pK}_a$  ( $\text{pK}_a = 9.6$ ). As the pH increases, the conversion of cationic species in the neutral one may result in greater hydrophobic interactions with Y200 and, at the same time, a lower solubility of the neutral ATN [43] which displays higher affinity with the sorbent surface rather than the liquid phase. Both these aspects could be responsible of the increase of ATN adsorption with pH.

## 2.2. Release

The performances of Y200 as a pre-concentration media for drugs enrichment was compared to a BEA zeolite having SAR 25, which was previously calcined (referred to as Beta25c), since it has been proved that this thermal treatment increases the adsorption efficiency of BEAs, thanks to the increase of acidity due to the thermal release of ammonia for  $\text{NH}_4$ -zeolites and to the increase of acidity as well as to surface and structural modifications induced by thermal treatments [15,18]. The extracting phases, at different pH and organic modifier contents, were selected in order to minimize the attractive

interactions between the sorbed drug and the zeolite framework (see Figure 4) and, at the same time, to favour the analyte's dissolution in the liquid phase. In general, for each zeolite-drug system, the following extracting phases were tested: Water, an organic polar solvent (methanol and acetonitrile), aqueous solutions at pH values where the adsorption has demonstrated to be low, mixtures organic modifier/formic acid or organic modifier/ammonium hydroxide. Despite the fact that in some cases acidic or alkaline extracting phases were employed, the time of contact of 5 min with the loaded zeolite (see Section 3.3) is too brief to induce structural degradation. Moreover, it should be considered that, in the studied pH range, it has been reported that zeolites [42,44] do not undergo degradation.

The release efficiency was calculated as a percentage recovery, according to Equation (2) [45]:

$$\%R = 100 \frac{C_f V_f}{C_i V_i} \quad (2)$$

where  $C_f$  corresponds to the concentration ( $\text{mg L}^{-1}$ ) of the released drug in the final volume  $V_f$  ( $0.2 \cdot 10^{-3}$  L),  $V_i$  is the initial volume ( $1 \cdot 10^{-3}$  L),  $C_i$  is the initial drug concentration (in the range  $0.05\text{--}1 \text{ mg L}^{-1}$ ). The details of the dispersive-SPE procedure were reported in Section 3.3. In Table 3, the results obtained from dispersive-SPE applied to KTP, at an initial concentration of  $1 \text{ mg L}^{-1}$ , are reported.

**Table 3.** Percentage Release of KTP at an Initial Concentration of  $1 \text{ mg L}^{-1}$  from Y200 and Beta25c ( $\pm$  SD: Standard Deviation).

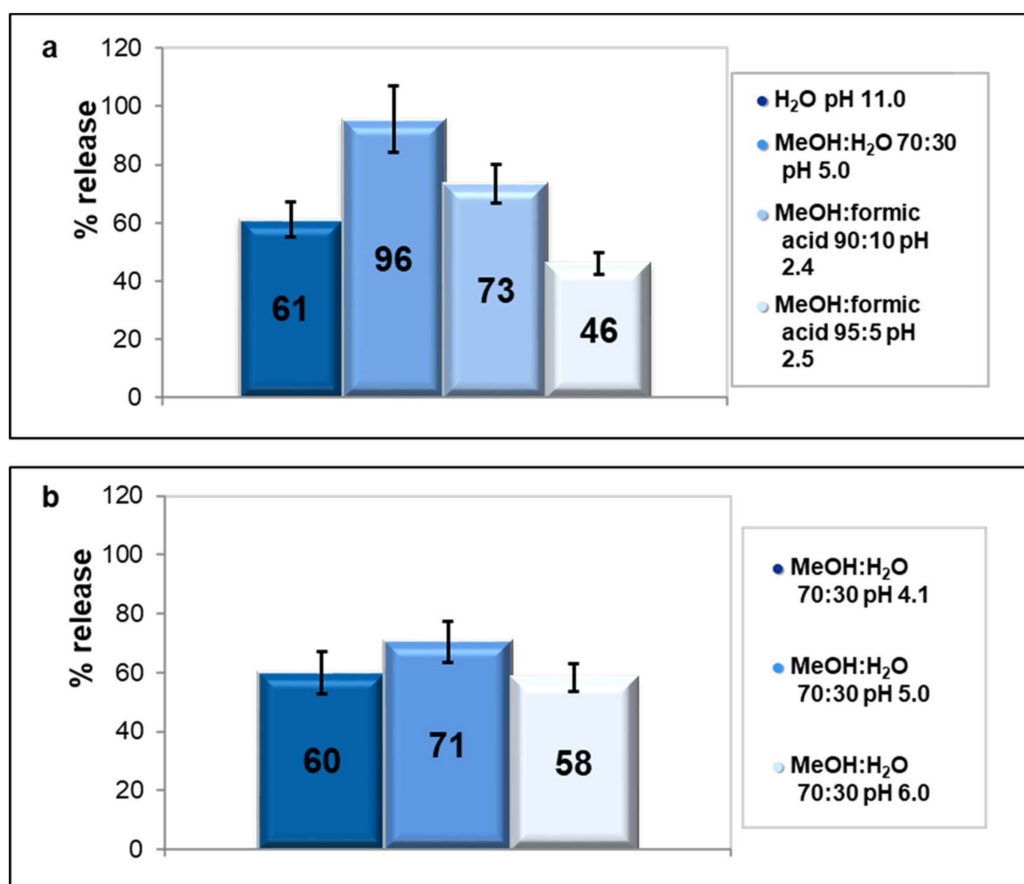
Extracting Phase	Y200	Beta25c
ACN	$53 \pm 4$	$53 \pm 5$
MeOH	$63 \pm 8$	$47 \pm 3$
MeOH:formic acid 90:10 pH 2.4	$94 \pm 14$	$115 \pm 17$
MeOH:formic acid 95:5 pH 2.5	$88 \pm 11$	$86 \pm 12$

For both zeolites, KTP is not at all released in water and the release is still negligible even by increasing the pH of water to 10. At this pH, KTP is negatively charged, hence electrostatic repulsions with a zeolite framework, negatively charged too, were expected. Percent recoveries higher than 80% were obtained with mixtures of methanol and formic acid, probably due to interactions between the neutral form of KTP at  $\text{pH} < \text{pK}_a$  and the extracting phase enriched in an organic modifier.

Some further experiments were carried out by varying the initial drug's concentration, in order to verify if such positive results could be achieved also in the low concentrations range. The data reported in Supplementary Materials (Figure S2) confirm that great recovery efficiencies were achieved with both zeolites also at low analyte concentrations ( $1, 0.1,$  and  $0.05 \text{ mg L}^{-1}$ ). The results of the present work were compared with those obtained by other studies [8,46] focused on solid phase extraction of KTP by using a commercial adsorbent and the efficiency was found comparable. Figure 5 shows some of the results obtained by extraction of HCT with different phases from both zeolites.

The release of HCT in water from Y200 is low but not negligible. However, a higher release ( $61 \pm 6\%$  as shown in Figure 5a) was obtained by increasing the pH to 10, because of electrostatic repulsions between the negatively charged drug and the zeolitic framework. A high recovery of  $96 \pm 11\%$  was obtained with MeOH:H<sub>2</sub>O = 70:30 at pH 5.0: analogously to KTP, in these conditions ( $\text{pH} < \text{pK}_a$ ) HCT is neutral and displays high affinity with the extracting phase which is mainly organic. Some experiments were carried out also at HCT concentrations lower than  $1 \text{ mg L}^{-1}$  (i.e.,  $0.1$  and  $0.05 \text{ mg L}^{-1}$ ): No significant differences were observed between the different concentrations, thus indicating that the dispersive SPE of the Y200-HCT system is effective also in the low concentrations range, similarly for what was observed for KTP. The recovery efficiency on Beta25c (Figure 5b) was evaluated by keeping constant the composition of the extracting phase and by varying the pH from 4 to 6. The highest recovery ( $71 \pm 7\%$ ) was obtained at pH 5 as already found for Y200, even if the extraction was less efficient. This could be due to higher affinities between HCT at low concentrations

and Beta25c (a binding constant of  $0.60 \text{ L mg}^{-1}$  was found [15]) with respect to Y200 ( $b = 0.037 \text{ L mg}^{-1}$  as reported in Table 1). Finally, for that which concerns ATN, this drug was not at all released from Y200 in water at pH 3, despite the fact that it was found that the adsorption is negligible at strongly acidic pH (Figure 4). Other experiments were performed at acidic pH by adding an organic modifier, and the best result ( $71 \pm 5\%$ ) was obtained with a mixture (ACN:formic acid) (95:5) as an extracting phase. Further tests were carried out at high pH values, by using extracting phases constituted by an organic modifier (MeOH, ACN, or a mixture of them) and ammonium hydroxide at different concentrations. These alkaline conditions should promote the dissolution of neutral ATN into the liquid phase which is mainly organic. The highest efficiency ( $83 \pm 9\%$ ) was obtained with an extracting phase composed by (MeOH:ACN 40:60):(NH<sub>4</sub> OH 5%) = 70:30. The solute enrichment obtained with the proposed procedure (five-fold enrichment of concentration, as described in Section 3.3) could be improved by using higher volumes of the initial drug solution. Moreover, the extraction efficiency could be enhanced by using longer time contact or higher volume of extraction phases. However, the results herein presented could be considered a good compromise between the efficiency of the enrichment process ( $> 80\%$ ) and the cost and time saving of the concentration procedure. Unfortunately, for the Beta25c-ATN system, very low recoveries were obtained with several extracting phases, in fact the best result was reached with a mixture (MeOH:ACN 40:60):(NH<sub>4</sub> OH 5%) = 80:20 which led to a scarce  $13 \pm 2\%$ . The differences in terms of recovery efficiencies between the two selected zeolites could be ascribed to the binding constants. The  $b$  parameter of the Beta25c-ATN system was found to be  $5.8 \pm 2.8 \text{ L mg}^{-1}$  [15], while that of the Y200-ATN system was  $0.11 \pm 0.03 \text{ L mg}^{-1}$  (Table 1). As already hypothesized for HCT and KTP, the lower recovery of ATN from Beta25c could be due to its higher affinity with respect to Y200.



**Figure 5.** Release of HCT  $1 \text{ mg L}^{-1}$  from Y200 with different extracting phases (a) and from Beta25c with mixture MeOH:H<sub>2</sub>O 70:30 at different pH (b).

### 3. Materials and Methods

#### 3.1. Materials

Technical grade (99% purity) ketoprofen (KTP), hydrochlorothiazide (HCT), and atenolol (ATN) were obtained from Sigma-Aldrich (Steinheim, Germany), as well as sodium phosphate monobasic for the HPLC eluent. HPLC grade acetonitrile (ACN) and methanol (MeOH) were purchased from VWR International PBI Srl (Radnor, PA, USA). The water was Milli-Q grade (Merck Millipore, Burlington, MA, USA). Formic acid and ammonium hydroxide solution were obtained from Merck (Darmstadt, Germany). Hydrochloric acid and sodium hydroxide (Alfa Aesar, Haverhill, MA, USA) were used for pH adjustment. The pH was measured with an Amel 2335 pH-meter (Milano, Italy). Zeolite powders were obtained from Zeolyst International (Conshohocken, PA, USA) and from Tosoh Corporation (Tokyo, Japan). The main features of the selected zeolites are reported in Supplementary Materials (Table S1). In our study, two USY zeolites with a Silica/Alumina Ratio (SAR) of 30 and 200 (referred as Y30 and Y200) and a BEA with SAR of 25 (referred as Beta25) have been employed. According to Čejka et al. [29], who discriminated between high-silica and low-silica zeolites when SAR was respectively above or below 5, the selected materials can be considered high-silica zeolites. Structures and chemical properties of the selected drugs are reported in Supplementary Materials (Table S2) [47–50].

#### 3.2. Sorption Studies

The adsorption experiments were carried out using the batch method, by putting in contact aqueous solutions of drugs at different concentrations in Milli-Q water with a known amount of zeolite. It has been reported in previous studies [15] that the equilibrium is quite fast, nevertheless in this work a contact time of 24 h was employed. Batch experiments were carried out in duplicate in 25 mL crimp top reaction glass flasks sealed with PTFE septa (Supelco, Bellefonte, PA, USA). During the equilibration, the solutions were thermostated at a temperature of  $25.3 \pm 0.5$  °C and continuously stirred at 700 rpm. The solid was separated from the solution by centrifugation (Eppendorf 5418, Hamburg, Germany) at 14,000 rpm for 10 min. For each level of concentration, the amount of analyte in the solution, before and after the contact with the adsorbent, was determined by HPLC-DAD as described in Supporting Information. Thermogravimetric and diffractometric analyses were performed on zeolites before and after saturation with the selected drugs. Thermogravimetric (TG) measurements were performed in air up to 900 °C, at  $10$  °C  $\text{min}^{-1}$  heating rate, using an STA 409 PC LUX<sup>®</sup> - Netzch Gerätebau GmbH (Verona, Italy). The X-ray diffraction analysis was carried out on a Bruker D8 Advance (Karlsruhe, Germany) diffractometer (Cu  $K\alpha_{1,2}$  radiation) equipped with a Si (Li)SOL-X solid-state detector. The GSAS software and the EXPGUI graphical interface were employed for structural refinements through a full profile Rietveld analysis. Statistical elaborations were carried out through MATLAB<sup>®</sup> ver. 9.1 software (The MathWorks Inc., Natick, MA, USA).

#### 3.3. Dispersive-SPE Studies

The dispersive-SPE procedure was carried out as follows: In a safe-lock microcentrifuge tube, 2 mg of zeolite were added to 1 mL of drug solution, in a concentration range of  $0.05$ – $1$  mg  $\text{L}^{-1}$  in Milli-Q water, and mixed for 5 min by vortex (VWR International PBI Srl, Radnor, PA, USA) equipped with a specific adapter for microcentrifuge tubes. The resulting suspension was centrifuged at 14,000 rpm for 5 min and the supernatant was analyzed by HPLC-DAD, in order to quantify the adsorption. In all cases, it was found that the drug concentration in the supernatant was below the instrumental limit of detection. Therefore, the drug was completely adsorbed in the brief time of contact, thanks to the fast kinetic offered by the zeolites [14,15], especially in the low concentration range. After the supernatant's removal, the loaded zeolite was re-suspended for 5 min with 500  $\mu\text{L}$  of solutions having different compositions (i.e., pH and organic modifier concentration) and then centrifuged at 14,000 rpm for 5 min. Finally, the supernatant was dried by evaporation under a gentle stream of nitrogen gas, dissolved with 200  $\mu\text{L}$  of the HPLC mobile phase (see Supplementary Materials) and analyzed by

HPLC-DAD for the quantification of the released drug. With the proposed procedure, a five-fold enrichment was achieved. All measurements were performed in triplicate.

#### 4. Conclusions

In this study, the adsorptive properties of two commercial high-silica Y zeolites, with a Silica/Alumina Ratio 30 and 200 (namely Y30 and Y200), toward drugs in a diluted aqueous solution were evaluated, with the aim to investigate their possible use in the enrichment step of the analysis. In fact, the determination of pharmaceuticals at trace levels in natural waters requires advanced analytical methodologies enabling a more efficient detection with lower limits of quantitation. Owing to their high surface area, hydrophobicity and water stability, the selected materials were demonstrated to be efficient sorbents, both in terms of saturation capacity and binding constant. Among the two Y-zeolites, in general better performances were observed for Y200. The structural analyses of saturated zeolites revealed that drugs adsorption occurred inside the porosities of Y200 leading to modifications of lattice parameters and channel ellipticity. Pharmaceuticals pre-concentration from dilute aqueous solutions was carried out through the dispersive-solid phase extraction technique, thanks to its attractive features, such as the short experimental times and small reagents amount required. As a pre-concentration medium, in addition to Y200, a calcined Beta-zeolite with Silica/Alumina Ratio 25 was tested. The dispersive-solid phase extraction experiments led to high recoveries, especially for ketoprofen and hydrochlorothiazide. These results are promising, especially by considering the short operational times required for the entire procedure.

**Supplementary Materials:** The following are available online at; Table S1: Zeolites characteristics; Table S2: Molecular structures and physical chemical properties of the studied drugs; Section S1: Experimental HPLC/DAD; Figure S1: Adsorption site in the supercage for ATN and KTP benzene ring; Figure S2: Release of KTP at three concentration levels with MeOH:formic acid 90:10 pH 2.4 as an extracting phase.

**Author Contributions:** Conceptualization, A.M. and L.P.; formal analysis, E.S., V.C., M.C., and L.P.; funding acquisition, L.P.; investigation, T.C., C.S., N.P., and G.B.; methodology, V.C., M.C., and L.P.; resources, A.C., A.M., and L.P.; supervision, E.S., A.C., A.M., and L.P.; visualization, E.S., A.M., and L.P.; writing—Original draft, E.S.; writing—Review and editing, E.S., A.M., and L.P. All authors have read and agreed to the published version of the manuscript.

**Funding:** This research was funded by the Ministry of Education, University and Research (MIUR) under the PRIN 2017 program grant agreement no. 2017Y2PAB8\_003, and from the 2014–2020 Interreg V-A Italy—Croatia CBC Programme, title of the project: PEPSEA (ID number 10047424).

**Conflicts of Interest:** The authors declare no conflict of interest. The funders had no role in the design of the study; in the collection, analyses, or interpretation of data; in the writing of the manuscript, or in the decision to publish the results.

#### References

1. Charuau, L.; Jarde, E.; Jaffrezic, A.; Thomas, M.; le Bot, B. Veterinary pharmaceutical residues from natural water to tap water: Sales, occurrence and fate. *J. Hazard. Mater.* **2019**, *361*, 169–186. [[CrossRef](#)] [[PubMed](#)]
2. Sharma, B.M.; Bečanová, J.; Scheringer, M.; Sharma, A.; Bharat, G.K.; Whitehead, P.G.; Klánová, J.; Nizzetto, L. Health and ecological risk assessment of emerging contaminants (pharmaceuticals, personal care products, and artificial sweeteners) in surface and groundwater (drinking water) in the Ganges River Basin, India. *Sci. Total Environ.* **2019**, *646*, 1459–1467. [[CrossRef](#)] [[PubMed](#)]
3. Yang, Y.; Ok, Y.S.; Kim, K.H.; Kwon, E.E.; Tsang, Y.F. Occurrences and removal of pharmaceuticals and personal care products (PPCPs) in drinking water and water/sewage treatment plants: A review. *Sci. Total Environ.* **2017**, *596*, 303–320. [[CrossRef](#)] [[PubMed](#)]
4. McCallum, E.S.; Krutzelmann, E.; Brodin, T.; Fick, J.; Sundelin, A.; Balshine, S. Exposure to wastewater effluent affects fish behaviour and tissue-specific uptake of pharmaceuticals. *Sci. Total Environ.* **2017**, *605*, 578–588. [[CrossRef](#)]
5. Wilkinson, J.; Hooda, P.S.; Barker, J.; Barton, S.; Swinden, J. Occurrence, fate and transformation of emerging contaminants in water: An overarching review of the field. *Environ. Pollut.* **2017**, *231*, 954–970. [[CrossRef](#)]

6. Yang, H.; Lu, G.; Yan, Z.; Liu, J.; Dong, H.; Jiang, R.; Zhou, R.; Zhang, P.; Sun, Y.; Nkoom, M. Occurrence, spatial-temporal distribution and ecological risks of pharmaceuticals and personal care products response to water diversion across the rivers in Nanjing, China. *Environ. Pollut.* **2019**, *255*, 113–132. [[CrossRef](#)]
7. Furlong, E.T.; Batt, A.L.; Glassmeyer, S.T.; Noriega, M.C.; Kolpin, D.W.; Mash, H.; Schenck, K.M. Nationwide reconnaissance of contaminants of emerging concern in source and treated drinking waters of the United States: Pharmaceuticals. *Sci. Total Environ.* **2017**, *579*, 1629–1642. [[CrossRef](#)]
8. Caban, M.; Lis, E.; Kumirska, J.; Stepnowski, P. Determination of pharmaceutical residues in drinking water in Poland using a new SPE-GC-MS(SIM) method based on Speedisk extraction disks and DIMETRIS derivatization. *Sci. Total Environ.* **2015**, *538*, 402–411. [[CrossRef](#)]
9. Comber, S.; Gardner, M.; Sörme, P.; Leverett, D.; Ellord, B. Active pharmaceutical ingredients entering the aquatic environment from wastewater treatment works: A cause for concern? *Sci. Total Environ.* **2018**, *613*, 538–547. [[CrossRef](#)]
10. Patrolecco, L.; Capri, S.; Ademollo, N. Occurrence of selected pharmaceuticals in the principal sewage treatment plants in Rome (Italy) and in the receiving surface waters. *Environ. Sci. Pollut. Res.* **2015**, *22*, 5864–5876. [[CrossRef](#)]
11. Carmalin, S.A.; Eder, C.L. Removal of emerging contaminants from the environment by adsorption. *Ecotox. Environ. Safe* **2018**, *150*, 1–17.
12. Patiño, Y.; Díaz, E.; Ordóñez, S. Pre-concentration of nalidixic acid through adsorption–desorption cycles: Adsorbent selection and modelling. *Chem. Eng. J.* **2016**, *283*, 486–494. [[CrossRef](#)]
13. Naing, N.N.; Li, S.F.Y.; Lee, H.K. Evaluation of graphene-based sorbent in the determination of polar environmental contaminants in water by micro-solid phase extraction-high performance liquid chromatography. *J. Chromatogr. A* **2016**, *1427*, 29–36. [[CrossRef](#)] [[PubMed](#)]
14. Martucci, A.; Pasti, L.; Marchetti, N.; Cavazzini, A.; Dondi, F.; Alberti, A. Adsorption of pharmaceuticals from aqueous solutions on synthetic zeolites. *Micropor. Mesopor. Mat.* **2012**, *148*, 174–183. [[CrossRef](#)]
15. Pasti, L.; Sarti, E.; Cavazzini, A.; Marchetti, N.; Dondi, F.; Martucci, A. Factors affecting drug adsorption on beta zeolites. *J. Sep. Sci.* **2013**, *36*, 1604–1611. [[CrossRef](#)]
16. Costa, A.A.; Wilson, W.B.; Wang, H.; Campiglia, A.D.; Dias, J.A.; Dias, S.C.L. Comparison of BEA, USY and ZSM-5 for the quantitative extraction of polycyclic aromatic hydrocarbons from water samples. *Micropor. Mesopor. Mat.* **2012**, *149*, 186–192. [[CrossRef](#)]
17. Wilson, W.B.; Costa, A.A.; Wang, H.; Campiglia, A.D.; Dias, J.A.; Dias, S.C.L. Pre-concentration of water samples with BEA zeolite for the direct determination of polycyclic aromatic hydrocarbons with laser-excited time-resolved Shpol'skii spectroscopy. *Microchem. J.* **2013**, *110*, 246–255. [[CrossRef](#)]
18. Sarti, E.; Chenet, T.; Pasti, L.; Cavazzini, A.; Rodeghero, E.; Martucci, A. Effect of silica alumina ratio and thermal treatment of Beta zeolites on the adsorption of toluene from aqueous solutions. *Minerals* **2017**, *7*, 22. [[CrossRef](#)]
19. Martucci, A.; Braschi, I.; Bisio, C.; Sarti, E.; Rodeghero, E.; Bagatin, R.; Pasti, L. Influence of water on the retention of methyl tertiary-butyl ether by high silica ZSM-5 and Y zeolites: A multidisciplinary study on the adsorption from liquid and gas phase. *RSC Adv.* **2015**, *5*, 86997–87006. [[CrossRef](#)]
20. Pasti, L.; Rodeghero, E.; Beltrami, G.; Ardit, M.; Sarti, E.; Chenet, T.; Stevanin, C.; Martucci, A. Insights into adsorption of chlorobenzene in high silica MFI and FAU zeolites gained from chromatographic and diffractometric techniques. *Minerals* **2018**, *8*, 80. [[CrossRef](#)]
21. Anastassiades, M.; Lehotay, S.J.; Stajnbaher, D.; Schenck, F.J. Fast and easy multiresidue method employing acetonitrile extraction/partitioning and “dispersive solid-phase extraction” for the determination of pesticide residues in produce. *J. AOAC Int.* **2003**, *86*, 412. [[CrossRef](#)] [[PubMed](#)]
22. Román, I.P.; Chisvert, A.; Canals, A. Dispersive solid-phase extraction based on oleic acid-coated magnetic nanoparticles followed by gas chromatography–mass spectrometry for UV-filter determination in water samples. *J. Chromatogr. A* **2011**, *1218*, 2467–2475. [[CrossRef](#)] [[PubMed](#)]
23. Wang, P.; Yang, X.; Wang, J.; Cui, J.; Dong, A.J.; Zhao, H.T.; Zhang, L.W.; Wang, Z.Y.; Xu, R.B.; Li, W.J. Multi-residue method for determination of seven neonicotinoid insecticides in grains using dispersive solid-phase extraction and dispersive liquid–liquid micro-extraction by high performance liquid chromatography. *Food Chem.* **2012**, *134*, 3–1691. [[CrossRef](#)]
24. Tsai, W.H.; Huang, T.C.; Huang, J.J.; Hsue, Y.H.; Chuang, H.Y. Dispersive solid-phase microextraction method for sample extraction in the analysis of four tetracyclines in water and milk samples by high-performance



- liquid chromatography with diode-array detection. *J. Chromatogr. A* **2009**, *1216*, 12–2263. [[CrossRef](#)] [[PubMed](#)]
25. Rodeghero, E.; Martucci, A.; Cruciani, G.; Bagatin, R.; Sarti, E.; Bosi, V.; Pasti, L. Kinetics and dynamic behaviour of toluene desorption from ZSM-5 using in situ high-temperature synchrotron powder X-ray diffraction and chromatographic techniques. *Catal. Today* **2016**, *277*, 118–125. [[CrossRef](#)]
  26. Rodeghero, E.; Pasti, L.; Sarti, E.; Cruciani, G.; Bagatin, R.; Martucci, A. Temperature-induced desorption of methyl tert-butyl ether confined on ZSM-5: An in situ synchrotron XRD powder diffraction study. *Minerals* **2017**, *7*, 34. [[CrossRef](#)]
  27. Archer, E.; Petrie, B.; Kasprzyk-Hordern, B.; Wolfaard, G.M. The fate of pharmaceuticals and personal care products (PPCPs), endocrine disrupting contaminants (EDCs), metabolites and illicit drugs in a WWTW and environmental waters. *Chemosphere* **2017**, *174*, 437–446. [[CrossRef](#)]
  28. Fernández-Perales, M.; Sánchez-Polo, M.; Rozalen, M.; López-Ramón, M.V.; Mota, A.J.; Rivera-Utrilla, J. Degradation of the diuretic hydrochlorothiazide by UV/Solar radiation assisted oxidation processes. *J. Environ. Manag.* **2020**, *257*, 109973. [[CrossRef](#)]
  29. Čejka, J.; van Bekkum, H.; Corma, A.; Schüth, F. *Introduction to Zeolite Science and Practice*, 3rd ed.; Elsevier: Amsterdam, The Netherlands, 2007; Volume 168, pp. 50–51.
  30. Hartig, D.; Schwindt, N.; Scholl, S. Using the local adsorption equilibrium distribution based on a Langmuir type adsorption model to investigate liquid phase adsorption of sugars on zeolite BEA. *Adsorption* **2017**, *23*, 433–441. [[CrossRef](#)]
  31. Jiang, N.; Shang, R.; Heijman, S.G.J.; Rietveld, L.C. High-silica zeolites for adsorption of organic micro-pollutants in water treatment: A review. *Water Res.* **2018**, *144*, 145–161. [[CrossRef](#)]
  32. Cuerda-Correa, E.M.; Domínguez-Vargas, J.R.; Olivares-Marín, F.J.; Beltrán de Heredia, J. On the use of carbon blacks as potential low-cost adsorbents for the removal of non-steroidal anti-inflammatory drugs from river water. *J. Hazard. Mater.* **2010**, *177*, 1046–1053. [[CrossRef](#)] [[PubMed](#)]
  33. Haro, N.K.; del Vecchio, P.; Marcilio, N.R.; Féris, L.A. Removal of atenolol by adsorption – Study of kinetics and equilibrium. *J. Clean. Prod.* **2017**, *154*, 214–219. [[CrossRef](#)]
  34. Fröhlich, A.C.; Foletto, E.L.; Dotto, G.L. Preparation and characterization of NiFe<sub>2</sub>O<sub>4</sub>/activated carbon composite as potential magnetic adsorbent for removal of ibuprofen and ketoprofen pharmaceuticals from aqueous solutions. *J. Clean. Prod.* **2019**, *229*, 828–837. [[CrossRef](#)]
  35. Arya, V.; Philip, L. Adsorption of pharmaceuticals in water using Fe<sub>3</sub>O<sub>4</sub> coated polymer clay composite. *Micropor. Mesopor. Mat.* **2016**, *232*, 273–280. [[CrossRef](#)]
  36. Wesolowski, M.; Rojek, B. Thermogravimetric detection of incompatibilities between atenolol and excipients using multivariate techniques. *J. Therm. Anal. Calorim.* **2013**, *113*, 169–177. [[CrossRef](#)]
  37. Silva Pires, M.A.; Souza dos Santos, R.A.; Sinisterra, R.D. Pharmaceutical composition of hydrochlorothiazide:  $\beta$ -cyclodextrin: Preparation by three different methods, physico-chemical characterization and in vivo diuretic activity evaluation. *Molecules* **2011**, *16*, 4482–4499. [[CrossRef](#)]
  38. Tița, B.; Fuliș, A.; Bandur, G.; Marian, E.; Tița, D. Compatibility study between ketoprofen and pharmaceutical excipients used in solid dosage forms. *J. Pharm. Biomed.* **2011**, *56*, 221–227. [[CrossRef](#)]
  39. Braschi, I.; Gatti, G.; Bisio, C.; Berlier, G.; Sacchetto, V.; Cossi, M.; Marchese, L. The role of silanols in the interactions between methyl tert-butyl ether and high-silica Faujasite Y: An infrared spectroscopy and computational model study. *J. Phys. Chem. C* **2012**, *116*, 6943–6952. [[CrossRef](#)]
  40. Fukahori, S.; Fujiwara, T.; Ito, R.; Funamizu, N. pH-Dependent adsorption of sulfa drugs on high silica zeolite: Modeling and kinetic study. *Desalination* **2011**, *275*, 237–242. [[CrossRef](#)]
  41. Kuzniatsova, T.; Kim, Y.; Shqau, K.; Dutta, P.K.; Verweij, H. Zeta potential measurements of zeolite Y: Application in homogeneous deposition of particle coatings. *Micropor. Mesopor. Mat.* **2007**, *103*, 102–107. [[CrossRef](#)]
  42. Lee, E.F.T.; Rees, L.V.C. Dealumination of sodium Y zeolite with hydrochloric acid. *J. Chem. Soc. Faraday Trans.* **1987**, *83*, 1531–1537. [[CrossRef](#)]
  43. Schönherr, D.; Wollatz, U.; Haznar-Garbacz, D.; Hanke, U.; Box, K.J.; Taylor, R.; Ruiz, R.; Beato, S.; Becker, D.; Weitschies, W. Characterisation of selected active agents regarding pKa values, solubility concentrations and pH profiles by Sirius T3. *Eur. J. Pharm. Biopharm.* **2015**, *92*, 155–170. [[CrossRef](#)] [[PubMed](#)]

44. Liu, X.; Mäki-Arvela, P.; Aho, A.; Vajglova, Z.; Gun'ko, V.M.; Heinmaa, I.; Kumar, N.; Murzin, D.Y. Zeta potential of beta zeolites: Influence of structure, acidity, pH, temperature and concentration. *Molecules* **2018**, *23*, 946. [[CrossRef](#)] [[PubMed](#)]
45. Bosi, V.; Sarti, E.; Navacchia, M.L.; Perrone, D.; Pasti, L.; Cavazzini, A.; Capobianco, M.L. Gold-nanoparticle extractioned reversed-electrode-polarity stacking mode combined to enhance capillary electrophoresis sensitivity for conjugated nucleosides and oligonucleotides containing thioether linkers. *Anal. Bioanal. Chem.* **2015**, *407*, 5405–5415. [[CrossRef](#)]
46. Santos, J.L.; Aparicio, I.; Alonso, E.; Callejón, M. Simultaneous determination of pharmaceutically active compounds in wastewater samples by solid phase extraction and high-performance liquid chromatography with diode array and fluorescence detectors. *Anal. Chim. Acta* **2005**, *550*, 116–122. [[CrossRef](#)]
47. Gantiva, M.; Martínez, F. Thermodynamic analysis of the solubility of ketoprofen in some propylene glycol + water cosolvent mixtures. *Fluid Phase Equilib.* **2010**, *293*, 242–250. [[CrossRef](#)]
48. Radjenović, J.; Petrović, M.; Ventura, F.; Barceló, D. Rejection of pharmaceuticals in nanofiltration and reverse osmosis membrane drinking water treatment. *Water Res.* **2008**, *42*, 3601–3610. [[CrossRef](#)]
49. Kadam, Y.; Yerramilli, U.; Bahadur, A.; Bahadur, P. Micelles from PEO–PPO–PEO block copolymers as nanocontainers for solubilization of a poorly water soluble drug hydrochlorothiazide. *Colloid. Surface B* **2011**, *83*, 49–57. [[CrossRef](#)]
50. Küster, A.; Alder, A.C.; Escher, B.I.K.; Duis, K.; Fenner, K.; Garric, J.; Hutchinson, T.H.; Lapen, D.R.; Péry, A.; Rö#xF6;mbke, J. Environmental risk assessment of human pharmaceuticals in the European Union: A case study with the  $\beta$ -blocker atenolol. *Integr. Environ. Assess. Manag.* **2010**, *6*, 514–523.

**Sample Availability:** Samples of the zeolites are available from the authors.



© 2020 by the authors. Licensee MDPI, Basel, Switzerland. This article is an open access article distributed under the terms and conditions of the Creative Commons Attribution (CC BY) license (<http://creativecommons.org/licenses/by/4.0/>).

# High-Silica Zeolites as Sorbent Media for Adsorption and Pre-Concentration of Pharmaceuticals in Aqueous Solutions

Elena Sarti <sup>1,\*</sup>, Tatiana Chenet <sup>1</sup>, Claudia Stevanin <sup>1</sup>, Valentina Costa <sup>1</sup>, Alberto Cavazzini <sup>1</sup>, Martina Catani <sup>1</sup>, Annalisa Martucci <sup>2</sup>, Nicola Precisvalle <sup>2</sup>, Giada Beltrami <sup>2</sup> and Luisa Pasti <sup>1</sup>

<sup>1</sup> Department of Chemical and Pharmaceutical Sciences, University of Ferrara, Via Luigi Borsari 46, 44121 Ferrara, Italy; tatiana.chenet@unife.it (T.C.); claudia.stevanin@unife.it (C.S.); valentina.costa@unife.it (V.C.), alberto.cavazzini@unife.it (A.C.); martina.catani@unife.it (M.C.); luisa.pasti@unife.it (L.P.)

<sup>2</sup> Department of Physics and Earth Sciences, University of Ferrara, Via Giuseppe Saragat 1, 44122 Ferrara, Italy; annalisa.martucci@unife.it (A.M.); nicola.precisvalle@unife.it (N.P.); giada.beltrami@unife.it (G.B.)

\* Correspondence: elena.sarti@unife.it, Tel: +39 0532 455189; Fax: +39 0532 455507

## Contains:

- Pages: 4
- Tables: 2
- Figures: 2

## Contents:

**Table S1.** Zeolites characteristics

**Table S2.** Molecular structures and physical chemical properties of the studied drugs

**Section S1. Experimental : HPLC/DAD**

**Figure S1.** Adsorption site in the supercage for ATN and KTP benzene ring

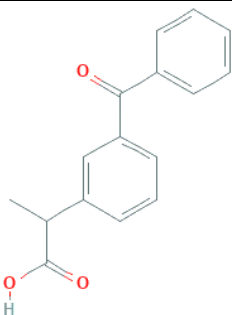

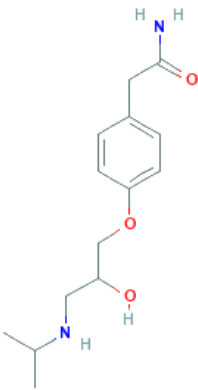
**Figure S2.** Release of KTP at three concentration levels with MeOH:formic acid 90:10 pH 2.4 as extracting phase

**References**

**Table S1.** Zeolites characteristics

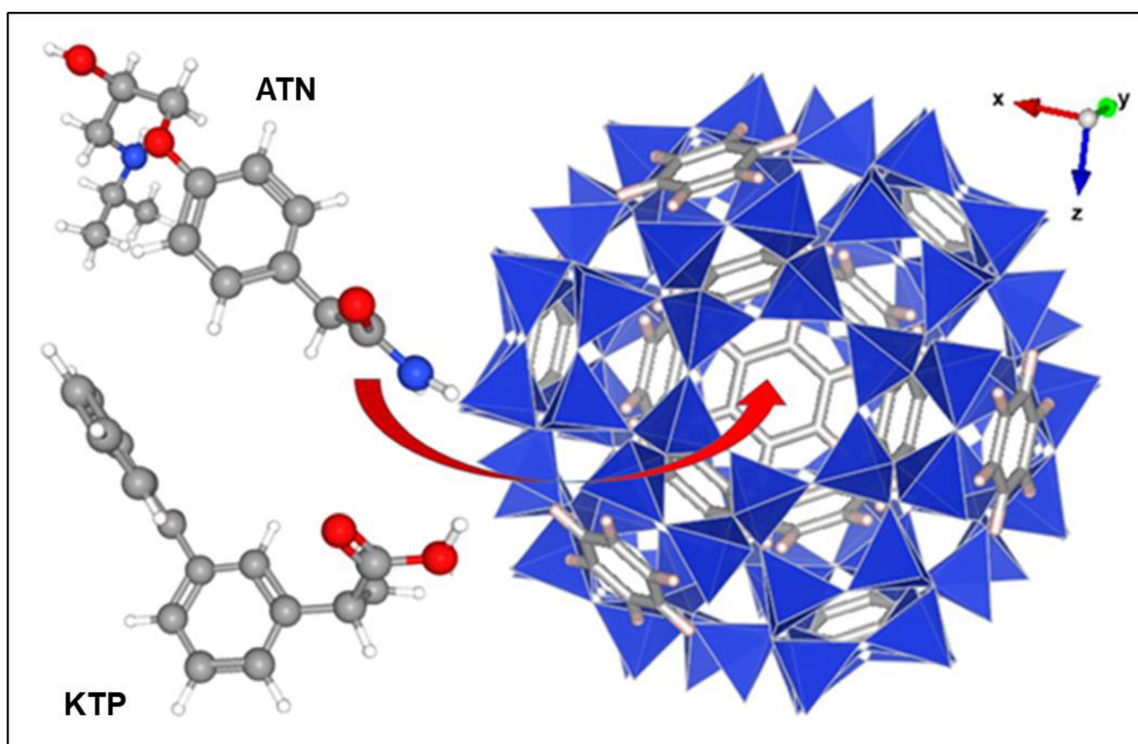
	Producer	SiO <sub>2</sub> /Al <sub>2</sub> O <sub>3</sub> ratio	Nominal cation form	Surface area (m <sup>2</sup> g <sup>-1</sup> )
Y200	Tosoh Corporation (HSZ-390HUA)	200	Hydrogen	630
Y30	Zeolyst (CBV 720)	30	Hydrogen	780
Beta25	Zeolyst (CP814E)	25	Ammonium	680

**Table S2.** Molecular structures and physical chemical properties of the studied drugs

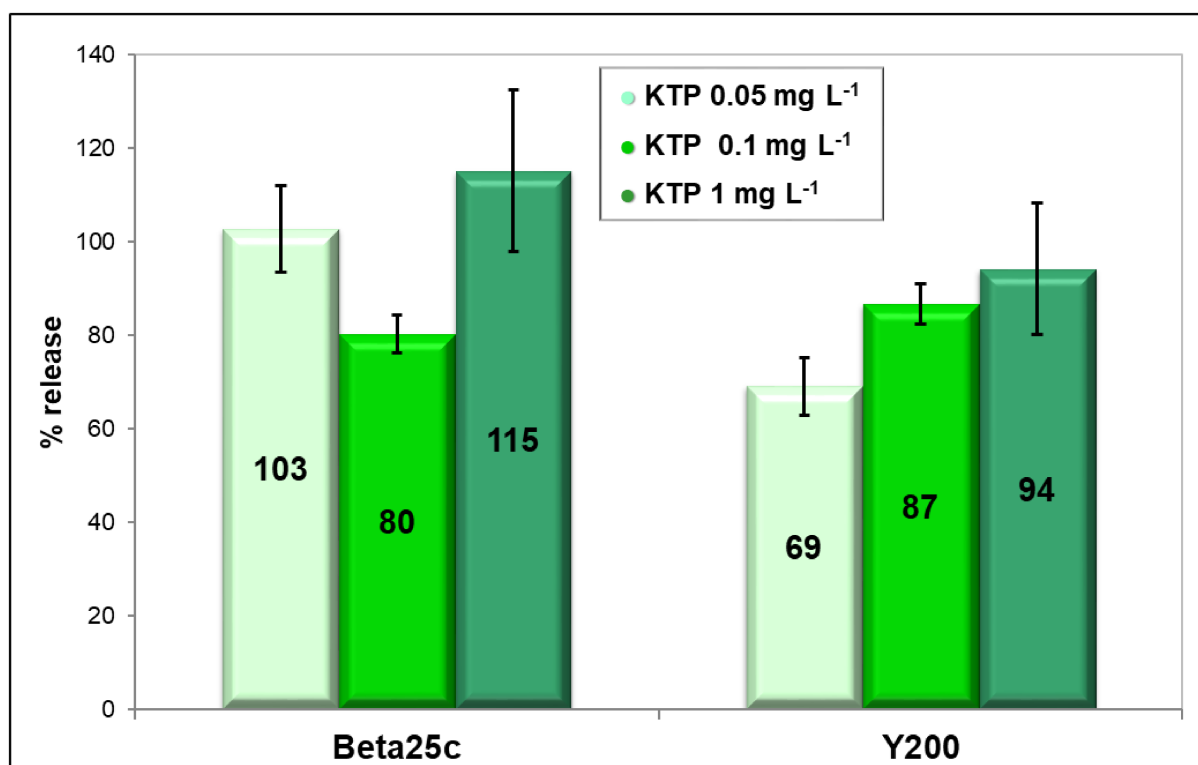
Drug	Formula	Molecular Weight	Structure	Water solubility (g L <sup>-1</sup> )	pK <sub>a</sub>	Log K <sub>ow</sub>
KTP	C <sub>16</sub> H <sub>14</sub> O <sub>3</sub>	254.28		0.11 [47]	4.0 [48]	3.1 [48]
HCT	C <sub>7</sub> H <sub>8</sub> ClN <sub>3</sub> O <sub>4</sub> S <sub>2</sub>	297.74		1.0 [49]	pK <sub>a1</sub> =7.9 pK <sub>a2</sub> =9.2 [48]	-0.07 [48]
ATN	C <sub>14</sub> H <sub>22</sub> N <sub>2</sub> O <sub>3</sub>	266.34		13 [50]	9.6 [50]	0.16-0.50 [50]

## S1. Experimental: HPLC/DAD

Drugs solutions were analysed by a Dionex HPLC (Thermo Fisher Scientific Inc., Waltham, MA, USA) equipped with a P680 pump and a UVD340U detector. The flow rate was kept at  $1 \text{ mL min}^{-1}$  under isocratic conditions. The reversed-phase C18 analytical column (Agilent Technologies, Santa Clara, CA, USA;  $150 \times 4.6 \text{ mm}$ , I.D.  $5 \mu\text{m}$ ) was thermostated at  $25 \text{ }^\circ\text{C}$ . The injection volume was  $20 \mu\text{L}$ . As mobile phases, the following mixtures were employed: for KTP (MeOH: phosphate buffer  $2\text{mM pH } 3$ ) (60:40), for HCT (MeOH: phosphate buffer  $2\text{mM pH } 3$ ) (15:85), for ATN (ACN: phosphate buffer  $2\text{mM pH } 3$ ) (5:95). The selected detection wavelengths were  $255 \text{ nm}$ ,  $224 \text{ nm}$  and  $225 \text{ nm}$  for KTP, HCT and ATN, respectively.



**Figure S1.** Adsorption site in the supercage for ATN and KTP benzene ring




**Figure S2.** Release of KTP at three concentration levels with MeOH:formic acid 90:10 pH 2.4 as extracting phase

## References

47. Gantiva M., Martínez F., Thermodynamic analysis of the solubility of ketoprofen in some propylene glycol + water cosolvent mixtures. *Fluid Phase Equilib.* 2010, 293, 242–250.
48. Radjenović J., Petrović M., Ventura F., Barceló D., Rejection of pharmaceuticals in nanofiltration and reverse osmosis membrane drinking water treatment. *Water Res.* 2008, 42, 3601 – 3610
49. Kadam Y., Yerramilli U., Bahadur A., Bahadur P., Micelles from PEO–PPO–PEO block copolymers as nanocontainers for solubilization of a poorly water soluble drug hydrochlorothiazide. *Colloid. Surface B* 2011, 83, 49–57
50. Küster A., Alder A. C., Escher B. I., K. Duis K., Fenner K., Garric J., Hutchinson T. H., Lapen D. R., Péry A., Römbke J., Snape J., Ternes T., Topp E., Wehrhan A., Knacker T., Environmental risk assessment of human pharmaceuticals in the European Union: A case study with the  $\beta$ -blocker atenolol; *Integr. Environ. Assess. Manage.* 2010, 6, 514–523.

Article

# Insights into Adsorption of Chlorobenzene in High Silica MFI and FAU Zeolites Gained from Chromatographic and Diffractometric Techniques

Luisa Pasti <sup>1,\*</sup>, Elisa Rodeghero <sup>2</sup>, Giada Beltrami <sup>2</sup>, Matteo Ardit <sup>2</sup>, Elena Sarti <sup>1</sup>, Tatiana Chenet <sup>1</sup>, Claudia Stevanin <sup>1</sup> and Annalisa Martucci <sup>2,\*</sup> 

<sup>1</sup> Department of Chemistry and Pharmaceutical Sciences, University of Ferrara, Via L. Borsari 46, 44121 Ferrara, Italy; elena.sarti@unife.it (E.S.); tatiana.chenet@unife.it (T.C.); claudia.stevanin@unife.it (C.S.)

<sup>2</sup> Department of Physics and Earth Sciences, University of Ferrara, Via Saragat 1, 44122 Ferrara, Italy; elisa.rodeghero@unife.it (E.R.); giada.beltrami@unife.it (G.B.); rdtmtt@unife.it (M.A.)

\* Correspondence: psu@unife.it (L.P.); mrs@unife.it (A.M.); Tel.: +39-0532-455346 (L.P.); +39-0532-974730 (A.M.)

Received: 9 January 2018; Accepted: 19 February 2018; Published: 26 February 2018

**Abstract:** In this work, the capability of two commercial high silica zeolites (HSZs), namely ZSM-5 and Y, for the removal of chlorobenzene (CB) from water was investigated by combining chromatographic and diffractometric techniques. The adsorption isotherms and kinetics of CB on ZSM-5 and Y zeolites were determined from batch tests. The adsorption kinetics were very fast; the time to reach equilibrium was less than 10 min. The equilibrium data of CB on the two HSZs showed dissimilarities that are particularly evident in the adsorption data concerning the low concentration range, where Y zeolite is characterized by low adsorption. On the contrary, at higher solution concentrations the adsorption capacity of Y is higher than that of ZSM-5. The crystalline structures of Y and ZSM-5 saturated with CB were investigated by X-ray diffraction (XRD) techniques. Rietveld refinement analyses of XRD data allowed for quantitative probing of the structural modifications of both zeolites after CB adsorption and provided insight into the preferred zeolite adsorption sites in both microporous materials. The refined framework–extraframework bond distances confirm that interactions between the selected organic contaminant and hydrophobic zeolites are mediated via co-adsorbed H<sub>2</sub>O. The occurrence of H<sub>2</sub>O–CB–framework oxygen oligomers explains variations in both the unit cell parameters and the shape of the channels, clearly confirming that water plays a very relevant role in controlling the diffusion and adsorption processes in hydrophobic zeolites.

**Keywords:** chlorobenzene; sorption; ZSM-5; X-ray powder diffraction; Rietveld structure refinement; chromatography

## 1. Introduction

Industrial and agricultural discharges, chlorine disinfection by-products (DBPs) of drinking water and wastewater, and incineration of wastes are the main sources of chlorine and organochlorine compounds (OCICs), such as chlorobenzene (CB). These compounds can cause toxic effects on both human health and environmental systems, even at low concentration [1]. In particular, the Environmental Protection Agency (EPA) fixed the maximum contaminant level (MCL) of CB at 0.1 mg/L; above this threshold value CB can cause negative health effects, such as gastrointestinal irritations, hepatotoxicity and kidney damages [2]. Therefore, it is important to remove this pollutant from the environment and different methodologies have been proposed.

Actually, the physical method based on adsorption processes is a recuperative method exploited for in situ water treatments which combines high flexibility of the system, efficiency even at low

concentration levels, low energy, cheap operating costs, and possible waste reductions [3]. Different adsorbent materials can be employed, and their efficiency depends on the host-guest interactions between sorbent and sorbate [4–13]. In general, carbonaceous adsorbents are low cost materials, widely employed in remediation technology. However, their applicability can be limited by fouling that cause a pore blocking (i.e., to the presence of dissolved organic matter), to low adsorption capacity, sharp rise of bed temperature and difficulty of regeneration [14–17]. In recent years, organic contaminants removal by single-walled carbon nanotubes (SWCNTs) has attracted great interest due to their chemical, electronic and mechanical properties [18]. However, the saturation capacity of these adsorbents for OCICs is moderate and functional groups on the surface of carbonaceous adsorbents can further reduce the adsorption features [19–21]. In the past few decades, surfactant modified clays have been proposed as a potential alternative to carbonaceous adsorbents for removing OCIC pollutants. Indeed, it has been proved that these materials are efficient and they can be easily regenerated. One of the main disadvantages is their limited stability due to a progressive release of surfactant which can have a negative impact on biota [22–25]. Synthetic and hydrophobic zeolites offer an attractive and efficient option for the removal of chlorine, and organochlorine compounds from water. The main advantages are related to their high surface area and porous structure, high specific capacity and organic pollutants selectivity. Additionally, fast kinetics, mechanical, biological and chemical stability make them promising and efficient adsorbents [4,6–8,26–28]. Furthermore, their high thermal stability guarantees the possibility of regeneration through thermal treatments in order to reintroduce them in new adsorption processes [5,29–33].

This work is part of a wider study aimed at systematically evaluating the adsorptive capacity of high silica zeolites (HSZ) (e.g., mordenite, ZSM-5, faujasite, beta, ferrierite [4,7,10,29,30]) for fuel-based compounds differing in chemical properties (e.g., polarity, functional groups, size, host-guest interactions, etc.), which can provide useful information to accurately predict the behavior of HSZs as well as improve their individual performance.

The objective of this study is to evaluate the capability of two commercial HSZs, ZSM-5 (MFI topology), and Y zeolite (FAU topology) [34], for removal of chlorobenzene (CB) from water. For that purpose, the adsorption process from water was investigated in order to gain information on the interactions between the selected organic contaminant and hydrophobic zeolites. The information gathered from this work provides a tool for the selection of adsorbent materials for environmental remediation. Additionally, the investigation of host-guest interactions can provide information on the fate and transport of OCICs in the environment, and in particular for the partition of those contaminants in the mineral fraction of soils, normally constituted by aluminosilicate.

## 2. Experimental Methods

### 2.1. Materials and Methods

High-silica Y (code HSZ-390HUA, 200 SiO<sub>2</sub>/Al<sub>2</sub>O<sub>3</sub> molar ratio, 750 m<sup>2</sup>/g surface area, 0.05 wt % Na<sub>2</sub>O content) and ZSM-5 (code CBV 28014, 280 SiO<sub>2</sub>/Al<sub>2</sub>O<sub>3</sub> molar ratio, 400 m<sup>2</sup>/g surface area, 0.01 wt % Na<sub>2</sub>O content) hydrophobic zeolites were purchased in their as-synthesized form by Tosoh Corporation (Tokyo, Japan) and Zeolyst International (Conshohocken, PA, USA) respectively.

Chlorobenzene (CB) in its anhydrous form (purity of 99.8%) was provided by Sigma-Aldrich (Steinheim, Germany) and used as received.

### 2.2. Batch Adsorption

The adsorption isotherm was determined using the batch method. Batch experiments were carried out in duplicate in 20 mL crimp top reaction glass flasks sealed with PTFE septa (Supelco, Bellefonte, PA, USA). The flasks were filled in order to have the minimum headspace and a solid:solution ratio of 1:2 (mg·mL<sup>-1</sup>) was employed. After equilibration, for 24 h at a temperature of 25.3 ± 0.5 °C under



stirring, the solids were separated from the aqueous solution using centrifugation (14,000 rpm for 30 min).

The concentration of contaminants in the aqueous solution, before and after the contact with the adsorbent was determined by Headspace Gas Chromatography coupled to Mass Spectrometry (HS-GC-MS). The analysis was carried out using an Agilent GC-MS system (Santa Clara, CA, USA) consisting of a GC 6850 Series II Network coupled to a Pal G6500-CTC injector and a Mass Selective Detector 5973 Network.

HS autosampler injector conditions are: incubation oven temperature 80 °C, incubation time 50 min, headspace syringe temperature 85 °C, agitation speed 250 rpm, agitation on time 30 s, agitation off time 5 s, injection volume 500 µL, fill speed 30 µL·s<sup>-1</sup>, syringe pull-up delay 5 s, injection speed 250 µL·s<sup>-1</sup>, pre-injection delay 0 s, post injection delay 2 s, syringe flush 30 s with nitrogen. A DB-624 UI GC column (L = 20 m, I.D. = 0.18 mm, df = 1.00 µm film thickness, Agilent, Santa Clara, CA, USA) was used. High purity helium was the carrier gas with a constant flow rate of 0.7 mL·min<sup>-1</sup>. The oven temperature gradient started at 40 °C for 4 min and then ramped to 130 °C at 15 °C·min<sup>-1</sup>. The injector temperature was kept at 150 °C. All samples were injected in split mode (10:1). The mass spectrometer operated in electron impact mode (positive ion, 70 eV). The source temperature and the quadrupole temperature were set to 230 °C and 150 °C, respectively. The mass spectra were acquired in full scan mode. The electronic scan speed was 1562 amu·s<sup>-1</sup> in a mass range from 30 to 300 amu. For identification and quantification of the target analyte the SIM (selected ion monitoring) chromatograms were extracted from the acquired signal by selecting the most abundant characteristic fragments at  $m/z = 112$ . Chromatographic peak of analytes was identified by comparison of the retention time and the mass spectrum with standard compound and library data; quantitative analysis was performed using calibration curves.

### 2.3. Thermal Analyses

The Netzsch STA 409 PC LUXX<sup>®</sup> (Gerätebau, Germany) simultaneous TG/DTA thermogravimetric balance was employed in order to carry out both thermogravimetric (TG) and differential thermal analyses (DTA) on Y and ZSM-5 zeolites before and after CB loading. The measurements were performed in constant air flux conditions using a heating rate of 10 °C/min, from room temperature (RT) to 900 °C.

### 2.4. X-ray Powder Diffraction Data Collection and Refinement Strategy

X-ray diffraction patterns on powders of Y and ZSM-5 zeolites loaded with CB were carried out on a Bruker D8 Advance (Karlsruhe, Germany) diffractometer (Cu K $\alpha_{1,2}$  radiation) equipped with a Sol-X detector. Diffraction data were collected at RT, in 3°–110° 2 $\theta$  (for ZSM-5) and 3°–100° 2 $\theta$  (for Y zeolite) 2 $\theta$  ranges respectively, with a counting time of 12 s each 0.02° 2 $\theta$ . Figure S1 reported observed, calculated and difference X-ray powder diffraction patterns of Y–CB (a) and ZSM-5–CB (b), respectively.

GSAS software [35] and the EXPGUI graphical interface [36] were employed for Y–CB and ZSM-5–CB structural refinements through a full profile Rietveld analysis. Unit-cell and structural parameters were determined starting from the monoclinic  $P2_1/n$  (for ZSM-5) and the cubic  $Fd-3$  (for Y) space groups of Martucci et al. [10], and Braschi et al. [11] structural models, respectively. The Bragg peak profiles were modelled by a Pseudo-Voigt function with 0.001% cut-off peak intensity. Refined coefficients were: two Gaussian terms (i.e., the  $\tan^2\theta$  dependent GU and the  $\theta$  independent GW), and two Lorentzian terms (i.e.,  $\cos\theta^{-1}$  dependent LX,  $\tan\theta$  dependent LY), respectively. A Chebyshev polynomial function with 24 and 22 coefficients was used in order to empirically fit the instrumental background for Y and ZSM-5, respectively. In both structural refinements, scale factor, 2 $\theta$ -zero shift and unit-cell parameters were also refined. Soft constraints were initially imposed on Si–O, O–O, C–C and C–Cl bond distances (tolerance ( $\sigma$ ) value of 0.04 Å) and completely removed in the final cycles. Finally, atomic coordinates, site occupancy and isotropic atomic displacement parameters were

refined. Furthermore, the displacement parameters for a given atom type were constrained to be equivalent (i.e., Si and O sites), thus limiting the number of refined atomic displacement parameters to two. Additionally, in Y-CB  $x/a$  and  $y/b$  parameters of the chlorobenzene molecule were constrained to be equal in order to maintain the planarity. Table 1 reports the details of the data collection and Rietveld refinements. In Supplementary Materials (Tables S1 and S2, respectively) the refined atomic coordinates, occupancies and isotropic thermal parameters of Y and ZSM-5 loaded structures are reported. Extraframework atomic fractional coordinates, thermal isotropic displacement factor and occupancy of Y-CB and ZSM-5-CB are in Tables S3 and S4, respectively. Selected bond distances (Å) and angles (°) within both the Y-CB and ZSM-5-CB framework and extraframework atoms are listed in Tables S5 and S6, respectively. CIFs for all reported crystal structures are added in Supplementary Materials as supplementary information.

**Table 1.** Details of the data collection and Rietveld refinements.

Parameter	ZSM-5	ZSM-5-CB	Y	Y-CB
	[Si <sub>96</sub> O <sub>192</sub> ]	[Si <sub>96</sub> O <sub>192</sub> ].6(C <sub>6</sub> H <sub>5</sub> Cl).8(H <sub>2</sub> O)	[Si <sub>192</sub> O <sub>384</sub> ]	[Si <sub>192</sub> O <sub>384</sub> ].32(C <sub>6</sub> H <sub>5</sub> Cl).70(H <sub>2</sub> O)
Space group	<i>P</i> 2 <sub>1</sub> / <i>n</i>	<i>P</i> 2 <sub>1</sub> / <i>n</i>	<i>Fd</i> -3 <i>m</i>	<i>Fd</i> -3
<i>a</i> (Å)	19.899(5)	19.919(1)	24.259(1)	24.263(1)
<i>b</i> (Å)	20.117(6)	20.107(1)	24.259(1)	24.263(1)
<i>c</i> (Å)	13.389(4)	13.3967(1)	24.259(1)	24.263(1)
$\alpha$ (°)	90	90	90	90
$\beta$ (°)	90.546(3)	90.528(3)	90	90
$\gamma$ (°)	90	90	90	90
<i>V</i> (Å <sup>3</sup> )	5359.9(3)	5365.7(5)	14,277.1(1)	14,284.4(6)
Wavelength (Å): Cu K $\alpha$ <sub>1</sub>	1.540593	1.540593	1.540593	1.540593
Cu K $\alpha$ <sub>2</sub>	1.544427	1.544427	1.544427	1.544427
Refined 2 $\theta$ (°) range	3°–110°	3°–110°	3°–100°	3°–100°
Contributing reflections	5861	6362	620	620
<i>N</i> <sub>obs</sub>	5350	5350	4850	4850
<i>N</i> <sub>var</sub>	289	301	40	40
<i>R</i> <sub>wp</sub> (%)	10.3	13.3	12.8	12.9
<i>R</i> <sub>p</sub> (%)	9.4	10.4	12.5	12.6
<i>R</i> <sub>F</sub> <sup>2</sup> (%)	7.00	7.25	9.95	10.0

$R_p = \sum |Y_{io} - Y_{ic}| / \sum Y_{io}$ ;  $R_{wp} = [\sum w_i (Y_{io} - Y_{ic})^2 / \sum w_i Y_{io}^2]^{0.5}$ ;  $R_F^2 = \sum |F_o^2 - F_c^2| / |F_o^2|$

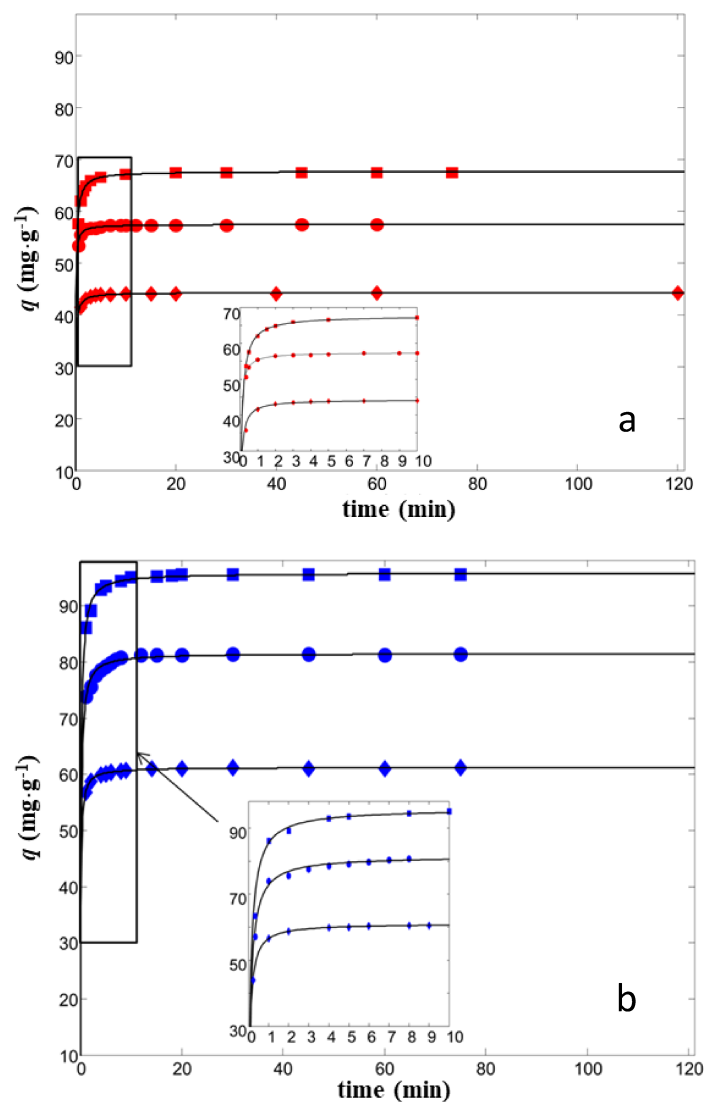
### 3. Results and Discussion

#### 3.1. Adsorption Isotherms from Aqueous Solutions

The uptake  $q$  (mg·g<sup>−1</sup>) was calculated as follows:

$$q = \frac{(C_0 - C)V}{m} \quad (1)$$

where  $C_0$  is the initial concentrations in solution (mg·L<sup>−1</sup>),  $C$  is the concentration at time  $t$  in kinetics experiments (mg·L<sup>−1</sup>),  $V$  is the solution volume (L) and  $m$  is the mass of sorbent (g). In Figure 1 the uptake data for CB on Y and ZSM-5 are reported.



**Figure 1.** Chlorobenzene (CB) uptake vs. contact time for ZSM-5 (a) and Y (b) for initial concentration of 35, 25, 15 mg/L. The insets: enlarged image of the boxed regions.

It can be seen that the kinetics of the adsorption process was very fast; the equilibrium was reached in about 10 min. Similar behaviors were also observed for the adsorption of other aqueous contaminants, such as dichloroethane and toluene onto ZSM-5 and Y zeolites [5–10,13].

We have previously verified [5–10,13] that uptake data of the investigated zeolites can be fitted by the pseudo-second order model as:

$$q_t = \frac{k_2 q_e^2 t}{1 + k_2 q_e t} \quad (2)$$

where  $q_t$  and  $q_e$  are the amounts of solute adsorbed per mass of sorbent at time  $t$  and at equilibrium, respectively, and  $k_2$  is the second-order adsorption rate constant. The values of equilibrium uptake  $q_e$  and the adsorption rate constant  $k_2$  were obtained from non-linear fit of  $q_t$  vs.  $t$  (see Table 2). Analogous to what was observed for the adsorption of other aqueous contaminants, the uptake data of CB can be modelled by a pseudo-second order kinetic model, as indicated from the high coefficient of determination.

**Table 2.** Estimated kinetics parameters (see Equation (2)). The confidence limits at 95% of probability of the estimated parameters are reported in brackets.

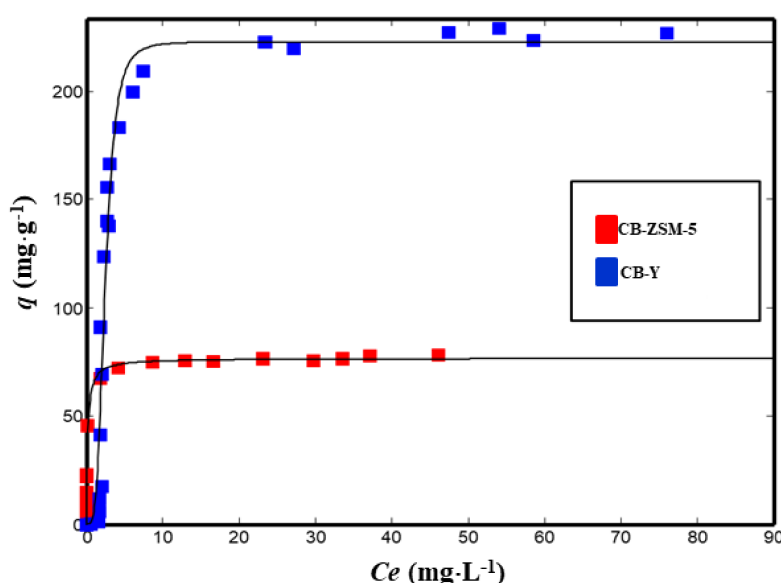
	$C_0$ (mg·L <sup>-1</sup> )	$q_t$ (mg·g <sup>-1</sup> )	$k_2$ (g·L <sup>-1</sup> ·mg <sup>-1</sup> )	$R^2$
ZSM-5	15	23.4 (23.3, 23.5)	0.44 (0.41, 0.47)	0.9845
	25	44.3 (44.2, 44.3)	0.37 (0.33, 0.41)	0.9803
	35	67.6 (67.5, 67.6)	0.21 (0.19, 0.23)	0.9985
Y	25	39.3 (39.2, 39.4)	0.14 (0.11, 0.17)	0.9822
	35	70.3 (70.2, 70.3)	0.13 (0.11, 0.15)	0.9969
	45	82.3 (82.4, 82.5)	0.10 (0.085, 0.12)	0.9935

Furthermore, for the adsorption of CB it can be noted that the kinetic constant decreases by increasing the initial concentration [37], and that the adsorption onto Y zeolites is characterized by a lower kinetic constant than that found for ZSM-5. These findings allow us to generalize the difference observed in the adsorption kinetics of these two zeolites. In particular, the adsorption kinetics of neutral organic molecules (namely, toluene, dichloroethane, methyl tert-butylether and CB), which differ from each other in physicochemical properties and molecular dimensions, is faster on ZSM-5 than on Y zeolite.

It has been already shown that adsorption of organics in aqueous solutions onto ZSM-5 hydrophobic zeolites are well fitted by the Langmuir equation [5,6,8,13], that assumes monolayer adsorption onto energetically equivalent adsorption sites and negligible sorbate–sorbate interactions. The relationships describing the Langmuir isotherm is [38]:

$$q = \frac{q_s b C_e}{1 + b C_e} \quad (3)$$

where  $b$  is the binding constant (L·mg<sup>-1</sup>) and  $q_s$  is the saturation capacity of the adsorbent material (mg·g<sup>-1</sup>). The experimental data obtained for the adsorption of CB on both ZSM-5 and Y are shown in Figure 2. It can be observed that the isotherms are shaped differently from each other; they can be classified as concave (Type I) and sigmoidal (Type V) isotherms, respectively.



**Figure 2.** Adsorption isotherms of CB for ZSM-5 (red squares) and Y (blue squares).

Similar differences in the adsorption of polar organic compound from aqueous solution onto ZSM-5 and Y were also observed for methyl tert-butylether and toluene. In such cases, a Hill isotherm model was employed:

$$q_e = q_s \frac{c_e^n}{K_H + c_e^n} \quad (4)$$

where  $K_H$  is the Hill constant, and  $n$  is the Hill coefficient which is related to the degree of cooperativity. The Hill isotherm is often employed to describe cooperative adsorption in biological systems, and it has also been used to model adsorption data on zeolites due to evidence of the presence of water-organic compound clusters [39] inside the zeolite frameworks. Since the tendency to form clusters increases by increasing the porosity dimensions, the clusters are more probably formed in the large cage of Y than in the channel system of ZSM-5 [40]. To evaluate if clusters can be formed for CB, a structural investigation was carried out (vide infra).

In Table 3, the isotherm parameters for ZSM-5 and Y estimated by non linear fitting of Equations (3) and (4) respectively, are reported. It can be seen that the saturation capacity of these zeolites are higher than those obtained with graphite materials (i.e., 28.3 mg/g for dichlorobenzene) [41], and in particular Y zeolite has a saturation value higher than adsorbents single-walled carbon nanotubes, especially if they are partially oxidized [42]. In addition HSZs can be regenerated without significant loss of their adsorption properties [5,6,29,30]. Therefore hydrophobic zeolites are very promising adsorbents for the removal of chlorinated aromatic compounds from water.

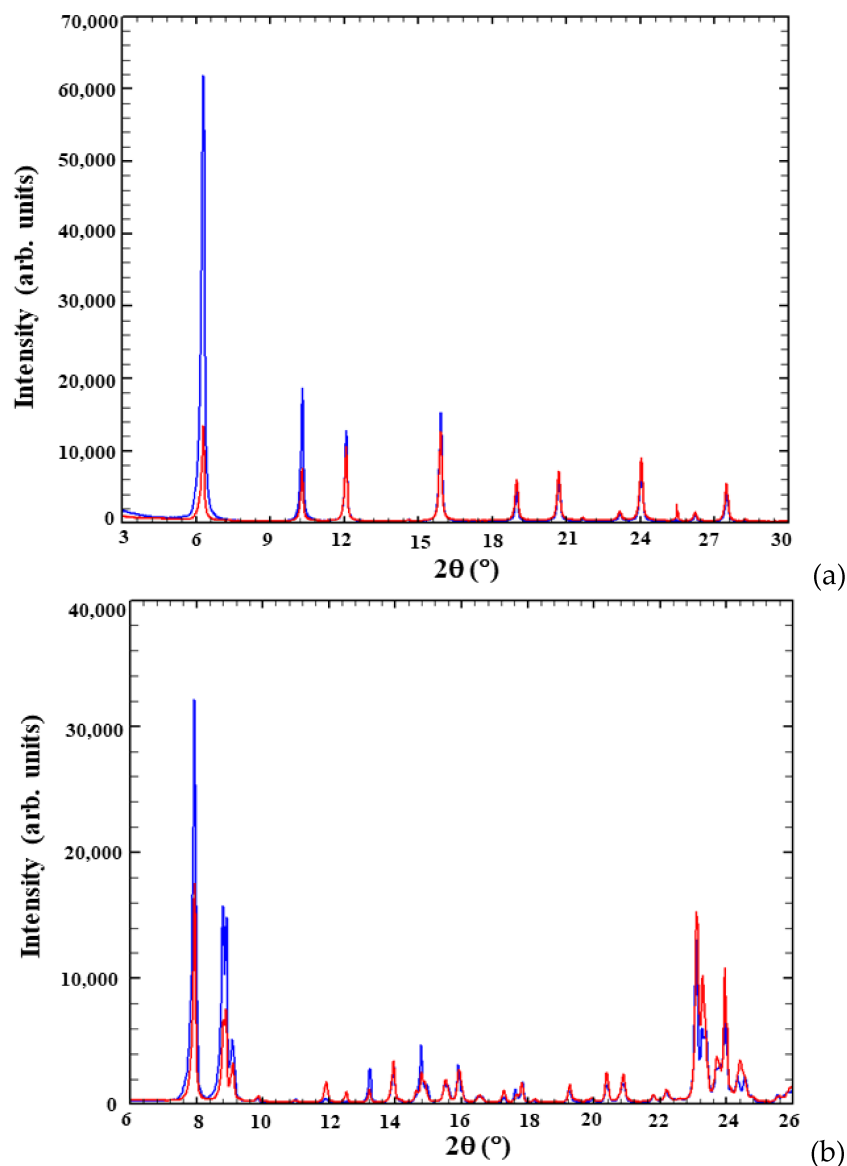
**Table 3.** Isotherm parameters for the adsorption of CB on ZSM-5 and Y. SSE: sum of squared errors.

			$R^2$	SSE
Langmuir				
CB-ZSM-5	$q_s$	76.6 (74.8, 79.5)	0.9874	198
	$b$	5.0 (3.7, 6.6)		
Hill				
CB-Y	$q_s$	227 (218, 245)	0.9654	2135
	$K_H$	9.2 (6.6, 12.1)		
	$n$	5.5 (4.3, 6.7)		

### 3.2. Structural Modifications upon Chlorobenzene Adsorption on High Silica Zeolites

#### 3.2.1. Y-CB

Y zeolite (FAU framework topology [34]) is built up of large cavities ( $\alpha$  cages or supercages) with a diameter of 12 Å linked to four other supercages through 12 membered-ring windows (diameter of 7.4 Å) and cuboctahedral  $\beta$  cages connected each other through double hexagonal rings (D6R). Topological symmetry of the unloaded material is cubic  $Fd-3m$ , but it has been highlighted that the embedding of organic compounds can decrease the symmetry to  $Fd-3$  [10–13,43]. A careful examination of powder diffraction patterns after chlorobenzene adsorption highlights that Y-CB peak positions are quite similar to those of the as-synthesized material in all the  $2\theta$  range investigated. Contrariwise, peak intensities strongly decrease after pollutant incorporation, especially at low  $2\theta$  angles (Figure 3).



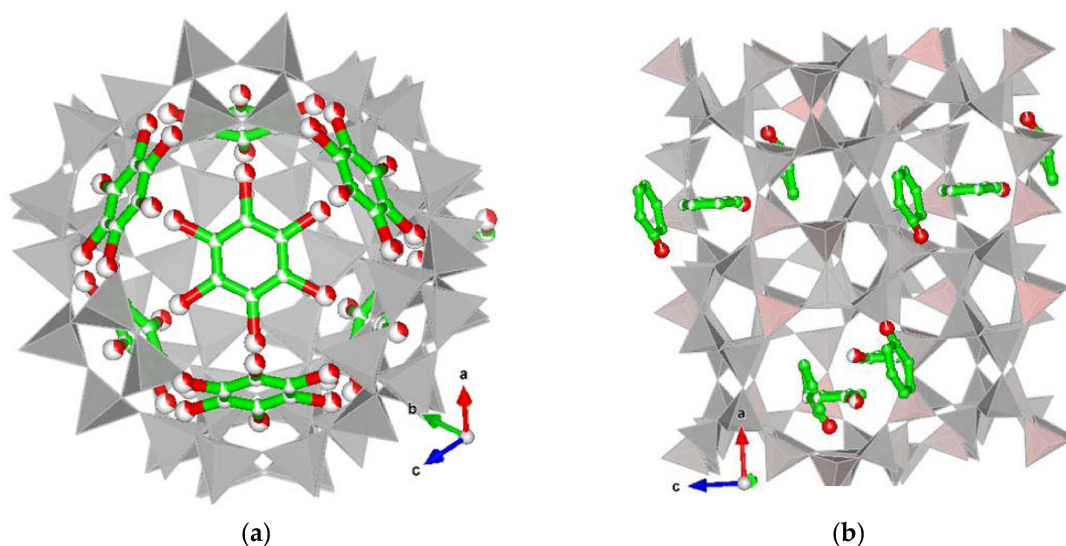
**Figure 3.** Observed powder diffraction patterns of Y-CB (a) and ZSM-5-CB (b), respectively, showing differences both in intensity and position of the diffraction peaks in the low and intermediate  $2\theta$  regions. Blue lines represent the unloaded samples, red lines the loaded ones.

These differences suggest variations in the extraframework species content as well as in the lattice parameters (Table 1), thus attesting to CB adsorption into the porous structure of the zeolite. After adsorption, the T1–O and T2–O mean distances are 1.621 and 1.620 Å, respectively, the O–T–O angles range from 103.3° to 112.3° (Table S5). The T–O–T bond angles adopt a wide range of values from 125° to 171° (mean value = 142°). The T–O, T–O–T and O–T–O grand mean values (Table S5) are in high agreement with those reported for other pure silica zeolites (PSZ) [44]. Furthermore, after adsorption the channel ellipticity  $\varepsilon$  (defined as the ratio between the smaller and larger O–O “free diameters” of the 12-rings) changed ( $\varepsilon = 1.02$  in Y,  $\varepsilon = 1.21$  in Y-CB) and at the same time, the openings reached a wider Crystallographic Free Area (C.F.A., sensu Baerlocher [34]) when compared with the as-synthesised material (Table 4), thus confirming the high flexibility of FAU-type materials [45,46].

**Table 4.** Crystallographic Free Area and ellipticity ( $\epsilon$ ) comparison between unloaded Y [11] and Y-CB systems. C.F.A. =  $\pi \cdot (\text{mean radius})^2$  ( $\text{\AA}^2$ );  $\epsilon$  = ratio between the longest and the shortest pore dimensions.

Parameter	Y-CB	Y [11]
O4–O4 distance ( $\text{\AA}$ )	11.16	9.81
O1–O1 distance ( $\text{\AA}$ )	9.68	9.70
Free diameter O4–O4 ( $\text{\AA}$ )	8.46	7.11
Free diameter O1–O1 ( $\text{\AA}$ )	6.98	7.00
Mean diameter ( $\text{\AA}$ )	7.72	7.06
Mean radius ( $\text{\AA}$ )	3.86	3.53
C.F.A. ( $\text{\AA}^2$ )	46.81	39.07
$\epsilon$	1.21	1.01

Rietveld structural refinement allows us to detect 32 CB molecules per unit cell (corresponding to ~22.0% dry weight, dw %) located within the Y supercage (Figure 4a). Chlorobenzene molecules occupy one crystallographic independent and partially occupied site (C and Cl atoms in Table S3), and statistically can assume six different orientations (Figure 4a).

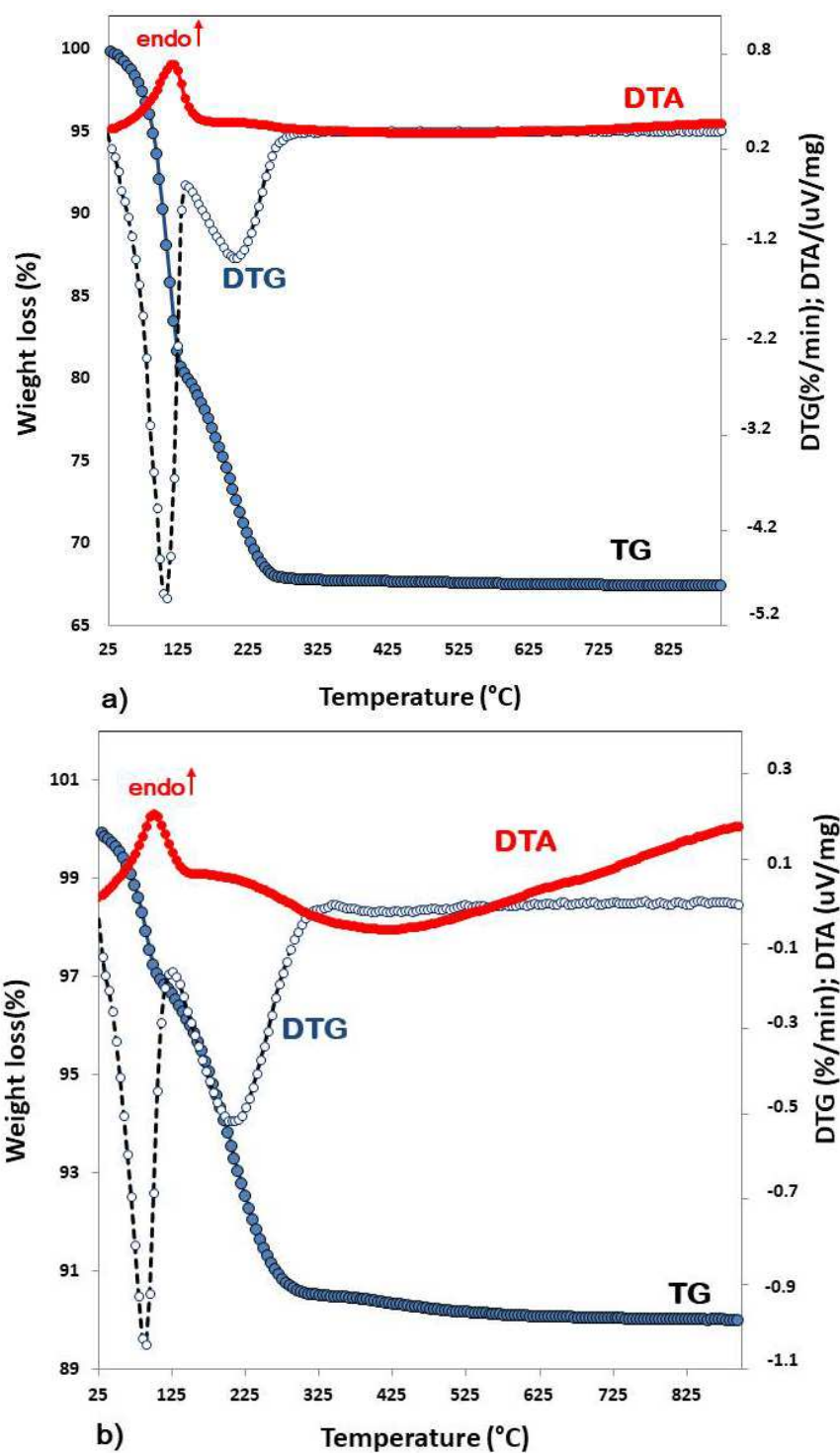


**Figure 4.** Distribution of CB molecules in Y (a) and ZSM-5 (b) zeolites, respectively. Chlorine (red circle) and carbon (green circle) are shown. Drawings produced by VESTA 3 [47].

Moreover, the evidence of relatively short Cl–O1 bond distances (i.e., Cl–O1 = 2.723(1)  $\text{\AA}$  and 2.680  $\text{\AA}$ , respectively) proves that chlorobenzene directly interacts with framework oxygens.

Furthermore, difference-Fourier maps of the electron density analysis revealed the presence of co-adsorbed  $\text{H}_2\text{O}$  molecules hosted in three additional extraframework sites (W1, W2 and W3 sites, respectively, Table S3). Additionally, based on the W sites refined distance these sites interact with both each other and chlorine atoms forming oligomers (W2–W2 = 2.93  $\text{\AA}$ , W3–Cl = 3.21  $\text{\AA}$  and W1–W2 = 2.93 and 2.74  $\text{\AA}$ , respectively) that strongly interact with the framework oxygen atoms via chlorine (Figure 4a). According to the recent literature [5–8,10–13,29,44], the strong interactions among organic molecules– $\text{H}_2\text{O}$  short chain-frameworks play a relevant role in stabilizing the guest structures within the zeolite porosity.

On a whole, on the basis of Rietveld refinement 70  $\text{H}_2\text{O}$  molecules (~8% dw %) were detected in good agreement with the TG curve (Figure 5a), which shows two main weight losses: the first one (about 7.3 dw % zeolite, 25–110  $^\circ\text{C}$ ) is related to desorption of species retained on the surface, the second one (23.5 dw % zeolite, 110–900  $^\circ\text{C}$ ) to the removal from the structure of loaded CB and  $\text{H}_2\text{O}$  molecules.



**Figure 5.** Thermal analysis of Y (a) and ZSM-5 (b) loaded with chlorobenzene from room temperature to 900 °C. In blue and gray circles, the total weight loss curve (TG) and the derivative of it (DTG); in red the differential thermal analysis (DTA) curve.

### 3.2.2. ZSM-5-CB

The ZSM-5 zeolite framework consists of two intersecting channel systems: a straight channel parallel to [010] direction and a sinusoidal one parallel to [100] direction [34]. Both channels are limited by 10MR of  $\text{TO}_4$  tetrahedra with free diameters of 5.4–5.6 Å and 5.1–5.5 Å for sinusoidal and straight channel, respectively. After CB adsorption, the evolution of the powder diffraction pattern



indicates that ZSM-5 maintains its crystallinity as well as the monoclinic  $P2_1/n$  symmetry. In Table 1, the comparison between refined lattice parameters of starting material and of the ZSM-5–CB system highlights the occurrence of chlorobenzene adsorption in the ZSM-5 micropores. The structural characterization was carried out starting with the model proposed by Rodeghero et al. [6] and an examination of the difference Fourier maps of the electron density suggested the presence of extraframework content. In detail, some of recognized maxima were reasonably attributed to chlorobenzene adsorption sites in both the sinusoidal channel (CB2 sites) and the intersection between sinusoidal and straight channels (CB1 sites) (Table S4, Figure 4b). On the whole, a total amount of about 6 molecules per unit cell (p.u.c.) of organics were detected. Besides, residual maxima of difference Fourier maps also indicate the presence of co-adsorbed H<sub>2</sub>O molecules (~1.5 dw %) hosted at W1 and W2 sites. In particular, based on the refined distances between the extraframework content and framework oxygen atoms strong interactions among chlorobenzene molecules hosted in both adsorption sites (CB1 and CB2), H<sub>2</sub>O molecules (W1 and W2 sites), and framework oxygen atoms occur (i.e., O4–C10 = 3.01(1) Å, O18–C9 = 2.61(1) Å, O31–C11 = 2.69(1) Å, O47–C11 = 2.99(1) Å, W2–W2 = 3.15(1) Å, O26–C12 = 3.03(3) Å, W1–C1 = 3.16(3) Å) (Figure 4b and Table S6). Additionally, thermogravimetric analysis (Figure 5b) indicated that relevant weight loss, occurring at temperatures higher than 100 °C (7% in weight), is due to the expulsion from the structure of extraframework ions embedded in the ZSM-5 channels. The residual one at lower temperature can be ascribed to the expulsion of water and/or CB molecules bonded to the surface (3% in weight below ~100 °C).

These results are quite well supported by the total amount of adsorbed molecules detected through both saturation capacity determined by the adsorption isotherm and the results obtained by Rietveld analysis. After adsorption, the T–O bond length ranges from 1.602 to 1.608 Å, the O–T–O angles varies from 96° to 125°, with a mean value of 109.4° (Table S6). According to Wragg et al. [44] the T–O–T bond angles adopt a wide range of values from 124° to 178° (Table S6). Regarding the channel geometry, after organics adsorption, any changes in both shape and channel dimension were also evaluated. Specifically, both straight and sinusoidal channels hosting the organic molecules change their shape and become more elliptical (Table 5).

**Table 5.** C.F.A. and ellipticity ( $\epsilon$ ) comparison between unloaded ZSM-5 [13] and ZSM-5–CB systems. C.F.A. =  $\pi \cdot (\text{mean radius})^2$  ( $\text{\AA}^2$ );  $\epsilon$  = ratio between the longest and the shortest pore dimensions.

Straight Channel						
O–O distance ( $\text{\AA}$ )	O7–O1	O8–O2	O31–O37	O44–O46	O47–O48	$\epsilon$
ZSM-5–CB	8.22	8.20	8.02	8.22	7.97	1.03
ZSM-5	7.90	7.94	8.04	8.41	7.80	1.08
Free diameter ( $\text{\AA}$ )	O7–O1	O8–O2	O31–O37	O44–O46	O47–O48	
ZSM-5–CB	5.52	5.50	5.32	5.52	5.27	-
ZSM-5	5.20	5.24	5.34	5.71	5.10	-
	Mean diameter ( $\text{\AA}$ )	Mean radius ( $\text{\AA}$ )	C.F.A. ( $\text{\AA}^2$ )			
ZSM-5–CB	5.43	2.71	23.12	-		
ZSM-5	5.32	2.66	22.20	-		
O–O distance ( $\text{\AA}$ )	O11–O5	O20–O18	O21–O22	O27–O33	O28–O34	$\epsilon$
ZSM-5–CB	8.08	7.89	8.11	8.22	8.08	1.04
ZSM-5	8.19	8.35	7.98	8.13	7.76	1.08
Free diameter ( $\text{\AA}$ )	O11–O5	O20–O18	O21–O22	O27–O33	O28–O34	
ZSM-5–CB	5.38	5.19	5.41	5.52	5.38	
ZSM-5	5.49	5.65	5.28	5.43	5.06	
	Mean diameter ( $\text{\AA}$ )	Mean radius ( $\text{\AA}$ )	C.F.A. ( $\text{\AA}^2$ )			
ZSM-5–CB	5.37	2.69	22.67			
ZSM-5	5.38	2.69	22.74			
Sinusoidal Channel						
O–O distance ( $\text{\AA}$ )	O20–O15	O24–O26	O27–O2	O28–O1	O41–O46	$\epsilon$
ZSM-5–CB	8.08	7.87	7.76	8.16	8.69	1.12
ZSM-5	8.15	8.07	7.97	7.76	8.51	1.10
Free diameter ( $\text{\AA}$ )	O20–O15	O24–O26	O27–O2	O28–O1	O41–O46	
ZSM-5–CB	5.38	5.17	5.06	5.46	5.99	
ZSM-5	5.45	5.37	5.27	5.06	5.81	
	Mean diameter ( $\text{\AA}$ )	Mean radius ( $\text{\AA}$ )	C.F.A. ( $\text{\AA}^2$ )			
ZSM-5–CB	5.41	2.71	23.01			
ZSM-5	5.39	2.70	22.82			
O–O distance ( $\text{\AA}$ )	O17–O18	O23–O25	O30–O5	O31–O4	O44–O43	$\epsilon$
ZSM-5–CB	7.50	8.58	8.20	7.89	7.75	1.14
ZSM-5	7.30	8.31	8.32	8.05	7.95	1.14
Free diameter ( $\text{\AA}$ )	O17–O18	O23–O25	O30–O5	O31–O4	O44–O43	
ZSM-5–CB	4.80	5.88	5.50	5.19	5.05	
ZSM-5	4.60	5.61	5.62	5.35	5.25	
	Mean diameter ( $\text{\AA}$ )	Mean radius ( $\text{\AA}$ )	C.F.A. ( $\text{\AA}^2$ )			
ZSM-5–CB	5.28	2.64	21.92			
ZSM-5	5.29	2.64	21.93			

#### 4. Conclusions

This work aims to highlight the adsorptive capacity of commercial high silica zeolites ZSM-5 (MFI topology), and Y zeolite (FAU topology), for removal of chlorobenzene (CB) from water. Both high silica ZSM-5 and Y zeolites are characterized by fast kinetics, that combined with good adsorption capacity, suggest they can be efficiently used as a sorbent media to control the concentration of chlorobenzene in water systems. In particular, ZSM-5 is more efficient in the removal of CB at low concentration level, while Y shows higher saturation capacity than ZSM-5. Difference Fourier maps of the electron density provide insight into the preferred zeolite adsorption sites in both microporous materials. The refined framework–extraframework bond distances highlight the existence of CB, and hydrophobic zeolites interactions mediated via co-adsorbed H<sub>2</sub>O molecules. Adsorption of CB on ZSM-5 and Y zeolites is accompanied by structural changes, i.e. variations in both unit-cell parameters and channel shape when compared to the as-synthesized microporous materials, clearly confirming the very relevant role of H<sub>2</sub>O molecules in both the diffusion and adsorption processes in hydrophobic zeolites. After adsorption, the channels become more distorted, thus indicating remarkable framework flexibility for both ZSM-5 and Y zeolites.

**Supplementary Materials:** The following are available online at [www.mdpi.com/2075-163x/8/3/80/s1](http://www.mdpi.com/2075-163x/8/3/80/s1), Figure S1: Observed (dotted line), calculated (solid line) and difference (bottom) X-ray powder diffraction patterns of Y–CB (a) and ZSM-5–CB (b), respectively, Table S1: Framework atomic fractional coordinates and thermal isotropic displacement factor of Y–CB, Table S2: Framework atomic fractional coordinates and thermal isotropic displacement factor of ZSM-5–CB, Table S3: Extraframework atomic fractional coordinates, thermal isotropic displacement factor and occupancy of Y–CB, Table S4: Extraframework atomic fractional coordinates, thermal isotropic displacement factor and occupancy of ZSM-5–CB; *x/a* atomic fractional coordinates of CB2 molecule atoms have exactly the same values, in order to maintain the molecule planarity, Table S5: Selected bond distances (Å) and angles (°) within both the Y–CB framework and extraframework atoms at  $T_{amb}$ , Table S6: Selected bond distances (Å) and angles (°) within both the ZSM-5–CB framework and extraframework atoms at  $T_{amb}$ . CIFs for all reported crystal structures are added as Supplementary Information.

**Acknowledgments:** The authors thank the Italian University and Scientific Research Ministry (Grant PRIN Prot. 2015HK93L7), the Istituto ENI Donegani-Environmental Technologies (Novara, Italy) and the Laboratory Terra&Acqua Tech, Technopole of Ferrara of Emilia-Romagna High Technology Network for their financial support.

**Author Contributions:** The manuscript was written with contributions from all authors. All authors have given approval to the final version of the manuscript. Annalisa Martucci wrote the paper and performed the X-ray and chromatographic experiments with Luisa Pasti; Elisa Rodeghero, Giada Beltrami and Matteo Ardit conceived and designed the XRD experiments and analyzed the data; Elena Sarti, Tatiana Chenet and Claudia Stevanin conceived and designed the adsorption experiments and analyzed the data.

**Conflicts of Interest:** The authors declare no conflict of interest.

#### References

1. Sennour, R.; Mimane, G.; Benghalem, A.; Taleb, S. Removal of the persistent pollutant chlorobenzene by adsorption onto activated montmorillonite. *Appl. Clay Sci.* **2009**, *43*, 503–506. [[CrossRef](#)]
2. McClenny, W.A.; Oliver, K.D.; Jacumin, H.H., Jr.; Daughtrey, E.H., Jr. Ambient level volatile organic compound (VOC) monitoring using solid adsorbents—Recent US EPA studies. *J. Environ. Monitor.* **2002**, *4*, 695–705. [[CrossRef](#)]
3. Khan, F.I.; Ghoshal, A.K. Removal of Volatile Organic Compounds from polluted air. *J. Prevent. Proc.* **2000**, *13*, 527–545. [[CrossRef](#)]
4. Sarti, E.; Chenet, T.; Pasti, L.; Cavazzini, A.; Rodeghero, E.; Martucci, A. Effect of silica alumina ratio and thermal treatment of beta zeolites on the adsorption of toluene from aqueous solutions. *Minerals* **2017**, *7*, 22. [[CrossRef](#)]
5. Rodeghero, E.; Pasti, L.; Sarti, E.; Cruciani, G.; Bagatin, R.; Martucci, A. Temperature-induced desorption of methyl tert-butyl ether confined on ZSM-5: An in situ synchrotron XRD powder diffraction study. *Minerals* **2017**, *7*, 34. [[CrossRef](#)]

6. Rodeghero, E.; Martucci, A.; Cruciani, G.; Bagatin, R.; Sarti, E.; Bosi, V.; Pasti, L. Kinetics and dynamic behaviour of toluene desorption from ZSM-5 using in situ high-temperature synchrotron powder X-ray diffraction and chromatographic techniques. *Catal. Today* **2016**, *227*, 118–125. [[CrossRef](#)]
7. Arletti, R.; Martucci, A.; Alberti, A.; Pasti, L.; Nassi, M.; Bagatin, R. Location of MTBE and toluene in the channel system of the zeolite mordenite: Adsorption and host–guest interactions. *J. Solid State Chem.* **2012**, *194*, 135–142. [[CrossRef](#)]
8. Pasti, L.; Rodeghero, E.; Sarti, E.; Bosi, V.; Cavazzini, A.; Bagatin, R.; Martucci, A. Competitive adsorption of VOCs from binary aqueous mixtures on zeolite ZSM-5. *RSC Adv.* **2016**, *6*, 54544–54552. [[CrossRef](#)]
9. Pasti, L.; Sarti, E.; Cavazzini, A.; Marchetti, N.; Dondi, F.; Martucci, A. Factors affecting drug adsorption on beta zeolites. *J. Sep. Sci.* **2013**, *36*, 1604–1611. [[CrossRef](#)] [[PubMed](#)]
10. Martucci, A.; Pasti, L.; Marchetti, N.; Cavazzini, A.; Dondi, F.; Alberti, A. Adsorption of pharmaceuticals from aqueous solutions on synthetic zeolites. *Micropor. Mesopor. Mat.* **2012**, *148*, 174–183. [[CrossRef](#)]
11. Braschi, I.; Blasioli, S.; Gigli, L.; Gessa, C.E.; Alberti, A.; Martucci, A. Removal of sulfonamide antibiotics from water: Evidence of adsorption into an organophilic zeolite Y by its structural modifications. *J. Hazard. Mater.* **2010**, *17*, 218–225. [[CrossRef](#)] [[PubMed](#)]
12. Blasioli, S.; Martucci, A.; Paul, G.; Gigli, L.; Cossi, M.; Johnston, C.T.; Marchese, L.; Braschi, I. Removal of sulfamethoxazole sulfonamide antibiotic from water by high silica zeolites: A study of the involved host–guest interactions by a combined structural, spectroscopic, and computational approach. *J. Colloid Interf. Sci.* **2014**, *419*, 148–159. [[CrossRef](#)] [[PubMed](#)]
13. Pasti, L.; Martucci, A.; Nassi, M.; Cavazzini, A.; Alberti, A.; Bagatin, R. The role of water in DCE adsorption from aqueous solutions onto hydrophobic zeolites. *Micropor. Mesopor. Mat.* **2012**, *160*, 182–193. [[CrossRef](#)]
14. Guo, Y.; Li, Y.; Zhu, T.; Ye, M.; Wang, X. Adsorption of SO<sub>2</sub> and chlorobenzene on activated carbon. *Adsorpt.* **2013**, *19*, 1109–1116. [[CrossRef](#)]
15. Crisafulli, R.; Milhome, M.A.L.; Cavalcante, R.M.; Silveira, E.R.; De Keukeleire, D.; Nascimento, R.F. Removal of some polycyclic aromatic hydrocarbons from petrochemical wastewater using low-cost adsorbents of natural origin. *Bioresour. Technol.* **2008**, *99*, 4515–4519. [[CrossRef](#)] [[PubMed](#)]
16. Kim, B.K.; Ryu, S.K.; Kim, B.J.; Park, S.J. Roles of Acid-Base Interactions in Hydrogen Chloride Removal by Activated Carbon Fibers. *J. Ind. Eng. Chem.* **2006**, *12*, 121–126.
17. Park, S.J.; Kim, B.J. Influence of oxygen plasma treatment on hydrogen chloride removal of activated carbon fibers. *J. Colloid Interf. Sci.* **2004**, *275*, 590–595. [[CrossRef](#)] [[PubMed](#)]
18. Chin, C.J.M.; Shih, M.W.; Tsai, H.J. Adsorption of nonpolar benzene derivatives on single-walled carbon nanotubes. *Appl. Surf. Sci.* **2010**, *256*, 6035–6039. [[CrossRef](#)]
19. Long, C.; Li, Q.; Li, Y.; Liu, Y.; Li, A.; Zhang, Q. Adsorption characteristics of benzene–chlorobenzene vapor on hypercrosslinked polystyrene adsorbent and a pilot-scale application study. *Chem. Eng. J.* **2010**, *160*, 723–728. [[CrossRef](#)]
20. Chen, W.; Duan, L.; Zhu, D. Adsorption of polar and nonpolar organic chemicals to carbon nanotubes. *Environ. Sci. Technol.* **2007**, *41*, 8295–8300. [[CrossRef](#)] [[PubMed](#)]
21. Balamurugan, K.; Subramanian, V. Adsorption of chlorobenzene onto (5,5) armchair single-walled Carbon nanotube and graphene sheet: Toxicity versus adsorption strength. *J. Phys. Chem. C* **2013**, *117*, 21217–21227. [[CrossRef](#)]
22. Lee, J.J.; Choi, J.; Park, J.W. Simultaneous sorption of lead and chlorobenzene by organobentonite. *Chemosphere* **2002**, *49*, 1309–1315. [[CrossRef](#)]
23. Witthuhn, B.; Klauth, P.; Pernyeszi, T.; Vereecken, H.; Klumpp, E. Organoclays for Aquifer Bioremediation: Adsorption of Chlorobenzene on Organoclays and its Degradation by RHODOCOCCUS B528. *Water Air Soil Poll. Focus* **2006**, *6*, 317–329. [[CrossRef](#)]
24. Jarraya, I.; Fourmentin, S.; Benzina, M.; Bouaziz, S. VOC adsorption on raw and modified clay materials. *Chem. Geol.* **2010**, *275*, 1–8. [[CrossRef](#)]
25. Altare, C.R.; Bowman, R.S.; Katz, L.E.; Kinney, K.A.; Sullivan, E.J. Regeneration and long-term stability of surfactant-modified zeolite for removal of volatile organic compounds from produced water. *Micropor. Mesopor. Mat.* **2007**, *105*, 305–316. [[CrossRef](#)]
26. Anderson, M.A. Removal of MTBE and Other Organic Contaminants from Water by Sorption to High Silica Zeolites. *Environ. Sci. Technol.* **2000**, *34*, 725–727. [[CrossRef](#)]

27. Damjanović, L.; Rakić, V.; Rac, V.; Stošić, D.; Auroux, A. The investigation of phenol removal from aqueous solutions by zeolites as solid adsorbents. *J. Hazard. Mat.* **2010**, *184*, 477–484. [[CrossRef](#)] [[PubMed](#)]
28. Perego, C.; Bagatin, R.; Tagliabue, M.; Vignola, R. Zeolites and related mesoporous materials for multi-talented environmental solutions. *Micropor. Mesopor. Mat.* **2013**, *166*, 37–49. [[CrossRef](#)]
29. Leardini, L.; Martucci, A.; Braschi, I.; Blasioli, S.; Quartieri, S. Regeneration of high-silica zeolites after sulfamethoxazole antibiotic adsorption: A combined in situ high-temperature synchrotron X-ray powder diffraction and thermal degradation study. *Mineral. Mag.* **2014**, *78*, 1141–1160. [[CrossRef](#)]
30. Braschi, I.; Blasioli, S.; Buscaroli, E.; Montecchio, D.; Martucci, A. Physicochemical regeneration of high silica zeolite Y used to clean-up water polluted with sulfonamide antibiotics. *J. Environ. Sci.* **2016**, *43*, 302–312. [[CrossRef](#)] [[PubMed](#)]
31. Vignola, R.; Cova, U.; Fabiani, F.; Sbardellati, T.; Sisto, R.; Vignola, R. Process for the regeneration of nonpolar adsorbing zeolites used for the treatment of contaminated water. Patent WO/2009/000429, 31 December 2008.
32. Alberti, A.; Martucci, A. Phase transformations and structural modifications induced by heating in microporous materials. *Stud. Surf. Sci. Catal.* **2005**, *155*, 19–43. [[CrossRef](#)]
33. Alberti, A.; Martucci, A. Reconstructive phase transitions in microporous materials: Rules and factors affecting them. *Micropor. Mesopor. Mat.* **2011**, *141*, 192–198. [[CrossRef](#)]
34. Baerlocher, C.; McCusker, L.B.; Olson, D.H. *Atlas of Zeolite Framework Types*, 6th ed.; Elsevier: Amsterdam, The Netherlands, 2007.
35. Larson, A.C.; Von Dreele, R.B. *GSAS General Structure Analysis System, LANSCE, MS-H805*; Los Alamos National Laboratory: Los Alamos, NM, USA, 1994.
36. Toby, B.H. EXPGUI, a graphical user interface for GSAS. *J. Appl. Crystallogr.* **2001**, *34*, 210–213. [[CrossRef](#)]
37. Azizian, S.; Haerifar, M.; Bashiri, H. Adsorption of methyl violet onto granular activated carbon: Equilibrium, kinetics and modeling. *Chem. Eng. J.* **2009**, *146*, 36–41. [[CrossRef](#)]
38. De Moor, B.A.; Reyniers, M.F.; Gobin, O.C.; Lercher, J.A.; Marin, G.B. Adsorption of C2–C8 *n*-Alkanes in Zeolites. *J. Phys. Chem. C* **2011**, *115*, 1204–1219. [[CrossRef](#)]
39. Martucci, A.; Braschi, I.; Bisio, C.; Sarti, E.; Rodeghero, E.; Bagatin, R.; Pasti, L. Influence of water on the retention of methyl tertiary-butyl ether by high silica ZSM-5 and Y zeolites: A multidisciplinary study on the adsorption from liquid and gas phase. *RSC Advances* **2015**, *5*, 86997–87006. [[CrossRef](#)]
40. Martucci, A.; Braschi, I.; Marchese, L.; Quartieri, S. Recent advances in clean-up strategies of waters polluted with sulfonamide antibiotics: A review of sorbents and related properties. *Mineral. Mag.* **2014**, *78*, 1115–1140. [[CrossRef](#)]
41. Li, X.; Chen, G.H. Surface modified graphite nanosheets used as adsorbent to remove 1,2-dichlorobenzene from water. *Mater. Lett.* **2009**, *63*, 930–932. [[CrossRef](#)]
42. Yu, F.; Ma, J.; Wu, Y. Adsorption of toluene, ethylbenzene and *m*-xylene on multi-walled carbon nanotubes with different oxygen contents from aqueous solutions. *J. Hazard. Mater.* **2011**, *192*, 1370–1379. [[CrossRef](#)] [[PubMed](#)]
43. Krishna, R.; van Baten, J.M. Highlighting a Variety of Unusual Characteristics of Adsorption and Diffusion in Microporous Materials Induced by Clustering of Guest Molecules. *Langmuir* **2010**, *26*, 8450–8463. [[CrossRef](#)] [[PubMed](#)]
44. Wragg, D.S.; Morris, R.E.; Burton, A.W. Pure silica zeolite-type frameworks: A structural analysis. *Chem. Mater.* **2008**, *20*, 1561–1570. [[CrossRef](#)]
45. Leardini, L.; Martucci, A.; Alberti, A.; Cruciani, G. Template burning effects on stability and boron coordination in boron lewyne studied by in situ time resolved synchrotron powder diffraction. *Micropor. Mesopor. Mater.* **2013**, *167*, 117–126. [[CrossRef](#)]
46. Baur, W.H. Self-limiting distortion by antirotating hinges is the principle of flexible but noncollapsible frameworks. *J. Solid State Chem.* **1992**, *97*, 243–247. [[CrossRef](#)]
47. Momma, K.; Izumi, F. VESTA 3 for three-dimensional visualization of crystal, volumetric and morphology data. *J. Appl. Crystallogr.* **2011**, *44*, 1272–1276. [[CrossRef](#)]



# Supplementary Materials: Insights into Adsorption of Chlorobenzene in High Silica MFI and FAU Zeolites Gained from Chromatographic and Diffractometric Techniques

Luisa Pasti, Elisa Rodeghero, Giada Beltrami, Matteo Ardit, Elena Sarti, Tatiana Chenet, Claudia Stevanin and Annalisa Martucci

**Figure S1.** Observed (dotted line), calculated (solid line) and difference (bottom) X-ray powder diffraction patterns of Y-CB (a) and ZSM-5-CB (b), respectively.

**Table S1.** Framework atomic fractional coordinates and thermal isotropic displacement factor of Y-CB.

**Table S2.** Framework atomic fractional coordinates and thermal isotropic displacement factor of ZSM-5-CB.

**Table S3.** Extraframework atomic fractional coordinates, thermal isotropic displacement factor and occupancy of Y-CB.

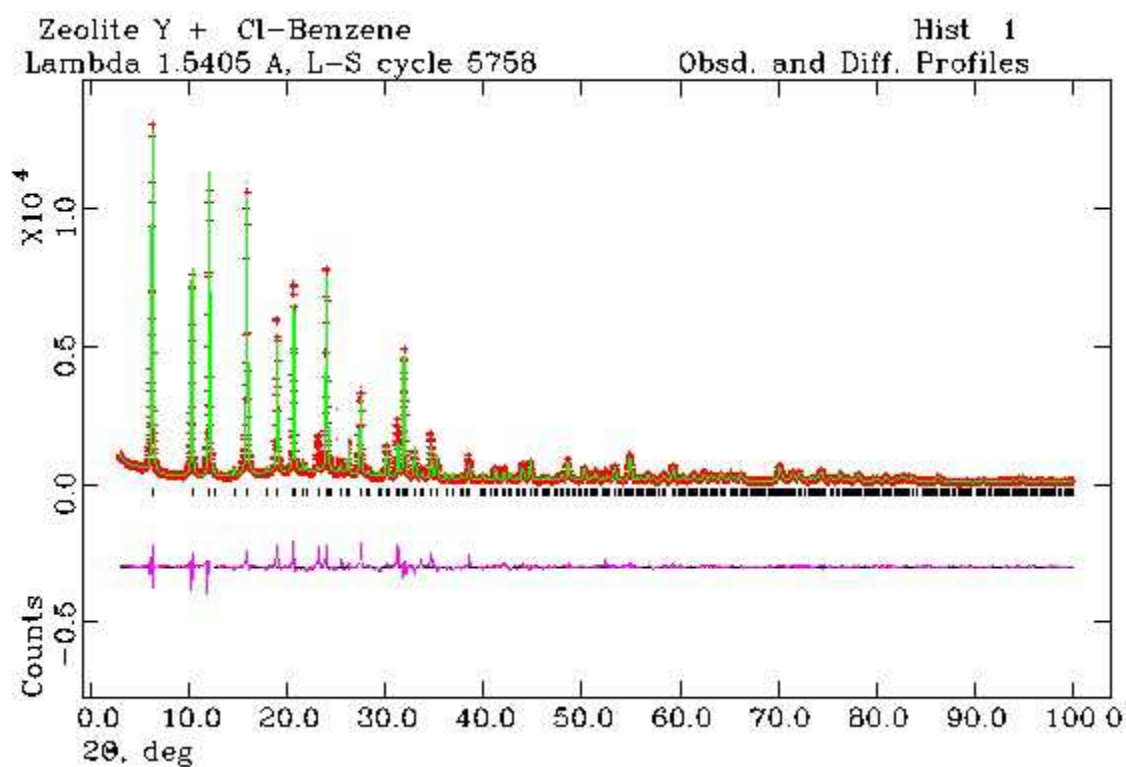
**Table S4.** Extraframework atomic fractional coordinates, thermal isotropic displacement factor and occupancy of ZSM-5-CB;  $x/a$  atomic fractional coordinates of CB2 molecule atoms have exactly the same values, in order to maintain the molecule planarity.

**Table S5.** Selected bond distances (Å) and angles (°) within both the Y-CB framework and extraframework atoms at  $T_{amb}$ .

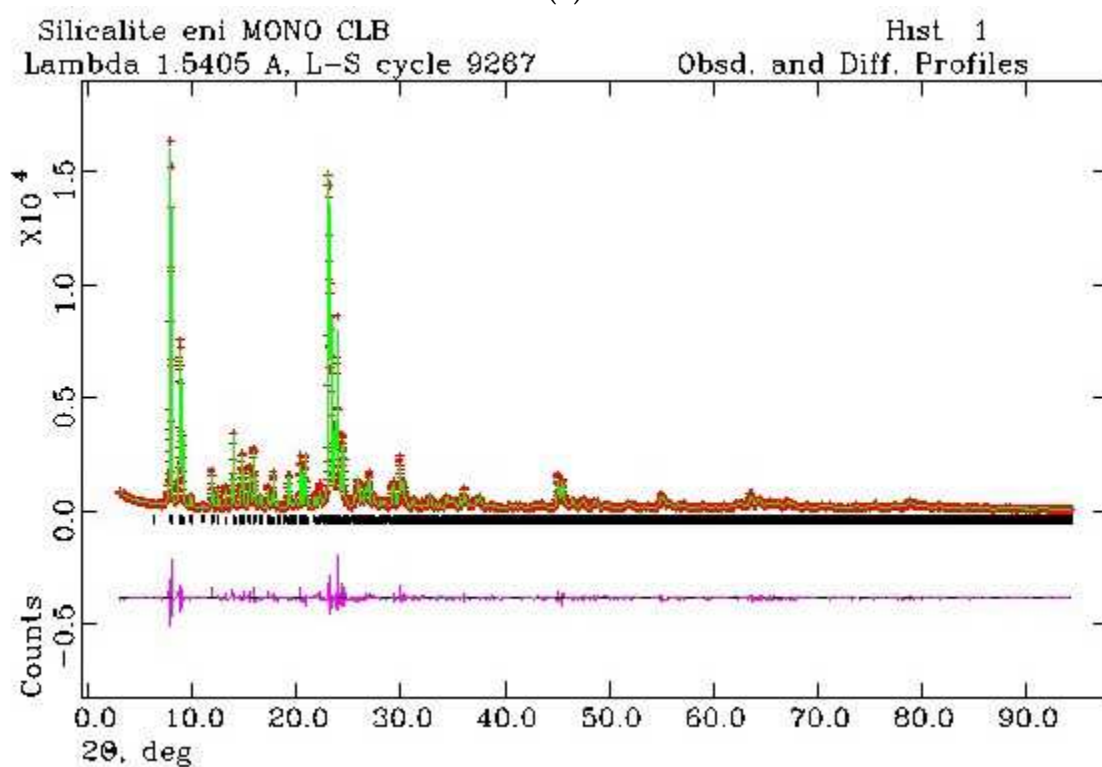
**Table S6.** Selected bond distances (Å) and angles (°) within both the ZSM-5-CB framework and extraframework atoms at  $T_{amb}$ .

Crystallographic Information File (CIF) of Y-CB

Crystallographic Information File (CIF) of ZSM-5-CB



(a)



(b)

**Figure S1.** Observed (dotted line), calculated (solid line) and difference (bottom) X-ray powder diffraction patterns of Y-CB (a) and ZSM-5-CB (b), respectively.

**Table S1.** Framework atomic fractional coordinates and thermal isotropic displacement factor of Y-CB.

Sites	$x/a$	$y/b$	$z/c$	$U_{iso}$ (Å <sup>2</sup> )	Fraction
T1	-0.0536(1)	0.1178(2)	0.0380(1)	0.002(1)	1.00
T2	-0.0534(1)	0.0330(1)	0.1234(1)	0.002(1)	1.00
O1	-0.1080(3)	-0.0029(1)	0.1099(1)	0.005(1)	1.00
O2	-0.0053(7)	-0.0094(1)	0.1417(2)	0.005(1)	1.00
O3	-0.0333(1)	0.0607(1)	0.0660(1)	0.005(1)	1.00
O4	-0.0546(2)	0.0858(1)	0.1640(1)	0.005(1)	1.00

**Table S2.** Framework atomic fractional coordinates and thermal isotropic displacement factor of ZSM-5-CB.

Sites	$x/a$	$y/b$	$z/c$	$U_{iso}$ (Å <sup>2</sup> )	Fraction
T1	0.0501(4)	0.4255(4)	-0.3339(5)	0.52(1)	1.00
T2	0.0303(4)	0.3159(4)	-0.1760(8)	0.52(1)	1.00
T3	0.0632(4)	0.2806(2)	0.0325(3)	0.52(1)	1.00
T4	0.0658(4)	0.1215(2)	0.0359(2)	0.52(1)	1.00
T5	0.0275(1)	0.0727(4)	-0.1785(5)	0.52(1)	1.00
T6	0.0590(4)	0.1914(4)	-0.3193(3)	0.52(1)	1.00
T7	-0.1748(3)	0.4261(1)	-0.3355(4)	0.52(1)	1.00
T8	-0.1296(3)	0.3149(1)	-0.1827(6)	0.52(1)	1.00
T9	-0.1757(3)	0.2712(1)	0.0337(6)	0.52(1)	1.00
T10	-0.1829(3)	0.1191(1)	0.0346(3)	0.52(1)	1.00
T11	-0.1309(2)	0.0698(4)	-0.1786(4)	0.52(1)	1.00
T12	-0.1638(5)	0.1882(2)	-0.3172(5)	0.52(1)	1.00
T13	0.4411(3)	0.4281(4)	-0.3370(4)	0.52(1)	1.00
T14	0.4721(2)	0.3179(4)	-0.1879(4)	0.52(1)	1.00
T15	0.4354(2)	0.2828(2)	0.0313(2)	0.52(1)	1.00
T16	0.4335(3)	0.1235(2)	0.0193(2)	0.52(1)	1.00
T17	0.4717(4)	0.0729(2)	-0.1960(2)	0.52(1)	1.00
T18	0.4361(4)	0.1930(4)	-0.3274(4)	0.52(1)	1.00
T19	0.6657(1)	0.4225(1)	-0.3232(2)	0.52(1)	1.00
T20	0.6305(2)	0.3069(4)	-0.1734(4)	0.52(1)	1.00
T21	0.6653(2)	0.2756(3)	0.0500(2)	0.52(1)	1.00
T22	0.6717(3)	0.1191(3)	0.0376(2)	0.52(1)	1.00
T23	0.6324(2)	0.0732(6)	-0.1837(4)	0.52(1)	1.00
T24	0.6815(4)	0.1911(4)	-0.3163(4)	0.52(1)	1.00
O1	0.0484(5)	0.3843(6)	-0.2314(4)	0.71(2)	1.00
O2	0.0738(3)	0.3144(2)	-0.0749(3)	0.71(2)	1.00
O3	0.0620(3)	0.2009(4)	0.0264(4)	0.71(2)	1.00
O4	0.0634(2)	0.1021(2)	-0.0803(3)	0.71(2)	1.00
O5	0.0453(6)	0.1197(4)	-0.2713(4)	0.71(2)	1.00
O6	0.0433(3)	0.2516(6)	-0.2444(4)	0.71(2)	1.00
O7	-0.1567(4)	0.3785(4)	-0.2429(3)	0.71(2)	1.00
O8	-0.1634(3)	0.3002(3)	-0.0765(4)	0.71(2)	1.00
O9	-0.1554(4)	0.1940(4)	0.0356(4)	0.71(2)	1.00
O10	-0.1594(3)	0.0884(4)	-0.0702(4)	0.71(2)	1.00



O11	-0.1567(5)	0.1152(4)	-0.2696(4)	0.71(2)	1.00
O12	-0.1385(4)	0.2480(3)	-0.2470(4)	0.71(2)	1.00
O13	-0.0498(5)	0.3216(4)	-0.1675(4)	0.71(2)	1.00
O14	-0.0516(3)	0.0682(4)	-0.1568(3)	0.71(2)	1.00
O15	0.1222(3)	0.4169(4)	-0.3852(4)	0.71(2)	1.00
O16	-0.0138(4)	0.4025(4)	-0.3986(4)	0.71(2)	1.00
O17	-0.1357(4)	0.4017(4)	-0.4332(4)	0.71(2)	1.00
O18	0.1338(4)	0.1817(4)	-0.3605(4)	0.71(2)	1.00
O19	-0.0011(3)	0.2057(4)	-0.3964(4)	0.71(2)	1.00
O20	-0.1322(3)	0.1841(4)	-0.4268(4)	0.71(2)	1.00
O21	0.0599(4)	0.0022(4)	-0.2069(4)	0.71(2)	1.00
O22	-0.1630(3)	-0.0006(3)	-0.2087(4)	0.71(2)	1.00
O23	-0.2552(4)	0.4281(3)	-0.3435(3)	0.71(2)	1.00
O24	-0.2411(3)	0.2009(3)	-0.3454(4)	0.71(2)	1.00
O25	-0.2543(3)	0.2769(3)	0.0577(3)	0.71(2)	1.00
O26	-0.2550(4)	0.1077(3)	0.0843(3)	0.71(2)	1.00
O27	0.4406(3)	0.3835(4)	-0.2378(4)	0.71(2)	1.00
O28	0.4396(3)	0.3142(3)	-0.0787(3)	0.71(2)	1.00
O29	0.4356(3)	0.2031(3)	0.0258(5)	0.71(2)	1.00
O30	0.4389(4)	0.0929(4)	-0.0910(3)	0.71(2)	1.00
O31	0.4357(3)	0.1213	-0.2750(3)	0.71(2)	1.00
O32	0.4574(3)	0.2530(4)	-0.2546(4)	0.71(2)	1.00
O33	0.6554(4)	0.3721(3)	-0.2317(3)	0.71(2)	1.00
O34	0.6562(3)	0.3066(4)	-0.0597(3)	0.71(2)	1.00
O35	0.6591(4)	0.1975(3)	0.0277(3)	0.71(2)	1.00
O36	0.6605(4)	0.0963(3)	-0.0764	0.71(2)	1.00
O37	0.6613(3)	0.1204(3)	-0.2698(3)	0.71(2)	1.00
O38	0.6620(4)	0.2454(4)	-0.2334	0.71(2)	1.00
O39	0.5503(4)	0.2996(3)	-0.1794(4)	0.71(2)	1.00
O40	0.5522(4)	0.0783(3)	-0.1942(3)	0.71(2)	1.00
O41	0.3779(4)	0.4188(4)	-0.4104(3)	0.71(2)	1.00
O42	0.5051(3)	0.4133(4)	-0.4057(3)	0.71(2)	1.00
O43	0.6415(3)	0.3911(3)	-0.4275(3)	0.71(2)	1.00
O44	0.3651(3)	0.1872(3)	-0.3836(3)	0.71(2)	1.00
O45	0.5017(3)	0.2017(3)	-0.3951(3)	0.71(2)	1.00
O46	0.6299(3)	0.1972(3)	-0.4084(3)	0.71(2)	1.00
O47	0.4484(3)	-0.0023(4)	-0.2169(3)	0.71(2)	1.00
O48	0.6539(4)	-0.0021(3)	-0.2070(4)	0.71(2)	1.00

---

**Table S3.** Extraframework atomic fractional coordinates, thermal isotropic displacement factor and occupancy of Y–CB.

Sites	<i>x/a</i>	<i>y/b</i>	<i>z/c</i>	<i>U</i> <sub>iso</sub> (Å <sup>2</sup> )	Fraction
C	0.4768(1)	0.4768(1)	0.5463(3)	0.161(3)	0.34(6)
Cl	0.4496(1)	0.4496(1)	0.6008(1)	0.161(3)	0.34(6)
W1	0.3096(4)	0.3096(4)	0.3096(4)	0.113(1)	0.82(1)
W2	0.4176(2)	0.4176(2)	0.4176(2)	0.113(1)	0.80(8)
W3	0.6277(1)	0.2209(1)	0.0081(1)	0.113(1)	0.18(1)

**Table S4.** Extraframework atomic fractional coordinates, thermal isotropic displacement factor and occupancy of ZSM-5–CB; *x/a* atomic fractional coordinates of CB2 molecule atoms have exactly the same values, in order to maintain the molecule planarity.

Sites	<i>x/a</i>	<i>y/b</i>	<i>z/c</i>	<i>U</i> <sub>iso</sub> (Å <sup>2</sup> )	Fraction
C1	0.7547(4)	0.5975(9)	0.0273(7)	0.211(7)	0.93(5)
C2	0.3017(5)	0.4444(9)	0.008(5)	0.211(7)	0.93(5)
C3	0.8151(8)	0.5686(7)	0.0564(6)	0.211(7)	0.93(5)
C4	0.8237(4)	0.5008(8)	0.0502(8)	0.211(7)	0.93(5)
C5	0.7110(7)	0.4899(6)	−0.0129(7)	0.211(7)	0.93(5)
C6	0.2285(7)	0.5386(9)	−0.0175(5)	0.211(7)	0.93(5)
Cl1	0.0991(2)	0.5357(2)	0.921(2)	0.211(7)	0.93(5)
C8	0.213(4)	0.1474(7)	0.7608(3)	0.285(2)	0.54(6)
C9	0.213(6)	0.0885(8)	0.7066(3)	0.285(2)	0.54(6)
C10	0.213(4)	0.0834(7)	0.9116(3)	0.285(2)	0.54(6)
C11	0.213(3)	0.1444(7)	0.8632(3)	0.285(2)	0.54(6)
C12	0.213(7)	0.0274(7)	0.8573(3)	0.285(2)	0.54(6)
C13	0.213(8)	0.0275(7)	0.7553(3)	0.285(2)	0.54(6)
Cl2	0.213(9)	−0.0544(7)	0.7127(3)	0.285(2)	0.54(6)
W1	0.7170(9)	0.7343(5)	0.1285(5)	0.193(3)	1.00(2)
W2	0.4209(7)	0.5034(5)	−0.0025(8)	0.193(3)	1.00(3)

**Table S5.** Selected bond distances (Å) and angles (°) within both the Y–CB framework and extraframework atoms at *T*<sub>amb</sub>.

Distance	Value (Å)	Distance	Value (Å)
T1–O1	1.629	T2–O1	1.619
T1–O2	1.612	T2–O2	1.620
T1–O3	1.622	T2–O3	1.621
T1–O4	1.620	T2–O4	1.619
Mean Value	1.621	Mean Value	1.620
Angle	Value (°)	Angle	Value (°)
O1–T1–O2	105.6	O1–T2–O2	107.7
O1–T1–O3	110.5	O1–T2–O3	107.3
O1–T1–O4	117.7	O1–T2–O4	122.3
O2–T1–O3	112.3	O2–T2–O3	106.4
O2–T1–O4	103.3	O2–T2–O4	110.4
O3–T1–O4	107.3	O3–T2–O4	101.6
Mean value	109.45	Mean value	109.3
Angle	Value (°)	Angle	Value (°)
T1–O1–T2	124.7	O1–Cl	2.680
T1–O2–T2	142.7	O1–Cl	2.723
T1–O3–T2	128.6	O4–Cl	2.599

T1–O4–T2	171.4	C–C	1.379
Mean value	141.8	Mean value	1.620
<b>Distance</b>	<b>Value (Å)</b>	<b>Distance</b>	<b>Value (Å)</b>
W2–W2	2.926	W1–W3	2.201
W2–W1	2.737	W3–CL	2.454
W2–W3	2.421	W3–CL	3.211

**Table S6.** Selected bond distances (Å) and angles (°) within both the ZSM-5–CB framework and extraframework atoms at  $T_{amb}$ .

<b>Distance</b>	<b>Value (Å)</b>
T1–O1	1.604
T1–O15	1.606
T1–O16	1.602
T1–O47	1.604
Mean value	1.604
T2–O1	1.604
T2–O2	1.604
T2–O6	1.606
T2–O13	1.605
Mean value	1.605
T3–O2	1.606
T3–O3	1.605
T3–O45	1.607
T3–O46	1.606
Mean value	1.606
T4–O3	1.604
T4–O4	1.605
T4–O42	1.605
T4–O43	1.602
Mean value	1.604
T5–O4	1.606
T5–O5	1.603
T5–O14	1.606
T5–O21	1.604
Mean value	1.605
T6–O5	1.603
T6–O6	1.605
T6–O18	1.604
T6–O19	1.603
Mean value	1.604
T7–O7	1.605
T7–O17	1.605
T7–O23	1.604
T7–O48	1.605
Mean value	1.605
T8–O7	1.604
T8–O8	1.606
T8–O12	1.606
T8–O13	1.605
Mean value	1.605
T9–O8	1.609

T9-O9	1.603
T9-O25	1.605
T9-O44	1.604
Mean value	1.605
<hr/>	
T10-O9	1.603
T10-O10	1.607
T10-O26	1.604
T10-O41	1.605
Mean value	1.605
<hr/>	
T11-O10	1.606
T11-O11	1.605
T11-O14	1.606
T11-O22	1.604
Mean value	1.605
<hr/>	
T12-O11	1.605
T12-O12	1.607
T12-O20	1.604
T12-O24	1.604
Mean value	1.605
<hr/>	
T13-O21	1.603
T13-O27	1.604
T13-O41	1.603
T13-O42	1.605
Mean value	1.604
<hr/>	
T14-O27	1.605
T14-O28	1.606
T14-O32	1.608
T14-O39	1.605
Mean value	1.606
<hr/>	
T15-O19	1.605
T15-O20	1.605
T15-O28	1.606
T15-O29	1.604
Mean value	1.605
<hr/>	
T16-O16	1.603
T16-O17	1.605
T16-O29	1.603
T16-O30	1.605
Mean value	1.604
<hr/>	
T17-O30	1.606
T17-O31	1.604
T17-O40	1.607
Mean value	1.605
<hr/>	
T18-O31	1.603
T18-O32	1.606
T18-O44	1.603
T18-O45	1.605
Mean value	1.604
<hr/>	
T19-O22	1.605
T19-O23	1.604
T19-O33	1.605
T19-O43	1.604

Mean value	1.605
T20-O33	1.605
T20-O34	1.603
T20-O38	1.607
T20-O39	1.605
Mean value	1.605
T21-O18	1.605
T21-O25	1.606
T21-O34	1.605
T21-O35	1.603
Mean value	1.605
T22-O15	1.606
T22-O26	1.602
T22-O35	1.602
T22-O36	1.608
Mean value	1.605
T23-O36	1.607
T23-O37	1.605
T23-O40	1.607
T23-O48	1.605
Mean value	1.606
T24-O24	1.605
T24-O37	1.605
T24-O38	1.606
T24-O46	1.605
Mean value	1.605
<b>Angle</b>	<b>Value (°)</b>
O1-T1-O15	109.6
O1-T1-O16	107
O1-T1-O47	96.1
O15-T1-O16	116.6
O15-T1-O47	105.3
O16-T1-O47	120.2
Mean value	109.1
O1-T2-O2	106.6
O1-T2-O6	112.8
O1-T2-O13	101.5
O2-T2-O6	112.2
O2-T2-O13	118.2
O6-T2-O13	105.1
Mean value	109.4
O2-T3-O3	112.3
O2-T3-O45	123.5
O2-T3-O46	102.1
O3-T3-O45	103.9
O3-T3-O46	108.3
O45-T3-O46	105.8
Mean value	109.3
O3-T4-O4	99.5
O3-T4-O42	116
O3-T4-O43	103.1
O4-T4-O42	110.4

O4-T4-O43	106.2
O42-T4-O43	119.5
Mean value	109.1
<hr/>	
O4-T5-O5	108.6
O4-T5-O14	107.7
O4-T5-O21	109.9
O5-T5-O14	113.4
O5-T5-O21	104.2
O14-T5-O21	113
Mean value	109.5
<hr/>	
O5-T6-O6	113.2
O5-T6-O18	100.9
O5-T6-O19	107
O6-T6-O18	119.6
O6-T6-O19	96.8
O18-T6-O19	119.4
Mean value	109.5
<hr/>	
O7-T7-O17	109.9
O7-T7-O23	106.5
O7-T7-O48	101.8
O17-T7-O23	116.3
O17-T7-O48	115.9
O23-T7-O48	105
Mean value	109.3
<hr/>	
O7-T8-O8	116.7
O7-T8-O12	111.3
O7-T8-O13	109.1
O8-T8-O12	105.9
O8-T8-O13	108.9
O12-T8-O13	104.1
Mean value	109.3
<hr/>	
O8-T9-O9	109
O8-T9-O25	108.2
O8-T9-O44	111.4
O9-T9-O25	108.2
O9-T9-O44	111.6
O25-T9-O44	108.3
Mean value	109.5
<hr/>	
O9-T10-O10	105.5
O9-T10-O26	115.9
O9-T10-O41	100.8
O10-T10-O26	125.1
O10-T10-O41	89.7
O26-T10-O41	114.6
Mean value	108.6
<hr/>	
O10-T11-O11	116.2
O10-T11-O14	101.2
O10-T11-O22	106.9
O11-T11-O14	117.3
O11-T11-O22	100.7
O14-T11-O22	114.7
Mean value	109.5

O11-T12-O12	115.2
O11-T12-O20	106.5
O11-T12-O24	108.7
O12-T12-O20	116.8
O12-T12-O24	108.3
O20-T12-O24	100.1
Mean value	109.3
O21-T13-O27	102.5
O21-T13-O41	108.8
O21-T13-O42	113.2
O27-T13-O41	115.7
O27-T13-O42	112.4
O41-T13-O42	104.5
Mean value	109.5
O27-T14-O28	104.9
O27-T14-O32	111.5
O27-T14-O39	126.5
O28-T14-O32	113.4
O28-T14-O39	108.8
O32-T14-O39	91.6
Mean value	109.4
O19-T15-O20	112.9
O19-T15-O28	116.8
O19-T15-O29	99.7
O20-T15-O28	101.9
O20-T15-O29	115.6
O28-T15-O29	110.5
Mean value	109.6
O16-T16-O17	100.6
O16-T16-O29	105.8
O16-T16-O30	117.3
O17-T16-O29	108.4
O17-T16-O30	107.9
O29-T16-O30	115.6
Mean value	109.3
O30-T17-O31	104
O30-T17-O40	112.4
O30-T17-O47	105.6
O31-T17-O40	114.3
O31-T17-O47	109.1
O40-T17-O47	110.8
Mean value	109.4
O31-T18-O32	114.3
O31-T18-O44	97.6
O31-T18-O45	110.7
O32-T18-O44	124.6
O32-T18-O45	92.8
O44-T18-O45	117.6
Mean value	109.6
O22-T19-O23	90.7
O22-T19-O33	113.6
O22-T19-O43	126.9

O23-T19-O33	107.7
O23-T19-O43	99.9
O33-T19-O43	112.2
Mean value	108.5
<hr/>	
O33-T20-O34	111.5
O33-T20-O38	105.2
O33-T20-O39	111.2
O34-T20-O38	110.4
O34-T20-O39	111
O38-T20-O39	107.2
Mean value	109.4
<hr/>	
O18-T21-O25	109.7
O18-T21-O34	115.7
O18-T21-O35	129.3
O25-T21-O34	99.1
O25-T21-O35	95.9
O34-T21-O35	101.6
Mean value	108.6
<hr/>	
O15-T22-O26	104.2
O15-T22-O35	113.7
O15-T22-O36	113.7
O26-T22-O35	108.3
O26-T22-O36	116.8
O35-T22-O36	100.4
Mean value	109.5
<hr/>	
O36-T23-O37	110.3
O36-T23-O40	113.5
O36-T23-O48	110.9
O37-T23-O40	105.1
O37-T23-O48	108.7
O40-T23-O48	108.1
Mean value	109.4
<hr/>	
O24-T24-O37	116.5
O24-T24-O38	108.8
O24-T24-O46	114.5
O37-T24-O38	105.7
O37-T24-O46	101.9
O38-T24-O46	108.9
Mean value	109.4
<hr/>	
T1-O1-T2	147.7
T2-O2-T3	133.7
T3-O3-T4	171.7
T4-O4-T5	153.4
T5-O5-T6	151.7
T2-O6-T6	175.3
T7-O7-T8	159.5
T8-O8-T9	161.3
T9-O9-T10	145.5
T10-O10-T11	170.5
T11-O11-T12	148.0
T8-O12-T12	167.0
T2-O13-T8	165.6



T5–O14–T11	158.6
T1–O15–T22	151.5
T1–O16–T16	168.2
T7–O17–T16	147.6
T6–O18–T21	124.0
T6–O19–T15	176.0
T12–O20–T15	129.3
T5–O21–T13	136.7
T11–O22–T19	142.9
T7–O23–T19	165.4
T12–O24–T24	147.8
T9–O25–T21	163.9
T10–O26–T22	129.4
T13–O27–T14	143.2
T14–O28–T15	151.4
T15–O29–T16	178.3
T16–O30–T17	158.8
T17–O31–T18	146.1
T14–O32–T18	173.5
T19–O33–T20	158.2
T20–O34–T21	154.7
T21–O35–T22	159.6
T22–O36–T23	167.5
T23–O37–T24	153.6
T20–O38–T24	165.2
T14–O39–T20	161.5
T17–O40–T23	171.3
T10–O41–T13	157.4
T4–O42–T13	164.6
T4–O43–T19	127.3
T9–O44–T18	136.6
T3–O45–T18	172.6
T3–O46–T24	157.5
T1–O47–T17	140.7
T7–O48–T23	148.0
<hr/>	
<b>Distance</b>	<b>Value (Å)</b>
C5–C6	1.39
C5–C4	2.40
C5–C2	1.35
C5–C3	2.76
C5–C1	2.39
C5–W2	2.64
C6–C5	1.39
C6–C4	1.38
C6–C2	2.41
C6–C3	2.38
C6–C1	2.76
C6–Cl1	2.70
C4–C5	2.40
C4–C6	1.38
C4–C2	2.83
C4–C3	1.38

---

C4-C1	2.40
C4-C11	1.75
C2-O20	3.03
C2-C5	1.35
C2-C6	2.41
C2-C4	2.83
C2-C3	2.49
C2-C1	1.48
C2-W2	2.66
C2-C14	2.97
C3-C5	2.76
C3-C6	2.38
C3-C4	1.38
C3-C2	2.49
C3-C1	1.39
C3-C12	2.94
C3-C7	2.72
C1-O24	3.21
C1-C5	2.39
C1-C6	2.76
C1-C4	2.40
C1-C2	1.48
C1-C3	1.39
C1-W1	3.16
C1-C14	2.76
C8-O18	2.36
C8-O25	3.19
C8-C9	1.39
C8-C10	2.40
C8-C11	1.37
C8-C12	2.74
C8-C13	2.41
C8-W1	3.13
C9-O18	2.61
C9-C8	1.39
C9-C10	2.75
C9-C11	2.38
C9-C12	2.36
C9-C13	1.39
C9-C12	2.87
C10-O4	3.01
C10-O43	2.64
C10-C8	2.40
C10-C9	2.75
C10-C11	1.39
C10-C12	1.34
C10-C13	2.38
C11-O4	3.19
C11-C8	1.37
C11-C9	2.38
C11-C10	1.39
C11-C12	2.35

---

C11–C13	2.76
C11–W1	2.81
C12–O21	3.20
C12–O26	2.95
C12–O41	2.93
C12–C8	2.74
C12–C9	2.36
C12–C10	1.34
C12–C11	2.35
C12–C13	1.37
C12–C14	2.54
C13–O21	3.14
C13–C8	2.41
C13–C9	1.39
C13–C10	2.38
C13–C11	2.76
C13–C12	1.37
C13–C12	1.74
W1–O20	3.33
W1–O28	3.33
W1–C1	3.16
W1–C8	3.13
W1–C11	2.81
W2–C5	2.64
W2–C2	2.66
W2–W2	3.15
CL2–O21	3.44
CL2–O26	3.03
CL2–O27	3.32
CL2–O41	3.26
CL2–C2	2.97
CL2–C3	2.94
CL2–C1	2.76
CL2–C9	2.87
CL2–C12	2.54
CL2–C13	1.74
Cl1–O31	2.69
Cl1–O44	3.17
Cl1–O47	2.99
Cl1–C6	2.70
Cl1–C4	1.75
Cl1–C3	2.72

---

**Crystallographic Information File (CIF) of Y-CBY-CB**

```
_symmetry_space_group_name_H-M 'Fd-3'  
_cell_length_a 24.263506  
_cell_length_b 24.263506  
_cell_length_c 24.263506  
_cell_angle_alpha 90.0000  
_cell_angle_beta 90.0000  
_cell_angle_gamma 90.0000  
loop_  
_atom_site_label  
_atom_site_type_symbol  
_atom_site_fract_x  
_atom_site_fract_y  
_atom_site_fract_z  
_atom_site_B_iso_or_equiv  
_atom_site_occupancy  
SI1 SI -0.05360 0.11780 0.03802 0.197391754562 1.00000  
SI2 SI -0.05346 0.03299 0.12335 0.197391754562 1.00000  
O1 O -0.10804 -0.00289 0.10993 0.394783509124 1.00000  
O2 O -0.00534 -0.00939 0.14171 0.394783509124 1.00000  
O3 O -0.03333 0.06065 0.06604 0.394783509124 1.00000  
O4 O -0.05463 0.08582 0.16401 0.394783509124 1.00000  
w2 O 0.41760 0.41760 0.41760 9.04496393424 0.80392  
w1 O 0.30959 0.30959 0.30959 9.04496393424 0.82154  
C1 C 0.47678 0.47678 0.54634 12.7041333236 0.33590  
w3 O 0.62774 0.22086 0.00814 9.04496393424 0.18780  
CL1 CL 0.44958 0.44958 0.60084 12.7041333236 0.33590
```

**Crystallographic Information File (CIF) of ZSM-5-CB**

```
_symmetry_space_group_name_H-M   'P21/n'  
_cell_length_a    19.919321  
_cell_length_b    20.109558  
_cell_length_c    13.395503  
_cell_angle_alpha  90.0000  
_cell_angle_beta  90.3905  
_cell_angle_gamma  90.0000  
loop_  
_atom_site_label  
_atom_site_type_symbol  
_atom_site_fract_x  
_atom_site_fract_y  
_atom_site_fract_z  
_atom_site_B_iso_or_equiv  
_atom_site_occupancy  
SI1 SI 0.05010 0.42550 -0.33391 0.41452268458 1.00000  
SI2 SI 0.03031 0.31594 -0.17604 0.41452268458 1.00000  
SI3 SI 0.06317 0.28059 0.03250 0.41452268458 1.00000  
SI4 SI 0.06578 0.12149 0.03589 0.41452268458 1.00000  
SI5 SI 0.02748 0.07270 -0.17852 0.41452268458 1.00000  
SI6 SI 0.05904 0.19140 -0.31926 0.41452268458 1.00000  
SI7 SI -0.17483 0.42614 -0.33549 0.41452268458 1.00000  
SI8 SI -0.12956 0.31494 -0.18272 0.41452268458 1.00000  
SI9 SI -0.17567 0.27118 0.03375 0.41452268458 1.00000  
SI10 SI -0.18289 0.11913 0.03461 0.41452268458 1.00000  
SI11 SI -0.13091 0.06979 -0.17856 0.41452268458 1.00000  
SI12 SI -0.16376 0.18816 -0.31719 0.41452268458 1.00000  
SI13 SI 0.44109 0.42809 -0.33705 0.41452268458 1.00000  
SI14 SI 0.47207 0.31785 -0.18791 0.41452268458 1.00000  
SI15 SI 0.43537 0.28278 0.03134 0.41452268458 1.00000  
SI16 SI 0.43351 0.12352 0.01930 0.41452268458 1.00000  
SI17 SI 0.47173 0.07287 -0.19599 0.41452268458 1.00000  
SI18 SI 0.43613 0.19295 -0.32742 0.41452268458 1.00000  
SI19 SI 0.66574 0.42249 -0.32322 0.41452268458 1.00000  
SI20 SI 0.63048 0.30694 -0.17338 0.41452268458 1.00000  
SI21 SI 0.66526 0.27562 0.04999 0.41452268458 1.00000  
SI22 SI 0.67166 0.11910 0.03762 0.41452268458 1.00000  
SI23 SI 0.63244 0.07315 -0.18366 0.41452268458 1.00000  
SI24 SI 0.68150 0.19112 -0.31632 0.41452268458 1.00000  
O1 O 0.04839 0.38426 -0.23144 0.557829098392 1.00000  
O2 O 0.07378 0.31442 -0.07487 0.557829098392 1.00000  
O3 O 0.06198 0.20090 0.02639 0.557829098392 1.00000  
O4 O 0.06341 0.10206 -0.08032 0.557829098392 1.00000  
O5 O 0.04533 0.11968 -0.27131 0.557829098392 1.00000  
O6 O 0.04327 0.25164 -0.24440 0.557829098392 1.00000  
O7 O -0.15674 0.37854 -0.24294 0.557829098392 1.00000  
O8 O -0.16344 0.30023 -0.07652 0.557829098392 1.00000  
O9 O -0.15544 0.19405 0.03559 0.557829098392 1.00000  
O10 O -0.15936 0.08842 -0.07025 0.557829098392 1.00000  
O11 O -0.15669 0.11520 -0.26963 0.557829098392 1.00000  
O12 O -0.13849 0.24803 -0.24695 0.557829098392 1.00000
```

O13 O -0.04984 0.32159 -0.16754 0.557829098392 1.00000  
O14 O -0.05156 0.06816 -0.15675 0.557829098392 1.00000  
O15 O 0.12220 0.41693 -0.38520 0.557829098392 1.00000  
O16 O -0.01379 0.40255 -0.39858 0.557829098392 1.00000  
O17 O -0.13567 0.40174 -0.43317 0.557829098392 1.00000  
O18 O 0.13382 0.18167 -0.36052 0.557829098392 1.00000  
O19 O -0.00109 0.20575 -0.39644 0.557829098392 1.00000  
O20 O -0.13217 0.18413 -0.42684 0.557829098392 1.00000  
O21 O 0.05992 0.00224 -0.20693 0.557829098392 1.00000  
O22 O -0.16296 -0.00064 -0.20872 0.557829098392 1.00000  
O23 O -0.25518 0.42810 -0.34345 0.557829098392 1.00000  
O24 O -0.24111 0.20091 -0.34537 0.557829098392 1.00000  
O25 O -0.25429 0.27687 0.05773 0.557829098392 1.00000  
O26 O -0.25498 0.10772 0.08435 0.557829098392 1.00000  
O27 O 0.44055 0.38346 -0.23782 0.557829098392 1.00000  
O28 O 0.43955 0.31423 -0.07868 0.557829098392 1.00000  
O29 O 0.43557 0.20310 0.02584 0.557829098392 1.00000  
O30 O 0.43888 0.09287 -0.09101 0.557829098392 1.00000  
O31 O 0.43565 0.12127 -0.27501 0.557829098392 1.00000  
O32 O 0.45736 0.25295 -0.25464 0.557829098392 1.00000  
O33 O 0.65543 0.37206 -0.23169 0.557829098392 1.00000  
O34 O 0.65621 0.30662 -0.05970 0.557829098392 1.00000  
O35 O 0.65912 0.19754 0.02769 0.557829098392 1.00000  
O36 O 0.66048 0.09635 -0.07639 0.557829098392 1.00000  
O37 O 0.66132 0.12040 -0.26983 0.557829098392 1.00000  
O38 O 0.66202 0.24538 -0.23343 0.557829098392 1.00000  
O39 O 0.55034 0.29961 -0.17937 0.557829098392 1.00000  
O40 O 0.55219 0.07833 -0.19416 0.557829098392 1.00000  
O41 O 0.37786 0.41880 -0.41044 0.557829098392 1.00000  
O42 O 0.50509 0.41334 -0.40569 0.557829098392 1.00000  
O43 O 0.64147 0.39114 -0.42750 0.557829098392 1.00000  
O44 O 0.36506 0.18718 -0.38359 0.557829098392 1.00000  
O45 O 0.50172 0.20171 -0.39509 0.557829098392 1.00000  
O46 O 0.62994 0.19723 -0.40843 0.557829098392 1.00000  
O47 O 0.44837 -0.00226 -0.21689 0.557829098392 1.00000  
O48 O 0.65387 -0.00214 -0.20702 0.557829098392 1.00000  
C5 C 0.71101 0.48992 -0.01282 16.5809073832 0.93337  
C6 C 0.22847 0.53856 -0.01752 16.5809073832 0.93337  
C4 C 0.82371 0.50085 0.05021 16.5809073832 0.93337  
C2 C 0.30172 0.44442 0.00800 16.5809073832 0.93337  
C3 C 0.81510 0.56856 0.05637 16.5809073832 0.93337  
C1 C 0.75470 0.59747 0.02726 16.5809073832 0.93337  
C8 C 0.21303 0.14737 0.76076 22.5394538431 0.54944  
C9 C 0.21303 0.08846 0.70666 22.5394538431 0.54944  
C10 C 0.21303 0.08337 0.91158 22.5394538431 0.54944  
C11 C 0.21303 0.14436 0.86321 22.5394538431 0.54944  
C12 C 0.21303 0.02742 0.85731 22.5394538431 0.54944  
C13 C 0.21303 0.02742 0.75525 22.5394538431 0.54944  
W1 O 0.71704 0.73433 0.12855 15.3066251725 1.00000  
W2 O 0.42098 0.50336 -0.00245 15.2497763471 1.00000  
CL-2 CL 0.21303 -0.05442 0.71269 22.5394538431 0.54947  
CL-1 CL 0.09900 0.53573 0.92100 16.5809073832 0.93333



# An advanced oxidation process by photoexcited heterogeneous sodium decatungstate for the degradation of drugs present in aqueous environment

Luisa Pasti<sup>a,\*</sup>, Elena Sarti<sup>a</sup>, Annalisa Martucci<sup>b</sup>, Nicola Marchetti<sup>a</sup>, Claudia Stevanin<sup>a</sup>,  
Alessandra Molinari<sup>a,\*</sup>

<sup>a</sup> Dipartimento di Scienze Chimiche e Farmaceutiche, Università di Ferrara, Via Luigi Borsari 46, 44121 Ferrara, Italy

<sup>b</sup> Dipartimento di Fisica e Scienze della Terra, Università di Ferrara, Via Saragat 1, 44123 Ferrara, Italy



## ARTICLE INFO

### Keywords:

Heterogeneous photocatalysis  
Sodium decatungstate  
Water remediation  
Drug mineralization  
•OH radicals

## ABSTRACT

The ability of decatungstate anion ( $W_{10}O_{32}^{4-}$ ) to photoproduce  $OH\cdot$  radicals from water is retained when the polyoxoanion is immobilized on solid supports and can be exploited as a heterogeneous photocatalytic process aimed to water remediation. However, we show that interaction between  $OH\cdot$  radicals and drug molecules depends on the physical chemical properties of the chosen support. In fact, we demonstrate that silica particles covered by decatungstate anions are not efficient in the degradation of carbamazepine and sulfamethoxazole (ubiquitous contaminants of natural waters) that are respectively neutral and negatively charged at operating pH of 6. On the contrary, entrapment of  $W_{10}O_{32}^{4-}$  inside a mesoporous organosilica matrix leads to a heterogeneous photocatalytic system with proper characteristic of hydrophobicity. Organic molecules enter mesopores and easily leave the aqueous environment. Inside pores, the reaction between photoproduced  $OH\cdot$  radicals is favored. Mono- and di-hydroxylated products precede fragmentation and degradation of the investigated drug.

## 1. Introduction

Water scarcity is a well-recognized challenge to the sustainable development of many countries that claims for further efforts to develop and improve water treatment technologies. It is therefore necessary the development of processes capable to ensure the total elimination of trace of organic contaminants from waters [1,2].

The use of advanced oxidation processes (AOPs) has been demonstrated to be a possible approach for the remediation of contaminated waters [3,4]. AOPs are based on the in situ production of free radical species, such as ( $OH\cdot$ ), which being a strong oxidant characterized by a very high standard reduction potential ( $E^\circ = +2.80$  V vs. SHE) rapidly oxidizes electron-rich organic compounds up to their mineralization [5]. Among the large variety of oxidation processes, photochemical methods offers the advantage of energy efficiency, rapidness and limited use of chemicals (oxidants), which together concur to the sustainability of the process [5]. In particular, photocatalysis with  $TiO_2$  has been demonstrated to be an efficient method for the destruction of low amounts of water-soluble organic pollutants [6–8], even if other semiconductor materials, such as  $WO_3$ , have been recently successfully utilized [9].

In water decontamination issue, the applicability of

polyoxotungstates for the degradation and mineralization of chlorophenols, chloroacetic acids and herbicide has been also explored [10,11]. Among polyoxotungstates, decatungstate anionic cluster has light absorption properties very similar to those of  $TiO_2$  and for this similarity it can be considered a soluble analogue of the most employed semiconductor. In addition, it has been demonstrated that photoexcitation of  $Na_4W_{10}O_{32}$  dissolved in water produces  $OH\cdot$  radicals from water oxidation [12]. The interest for heterogeneous decatungstate photocatalyst in advanced oxidation processes framework has led to the development of several heterogenization procedures, such as impregnation on a solid support [13] and ion exchange [14,15]. Indeed, heterogeneous (photo)catalysis has the advantage of easy separation and recovery.

Recently, a heterogeneous photocatalytic system obtained by immobilization of the anionic decatungstate cluster on silica particles functionalized with  $-NH_2$  groups has been employed for the degradation of some contaminants of emerging concerns in aqueous matrix [16]. It was proved that the photocatalytic system was efficient and recyclable. The degradation process is achieved by photoexcitation of heterogeneous decatungstate that results in the formation of  $OH\cdot$  radicals as revealed by EPR spin trapping spectroscopy.

In addition, studies on the reaction mechanism of heterogeneous

\* Corresponding authors.

E-mail addresses: [luisa.pasti@unife.it](mailto:luisa.pasti@unife.it) (L. Pasti), [alessandra.molinari@unife.it](mailto:alessandra.molinari@unife.it) (A. Molinari).

<https://doi.org/10.1016/j.apcatb.2018.08.015>

Received 28 May 2018; Received in revised form 2 August 2018; Accepted 4 August 2018

Available online 16 August 2018

0926-3373/ © 2018 Elsevier B.V. All rights reserved.

polyoxotungstates indicate that the selectivity and efficiency of these photocatalysts depend on the support characteristics. In general, pore structures, distributions of the active sites and hydrophilic–hydrophobic interactions with the substrate are key factors for the catalytic activity and selectivity of solid heterogeneous catalysts [17–19]. Therefore, the choice of support matrices is very important for highly efficient catalytic systems. In this paper, we show how support matrix properties can tune the degradation ability of immobilized decatungstate with respect to three target molecules in dilute aqueous solutions: propranolol, carbamazepine and sulfamethoxazole. These molecules are selected as probes since all of them are ubiquitous contaminants of natural waters. In particular, carbamazepine is a psychotic drug, resistant to conventional wastewater treatment and sulfamethoxazole is an antimicrobial largely employed, which has been detected in surface and drinking waters [20].

Two different heterogeneous photocatalysts, obtained either by immobilization of  $W_{10}O_{32}^{4-}$  by an ion exchange mechanism [16] or by encapsulation of the anionic cluster into a silicate structure [21], that were proved to be able to oxidize organic compounds, are here investigated.

In particular, their photocatalytic degradation activity with respect to contaminants of emerging concern is evaluated and the observed differences are related to both the support and the drug molecule physical chemical properties. EPR spin trapping technique and HPLC-MS analysis are employed to gain information about the operating degradative mechanism and the nature of reaction intermediates. In addition, composition and structural properties of the heterogeneous photocatalytic system are more deeply investigated. To the best of our knowledge, this is the first contribution where the photoactivity of decatungstate anion heterogenized on two different supports is compared, thus demonstrating that it is possible to tune the photocatalytic activity of the polyoxoanion by varying the chemical-physical properties of the support.

## 2. Experimental

### 2.1. Materials

Propranolol (PRP, purity 99.8%), carbamazepine (CBZ, purity 99.8%), sulfamethoxazole (SMX, purity 99.8%) and formic acid were purchased from Fluka (Fluka Chemie AG, Switzerland). Sodium hydroxide (Titolchimica, Rovigo, Italy), hydrochloric acid (Carlo Erba, Milano, Italy) of analytical grade were employed to adjust the pH of diluted drugs solutions. The pH was measured using an AMEL pHmeter (Milano, Italy). High-performance liquid chromatography (HPLC) grade acetonitrile (ACN) was purchased from Merck (Darmstadt, Germany). The water was Milli-Q<sup>®</sup> grade (Millipore, MA, USA).

### 2.2. Photocatalysts preparation

Sodium decatungstate ( $Na_4W_{10}O_{32}$ ) was synthesized following reported literature procedures [22,23]. The heterogeneous photocatalysts silica- $NH_3^+ / Na_3W_{10}O_{32}^-$  have been prepared carrying out the procedure recently published [16].  $Na_4W_{10}O_{32}/SiO_2/BTESE$  was prepared by simultaneous hydrolysis of tetraethylorthosilicate (TEOS, 23 mmol) and 1,2-bis(triethoxysilyl)ethane (BTESE, 2.3 mmol) in an acid aqueous solution of  $Na_4W_{10}O_{32}$  [21]. The obtained material has a content of decatungstate of 0.33 mmol/g. The composition was determined by Inductively Coupled Plasma-Optical Emission Spectrometer ICP-OES (Perkin-Elmer Optima 3100 XL) equipped with an axial torch, segmented array charge coupled device (SCD) detector and Babington-type nebulizer with cyclonic spray chamber for sample introduction. Plasma conditions were: RF power of 1.40 kW applied to the plasma; 15 L  $min^{-1}$  flow rate for plasma and 0.5 L  $min^{-1}$  for auxiliary gas. Nebulizer gas flow rate was 0.65 L  $min^{-1}$ . Sample uptake was 1.5 mL  $min^{-1}$  for each of three replicate scans. 0.5 g of samples were mineralized by microwave

acid digestion ( $HNO_3$ , HF and  $H_3BO_3$ ) at 200 °C and high pressure (200 psi), with 20 min dwell time.

At the end of preparation, UV–vis spectra of washing water aliquots showed that polyoxoanion was not released in the solution.

### 2.3. Photocatalytic experiments with homogeneous $Na_4W_{10}O_{32}$

An aerated aqueous solution (3 mL, final pH = 6) containing dissolved  $Na_4W_{10}O_{32}$  ( $2 \cdot 10^{-4}$  M) and the drug of interest ( $C_0 = 10$  mg  $L^{-1}$ ) was put into a spectrophotometric cell (optical path 1 cm) and placed in front of a Hg medium pressure lamp (Helios Italquartz, 15 W  $cm^{-2}$ ). The solution is magnetically stirred and irradiation was carried out using a cut-off filter, placed between the lamp slit (1 cm x 3 cm) and the cuvette in order to select the suitable wavelength range (PRP,  $\lambda > 330$  nm, SMX  $\lambda > 335$  nm; CBZ,  $\lambda > 300$  nm). Selection of suitable cut off filter was performed in order to avoid direct photolysis of the drug compound. At the end of illumination, the sample was filtrated with 0.22  $\mu m$  PVDF membrane filters Captiva Econofilter Agilent Technologies (Santa Clara, CA, USA) and HPLC analysis was performed. Samples containing dissolved decatungstate anion have been kept in the dark and then analyzed.

### 2.4. Photocatalytic experiments with heterogeneous $Na_4W_{10}O_{32}$

In a typical photocatalytic experiment, the optimal amount determined elsewhere [16,21] of silica- $NH_3^+ / Na_3W_{10}O_{32}^-$  (5 g/L) or of  $Na_4W_{10}O_{32}/SiO_2/BTESE$  (8 g/L) was kept in suspension in aqueous solution (3 mL, pH = 6) containing the drug of interest ( $C_0 = 10$  mg  $L^{-1}$ ) inside a spectrophotometric cell. Then, irradiation was carried out for the required period of time with the selected cut off filter (PRP,  $\lambda > 330$  nm, SMX  $\lambda > 335$  nm; CBZ,  $\lambda > 300$  nm) and at the end of irradiation the solution was analyzed as described above.

After irradiation, the solutions were centrifuged to separate the heterogeneous photocatalysts and UV–vis spectra have been recorded to evaluate leaching of decatungstate anion. Moreover, these solutions have been subsequently irradiated to establish eventual photoactivity of traces of decatungstate cluster, leached into the solution and not detected by spectrophotometric analysis.

Some photocatalytic experiments have been carried out to evaluate the stability of decatungstate on the support, by recovering  $Na_4W_{10}O_{32}/SiO_2/BTESE$  (8 g/L) after the first photocatalytic experiment, washing with aliquots of acetonitrile and drying in the oven at 373 K for 60 min. The photocatalytic system has been reused in a second experiment, suspending it in an aqueous solution (3 mL, pH = 6) containing CBZ ( $C_0 = 10$  mg  $L^{-1}$ ) and irradiated as described above. The irradiated solution was then analysed.

### 2.5. HPLC analysis

A HPLC/DAD (Waters, MA, USA pump: Waters 515, DAD: Waters PDA 996) was employed under isocratic elution conditions, reported in Table 2. The flow rate was 1 mL  $min^{-1}$ , while the column was thermostated at 25 °C. The column was 150 × 4.6 mm (Phenomenex, CA, USA) and packed with a C18 silica-based stationary phase with a particle diameter of 5  $\mu m$ . The injection volume was 20  $\mu L$  for all standards and samples.

### 2.6. HPLC/MS analysis

HPLC/MS analyses were carried out by means of Surveyor Plus micro-HPLC hyphenated to a linear ion trap mass spectrometer (LTQ XL Thermo Scientific, Waltham, MA, USA). The HPLC apparatus was composed of a solvent delivery system, a quaternary pump (including a membrane degasser) and an autosampler (including a thermostated column compartment). The LTQ system was equipped with an electrospray ionization (ESI) ion source. The mobile phase was obtained as



a mixture of ACN and formic acid 0.1% v/v: water formic acid 0.1% v/v. Chromatographic separation was performed under gradient elution conditions: 0–6 min 5% ACN, 6–14 min 5–70% ACN, 14–15 min 70% ACN, then held isocratically at 95% of ACN for 3 min before reconditioning the column. The flow rate was  $100 \mu\text{L min}^{-1}$ , while the column was thermostated at  $25^\circ\text{C}$ . The column was  $50 \times 2.1 \text{ mm}$  (Restek, Bellefonte, PA, USA) packed with a C18 silica-based stationary phase with a particle diameter of  $3 \mu\text{m}$ . The injection volume was  $5 \mu\text{L}$  for all standards and samples. MS experimental conditions were as follows: spray voltage 4 kV, capillary temperature  $275^\circ\text{C}$ , capillary voltage 11 V and tube lens 25 V for positive ESI conditions.

## 2.7. EPR-spin trapping experiments

EPR-spin trapping experiments were carried out with a Bruker ER200 MRD spectrometer equipped with a TE201 resonator (microwave frequency of 9.4 GHz). The homogeneous samples were aqueous solutions containing 5,5'-dimethylpyrroline N-oxide (DMPO,  $5 \times 10^{-2} \text{ M}$ ) as spin trap and  $\text{Na}_4\text{W}_{10}\text{O}_{32}$  ( $2 \times 10^{-4} \text{ M}$ ). In heterogeneous experiments, silica- $\text{NH}_3^+/\text{Na}_3\text{W}_{10}\text{O}_{32}^-$  was suspended in an analogous solution. When requested, CBZ ( $C_0 = 10 \text{ mg L}^{-1}$ ) was introduced together with the spin trap. The samples were put into a flat quartz cell and directly irradiated in the EPR cavity with a medium pressure Hg lamp equipped with cut off filter ( $\lambda > 300 \text{ nm}$ ). No signals were obtained in the dark or during irradiation of the solution in the absence of decatungstate.

## 2.8. XRD analysis

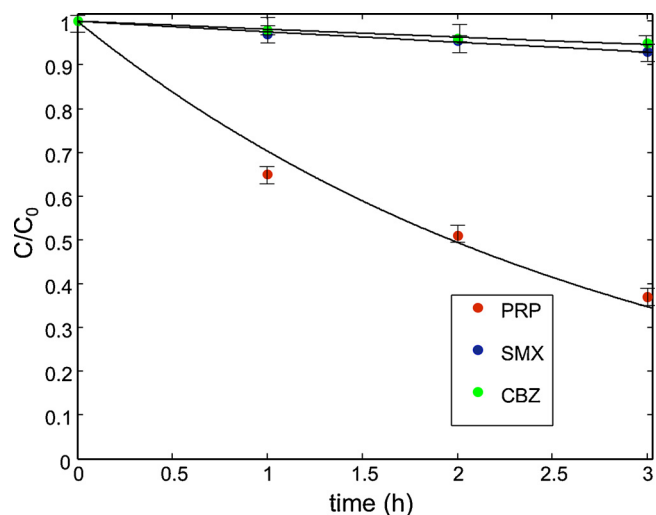
X-ray diffraction was used to verify the incorporation of BTESE on silica-based support. Powder patterns were measured on a Bruker D8 Advance Diffractometer equipped with a Sol-X detector, using  $\text{Cu K}\alpha_1, \alpha_2$  radiation in the  $3\text{--}110$   $2\theta$  range and a counting time of 12 s/step. Table 2S reports reflection information for  $\text{Na}_4\text{W}_{10}\text{O}_{32}/\text{SiO}_2/\text{BTESE}$  phase, where  $hkl$ , STOL is the value of  $\sin\theta/\lambda$ , TTH is the  $2\theta$  position of the reflection, FWHM is the full width at half maximum of the reflection, FOSQ is  $F_0^2$ , SIG is an estimate of  $\sigma F_0^2$ , FOBS is  $F_0$ . The GSAS LeBail computer program with the EXPGUI interface (Larson, A. C., & Von Dreele, R. B. General Structure Analysis System (GSAS); Los Alamos National Laboratory: Los Alamos, NM, 2000, 86–748).

## 3. Results and discussion

### 3.1. Sodium decatungstate heterogenized on modified silica particles (silica- $\text{NH}_3^+/\text{Na}_3\text{W}_{10}\text{O}_{32}^-$ )

We recently demonstrated that a robust and recyclable photocatalytic system can be obtained by immobilization of the anionic cluster on silica particles functionalized with  $-\text{NH}_2$  groups [16]. Moreover, photoexcitation of heterogeneous decatungstate (5 g/L) suspended in aqueous solutions (pH = 6) containing one among levofloxacin or trimethoprim or atenolol ( $C_0 = 10 \text{ mg/L}$ ) caused drug degradation mediated by  $\text{OH}\cdot$  radicals, whose formation has been pointed out by EPR spin trapping spectroscopy [16].

With the aim of evaluating the wide scope of the found method, we decided both to confirm the observed performance by using propranolol (PRP), another  $\beta$ -blocker similar in structure to the previous studied atenolol, and to prove the photocatalytic method extending to other two drugs having different structure and physical chemical properties. In particular, we choose the antibiotic sulfamethoxazole (SMX, often used in combination with the studied trimethoprim) and the antidepressant carbamazepine (CBZ), which is known as a very recalcitrant drug. The degradation of each substrate is followed during irradiation time and it is expressed as ratio  $C/C_0$  (where  $C$  is the drug concentration at a certain time and  $C_0$  is the initial one). Interestingly, we observe (Fig. 1) that PRP behaves similarly to atenolol and after 3 h irradiation about 60–65% of degradation was obtained. On the contrary,



**Fig. 1.** Degradation kinetics of drugs by photoexcitation of silica- $\text{NH}_3^+/\text{Na}_3\text{W}_{10}\text{O}_{32}^-$  (5 g/L) suspended in an aqueous solution (pH 6) containing propranolol (PRP), or sulfamethoxazole (SMX) or carbamazepine (CBZ).  $C_0 = 10 \text{ mg/L}$ . PRP,  $\lambda > 330 \text{ nm}$ ; SMX  $\lambda > 335 \text{ nm}$ ; CBZ,  $\lambda > 300 \text{ nm}$ .

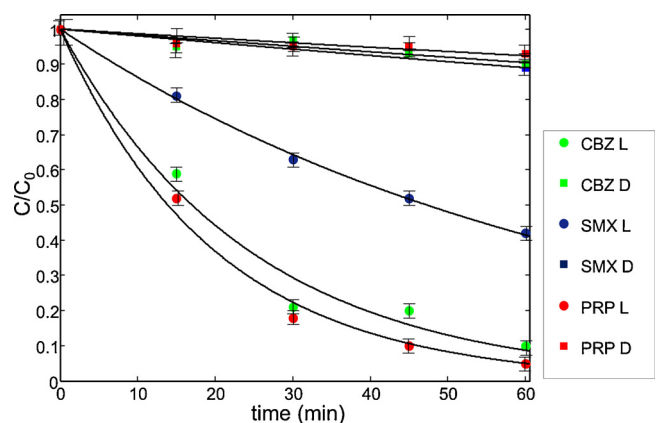
irradiation of the silica- $\text{NH}_3^+/\text{Na}_3\text{W}_{10}\text{O}_{32}^-$  system does not cause any appreciable photocatalytic degradation of both SMX and CBZ.

On the basis of these results, we propose that the inefficient degradation of both SMX and CBZ could be due to one of the following factors: i) low photoactivity of the polyoxoanion with respect to these molecules; ii) scarce affinity of the catalyst support for the two drugs; iii) combination of factors ascribable to decatungstate and its support.

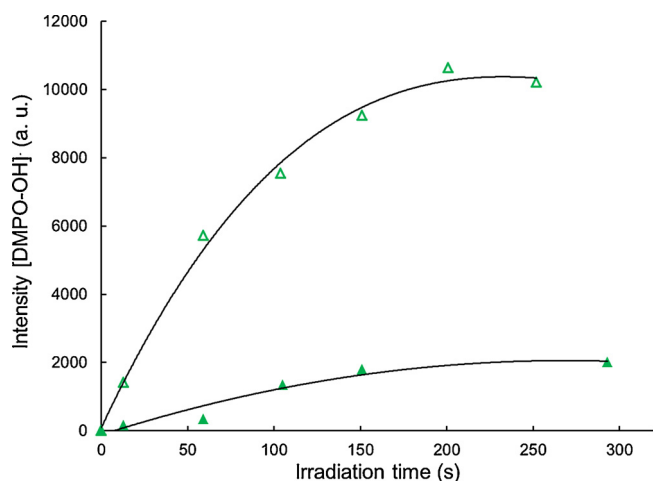
In order to evaluate the photocatalytic activity of decatungstate anion itself, experiments are carried out in homogeneous phase irradiating aqueous solutions containing dissolved  $\text{Na}_4\text{W}_{10}\text{O}_{32}$  ( $2 \times 10^{-4} \text{ M}$ ) and CBZ, SMX or PRP ( $C_0 = 10 \text{ mg/L}$ ). Obtained results are reported in Fig. 2 (circles), together with control experiments in which analogous samples are kept in the dark (squares).

It is shown that around 90% of starting CBZ and PRP are degraded after 60 min of illumination in the presence of homogeneous sodium decatungstate, and a lower degradation efficiency is obtained with SMX that is, however, photodegraded of about 60% in the first hour of irradiation. This decrease is attributable to the photocatalytic activity of  $\text{W}_{10}\text{O}_{32}^{4-}$  since the decrease in the dark of CBZ, SMX or PRP never exceeds 10% (Fig. 2, squares).

Furthermore, EPR-spin trapping experiments support this statement.

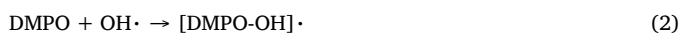
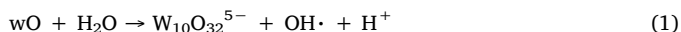


**Fig. 2.** Degradation kinetics of carbamazepine (CBZ), sulfamethoxazole (SMX) and propranolol (PRP) by photoexcitation of  $\text{Na}_4\text{W}_{10}\text{O}_{32}$  ( $2 \times 10^{-4} \text{ M}$ ) dissolved in water at pH 6 (circles). Control experiments are carried out in the dark (squares).  $C_0 = 10 \text{ mg L}^{-1}$ . CBZ,  $\lambda > 300 \text{ nm}$ ; SMX,  $\lambda > 335 \text{ nm}$ ; PRP,  $\lambda > 330 \text{ nm}$ .



**Fig. 3.** Fixed-field signal intensity of the [DMPO-OH]· adduct in time upon irradiation ( $\lambda > 300$  nm) of  $\text{Na}_4\text{W}_{10}\text{O}_{32}$  ( $2 \times 10^{-4}$  M) dissolved in water containing DMPO ( $5 \times 10^{-2}$  M): in the absence (full triangles) and in the presence (empty triangles) of CBZ (10 mg/L). Reported values are the mean of three repeated experiments. Errors do not exceed +10%.

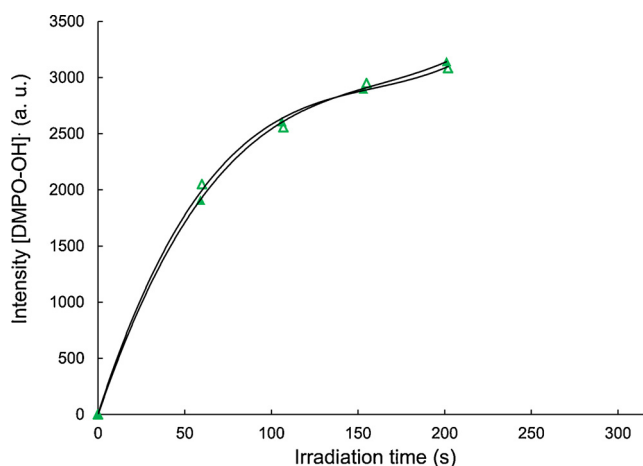
In fact, photoexcitation of  $\text{Na}_4\text{W}_{10}\text{O}_{32}$  dissolved in water in the presence of the spin trap DMPO causes the formation of a quartet 1:2:2:1 ( $a_N = a_H = 14.8$  G) ascribable to the paramagnetic adduct [DMPO-OH]· in accordance to previous investigation [12]. As shown in Fig. 3, the intensity of this signal increases by increasing the irradiation time, showing that reactions:



efficiently occur. Interestingly, addition of CBZ (10 mg/L) to the solution causes an important decrease of [DMPO-OH]· signal. This could be an indication that CBZ competes with DMPO in the reaction with OH· radicals, and probably this reaction is the first step of the photocatalytic drug degradation pathway.

Analogous EPR spin trapping experiments carried out irradiating silica- $\text{NH}_3^+$  /  $\text{Na}_3\text{W}_{10}\text{O}_{32}^-$  suspended in water containing DMPO show that the paramagnetic adduct [DMPO-OH]· is still formed, indicating that the primary photochemical process (reaction 1) that produces OH· radicals is operating also with the heterogeneous system. Contrarily to what observed for homogeneous decatungstate, the addition of CBZ does not cause any decrease in the intensity of the paramagnetic adduct (Fig. 4). This indicates that OH· radicals generated by photoexcited silica- $\text{NH}_3^+$  /  $\text{Na}_3\text{W}_{10}\text{O}_{32}^-$  do not quickly react with CBZ, in agreement with the absence of degradation of this drug shown in Fig. 1. Possibly, CBZ does not adequately approach the surface of the heterogeneous photocatalyst where OH· radicals are produced or CBZ concentration in the solution in contact with the particle is insufficient to favor the reaction between them two.

The different behavior of silica- $\text{NH}_3^+$  /  $\text{Na}_3\text{W}_{10}\text{O}_{32}^-$  with respect to the studied drugs can be tentatively rationalized considering their distribution diagrams (Fig. S1): at the operative pH of 6, while the  $\beta$ -blockers (PRP and atenolol, ATN) are mainly present in solution as cations, the same is not for CBZ and SMX. In fact, CBZ is in its neutral form and SMX presents an equilibrium between neutral and even negative form. Since the silica particles are covered by decatungstate anions, it can be supposed that immobilized decatungstate anions and CBZ or SMX are not sufficiently close each other, a needed requirement for the reaction between drug molecule and photogenerated OH· radicals.



**Fig. 4.** Fixed-field signal intensity of the [DMPO-OH]· adduct in time upon irradiation ( $\lambda > 300$  nm) of silica- $\text{NH}_3^+$  /  $\text{Na}_3\text{W}_{10}\text{O}_{32}^-$  suspended in an aqueous solution containing DMPO ( $5 \times 10^{-2}$  M): in the absence (full symbols) and in the presence of CBZ (10 mg/L) (empty symbols). Reported values are the mean of three repeated experiments. Errors do not exceed  $\pm 5\%$ .

### 3.2. Sodium decatungstate heterogenized on hydrophobic mesoporous silica support ( $\text{SiO}_2/\text{BTESE}/\text{Na}_4\text{W}_{10}\text{O}_{32}$ )

One of the main advantages of heterogeneous photocatalysis is the flexibility in choosing the support with the proper characteristics. Starting from the fact that silica- $\text{NH}_3^+$  /  $\text{Na}_3\text{W}_{10}\text{O}_{32}^-$  is not able to perform efficient photocatalytic degradation of CBZ and SMX (Fig. 1), we thought that a heterogeneous photocatalyst obtained by direct hydrolysis of TEOS and of an organotrialkoxy silane (BTESE) should be hydrophobic enough to favor the approach of organic drugs dissolved in an aqueous matrix. Morphological features of  $\text{SiO}_2/\text{BTESE}/\text{Na}_4\text{W}_{10}\text{O}_{32}$  have been determined: we have checked that  $\text{SiO}_2/\text{BTESE}/\text{Na}_4\text{W}_{10}\text{O}_{32}$  employed in this research presents similar morphological characteristics to those of an analogous heterogeneous system previously used [21]. In particular, the specific surface area is roughly  $700 \text{ m}^2 \text{ g}^{-1}$  and about 80% of total pore volume are classified as mesopores. Additionally, FTIR spectra clearly showed that organic fragments (coming from BTESE) and silica moieties are distributed within the framework and microgravimetric adsorption isotherms pointed out that  $\text{SiO}_2/\text{BTESE}/\text{Na}_4\text{W}_{10}\text{O}_{32}$  enhances adsorption of toluene vapors with respect to that of water [21]. To complete the characterization, XRD was used to determine  $\text{Na}_4\text{W}_{10}\text{O}_{32}$  unit cell parameters starting from the CIF file deposited with the Cambridge Crystallographic Data Center under number CCDC 1548831. The  $\text{Na}_4\text{W}_{10}\text{O}_{32}/\text{SiO}_2/\text{BTESE}$  refined XRD pattern is shown in Fig. 5.

From Fig. 5 the peaks at scattering angle ( $2\theta$ ) values of  $16.52^\circ$ ,  $25.57^\circ$ ,  $34.22^\circ$  and  $35.04^\circ$  were assigned to  $\text{Na}_4\text{W}_{10}\text{O}_{32}$  respectively. The main crystallographic data and refinement results are as follows: triclinic crystal symmetry, space group  $P_{-1}$ ,  $a = 11.9532(6)$  Å,  $b = 12.2201(7)$  Å,  $c = 12.1898(8)$  Å,  $\alpha = 75.343^\circ(4)$ ,  $\beta = 71.525^\circ(4)$ ,  $\gamma = 88.083^\circ(5)$ , cell volume =  $1631.70(17)$  Å<sup>3</sup>. Values in parenthesis represent the standard deviations of the parameters computed on the basis of 8467 independent observations. Final reliability factors over the observed reflections  $R_p = 0.0403$ ,  $R_{wp} = 0.0535$ ,  $\chi^2 = 1.029$  (where  $R_p = \sum|Y_{io} - Y_{ic}|/\sum Y_{io}$ ;  $R_{wp} = [\sum w_i(Y_{io} - Y_{ic})^2/\sum w_i Y_{io}^2]^{0.5}$ ).

These data allows us to infer that decatungstate anion is not significantly modified during the synthesis of the heterogeneous system via hydrolysis of TEOS and of BTESE. In addition, XRD analysis shows that it is encapsulated inside the mesoporous network. Finally, the decatungstate content was determined by ICP-OES measurement (see par. 2.2).

As described in the Experimental Section, the synthesis process of  $\text{SiO}_2/\text{BTESE}/\text{Na}_4\text{W}_{10}\text{O}_{32}$  includes the hydrolysis of TEOS and of BTESE

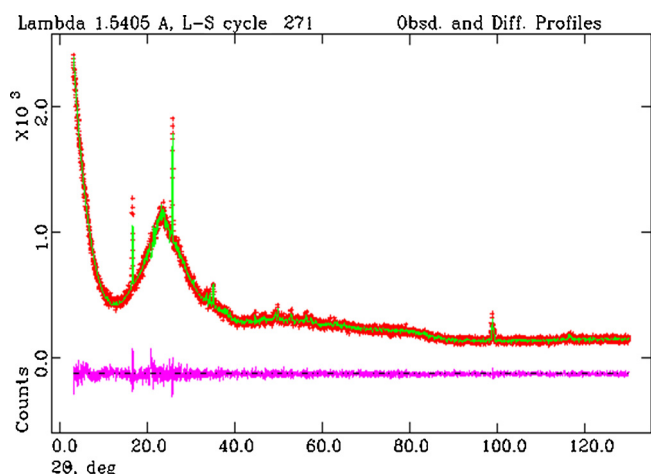


Fig. 5. Observed (red dotted line), calculated (green solid line) and difference (purple bottom line) X-ray powder diffraction patterns for  $\text{Na}_4\text{W}_{10}\text{O}_{32}/\text{SiO}_2/\text{BTESE}$ . (For interpretation of the references to colour in this figure legend, the reader is referred to the web version of this article).

in the presence of an acid solution of sodium decatungstate. Silanol groups ( $\equiv\text{Si}-\text{OH}$ ) can be protonated in the acidic medium to form  $\equiv\text{Si}-\text{OH}_2^+$ . These groups, in turn, should act as counterions for decatungstate anion, that on the basis of XRD results is entirely encapsulated in the mesopores, leading to  $(\equiv\text{Si}-\text{OH}_2^+)(\text{Na}_3\text{W}_{10}\text{O}_{32}^-)$  [24]. This strong interaction is confirmed by UV-vis spectra of washing water aliquots showing that polyoxoanion was not released in the solution.

Therefore, this heterogeneous photocatalytic system was used for attempting the degradation of CBZ and SMX and, in a typical experiment,  $\text{SiO}_2/\text{BTESE}/\text{Na}_4\text{W}_{10}\text{O}_{32}$ , suspended in an aqueous solution containing the drug of interest, is irradiated for a desired time (see Experimental section). In parallel, samples prepared in an analogous way are kept in the dark for the same period. The degradation of each substrate is expressed, as before, in terms of  $C/C_0$  ratio vs time (Fig. 6).

One can observe that CBZ and SMX are now degraded upon photoexcitation of decatungstate. After 4 h illumination, more than 80% of CBZ and of SMX disappear from the aqueous solution. To verify the photoactivity of eventual leached polyoxoanion, the solution after one hour irradiation was separated from the heterogeneous photocatalyst, analyzed and then directly irradiated for an hour. The final analysis of these samples do not show a significant change ( $< 2\%$ ) in remained

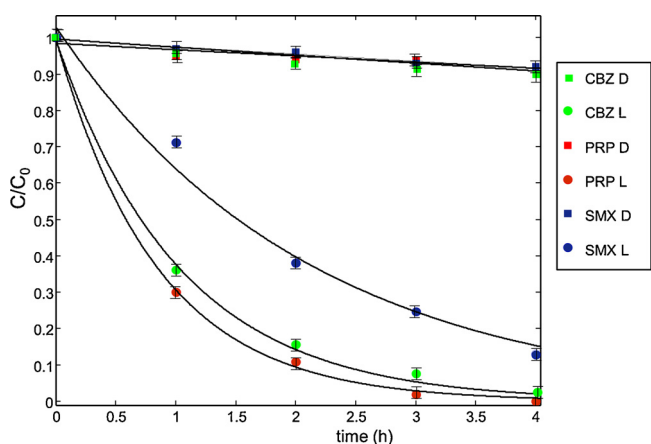


Fig. 6. Degradation kinetics of carbamazepine (CBZ), sulfamethoxazole (SMX) and propranolol (PRP) by photoexcitation of  $\text{SiO}_2/\text{BTESE}/\text{Na}_4\text{W}_{10}\text{O}_{32}$  ( $500 \text{ g L}^{-1}$ ) suspended in water at pH 6 (circles). Control experiments are carried out in the dark (squares).  $C_0 = 10 \text{ mg L}^{-1}$ . CBZ,  $\lambda > 300 \text{ nm}$ ; SMX,  $\lambda > 335 \text{ nm}$ ; PRP,  $\lambda > 330 \text{ nm}$ .

Table 1

Kinetic constants obtained by fitting the experimental data with a first order kinetic equation ( $C/C_0 = \exp(-kt)$ ). Data in parenthesis are the confidence limits at 95% of probability.

Photocatalyst	drug	k ( $\text{h}^{-1}$ )	R <sup>2</sup>
$\text{Na}_4\text{W}_{10}\text{O}_{32}$ solution	CBZ	2.46 (2.10, 2.82)	0.9808
	PRP	2.94 (2.73, 3.05)	0.9934
	SMX	0.90 (0.89, 0.91)	0.9987
$\text{SiO}_2-\text{NH}_3^+ / \text{Na}_3\text{W}_{10}\text{O}_{32}^-$	CBZ	0.024 (0.021, 0.027)	0.9837
	PRP	0.35 (0.28, 0.42)	0.9867
	SMX	0.021 (0.018, 0.024)	0.9881
$\text{SiO}_2/\text{BTESE}/\text{Na}_4\text{W}_{10}\text{O}_{32}$	CBZ	0.97 (0.83, 1.11)	0.9977
	PRP	1.18 (1.08, 1.28)	0.9982
	SMX	0.48 (0.36, 0.60)	0.9825

drug concentration indicating that release of decatungstate into the solution is negligible. These results allow us to infer that the removal of CBZ and SMX occurs via the heterogeneous photocatalytic system employed. Moreover, the charge taken by the drug molecule at pH 6 (Fig. S1) that was an obstacle in the case of  $\text{SiO}_2-\text{NH}_3^+ / \text{Na}_3\text{W}_{10}\text{O}_{32}^-$  is overcome by this kind of support.

Concerning the stability of the material,  $\text{SiO}_2/\text{BTESE}/\text{Na}_4\text{W}_{10}\text{O}_{32}$  was recovered, washed with acetonitrile, dried at 373 K for 60 min and then used in a second experiment. The loss of activity in terms of both adsorption and photocatalytic degradation was within 10% after the two cycles, in agreement with the lack of release of anion during the experiment.

In Table 1 the kinetic constants obtained by fitting the data with a pseudo first order kinetic model are reported. A comparison can be made between homogeneous samples and heterogeneous experiments. One can additionally observe that SMX degradation kinetic is the slowest also with homogeneous sodium decatungstate, reinforcing the idea that the ionic charge of the drug molecule at pH 6 has a relevant role for the beginning of the oxidation process.

From these results, we suggest that the ability of  $\text{SiO}_2/\text{BTESE}/\text{Na}_4\text{W}_{10}\text{O}_{32}$  to photodegrade CBZ and SMX can be attributed to the hydrophobicity induced by BTESE to the heterogeneous photocatalytic system. From Table S1, CBZ and SMX are hydrophobic (see  $\log k_{ow}$ ) and it has been already proved that they are adsorbed by high silica microporous material [25,26]. Moreover, the molecular dimensions are suitable with the pore sizes of the support where decatungstate anion is encapsulated. This can facilitate their approach to  $\text{OH}\cdot$  radicals photoproduced nearby.

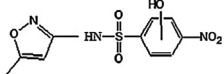
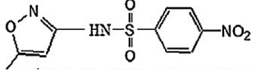
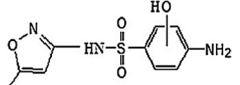
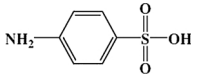
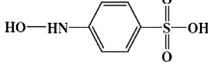
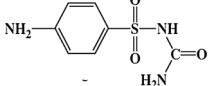
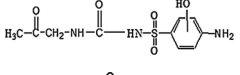
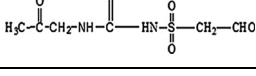
In addition  $\text{SiO}_2/\text{BTESE}/\text{Na}_4\text{W}_{10}\text{O}_{32}$  maintains a very good performance also in the degradation of PRP, showing that hydrophobicity introduced in the support does not preclude positively charged molecules from approaching the polyoxoanion (Fig. 1S). This result is particularly relevant since drugs photodegradation can be performed despite the form (charged or not) mainly present at the working conditions and answers to the requirement of general applicability.

### 3.3. HPLC/MS analysis

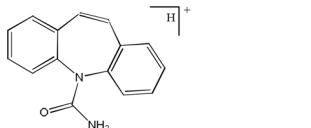
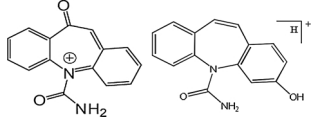
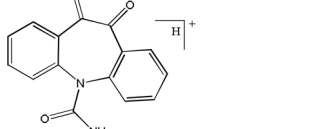
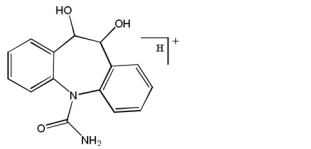
Degradation mechanism of drug molecules by  $\text{SiO}_2/\text{BTESE}/\text{Na}_4\text{W}_{10}\text{O}_{32}$  was investigated analyzing irradiated solution by HPLC-MS. Identification of the degradation byproducts was based on the analysis of the total ion current (TIC) and on the corresponding mass spectra. The identified intermediates for the case of SMX and of CBZ are reported in Tables 2 and 3 respectively.

The intermediate with 301  $m/z$  corresponds to a monohydroxylation of the aromatic ring and a nitration of the amino group of SMX. The product with 283  $m/z$  derives from the oxidation of the amino group to nitro derivative, whereas the intermediate with 270  $m/z$  correspond to the hydroxylation of SMX aromatic ring. Oxidation of the isoxazole ring of 270  $m/z$  results in the formation of 288  $m/z$  and 228  $m/z$

**Table 2**  
SMX: degradation intermediates, retention times, fragment ions and proposed structures.

Precursor Ion (m/z)	t <sub>r</sub> (min)	MS <sup>2</sup> (m/z)	Structure
301	9.18	177 133	
283	9.18	239 177 133	
270	10.25	206 228	
174	10.20	156	
190	3.76	158	
216	13.54	198	
288	14.46	270	
228	14.70		

**Table 3**  
CBZ: degradation intermediates, retention times, fragment ions and proposed structures.

Precursor Ion (m/z)	t <sub>r</sub> (min)	MS <sup>2</sup> (m/z)	Structure
237.1	14.35	194.01 220.06	
251.1 253.1	12.3	208.0 210.0 236.0	
267.1	16.2	168 196.1 211.1	
271.1	9.6	210 253	

intermediate and the intermediate with 216 m/z can derive from the opening of the isoxazole ring of SMX. The cleavage of bond between isoxazole ring and the amine group of SMX, can generate the 174 m/z by-product. The compound with 190 m/z was identified as an

hydroxylated form of the amino group of 174 m/z derivative. Structures similar to those described were observed also in the photo-Fenton degradation of SMX [27].

From Table 2 it is seen that hydroxylation of SMX by hydroxyl radical (OH·) attack could be an important reaction for the subsequent degradation of SMX. Indeed, three mono-hydroxylated byproducts (i.e. 301 m/z, 270 m/z and 288 m/z) are revealed.

Mono and dihydroxylated intermediates were also identified in the CBZ degradation by photoexcited /SiO<sub>2</sub>/BTESE/Na<sub>4</sub>W<sub>10</sub>O<sub>32</sub> catalyst in aqueous solution and they correspond to the intermediates 253 and 271 m/z respectively in Table 3. Further oxidation of both these compounds leads to the formation of 251 and 267 m/z intermediates. The detection of these intermediates indicates that hydroxylation and oxidation are the main reactions responsible for CBZ degradation.

On the basis of reported and previous results we propose a reaction mechanism for photoexcited /SiO<sub>2</sub>/BTESE/Na<sub>4</sub>W<sub>10</sub>O<sub>32</sub> that can be considered general for pharmaceutical photocatalytic degradation. Photoexcitation of decatungstate anion dissolved or suspended in an aqueous environment causes the oxidation of water to OH· radicals [12], as shown in reaction 1. EPR spin trapping experiments and HPLC-MS point out that hydroxyl radicals attack drug molecules giving mono- or dihydroxylated intermediates. Their formation is the prelude to fragmentation.

#### 4. Conclusions

The ability of photoexcited sodium decatungstate to oxidize water producing OH· radicals, already observed in homogeneous conditions, is kept also when the polyoxoanion is heterogenized on siliceous supports. In this paper, we demonstrate that support characteristics are of paramount importance when reaction between OH· radicals and the organic molecule is the first step of its degradative pathway. In particular, silica-NH<sub>3</sub><sup>+</sup> / Na<sub>3</sub>W<sub>10</sub>O<sub>32</sub><sup>-</sup> system, constituted by particles covered by decatungstate anions, is not efficient in the degradation of carbamazepine and sulfamethoxazole, which are neutral or negatively charged at the operating pH. On the contrary, entrapment of Na<sub>4</sub>W<sub>10</sub>O<sub>32</sub><sup>-</sup> inside a mesoporous organosilica matrix leads to a heterogeneous photocatalytic system with proper characteristic of hydrophobicity that is able to degrade not only carbamazepine and sulfamethoxazole but also all the other categories previously studied. In fact, the higher hydrophobicity of the organosilica support with respect to the aqueous environment favors adsorption of organic molecules, which enter the mesopores. Here, their proximity to photoproducted OH· radicals favors the hydroxylation of drug molecule. HPLC-MS investigation points out that mono- and di-hydroxylated products are formed and precede fragmentation pathways and degradation. Results obtained from the used independent techniques and methods allow us to formulate a general advanced oxidation process mechanism for the photocatalytic degradation of drug molecules by heterogeneous sodium decatungstate.

#### Acknowledgement

We kindly acknowledge University of Ferrara (FAR 2016) for financial support.

#### Appendix A. Supplementary data

Supplementary material related to this article can be found, in the online version, at doi:<https://doi.org/10.1016/j.apcatb.2018.08.015>.

#### References

- [1] B. Subedi, K. Kannan, Mass loading and removal of select illicit drugs in two wastewater treatment plants in New York state and estimation of illicit drug usage in communities through wastewater analysis, *Environ. Sci. Technol.* 48 (2014)

- 6661–6670.
- [2] M.J. Benotti, R.A. Trenholm, B.J. Vanderford, J.C. Holady, B.D. Stanford, S.A. Snyder, Pharmaceuticals and endocrine disrupting compounds in U.S. drinking water, *Environ. Sci. Technol.* 43 (2009) 597–603.
- [3] M.N. Chong, A.K. Sharma, S. Burn, C.P. Saint, Feasibility study on the application of advanced oxidation technologies for decentralised wastewater treatment, *J. Clean. Prod.* 35 (2012) 230–238.
- [4] J.L. Wang, L. Xu, Advanced oxidation processes for wastewater treatment: formation of hydroxyl radical and application, *Critic. Rev. Environ. Sci. Technol.* 42 (2012) 251–325.
- [5] U.I. Gaya, A.H. Abdullah, Heterogeneous photocatalytic degradation of organic contaminants over titanium dioxide: a review of fundamentals, progress and problems, *J. Photochem. Photobiol. C: Photochem. Rev.* 9 (2008) 1–12 and references therein.
- [6] M. Addamo, V. Augugliaro, A. Di Paola, E. Garcia-Lopez, V. Loddo, G. Marci, Removal of drugs in aqueous systems by photoassisted degradation, *J. Appl. Electrochem.* 35 (2005) 765–774.
- [7] L.A. Ioannou, E. Hapeshi, M.I. Vasquez, D. Mantzavinos, D. Fatta-Kassinos, Solar/ $\text{TiO}_2$  photocatalytic decomposition of  $\beta$ -blockers atenolol and propranolol in water and wastewater, *Sol. Energy* 85 (2011) 1915–1926.
- [8] L. Haroune, M. Salaun, A. Menard, C.Y. Legault, J.P. Bellenger, Photocatalytic degradation of carbamazepine and three derivatives using  $\text{TiO}_2$  and ZnO: effect of pH, ionic strength, and natural organic matter, *Sci. Total Environ.* 475 (2014) 16–22.
- [9] G. Longobucco, L. Pasti, A. Molinari, N. Marchetti, S. Caramori, V. Cristino, R. Boaretto, C.A. Bignozzi, Photoelectrochemical mineralization of emerging contaminants at porous  $\text{WO}_3$  interfaces, *Appl. Catal. B: Environ.* 204 (2017) 273–282.
- [10] P. Kormali, D. Dimotikali, D. Tsipi, A. Hiskia, E. Papaconstantinou, Photolytic and photocatalytic decomposition of fenitrothion by  $\text{PW}_{12}\text{O}_{40}^{3-}$  and  $\text{TiO}_2$ : a comparative study, *Appl. Catal. B: Environ.* 48 (2004) 175–183.
- [11] P. Kormali, A. Troupis, T. Triantis, A. Hiskia, E. Papaconstantinou, Photocatalysis by polyoxometallates and  $\text{TiO}_2$ : a comparative study, *Catal. Today* 124 (2007) 149–155.
- [12] A. Molinari, R. Argazzi, A. Maldotti, Photocatalysis with  $\text{Na}_4\text{W}_{10}\text{O}_{32}$  in water system: formation and reactivity of  $\text{OH}^\bullet$  radicals, *J. Mol. Catal. A Chem.* 372 (2013) 23–28.
- [13] A. Maldotti, A. Molinari, G. Varani, M. Lenarda, L. Storaro, F. Bigi, R. Maggi, A. Mazzacani, G. Sartori, Immobilization of (n-Bu<sub>4</sub>N)<sub>4</sub>W<sub>10</sub>O<sub>32</sub> on mesoporous MCM-41 and amorphous silicas for photocatalytic oxidation of cycloalkanes with molecular oxygen, *J. Catal.* 209 (2002) 210–216.
- [14] E.S. Da Silva, V. Prevot, C. Forano, P. Wong-Wah Chung, H.D. Burrows, M. Sarakha, Heterogeneous photocatalytic degradation of pesticides using decatungstate intercalated macroporous layered double hydroxides, *Environ. Sci. Pollut. Res.* 21 (2014) 11218–11227.
- [15] A. Molinari, G. Varani, E. Polo, S. Vaccari, A. Maldotti, Photocatalytic and catalytic activity of heterogenized  $\text{W}_{10}\text{O}_{32}^{4-}$  – in the bromide-assisted bromination of arenes and alkenes in the presence of oxygen, *J. Mol. Catal. A Chem.* 262 (2007) 156–163.
- [16] A. Molinari, E. Sarti, N. Marchetti, L. Pasti, Degradation of emerging concern contaminants in water by heterogeneous photocatalysis with  $\text{Na}_4\text{W}_{10}\text{O}_{32}$ , *Appl. Catal. B: Environ.* 203 (2017) 9–17.
- [17] S.-S. Wang, G.-Y. Yang, Recent advances in polyoxometalate-catalyzed reactions, *Chem. Rev.* 115 (2015) 4893–4962.
- [18] F. Zaera, The new materials science of catalysis: toward controlling selectivity by designing the structure of the active site, *J. Phys. Chem. Lett.* 1 (2010) 621–627.
- [19] A. Maldotti, R. Amadelli, A. Molinari, M.G. Clerici, O. Kholdeeva (Eds.), *Liquid Phase Oxidation via Heterogeneous Catalysis*, Wiley, 2013, pp. 411–450 ch. 9.
- [20] A.J. Ebele, M. Abou-Elwafa Abdallah, S. Harrad, Pharmaceuticals and personal care products (PPCPs) in the freshwater aquatic environment, *Emerg. Contam.* 3 (2017) 1–16.
- [21] A. Molinari, G. Magnacca, G. Papazzoni, A. Maldotti, Hydrophobic  $\text{W}_{10}\text{O}_{32}^{4-}$ /silica photocatalyst for toluene oxidation in water system, *Appl. Catal. B: Environ.* 138–139 (2013) 446–452.
- [22] D.C. Duncan, T.C. Netzel, C.L. Hill, Early-time dynamics and reactivity of polyoxometalate excited states. identification of a short-lived LMCT excited state and a reactive long-lived charge-transfer intermediate following picosecond flash excitation of  $[\text{W}_{10}\text{O}_{32}]^{4-}$  in acetonitrile, *Inorg. Chem.* 34 (1995) 4640–4646.
- [23] F. Bigi, A. Corradini, C. Quarantelli, G. Sartori, Silica-bound decatungstates as heterogeneous catalysts for  $\text{H}_2\text{O}_2$  activation in selective sulfide oxidation, *J. Catal.* 250 (2007) 222–230.
- [24] Y. Guo, C. Hu, X. Wang, Y. Wang, E. Wang, Microporous decatungstates: synthesis and photochemical behavior, *Chem. Mater.* 13 (2001) 4058–4064.
- [25] A. Martucci, L. Pasti, N. Marchetti, A. Cavazzini, F. Dondi, A. Alberti, Adsorption of pharmaceuticals from aqueous solutions on synthetic zeolites, *Microporous Mesoporous Mater.* 148 (2012) 174–183.
- [26] S. Blasioli, A. Martucci, G. Paul, L. Gigli, M. Cossi, C.T. Johnston, L. Marchese, I. Braschi, Removal of sulfamethoxazole sulfonamide antibiotic from water by high silica zeolites: a study of the involved host–guest interactions by a combined structural, spectroscopic, and computational approach, *J. Colloid Interface Sci.* 419 (2014) 148–159.
- [27] O. González, S. Carme, S. Esplugas, Sulfamethoxazole abatement by photo-Fenton: toxicity, inhibition and biodegradability assessment of intermediates, *J. Hazard. Mater.* 146 (2007) 459–464.



## Photoelectrochemical degradation of pharmaceuticals at $\beta$ 25 modified $\text{WO}_3$ interfaces

Vito Cristino<sup>a</sup>, Gelsomina Longobucco<sup>a</sup>, Nicola Marchetti<sup>a</sup>, Stefano Caramori<sup>a,\*</sup>, Carlo Alberto Bignozzi<sup>a</sup>, Annalisa Martucci<sup>b</sup>, Alessandra Molinari<sup>a</sup>, Rita Boaretto<sup>a</sup>, Claudia Stevanin<sup>a</sup>, Roberto Argazzi<sup>a</sup>, Maurizio Dal Colle<sup>a</sup>, Renzo Bertinello<sup>c</sup>, Luisa Pasti<sup>a,\*</sup>

<sup>a</sup> Department of Chemical and Pharmaceutical Sciences, Via Luigi Borsari 46, 44121, Ferrara, Italy

<sup>b</sup> Department of Physics and Earth Sciences, University of Ferrara, Via Saragat 1, 44121, Ferrara, Italy

<sup>c</sup> Department of Chemical Sciences, University of Padua, Via Marzolo 1, 35131, Padua, Italy

### ARTICLE INFO

#### Keywords:

$\text{WO}_3$   
Zeolite  
Photoelectrochemistry  
Photocatalysis  
Environmental remediation

### ABSTRACT

In this contribution we have explored the applications of  $\text{WO}_3$  based nanomaterials to the degradation of Ketoprofen and Levofloxacin, selected among the most widely used anti-inflammatory and analgesic species and antibiotics and representing thus ubiquitous water contaminants of emerging concern. Compared to conventional photocatalytic conditions, which were not effective in the oxidative degradation of Ketoprofen, the application of the electric bias was successful in promoting a 50% Ketoprofen degradation after 5 h illumination, with a degradation rate constant of  $0.22 \text{ h}^{-1}$ . A similar improvement was found with Levofloxacin. The degradation rate was further accelerated by exploiting  $\text{WO}_3$  films modified with  $\beta$ 25 zeolites which achieved, on the same time scale, > 65% degradation with Ketoprofen and ca. 90% with Levofloxacin. The complete disappearance of the oxidation intermediates of these two drugs was observed on a time scale of ca. 20 h, indicative of the achievement of complete drug mineralization at the illuminated  $\beta$ 25/ $\text{WO}_3$  interface under 1 sun illumination.

### 1. Introduction

Among the wide variety of Contaminants of Emerging Concerns (CECs) pharmaceuticals, personal care products and their metabolites have especially alarmed the public and regulators. Although adverse human health consequences from the existing trace levels of these substances in natural or drinking water are in general unlikely, their impact to aquatic ecosystems is more evident [1]. Some of these emerging pollutants are indeed very stable molecules, capable to survive the current potabilization and water remediation processes [2] and are thus able to reach and impact the aqueous environment with unaltered efficacy. In view of the growing world population, increasing industrialization of emerging countries and climate change, the re-use and re-cycle of water and the protection of aqueous ecosystems represent major societal challenges. Photocatalytic routes to the degradation of harmful organics, exploiting sunlight to trigger the formation of high energy electron/hole pairs (e/h) within dispersed semiconductor (nano)particles, to promote direct or indirect (mediated for example by oxidants like  $\cdot\text{O}_2^-$ ,  $\text{H}_2\text{O}_2$ ,  $\cdot\text{OH}$ ) oxidation reactions is an

established approach, particularly with  $\text{TiO}_2$  [3–6] and  $\text{ZnO}$  [7–9] based materials. Some of the present authors also employed a decatungstate polyoxoanion heterogenized on silica particles in the photomineralization of pharmaceuticals [10]. The common feature of all these materials is the ability to photoproduce  $\cdot\text{OH}$  radicals, whose oxidation potential ( $E^\circ = 2.1 \text{ V}$  vs NHE) allows for the oxidation of a variety of organic compounds leading, with sufficient time, to their mineralization [11]. In the absence of visible absorbing dye sensitizers [12,13], an important drawback of the materials and molecular clusters mentioned above is their limited capacity of harvesting the solar spectrum, with no practical photochemical activity beyond 420 nm. Other semiconductors, and among them  $\text{WO}_3$ , offer a lower band gap (ca.  $2.7 \pm 0.1 \text{ eV}$ ) [14] for harvesting a sizable portion of the visible region, up to 460 nm, with a valence band edge suitable for the production of  $\cdot\text{OH}$  radicals following monoelectronic oxidation of water [15]. The application of electric potential (bias) to a nanocrystalline thin film semiconductor, allows to optimize the charge separation at the Semiconductor/Electrolyte Interface (SEI), improving the rate of degradation of organic targets [16,17]. Recently, the

\* Corresponding authors.

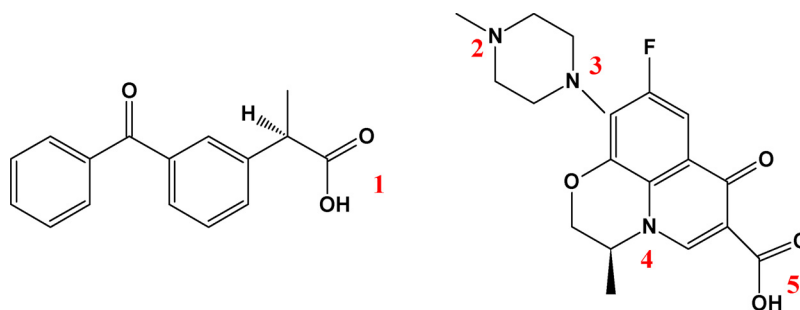
E-mail addresses: [cte@unife.it](mailto:cte@unife.it) (S. Caramori), [psu@unife.it](mailto:psu@unife.it) (L. Pasti).

<https://doi.org/10.1016/j.cattod.2018.09.020>

Received 15 June 2018; Received in revised form 25 September 2018; Accepted 28 September 2018

Available online 15 October 2018

0920-5861/ © 2018 Elsevier B.V. All rights reserved.



**Chart 1.** Molecular structures of KTP (left) and LFX (right). Both molecules are represented in their neutral form. Red numbers refer to the ionizable groups in their molecular structures. (For interpretation of the references to colour in this figure legend, the reader is referred to the web version of this article.)

photoelectrochemical approach employing  $\text{WO}_3$  photoanodes to the degradation of CECs, represented by either neutral (Carbamazepin, CBZ) or positively charged (Atenolol, ATN) molecular species, outperformed open circuit photocatalysis by a factor of three-to-five [18].

In this contribution we have focused on the degradation of Ketoprofen (KTP) and Levofloxacin (LFX) (Chart 1) in diluted aqueous electrolytes ( $[\text{Na}_2\text{SO}_4] = 7 \times 10^{-4} \text{ M}$ ) at pH 6. These targets were selected among the most widely used anti-inflammatory and analgesic species (KTP) and antibiotics (LFX). LFX is an antibacterial fluoroquinolone widely used in the treatment of respiratory diseases and bacterial infections. The urinary excretion of fluoroquinolones delivers about 85% of the unmodified parent compounds, consequently a considerable amount of active drugs is present in waste waters [19]. Concerning the widely used KTP, roughly 80% of the administered dose is excreted in the urine, primarily as the glucuronide metabolite explaining its abundance in waste waters [20]. Additionally, these substances have been chosen as target molecules for their different acid/base characteristics, that allow us to investigate how the photocatalyst activity is influenced by the structure and physico-chemical properties of the target substrate. Indeed, KTP carries a carboxylic acid (see 1 in Chart 1), which dissociates at  $\text{pH} \geq 6$  having a typical  $\text{pK}_a \approx 4.5$  [21] resulting in an anionic species within the pH selected for the photo-degradation experiments. LFX has a carboxylic group as well (5), but it also possesses two tertiary  $\text{sp}^3$  nitrogens (2–4) one of which can be protonated at neutral and acidic pH. The protonation constants indicate that this compound is present mainly as a zwitterionic form at pH 6, whereas at pH higher than 7 it prevails in the negative form [22]. Available nitrogen lone pairs in LFX might also interact with  $\text{W}^{6+}$  acid groups at  $\text{WO}_3$  surface, favoring the contact between LFX and the oxidant species generated by the photocatalyst. Interestingly, while it has been found that LFX is effectively degraded under both photocatalytic (no bias) and photoelectrochemical (applied bias) conditions, in the case of KTP there is an extreme difference in the photochemical vs photoelectrochemical degradation kinetic: under conventional photocatalytic conditions, KTP does not show any appreciable photocatalytic degradation, whereas under applied bias its degradation is roughly 70% complete within a 5 h illumination cycle. This behavior was explained by the induction of a local excess of KTP at the  $\text{WO}_3$  SEI under positive potential, allowing a faster reaction with surface generated  $\cdot\text{OH}$  radicals. In the absence of positive bias, at pH 6, such interaction does not occur, due to electrostatic repulsion between the anionic KTP and the negatively charged  $\text{WO}_3$  surface, having zero zeta potential below pH 2. This indicates that besides modulating the charge separation rate at the SEI, the electric bias is useful to tune the solar degradation of otherwise impervious molecular species, ostensibly acting through double layer effects which result in an increased concentration of the molecular targets in proximity of the mesoporous photoactive material.

Finally, the degradation activity of  $\text{WO}_3$  was enhanced by incorporating an adsorbent material, in particular a Beta zeolite (BEA) having  $\text{SiO}_2/\text{Al}_2\text{O}_3$  ratio equal to 25 ( $\beta 25$ ) [23]. The use of composite materials based on  $\text{WO}_3$  modified with zeolites has been reported in

catalysis, [24] sensor application [25] and, more recently, in gas phase photocatalysis [26], but, to the best of our knowledge, it was never reported for the degradation of these emerging contaminants in aqueous solution in a photoelectrochemical cell. The combination of the photocatalyst with the adsorbent allows to collect and trap contaminant molecules in proximity of the surface, where  $\cdot\text{OH}$  photogeneration occurs, allowing to increase the chance of bimolecular encounter between the target and this highly reactive oxidant. This strategy thus results in efficient degradation of species, such as KTP, even under purely photocatalytic (no bias) conditions.

## 2. Experimental

### 2.1. Chemicals for analytical and photo-electrochemical measurements

Levofloxacin (Fluka, purity > 98%), ketoprofen (Sigma-Aldrich, purity > 98%), sodium sulfate (Sigma-Aldrich, purity, 99%), sulfuric acid (Sigma-Aldrich, 95%), were used as received. Zeolite Beta (Zeolyst International) in its ammonium cation form, having a  $\text{Na}_2\text{O}$  content lower than 0.05% wt was employed after a calcination process. Calcination was carried out by raising the temperature from room temperature to  $600^\circ\text{C}$  in 1 h, then holding at  $600^\circ\text{C}$  for 4 h. Finally, the adsorbents were kept at room temperature for 3 h. High-performance liquid chromatography (HPLC) grade acetonitrile (ACN) was purchased from Merck (Darmstadt, Germany). The water was Milli-Q® grade (Millipore, MA, USA).

A dilute aqueous solution of sulfuric acid was employed to adjust at 6 the pH of the drug solution (in the range 30–2 ppm Levofloxacin or Ketoprofen) containing 0.7 mM of sodium sulfate as supporting electrolyte. The saline concentration was chosen to reproduce the average salinity of freshwater [27]. The pH of the drug solutions was measured with a combined glass electrode connected to an AMEL pH-meter (Milano, Italy).

### 2.2. Preparation of materials and thin films for photocatalysis and photoelectrocatalysis

Nanocrystalline  $\text{WO}_3$  was prepared by following a published procedure [15]. Briefly,  $\text{H}_2\text{WO}_4$  was generated from 2.5 g of  $\text{Na}_2\text{WO}_4$  (Alfa Aesar) dissolved in 100 mL of Millipore water by addition of 20 ml of concentrated HCl (Sigma-Aldrich), followed by several washings in order to eliminate NaCl. The colloidal suspension of  $\text{H}_2\text{WO}_4$  nanoparticles was obtained by dissolving the  $\text{H}_2\text{WO}_4$  gel in 3 M oxalic acid (2.5 ml) at  $60^\circ\text{C}$  (Sigma-Aldrich) and stabilized by addition of 20% w/w Carbowax (Sigma-Aldrich, 15,000–20,000 u) and Triton X-100 (Fluka) (1 drop/2 g of colloidal precursor) which acted as densifier/sintering agent and tensioactive respectively.  $\text{WO}_3$  electrodes (active area  $1 \text{ cm}^2$ ) were fabricated by spin casting (600 rpm for 6 s followed by 2000 rpm for 20 s) colloidal  $\text{H}_2\text{WO}_4$  onto well cleaned FTO substrates (Fluorine Tin Oxide, Pilkington TEC 8) glass, followed by firing at  $550^\circ\text{C}$ . This procedure was repeated six times in order to obtain films

having a thickness of ca. 2  $\mu\text{m}$  and a photoresponse up to 470 nm, as shown by a typical photoaction spectrum in sulfuric acid (Fig. S1).

Deposition of zeolites on  $\text{WO}_3$  electrodes was achieved by repeated spin coating ( $4\times$ , 600 rpm for 6 s followed by 2000 rpm for 20 s) of a 4% w/v  $\beta\text{25}$  suspension in water. After each deposition of  $\beta\text{25}$ , the electrode was heated at 550  $^\circ\text{C}$  to consolidate deposition.

$\beta\text{25}/\text{WO}_3$  nanocrystalline powder was prepared by adding 0.1 g of  $\beta\text{25}$  zeolite to the  $\text{H}_2\text{WO}_4$  gel obtained as previously described, followed by stirring for 24 h. The resulting solid was separated by centrifugation and heated at 550  $^\circ\text{C}$  for 8 h to obtain a powder.

### 2.3. AFM

Atomic force microscopy (AFM) images were collected using a Digital Instruments Nanoscope III scanning probe Microscope (Digital Instruments, CA). The instrument was equipped with a silicon tip (RTESP-300 Bruker) and operated in tapping mode. Surface topographical analysis of raw AFM images was carried out with NanoScope analysis 1.5 and Gwyddion, a free modular program for SPM (scanning probe microscopy) data visualization.

### 2.4. XRD and XPS

X-ray diffraction (XRD) measurements were performed using a BRUKER D8 Advance X-ray diffractometer equipped with a Sol-X detector, working at 40 kV and 40 mA. The X-ray diffraction patterns were collected in a step-scanning mode with steps of  $\Delta 2\theta = 0.01^\circ$  and a counting time of 12 s/step using Cu  $\text{K}\alpha 1$  radiation ( $\lambda = 1.54056 \text{ \AA}$ ) in the  $2\theta$  range 3–100 $^\circ$ .

XPS experiments were conducted using a  $\Phi 5600\text{ci}$  X-Ray Photoelectron spectrometer (Perkin Elmer, Waltham, MA, USA) with an Mg K anode X-ray source (1253.6 eV) with a primary beam energy of 14 kV and an electron current of 20 mA. A CHA (Concentric Hemispherical Analyser) was used to collect the output signals. Analysed areas were circles of 0.8 mm in diameter. Multiplex scan mode was performed with a 0.125 eV steps (pass energy 23.50 eV). BEs were calibrated against the C1s peak (285 eV).

### 2.5. Photocatalytic experiments

In photocatalytic measurements the electrode (either  $\text{WO}_3$  or  $\beta\text{25}/\text{WO}_3$ , having 1  $\text{cm}^2$  geometric active area) was immersed in 10 mL of electrolyte solution comprising 0.7 mM  $\text{Na}_2\text{SO}_4$  and KTP or LFX in 30–10 ppm concentration at pH 6. The photoanode was irradiated under open circuit conditions (disconnected wires) with a Hg medium pressure lamp at 0.128  $\text{W}/\text{cm}^2$ . In order to avoid decomposition pathways arising from direct photochemical excitation of the pharmaceutical targets, appropriate cut-off filters were interposed between the source and the cell (360 nm for LFX, 380 nm for KTP, in accordance to the absorption threshold of the respective molecules). Typical photocatalytic experiments were carried out for five hours, monitoring the target concentration at 1, 3 and 5 h intervals.

### 2.6. Photo-electrochemical experiments

Photodegradation experiments under photo-electrochemical conditions were carried out in a two electrode cell (volume = 10 mL) under potentiostatic conditions controlled by an Eco Chemie PGSTAT 101 potentiostat/galvanostat running under Nova environment. The working electrode (photoanode) was either a  $\text{WO}_3$  or a  $\beta\text{25}/\text{WO}_3$  thin film supported on FTO, while the counter electrode was a platinum grid. An ABET sun simulator (AM 1.5 G with the appropriate cut offs) was used as an illumination source for photoelectrochemical experiments. Constant potential photoelectrolysis was conducted in aerated 0.7 mM  $\text{Na}_2\text{SO}_4$  aqueous solutions at pH 6 by applying a constant bias of 1.2 V for KTP and 0.4 V for LFX respectively. These potential values

were selected on the basis of the respective current density vs potential (J/V) curves (see Results and Discussion section). Typical experiments had a duration of 5 h, during which depolarization cycles at 0 V for 10 min were introduced between polarization cycles of the duration of 30 min in order to ensure a reproducible and stable operation of the photoelectrode. Longer experiments, aimed at the determination of decomposition intermediates were carried out for 20 h, by adopting the same electrochemical program specified above.

### 2.7. HPLC/DAD analysis

A HPLC/DAD (Waters, MA, USA pump:Waters 515, DAD:Waters PDA 996) was employed under isocratic elution condition, the eluent was 18:82 ACN: phosphate buffer 25 mM at pH 4 and 60:40 MeOH: phosphate buffer 2 mM at pH 3.3 for LFX and KTP respectively. The flow rate was 1 mL/min. The column was  $4.6 \times 150$  mm Kromasil Eternity-5-C18. The injection volume was 20  $\mu\text{L}$  for all standards and samples.

### 2.8. HPLC/MS analysis

HPLC/MS analyses were made by means of Surveyor micro-HPLC hyphenated to a linear trap quadrupole mass spectrometer (LTQ XL Thermo Scientific, Waltham, MA, USA). The HPLC apparatus was composed of a solvent delivery system, a quaternary pump (including a membrane degasser) and an autosampler (including a thermostated column compartment). The LTQ system was equipped with an electrospray ionization (ESI) ion source. The mobile phase was obtained as a mixture of acetonitrile (ACN) formic acid 0.1% v/v : water formic acid 0.1% v/v. Chromatographic separation was performed under gradient elution conditions: 0–6 min 5% ACN, 6–14 min 5–70% ACN, 14–15 min 70% ACN, then held isocratically at 95% of ACN for 3 min before re-conditioning the column. The flow rate was 100  $\mu\text{L}/\text{min}$ , while the column was thermostated at 25  $^\circ\text{C}$ . The column was  $50 \times 2.1$  mm (Restek, Bellefonte, PA, USA) and packed with a C18 silica-based stationary phase with a particle diameter of 3  $\mu\text{m}$ . The injection volume was 5  $\mu\text{L}$  for all standards and samples. MS experimental conditions were as follows: spray voltage 4 kV, capillary temperature 275  $^\circ\text{C}$ , capillary voltage 11 V and tube lens 25 V for positive ESI conditions.

## 3. Results and discussion

### 3.1. Morphological, structural, optical and electrochemical properties

Structural and morphological properties of colloidal  $\text{WO}_3$  films prepared by sequential spin coating-annealing cycles by our group, were reported previously [15,28]. AFM images taken on the  $\beta\text{25}/\text{WO}_3$  composite are consistent with previous results taken on unmodified films, showing a network of rather polydisperse, partly fused, roughly spherical particles, whose diameter varies between 60 and 30 nm. The film shows mesopores of the order of 50–100 nm, which allow for electrolyte percolation through the film, more evident at intermediate magnification (scale bar 1  $\mu\text{m}$  in Fig. 1A, B). Smaller interstices are evident between nanoparticle interconnections at higher magnification in Fig. 1C.  $\beta\text{25}$  modified  $\text{WO}_3$  displays the presence of comparatively larger elongated prismatic structures, having a ca. 1:2 aspect ratio and a length of ca. 200–250 nm assigned by comparison with pure  $\beta\text{25}$  zeolites. These are prevalently distributed at the surface of the film, and are often embedded and surrounded by the outermost layers of  $\text{WO}_3$  nanoparticles. This is consistent with the two step preparation route of  $\beta\text{25}$  modified  $\text{WO}_3$  surfaces which is based on the spin casting of zeolite suspensions on the pre-formed  $\text{WO}_3$  film. Attempts to disperse zeolites within the bulk of the film, by modifying with zeolites the colloidal precursor for one-step film deposition, were successful from the synthetic point of view, but led to photoanodes having poor photoelectrochemical reproducibility due to scarce film adhesion to the ohmic



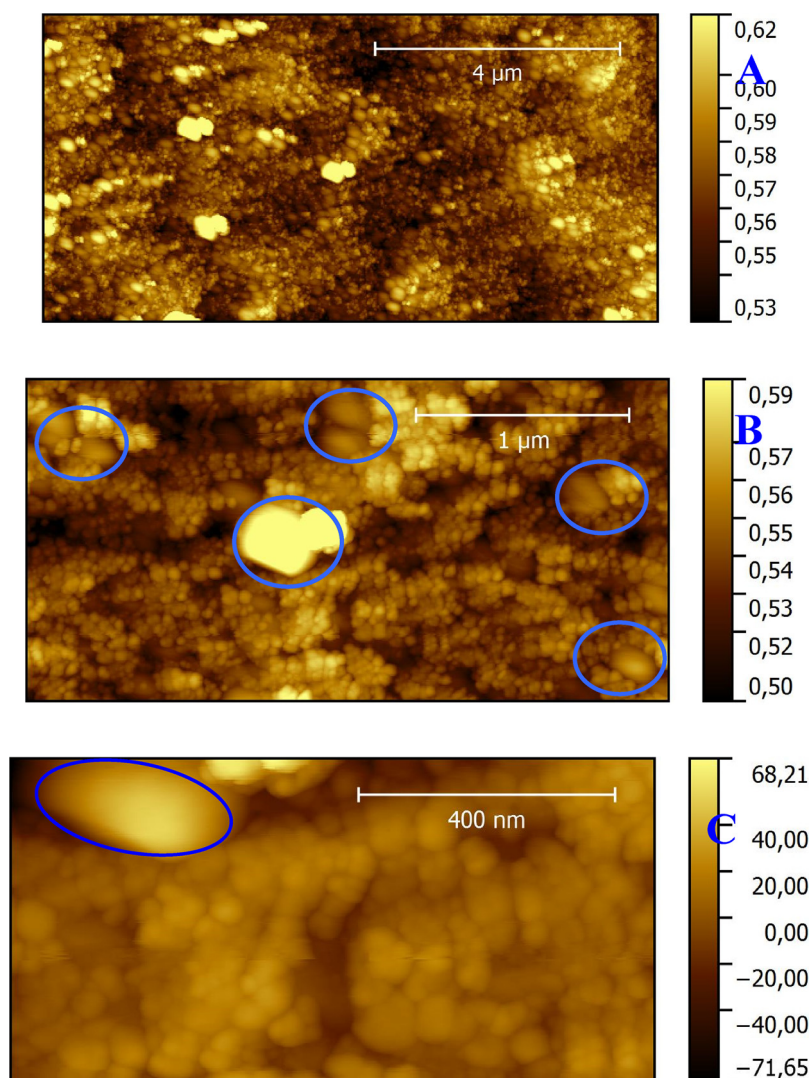


Fig. 1. AFM micrographs showing the surface of  $\beta 25/\text{WO}_3$ . Blue circles indicate some zeolite structures at the surface and embedded within the outermost layers of much smaller  $\text{WO}_3$  particles. (For interpretation of the references to colour in this figure legend, the reader is referred to the web version of this article.)

contact and were early abandoned for this work.

X-ray powder diffraction patterns of  $\beta 25$  before and after  $\text{WO}_3$  embedding are shown in Fig. 2. The strong changes in the XRD patterns can be interpreted by assuming the presence of two phases:  $\beta 25$  and tungsten trioxide  $\text{WO}_3$  with monoclinic symmetry. The evidence for the monoclinic-type phase of  $\text{WO}_3$  is strongly supported by the occurrence of new diffraction peaks (PDF file # 83-0951).  $\text{WO}_3$  phase showed a high intensity peak at (020) reflection as well as lower intensity ones corresponding to (212), (410), (240) reflections.

Comparative XPS measurements (Fig. 3) carried out on the thin film electrodes supported on FTO show that both the tungsten  $\text{W}4f_{7/2}$  and the  $\text{O}1s$  peaks associated to  $\text{WO}_3$  in the  $\beta 25$  modified film are essentially unchanged with regard to binding energy, peak intensity ratio and FWHM (1.4 (W) and 1.6 (O) eV) with respect to the unmodified  $\text{WO}_3$  where BEs of 35.7 eV (W) and 530.5 (O) perfectly match with known literature data for such material ( $35.7 \pm 0.1$  and  $530.5 \pm 0.1$  eV for W and O in  $\text{WO}_3$  respectively) [29], suggesting a negligible electronic perturbation to the W core levels upon physical

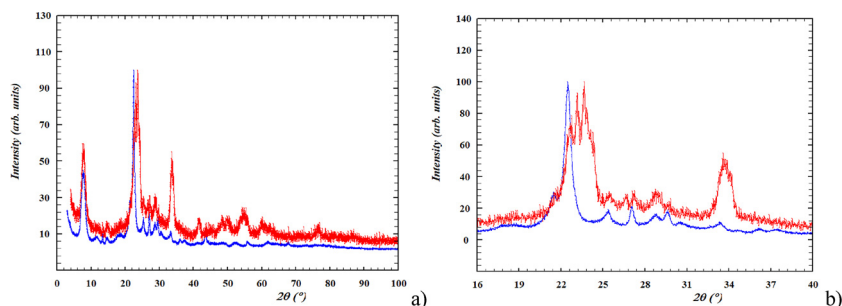


Fig. 2. (a) Intensity-normalized X-ray diffraction patterns of  $\beta 25$  (blue line) and  $\beta 25/\text{WO}_3$  in the  $3\text{--}100^\circ$   $2\theta$  range. (b) The occurrence of new peaks related to the embedding of  $\text{WO}_3$ . (For interpretation of the references to colour in this figure legend, the reader is referred to the web version of this article.)

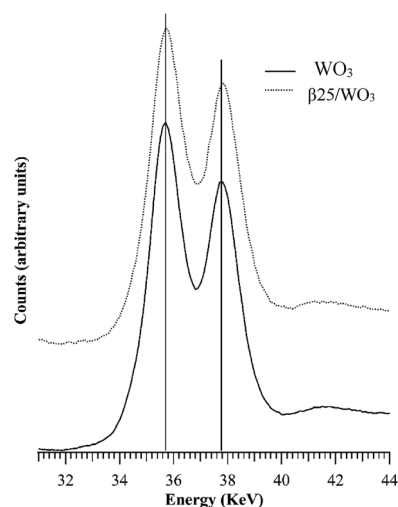


Fig. 3. W4f7/2 XPS peaks observed in unmodified WO<sub>3</sub> and beta25 modified thin films supported on FTO.

deposition of beta25 on the nanocrystalline WO<sub>3</sub>.

Consistent with the XPS evidence, the electronic spectra and the cyclic voltammetry of pure WO<sub>3</sub> and of beta25 modified WO<sub>3</sub> electrodes are substantially super-imposable, (Fig. 4A,B) corroborating the fact that no new electronic levels in the semiconductor are introduced upon casting of the zeolite on the pre-formed WO<sub>3</sub> thin films. In both unmodified and beta25 modified materials, the absorption spectra are characterized by the same onset of the visible absorption at 450 nm, as one should expect from the forbidden gap value of WO<sub>3</sub>. The presence of zeolites, larger than the average WO<sub>3</sub> nanoparticles, as shown by AFM, contributes to the increased light scattering from the beta25/WO<sub>3</sub> film, evident from the increased background at  $\lambda > 450$  nm, where the electronic transitions of the semiconductor are absent. Cyclic voltammetry, reported in Fig. 4B, shows similar capacitive charging currents at positive potentials (i.e.  $> 0$  V vs SCE) where faradaic processes are absent. Also, WO<sub>3</sub> and beta25/WO<sub>3</sub> show the same onset of the W<sup>6+</sup> / W<sup>5+</sup> reduction (ca. 0 V vs SCE), corresponding to trapping of electrons in defects and surface states close to the conduction band edge, confirming the marginal impact coming from zeolite modification to the semiconductor energetics. In both WO<sub>3</sub> and beta25/WO<sub>3</sub>, the similar intensity of the faradaic reductive wave, where charge compensation of the W<sup>6+</sup> / W<sup>5+</sup> process occurs by movement of cations from the electrolyte (in our specific case Na<sup>+</sup>) to the porous semiconductor, indicates that after coating with zeolites the WO<sub>3</sub> porous film maintains its permeability to the electrolyte, with an electrochemically active area comparable to that of pristine WO<sub>3</sub>. This is again consistent with AFM, where the presence of rather sparse zeolitic structures decorating the surface of the semiconductor, cannot preclude the access of the electrolyte to most of the porous photoelectrode.

### 3.2. Photochemical and photoelectrochemical degradation of KTP and LFX at WO<sub>3</sub> electrodes

Photochemical degradation experiments were initially carried out on 0.7 mM Na<sub>2</sub>SO<sub>4</sub> aqueous solutions containing 10 mg/L of drug (KTP or LFX) where the electrolyte was added to reproduce the overall ionic content of natural freshwaters and to provide, for comparative purposes, the same ionic environment established at the SEI under photoelectrochemical conditions. In photochemical experiments, colloidal WO<sub>3</sub> films were employed in the absence of applied potential bias. Under such conditions WO<sub>3</sub> electrons are promoted by valence band excitation under  $\lambda > 360$  nm, into both delocalized (conduction band) and localized (trap) states, while holes, surviving recombination, are scavenged by water (leading to  $\cdot$ OH formation) or by direct reaction with the organics interacting with the WO<sub>3</sub> surface. In the absence of surface co-catalysts [30], production of oxidizing intermediates via reduction of molecular oxygen by surface trapped electrons is considered to be slow and inefficient at WO<sub>3</sub> nanoparticles having  $> 30$  nm size, exhibiting no quantum confinement [31], thus the oxidation reactions are, in our case, mainly carried out by photogenerated holes. Clearly both the direct (via reaction with holes having an approximate quasi-Fermi potential of 2.7 V vs SCE) and the indirect pathway, via  $\cdot$ OH mediated oxidation, would lead to the oxidative degradation of these organic species.

Flat band conditions are quickly established in the solid under illumination due to electron accumulation, neutralizing the positive charges within the depletion layer formed upon initial Fermi level equilibration following contact between the solid and the liquid phases. In these stationary conditions no electric field should exist in the semiconductor film and transport of holes to the WO<sub>3</sub> surface, where scavenging occurs, takes place solely by diffusion. Fig. 5 shows that photochemical degradation of 10 ppm LFX is ca. 75% complete after 5 h of illumination at ca. 0.13 W/cm<sup>2</sup>, according to a monoexponential kinetic with a rate constant of 0.27 h<sup>-1</sup>. On the contrary, in the same experimental conditions, KTP is not degraded, showing no deviations in the solution concentration from the initial 10 ppm value, which remains substantially constant, within the experimental error, during an irradiation cycle of 5 h. This finding can be possibly explained by considering the electrostatic repulsion between the negative charge of KTP at pH 6 and the negatively charged WO<sub>3</sub> surface [32,33]. This would cause a depletion of KTP from the immediate proximity of the semiconductor surface reducing the probability of direct scavenging by reaction with holes and also the likelihood of bi-molecular reaction with  $\cdot$ OH which, being highly reactive species, are not expected to diffuse very far from the surface whereupon are generated under illumination. Competitive reaction of  $\cdot$ OH with SO<sub>4</sub><sup>2-</sup> to form S<sub>2</sub>O<sub>8</sub><sup>2-</sup>, bi-molecular events yielding H<sub>2</sub>O<sub>2</sub> or electron recapture on the semiconductor surface leading to reformation of water will indeed limit the lifetime of  $\cdot$ OH and hence their diffusional path.

In the photoelectrochemical experiment, the application of a 1.2 V vs Pt potential bias to a WO<sub>3</sub> film, significantly improves the

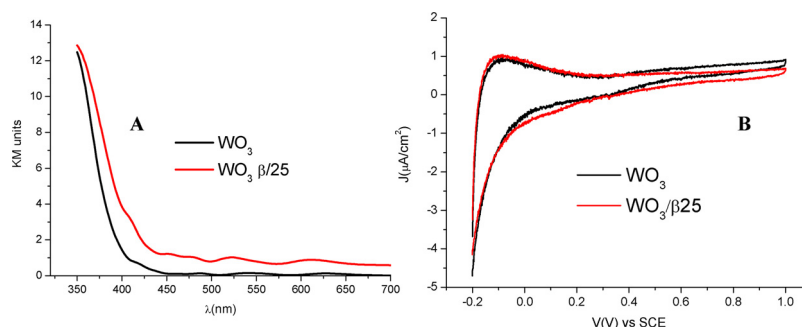
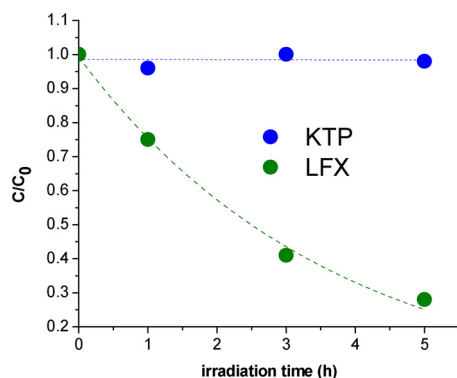
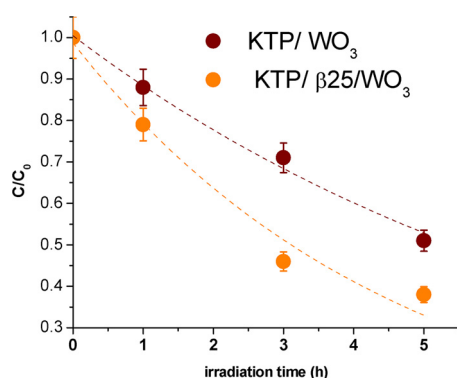


Fig. 4. Electronic absorption spectra (A) and cyclic voltammetry (20 mV/s) in 0.5 M Na<sub>2</sub>SO<sub>4</sub> recorded on WO<sub>3</sub> and beta25/WO<sub>3</sub> electrodes.



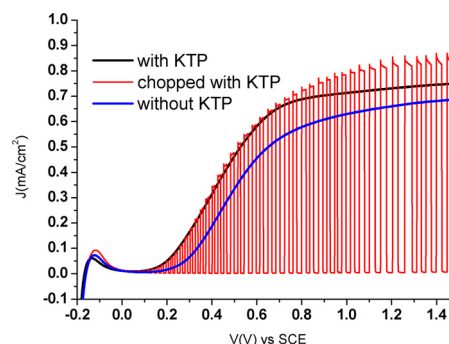
**Fig. 5.** Photocatalytic degradation kinetics (no applied potential) of 10 ppm KTP ( $\lambda > 380$  nm) and of LFX ( $\lambda > 360$  nm) on colloidal WO<sub>3</sub> thin films (area = 1 cm<sup>2</sup>) at pH 6 in 0.7 mM Na<sub>2</sub>SO<sub>4</sub>. Hg medium pressure mercury lamp 0.128 W/cm<sup>2</sup>.



**Fig. 6.** Photoelectrochemical degradation kinetics of 10 ppm KTP (AM 1.5 G and  $\lambda > 380$  nm) at WO<sub>3</sub> (area = 1 cm<sup>2</sup>) (brown) and at β<sub>25</sub>/WO<sub>3</sub> (orange) at pH 6 in 0.7 mM Na<sub>2</sub>SO<sub>4</sub> under 1.2 V vs Pt bias.

degradation of KTP under simulated solar illumination (AM 1.5 G + 380 nm cut off filter) resulting in a ca. 50% abatement of the initial concentration of KTP after 5 h of illumination, with a rate constant of 0.13 h<sup>-1</sup> (Fig. 6, brown circles). The applied potential bias was set at 1.2 V since at this value no substantial dark anodic current is observed, (Fig. S2), while the photoanodic plateau (i.e. the maximum rate of hole extraction from the semiconductor) is reached (Fig. S3). Additionally, from chronoamperometry data (Fig. S4) it can be observed that the photocurrent is essentially constant and reproducible, with a steady state photoanodic current density of ca. 100 μA/cm<sup>2</sup>, during 10 polarization cycles at 1.2 V vs Pt, each of the duration of 30 min, confirming the stability of the photoanodic response of WO<sub>3</sub> employed for the decontamination process.

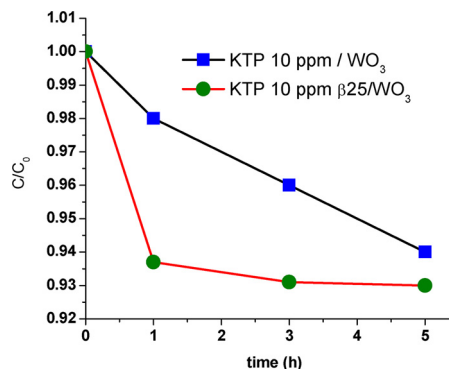
Since a 10 ppm concentration of KTP in the poorly conductive 0.7 mM Na<sub>2</sub>SO<sub>4</sub> solution was not ideal to observe the direct impact of the photo-oxidation of this drug on the resulting J-V characteristic of the WO<sub>3</sub> photoelectrode, three electrode potentiodynamic experiments were carried out in 0.5 M Na<sub>2</sub>SO<sub>4</sub> at pH 6 in the presence of 10<sup>-3</sup> M KTP, representing the drug solubility limit in water at pH 6. Compared to the blank electrolyte made of 0.5 M Na<sub>2</sub>SO<sub>4</sub> at pH 6 (Fig. 7 blue line), the presence of 10<sup>-3</sup> M KTP (Fig. 7, black line) induces a ca. 100 mV anticipated photoanodic response, while the photocurrent in the activation region of the curve, i.e. between 0.2 and 0.4 V vs SCE, where minority carrier recombination is more significant, is ca. twice higher, with a good matching of the steady state JV with square shaped photoanodic transients (red line, Fig. 7). All these photoelectrochemical features provide unambiguous evidence of reduced photogenerated carrier recombination thanks to the participation of KTP to hole scavenging (or ·OH scavenging) processes at the SEI under positive



**Fig. 7.** JV characteristic of colloidal WO<sub>3</sub> thin films (area = 1 cm<sup>2</sup>) under AM 1.5 illumination with 380 nm cut-off filter at pH 6 in 0.5 M Na<sub>2</sub>SO<sub>4</sub> in the presence (black and red curves) and in the absence of 10<sup>-3</sup> M KTP (blue). (For interpretation of the references to colour in this figure legend, the reader is referred to the web version of this article.)

polarization.

The improved degradation of KTP under applied bias can be explained by the combination of two factors. First, the positive polarization reduces recombination, by continuously removing photogenerated electrons from conduction band and sub-band gap states, increasing the flux of holes through the SEI where scavenging by the electrolyte occurs. Second, the positive charges induced on the electrode, comprising both the underlying FTO contact and mesoporous WO<sub>3</sub> are counterbalanced by anionic species in the electrolyte. The ionic cloud surrounding the electrode is generally described in the framework of the Stern-Graham model, where the first linear potential drop in the electrolyte takes place within the Helmholtz plane, i.e. a compact sheet of ionic charge at a fixed distance from the electrochemical surface, followed by a diffuse layer, where the potential drop, according to a linear approximation of the Poisson-Boltzmann equation occurs exponentially [34]. The induction of an ionic cloud, constituted by SO<sub>4</sub><sup>2-</sup> and KTP, having charge opposite to that of the electrode surface, thus results in a local surface excess of KTP, favoring the effective bimolecular encounter with an increased flux of photogenerated ·OH, leading to enhanced oxidative degradation. Possible chemical interactions of KTP with the electrode surface, consisting for instance in the coordination of the carboxylate group to either Sn<sup>4+</sup> of FTO or W<sup>6+</sup> of WO<sub>3</sub> could also result from the electrostatically increased surface excess of KTP. The local uptake of KTP by the mesoporous electrode under 1.2 V vs Pt polarization was confirmed by HPLC analysis carried out on 10 ppm KTP/0.7 mM Na<sub>2</sub>SO<sub>4</sub>, within a time interval spanning 5 h, during which the solution was left to equilibrate with the electrode under positive polarization in the dark. We can indeed observe in Fig. 8 (blue squares) a slow depletion of KTP from the solution, slowly decreasing to a ca.



**Fig. 8.** KTP (10 ppm in 0.7 mM Na<sub>2</sub>SO<sub>4</sub>) uptake by WO<sub>3</sub> (blue) and β<sub>25</sub>/WO<sub>3</sub> (green) in the dark under 1.2 V vs Pt polarization. (For interpretation of the references to colour in this figure legend, the reader is referred to the web version of this article.)

10% uptake after 5 h.

Photoelectrochemical KTP degradation is further accelerated by exploiting the  $\beta$ 25 modified  $\text{WO}_3$  film, giving a > 65% abatement (orange circles, Fig. 4) and a degradation rate constant of  $0.22 \text{ h}^{-1}$  within the same time interval and in otherwise identical conditions. The photoanodic current density, recorded during such experiment was also comparable with that delivered by the unmodified  $\text{WO}_3$  SEI, with a steady state value ranging between 100 and  $150 \mu\text{A}/\text{cm}^2$  (Fig. S5).

Consistent with the degradation results, the  $\beta$ 25/ $\text{WO}_3$  electrode shows a much faster KTP uptake, (Fig. 8 green dots), with 90% of the relative variation occurring within the first hour, indicating a favorable trapping and confinement of KTP within the zeolites [35] embedded in the  $\text{WO}_3$  film. This well explains the faster degradation kinetics observed under photoelectrochemical conditions with the  $\beta$ 25/ $\text{WO}_3$  modified electrode. Imprisoning of KTP inside zeolites is also consistent with the high photoactivity of  $\beta$ 25/ $\text{WO}_3$  in the absence of applied bias (Fig. S6) where degradation of KTP was achieved with a time constant of  $0.27 \text{ h}^{-1}$  under medium pressure Hg lamp ( $\lambda > 380 \text{ nm}$ ) illumination. It should be recalled that in otherwise identical conditions, no significant KTP degradation was observed with the unmodified  $\text{WO}_3$  film. This piece of evidence suggests that direct reaction of KTP with photogenerated holes at the SEI is not the likely mechanism for drug degradation, since in the case of KTP trapping inside  $\beta$ 25, the direct contact between such organic species and the semiconductor surface is precluded. Rather, the degradation most probably involves reaction with  $\cdot\text{OH}$  diffusing away from the semiconductor surface upon primary hole scavenging by water.

In the case of LFX, for which a satisfactory performance was already observed (see Fig. 1) under purely photocatalytic (no bias) conditions, the application of the potential to either  $\text{WO}_3$  or  $\beta$ 25/ $\text{WO}_3$  also translates in a significant acceleration of the oxidative degradation of this drug at the SEI under illumination. Differently from KTP, which was essentially stable showing only a slight decrease at 1.5 V bias, probably due to surface uptake upon polarization, LFX is appreciably degraded by electrolysis at potential > 0.4 V vs. Pt, (Fig. 9), consistent with the observation of a dark electrochemical process, occurring at the exposed back contact (FTO) of the photoanode, having a threshold at 0.6 V vs Pt (Fig. S7). In order to avoid spurious electrochemical contributions to drug degradation, the rate of LFX degradation was monitored at a bias of 0.4 V vs Pt, a potential at which only photoinduced charge separation within  $\text{WO}_3$  should be active in triggering oxidative processes. Unsurprisingly, due to reduced bias, the photoanodic current generated by  $\text{WO}_3$  in 10 ppm LFX dissolved in 0.7 mM  $\text{Na}_2\text{SO}_4$  at pH 6, was smaller than in the KTP case, being in the order of ca.  $50 \mu\text{A}/\text{cm}^2$ . Nevertheless the photocurrent was satisfactorily stable and reproducible during prolonged experiments (Fig. S8).

Essentially, in this case the enhanced activity stems from an increased hole flux reaching the SEI: under 0.4 V vs Pt and AM 1.5 G (> 380 nm) illumination, causing the initial concentration of LFX to drop to less than 90% within 5 h, according to a rate constant of  $0.69 \text{ h}^{-1}$  (Fig. 10). No obvious advantages were found from the use of a  $\beta$ 25 modified  $\text{WO}_3$  thin film, given the fact that LFX is already likely to display a good interaction with the semiconductor surface, either

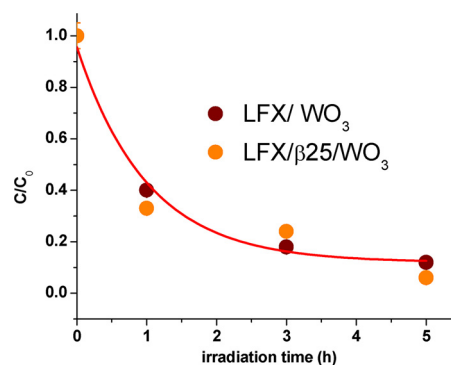


Fig. 10. Photoelectrochemical degradation kinetics of 10 ppm LFX, under AM 1.5 G and  $\lambda > 380 \text{ nm}$  illumination at  $\text{WO}_3$  (area =  $1 \text{ cm}^2$ ) (brown) and  $\beta$ 25/ $\text{WO}_3$  (orange) at pH 6 in 0.7 mM  $\text{Na}_2\text{SO}_4$  under 0.4 V vs Pt bias.

through electrostatic interactions or by surface adsorption via nitrogen lone pairs. Compared to KTP, LFX is also an easier to oxidize species, which may react with a wider family of oxidant intermediates, like  $\text{H}_2\text{O}_2$ , generated upon primary water photooxidation by the coupling of two  $\cdot\text{OH}$  radicals.

### 3.3. Drug mineralization and characterization of the degradation intermediates

The main degradation products of both KTP and LFX generated during the photo-electrocatalytic process were identified. The structural assignments of the intermediates were done on the basis of the comparison of the fragment ions detected in the MS-MS spectra with those reported in previous studies [36,37].

Concerning LFX, in addition to the parent molecule, five intermediate products were identified (Table 1) in the withdrawal solutions obtained during photoelectrochemical degradation. These compounds have molecular ions at  $m/z$  335, 278, 337, 347 and 364. All of them correspond to the protonated molecule  $[\text{M} + \text{H}]^+$ .

The byproduct having  $m/z$  335 corresponds to the partial degradation of the piperazynilic ring, it is 27 Da lighter than LFX, and it could correspond to a secondary amine generated by the net loss of  $\text{C}_2\text{H}_2$  from the piperazynic moiety consistent with a previous observation by El Najjar et al. [38]

The product with  $m/z$  278 can be attributed to the oxidation of the piperazine side-chain in analogy to previously reported floxacin degradation products [39]. The intermediate with  $m/z$  of 364 possibly derives from the ring-opening at the N1 position (see Chart 1) followed by further oxidation via OH radical [40]. The fragment at  $m/z$  347 may be generated through the transformation of the molecule chromophoric group. Additionally, literature data suggest that even the oxidation of quinolone moiety is mediated by  $\cdot\text{OH}$  [41].

The product having  $m/z$  347 possibly derives from demethylation ( $-14 \text{ Da}$ ) of the parent compound  $m/z$  362. [40]. The exact concentrations of the intermediates have not been quantified since the corresponding standards for calibration are not commercially available.

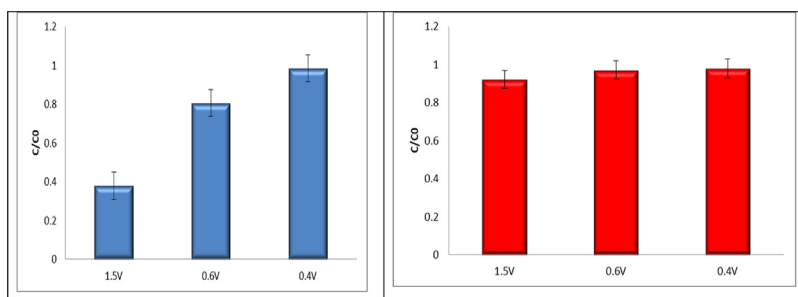
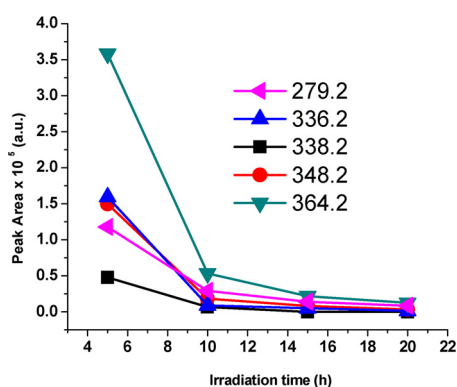


Fig. 9. Electrodegradation of LFX (blue bars) and KTP (red bars) in the dark at the  $\text{WO}_3$  SEI biased at various anodic potentials. The ratio of the concentration of either LFX or KTP with respect to their respective initial concentration (10 ppm) is reported after 3 h of anodic polarization at 0.4, 0.6 and 1.5 V vs Pt in the dark at pH 6 in 0.7 mM  $\text{Na}_2\text{SO}_4$ . (For interpretation of the references to colour in this figure legend, the reader is referred to the web version of this article.)

**Table 1**  
Structure of the photoelectrochemical degradation products of LFX identified by mass spectrometry.

Precursor ion	tr	MS <sup>2</sup>	Structure
362	7.18	362 318	
279	9.79	261	
336	6.96	261 235	
338	4.48	320 310 294 292	
348	7.10	304 284 261	
364	6.51	346 333 289 261 235	



**Fig. 11.** Photoelectrochemical degradation of the LFX intermediates at the  $\beta$ 25/ $\text{WO}_3$  SEI under AM 1.5 G illumination with 380 nm cut off.

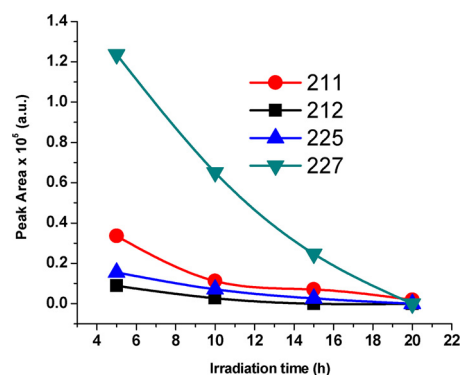
However, the relative abundance of the oxidation products can be evaluated from their associated peak integral. Fig. 11 shows that the intermediates described above underwent a complete degradation, generally resulting below the detection limit of this analytical technique after 20 h of photoelectrolysis employing  $\beta$ 25- $\text{WO}_3$  photoelectrodes, consistent with the mineralization of LFX.

In the degradation of KTP, the four most abundant intermediates observed have  $m/z$  227, 225, 212 and 211 (see Table 2).

The molecular weight of KTP is 254, whereas the intermediate having  $m/z$  211, reported in Table 2, show a 44 Da decrease in the molar mass suggesting a decarboxylation of the parent compound. The most significant ( $\text{MS}^2$ ) fragments obtained from the  $m/z$  211 compound, are reported in Table 2 alongside with the structural assignment performed on the basis of the comparison of the  $m/z$  fragments with the work by Szabò et al. [42]. It is thus possible to identify this compound as 3-ethylbenzophenone (EB). The  $m/z$  212 intermediate seems to correspond to 3-hydroxymethyl-benzophenone, possibly deriving from oxidation of EB. On a similar basis, the fragment analysis of the intermediates with  $m/z$  227 and 225 leads to 3-acetylbenzophenone and 3-hydroxyethyl benzophenone. The peak area of the fragments vs. irradiation time is reported in Fig. 12, where it can be observed that also for KTP the intermediates become undetectable after 20 h of photoelectrolytic process, consistent with the achievement of drug

**Table 2**  
Structures of the detected photoelectrochemical degradation products of KTP.

Precursor Ion	Tr	MS <sup>2</sup>	Structure
211	17.17	196 182 183 154	
212	14.35	105	
225	15.48	183 147	
227	13.59	76 105 209	



**Fig. 12.** Photoelectrochemical degradation of the KTP intermediates at the  $\beta$ 25/ $\text{WO}_3$  SEI under AM 1.5 G illumination and 380 nm cutoff.

mineralization.

#### 4. Conclusions

In this contribution we have explored the applications of  $\text{WO}_3$  based nanomaterials to the degradation of Ketoprofen (KTP) and Levofloxacin (LFX), representing ubiquitous water contaminants of emerging concern. Interestingly, it was found that, while LFX is effectively degraded under both photocatalytic (no bias) and photoelectrochemical (applied bias) conditions, in the case of KTP there is an extreme difference in the photochemical vs. photoelectrochemical degradation kinetic: under conventional photocatalytic conditions, KTP does not show any appreciable degradation, whereas under applied bias its degradation is roughly 70% complete during a 5 h illumination cycle with  $\lambda > 380$  nm. This behavior was explained by the induction of a local excess of KTP at the  $\text{WO}_3$  SEI under positive potential, allowing a faster reaction with surface generated  $\cdot\text{OH}$  radicals. In the absence of positive bias, at pH 6, such interaction does not occur, due to electrostatic repulsion between the anionic KTP and the negatively charged  $\text{WO}_3$  surface, having point of zero charge at pH lower than 2. This indicates that besides modulating the charge separation rate at the SEI, the electric bias could be useful to tune the solar degradation of otherwise impervious molecular species via double-layer effects.

Further, in the case of KTP, the degradation activity of  $\text{WO}_3$  could be further enhanced by incorporating  $\beta$ 25 zeolites into the photoactive semiconductor, allowing to trap and confine KTP in the immediate proximity of the  $\text{WO}_3$  surface, where the exposure to the flux of  $\cdot\text{OH}$  generated by mono-electronic oxidation of water should be optimal. Indeed, under appropriate photoelectrochemical conditions,  $\beta$ 25- $\text{WO}_3$  led to the complete degradation of both KTP and LFX, as well as of their respective oxidation intermediates following 20 h of illumination.

Our research is now directed towards the fabrication of thick  $\text{WO}_3$

films optimized for application under solar concentration and to the exploitation of WO<sub>3</sub>/BiVO<sub>4</sub> junctions, where the better light harvesting should allow for a considerable acceleration of the photoelectrochemical degradation of CECs.

## Acknowledgements

This work is part of the HP-Solar Project supported by Regione Emilia Romagna under POR/FESR 2014-2020 program and PRIA project founded by the University of Ferrara.

## Appendix A. Supplementary data

Supplementary data associated with this article can be found, in the online version, at <https://doi.org/10.1016/j.cattod.2018.09.020>.

## References

- [1] M. La Farre, S. Perez, L. Kantiani, D. Barcelò, *Trends Analyt. Chem.* 27 (2008) 991–1007.
- [2] M. Schriks, M.B. Heringa, M.M. van de Krooi, P. de Voogt, A.P. van Wezel, *Water Res.* 44 (2010) 461–476.
- [3] K. Hashimoto, H. Irie, A. Fujishima, *Jpn. J. Appl. Phys.* 44 (2005) 8269–8285.
- [4] X. Chen, S.S. Mao, *Chem. Rev.* 107 (2007) 2891–2959.
- [5] M.A. Henderson, *Surf. Sci. Rep.* 66 (2011) 185–297.
- [6] J. Schneider, M. Matsuoka, M. Takeuchi, J. Zhang, Y. Horiuchi, M. Anpo, D.W. Bahnemann, *Chem. Rev.* 114 (2014) 9919–9986.
- [7] N. Daneshvar, D. Salari, A.R. Khataee, *J. Photochem. Photobiol. A: Chem.* 162 (2004) 317–322.
- [8] E.S. Elmolla, M. Chaudhri, *J. Hazard. Mater.* 173 (2010) 445–449.
- [9] E.S. Elmolla, M. Chaudhuri, *Desalination* 256 (2010) 43–47.
- [10] A. Molinari, E. Sarti, N. Marchetti, L. Pasti, *Appl. Catal. B: Environ.* 203 (2017) 9–17.
- [11] A. Molinari, R. Argazzi, A. Maldotti, *J. Mol. Catal. A: Chem.* 372 (2013) 23–28.
- [12] G. Liu, T. Wu, H. Hidaka, N. Serpone, *Environ. Sci. Technol.* 33 (1999) 2081–2087.
- [13] C. Chen, W. Zhao, P. Lei, J. Zhao, N. Serpone, *Chem. Eur. J.* 10 (2004) 1956–1965.
- [14] A. Tanaka, K. Hashimoto, H. Kominami, *J. Am. Chem. Soc.* 136 (2013) 586–589.
- [15] V. Cristino, M. Sabrina, A. Molinari, S. Caramori, S. Carli, R. Boaretto, R. Argazzi, L. Meda, C.A. Bignozzi, *J. Mater. Chem. A* 4 (2016) 2995–3006.
- [16] I. Tantis, L. Bousiakou, Z. Frontistis, D. Mantzavinos, I. Konstantinou, M. Antonopoulou, G.-A. Karikas, P. Lianos, *J. Hazard. Mater.* 294 (2015) 57–63.
- [17] I. Tantis, E. Stathatos, D. Mantzavinos, P. Lianos, *J. Chem. Technol. Biotechnol.* 90 (2015) 1338–1344.
- [18] G. Longobucco, L. Pasti, A. Molinari, N. Marchetti, S. Caramori, V. Cristino, R. Boaretto, C.A. Bignozzi, *Appl. Catal. B: Environ.* 204 (2017) 273–228/272.
- [19] M. Ferech, S. Coenen, S. Malhotra-Kumar, K. Dvorakova, E. Hendrickx, C. Suetens, H. Goossens, *J. Antimicrob. Chemother.* 58 (2006) 423–427.
- [20] C. Tixier, H.P. Singer, S. Oellers, S.R. Muller, *Environ. Sci. Technol.* 37 (2003) 1061–1068.
- [21] H.R. Lozano, F. Martinez, *Braz. J. Pharm. Sci.* 42 (2006) 601–613.
- [22] J.A.O. Gonzalez, M.C. Mochon, F.J.B. de la Rosa, *Talanta* 52 (2000) 1149–1156.
- [23] J.M. Newsam, M.M.J. Treacy, W.T. Koetsier, C.B. De Gruttyer, *Proc. R. Soc. Lond. Ser. A* 420 (1988) 375–405.
- [24] H. Liu, S. Huang, L. Zhang, S. Liu, W. Xin, *Catal. Commun.* 10 (2009) 544–558.
- [25] P. Varsani, A. Afonja, D.E. Williams, I.P. Parkin, R. Binions, *Sens. Actuators B* 160 (2011) 475–482.
- [26] I. Jansson, K. Yosshiiri, H. Hori, F.J. Garcia-Garcia, S. Rojas, B. Sanchez, B. Ohtani, S. Suarez, *Appl. Catal. A: Gen.* 521 (2016) 208–219.
- [27] [https://www3.epa.gov/caddis/ssr\\_ion\\_int.html](https://www3.epa.gov/caddis/ssr_ion_int.html).
- [28] L. Meda, G. Tozzola, A. Tacca, G.L. Marra, S. Caramori, V. Cristino, C.A. Bignozzi, *Sol. Energy. Mat. Sol. Cells* 94 (2010) 788–796.
- [29] [https://srdata.nist.gov/xps/main\\_search\\_menu.aspx](https://srdata.nist.gov/xps/main_search_menu.aspx).
- [30] H. Irie, S. Miura, K. Kamiya, K. Hashimoto, *Chem. Phys. Lett.* 457 (2008) 202–205.
- [31] T. Suzuki, H. Watanabe, Y. Oaki, H. Imai, *Chem. Commun.* 52 (2016) 6185–6188.
- [32] M. Anik, T. Cansizoglu, *J. Appl. Electrochem.* 36 (2006) 603–608.
- [33] S. Yamazaki, T. Yamate, K. Adachi, *Appl. Catal. A: Gen.* 454 (2013) 30–36.
- [34] J.O.M. Bockris, A.K.N. Reddy, M. Gamboa-Aldeco, *Modern Electrochemistry 2A: Fundamentals of Electrode Processes*, Kluwer Academic Publishers, New York, Boston, Dordrecht, London, Moscow, 2002.
- [35] L. Pasti, E. Sarti, A. Cavazzini, N. Marchetti, F. Dondi, A. Martucci, *J. Sep. Sci.* 36 (2013) 1604–1611.
- [36] Y. Gong, J. Li, Y. Zhang, M. Zhang, X. Tian, A. Wang, *J. Hazard. Mater.* 304 (2016) 320–328.
- [37] T. Kosjek, S. Perko, E. Heath, B. Kralj, D. Zigon, *J. Mass Spectrom.* 46 (2011) 391–401.
- [38] N.H. El Najjar, A. Touffet, M. Deborde, R. Journal, N.K.V. Leitner, *Chemosphere* 93 (2013) 604–611.
- [39] A.S. Maia, A.R. Ribeiro, C.L. Amorim, J.C. Barreiro, Q.B. Cass, P.M. Castro, M.E. Tiritan, *J. Chromatogr. A* 1333 (2014) 87–98.
- [40] I. Michael, E. Hapeshi, J. Acena, S. Perez, M. Petrovic, A. Zapata, D. Fatta-Kassinos, *Sci. Total Environ.* 461 (2013) 39–48.
- [41] P. Calza, C. Medana, F. Cabone, V. Giancotti, C. Baiocchi, *Rapid Commun. Mass Spectrom.* 22 (2008) 1533–1552.
- [42] R.K. Szabo, C. Megyeri, E. Illes, K. Gajda-Schranz, P. Mazellier, A. Dombi, *Chemosphere* 84 (2011) 1658–1663.

## Supporting Information to

ha formattato: Inglese (Regno Unito)

### Photoelectrochemical Degradation of Pharmaceuticals at $\beta$ 25-modified $\text{WO}_3$ interfaces

Vito Cristino<sup>a</sup>, Gelsomina Longobucco<sup>a</sup>, Nicola Marchetti<sup>a</sup>, Stefano Caramori<sup>\*a</sup>, Carlo Alberto Bignozzi<sup>a</sup>, Annalisa Martucci<sup>b</sup>, Alessandra Molinari<sup>a</sup>, Rita Boaretto<sup>a</sup>, Claudia Stevanin<sup>a</sup>, Roberto Argazzi<sup>a</sup>, Maurizio Dal Colle,<sup>a</sup> Renzo Bertoncetto<sup>c</sup> and Luisa Pasti<sup>\*a</sup>.

(a) Department of Chemical and Pharmaceutical Sciences, University of Ferrara, 44121, Via Luigi Borsari 46, 44121

(b) Department of Physics and Earth Sciences, University of Ferrara, Via Saragat 1, 44121 Ferrara.

(c) Department of Chemical Sciences, University of Padua, Via Marzolo 1, 35131, Padua.

(\*) [psu@unife.it](mailto:psu@unife.it); [cte@unife.it](mailto:cte@unife.it)

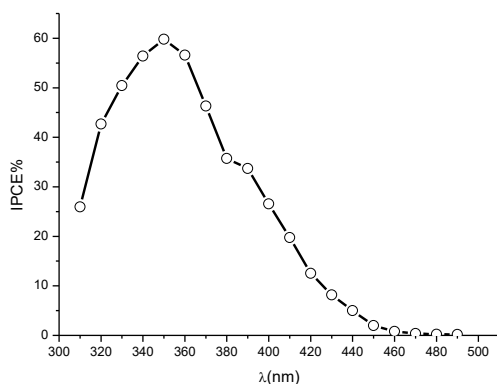


Figure S1. Typical photoaction spectrum of the  $\text{WO}_3$  colloidal film used for the photoelectrochemical degradation studies. Data recorded in 1 M  $\text{H}_2\text{SO}_4$  at 1.5 V vs SCE.

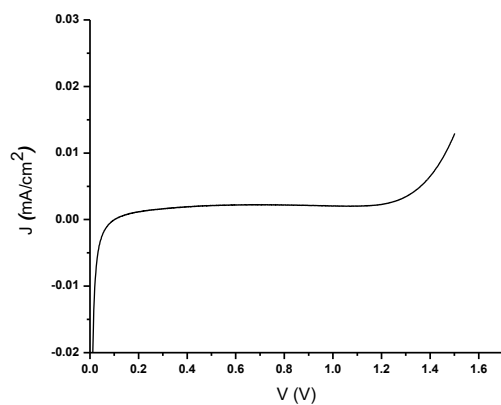


Figure S2. Dark JV characteristic of colloidal  $\text{WO}_3$  thin films (area =  $1 \text{ cm}^2$ ) at pH 6 in  $0.7 \text{ mM Na}_2\text{SO}_4$  in the presence of  $10 \text{ ppm KTP}$ . The onset of the dark anodic current at voltages  $> 1.3 \text{ V}$  vs Pt is due to water oxidation at the exposed FTO back contact.

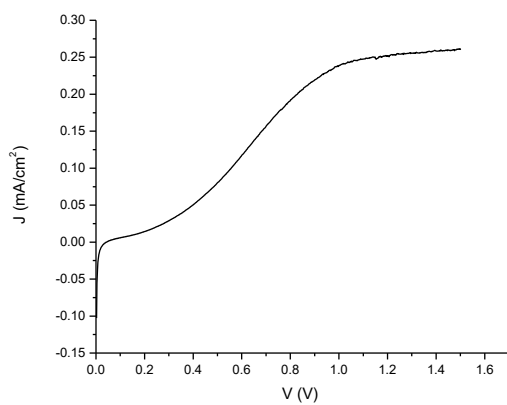


Figure S3. Potentiodynamic (scan rate =  $10 \text{ mV/s}$ ) J-V characteristic of colloidal  $\text{WO}_3$  thin films (area =  $1 \text{ cm}^2$ ) at pH 6 in  $0.7 \text{ mM Na}_2\text{SO}_4$  in the presence of  $10 \text{ ppm KTP}$ . Under AM1.5 G,  $\lambda > 380 \text{ nm}$  illumination, the photoanodic plateau is reached at a voltage  $\geq 1 \text{ V}$ , at which the dark current is still negligible.



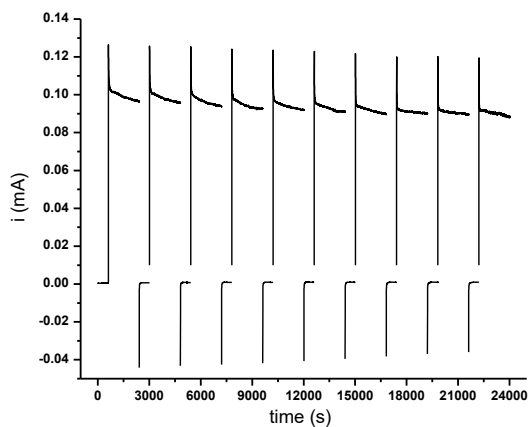


Figure S4. Chronoamperogram recorded with colloidal  $\text{WO}_3$  thin films (area =  $1 \text{ cm}^2$ ) at pH 6 in  $0.7 \text{ mM Na}_2\text{SO}_4$  in the presence of  $10 \text{ ppm KTP}$  AM 1.5 G  $\lambda > 380 \text{ nm}$  illumination. During a typical 5 hours experiment 10 irradiation cycles of the duration of 30 minutes at  $1.2 \text{ V vs Pt}$  are separated by 10 minutes rest cycles at  $0 \text{ V vs Pt}$ .

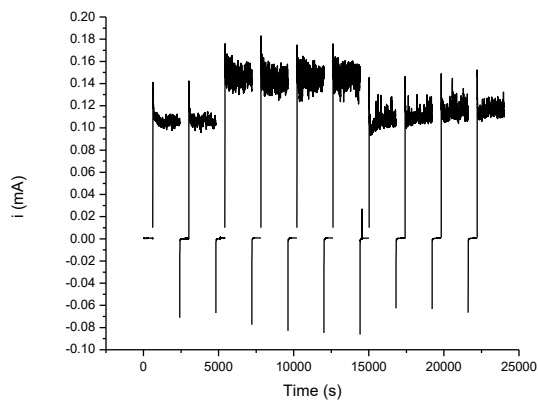


Figure S5. Chronoamperogram recorded with colloidal  $\text{WO}_3$ - $\beta 25$  modified thin films (area =  $1 \text{ cm}^2$ ) at pH 6 in  $0.7 \text{ mM Na}_2\text{SO}_4$  in the presence of  $10 \text{ ppm KTP}$ . AM 1.5 G  $\lambda > 380 \text{ nm}$  illumination. During a typical 5 hours experiment 10 irradiation cycles of the duration of 30 minutes at  $1.2 \text{ V vs Pt}$  are separated by 10 minutes rest cycles at  $0 \text{ V vs Pt}$ .

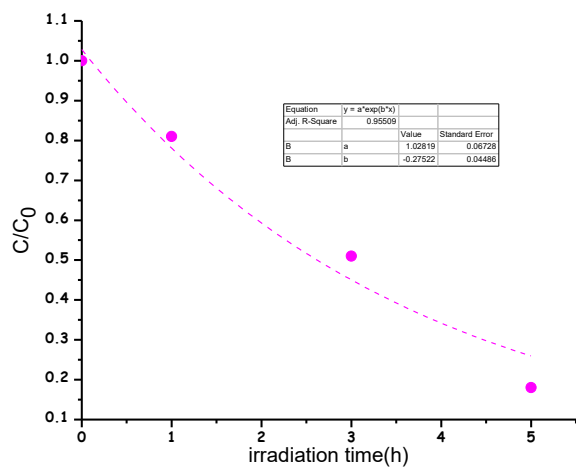


Figure S6. 30 ppm KTP degradation kinetics at  $\text{WO}_3\text{-}\beta\text{25 SEI}$  (area =  $1 \text{ cm}^2$ ) under medium pressure Hg lamp illumination ( $\lambda > 380 \text{ nm}$ ).  $0.7 \text{ mM Na}_2\text{SO}_4$  at pH 6.

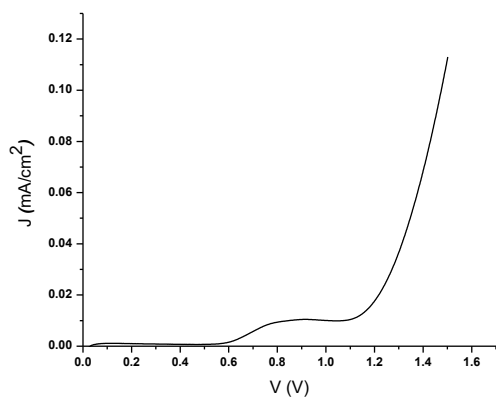


Figure S7. Dark J-V characteristic of the  $\text{WO}_3$  SEI in the presence of  $10^{-5} \text{ M LFX}$  in  $0.1 \text{ M Na}_2\text{SO}_4$ . A diffusion limited oxidation wave, assigned to electrochemical LFX oxidation at the exposed FTO back contact, is observed starting at  $0.6 \text{ V vs Pt}$ , followed by another faradaic process at  $> 1.2 \text{ V vs Pt}$ , overlapping with the onset of water oxidation.

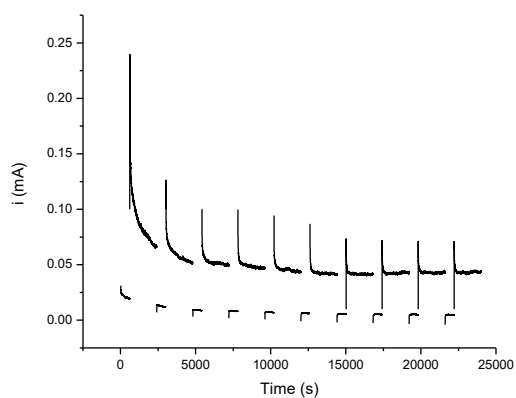


Figure S8. Chronoamperogram recorded with colloidal  $\text{WO}_3$  thin film (area =  $1 \text{ cm}^2$ ) at pH 6 in  $0.7 \text{ mM Na}_2\text{SO}_4$  in the presence of  $10 \text{ ppm LFX}$ . AM  $1.5 \text{ G } \lambda > 380 \text{ nm}$  illumination. During a typical 5 hours experiment 10 irradiation cycles of the duration of 30 minutes at  $0.4 \text{ V vs Pt}$  are separated by 10 minutes rest cycles at  $0 \text{ V vs Pt}$ .

Article

# Anticancer Activity of Aqueous Extracts from *Asparagus officinalis* L. Byproduct on Breast Cancer Cells

Arianna Romani <sup>1,†</sup>, Fabio Casciano <sup>1,2,†</sup>, Claudia Stevanin <sup>3</sup>, Annalisa Maietti <sup>3,4</sup>, Paola Tedeschi <sup>3,4</sup>, Paola Secchiero <sup>1</sup>, Nicola Marchetti <sup>3,4,\*</sup> and Rebecca Voltan <sup>1,\*</sup>

<sup>1</sup> Department of Translational Medicine and LTTA Centre, University of Ferrara, 44121 Ferrara, Italy; arianna.romani@unife.it (A.R.); fabio.casciano@unife.it (F.C.); paola.secchiero@unife.it (P.S.)

<sup>2</sup> Interdepartmental Research Center for the Study of Multiple Sclerosis and Inflammatory and Degenerative Diseases of the Nervous System, University of Ferrara, 44121 Ferrara, Italy

<sup>3</sup> Department of Chemistry, Pharmaceutical and Agricultural Sciences, University of Ferrara, 44121 Ferrara, Italy; claudia.stevanin@unife.it (C.S.); annalisa.maietti@unife.it (A.M.); paola.tedeschi@unife.it (P.T.)

<sup>4</sup> Terra&Acqua Tech Lab, Ferrara Technopole, 44121 Ferrara, Italy

\* Correspondence: nicola.marchetti@unife.it (N.M.); rebecca.voltan@unife.it (R.V.)

† Co-first author.

**Abstract:** Cultivation of asparagus (*Asparagus officinalis* L.; Asp) for food and medicinal use has taken place since the early Roman Empire. Today, Asp represents a worldwide diffuse perennial crop. Lower portions of the spears represent a food industry waste product that can be used to extract bioactive molecules. In this study, aqueous extracts derived from the non-edible portion of the plant (hard stem) were prepared and characterized for chemical content. Furthermore, the biocompatibility and bioactivity of Asp aqueous extracts were assessed *in vitro* on normal fibroblasts and on breast cancer cell lines. Results showed no interference with fibroblast viability, while a remarkable cytostatic concentration-dependent activity, with significant G1/S cell cycle arrest, was specifically observed in breast cancer cells without apoptosis induction. Asp extracts were also shown to significantly inhibit cell migration. Further analyses showed that Asp extracts were characterized by specific pro-oxidant activity against tumoral cells, and, importantly, that their combination with menadione resulted in a significant enhancement of oxidants production with respect to menadione alone in breast cancer cells but not in normal cells. This selectivity of action on tumoral cells, together with the easiness of their preparation, makes the aqueous Asp extracts very attractive for further investigation in breast cancer research, particularly to investigate their role as possible co-adjuvant agents of clinical drug therapies.

**Keywords:** *Asparagus officinalis*; breast cancer; cellular migration; reactive oxygen species (ROS)

**Citation:** Romani, A.; Casciano, F.; Stevanin, C.; Maietti, A.; Tedeschi, P.; Secchiero, P.; Marchetti, N.; Voltan, R. Anticancer Activity of Aqueous Extracts from *Asparagus officinalis* L. Byproduct on Breast Cancer Cells. *Molecules* **2021**, *26*, 6369. <https://doi.org/10.3390/molecules26216369>

Academic Editor: Roberta Costi

Received: 12 August 2021

Accepted: 19 October 2021

Published: 21 October 2021

**Publisher's Note:** MDPI stays neutral with regard to jurisdictional claims in published maps and institutional affiliations.



**Copyright:** © 2021 by the authors. Licensee MDPI, Basel, Switzerland. This article is an open access article distributed under the terms and conditions of the Creative Commons Attribution (CC BY) license (<http://creativecommons.org/licenses/by/4.0/>).

## 1. Introduction

Breast cancer (BC) is the most common cancer among women [1]. It is classified mainly based on the expression of three receptors that determine its pharmacological response and, therefore, severity: estrogen receptor (ER), progesterone receptor (PgR), and epidermal growth factor receptor 2 (HER2). The majority of cases are hormone-dependent, showing overexpression of ER and PgR [2]. In those patients, endocrine-based treatment is used as a first-line treatment; however, after its initial efficacy, about 50% of patients develop endocrine resistance and treatment failure, requiring different choices or use of combined therapy [3]. Triple-negative breast cancers (TNBC; ER-, PgR-, HER2-), on the other hand, account for 10–15% of cases and still do not have efficient treatment. Since TNBC show an unfavorable prognosis and hormone-dependent BC has a 5-year survival rate of 25%, it is important to find an efficient and relatively safe cure to improve patients' survival [4].

Increasing attention in novel drug research has been focused on natural products as a source of compounds that exhibit few adverse effects [5,6]. One of the most common vegetables reported with therapeutic proprieties is asparagus, a plant nutritionally and commercially important belonging to the Asparagaceae family. Worldwide, more than 200 species have been identified [7], and among them, *Asparagus officinalis* L. (Asp) is the main species cultivated and commercialized [8]. The 2019 survey by FAO (<http://www.fao.org/faostat/en/#data>, on 5 October 2021 ) evidenced that asparagus cultivation is distributed worldwide, even if only six countries demonstrate major production: China (over 8 million tons); Peru (367,000 tons); Mexico (272,000 tons); Germany (131,000 tons); Spain (59,000 tons); Italy (50,000 tons). Italy has the largest yield in Europe and holds third place globally (7 tons per hectare), while the top yield globally belongs to Peru (11.5 tons per hectare). In Italy, asparagus production is focused only on five regions, with nearly 10,000 hectares cultivated (CSO Italy, Centro Servizi Ortofrutticoli, <https://www.csoservizi.com/focus-prodotti/asparagi/>, on 5 October 2021) by large agri-food farms. Hence, it is promptly understandable that potential solutions facing the recovery of bioactive molecules with asparagus waste material (i.e., hard stems, roots, plant aerial parts) might have a great impact on this agri-food chain.

Different factors, including species, type of cultivation, seasons, or plant section used greatly change the content of the active biological molecules extracted [9]. Previous studies, focused mainly on the stem portion, have identified phenolic compounds, saponins, sterols, sulfur-containing acid, carotenoid, and amino acids as the main bioactive components [10]. Components such as flavonoids and carotenoids are well known for their antioxidant activity; others, such as saponins, have been reported to possess cell cycle modulatory activity in cancer cells [11]. Lately, asparagus methanol extracts from *Asparagus laricinus* have been reported to induce cytotoxicity in breast and prostate cancer cell lines [12].

More recently, Asp has become of interest for the possibility to extract bioactive molecules from non-edible portions [13]. Indeed, besides edible stems used in industrial processing, hard stems and roots, which are normally discarded, have been suggested to be used to extract phytochemicals with biological activities [7,14]. Recycling food industry byproducts will be beneficial from both economic and ecological points of view.

Therefore, the present study first had the purpose of characterizing the chemical composition of hard stem Asp extracts prepared by a simple aqueous method that does not alter the structure nor the biological activity of important functional molecules. Then, the next aim of the study was to investigate *in vitro* the biological effects of the water extracts on survival and proliferation, oxidative balance and migration of BC cell lines belonging to different phenotypes, as well as in a normal cell line.

The simple procedure to obtain water extracts of Asp hard stem, its chemical composition and its bioactivity on breast cancer cell lines represent the most innovative key-points of this study.

## 2. Results

### 2.1. *Asparagus* Extracts

Asparagus matrix has a moisture content of about  $89.9\% \pm 0.1\%$  *w/w*, as estimated by freeze-drying. The yield of water extraction was  $7.25\% \pm 0.23\%$  *w/w*. The estimation of total phenolic content (TPC), total flavonoid content (TFC) and antioxidant activity (DPPH and ABTS) for aqueous extract are reported in Table 1. TPC value evidenced a moderate amount of phenols extracted in Asp hard stem, confirmed also by low levels of antioxidant activity. As a matter of fact, the water extract contains 3.6% of phenolic compounds and 4% of flavonoids that constitute the hard stem matrix (see Table S1, Supplementary Material). It seems, therefore, that the aqueous extract is made of similar relative amounts of TPC and TFC than those available in ASP hard stem for extraction. Interestingly, flavonoids represent about 92.3% of water-extracted phenolic compounds, while in the

hard stem, their relative amount is 83.8% of total phenolics on a dry matter basis. Thus, since phenolic compounds and flavonoids are water-extracted to the same extent (3.6% and 4%, respectively), and the relative amount of flavonoids is about 8.5% higher in dry water extracts than in dry hard stems, this can be interpreted in two ways: the dry water extract contains a slightly larger representative fraction of flavonoids than ASP hard stem matrix; or part of the water-extracted phenolics are lost during the lyophilization process and the relative amount of flavonoids results a bit higher.

**Table 1.** Values of total phenolic content (TPC), total flavonoid content (TFC) and antioxidant activities (DPPH and ABTS) in water extracts from asparagus hard stem byproducts. Values are expressed in terms of gallic acid equivalents (GAE) and Trolox equivalents (TE) per mg of dry extract ( $\text{mg}_{\text{de}}$ ).

<b>TPC</b> ( $\mu\text{g}_{\text{GAE}}/\text{mg}_{\text{de}}$ )	10.09 $\pm$ 1.23
<b>TFC</b> ( $\mu\text{g}_{\text{GAE}}/\text{mg}_{\text{de}}$ )	9.31 $\pm$ 0.74
<b>DPPH</b> ( $\mu\text{mol}_{\text{TE}}/\text{mg}_{\text{de}}$ )	0.010 $\pm$ 0.006
<b>ABTS</b> ( $\mu\text{mol}_{\text{TE}}/\text{mg}_{\text{de}}$ )	0.017 $\pm$ 0.006

## 2.2. LC-MS/MS Analysis of Asparagus Extracts

### 2.2.1. Free Amino Acid Profile

Proteins and peptides in the hard stem represent about 1.85% *w/w* on a fresh matter basis and exhibit antioxidant and ACE inhibitory properties, as already evidenced recently [15]. Here, we mainly focused on the free aminoacidic profile. Single amino acid concentrations are reported in Table 2. Ion transitions (i.e., MRM (*m/z*) column) allowed us to correctly identify all amino acids, except for leucine (LEU) and Isoleucine (ILE). These two were quantified together. The total amount of free amino acids in the hard stem is noticeably higher (i.e., 45  $\mu\text{g}/\text{mg}_{\text{de}}$ ) than in the edible stem (i.e., 32.7  $\mu\text{g}/\text{mg}_{\text{de}}$ ) (data not published). The most abundant free amino acids in the hard stem are lysine (56.3%) and asparagine (30.3%). Proline, alanine, valine and glutamic acid are in the range 1–3%. Arginine, aspartic acid, histidine, leucine and isoleucine, methionine, phenylalanine, serine, threonine and tryptophan are in the range 0.1–0.9%, while only tyrosine is below 0.1%. Tryptophane is about 35 times more concentrated in the hard stem than in the edible part of the stem, while histidine and arginine are only 1.9 and 1.5 times higher in the hard stem. Additionally, levels of lysine and asparagine are higher in the hard stem than in the whole edible stem and spear: even though they are still the most abundant amino acids in the edible part, lysine is about 1.4 times and asparagine is 1.7 times more abundant in the hard stem (see Table S2, Supplementary Material, for the free amino acid profile in the edible stem).

**Table 2.** Quantitative determination of free amino acids in asparagus hard stem byproducts.

Amino Acid	Concentration ( $\mu\text{g}/\text{mg}_{\text{de}}$ )	MRM ( $m/z$ )
ALA	$0.101 \pm 0.023$	90.2 $\rightarrow$ 44.2
ARG	$0.369 \pm 0.019$	175.1 $\rightarrow$ 70.1
ASN	$13.65 \pm 1.12$	133.1 $\rightarrow$ 74.1
ASP	$0.322 \pm 0.022$	134.1 $\rightarrow$ 74.1
GLU	$0.451 \pm 0.027$	148.2 $\rightarrow$ 84.2
HIS	$0.254 \pm 0.015$	156.1 $\rightarrow$ 110.2
LEU+ILE	$0.368 \pm 0.018$	132.1 $\rightarrow$ 86.1
LYS	$25.33 \pm 1.75$	147.1 $\rightarrow$ 84.1
MET	$0.069 \pm 0.004$	150.2 $\rightarrow$ 104.1
PHE	$0.117 \pm 0.012$	166.2 $\rightarrow$ 120.2
PRO	$1.434 \pm 0.068$	116.1 $\rightarrow$ 70.1
SER	$0.364 \pm 0.016$	106.1 $\rightarrow$ 60.1
THR	$0.253 \pm 0.011$	120.1 $\rightarrow$ 74.1
TRP	$0.144 \pm 0.009$	205.2 $\rightarrow$ 146.2
TYR	$0.039 \pm 0.007$	182.2 $\rightarrow$ 136.2
VAL	$0.814 \pm 0.034$	118.1 $\rightarrow$ 72.1

### 2.2.2. Organic Acids, Phenolic Acids, Polyphenols and Derivatives

Few secondary metabolites were identified in water extracts. Their tentative LC-MS/MS identification is reported in Table 3. Compounds are grouped based on their most intense ionization mode. The second column presents the precursor ion, while the third column contains all informative fragment ions useful for compound identification. Numbers in parenthesis are the ion relative intensity. The last column reports the relative abundance for each identified compound, calculated on the basis of peak area.

Among common organic acids (i.e., malic and quinic) and phenolic acid esters (i.e., dicaffeoyltartaric acid, caftaric acid, caffeoylquinic acid, feruloylquinic acid), important free aglycones were found: three flavonols (i.e., quercetin, kaempferol and syringetin), two isoflavones (i.e., genistein and prunetin) and one flavone (i.e., apigenin). Additionally, some common and less common glycosylated flavonoids were identified, such as myricetin-O-rhamnoside, tricetin-O-glucoside, isorhamnetin-O-glucuronide, laricitrin-O-glucoside and rutin. Interestingly, two anthocyanins were identified (i.e., petunidin- and malvidin-O-pentoside derivatives) and listed separately as [M]<sup>+</sup>.

Both isoflavones and flavonols are known to play important bioactive roles as estrogens and antioxidants. Hence, alone or in synergy with all compounds identified in water extracts, they may have captivating effects on cancer cells.

**Table 3.** Tentative LC-MS/MS identification of most abundant compounds in asparagus hard stem.

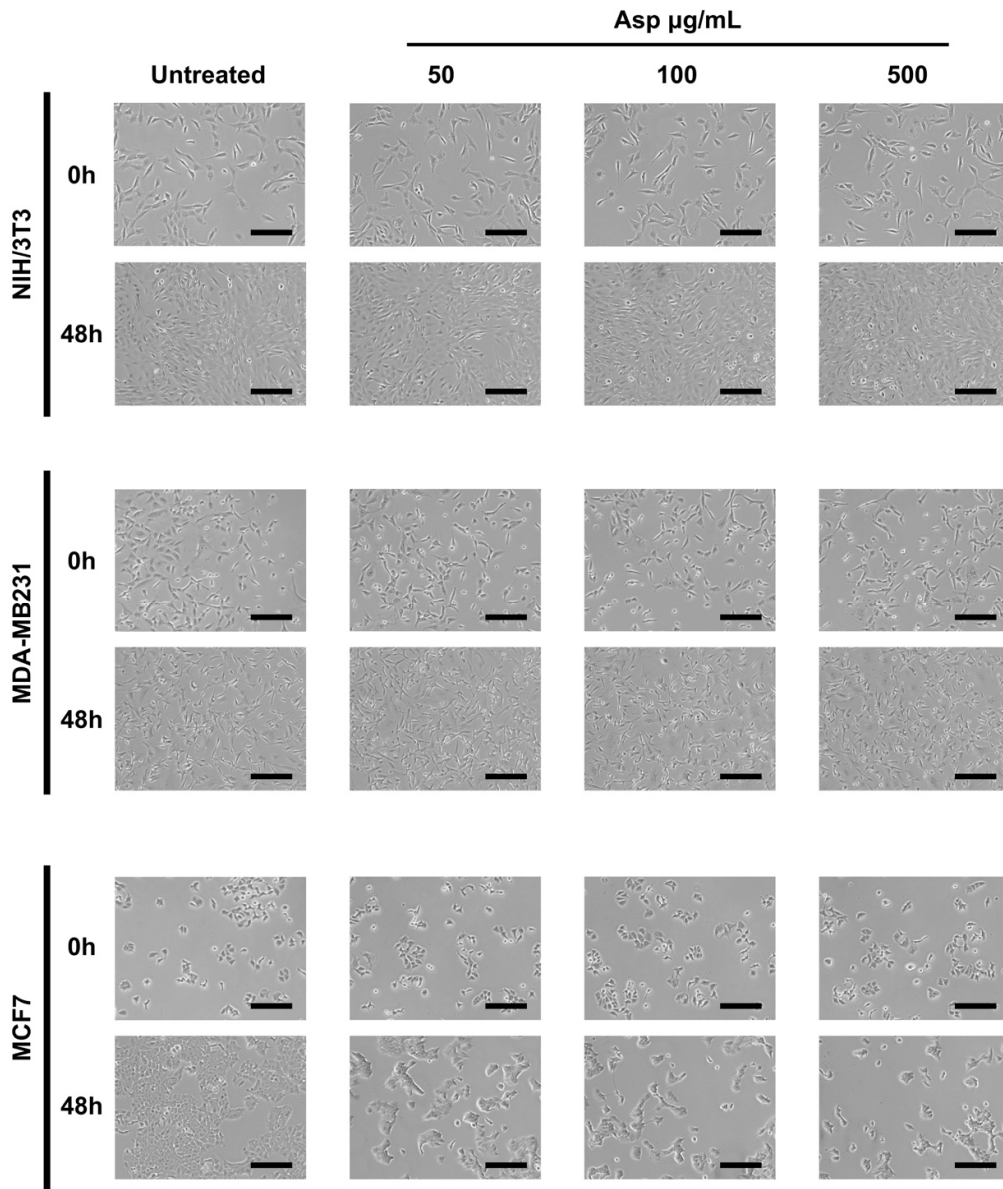
Compound	[M – H] <sup>–</sup> (m/z)	MS/MS Fragments (m/z)	Relative Abundance
Dicaffeoyltartaric acid	473	311 (100), 293 (80) 179 (5), 149 (3)	0.5%
Caftaric acid	311	149 (100), 179 (55), 135 (5)	6.7%
Caffeoylquinic acid	353	191 (100), 179 (5)	0.27%
Malic acid	133	115 (100)	48.8%
Myricetin-O-rhamnoside	463	316 (100), 317 (50), 271 (15)	0.40%
Quinic acid	191	111 (100), 173 (20)	38.0%
Feruloylquinic acid	367	191 (100), 173 (5)	0.04%
Quercetin	301	179 (100), 151 (75), 273 (15), 257 (10)	0.03%
Tricin-O-glucoside	491	476 (100), 329 (70), 328 (15), 314 (5)	0.2%
Isorhamnetin-O-glucuronide	491	315 (100), 255 (10), 151 (5)	0.02%
<b>[M + H]<sup>+</sup> (m/z)</b>			
Laricitrin-O-glucoside	495	333 (100)	0.04%
Syringetin	347	291 (100), 153 (50), 287 (20)	0.08%
Kaempferol	287	153 (100), 121 (50), 213 (20), 229 (5)	0.1%
Apigenin	271	153 (100), 229 (30), 225 (30), 119 (10)	0.3%
Rutin	611	303 (100), 465 (30)	2.4%
Genistein	271	153 (100), 215 (85), 243 (60), 149 (25)	0.2%
Prunetin	285	229 (100), 257 (60), 267 (30), 163 (25)	1.2%
<b>[M]<sup>+</sup> (m/z)</b>			
Petunidin-O-pentoside	449	317 (100)	0.4%
Malvidin-O-pentoside	463	331 (100)	0.3%

Compounds tentatively identified in Asp hard stem aqueous extracts are in accordance with literature works, although most of them concerned more exhaustive hydro-alcoholic extracts and most of the extensive chemical characterization regards the edible part [11,16–20].

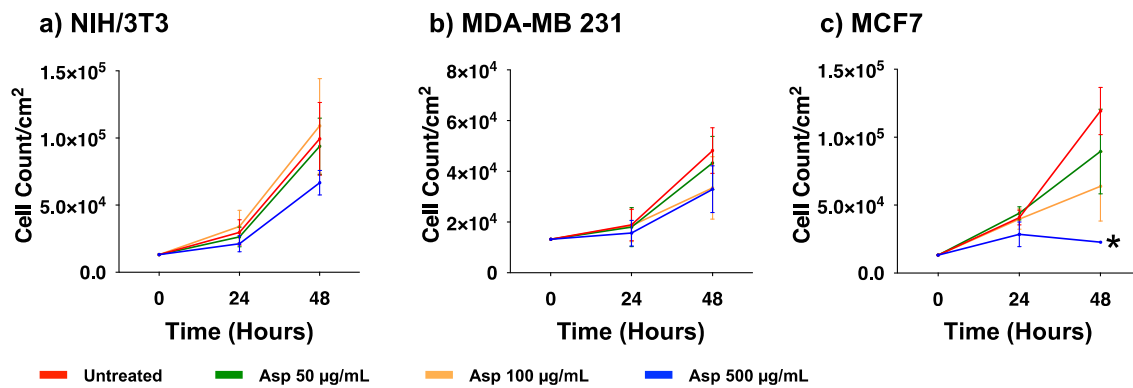
### 2.3. Asparagus Extracts Affect Viability of MCF-7 Breast Cancer Cells through Cell Cycle Block

To evaluate the biological effects of Asp extracts on cellular activities, cellular morphology, replication and apoptosis were assessed on NIH/3T3 fibroblasts and breast cancer cell lines MDA-MB231 and MCF7, before and after treatments with several doses of Asp extracts. As shown in Figure 1, no changes in morphology and distribution were observed in NIH/3T3 as well as in MDA-MB231 cells until 48 h after treatments. However, a remarkable reduction in cell density coupled with cell size increase (typical of cellular senescence) was observed in MCF7 cells treated for 48 h with Asp with respect to the untreated. In agreement, as reported in the panels in Figure 2a,b, no significant changes in the number of viable cells were identified in NIH/3T3 and MDA-MB231 cells. On the contrary, a significant reduction in the number of viable cells was identified in the MCF7 cell line treated with 500 µg/mL Asp extracts for 48 h, compared with untreated cells maintained in culture in the same condition (Figure 2c; *p*-value 0.0434).





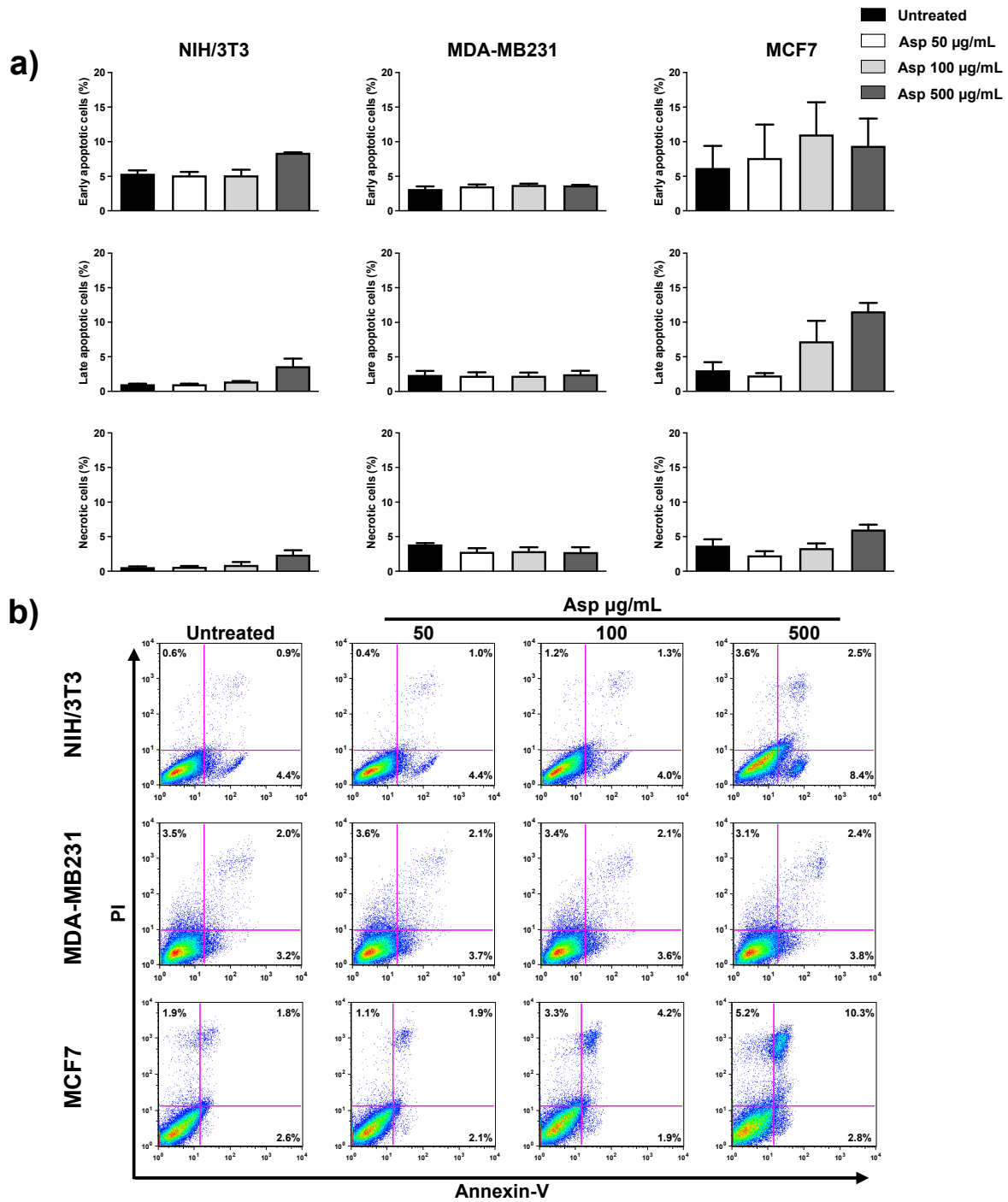
**Figure 1.** Representative images were taken by light microscopy of NIH/3T3, MDA-MB231 and MCF7 cells untreated or treated with 50, 100, and 500  $\mu\text{g/mL}$  of Asparagus extracts (Asp) for 48 h. Magnification 10 $\times$ , scale bar 200  $\mu\text{m}$ .



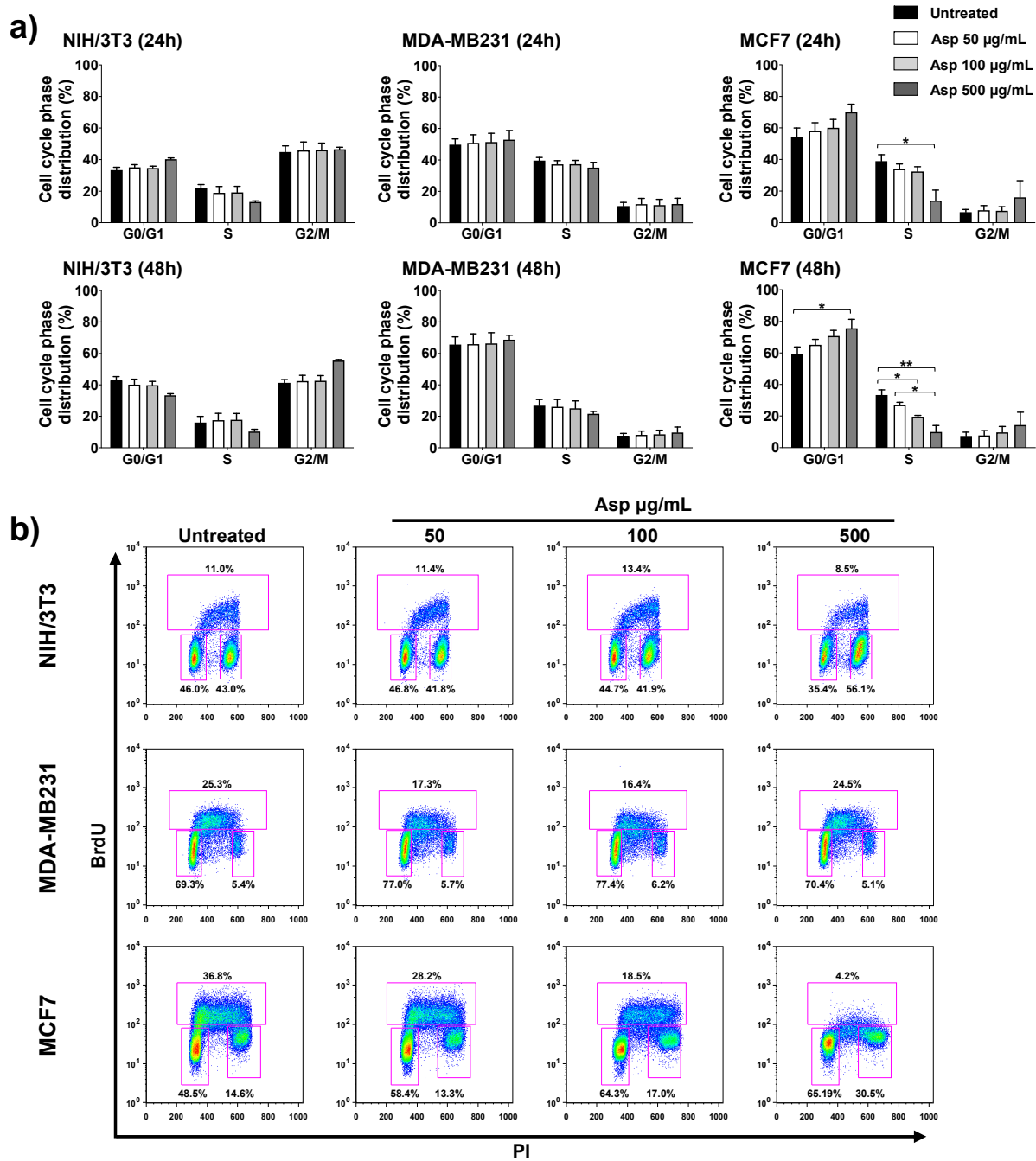
**Figure 2.** Cell viability of (a) NIH/3T3, (b) MDA-MB231, (c) MCF7 exposed to 50, 100, and 500 µg/mL of Asp for 24 and 48 h. Data are reported as mean ± standard error of the mean from three independent experiments. Statistical analysis was performed by ANOVA followed by Bonferroni's post hoc test. \*  $p \leq 0.05$  vs. untreated at the same incubation time.

Next, we investigated whether induction of apoptosis was responsible for the observed effects on cell viability. As reported in Figure 3, there were no significant differences between treated and untreated samples for all three cell lines, analyzing early and late apoptotic events, as well as necrotic events. Only for the MCF7 cell line, an increasing trend was observed for late apoptotic population in response to increasing concentrations of extracts, even if it was not significant with respect to the untreated control.

To further investigate the possible implication of Asp extracts on cell proliferation, the cell cycle was analyzed by flow cytometry upon BrdU incorporation. In agreement with cell viability results, Asp treatment on NIH/3T3 and MDA-MB-231 cells did not modify the cell cycle phase distribution either after 24 h or 48 h of treatment (Figure 4). By contrast, in MCF7 cells, Asp (500 µg/mL) induced a relevant contraction of the number of cells in S phase already after 24 h, when compared with untreated ( $p$ -value = 0.0169). Extending the treatment to 48 h, the alteration of cell cycle phases was more marked, showing a concentration-dependent effect with a significant reduction in cells in the S phase (100 µg/mL vs. untreated,  $p$ -value = 0.0469; 500 µg/mL vs. untreated,  $p$ -value = 0.0016; Asp 50 µg/mL vs. Asp 500 µg/mL,  $p$ -value = 0.0205), accumulation in G1 (500 µg/mL vs. untreated,  $p$ -value = 0.0169) and consequent induction of cell cycle blockade.



**Figure 3.** NIH/3T3; MDA-MB231; MCF7 percentage of apoptotic cells after 48 h, calculated from the flow cytometry dot plots after Annexin V/PI staining. (a) Results from untreated or treated with 50, 100, and 500 µg/mL Asp extracts were expressed as a percentage of the total population. Data are reported as mean ± standard error from three independent experiments. (b) Representative flow cytometry dot plots. The axis scales for fluorescence are reported as logarithmic.



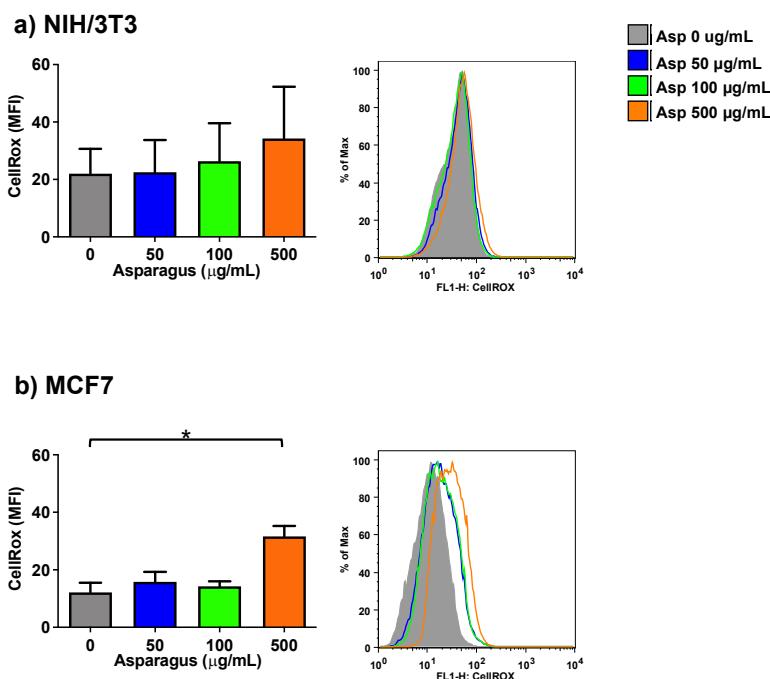
**Figure 4.** NIH/3T3; MDA-MB231; MCF7 cell distribution in the different phases of the cell cycle calculated from the flow cytometry dot plots after BrdU/PI staining of cultures after 24 or 48 h. **(a)** Results from cells untreated or treated with 50, 100, and 500 µg/mL of Asp extracts were expressed as a percentage of the total population. Data are reported as mean ± standard error from three independent experiments. Statistical analysis was performed by ANOVA followed by Bonferroni's post hoc test.  $p$ -values  $\leq 0.05$  were considered significant: \*  $p \leq 0.05$ , \*\*  $p \leq 0.01$ ; **(b)** Representative flow cytometry dot plots of cell cycle profiles after 48 h of treatments. The PI axes scale is reported as linear and the BrdU axes scale is reported as logarithmic.

#### 2.4. Asparagus Extracts Cause ROS Production in Breast Cancer Cells But Not in Normal Cells

To further study the biological effects of Asp extracts in normal (NIH/3T3) and tumoral (MCF7) cell lines, a possible role of Asp in modulating the production of oxidants

upon treatment was assessed by a method that enables the flow cytometric detection of reactive oxygen species (ROS) in live cells (CellROX Green Flow Cytometry Assay).

As depicted in Figure 5, following exposure to several Asp concentrations, normal cells did not significantly change their ROS level, while a significant increase in the production of oxidant species was observed in breast cancer MCF7 cells treated with 500  $\mu\text{g}/\text{mL}$  of Asp for 48 h, with respect to the untreated sample (Asp 0  $\mu\text{g}/\text{mL}$ ) ( $p$ -value = 0.0126).

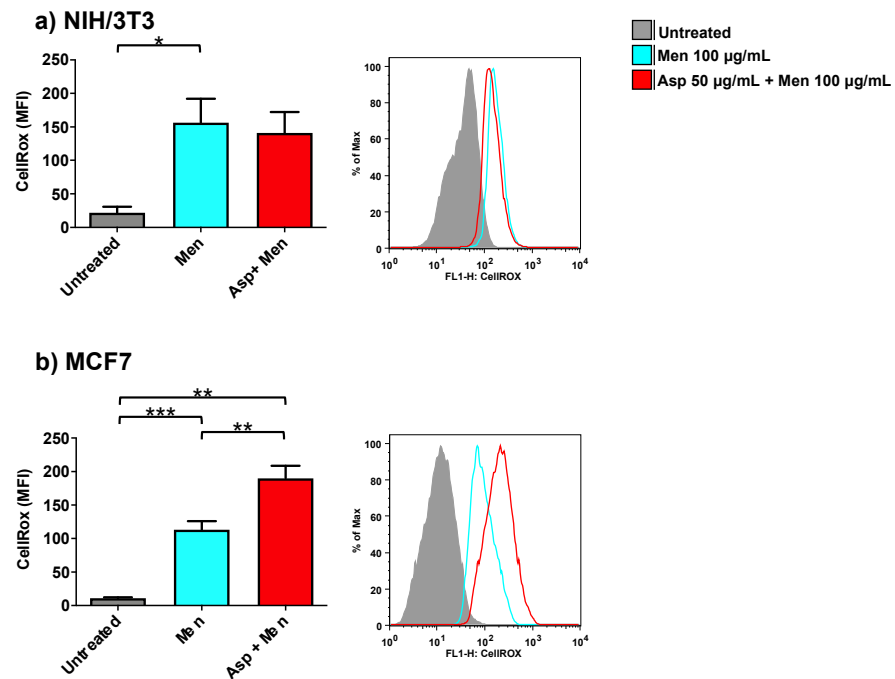


**Figure 5.** NIH-3T3 (a) or MCF7 (b) cells were treated with 0, 50, 100 or 500  $\mu\text{g}/\text{mL}$  of Asp extracts for 48 h and incubated with CellROX Green Reagent to investigate the oxidation level (stress) of the cells. Left panels: MFI data are reported as mean  $\pm$  standard error of results from three independent experiments; right panels: super imposed graphs from flow cytometry dot plots data of a representative experiment. The axes scale for fluorescence is reported as logarithmic. Statistical analyses were performed by ANOVA followed by Bonferroni's post hoc test. \*  $p < 0.05$ .

### 2.5. Asparagus Extracts Increase Oxidant Activity of Menadione in Breast Cancer Cells

In order to investigate the role of Asp extracts on oxidative balance, both normal (NIH/3T3) as well as tumoral cells (MCF7) were exposed to Asp and then triggered with a pro-oxidant concentration of menadione (Figure 6). Asp 50  $\mu\text{g}/\text{mL}$  was chosen as the pre-treatment dose to exclude concomitant effects derived from an alteration in viability or cell cycle modulation.

As expected, cells treated only with Menadione (positive control) showed a significant increase in oxidant production compared to untreated cells ( $p$ -value 0.0425 and  $p$ -value  $\leq 0.0001$  for NIH/3T3 and MCF7, respectively). Interestingly, cells pre-treated with Asp extracts showed an opposite response in normal and cancerous cells when triggered with Menadione. Indeed, in fibroblasts (Figure 6a), Asp did not induce a significant variation with respect to Menadione; however, in MCF7 cells (Figure 6b), a combination of Asp and Menadione significantly enhanced oxidant production compared to cells treated with Menadione alone ( $p$ -value = 0.0038).

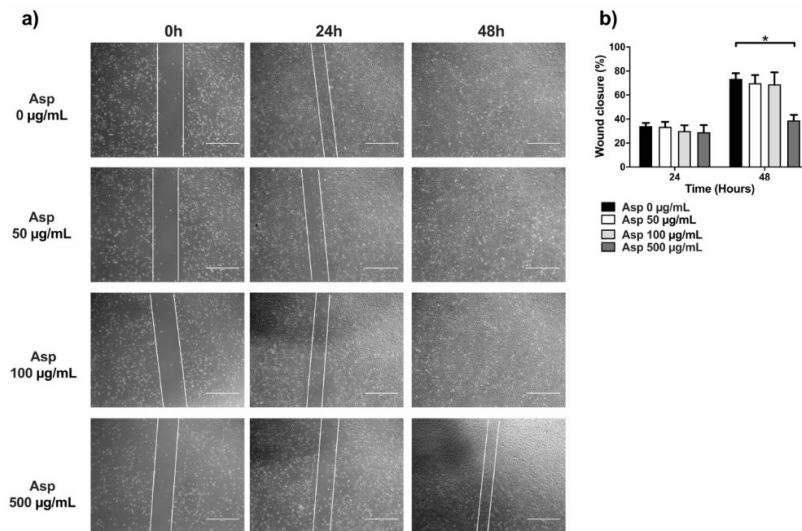


**Figure 6.** NIH/3T3 (a) or MCF7 (b) were treated with 50 µg/mL Asp for 48 h and then triggered with oxidative stimulation performed by Menadione (Men) 100 µM for 30 min. The left panels reported data as mean ± standard error of results from at least three independent experiments. Right panels: representative flow cytometry dot plots. The axes scale for fluorescence is reported as logarithmic. Statistical analysis was performed by ANOVA followed by Bonferroni post hoc test; \*  $p < 0.05$ , \*\*  $p < 0.01$  and \*\*\*  $p < 0.001$ .

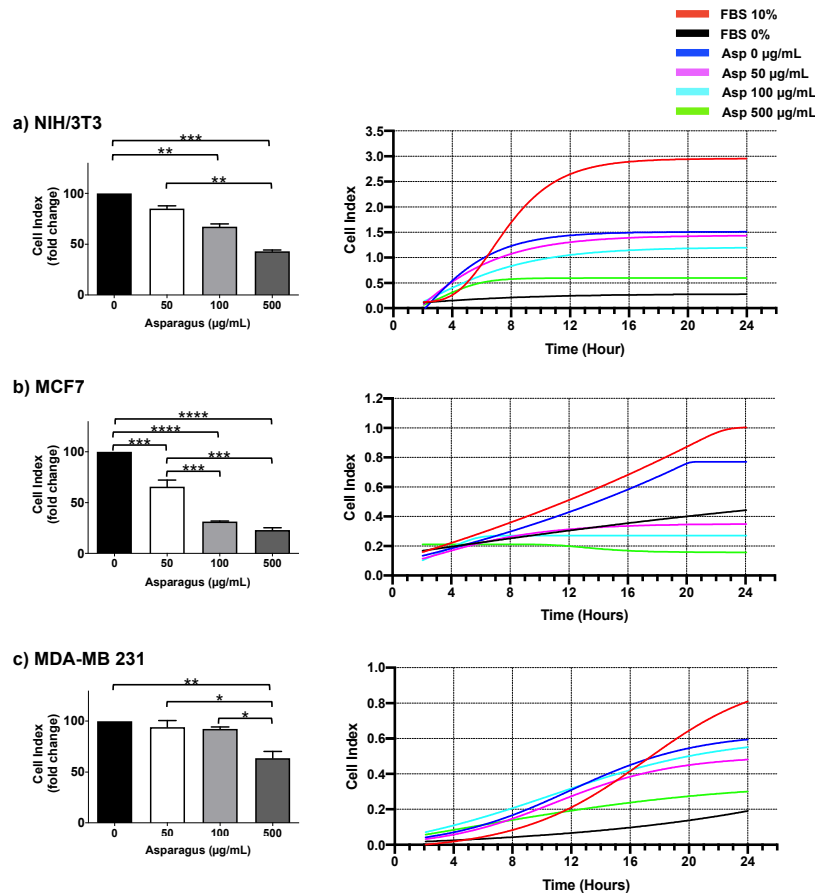
### 2.6. Asparagus Extracts Impair Cell Migration

To complete the characterization of biological activities of Asp on cells, we first assessed effects on migration by using traditional wound repair. A single scratch was manually performed on NIH/3T3 cells grown with a reduced concentration of serum (5% FBS) to lower interference from normal cell replication. Cells were treated with Asp at different doses and pictures were taken at different time points until 48 h of incubation (Figure 7). At 24 h, no significant variation in wound area was found, although a significant reduction in wound closure was observed in fibroblasts treated with 500 µg/mL of Asp compared with untreated cells (Asp 0 µg/mL) after 48 h of treatment ( $p$ -value = 0.0103).

To deeply investigate the role of Asp extracts in cell motility, dynamic high-resolution assessments of migration using the xCELLigence assay were performed on both normal and breast cancer cells. Results showed a significant inhibitory effect on cell migration mediated by Asp extracts, with respect to untreated, in all cell line tested (Figure 8). In detail, a significant reduction in NIH/3T3 cell migration was observed in response to 100 and 500 µg/mL ( $p$ -value 0.0068 and  $\leq 0.0001$ , respectively), confirming data from wound repair. Importantly, MCF7 cell lines showed a significant reduction in migration in a concentration-dependent manner ( $p$ -value  $\leq 0.0001$  for all dosed vs. untreated;  $p$ -value  $\leq 0.001$  for 100 µg/mL and 500 µg/mL vs. 50 µg/mL), reducing the migration of this cell line below the basal threshold (0% FBS). Of note, migration was also significantly impaired in triple-negative MDA-MB231 cells after treatment with Asp 500 µg/mL ( $p$ -value 0.0038 vs. untreated;  $p$ -value 0.0115 vs. Asp 50 µg/mL;  $p$ -value 0.0162 vs. Asp 100 µg/mL).



**Figure 7.** Scratch assay performed on fibroblasts (NIH/3T3). (a) Representative images were taken under light microscopy of fibroblast monolayers untreated or treated with 50, 100, and 500 µg/mL of asparagus (Asp) at 0 h (immediately after scratch were performed), 24 or 48 h. Scale bar 1000 µm. (b) Data from four independent experiments are reported as mean ± standard error. Statistical analyses were performed by ANOVA followed by Bonferroni’s post hoc test. \*  $p < 0.05$ .



**Figure 8.** NIH-3T3 (a), MCF7 (b) and MDA-MB231 (c) cells were seeded in the upper chamber of CIM plate and monitored for migration through the lower chamber in response to different concentrations of Asp (0–500 µg/mL) with the xCELLigence system (DP-RTCA) for 24 h. Positive controls were performed by using medium with 10% FBS in the lower chamber as the chemoattractant, while negative controls were performed by using medium without FBS (0% FBS). In the

left panels, data are expressed as fold change compared to untreated cells of results from three independent experiments and are reported as mean  $\pm$  standard error. Statistical analysis was performed by ANOVA followed by Bonferroni's post hoc test.  $p$ -values  $\leq 0.05$  were considered significant: \*  $p \leq 0.05$ , \*\*  $p \leq 0.005$ , \*\*\*  $p \leq 0.001$  \*\*\*\*  $p \leq 0.0001$ . Right panels show representative graphs from RTCA software reporting overtime cell index.

### 3. Discussion

In recent years, increasing attention has been paid to sustainable recycling of food waste, mainly focusing on recovering bioactive molecules. This might represent a new source for drug production [21], especially for fields such as cancer where drug resistance or side effects still cause treatment interruption or failure. In the present study, we characterized the chemical composition and biological activities of hard stem asparagus aqueous extracts obtained from food industry waste recycling.

The chemical composition analyses revealed the absence of many antioxidants that were frequently found on edible stems of asparagus. However, the presence of isoflavones, flavonols and flavones together with other glycosylated flavonoids might result in an effective pool of molecules with bioactivity on breast cancer cells. In particular, a relevant feature is represented by the presence of two isoflavones (i.e., prunetin and genistein) and one flavone (i.e., apigenin), counting all three together for the 1.7% relative amount in the extracts. It is known that these compounds might exert some antiestrogenic activity on estrogen-receptor- $\alpha$  positive tumor cells, such as MCF7.

Indeed, we demonstrated *in vitro*, on cellular models of breast cancer with different phenotypes, specific anticancer effects, mainly attributable to cell cycle arrest, migration inhibition and oxidant production.

Firstly, we observed a significant reduction in the proliferation rate of the MCF7 breast cancer cell line (expressing HR<sup>+</sup>/HER2<sup>-</sup> phenotype), associated with a significant blockade of the cell cycle and low levels of apoptosis. This evidence is in accordance with other reports demonstrating cell cycle arrest in different cancer cell types following treatment with asparagus extracts [11,12]. However, studies are difficult to compare, since they use different raw materials and different methods for the extraction. We believe that the antiproliferative effect of Asp extracts on these cells might be the final result due to the combined effects of antiestrogenic phytochemicals and other antioxidants, mainly rutin, which is the most abundant flavonoid (i.e., 2.4%). Undoubtedly, the copresence of different components with activities connected to antitumor effects (i.e., anti-inflammatory), together with the antioxidant one (see rutin), might end up with particularly efficacious bioactivity against hormone-sensitive tumor cells. On the contrary, no direct involvement in these types of effects concerns the two organic acids (i.e., malic and quinic acids), which are the most abundant compounds in the extracts (i.e., 49% and 38%, respectively) and they are known to have antibacterial and anticholinesterase properties. Nonetheless, it is possible that malic and quinic acids can contribute somehow to the overall antioxidant property of the extract, as well as kaempferol and the other glycosylated flavonoids. Instead, three phenolic acids, such as caftaric (6.7%), dicaffeoyltartaric (0.5%) and caffeoylquinic (0.3%), can play a supportive role in affecting the tumor cell cycle and its response to other compounds.

Our results also indicated that any significant changes in proliferation, cell cycle and apoptosis were observed in MDA-MB-231 triple-negative cells (representative of a more aggressive phenotype of breast cancer), but not in NIH/3T3 noncancer cells.

Phytochemicals are commonly associated with beneficial effects, mainly for the presence of antioxidant molecules; however, the asparagus extracts used in our study, derived from the portion discarded from the food industry, were characterized by poor antioxidant content. This apparent defect translated into an advantage when we assessed the extracts on MCF7 tumoral cells. Indeed, in this model, we demonstrated a specific significant pro-oxidant activity of the extracts used alone at high dosage and, importantly, their capability at low dosage to enhance the level of ROS production induced by menadione. To explain this last feature, we can assume that the antioxidant molecules,



even if present at low levels in the extracts, might be sufficient to induce redox amplification, cooperating in the ROS production prompted by menadione. This concept is supported by other authors that previously demonstrated an interaction between menadione and antioxidant molecules, resulting in increased oxidative stress in the same model—the MCF7 cells [22]. They reported apoptosis induction by ascorbate/menadione combination treatment, suggesting inhibition of ERK2 induced by H<sub>2</sub>O<sub>2</sub> generated from menadione redox cycling, with specific action on cancer cells. Our results similarly showed a specific cooperative effect on HR<sup>+</sup>/HER2<sup>-</sup> cells (MCF7), while preserving normal control fibroblasts. To further support our theory, it is of interest to cite Bakalova et al., who demonstrated that using menadione/ascorbate in combination with 13 conventional clinically used drugs for leukemia treatment did not induce cytotoxicity in cancer cells, but instead, caused irreversible metabolic changes, increasing sensitivity toward conventional therapy [23]. These observations are particularly important because they lay the foundations for future use of extracts to enhance the effects of clinically used drugs that act on breast cancer cells through the induction of oxidative stress, such as tamoxifen (used for hormonal therapy) or paclitaxel (used for chemotherapy). This aspect deserves further preclinical studies to evaluate its feasibility and effectiveness.

Next, we observed a significant inhibition of concentration-dependent migration of MCF7 cells and, surprisingly, even of the triple negative MDA-MB-231 cells. In particular, for MCF7, which showed a low degree of apoptosis after treatment with ASP, we exclude the role of cell death due to the intrinsic characteristics of the assay that allows seeding of the cells in the upper chamber, while the medium with treatment is placed only in the lower chamber. Inhibition of cell migration on MDA-MB-231 cell models has been described following treatments with traditional anticancer drugs (e.g., cisplatin) [24] and purified molecules (e.g., curcumin) [25]. Interference with cellular migration represents a pivotal effect of the anticancer activity of the extracts, suggesting a possible role in inhibition of the metastatic process. A separate explanation is needed to interpret the data obtained on the migration of NIH/3T3 noncancer cells. In fact, these cells are fibroblasts and, as cells normally present in the connective tissue, in the case of tumors, they become part of the tumor microenvironment. Here, they are known to release substances that promote tumor proliferation [26]. In addition, they are also able to migrate to tumor implantation sites (or metastases) to support their growth through the induction of angiogenesis [27]. Therefore, inhibiting the migration of these cells, even if of the nontumor phenotype, has important implications in preventing the development of a tumor-friendly microenvironment.

This is a preliminary study that will need more investigations to comprehend the molecular mechanisms involved in the observed biological effects, as well as to understand the efficacy of the combined use of Asp extracts with traditional drugs by using preclinical *in vitro* and *in vivo* models. Nonetheless, we believe that our results will open up new opportunities to use natural products, alone or combined with traditional treatment, to improve therapy for BC. In particular, observations reporting the inhibition of proliferation and menadione combined oxidant production in HR<sup>+</sup> cells, as well as migration reduction in both HR<sup>+</sup> and TNBC cells, seem to be particularly relevant for patients who develop drug resistance.

#### 4. Materials and Methods

##### 4.1. Preparation of Asparagus Extracts, Phenolic Content, Total Flavonoids and Antioxidant Activity

Asp hard stem samples employed in this study were from a farm located in the Province of Rovigo (Veneto Region, Italy). They were waste materials from greenhouse cultivation of Asp obtained when harvested spears are sorted and packed for the market.

Aqueous extracts from lyophilized Asp hard stems were obtained by the following procedure, which has already been applied with modifications to other vegetable matrices

[15,28–30]: ultraturrax (T18 model by IKA-Werke, Staufen, Germany) mechanical homogenization of 1 gram (dry matrix) in 25 mL of water (1:25 *w/v*) for 1 min; ultrasound bath (Elmasonic S 30 H, Elma Schmidbauer, Singen, Germany) for 10 min at 37 kHz (80 W effective ultrasonic power); suspension centrifuged at 10,000 g for 10 min (model PK121R, Thermo Fisher Scientific, Waltham, MA, USA). Then, water supernatants were recovered, and the extract was lyophilized.

Phenolic content and antioxidant activity were determined by means of four different parameters: total phenolic compounds (TPC); total flavonoids (TFC); two Trolox equivalent antioxidant capacity (TEAC) assays based on DPPH and ABTS radicals. TPC and TFC are reported as  $\mu\text{g}$  of gallic acid equivalents per mg of dry extract ( $\mu\text{g}_{\text{GAE}}/\text{mg}_{\text{de}}$ ) and they were determined in accordance with Singleton [31] and the aluminum chloride colorimetric method [32,33], respectively. Results for DPPH and ABTS assays were calculated as  $\mu\text{mol}$  of Trolox equivalents per mg of dry extract ( $\mu\text{mol}_{\text{TE}}/\text{mg}_{\text{de}}$ ).

These parameters were also estimated for hard stems (on dry basis) by using an overnight hydroalcoholic extraction (80:20 methanol:water + 0.1% *v/v* of formic acid) [25]. They were similarly expressed as  $\mu\text{g}_{\text{GAE}}/\text{mg}_{\text{dm}}$  and  $\mu\text{mol}_{\text{TE}}/\text{mg}_{\text{dm}}$ , where  $\text{mg}_{\text{dm}}$  means mg of dry matter (i.e., lyophilized ASP byproducts).

#### 4.2. LC-MS/MS Analysis of Asparagus Extracts

##### 4.2.1. Free Amino Acid Profile

Protein content and bioactive peptides in this byproduct matrix have already been investigated by the same authors [14]. Thus, here, we focused more on the determination of free amino acids. They were determined by external calibration method. Liquid chromatographic separation was obtained on a Restek Raptor Polar X column (100 × 2.1 mm) packed with superficially porous particles (diameter 2.7  $\mu\text{m}$ ). The mobile phase was a mixture of water + formic acid 0.1% (*v/v*) (A) and acetonitrile + formic acid 0.1% (*v/v*) (B). Chromatographic runs were conducted under gradient elution conditions (from 25% to 70% of A in 10 min) at a mobile phase flow rate of 150  $\mu\text{L}/\text{min}$ .

MS/MS detection was carried out under MRM mode (multiple reaction monitoring) with the positive ESI mode (see Section 2.2.1 for ion transitions and results).

##### 4.2.2. Organic Acids, Phenolic Acids, Polyphenols and Derivatives

Untargeted LC-MS/MS analysis of phenolics was carried out by means of a 2.1 × 150 mm Symmetry C18 column (Waters, Milford, MA, USA), packed with 3.0 mm fully porous particles, thermostated at 30 °C, under gradient elution conditions. Mobile phases were mixtures of water and formic acid 0.1% (*v/v*), channel A, and acetonitrile and formic acid 0.1% (*v/v*), channel B. The gradient elution was obtained with 5% to 70% channel B in 25 min. MS detection was achieved with a Thermo LTQ XL linear ion trap, equipped with an ESI interface (both positive and negative ionization modes were used).

#### 4.3. Cell Culture and Treatment

Mouse embryo fibroblasts (NIH/3T3) and human breast cancer cell lines MDA-MB-231 (TNBC) and MCF7 (ER<sup>+</sup>, HER2<sup>-</sup>) were purchased from Lonza (Basel, Switzerland) and grown in DMEM (4.5 g/L glucose) containing 10% FBS, 1% pen/strep and L-glut (all from Life Technologies, Monza, Italy). Cells were maintained at 37 °C in a humidified atmosphere with 5% CO<sub>2</sub>. Doubling times of the three cell lines were determined by the calculator available at <http://www.doubling-time.com/compute.php> on 28 September 2021 (Roth V. 2006 Doubling Time Computing; NIH/3T3: 15 ± 1 h; MCF7: 15 ± 2 h; MDA-MB231: 22 ± 2 h). Lyophilized Asp extracts were dissolved in DMEM containing 1% FBS, 1% pen/strep, and L-glut, sterilized by filtration and used for *in vitro* treatment at predetermined concentrations of 50, 100, and 500  $\mu\text{g}/\text{mL}$  for 24 and 48 h on NIH/3T3, MDA-MB231 and MCF7 cells seeded at the density of 25,000 cells/cm<sup>2</sup>. Cells were analyzed for cell shape and growth changes. Phase-contrast images were recorded with

an EVOS digital microscope (Advanced Microscopy Group, Bothell, WA, USA). Recorded images were normalized for brightness with Fiji software [34].

#### 4.4. Assessment of Cell Viability, Cell Cycle Profile and Apoptosis

Twenty-four and 48 hours after treatment with Asp extracts, cell viability was examined by Trypan blue exclusion dye. Cell cycle profiles were analyzed by 5-bromodeoxyuridine (BrdU; Sigma, St Louis, MO, USA) incorporation, as previously described [35]. Briefly, cells after incubation with 50  $\mu$ M BrdU for 1 h at 37 °C were stained with primary mouse anti-BrdU antibody (clone 3D4, BD Bioscience, San José, CA, USA), goat F(ab')<sub>2</sub> anti-mouse IgG (H+L) fluorescein isothiocyanate-conjugated secondary antibody (Beckman Coulter, Brea, CA) and propidium iodide (PI; Sigma, St Louis, MO, USA), and were acquired using an FACS Calibur flow cytometer (BD Bioscience, San José, CA, USA) [36]. Apoptosis was analyzed in flow cytometry by Annexin V-FITC/propidium iodide (PI) staining (Immunotech, Marseille, France), as previously reported [36]. Flow cytometric acquisition was analyzed with the FlowJo software (Tree Star, Ashland, OR, USA).

#### 4.5. Analysis of ROS

Changes in intracellular reactive oxygen species (ROS) levels were determined by cell-permeable CellRox<sup>®</sup> Green Oxidative Stress Reagent (Molecular Probes, Life Technologies) and analyzed using FACS Calibur flow cytometer. CellRox<sup>®</sup> is a nonfluorescent (or very weak fluorescent) dye in a reduced state, which is used for ROS measurement in live cells based on the strong fluorogenic signal developed after oxidation. Briefly, 50,000 NIH/3T3 or MCF7 cells were seeded on 24-well plates and grown for 24 h. The next day, the medium was removed, and cells were treated with 50  $\mu$ g/mL of Asp extracts (diluted in fresh medium) for 48 h or left untreated as a negative control. As a positive ROS control, cells were treated with 100  $\mu$ M Menadione (Sigma-Aldrich, St Louis, MO, USA) for 30 min. Cells were then stained with 2.5  $\mu$ M CellRox<sup>®</sup> reagent for 30 min at 37 °C protected from light.

Cells were harvested by trypsinization, washed with PBS and centrifuged at 125xg for 5 min. In the end, cells were re-suspended in PBS with 0.5  $\mu$ g/mL 7-AAD (BD Bioscience, San José, CA, USA) and analyzed by flow cytometry. Dead cells, positive for 7-AAD staining, were excluded from the analysis. Flow cytometric acquisition was analyzed with the FlowJo software (Tree Star, Ashland, OR, USA).

In some experiments, 100  $\mu$ M menadione was added for 30 min to NIH/3T3 or MCF7 pretreated with 50  $\mu$ M Asp for 48 h and then stained with 2.5  $\mu$ M CellRox<sup>®</sup> reagent for 30 min at 37 °C protected from light. Flow cytometric acquisition was performed as reported above.

#### 4.6. Wound Healing Assay

NIH-3T3 cells were seeded on a 6-well plate (13,000 cell/cm<sup>2</sup>) in DMEM, 5% FBS, 1% sodium pyruvate, 1% pen/step and L-glut and left to grow for 24 h. A linear scratch was performed in the middle of each well using a p200 tip; then, the medium was removed and cells were washed twice with PBS before adding fresh media containing a predetermined concentration of 5% FBS and Asp extracts (0, 50, 100 or 500  $\mu$ g/mL). Phase-contrast images were recorded with an EVOS digital microscope. Four frames for each well were taken following the scratch length at different time points (immediately after the scratch was performed, after 24 and 48 h). For each well, analysis of the scratched area was performed by the Fiji software edge recognition tool and calculated by the following formula:

$$\text{Wound closure (\%)} = \left[ \frac{A_{t_0} - A_{\Delta t}}{A_{t_0}} \right] \times 100$$

where  $A_{t_0}$  is the average of four frames measured immediately after scratching and  $A_{\Delta t}$  is the average of four frames measured after 24 or 48 h after scratching. Wound closure in cells treated with Asp extracts was compared with untreated cells at the same time point.

#### 4.7. Assessment of Cell Migration

Cell migrations were performed using a DP-RTCA xCELLigence real-time cell analyzer (F. Hoffmann-La Roche SA, Basel, Switzerland) which records changes in impedance (reported as Cell Index) over time in a non-invasive system. Migration assay was performed using RTCA DP CIM-Plates 16. Cells were starved for 2 h with DMEM containing 0.2% FBS, 1% pen/strep, and L-glut and then seeded (40,000 cells/well) in the upper chamber in DMEM containing 1% FBS, 1% pen/strep, and L-glut. A 1% FBS concentration was experimentally established to support the length (24 h) of the experiments. Each condition was run in triplicate. Cells were left to equilibrate at RT for 30 min. Migration kinetics were analyzed in the presence of Asp (0, 50, 100, 500  $\mu\text{g/mL}$  in DMEM containing 1% FBS, 1% pen/strep, and L-glut) in the lower chamber and recorded every 15 min for 48 h. The positive control was performed using DMEM containing 10% FBS in the lower chamber as the chemoattractant. Data were analyzed using the RTCA software (F. Hoffmann-La Roche, version 1.2.1, Basel, Switzerland) and expressed as fold change  $\pm$  SEM of CI of migration with respect to untreated cultured set.

#### 4.8. Statistical Analysis

All data, obtained from independent experiments, were tested for normal distribution by the Shapiro–Wilk normality test and for homogeneity of variance by the Brown–Forsythe test. Results were evaluated by one-way ANOVA followed by Bonferroni post hoc test (from multiple corrections) using GraphPad Prism (GraphPad Software, San Diego, CA, USA). Results were expressed as mean  $\pm$  standard error of the mean (SEM) of replicate experiments. Statistical significance was defined as  $p < 0.05$ .

**Supplementary Materials:** The following are available online. Table S1: Values of total phenolic content (TPC), total flavonoid content (TFC) and antioxidant activities (DPPH and ABTS) in hydroalcoholic extract from asparagus hard-stem by-products, Table S2: Quantitative determination of free amino acids in asparagus edible-stem extract, Figure S1: LC-MS/MS ESI negative ion extracted chromatograms of identified compounds listed in Table 3, Figure S2: LC-MS/MS ESI positive ion extracted chromatograms of identified compounds listed in Table 3.

**Author Contributions:** Conceptualization, R.V. and N.M.; methodology and formal analysis, A.R., F.C., C.S., P.T. and A.M.; data curation, A.R., R.V. and N.M.; writing—original draft preparation, A.R. and N.M.; writing—review and editing, R.V.; supervision, R.V., P.S. and N.M.; funding acquisition, R.V., P.S. and N.M. All authors have read and agreed to the published version of the manuscript.

**Funding:** This research was partially funded by the following grants by the University of Ferrara: FIR 2018 “Fondo per l’Incentivazione della Ricerca” to N.M.; FFABR 2017 “Fondo per il finanziamento delle attività base di ricerca” to N.M. and R.V.

**Institutional Review Board Statement:** Not applicable.

**Informed Consent Statement:** Not applicable.

**Conflicts of Interest:** The authors declare no conflict of interest. The funders had no role in the design of the study; in the collection, analyses, or interpretation of data; in the writing of the manuscript, or in the decision to publish the results.

## References

1. Siegel, R.L.; Miller, K.D.; Jemal, A. Cancer Statistics. *CA Cancer J. Clin.* **2019**, *69*, 7–34, doi:10.3322/caac.21551.
2. Tagliaferri, B.; Quaquerini, E.; Palumbo, R.; Balletti, E.; Presti, D.; Malovini, A.; Agozzino, M.; Teragni, C.M.; Terzoni, A.; Bernardo, A.; et al. Role of Androgen Receptor Expression in Early Stage ER+/PgR-/HER2- Breast Cancer. *Ther. Adv. Med. Oncol.* **2020**, *12*, 1758835920958355, doi:10.1177/1758835920958355.

3. Kwapisz, D. Cyclin-Dependent Kinase 4/6 Inhibitors in Breast Cancer: Palbociclib, Ribociclib, and Abemaciclib. *Breast Cancer Res. Treat.* **2017**, *166*, 41–54, doi:10.1007/s10549-017-4385-3.
4. Presti, D.; Qua Quarini, E. The PI3K/AKT/MTOR and CDK4/6 Pathways in Endocrine Resistant HR+/HER2- Metastatic Breast Cancer: Biological Mechanisms and New Treatments. *Cancers* **2019**, *11*, 1242, doi:10.3390/cancers11091242.
5. Almehdar, H.; Abdallah, H.M.; Osman, A.-M.M.; Abdel-Sattar, E.A. In Vitro Cytotoxic Screening of Selected Saudi Medicinal Plants. *J. Nat. Med.* **2012**, *66*, 406–412, doi:10.1007/s11418-011-0589-8.
6. Sethi, G.; Shanmugam, M.; Warriar, S.; Merarchi, M.; Arfuso, F.; Kumar, A.; Bishayee, A. Pro-Apoptotic and Anti-Cancer Properties of Diosgenin: A Comprehensive and Critical Review. *Nutrients* **2018**, *10*, 645, doi:10.3390/nu10050645.
7. Chitrakar, B.; Zhang, M.; Adhikari, B. Asparagus (*Asparagus officinalis*): Processing Effect on Nutritional and Phytochemical Composition of Spear and Hard-Stem Byproducts. *Trends Food Sci. Technol.* **2019**, *93*, 1–11, doi:10.1016/j.tifs.2019.08.020.
8. Adouni, K.; Chahdoura, H.; Mosbah, H.; Santos-Buelga, C.; González-Paramás, A.M.; Ciudad-Mulero, M.; Fernandes, Â.; Calhelha, R.C.; Morales, P.; Flamini, G.; et al. Revalorization of Wild Asparagus Stipularis Forssk. as a Traditional Vegetable with Nutritional and Functional Properties. *Food Funct.* **2018**, *9*, 1578–1586, doi:10.1039/c7fo01687e.
9. Singh, R. *Asparagus racemosus*: A Review on Its Phytochemical and Therapeutic Potential. *Nat. Prod. Res.* **2016**, *30*, 1896–1908, doi:10.1080/14786419.2015.1092148.
10. Rodríguez, R.; Jaramillo, S.; Rodríguez, G.; Espejo, J.A.; Guillén, R.; Fernández-Bolaños, J.; Heredia, A.; Jiménez, A. Antioxidant Activity of Ethanolic Extracts from Several Asparagus Cultivars. *J. Agric. Food Chem.* **2005**, *53*, 5212–5217, doi:10.1021/jf050338i.
11. Zhang, F.; Zhang, Y.-Y.; Sun, Y.-S.; Ma, R.-H.; Thakur, K.; Zhang, J.-G.; Wei, Z.-J. Asparanin A from *Asparagus officinalis* L. Induces G0/G1 Cell Cycle Arrest and Apoptosis in Human Endometrial Carcinoma Ishikawa Cells via Mitochondrial and PI3K/AKT Signaling Pathways. *J. Agric. Food Chem.* **2020**, *68*, 213–224, doi:10.1021/acs.jafc.9b07103.
12. Mfengwana, P.H.; Mashele, S.S.; Manduna, I.T. Cytotoxicity and Cell Cycle Analysis of Asparagus Laricinus Burch. and Senecio Asperulus DC. on Breast and Prostate Cancer Cell Lines. *Heliyon* **2019**, *5*, e01666, doi:10.1016/j.heliyon.2019.e01666.
13. Fuentes-Alventosa, J.M.; Jaramillo-Carmona, S.; Rodríguez-Gutiérrez, G.; Guillén-Bejarano, R.; Jiménez-Araujo, A.; Fernández-Bolaños, J.; Rodríguez-Arcos, R. Preparation of Bioactive Extracts from Asparagus By-Product. *Food Bioprod. Process.* **2013**, *91*, 74–82, doi:10.1016/j.fbp.2012.12.004.
14. Montone, C.M.; Zenezini Chiozzi, R.; Marchetti, N.; Cerrato, A.; Antonelli, M.; Capriotti, A.L.; Cavaliere, C.; Piovesana, S.; Laganà, A. Peptidomic Approach for the Identification of Peptides with Potential Antioxidant and Anti-Hypertensive Effects Derived From Asparagus By-Products. *Molecules* **2019**, *24*, 3627, doi:10.3390/molecules24193627.
15. Bergantin, C.; Maietti, A.; Tedeschi, P.; Font, G.; Manyes, L.; Marchetti, N. HPLC-UV/Vis-APCI-MS/MS Determination of Major Carotenoids and Their Bioaccessibility from “Delica” (*Cucurbita Maxima*) and “Violina” (*Cucurbita Moschata*) Pumpkins as Food Traceability Markers. *Molecules* **2018**, *23*, 2791, doi:10.3390/molecules23112791.
16. Zhao, J.; Zhang, W.; Zhu, X.; Zhao, D.; Wang, K.; Wang, R.; Qu, W. The Aqueous Extract of *Asparagus officinalis* L. by-Product Exerts Hypoglycaemic Activity in Streptozotocin-Induced Diabetic Rats. *J. Sci. Food Agric.* **2011**, *91*, 2095–2099, doi:10.1002/jsfa.4429.
17. Fan, R.; Yuan, F.; Wang, N.; Gao, Y.; Huang, Y. Extraction and Analysis of Antioxidant Compounds from the Residues of *Asparagus officinalis* L. *J. Food Sci. Technol.* **2015**, *52*, 2690–2700, doi:10.1007/s13197-014-1360-4.
18. Rodríguez, R.; Jaramillo, S.; Guillén, R.; Jiménez, A.; Fernández-Bolaños, J.; Heredia, A. Cell Wall Phenolics of White and Green Asparagus. *J. Sci. Food Agric.* **2005**, *85*, 971–978, doi:10.1002/jsfa.2053.
19. Fuentes-Alventosa, J.M.; Jaramillo-Carmona, S.; Rodríguez-Gutiérrez, G.; Rodríguez-Arcos, R.; Fernández-Bolaños, J.; Guillén-Bejarano, R.; Espejo-Calvo, J.A.; Jiménez-Araujo, A. Effect of the Extraction Method on Phytochemical Composition and Antioxidant Activity of High Dietary Fibre Powders Obtained from Asparagus By-Product. *Food Chem.* **2009**, *116*, 484–490, doi:10.1016/j.foodchem.2009.02.074.
20. Fuentes-Alventosa, J.M.; Rodríguez-Gutiérrez, G.; Jaramillo-Carmona, S.; Espejo-Calvo, J.A.; Rodríguez-Arcos, R.; Fernández-Bolaños, J.; Guillén-Bejarano, R.; Jiménez-Araujo, A. Effect of Extraction Method on Chemical Composition and Functional Characteristics of High Dietary Fibre Powders Obtained from Asparagus By-Products. *Food Chem.* **2009**, *2*, 665–671, doi:10.1016/j.foodchem.2008.07.075.
21. Kumar, K.; Yadav, A.N.; Kumar, V.; Vyas, P.; Dhaliwal, H.S. Food Waste: A Potential Bioresource for Extraction of Nutraceuticals and Bioactive Compounds. *Bioresour. Bioprocess.* **2017**, *4*, 18, doi:10.1186/s40643-017-0148-6.
22. Beck, R.; Verrax, J.; Dejeans, N.; Taper, H.; Calderon, P.B. Menadione Reduction by Pharmacological Doses of Ascorbate Induces an Oxidative Stress That Kills Breast Cancer Cells. *Int. J. Toxicol.* **2009**, *28*, 33–42, doi:10.1177/1091581809333139.
23. Bakalova, R.; Semkova, S.; Ivanova, D.; Zhelev, Z.; Miller, T.; Takeshima, T.; Shibata, S.; Lazarova, D.; Aoki, I.; Higashi, T. Selective Targeting of Cancerous Mitochondria and Suppression of Tumor Growth Using Redox-Active Treatment Adjuvant. *Oxid. Med. Cell. Longev.* **2020**, *2020*, e6212935, doi:10.1155/2020/6212935.
24. Yang, M.-D.; Sun, Y.; Zhou, W.-J.; Xie, X.-Z.; Zhou, Q.-M.; Lu, Y.-Y.; Su, S.-B. Resveratrol Enhances Inhibition Effects of Cisplatin on Cell Migration and Invasion and Tumor Growth in Breast Cancer MDA-MB-231 Cell Models In Vivo and In Vitro. *Molecules* **2021**, *26*, 2204, doi:10.3390/molecules26082204.
25. Mukherjee, S.; Mazumdar, M.; Chakraborty, S.; Manna, A.; Saha, S.; Khan, P.; Bhattacharjee, P.; Guha, D.; Adhikary, A.; Mukherjee, S.; et al. Curcumin Inhibits Breast Cancer Stem Cell Migration by Amplifying the E-Cadherin/ $\beta$ -Catenin Negative Feedback Loop. *Stem Cell Res. Ther.* **2014**, *5*, 116, doi:10.1186/scrt506.

26. Shiga, K.; Hara, M.; Nagasaki, T.; Sato, T.; Takahashi, H.; Takeyama, H. Cancer-Associated Fibroblasts: Their Characteristics and Their Roles in Tumor Growth. *Cancers* **2015**, *7*, 2443–2458, doi:10.3390/cancers7040902.
27. Wan, X.; Guan, S.; Hou, Y.; Qin, Y.; Zeng, H.; Yang, L.; Qiao, Y.; Liu, S.; Li, Q.; Jin, T.; et al. FOSL2 Promotes VEGF-Independent Angiogenesis by Transcriptionally Activating Wnt5a in Breast Cancer-Associated Fibroblasts. *Theranostics* **2021**, *11*, 4975–4991, doi:10.7150/thno.55074.
28. Marchetti, N.; Bonetti, G.; Brandolini, V.; Cavazzini, A.; Maietti, A.; Meca, G.; Mañes, J. Stinging Nettle (*Urtica dioica* L.) as a Functional Food Additive in Egg Pasta: Enrichment and Bioaccessibility of Lutein and  $\beta$ -Carotene. *J. Funct. Foods* **2018**, *47*, 547–553, doi:10.1016/j.jff.2018.05.062.
29. Alonso-Garrido, M.; Tedeschi, P.; Maietti, A.; Font, G.; Marchetti, N.; Manyes, L. Mitochondrial Transcriptional Study of the Effect of Aflatoxins, Enniatins and Carotenoids in Vitro in a Blood Brain Barrier Model. *Food Chem. Toxicol.* **2020**, *137*, 111077, doi:10.1016/j.fct.2019.111077.
30. Bergantin, C.; Maietti, A.; Cavazzini, A.; Pasti, L.; Tedeschi, P.; Brandolini, V.; Marchetti, N. Bioaccessibility and HPLC-MS/MS Chemical Characterization of Phenolic Antioxidants in Red Chicory (*Cichorium Intybus*). *J. Funct. Foods* **2017**, *33*, 94–102, doi:10.1016/j.jff.2017.02.037.
31. Singleton, V.L.; Orthofer, R.; Lamuela-Raventós, R.M. Analysis of Total Phenols and Other Oxidation Substrates and Antioxidants by Means of Folin-Ciocalteu Reagent. *Methods Enzymol.* **1999**, *299*, 152–178, doi:10.1016/S0076-6879(99)99017-1.
32. Miliauskas, G.; Venskutonis, R.P.; Beek, T.A. van Screening of Radical Scavenging Activity of Some Medicinal and Aromatic Plant Extracts. *Food Chem.* **2004**, *85*, 231–237, doi:10.1016/j.foodchem.2003.05.007.
33. Chang, C.; Yang, M.; Wen, H.; Chern, J. Estimation of Total Flavonoid Content in Propolis by Two Complementary Colometric Methods. *J. Food Drug Anal.* **2002**, *10*, 178–182, doi:10.38212/2224-6614.2748.
34. Schindelin, J.; Arganda-Carreras, I.; Frise, E.; Kaynig, V.; Longair, M.; Pietzsch, T.; Preibisch, S.; Rueden, C.; Saalfeld, S.; Schmid, B.; et al. Fiji: An Open-Source Platform for Biological-Image Analysis. *Nat. Methods* **2012**, *9*, 676–682, doi:10.1038/nmeth.2019.
35. Trapella, C.; Rizzo, R.; Gallo, S.; Alogna, A.; Bortolotti, D.; Casciano, F.; Zauli, G.; Secchiero, P.; Voltan, R. HelixComplex Snail Mucus Exhibits Pro-Survival, Proliferative and pro-Migration Effects on Mammalian Fibroblasts. *Sci. Rep.* **2018**, *8*, 17665, doi:10.1038/s41598-018-35816-3.
36. Voltan, R.; Rimondi, E.; Melloni, E.; Rigolin, G.M.; Casciano, F.; Arcidiacono, M.V.; Celeghini, C.; Cuneo, A.; Zauli, G.; Secchiero, P. Ibrutinib Synergizes with MDM-2 Inhibitors in Promoting Cytotoxicity in B Chronic Lymphocytic Leukemia. *Oncotarget* **2016**, *7*, 70623–70638, doi:10.18632/oncotarget.12139.

Article

# Anticancer activity of aqueous extract from *Asparagus officinalis* L. by-product on breast cancer cells

Arianna Romani <sup>1,#</sup>, Fabio Casciano <sup>1,2,#</sup>, Claudia Stevanin <sup>3</sup>, Annalisa Maietti <sup>3,4</sup>, Paola Tedeschi <sup>3,4</sup>, Paola Secchiero <sup>1</sup>, Nicola Marchetti <sup>3,4,\*</sup> and Rebecca Voltan <sup>1\*</sup>

<sup>1</sup> Department of Translational Medicine and LTTA Centre, University of Ferrara, 44121 Ferrara, Italy

<sup>2</sup> Interdepartmental Research Center for the Study of Multiple Sclerosis and Inflammatory and Degenerative Diseases of the Nervous System, University of Ferrara, 44121 Ferrara, Italy

<sup>3</sup> Department of Chemistry, Farmaceutical and Agricultural Sciences, University of Ferrara, Italy

<sup>4</sup> Terra&Acqua Tech Lab, Ferrara Technopole, Italy

# Co-first author

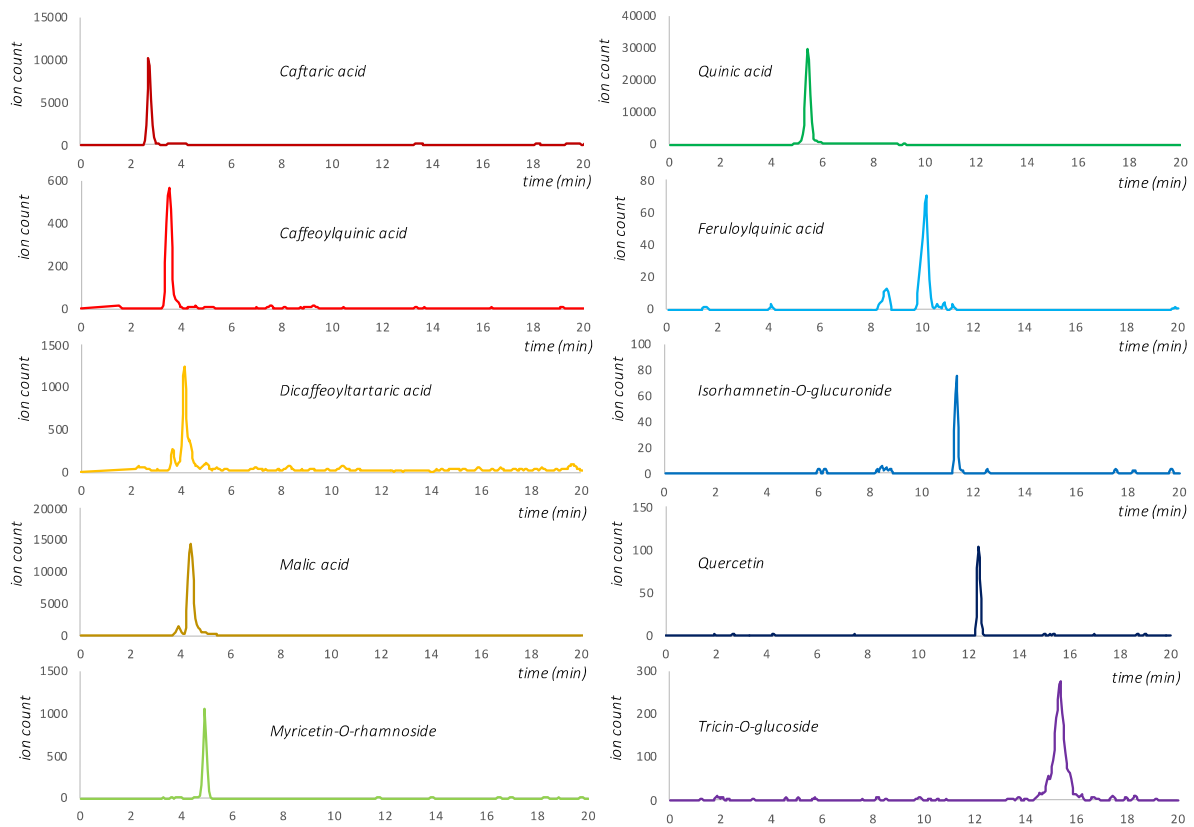
\* Correspondence: nicola.marchetti@unife.it (NM); rebecca.voltan@unife.it (RV)

**Table S1.** Values of total phenolic content (TPC), total flavonoid content (TFC) and antioxidant activities (DPPH and ABTS) in hydroalcoholic extract from asparagus hard-stem by-products. Values are expressed in terms of gallic acid equivalents (GAE) and trolox equivalents (TE) per mg of dry matter (mg<sub>de</sub>).

TPC ( $\mu\text{g}_{\text{GAE}}/\text{mg}_{\text{dm}}$ )	276.1 ± 33.5
TFC ( $\mu\text{g}_{\text{GAE}}/\text{mg}_{\text{dm}}$ )	231.4 ± 18.4
DPPH ( $\mu\text{mol}_{\text{TE}}/\text{mg}_{\text{dm}}$ )	0.271 ± 0.164
ABTS ( $\mu\text{mol}_{\text{TE}}/\text{mg}_{\text{dm}}$ )	0.426 ± 0.032

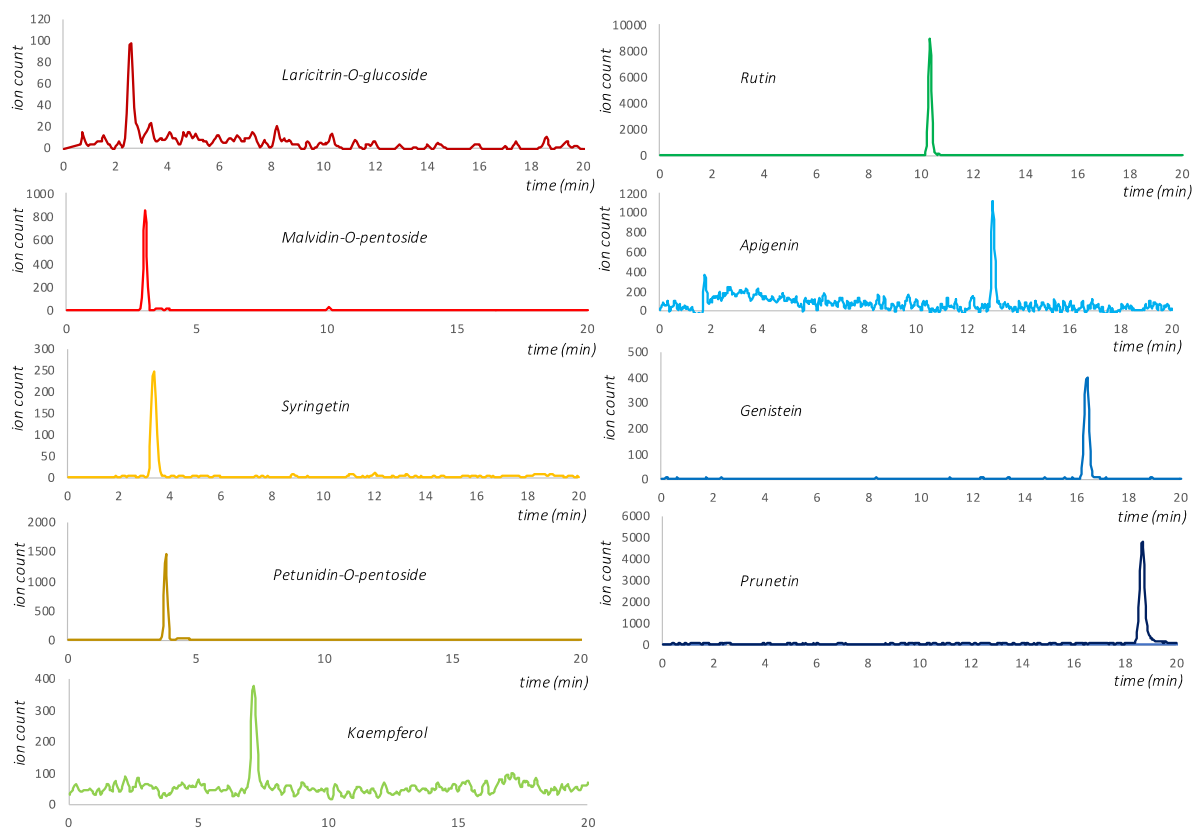
**Table S2.** Quantitative determination of free amino acids in asparagus edible-stem extract.

Amino acid	Concentration ( $\mu\text{g}/\text{mg}_{\text{de}}$ )
ALA	0.016 ± 0.019
ARG	0.234 ± 0.025
ASN	8.02 ± 0.94
ASP	0.379 ± 0.035
GLU	0.754 ± 0.033
HIS	0.135 ± 0.011
LEU+ILE	0.341 ± 0.024
LYS	17.54 ± 1.17
MET	0.211 ± 0.013
PHE	0.135 ± 0.017
PRO	1.463 ± 0.055
SER	1.159 ± 0.048
THR	0.223 ± 0.009
TRP	0.014 ± 0.005
TYR	0.054 ± 0.011
VAL	1.088 ± 0.031



**Figure S1.** LC-MS/MS ESI negative ion extracted chromatograms of identified compounds listed in Table 3.





**Figure S2.** LC-MS/MS ESI positive ion extracted chromatograms of identified compounds listed in Table 3.



## Dottorati di ricerca

Il tuo indirizzo e-mail

stvclld@unife.it

Oggetto:

Dichiarazione di conformità della tesi di Dottorato

Io sottoscritto Dott. (Cognome e Nome)

Stevanin Claudia

Nato a:

Rovigo

Provincia:

Rovigo

Il giorno:

17/09/1992

Avendo frequentato il Dottorato di Ricerca in:

Scienze Chimiche

Ciclo di Dottorato

34

Titolo della tesi:

CHARACTERIZATION OF NANOSTRUCTURED ADSORBENT MATERIALS FOR ENVIRONMENTAL APPLICATIONS

Titolo della tesi (traduzione):

CARATTERIZZAZIONE DI MATERIALI ADSORBENTI NANOSTRUTTURATI PER APPLICAZIONI AMBIENTALI

Tutore: Prof. (Cognome e Nome)

Pasti Luisa

Settore Scientifico Disciplinare (S.S.D.)

CHIM/01

Parole chiave della tesi (max 10):

Materiali nanostrutturati, adsorbimento, zeoliti, membrane matrice mista, fotocatalisi, contaminanti emergenti Nanostructured materials, adsorption, zeolites, mixed matrix membranes, photocatalysis, emerging contaminants

Consapevole, dichiara

CONSAPEVOLE: (1) del fatto che in caso di dichiarazioni mendaci, oltre alle sanzioni previste dal codice penale e dalle Leggi speciali per l'ipotesi di falsità in atti ed uso di atti falsi, decade fin dall'inizio e senza necessità di alcuna formalità dai benefici conseguenti al provvedimento emanato sulla base di tali dichiarazioni; (2) dell'obbligo per l'Università di provvedere al deposito di legge delle tesi di dottorato al

fine di assicurarne la conservazione e la consultabilità da parte di terzi; (3) della procedura adottata dall'Università di Ferrara ove si richiede che la tesi sia consegnata dal dottorando in 2 copie, di cui una in formato cartaceo e una in formato pdf non modificabile su idonei supporti (CD-ROM, DVD) secondo le istruzioni pubblicate sul sito : <http://www.unife.it/studenti/dottorato> alla voce ESAME FINALE – disposizioni e modulistica; (4) del fatto che l'Università, sulla base dei dati forniti, archiverà e renderà consultabile in rete il testo completo della tesi di dottorato di cui alla presente dichiarazione attraverso l'Archivio istituzionale ad accesso aperto "EPRINTS.unife.it" oltre che attraverso i Cataloghi delle Biblioteche Nazionali Centrali di Roma e Firenze. DICHIARO SOTTO LA MIA RESPONSABILITÀ: (1) che la copia della tesi depositata presso l'Università di Ferrara in formato cartaceo è del tutto identica a quella presentata in formato elettronico (CD-ROM, DVD), a quelle da inviare ai Commissari di esame finale e alla copia che produrrà in seduta d'esame finale. Di conseguenza va esclusa qualsiasi responsabilità dell'Ateneo stesso per quanto riguarda eventuali errori, imprecisioni o omissioni nei contenuti della tesi; (2) di prendere atto che la tesi in formato cartaceo è l'unica alla quale farà riferimento l'Università per rilasciare, a mia richiesta, la dichiarazione di conformità di eventuali copie. PER ACCETTAZIONE DI QUANTO SOPRA RIPORTATO

Dichiarazione per embargo

18 mesi

Richiesta motivata embargo

5. Tutela della proprietà intellettuale

Liberatoria consultazione dati Eprints

Consapevole del fatto che attraverso l'Archivio istituzionale ad accesso aperto "EPRINTS.unife.it" saranno comunque accessibili i metadati relativi alla tesi (titolo, autore, abstract, ecc.)

Firma del dottorando

Ferrara, li 09/02/2022 Firma del Dottorando Claudia Stevanin



Firma del Tutore

Visto: Il Tutore Si approva Firma del Tutore Luisa Pasti





# Università degli Studi di Ferrara

UFFICIO DOTTORATI DI RICERCA

AL MAGNIFICO RETTORE  
UNIVERSITÀ DEGLI STUDI DI FERRARA  
UFFICIO DOTTORATO  
Via delle Scienze, n. 41/B – 44121 Ferrara

Richiesta di embargo della tesi di dottorato oltre i 12 mesi (da allegare alla dichiarazione di conformità)			
Nome e cognome del dottorando:	Claudia Stevanin		
Corso di dottorato:	Scienze Chimiche		
Matricola:	108395		
Ciclo:	34		
E-mail per contatti:	stvcl@unife.it		
Anno dell'esame finale:	2022		
Nome e cognome del Tutore:	Luisa Pasti		
<b>Titolo della tesi:</b>			
CHARACTERIZATION OF NANOSTRUCTURED ADSORBENT MATERIALS FOR ENVIRONMENTAL APPLICATIONS			
Periodo di secretazione:	<input checked="" type="checkbox"/> 18 mesi	<input type="checkbox"/> 24 mesi	<input type="checkbox"/> 36 mesi
<b>Motivo dell'embargo:</b>			
Tesi in corso di pubblicazione	<input type="checkbox"/>	Tesi già sottoposte a un editore che non consenta l'accesso aperto prima dell'avvenuta pubblicazione	
Motivi di pubblica sicurezza	<input type="checkbox"/>	Quando la tesi può mettere a rischio la sicurezza pubblica e/o nazionale o per motivi di rispetto della Legge vigente	
Tutela della proprietà intellettuale	<input checked="" type="checkbox"/>	Diritto d'autore, brevetti, copyright etc.	
Tesi previo accordo con terze parti	<input type="checkbox"/>	Lavoro prodotto nell'ambito di un progetto di ricerca per il quale sia stato stipulato un accordo con un ente di ricerca esterno o con un ente finanziatore che preveda la divulgazione della tesi solo dopo il completamento dell'intero progetto di ricerca	
Privacy	<input type="checkbox"/>	Qualora la ricerca verta su una o più persone per cui si tema di violare il diritto alla riservatezza	
<b>Descrizione dettagliata della richiesta di secretazione:</b>			
<i>Indicare in modo esaustivo le ragioni per cui si chiede l'embargo, citando gli estremi di eventuali accordi editoriali, contratti commerciali, progetti di ricerca etc. per cui sia richiesta la non accessibilità temporanea ai contenuti del lavoro</i> <b>La richiesta di embargo per più di 12 mesi è dovuta alla presenza all'interno della tesi di risultati non ancora pubblicati che possono essere oggetto di brevetto.</b>			
Data:	09/02/2022		
Firma del dottorando:			
Firma del Tutore:			
Come previsto dal Regolamento in materia di Dottorato di Ricerca dell'Università di Ferrara, che stabilisce l'obbligo di deposito delle tesi di Dottorato nell'archivio istituzionale d'Ateneo ad accesso aperto, la presente istanza dovrà essere sottoposta all'eventuale approvazione da parte del Consiglio di "IUSS Ferrara 1391"			